



ШЕСТНАДЦАТЫЙ
МОСКОВСКИЙ
МЕЖДУНАРОДНЫЙ
СИМПОЗИУМ
ПО ИССЛЕДОВАНИЯМ
СОЛНЕЧНОЙ СИСТЕМЫ

20-24 ОКТЯБРЯ 2023

ИНСТИТУТ
КОСМИЧЕСКИХ
ИССЛЕДОВАНИЙ
МОСКВА

THE SIXTEENTH
MOSCOW
SOLAR SYSTEM
SYMPOSIUM

20-24 OCTOBER 2023

SPACE RESEARCH
INSTITUTE
MOSCOW

20 OCTOBER:
SESSION MARS

21 OCTOBER:
SESSION MOON AND MERCURY

22 OCTOBER:
SESSION VENUS

23 OCTOBER:
SESSION SMALL BODIES
(INCLUDING COSMIC DUST)

24 OCTOBER:
SESSION EXTRASOLAR PLANETS
SESSION GIANT PLANETS
SESSION ASTROBIOLOGY

ШЕСТНАДЦАТЫЙ МОСКОВСКИЙ СИМПОЗИУМ ПО ИССЛЕДОВАНИЯМ СОЛНЕЧНОЙ СИСТЕМЫ 16M-S³

**октябрь 20-24, 2025
ИНСТИТУТ КОСМИЧЕСКИХ ИССЛЕДОВАНИЙ
РОССИЙСКОЙ АКАДЕМИИ НАУК
МОСКВА, РОССИЯ**

THE SIXTEENTH MOSCOW SOLAR SYSTEM SYMPOSIUM 16M-S³

**october 20-24, 2025
SPACE RESEARCH INSTITUTE
OF RUSSIAN ACADEMY OF SCIENCES
MOSCOW, RUSSIA**

спонсоры:

- Институт космических исследований РАН
- Институт геохимии и аналитической химии им. Вернадского РАН
- Брауновский университет (США)

sponsored by:

- Space Research Institute RAS
- Vernadsky Institute of Geochemistry and Analytical Chemistry RAS
- Brown University, USA

ISBN: 978-5-00015-071-9

DOI: 10.21046/16MS3-2025

© Федеральное Государственное Бюджетное Учреждение Науки
ИНСТИТУТ КОСМИЧЕСКИХ ИССЛЕДОВАНИЙ РОССИЙСКОЙ АКАДЕМИИ НАУК (ИКИ РАН)
2025

TABLE OF CONTENT

INTRODUCTION

PROGRAM COMMITTEE

PROGRAM

overview PROGRAM

scientific PROGRAM

ABSTRACTS

INFORMATION

ADDRESS

METRO MAP

REGISTRATION AND INFORMATION DESK

ORAL SESSIONS, location

POSTER SESSIONS, location

INTERNET ACCESS AND WiFi

SOCIAL PROGRAM

LUNCH POINTS

THE SIXTEENTH MOSCOW SOLAR SYSTEM SYMPOSIUM 16M-S³

**SPACE RESEARCH INSTITUTE
MOSCOW, RUSSIA
october 20–24, 2025**

Starting from 2010, the Space Research Institute holds annual international symposia on Solar system exploration. Main topics of these symposia include wide range of problems related to formation and evolution of Solar system, planetary systems of other stars; exploration of Solar system planets, their moons, small bodies; interplanetary environment, astrobiology problems. Experimental planetary studies, science instruments and preparation for space missions are also considered at these symposia.

The Sixteenth Moscow international Solar System Symposium (16M-S³) will be held from October 20 till 24, 2025

THE FOLLOWING SESSIONS WILL BE HELD DURING THE SYMPOSIUM:

OPENING SESSION

- Session. MARS
- Session. MOON AND MERCURY
- Session. VENUS
- Session. SMALL BODIES (INCLUDING COSMIC DUST)
- Session. EXTRASOLAR PLANETS
- Session. GIANT PLANETS
- Session. ASTROBIOLOGY

Space Research Institute holds this symposium with participation of the following organizations:

- Vernadsky Institute of Geochemistry and Analytical Chemistry RAS, Russia
- Brown University, USA
- Schmidt Institute of Physics of the Earth RAS, Russia
- Keldysh Institute of Applied Mathematics RAS, Russia
- Kotelnikov Institute of Radio-engineering and Electronics RAS, Russia
- Sternberg Astronomical institute, Moscow State University, Russia

Symposium website: <https://ms2025.cosmos.ru>

Contact email address: ms2025@cosmos.ru

PROGRAM COMMITTEE

chair:

acad. **ZELNYI L.M.** IKI RAS

members:

BAZILEVSKIY A.T. GEOHI RAS

BIBRING J.-P. IAS, CNRS, France

BOROVIN G.K. Keldysh AMI RAS

HEAD III J. Brown University, USA

JHEETA S. NoRCEL, United Kingdom

KORABLEV O.I. IKI RAS

KOSTITSYN Y.A. GEOHI RAS

KOTSYURBENKO O.R. Yugra State University

MITROFANOV I.G. IKI RAS

RODIN A.V. IKI RAS

SHEVCHENKO V.V. GAISH MSU

SMIRNOV V.M. IRE RAS

TAVROV A.V. IKI RAS

VAISBERG O.L. IKI RAS

ZAKHAROV A.V. IKI RAS

ZASOVA L.V. IKI RAS

secretary:

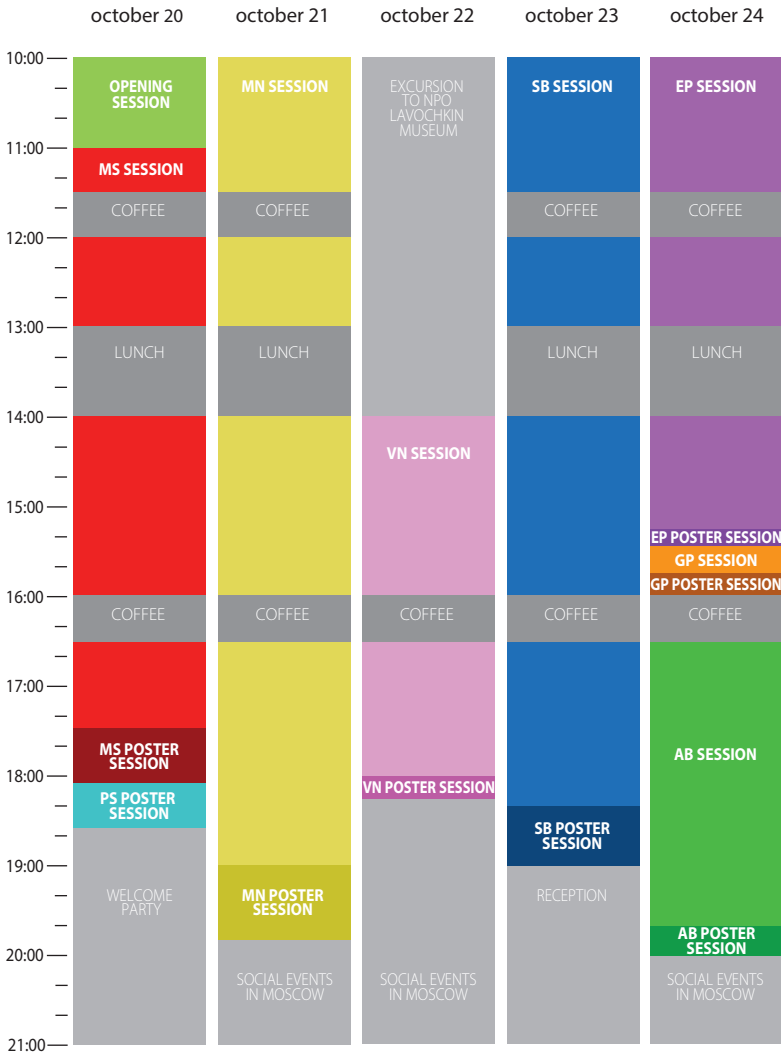
ROSTE O.Z. IKI RAS

PROGRAM

overview 16M-S³ program

THE SIXTEENTH MOSCOW SOLAR SYSTEM SYMPOSIUM

Space Research Institute, 20–24 October 2025



- **MS SESSION:** MARS SESSION
- **MN SESSION:** MOON AND MERCURY SESSION
- **VN SESSION:** VENUS SESSION
- **SB SESSION:** SMALL BODIES (INCLUDING COSMIC DUST) SESSION
- **EP SESSION:** EXTRASOLAR PLANETS SESSION
- **GP SESSION:** GIANT PLANETS SESSION
- **AB SESSION:** ASTROBIOLOGY SESSION
- **PS POSTER SESSION:** POSTER SESSION FOR ALL SESSIONS

16M-S³ SCIENTIFIC PROGRAM

MONDAY, 20 OCTOBER 2025

10.00–11.00

OPENING SESSION

Lev ZELENYI

Opening Remarks

Ji WU

Discovering the Sky at the Longest wavelength (DSL)
(Plenary Report)

11.00–18.05

MARS SESSION

Convener: **Oleg KORABLEV**
conference hall, second floor

11.00–11.15 **Anna FEDOROVA et al** Long-term observations of aerosol vertical distribution on Mars by SPICAM IR on Mars-Express 16MS3-MS-01

11.15–11.30 **Alexander TROKHIMOVSKIY and Oleg KORABLEV** The ACAE spectrometers for Tianwen-3 Mars mission 16MS3-MS-02

11.30–12.00

COFFEE-BREAK

12.00–12.15 **Mikhail LUGININ et al** Evidence of bimodality in Martian water ice clouds from the ACS/TGO solar occultation observations 16MS3-MS-03

12.15–12.30 **Mariya ZHARIKOVA et al** Comparison of the MAOAM water vapor modeling results with ExoMars ACS data 16MS3-MS-04

12.30–12.45 **Ekaterina STARICHENKO et al** The vertical damping of gravity waves in the Martian atmosphere from the ACS/TGO solar occultation experiment 16MS3-MS-05

12.45–13.00 **Artem ALIAKIN et al** The influence of infrared transparency windows in the Martian atmosphere on the greenhouse effect 16MS3-MS-06

13.00–14.00

LUNCH

14.00–14.15 **Andrey KIRILLOV** Electronic kinetics of carbon monoxide in the upper atmospheres of Mars and planets of Solar System 16MS3-MS-07

14.15–14.30 **Jordanka SEMKOVA et al** Dose rate and particle flux of cosmic rays in the free space at 1.5 AU during different phases of solar activity according measurements by Liulin-MO dosimeter on Trace Gas Orbiter 16MS3-MS-08

14.30–14.45 **Paparin AMLONGKUL et al** Comparing MEREM radiation environment simulations with observations in Mars orbit 16MS3-MS-09

14.45–15.00	Thanayuth ANYALERT et al	Simulation-Based Study of RAAN Effects on Jovian Magnetic Connectivity: Application to the TW-3 MARCH Payload	16MS3-MS-10
15.00–15.15	Alexey IVANYUKHIN and A.P. PLOKHIKH	Improvement of radio communication performance via an accompanying relay spacecraft for round-trip missions to Mars	16MS3-MS-11
15.15–15.30	Olga POPOVA et al	Cluster analysis of recently formed Martian crater fields	16MS3-MS-12
15.30–15.45	Elena PODOBNAYA et al	Distribution of crater sizes in recently formed Martian crater fields	16MS3-MS-13
15.45–16.00	Boris IVANOV	New craters on Mars – 2024–2025 catalog expansion	16MS3-MS-14
16.00–16.30	COFFEE-BREAK		
16.30–16.45	Georg SKREBEC	Polycyclic nature of Martian outflow channel activity: chronostratigraphic constraints	16MS3-MS-15
16.45–17.00	Jun CHU et al	Impact-induced hydrothermal clay formation on Mars – geometrical evidence in Holden crater	16MS3-MS-16
17.00–17.15	Alexander LOMAKIN et al	Some miscellaneous findings in the SPICAM-IR nadir dataset	16MS3-MS-17
17.15–17.30	Egor KULIK and Tamara GUDKOVA	Effect on the Chandler Wobble period of Mars by mantle mineralogy and temperature profile	16MS3-MS-18
17.30–18.05	POSTER SESSION, SESSION MARS		
	7 posters * 5 min		
	Alexey BATOV and Tamara GUDKOVA	Non-hydrostatic stresses in the interiors of Mars excluding long-wave component	16MS3-MS-PS-01
	Vladimir CHEPTSOV et al	Perchlorate radiolysis under simulated Martian conditions	16MS3-MS-PS-02
	Ekaterina FABER	Deep Learning for Hyperspectral Unmixing of CRISM Data: Application to Mineral Mapping on Mars	16MS3-MS-PS-03
	Polina SAZONOVA et al	Effect of sodium perchlorate on soil prokaryotic complexes under limited available moisture conditions	16MS3-MS-PS-04
	Alexander LOMAKIN et al	Co-located SPICAM-IR and OMEGA observations of Martian polar caps	16MS3-MS-PS-05

Dariia KOSSOVA et al	Structure of the upper Martian atmosphere from the homopause to the CO ₂ exobase as observed by ACS/TGO	16MS3-MS-PS-06
Vladimir OGIBALOV	Radiative transfer in the NIR bands of CO ₂ and CO molecules under breakdown of vibrational LTE in the daytime Martian atmosphere. Effect of radiation absorption by aerosols on vibrational state populations	16MS3-MS-PS-07

18.05–18.35

POSTER SESSION, FOR ALL SESSIONS

18.35–19.30

WELCOME PARTY

10.00–19.50

2 MOON AND MERCURY SESSION

Conveners: **Igor MITROFANOV, Maxim LITVAK**
conference hall, second floor

10.00–10.20	Alexander KOZYREV et al	MGNS: the first data on Mercury's gamma-ray radiation	16MS3-MN-01
10.20–10.40	Victor GUBAREV et al	Galactic cosmic rays in the vicinity of Mercury	16MS3-MN-02
10.40–11.00	Alexander LAVRUKHIN et al	Determination of the Mercury's internal dipole parameters using MESSENGER spacecraft data	16MS3-MN-03
11.00–11.20	Alexey BEREZHNOY et al	About the origin of high-speed Ca atoms in the Hermean exosphere	16MS3-MN-04
11.20–11.40	Lianghai XIE and Lei LI	Monte Carlo simulation of the global migration of lunar hydroxyl from a magnetic-shielded solar wind source	16MS3-MN-05

11.40–12.00 COFFEE-BREAK

12.00–12.20	Alexander BASILEVSKY et al	Surface morphology of partially shadowed floors of three near-pole lunar craters	16MS3-MN-06
12.20–12.40	Svetlana DEMIDOVA et al	Metal-sulfide mineralization of Chang'E-5 soil sample	16MS3-MN-07
12.40–13.00	Alexander KRASILNIKOV and Mikhail IVANOV	Determination of the mixing factor of local and foreign material in the Langrenus and Cavalerius craters ejecta	16MS3-MN-08

13.00–14.00 LUNCH

14.00–14.20	Lev ZELENYI et al	The lunar segment of the Federal Space science project	16MS3-MN-09
14.20–14.40	Anatoly PETRUKOVICH et al	Lunar exploration from polar orbit: Luna-26	16MS3-MN-10
14.40–15.00	Igor MITROFANOV et al	Science at the lunar poles: Luna-27.1 and Luna-27.2	16MS3-MN-11
15.00–15.20	Mikhail SACHKOV et al	Toward multiwavelength distributed astronomical observations from the Moon	16MS3-MN-12
15.20–15.40	SenthilKumar MEGALA	Salient Science outcome from Chandrayaan-3 Mission	16MS3-MN-13
15.40–16.00	Huijuan WANG et al	Preliminary considerations on the AI requirements in lunar-based astronomical observations at ILRS	16MS3-MN-14

16.00–16.20 COFFEE-BREAK

16.20–16.40	Habibullo ABDUSSAMATOV	Permanent protection system of the astronaut spacesuit, optical surfaces and all other equipment against charged particles of lunar dust	16MS3-MN-15
16.40–17.00	Alexander GUSEV and J.G. MENG	Geophysical exploration of the Moon XI: 3D pits and caves	16MS3-MN-16
17.00–17.20	Artem LYSENKO et al	Experimental study of the dependence of the compressive strength of samples of the lunar regolith simulant on the parameters of selective laser melting	16MS3-MN-17
17.20–17.40	Ivan AGAPKIN et al	Preliminary Results on the Application of Selective Microwave Sintering for Lunar Soil Analogue VI-LH1	16MS3-MN-18
17.20–18.00	Olga TURCHINSKAYA et al	Comparative analysis of potential sites for lunar base deployment in the Northern Polar region	16MS3-MN-19
18.00–18.20	Sergey VOROPAEV et al	Remote sensing of lunar surface: the search for isotopic forms of water	16MS3-MN-20
18.20–18.40	Alexey ANDREEV and Yury NEFEDYEV	Development of a selenocentric dynamic reference system based on data from modern lunar missions and the application of regression modeling methods	16MS3-MN-21
18.40–19.00	Li DENG et al	Lunar orbit satellite formation: Distributed low frequency interferometric imaging spectrometer	16MS3-MN-22

19.00–19.50

POSTER SESSION, SESSION MOON AND MERCURY

16 posters * 3 min

Lidiia LAKHMANOVA et al	Basaltic clasts population in the lunar meteorite Dhofar 280	16MS3-MN-PS-01
Pradiphat MUANGHA et al	Conceptual Design and Performance Simulation of a Dual-Particle Albedo Detector for Chang'e-8 Mission in the Lunar South Polar Region	16MS3-MN-PS-02
Ricardo Tomás FERREYRA and Michael SHPEKIN	The underground propagation of new conical shock waves generated by the falling impactors on planets	16MS3-MN-PS-03
Michael SHPEKIN and Ricardo Tomás FERREYRA	The problem of propagation and some properties of shock waves generated by the falling impactors on the Solar System planets	16MS3-MN-PS-04

Michael SHPEKIN and A.D. GABDULKHAKOV	Aposterior analysis of the orbital motion of the Apollo 17 spacecraft in near-lunar space	16MS3-MN-PS-05
Bintang ALAM SEMESTA WISLAN	The Technical Feasibility of Dust Tracking & Characterization Technology for Lunar Base Settlement	16MS3-MN-PS-06
Ekaterina FEOKTISTOVA and M.P. SHCHERBINA	Mons Muton on the Moon	16MS3-MN-PS-07
Ekaterina GRISHAKINA	Analysis of lunar craters larger than 10 km formed in the Moon's first billion years	16MS3-MN-PS-08
Egor SOROKIN et al	Chemical composition of metallic iron spherules in the lunar soil of Chang'e-5	16MS3-MN-PS-09
Andrey MITUSOV and Vladislav KHRISANOV	Breaking the Shadows: New Targets on Shackleton Crater Floor, lunar South Pole	16MS3-MN-PS-10
Sergei IPATOV	Exchange of ejected material between the Moon and the terrestrial planets	16MS3-MN-PS-11
Vasily MARCHUK and O. YUSHKOVA	Preliminary algorithm for data processing of the radar complex RLK-L	16MS3-MN-PS-12
Alexander KOSOV et al	Ground Station for Radio Science Experiment with Ka-band Receiver (PKD) onboard of Luna-26 orbiter	16MS3-MN-PS-13
Mikhail MALENKOV et al	Unloading, transporting and assembling lunar station modules on the lunar surface: design development of the mobile robotics concept	16MS3-MN-PS-14
Marina KUZMICHEVA	Magnetic field anomalies of Bosumtwi and Zhamanshin craters on the Earth: analysis based on numerical simulations	16MS3-MN-PS-15
Alexey IVANYUKHIN and V. IVASHKIN	Fast Free-Return Trajectories in the Earth-Moon System	16MS3-MN-PS-16

08.00–14.00

EXCURSION TO NPO LAVOCHKIN MUSEUM

14.00–18.15

3

VENUS SESSION

Conveners: **Ludmila ZASOVA, Dmitry GORINOV**
conference hall, second floor

14.00–14.20	Lev ZELENYI et al	The Venera-D mission for a comprehensive study of Venus	16MS3-VN-01
14.20–14.40	Mikhail IVANOV and James HEAD	The history of the long-wavelength topography on Venus	16MS3-VN-02
14.40–15.00	Justin FILIBERTO et al	Assessing the evidence for active volcanism on Venus: current limitations and prospects for future investigations	16MS3-VN-03
15.00–15.20	Sriram BHIRAVARASU et al	Venus surface studies using VSAR onboard ISRO's Venus Orbiter mission	16MS3-VN-04
15.20–15.40	Danil MALYSHEV et al	Clustering of Volcanoes and Coroneae on Venus Based on Neural Network Processing	16MS3-VN-05
15.40–16.00	Ivan BORONIN and Tamara GUDKOVA	Modeling the Internal Structure of Venus Using the Monte Carlo Method	16MS3-VN-06

16.00–16.20

COFFEE-BREAK

16.20–16.40	Daria EVDOKIMOVA et al	Venus lower atmosphere and surface from SPICAV-IR/VEx observations in NIR transparency windows at 0.8–1.3 μm	16MS3-VN-07
16.40–17.00	Denis BELYAEV et al	VIRAL experiment for ISRO's Venus Orbiter Mission: scientific concept	16MS3-VN-08
17.00–17.20	Joshita SHARMA	Long Duration Payload Bay for Venus Exploration	16MS3-VN-09
17.20–17.40	Nikolay TKACHEV et al	Simulation Modeling Application for the Design Analysis of the Operation of a Venus Exploration Aerobot	16MS3-VN-10
17.40–18.00	Vladislav ZUBKO et al	The Venus-asteroid resonance transfers for expanding the planetary exploration framework	16MS3-VN-11

18.00–18.15

POSTER SESSION, SESSION VENUS

5 posters * 3 min

Elizaveta STEPANOVA et al	Thermal structure of the upper atmosphere of Venus from occultation experiments	16MS3-VN-PS-01
----------------------------------	---	----------------

Evgeniya GUSEVA and Mikhail IVANOV	Volcanic features of concentration regions of large volcanoes and coronae, Venus	16MS3-VN-PS-02
Arina SHIMOLINA et al	1:500,000 scale mapping and analysis of radiating, circumferential and linear dyke swarm patterns of Beta Regio, Venus	16MS3-VN-PS-03
Tamara GUDKOVA and A.V. BATOV	Non-hydrostatic stresses beneath Atla Regio and Beta Regio on Venus	16MS3-VN-PS-04
Vladimir OGIBALOV et al	The effect of the contour shape of spectral lines on the emission in the 4.3 μm band of CO_2 molecules outgoing from the planetary atmosphere in the presence of macroscopic wind velocity gradient	16MS3-VN-PS-05

10.00–19.00

4

SMALL BODIES SESSION
including cosmic dustConveners: **Alexander BASILEVSKY, Alexander ZAKHAROV**
conference hall, second floor

10.00–10.15	Sergey KRASILNIKOV et al	Water Ice Exposure on the Surface of Comet 67P/Churyumov-Gerasimenko	16MS3-SB-01
10.15–10.30	Gleb KUCHEROV et al	Possibility of liquid water formation in icy bodies due to the process of rapid recombination of accumulated radicals	16MS3-SB-02
10.30–10.45	Anatoliy PAVLOV et al	Outbursts of icy bodies in Kuiper Belt and beyond, as possible new source of dust to explain New Horizons observations	16MS3-SB-03
10.45–11.00	Vacheslav EMEL'YANENKO	Distant trans-Neptunian objects produced by perturbations of migrating outer planets and massive planetesimals	16MS3-SB-04
11.00–11.15	Alina MERKULOVA et al	Cometary outbursts in the Early Solar System	16MS3-SB-05
11.15–11.30	Sergey POPEL et al	Dusty plasma formation near 67P/Churyumov-Gerasimenko comet: importance of albedo	16MS3-SB-06

11.30–12.00

COFFEE-BREAK

12.00–12.15	Maria KIRSANOVA and Ya.N. PAVLYUCHENKO	Pre-perihelion observations and interpretation of CH ₃ OH, CO and HCN line emission in the Oort cloud comet C/2017 K2 (PANSTARRS)	16MS3-SB-07
12.15–12.30	Alexey DROZDOV and N.V. EMEL'YANOV	Calculation of the Pluto surface composition map based on the LEISA infrared spectrum of the New Horizons spacecraft	16MS3-SB-08
12.30–12.45	Nikolai KISELEV et al	Comparison of polarization phase dependence of NEA 2100 Ra-Shalom with the dependencies for others low-albedo NEAs	16MS3-SB-09
12.45–13.00	Nuraddin ADIGOZALOV and Vladislav SIDORENKO	Asteroids of the Hungaria family and the Earth's co-orbital population	16MS3-SB-10

13.00–14.00

LUNCH

14.00–14.15	Maxim PUPKOV et al	Designing halo orbits passing through the trajectories of near-Earth asteroids	16MS3-SB-11
-------------	---------------------------	--	-------------

14.15–14.30	Alexander SUKHANOV	On the Possibility of Flybys of a Large Number of Main Belt Asteroids	16MS3-SB-12
14.30–14.45	Tatyana GALUSHINA et al	About the influence of non-gravitation perturbations on the motion of asteroids approaching Jupiter	16MS3-SB-13
14.45–15.00	Olga CHERNENKO et al	Selection of near-Earth asteroids and initial trajectory design for transfer to Earth-resonant orbit	16MS3-SB-14
15.00–15.15	Eduard KUZNETSOV et al	Scenarios for the formation of the young Emilkovalski asteroid family	16MS3-SB-15
15.15–15.30	Maksim KHOVRICHEV et al	izMeteors: meteor event detection network and database	16MS3-SB-16
15.30–15.45	Stanislav KUZNETSOV and Vladimir BUSAREV	Modeling the dynamics of dust particles in the gravitational and electrostatic fields of a primitive asteroid taking into account the sublimation of water ice	16MS3-SB-17
15.45–16.00	Anna KARTASHOVA and G. KOKHIROVA	Meteor observations from Russia and Tajikistan stations	16MS3-SB-18
16.00–16.20	COFFEE-BREAK		
16.20–16.35	Yuriy CHETVERIKOV et al	Cosmic dust collection near Vostok station in Central Antarctica: Research problems and prospects	16MS3-SB-19
16.35–16.50	Nikolay BORISOV	Peculiarities of dynamics of charged dust grains ejected from the surfaces of Phobos and Deimos	16MS3-SB-20
16.50–17.05	Evgeniya PETROVA and V.I. GROKHOVSKY	Meteorite fusion crust as a result of the impact of ablation processes on the meteoroid substance	16MS3-SB-21
17.05–17.20	Mohamad ABDELAAL et al	Investigation of Electromagnetic Processes in Planetary Atmospheres	16MS3-SB-22
17.20–17.35	Yulia SOROKOLETOVA et al	Operation of a spacecraft with a parabolic solar sail for space debris removal	16MS3-SB-23
17.35–17.50	Steven WIJAYA et al	Application of Artificial Neural Network to Identify Orbital Resonances in the Motion of Artificial Earth Satellites	16MS3-SB-24
17.50–18.05	Sergei IPATOV	Migration of bodies ejected from Mercury and Venus	16MS3-SB-25

18.05–18.20	Maxim NYRTSOV et al	Coordinate system transformations in extraterrestrial cartography	16MS3-SB-26
-------------	----------------------------	---	-------------

18.20–19.00

**POSTER SESSION,
SESSION SMALL BODIES (INCLUDING COSMIC DUST)**

11 posters * 3 min

Anna KUZOVCHIKOVA et al	Pyrrhotite and ilmenite as supplements for lunar regolith simulants improving the conditions of microwave breakdown and the formation of plasma-dust clouds	16MS3-SB-PS-01
Yangyang TIAN et al	Algorithm for image segmentation of particle tracks in the dusty plasma near the surface of atmosphereless bodies	16MS3-SB-PS-02
Vladimir EFREMOV et al	Estimating of the meteor parameters	16MS3-SB-PS-03
Tatiana MOROZOVA and Sergey POPEL	Lower-hybrid drift waves in plasma of meteoroid tails in the Earth's ionosphere	16MS3-SB-PS-04
Yuri MEDVEDEV and S.R. PAVLOV	Systematic Biases in Positional Observations of Interstellar Comet 31/ATLAS	16MS3-SB-PS-05
Andrey DUBINSKY et al	On Anomalous Dissipation in Dusty Plasmas in the Vicinity of Comet Nuclei and Active Asteroids	16MS3-SB-PS-06
Sergey KOPNIN et al	Dust particles above the surface of Enceladus	16MS3-SB-PS-07
Yulia IZVEKOVA et al	Solitons and periodic nonlinear dust acoustic waves near the satellites of Mars	16MS3-SB-PS-08
Yulia IZVEKOVA et al	Nonlinear dust acoustic waves in Saturn's magnetosphere	16MS3-SB-PS-09
Nikolay PEROV and O.A. KIRSHINA	Search for ordered trajectories of dust particles in the Sun and Mars system	16MS3-SB-PS-10
Maria SERGIENKO et al	Dynamic evolution of Near-Earth asteroids associated with the α -Capricornids meteoroid stream	16MS3-SB-PS-11

19.00–21.00

RECEPTION

10.00–15.25

5 EXTRASOLAR PLANETS SESSION

Convener: **Alexander TAVROV**
conference hall, second floor

10.00–10.15	Marina RUMENSKIKH et al	Interpretation of absorption of hot exoplanets during the transit of helium tails	16MS3-EP-01
10.15–10.25	Marina RUMENSKIKH et al	Experiment on the modeling transit absorptions of hot exoplanets	16MS3-EP-02
10.25–10.40	Ildar SHAIKHISLAMOV et al	Complex plane numerical modeling of hot exoplanet atmospheres and interpretation of multi-line transit observations	16MS3-EP-03
10.40–10.50	Anton KROTOV and Elena BELENKAYA	Comparison of the magnetosphere of Osiris in the paraboloid and MHD models	16MS3-EP-04
10.50–11.05	Grigory TSURIKOV et al	Search for habitable worlds: potentially observable biomarkers to probe in the atmospheres of exoplanets	16MS3-EP-05
11.05–11.20	Grigory TSURIKOV et al	Planetary magnetic field as a property of weakening the precipitating electrons flux into the Earth's atmosphere	16MS3-EP-06
11.20–11.30	Alexander TAVROV et al	Techniques for exoplanet direct imaging, updated analysis and the proposal for a high contrast imaging instrument onboard the WSO-UV 1.7 meter telescope	16MS3-EP-07
11.30–11.40	Oleg YAKOVLEV et al	Multicolor Photometric Validation of the Exoplanet Candidate around SOI-3	16MS3-EP-08
11.40–12.00	COFFEE-BREAK		
12.00–12.10	Anastasiia IVANOVA et al	Validation of exoplanet candidates using spectroscopic observations from BTA-6	16MS3-EP-09
12.10–12.20	Vladislava ANANYEVA and Alexander TAVROV	Mass distribution of giant planets in transit discovered by the TESS mission	16MS3-EP-10
12.20–12.30	Lomara MAKSIMOVA et al	Approach of the Orion Sword Complex (NGC 1977) to Stars with Planetary Systems (TOI-2796)	16MS3-EP-11
12.30–12.45	Grigory MOROZOV and Elena BELENKAYA	Characteristics of exoplanets depending on the spectral class of the parent star	16MS3-EP-12

12.45–13.00	Elza BUSLAEVA and Elena BELENKAYA	The Influence of Stellar Metallicity on Planet Formation	16MS3-EP-13
13.00–14.00	LUNCH		
14.00–14.15	Piero D'INCECCO et al	Venus and Earth as laboratories for understanding terrestrial exoplanets: surface spectral signatures, planetary synergies, and the AVENGERS initiative	16MS3-EP-14
14.15–14.30	Olga OLEJNIK and V.V. EMEL'YANENKO	Migration of Earth-like planets in planetesimal disks causing the formation of debris disks	16MS3-EP-15
14.30–14.45	Gleb MALYGIN et al	Ultra-cool brown dwarfs with and without circum-substellar plasma disks: possible consequences	16MS3-EP-16
14.45–15.00	Eduard KUZNETSOV and Alexander PERMINOV	Stability and dynamics of the compact planetary system Kepler-51	16MS3-EP-17
15.00–15.15	Roman EVDOKIMOV and Valery SHEMATOVICH	The Influence of Water Content in the Cores of Mini-Neptunes on the Rate of Primary Atmosphere's Core-Powered Mass-Loss	16MS3-EP-18

15.15–15.25

POSTER SESSION, SESSION EXTRASOLAR PLANETS

2 posters * 5 min

Evdokiia SAVINTSEVA et al	Numerical modeling of the hot Saturn atmosphere Hat-P-18b	16MS3-EP-PS-01
Valery KOTOV	Motion of superfast exoplanets and Solar system	16MS3-EP-PS-02

15.25–15.55

6

GIANT PLANETS SESSION

Convener: **Valery SHEMATOVICH**
conference hall, second floor

15.25–15.45	Alexander PERMINOV and Eduard KUZNETSOV	The semi-analytical motion theory of major planets of the Solar system	16MS3-GP-01
-------------	--	--	-------------

15.45–15.55

POSTER SESSION, SESSION GIANT PLANETS

2 posters * 5 min

Sergey SALAMAKHIN and A.M. KARIMOV	Features of methane and ammonia absorption along the central meridian of Jupiter and in the Great Red Spot in 2023	16MS3-GP-PS-01
Anastasiia IVANOVA et al	Spatial variations of Jovian tropospheric ammonia obtained from SAO RAS observations	16MS3-GP-PS-02

16.00–16.20

COFFEE-BREAK

16.20–20.00

7 ASTROBIOLOGY SESSION

Convener: **Oleg KOTSYURBENKO**
conference hall, second floor

16.20–16.40	Vladimir KOMPANICHENKO	Stimulation of the origin-of-life process by high-frequency oscillations in hydrothermal medium:suggested experiments	16MS3-AB-01
16.40–17.00	Sohan JHEETA	From Prebiotic Earth to Astroscience Empowerment: The NoRCEL Institute's Educational Journey Across the Global South	16MS3-AB-02
17.00–17.20	Oleg KOTSYURBENKO	Astroecology as a new scientific direction within astrobiology	16MS3-AB-03
17.20–17.40	Anton VASYUNIN et al	Theoretical and experimental studies of interstellar ices	16MS3-AB-04
17.40–18.00	Varvara KARTEYEVA et al	Nitrous oxide in interstellar ice	16MS3-AB-05
18.00–18.20	Ruslan NAKIBOV et al	Methane environment in interstellar ice	16MS3-AB-06
18.20–18.40	Roman EVDOKIMOV and Valery SHEMATOVICH	On the formation and stability of residual hydrogen-helium atmospheres of mini-Neptunes depending on possible atmospheric loss processes	16MS3-AB-07
18.40–19.00	Ivan KOZLOV et al	Effect of two-year exposure in Low Earth Orbit conditions on the prokaryotic community of grey forest soil	16MS3-AB-08
19.00–19.20	Maxim ZAITSEV et al	Abiotic synthesis of organic compounds in plasma-dust clouds initiated by microwave discharge in the mineral simulant of lunar regolith	16MS3-AB-09
19.20–19.40	Tatiana MOROZOVA	Alternative life forms under extreme conditions	16MS3-AB-10

19.40–20.00

POSTER SESSION, SESSION ASTROBIOLOGY

4 posters * 5 min

Vladimir CHEPTSOV et al	Effect of perchlorate on bacteria radioresistance under simulated Martian conditions	16MS3-AB-PS-01
Valeria BADYA et al	Remote sensing of Earth's ecosystems	16MS3-AB-PS-02
Polina BESOGONOVA et al	Closed artificial ecosystems in space exploration	16MS3-AB-PS-03
Alexander TERTYSHNIKOV	Maxima of strong meteor showers in blood markers	16MS3-AB-PS-04

ABSTRACTS

SESSION 1. MARS (MS)
ORAL SESSION

LONG-TERM OBSERVATIONS OF AEROSOL VERTICAL DISTRIBUTION ON MARS BY SPICAM IR ON MARS-EXPRESS

A. A. Fedorova¹, M. Luginin¹, F. Montmessin², O. I. Korablev¹, J.-L. Bertaux², A. Stcherbinine³, A. Määttänen², F. Lefèvre²

¹ Space Research Institute RAS, Moscow, Russia, fedorova@cosmos.ru

² LATMOS/CNRS, Université Paris-Saclay, Sorbonne Université Guyancourt, France

³ Institut de Recherche en Astrophysique et Planétologie, Centre National d'Études Spatiales, Toulouse, France

KEYWORDS:

Mars, atmospheres, solar occultations, spectroscopy, dust, clouds

INTRODUCTION:

The atmospheric aerosols are an important component of Mars' atmosphere. The climate on Mars is constantly and globally regulated by the presence of suspended particles, which consist of mineral dust and icy condensates such as water and carbon dioxide ice. These aerosols interact with solar and planetary radiation, influencing the atmospheric dynamics [1, 2]. Therefore, comprehending the characteristics of aerosols and their seasonal and spatial distribution is essential for climate modeling. Furthermore, measurements of gaseous concentrations through remote sensing are highly sensitive to the aerosol concentration and vertical distribution in the atmosphere.

The infrared channel of the SPICAM spectrometer onboard the Mars-Express mission provides the continuous monitoring of aerosols in the Martian atmosphere since 2005 by solar occultation method [3, 4]. We present a multi-year survey of these measurements from Martian year (MY) 28 to 36 to study the seasonal and spatial variation of vertical distribution of extinctions, particle size and density for dust and water ice in the atmosphere. The dataset covers nine Martian years and includes more than 2000 retrieved profiles. Within the SPICAM spectral range, we cannot distinguish between absorption due to dust or water ice. We employ an algorithm to separate the two types of aerosols based aerosol measurements of the MCS (Mars Climate Sounder) on MRO (Mars Reconnaissance Orbiter) [5], SPICAM water vapor observations [6] and predictions of general circulation model [7].

RESULTS:

The extinction profiles demonstrate prominent seasonal variations with 80 km elevation in the perihelion season and 40 km in the aphelion season. There is a strong seasonal variation of extinction altitude in the Southern hemisphere while this variation is much weaker in the Northern hemisphere. The effective radius of dust was found to range from 0.3 to 1 μm , and the number density varies from <0.1 to 10 cm^{-3} with a slight seasonal dependence. The effective radius of water ice was found to vary between 0.1 and 3 μm , with a number density varying between 0.1 and 100 cm^{-3} . Compared to water, the particle distribution of dust is on average closer to uniform with altitude, which may be explained by the specific dust/ice selection. High-altitude mesospheric clouds were observed at 70–90 km during the global and regional dust events, such as GDS of MY28 and 34 and regional dust storm C. The Southern and Northern hood clouds were characterized by an optical depth >0.1 , small particle sizes varying from 0.2 to 1.2 μm in radius and a high number density $>5 \text{ cm}^{-3}$. The mass mixing ratio of both water ice and dust by SPICAM is consistent with MCS and MCD values, except for the days close to perihelion and the C storm, which are underestimated by the model. The algorithm was validated against simultaneous aerosol measurements from ACS/TGO to demonstrate a good selective performance for dust and ice clouds.

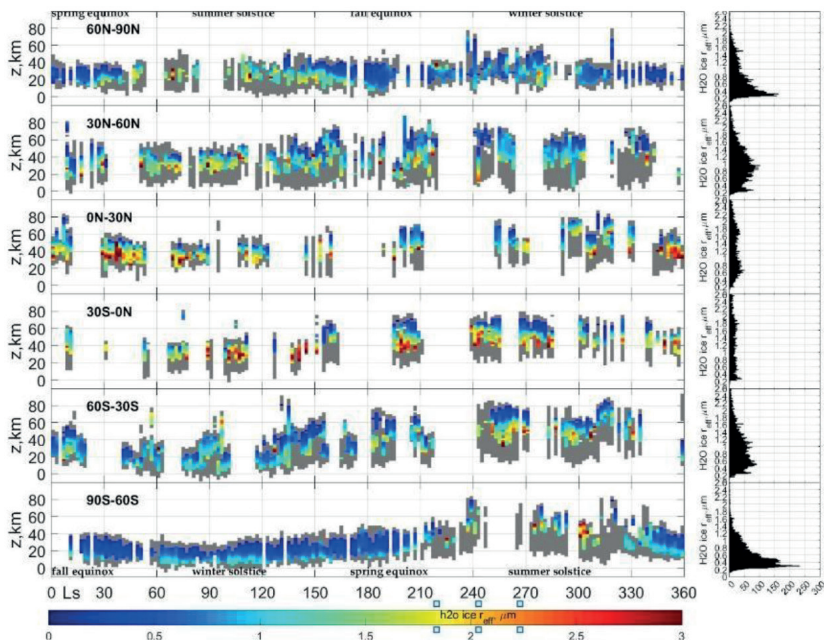


Figure 1. The distribution of water ice effective radius with altitude as a function of L_s for 6 latitude bins from the Northern to Southern hemisphere. The altitudes and L_s have been arranged into $2\text{ km} \times 2^\circ$ bins. The dataset for the GDS of MY28 and 34 were excluded. The y-axis shows the altitude above the areoid.

ACKNOWLEDGMENTS:

We acknowledge Russian Science Foundation grant No.23-12-00207 (<https://rscf.ru/project/23-12-00207/>).

REFERENCES:

- [1] Kahre M. A., Murphy J. R., Newman C. E. et al. The Mars Dust Cycle // The Atmosphere and Climate of Mars / eds. Haberle R.M. et al. Cambridge University Press, 2017. P. 295–337.
- [2] Clancy R. T., Montmessin F., Benson J. et al. Mars Clouds. // The Atmosphere and Climate of Mars / eds. Haberle R.M. et al. Cambridge University Press, 2017. P. 76–105.
- [3] Korablev O., Bertaux J.-L., Fedorova A. et al. SPICAM IR acousto-optic spectrometer experiment on Mars Express // J. Geophysical Research: Planets. 2006. V. 111. Iss. 9. Article E09S03. DOI: 10.1029/2006JE002696.
- [4] Fedorova A.A., Korablev O.I., Bertaux J.-L. et al. Solar infrared occultations by the SPICAM experiment on Mars Express: Simultaneous observations of H_2O , CO_2 and aerosol vertical distribution // Icarus. 2009. V. 200. Iss. 1. P. 96–117. DOI: 10.1016/j.icarus.2008.11.006.
- [5] Kleinböhl A., Kass D. M., Schreier M. et al. Far infrared radiative properties of Mars atmospheric aerosols and their application to Mars Climate Sounder retrievals of aerosol profiles, aerosol columns and surface temperatures // Icarus. 2024. V. 419. Article 116000. <https://doi.org/10.1016/j.icarus.2024.116000>.
- [6] Fedorova A., Montmessin F., Korablev O. et al. Multi-annual monitoring of the water vapor vertical distribution on Mars by SPICAM on Mars Express // J. Geophysical Research: Planets. 2021. V. 126. Iss. 1. Article e2020JE006616. <https://doi.org/10.1029/2020JE006616>.
- [7] Millour E., Forget F., Spiga A. et al. The Mars Climate Database (Version 6.1) // Europlanet Science Congress. V. 16. EPSC2022-786. 2022. <https://doi.org/10.5194/epsc2022-786>.

THE ACAE SPECTROMETERS FOR TIANWEN-3 MARS MISSION

A. Trokhimovskiy, O. Korablev

Space Research Institute RAS, Moscow, Russia, trokh@cosmos.ru

KEYWORDS:

Mars, atmosphere, spectrometer

ABSTRACTS

ACAE (Atmospheric Climate and Escape) is a joint proposal of the Space Research Institute (IKI), Tsinghua University and Sun Yat-sen University. Among them, IKI serves as the responsible institution on the Russian side, while Tsinghua University is the lead institution on the Chinese side, with Sun Yat-sen University participating as a supporting Chinese institution. The ACAE project proposes advanced infrared (IR) and ultraviolet (UV) spectrometers, which are planned to be mounted on the orbiter module of the Chinese Tianwen-3 Mars mission. These instruments are intended for studying the composition and dynamics of the Martian atmosphere. It continues the legacy of missions like Mars Express and ExoMars, focusing on CO₂, water vapor, ozone, dust, and upper atmosphere escape processes. The instrument features an enhanced IR channel (adapted from ACS-NIR Exomars TGO, with a flight heritage and flight hardware available) to be supplied by IKI and a UV spectrometer newly developed under supervision of Tsinghua University. The mass of the units will be 3.2 kg for the IR, 1.8 kg for the UV, all combined in a unified structure having joint mechanical, thermal, electrical, etc. interfaces with the spacecraft. The instrument will have two optical ports. The main port is to observe the Mars atmosphere in nearly-nadir direction by registering the reflected solar light. The solar port serves to profile the atmosphere in solar occultations by pointing to the sun and registering the direct solar light, which passed through the atmosphere. Combining different observations, ACAE enables comprehensive atmospheric studies through high-resolution mapping and vertical structure analysis.

EVIDENCE OF BIMODALITY IN MARTIAN WATER ICE CLOUDS FROM THE ACS/TGO SOLAR OCCULTATION OBSERVATIONS

M. Luginin, N. Ignatiev, A. Fedorova, A. Trokhimovskiy, O. Korablev
Space Research Institute RAS, Moscow, Russia, mikhail.luginin@cosmos.ru

KEYWORDS:

infrared observations, atmosphere of Mars, solar occultation, water ice, clouds

ABSTRACT:

Water ice clouds significantly impact the water cycle by modifying the global transport of water vapor [1], influencing the Martian climate through radiative effects [2], and altering dust distribution by scavenging dust aerosol particles during ice condensation [3]. Further observations of vertical distribution and microphysical properties of water ice aerosols in the Martian atmosphere are needed for a better understanding and modeling of Martian climate and water cycle.

The ExoMars Trace Gas Orbiter (TGO) is a collaborative mission between ESA and Roscosmos aimed at exploring Mars, which commenced its scientific observations in April 2018. The Atmospheric Chemistry Suite (ACS) consists of three infrared spectrometers: Near Infrared (NIR), Mid-Infrared (MIR), and Thermal Infrared (TIRVIM). In this work, we have analyzed 910 solar occultation observations from the TIRVIM instrument, collected between April 28, 2018 and December 2, 2019. Out of these, 826 observations were measured jointly with NIR profiles.

TIRVIM is a Fourier-transform spectrometer covering 1.7–17 μm spectral range. Aerosol properties from TIRVIM solar occultation data were retrieved from 20 wavelengths in the spectral range of 2–6 μm (1700–5000 cm^{-1}), chosen outside of strong-gas-absorption bands.

NIR is an echelle spectrometer covering spectral range 0.7–1.7 μm , with selection of diffraction orders performed by an acousto-optical tunable filter. For the aerosol retrieval, diffraction orders centered at 0.76, 0.86, 0.99, 1.38, and follows 1.57 μm were used.

The scheme for retrieval of aerosol extinction and obtaining aerosol microphysical properties mostly follows [5]. Firstly, aerosol extinction coefficient is retrieved using the standard ‘onion peeling’ method. Next, particle size distribution is determined by fitting spectral dependence of experimental normalized aerosol extinctions to their corresponding theoretical values. The aerosol extinction is modeled according to Mie theory. Composition of aerosols is *a priori* unknown, therefore we use four competing models in our fitting procedure: an unimodal distribution consisting of either dust or water ice, or simultaneous presence of water ice and dust (water ice) modes, forming a bimodal distribution. We assume that each mode is characterized by a lognormal distribution. The model with the lowest χ^2 is considered the best. Finally, aerosol number density is calculated as a ratio of experimental extinction coefficient to modeled extinction cross section. In this work, we will present results of observations of bimodal water ice particle size distribution in Martian clouds from the ACS solar occultation in the period from April 2018 to December 2019.

ACKNOWLEDGMENTS:

This work has been funded by grant No. 23-12-00207 of the Russian Science Foundation (<https://rscf.ru/project/23-12-00207/>).

REFERENCES:

- [1] *Richardson M.I., Wilson R.J.* Investigation of the nature and stability of the Martian seasonal water cycle with a general circulation model // *J. Geophysical Research*. 2002. V. 107. Iss. E5. Article 5031. P. 7-1–7-28. <https://doi.org/10.1029/2001JE001536>.

- [2] *Madeleine J.-B., Forget F., Spiga A. et al.* Aphelion water-ice cloud mapping and property retrieval using the OMEGA imaging spectrometer onboard Mars Express // *J. Geophysical Research*. 2012. V. 117. Iss. E11. <https://doi.org/10.1029/2011JE003940>.
- [3] *Navarro T., Forget F., Millour E., Greybush S.J.* Detection of detached dust layers in the Martian atmosphere from their thermal signature using assimilation // *Geophysical Research Letters*. 2014. V. 41. Iss. 19. P. 6620–6626. <https://doi.org/10.1002/2014GL061377>.
- [4] *Korablev o., Montmessin F., Trokhimovskiy A. et al.* The Atmospheric Chemistry Suite (ACS) of Three Spectrometers for the ExoMars 2016 Trace Gas Orbiter // *Space Science Reviews*. 2018. V. 214. No. 1. Article 7. <https://doi.org/10.1007/s11214-017-0437-6>.
- [5] *Luginin M., Fedorova A., Ignatiev N. et al.* Properties of Water Ice and Dust Particles in the Atmosphere of Mars During the 2018 Global Dust Storm as Inferred From the Atmospheric Chemistry Suite // *J. Geophysical Research*. 2020. V. 125. Iss. 11. Article e2020JE006419. 22 p. <https://doi.org/10.1029/2020JE006419>.

COMPARISON OF THE MAOAM WATER VAPOR MODELING RESULTS WITH EXOMARS ACS DATA

M. S. Zharikova¹, A. S. Medvedev², A. A. Fedorova¹,
D. S. Shaposhnikov¹, D. A. Belyaev¹, M. S. Luginin¹

¹ Space Research Institute RAS, Moscow, Russia
mariyazharikova96@yandex.ru

² Max Planck Institute for Solar System Research, Göttingen, Germany

KEYWORDS:

atmosphere, Mars, model, water vapor, dust

INTRODUCTION:

The water cycle is one of the key climatic processes in the Martian atmosphere. Despite the low water content —approximately 10 precipitable microns — water transport into the upper atmosphere plays a crucial role in Mars' long-term water loss. Therefore, it is of significant interest for scientific investigation.

MAOAM:

The MAOAM model is based on the terrestrial KMCM model with a spectral dynamical core. To solve the advection equation for minor constituents, it employs a second-order semi-Lagrangian explicit monotonic hybrid scheme [1]. The model's hydrological module includes water vapor and ice microphysics, heterogeneous nucleation, sedimentation, photodissociation, water transport processes, and interaction with the surface.

ACS:

The Atmospheric Chemistry Suite (ACS) is an instrument aboard the ExoMars Trace Gas Orbiter (TGO), which has been orbiting Mars since October 2016. It comprises three infrared spectrometers: near-infrared (NIR), mid-infrared (MIR), and thermal infrared (TIRVIM) [2]. In this study we use data from the NIR and MIR channels.

We plan to present updated comparisons between MAOAM water vapor simulations and ACS data, as well as discuss the impact of dust on the modeling of water vapor distribution and temperature.

REFERENCES:

- [1] *Shaposhnikov D. S., Medvedev A. S., Rodin A. V., Hartogh P.* Seasonal water "pump" in the atmosphere of Mars: Vertical transport to the thermosphere // *Geophysical Research Letters*. 2019. V. 46. Iss. 8. P. 4161–4169. <https://doi.org/10.1029/2019GL082839>.
- [2] *Korablev O., Vandaele A. C., Montmessin F. et al.* The Atmospheric Chemistry Suite (ACS) of three spectrometers for the ExoMars 2016 Trace Gas Orbiter // *Space Science Reviews*. 2018. V. 214. P. 1–41. DOI: 10.1007/s11214-017-0437-6.

THE VERTICAL DAMPING OF GRAVITY WAVES IN THE MARTIAN ATMOSPHERE FROM THE ACS/TGO SOLAR OCCULTATION EXPERIMENT

E. D. Starichenko¹, D. A. Belyaev¹, A. S. Medvedev², A. A. Fedorova¹, O. I. Korablev¹, F. Montmessin³, A. Trokhimovskiy¹

¹ Space Research Institute RAS, Moscow, Russia
starichenko.ed@phystech.edu

² Max Planck Institute for Solar System Research, Göttingen, Germany

³ LATMOS/IPSL, UVSQ Université Paris-Saclay, UPMC Univ., CNRS
Guyancourt, France

KEYWORDS:

gravity waves, Martian atmosphere, Trace Gas Orbiter, Atmospheric Chemistry Suite, solar occultation

INTRODUCTION:

Gravity waves (GWs) are omnipresent in planetary atmospheres and originate from displacements of air parcels. They are generated in the lower and denser atmosphere and propagate to the upper and thinner atmosphere growing in their amplitude. Along the way GWs are reduced by various processes and redistribute their energy and momentum to the surrounding atmosphere, affecting the atmospheric dynamics and climatology of the planet. In this work, we study some of the mechanisms of GWs' damping the Martian atmosphere. We use data from solar occultation experiments conducted by the infrared spectrometers of Atmospheric Chemistry Suite (ACS) [1] on board the Trace Gas Orbiter (TGO).

OBSERVATIONS:

ACS is a part of the TGO, which represents the ESA-Roscosmos ExoMars 2016 collaborative mission. The instrument consists of three infrared channels [1]: near-IR (NIR, 0.73–1.6 μm), middle-IR (MIR, 2.3–4.2 μm) and thermal-IR (TIRVIM, 1.7–17 μm). In this work, we use the data obtained from the MIR and NIR instruments, operating in solar occultation mode since April 2018. ACS-MIR is a cross-dispersion echelle spectrometer that allows for retrieving temperature and density vertical profiles in the strong 2.7 μm CO₂ absorption band covering the broad altitude range of 20–180 km [2, 3]. ACS-NIR, an echelle spectrometer combined with an acousto-optic tunable filter, measures the atmospheric structure in the 1.57 μm CO₂ band at altitudes from 10 to 100 km [4, 5]. Both ACS channels possess a high resolving power, exceeding $\sim 25\,000$, signal to noise ratio more than 1000, and sound the atmosphere with the vertical resolution of 0.5–2.5 km. During simultaneous occultations, the instruments lines of sight target identical tangent points that provide confidential cross validation between the retrieved atmospheric profiles. Presently, we report the observations for 3.0–3.5 Martian years (MY), from the middle of MY34 (April 2018) to the end of MY37 (October 2024), counting ~ 1100 occultations of MIR and ~ 12300 occultations of NIR.

RESULTS:

For the analysis of GWs' damping, we use such characteristic of GWs as amplitude of relative temperature perturbations $|T - \bar{T}| / \bar{T}$, where T is a vertical temperature profile and \bar{T} — mean temperature profile. Additionally we use such parameters as vertical flux of horizontal momentum (per unit mass) F , Brunt-Väisälä frequency, which characterizes the stability of GWs propagation. In order to derive these parameters of GWs, we use the method described in (Starichenko et al., 2021, 2024) [6, 7].

Figure 1 depicts the seasonal data coverage along the seasonal distributions of relative temperature disturbances and momentum fluxes. GW activity is more intense in the winter seasons. The magnitudes of F in the middle atmosphere are larger and occur lower in the southern hemisphere

during aphelion winters, while the peaks extend higher (up and above 100 km) during the perihelion winters. The figure shows that filtering and breaking/saturation processes greatly restrict wave amplitudes in the upper atmosphere.

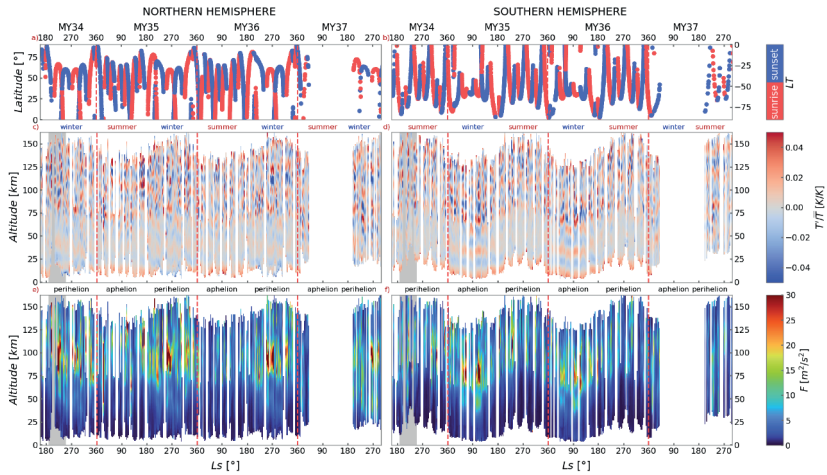


Figure 1. Upper row: Latitude coverage of ACS measurements as a function of the solar longitude Ls; color indicates the local time of observations. Middle and bottom rows: seasonal-altitude distribution of relative temperature perturbations and wave momentum flux (per unit mass), correspondingly (shown in color bars). The left and right columns present the data for the northern and southern hemispheres, respectively. Gray shaded area denotes the period of global dust storm (GDS). Red dashed lines separate Martian years MY34 to MY37

ACKNOWLEDGMENTS:

The data analysis in IKI RAS is supported by the RSF grant No. 25-22-00494.

REFERENCES:

- [1] Korablev O., Montmessin F., ACS Team. The Atmospheric Chemistry Suite (ACS) of three spectrometers for the ExoMars 2016 Trace Gas Orbiter // Space Science Reviews. 2018. V. 214. Article 7. DOI: 10.1007/s11214-017-0437-6.
- [2] Belyaev D., Fedorova A.A., Trokhimovskiy A. et al. Revealing a high water abundance in the upper mesosphere of Mars with ACS onboard TGO // Geophysical Research Letters. 2021. V. 48. Article e2021GL093411. DOI: 10.1029/2021GL093411.
- [3] Belyaev D., Fedorova A.A., Trokhimovskiy A. et al. Thermal Structure of the Middle and Upper Atmosphere of Mars from ACS/TGO CO₂ Spectroscopy // J. Geophysical Research: Planets. 2022. V. 127. Iss. 10. Article e2022JE007286. <https://doi.org/10.1029/2022JE007286>.
- [4] Fedorova A., Montmessin F., Korablev O. et al. Stormy water on Mars: The distribution and saturation of atmospheric water during the dusty season // Science. 2020. V. 367. Iss. 6475. Article eaay9522. P. 297–300. DOI: 10.1126/science.aay9522.
- [5] Fedorova A., Montmessin F., Trokhimovskiy A. et al. A two-Martian year survey of the water vapor saturation state on Mars based on ACS NIR/TGO occultations // J. Geophysical Research: Planets. 2022. V. 128. Iss. 1. Article e2022JE007348. DOI: 10.1029/2022JE007348.
- [6] Starichenko E.D., Belyaev D.A., Medvedev A.S. et al. Gravity wave activity in the Martian atmosphere at altitudes 20–160 km from ACS/TGO occultation measurements // J. Geophysical Research: Planets. 2021. V. 126. Iss. 8. Article e2021JE006899. DOI: 10.1029/2021JE006899.
- [7] Starichenko E.D., Medvedev A.S., Belyaev D.A. et al. Climatology of gravity wave activity based on two Martian years from ACS/TGO observations // Astronomy and Astrophysics. 2024. V. 683. Article A206. <https://doi.org/10.1051/0004-6361/202348685>.

THE INFLUENCE OF INFRARED TRANSPARENCY WINDOWS IN THE MARTIAN ATMOSPHERE ON THE GREENHOUSE EFFECT

A. V. Aliakin¹, A. V. Karnaukhov², M. E. Prokhorov¹

¹ Sternberg Astronomical Institute Moscow University, Moscow, Russia
alyakinav@my.msu.ru

² Institute of Cell Biophysics RAS, Pushchino, Moskovskaya obl., Russia

KEYWORDS:

Mars, greenhouse effect, transparency windows

ABSTRACT:

Thermal radiation from the planet's surface is partially absorbed by the atmosphere if it contains greenhouse gases. Most greenhouse gases have transparency windows, the spectral range of which decreases with increasing concentration of greenhouse gases in the atmosphere. For example, the atmosphere of Mars has wide transparency windows due to the rarefaction of the atmosphere, while in the atmosphere of Venus there are practically no transparency windows. In the atmosphere of the Earth, the size of the transparency windows is intermediate. The report examines this issue for Mars and the terrestrial planets. The spectral range of the transparency windows significantly affects the magnitude of the greenhouse effect: on Mars these are units of Kelvin, on Earth about 39 K [1]. It should be noted that without the greenhouse effect, the Earth would be outside the habitable zone.

REFERENCES:

- [1] Karnaukhov A. V. Initial stage of the Mars evolution might be suitable for a life appearance because of greenhouse effect. Theoretical model // Proc. 3rd European Workshop on Exo-Astrobiology "Mars: The Search for Life". 2004. P. 213–214.

ELECTRONIC KINETICS OF CARBON MONOXIDE IN THE UPPER ATMOSPHERES OF MARS AND PLANETS OF SOLAR SYSTEM

A. S. Kirillov

Polar Geophysical Institute, Apatity, Murmansk region, Russia, kirillov@pgia.ru

KEYWORDS:

Mars, planets, upper atmosphere, carbon monoxide, molecular nitrogen, electronic kinetics

ABSTRACT:

Auroral emissions in the atmosphere of Mars was discovered by SPICAM (Bertaux et al., 2005, Nature). The main emissions in the net auroral spectrum are the CO $a^3\Pi-X^1\Sigma$ Cameron bands between 180 and 240 nm, long observed on the Martian dayside [1]. In CO₂-rich atmosphere there is a production of electronically excited carbon monoxide CO by impact of energetic particles with CO₂ molecules. We study the kinetics of the triplet $a^3\Pi$, $a^3\Sigma^+$, $d^3\Delta$, $e^3\Sigma^-$ states of carbon monoxide at altitudes of the atmosphere of Mars during the precipitation high energetic particles. The intensities of the CO $a^3\Pi-X^1\Sigma$ Cameron bands are calculated for conditions of auroral precipitations in Martian atmosphere. In N₂-rich atmospheres of Titan, Triton, Pluto there is a production of metastable molecular nitrogen N₂($A^3\Sigma_u^+$) by impact of energetic particles on N₂ molecules and in cascade processes from triplet states of electronically excited nitrogen molecules. The interaction of N₂($A^3\Sigma_u^+$) with minor component CO in the atmospheres causes the effective production of CO($a^3\Pi$) in intermolecular electron energy transfer processes. Moreover, there is vibrational excitation of ground-state N₂($X^1\Sigma_g^+$) and CO($X^1\Sigma^+$) in the intermolecular and intramolecular processes.

REFERENCES:

- [1] Barth C. A., Wallace L., Pearce J. B. Mariner 5 measurement of Lyman alpha radiation near Venus // J. Geophysical Research. 1971. V. 76. P. 2213–2227 p.

DOSE RATE AND PARTICLE FLUX OF COSMIC RAYS IN THE FREE SPACE AT 1.5 A. U. DURING DIFFERENT PHASES OF SOLAR ACTIVITY ACCORDING MEASUREMENTS BY LIULIN-MO DOSIMETER ON TRACE GAS ORBITER

J. Semkova¹, R. Koleva¹, V. Benghin³, K. Krastev¹, Yu. Matviichuk¹,
B. Tomov¹, N. Bankov¹, St. Maltchev¹, Ts. Dachev¹, I. Mitrofanov²,
D. Golovin², M. Mokrousov², M. Litvak², N. Lukyanov²,
V. Shurshakov³, S. Drobyshev³

¹ Space Research and Technology Institute, Bulgarian Academy of Sciences
Sofia, Bulgaria, jsemkova@stil.bas.bg

² Space Research Institute RAS, Moscow, Russia

³ State Scientific Center of Russian Federation — Institute of Biomedical
Problems RAS, Moscow, Russia

KEYWORDS:

Mars, free space, ExoMars TGO, radiation measurements, galactic cosmic rays (GCR), solar energetic particles (SEP), solar cycle

INTRODUCTION:

Mars is an ambitious target for future human exploration. The radiation environment during the transit and in Mars vicinity can be very hazardous for future human missions to the planet. In the interplanetary space and at Mars orbit the radiation field consists of two types of primary particles: galactic cosmic rays (GCR) and solar energetic particles (SEPs).

The dosimetric telescope Liulin-MO for measuring the ionizing radiation environment onboard the ExoMars Trace Gas Orbiter (TGO) is a module of the Fine Resolution Epithermal Neutron Detector (FREND) [1, 2].

Liulin-MO data about the radiation environment during TGO cruise to Mars and in high elliptic Mars orbits were taken in the period from April 2016 to March 2017. Since May 2018 Liulin-MO investigates the radiation conditions at Mars science orbit, which is a circular orbit with 400 km altitude.

Liulin-MO measurements to date cover the decreasing and minimum phases of the solar activity in solar cycle 24 and the rising phase, maximum, and decreasing phase near the maximum of cycle 25.

In this paper we present and discuss the results for the charged particle fluxes and dose rates at 1.5 a. u. during different phases of the solar activity cycle. The results are based on measurements by Liulin-MO dosimeter on TGO in the period April 2016 – July 2025.

Discussed is the selection of the best time interval in the solar cycle for a future manned trip to Mars, regarding the radiation safety. The obtained results may be used for verification and benchmarking of the galactic and

REFERENCES:

- [1] Mitrofanov I., Malakhov A., Bakhtin B. et al. Fine Resolution Epithermal Neutron Detector (FREND) onboard the ExoMars Trace Gas Orbiter // Space Science Reviews. 2018. V. 214. Article 86. <https://doi.org/10.1007/s11214-018-0522-5>.
- [2] Semkova J., Koleva R., Benghin V. et al. Charged particles radiation measurements with Liulin-MO dosimeter of FREND instrument aboard ExoMars Trace Gas Orbiter during the transit and in high elliptic Mars orbit // Icarus. 2018. V. 303. P. 53–66. <https://doi.org/10.1016/j.icarus.2017.12.034>.

COMPARING MEREM RADIATION ENVIRONMENT SIMULATIONS WITH OBSERVATIONS IN MARS ORBIT

P. Jamlongkul¹, T. Panyalert¹, P. Torteeka¹, S. Manuthasna¹, D. Ruffolo², W. Mitthumsiri², K. Chaiwongkhot², K. Puprasit^{2,3}, P. Muangha¹, T. Marsri¹, P. Charoenvicha¹, P. Khonsri¹, Y. Pittayang¹, K. Anuchit¹, W. Sophonamphonsucha¹

¹ National Astronomical Research Institute of Thailand (Public Organization) Chiang Mai, Thailand

² Mahidol University, Bangkok, Thailand

³ Chulabhorn Royal Academy, Bangkok, Thailand

KEYWORDS:

Mars orbital radiation environment, MEREM, solar energetic particles, SEP, Galactic cosmic rays, GCRs, Mars orbital operations, Tianwen-3, astrobiology, mission planning

INTRODUCTION:

Comparing in-situ radiation and charged particle data from observation missions with simulation outputs from the Mars Energetic Radiation Environment Model (MEREM) [1] provides a foundation for selecting criteria to adapt for future Mars mission planning, astronaut safety, and detector development [3]. Building on prior MEREM-based studies, this work systematically examines solar energetic particle (SEP) spectra and fluxes [2, 6], along with Galactic cosmic rays (GCRs) [3], by contrasting model outputs with observational data collected during Mars orbital operations [2, 4]. This comparison is intended to integrate observational insights with simulation frameworks under varying solar and heliospheric conditions [6], supporting the development of preliminary radiation environment estimates for future Mars missions [5, 7]. Additionally, insights from this comparison may inform broader considerations of how the Mars orbital radiation environment could influence organic molecule preservation [8], which is relevant for Mars sample-return missions such as Tianwen-3 [10] and future astrobiological studies [9]. By focusing on aligning empirical datasets with simulation frameworks, this study aims to support the refinement of mission-specific criteria in Mars orbital radiation environment assessments, facilitating mission design, risk mitigation, and maximizing scientific return during Mars exploration efforts [5, 7].

REFERENCES:

- [1] Heynderickx D., Quaghebeur B., Wera J. et al. New radiation environment and effects models in the European Space Agency's Space Environment Information System (SPENVIS) // Space Weather. 2004. V. 2. No. 10. Article S10S03. 4 p. DOI: 10.1029/2004SW000073.
- [2] Larson D.E., Lillis R.J., Lee C.O. et al. The MAVEN Solar Energetic Particle Investigation // Space Science Reviews. 2015. V. 195. P. 153–172. DOI: 10.1007/s11214-015-0218-z.
- [3] Zeitlin C., Hassler D.M., Cucinotta F.A. et al. Measurements of energetic particle radiation in transit to Mars on the Mars Science Laboratory // Science. 2013. V. 340. No. 6136. P. 1080–1084. DOI: 10.1126/science.1235989.
- [4] Jakosky B.M., Lin R.P., Grebowsky J.M. et al. The Mars Atmosphere and Volatile Evolution (MAVEN) Mission // Space Science Reviews. 2015. V. 195. P. 3–48. DOI: 10.1007/s11214-015-0139-x.
- [5] Guo J., Zeitlin C., Wimmer-Schweingruber R.F. et al. Variations of dose rate observed by MSL/RAD in transit to Mars and on Mars surface during the solar cycle 24 // Astronomy and Astrophysics. 2015. V. 577. Article A58. 6 p. DOI: 10.1051/0004-6361/201525680.
- [6] Mewaldt R.A. Solar energetic particle composition, energy spectra, and space weather // Space Science Reviews. 2006. V. 124. P. 303–316. DOI: 10.1007/s11214-006-9091-0.
- [7] Hassler D.M., Zeitlin C., Wimmer-Schweingruber R.F. et al. Mars' surface radiation environment measured with the Mars Science Laboratory's Curiosity rover // Science. 2013. V. 343. No. 6169. 11 p. DOI: 10.1126/science.1244797.

- [8] Pavlov A. A., Vasilyev G., Ostryakov V. M. et al. Degradation of the organic molecules in the shallow subsurface of Mars due to irradiation by cosmic rays // *Geophysical Research Letters*. 2012. V. 39. No. 13. Article L13202. 5 p. DOI: 10.1029/2012GL052166.
- [9] Eigenbrode J. L., Summons R. E., Steele A. et al. Organic matter preserved in 3-billion-year-old mudstones at Gale crater, Mars // *Science*. 2018. V. 360. No. 6393. P. 1096–1101. DOI: 10.1126/science.aas9185.
- [10] Chinese Academy of Sciences. China's Tianwen-3 Mars sample return mission: Opportunities and challenges // CAS Newsroom. 02.07.2025. https://english.casad.cas.cn/newsroom/ma/202507/t20250702_1046646.html.

SIMULATION-BASED STUDY OF RAAN EFFECTS ON JOVIAN MAGNETIC CONNECTIVITY: APPLICATION TO THE TW-3 MARCH PAYLOAD

Thanayuth Panyalert¹, Peerapong Torteeka¹, Shariff Manuthasna¹, Kanatip Anuchit¹, Pradiphat Muangha¹, Paporin Jamlongkul¹, Kullapha Chaiwongkhot², Kunlanan Puprasit³, Warit Mitthumsiri², Xu He⁴, Tanawish Marsri¹, Popefa Charoenvicha¹, Yaowarat Pittayang¹, Pakorn Khonsri¹, Patcharin Kamsing⁵, Jidapa Lakronwat², Petchara Pattarakijwanich², David Ruffolo², Wiphu Rujopakarn¹

¹ National Astronomical Research Institute of Thailand (Public Organization) Chiang Mai, Thailand, peerapong@narit.or.th

² Mahidol University, Bangkok, Thailand

³ Chulabhorn Royal Academy, Bangkok, Thailand

⁴ Changchun Institute of Optics, Fine Mechanics and Physics, Chinese Academy of Sciences, Changchun, China

⁵ Air-Space Control, Optimization and Management Laboratory, Department of Aeronautical Engineering, International Academy of Aviation Industry, King Mongkut's Institute of Technology Ladkrabang, Bangkok, Thailand

KEYWORDS:

Mars orbit, Tianwen-3, Jovian electrons, magnetic connectivity, parker spiral, RAAN sweep, interplanetary magnetic field (IMF), highly elliptical orbit, space weather observations, MARCH payload

INTRODUCTION:

Understanding the transport and detectability of energetic electrons originating from Jupiter has long been a subject of heliospheric studies, particularly due to their unique propagation behavior along interplanetary magnetic field (IMF) lines shaped by the Parker spiral [1, 2]. Jovian electrons, typically in the MeV range, can reach inner heliospheric locations such as Earth and Mars under favorable magnetic connectivity conditions [3, 4]. These conditions are governed by the relative heliolongitude between Jupiter and the observer, the structure of the solar wind, and the orientation of the IMF [5, 6]. Several modeling studies have explored the propagation of Jovian and galactic electrons through the heliosphere [7, 8], and have highlighted the importance of turbulence and magnetic field line topology on particle transport [9, 10]. At Mars, detection of charged particles from both solar and interplanetary sources has been made possible by instruments aboard orbiters and surface missions [11], [12], yet the potential to observe Jovian electrons from Mars orbit remains underexplored.

The Mars Aiming Radiation Collection Hodoscope (MARCH) is a proposed Thai-Chinese space radiation detector, currently under mission proposal development. Planned for potential deployment aboard China's Tianwen-3 Mars orbiter, MARCH is designed to detect energetic electrons and ions originating from solar, galactic, and Jovian sources. The Tianwen-3 orbiter will operate in a highly elliptical orbit with a periapsis of 400 km, an apoapsis of 76,000 km, and an inclination of approximately 54°. Although the Right Ascension of the Ascending Node (RAAN) has already been defined internally for the mission, it has not been publicly disclosed. This study therefore adopts a simulation-based approach to sweep RAAN values parametrically, with the aim of evaluating how orbital orientation affects the detector's magnetic connectivity with Jupiter. In this study, we simulate the detector's magnetic connectivity to Jupiter across a range of RAAN values, assuming a fixed anti-nadir pointing configuration of the instrument. We quantify connectivity using the "Jovian magnetic connectivity duty cycle" the fraction of time when the detector boresight falls within a threshold angle of

the Parker spiral direction emanating from Jupiter [13, 14]. By combining orbit propagation and magnetic field modeling, we assess how orbital orientation affects the detector's observational potential. The results provide a practical strategy for optimizing the geometry of deep-space missions targeting interplanetary particle populations, especially when constrained by fixed-pointing instruments in a complex heliospheric environment [15, 16].

REFERENCES:

- [1] *Chenette D.L.* The propagation of Jovian electrons to Earth orbit // *J. Geophysical Research*. 1980. V. 85. Iss. A5. P. 2243–2256. <https://doi.org/10.1029/JA085iA05p02243>
- [2] *Teegarden B.J., McDonald F.B., Trainor J.H. et al.* Interplanetary MeV electrons of Jovian origin // *J. Geophysical Research*. 1974. V. 79. Iss. 25. P. 3615–3622. <https://doi.org/10.1029/JA079i025p03615>.
- [3] *Strauss R.D., Potgieter M.S., Ferreira S.E.S.* Modelling and observing Jovian electron propagation times in the inner heliosphere // *Advances in Space Research*. 2013. V. 51. Iss. 3. P. 339–349. <https://doi.org/10.1016/j.asr.2012.09.035>.
- [4] *Ndanganeni R.R., Potgieter M.S.* The global modulation of Galactic and Jovian electrons in the heliosphere // *Astrophysics and Space Science*. 2018. V. 363. Iss. 7. Article 156. 8 p. DOI: 10.1007/s10509-018-3377-z.
- [5] *Chhiber R., Subedi P., Usmanov A.V. et al.* Cosmic-Ray Diffusion Coefficients throughout the Inner Heliosphere from a Global Solar Wind Simulation // *Astrophysical J. Supplement Ser.* 2017. V. 230. Iss. 2. Article 21. 15 p. DOI: 10.3847/1538-4365/aa74d2.
- [6] *Engelbrecht N.E., Effenberger F., Florinski V. et al.* Theory of Cosmic Ray Transport in the Heliosphere // *Space Science Reviews*. 2022. V. 218. Iss. 4. Article 33. DOI: 10.1007/s11214-022-00896-1.
- [7] *Evenson P.* Cosmic Ray Electrons // *Space Science Reviews*. 1998. V. 83. Iss. 1/2. P. 63–73.
- [8] *Ferreira S.E.S.* The transport of Galactic and Jovian cosmic ray electrons in the heliosphere // *Advances in Space Research*. 2005. V. 35. Iss. 4. P. 586–596. <https://doi.org/10.1016/j.asr.2004.11.032>.
- [9] *Chuychai P., Ruffolo D., Matthaeus W.H., Meechai J.* Trapping and diffusive escape of field lines in two-component magnetic turbulence // *Astrophysical J.* 2007. V. 659. Iss. 2. P. 1761–1776. DOI: 10.1086/511811.
- [10] *Ruffolo D., Matthaeus W.H., Chuychai P.* Trapping of solar energetic particles by the small-scale topology of solar wind turbulence // *Astrophysical J.* 2003. V. 597. Iss. 2. P. L169–L172. DOI: 10.1086/379847.
- [11] *Guo J., Lillis R., Wimmer-Schweingruber R.F. et al.* Measurements of Forbush decreases at Mars: both by MSL on ground and by MAVEN in orbit // *Astronomy and Astrophysics*. 2018. V. 611. Article A79. 14 p. <https://doi.org/10.1051/0004-6361/201732087>.
- [12] *Zhang J., Guo J., Zhang Y. et al.* The 2022 February 15 solar energetic particle event at Mars // *Geophysical Research Letters*. 2024. V. 51. Iss. 19. Article e2024GL111775. DOI: 10.1029/2024GL111775.
- [13] *Strauss R.D., Dresing N., Engelbrecht N.E. et al.* Jovian electrons in the inner heliosphere: Opportunities for multi-spacecraft observations and modeling // *Astrophysical J.* 2024. V. 961. Iss. 1. Article 57. DOI: 10.3847/1538-4357/ad11db.
- [14] *Ruffolo D., Seripienlert A., Tooprakai P. et al.* Squeezing of particle distributions by expanding magnetic turbulence and space weather variability // *Astrophysical J.* 2013. V. 779. Iss. 1. Article 74. 6 p. DOI: 10.1088/0004-637X/779/1/74.
- [15] *Curtis H.D.* *Orbital Mechanics for Engineering Students*. Amsterdam: Butterworth-Heinemann, 2019. 692 p.
- [16] *Jiang C., Liu Y., Jiang Y., Li H.* Orbital design and control for Jupiter-observation spacecraft // *Aerospace*. 2021. V. 8. Iss. 10. Article 282. <https://doi.org/10.3390/aerospace8100282>.

IMPROVEMENT OF RADIO COMMUNICATION PERFORMANCE VIA AN ACCOMPANYING RELAY SPACECRAFT FOR ROUND-TRIP MISSIONS TO MARS

A. V. Ivanyukhin^{1,2}, A. P. Plokhikh³

¹ *Research Institute of Applied Mechanics and Electrodynamics (Moscow Aviation Institute), Moscow, Russia, ivanyukhin.a@yandex.ru*

² *RUDN University, Moscow, Russia*

³ *Moscow Aviation Institute, Moscow, Russia*

Keywords:

interplanetary transfers, Mars missions, cycler, relay spacecraft, space communications

ABSTRACT:

The study addresses the problem of ensuring stable high-speed radio communication during the trajectories of Earth-Mars and Mars-Earth flight missions using relay spacecraft on heliocentric orbits [1, 2]. The relay spacecraft are proposed to be placed on resonant orbits, enabling their repeated use for a selected class of Earth-Mars flights, which is conceptually equivalent to the Cycler approach [3]. The orbits of Earth and Mars are assumed to be circular and coplanar.

A family of trajectories for round-trip Mars expeditions, differing in mission duration, is examined. The analyzed range includes flight durations from the energetically optimal Hohmann transfer (259 days) to fast transfers lasting 115 days, corresponding to the planned SpaceX Starship missions. Each trajectory within this family follows a two-impulse Earth-Mars and Mars-Earth transfer scheme, optimized for total delta-v expenditure, and is determined by solving Lambert's problem [4, 5].

An analysis is presented of communication links between Earth, Mars, the target spacecraft, and the relay satellite. Requirements for possible positioning regions of the relay satellite in the interplanetary space between Earth and Mars are formulated [1, 2]. Families of resonant orbits for relay satellites have been identified to achieve the specified communication channel capacity during the transfer phase. The most promising relay satellite orbital configurations have been determined, providing 100% channel availability while maximizing data throughput during the mission. The performance gain of the proposed relay architecture has been quantified in comparison with direct Earth communication links.

The analysis of low-thrust maneuvers for relay satellite deployment and station-keeping has been conducted, including delta-v cost estimates for repeated Earth-Mars-Earth mission cycles. Optimal launch windows for both the target spacecraft and relay satellite have been determined for upcoming synodic periods.

ACKNOWLEDGMENTS:

The study was supported by the Russian Science Foundation grant No. 23-19-00515, <https://rscf.ru/project/23-19-00515/>.

REFERENCES:

- [1] *Volkovskii A. S., Vazhenin N. A., Plokhikh A. P., Boriskin D. D.* Information capacity improvement for deep space communication radio systems using companion relay satellites // *Russian Aeronautics*. 2024. V. 67. No. 4. P. 942–950. <https://doi.org/10.3103/S1068799824040238>.
- [2] *Plokhikh A. P., Ivanyukhin A. V., Boriskin D. D., Vazhenin N. A.* Evaluation of the possibility of using resonant orbits for accompanying relay satellites // *Cosmic Research*. 2024. V. 62. No. 6. P. 643–653. <https://doi.org/10.1134/S0010952524600999>.
- [3] *Byrnes D. V., Longuski J. M., Aldrin B.* Cycler orbit between Earth and Mars // *J. Spacecraft and Rockets*. 1993. V. 30. No. 3. P. 334–336. <https://doi.org/10.2514/3.25519>.

- [4] *Kravchenko V. S., Ivanyukhin A. V.* Two-Impulse Orbital transfer based on the solution of Lambert problem with optimal flight time // Proc. Intern. Astronautical Congress. 2023. Paper IAC-23.IPB.26.
- [5] *Ivanyukhin A. V., Ivashkin V. V.* Solution of the Euler–Lambert problem based on the Okhotsimsky–Egorov ballistic approach // Solar System Research. 2024. V. 58. No. 6. P. 769–779. <https://doi.org/10.1134/S0038094624700527>.

CLUSTER ANALYSIS OF RECENTLY FORMED MARTIAN CRATER FIELDS

O. P. Popova, E. D. Podobnaya, D. O. Glazachev

Sadovsky Institute of Geosphere Dynamics RAS, Moscow, Russia
o9055610006@gmail.com

KEYWORDS:

Mars, fresh impacts, crater cluster, fragmentation, cluster analysis

INTRODUCTION:

The catalog of recently formed meteorite impact sites on Mars provides an opportunity to study the meteorite population common to Earth and Mars [1, 2]. About 60 % of the impactors disintegrated in the atmosphere and formed crater clusters [2]. Crater fields are very diverse in terms of both the number of craters they contain and the size of the scattering field (and the distance between craters). The characteristics of crater fields depend, among other things, on the properties of the impactor, so it can be assumed that among the crater clusters there should be groups associated with different types of impactors.

CLUSTER ANALYSIS:

Cluster analysis was used to analyze the catalog data. This method divides sets of objects into subsets (clusters) so that objects from the same group are more similar to each other than to objects from other clusters according to some criterion. The parameters of crater fields, which are considered as input variables, include the height of the cluster above the average surface of Mars H_{elev} , the number of craters in the cluster N , the average size of the cluster D_{med} , the normalized masses of fragments (M_1/M_0 , M_2/M_0 , etc.) (where M_i is the mass of a fragment and M_0 is the total mass of all fragments). The masses are estimated based on the size of the impactor for each crater in the cluster, and the size of the impactor itself is determined by the similarity ratio for craters [3].

RESULTS:

The number of groups identified varies depending on the method chosen; however, regardless of the method, clusters with a dominant main crater and clusters with a large number of relatively small craters are identified as separate groups. The third frequently distinguished group is the group in which there are two comparable large craters. The cumulative distributions of craters in clusters by mass showed that the slope of the distribution differs significantly for the group with small craters. Cluster analysis suggested a division into groups that correlates with previously proposed cluster classifications. Attempts to find a division into groups that reflects the relationship between height above the average surface and average cluster size did not yield positive results, nor is there any apparent dependence of the number of craters on height above the average surface.

ACKNOWLEDGMENTS:

This work was carried out within the framework of the state assignment of the Ministry of Science and Higher Education of the Russian Federation No. 125012200624-5.

REFERENCES:

- [1] *Daubar I.J., Dundas C.M., McEwen A.S. et al.* New Craters on Mars: An Updated Catalog // *J. Geophysical Research: Planets*. 2022. V.127. Iss.7. Article e2021JE007145. <https://doi.org/10.1029/2021JE007145>.
- [2] *Podobnaya E., Glazachev D., Popova O., Ivanov B.* Classification of craters clusters in the expanded catalog of fresh impact sites on Mars // *Solar System Research*. 2025. V. 59(5). P. 46–51. DOI: 10.1134/S003809462460207X.
- [3] *Holsapple K.A., Housen K.R.* A crater and its ejecta: An interpretation of Deep Impact // *Icarus*. 2007. V. 187. Iss. 1. P. 345–356. DOI: 10.1016/j.icarus.2006.08.029.

DISTRIBUTION OF CRATER SIZES IN RECENTLY FORMED MARTIAN CRATER FIELDS

E. D. Podobnaya, O. P. Popova, D. O. Glazachev

Sadovsky Institute of Geosphere Dynamics RAS, Moscow, Russia
epodobnaya@idg.ras.ru

KEYWORDS:

Mars, impact site, cluster, crater, size-frequency distribution, numerical modelling

INTRODUCTION:

Meteoroids, which enter the atmospheres of Earth and Mars belong to the same population of small solar system bodies and have different fates. On the Earth, meters-scale meteoroids deposit the most part of their mass and energy in the atmosphere, in rare cases their fragments may be found as meteorites. On Mars, due to the thinner atmosphere, they form impact craters or clusters of craters on the surface. These clusters provide a unique opportunity to estimate meteoroid parameters.

Repeated imaging of the Martian surface allowed to find new dated impact sites of meter-scaled meteoroids. Up to date more than 1400 freshly formed impact sites were discovered [1, 2]. For 1336 of them there is information about size and location of craters. More than a half (62 %) of the impacting bodies break up in the atmosphere and form clusters of craters [3].

SIZE-FREQUENCY DISTRIBUTION:

The size-frequency distribution (SFD) of small bodies in the Solar System, as well as the distribution of craters they form, provides insight into their origin and evolution. The cumulative distribution of small bodies is often described by the power law with power exponent b :

$$N(>D) \sim D^{-b}.$$

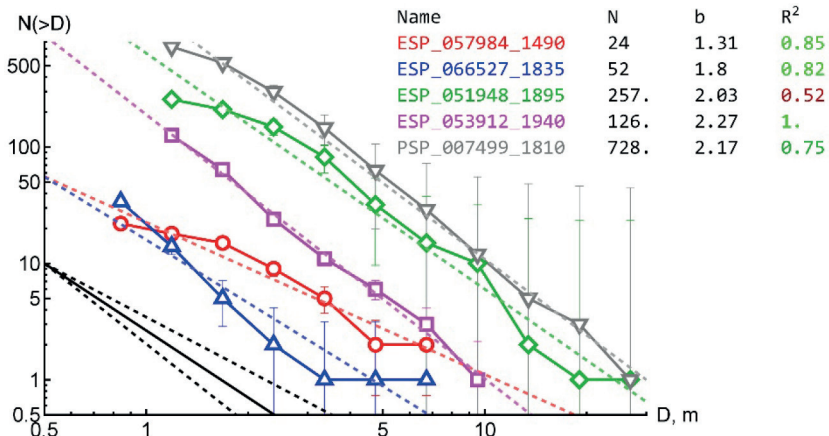


Figure 1. Cumulative SFD of few densely populated clusters (group 2, clusters include more than 20 craters). Black solid line starts from approximately mean number of craters in the catalog ($N = 10$) and demonstrates the average inclination, dashed black lines differ from the mean slope on its standard deviation. Root of variance estimation is shown as error bars. The legend contains information about cluster (its identification name and number of craters inside) and power fit parameters (obtained power exponent b and coefficient of determination R^2)

Previously three types of fresh Martian clusters were identified [4]. The first one includes clusters with one major crater supplemented by some much smaller ones; densely populated clusters (with more than 20 craters) correspond to the second type and the final group relates to sparsely populated

clusters (less than 20 craters), which have 2 or more comparable largest craters (Figure 1). The distributions for each group are characterized by various average power exponents [4]. They were estimated as 1.1, 1.9 and 1.4 for groups 1, 2 and 3 correspondingly. The various proposed groups may correspond to different fragmentation scenarios and/or meteoroid properties. In geosciences, observed data often cover a wide range of scales, but the applicability of the power-law relationship is often limited. The smallest events are below the sensitivity threshold of the instruments, while the large ones are constrained by the physical boundaries of the system itself. It was proposed to describe such distributions by an upper-truncated power law (2), at which there are no objects of size larger than D_T [5]:

$$N(> D) \sim (D^{-b} - D_T^{-b}).$$

Considered size-frequency distribution of Martian craters sizes is limited by the resolution of satellite cameras for small craters and by the largest crater in cluster. To better describe the limitations, the distribution was described by a truncated power law. Results will be compared with classic power law and independent works.

NUMERICAL SIMULATION:

Cluster groups may be modeled in the frame of an entry fragmentation model taking into account different fragment distributions in selected groups, entry velocities and angles, elevations and meteoroid strengths. Numerical modeling of characteristic clusters will allow us to determine the most suitable parameters of meteoroids and the corresponding fragmentation features. It will be shown that the characteristic clusters in each group are in good agreement with the real ones.

ACKNOWLEDGEMENTS:

This work was carried out within the framework of the state assignment of the Ministry of Science and Higher Education of the Russian Federation No. 125012200624-5.

REFERENCES:

- [1] Malin M.C., Edgett K.S., Posiolova L.V. et al. Present-day impact cratering rate and contemporary gully activity on Mars // *Science*. 2006. V. 314. Iss. 5805. P. 1573–1577. DOI: 10.1126/science.1135156
- [2] Daubar I.J., Dundas C.M., McEwen A.S. et al. New Craters on Mars: An Updated Catalog // *J. Geophysical Research: Planets*. 2022. V. 127. Iss. 7. Article e2021JE007145. <https://doi.org/10.1029/2021JE007145>.
- [3] Podobnaya E., Popova O., Ivanov B., Glazachev D. Classification of the updated catalog of recent impact sites on Mars // *Dynamic Processes in Geospheres*. 2023. V. 15. No. 4. P. 72–82 (in Russian).
- [4] Podobnaya E., Popova O., Ivanov B., Glazachev D. Classification of Craters Clusters in the Expanded Catalog of Fresh Impact Sites on Mars // *Solar System Research*. 2025. V. 59. No. 5. Article 46. <https://doi.org/10.1134/S003809462460207X>.
- [5] Corral Á., González Á. Power law size distributions in geoscience revisited // *Earth and Space Science*. 2019. V. 6. Iss. 5. P. 673–697. DOI: 10.1029/2018EA000479.

NEW CRATERS ON MARS — 2024–2025 CATALOG EXPANSION

B. A. Ivanov

Institute of Geosphere Dynamics RAS, Moscow, Russia
ivanov.ba@idg.ras.ru, baivanov@idg.chph.ras.ru

KEYWORDS:

Mars, impact craters, atmospheric shock waves, dust, HiRise

INTRODUCTION:

The last year presentation included HiRise Images up to ESP_084845_1925 filmed 01 September 2024. Here we present new images, outlining most interesting cites.

DATED “NEW” MARTIAN CRATERS:

The technique to find an approximate age of small new impact craters with repetitive imaging “before” and “after” a crater formation proposed by Malin et al. [1] has been successfully applied for craters, recorded with the HiRise camera [2]. The collection published in [2] has been expanded to 1700 recorded cases in 2024 [3] (Figure 1). During the last calendar year (2024–2025) the collection of dated “new” craters has been expanded with about 150 cases.

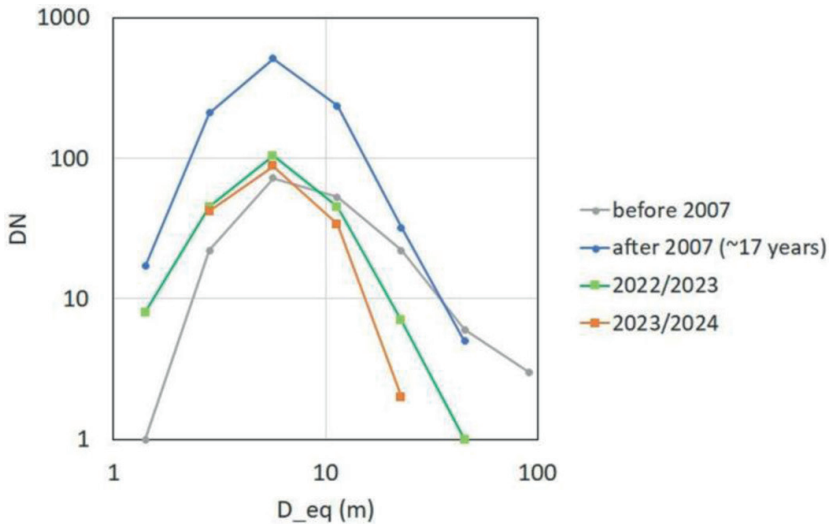


Figure 1. Evolution of the differential crater size distribution in diameter bins 1 to 2 m, 2 to 4 m, etc. After 2007 the finding rate of craters with $D < 20$ m was highly improved due to the increased surface coverage with CTX images

ATMOSPHERIC SHOCK WAVE’S FOOTPRINTS:

One of the most interesting features found around small “new” craters are footprints of atmospheric shock wave collision with the dusty Martian surface. A kind of these footprints named “scimitars” seems to be formed due to collision of ballistic sonic waves and hemispherical shock waves from the point of impact [4].

In the presented work we analyze several new impacts recorded by the HiRise team during the last year, including a few new cases of scimitar’s formation.

ESP_086005_1955

Figure 2 presents an example of a scimitar near the “new” crater at the HiRise image ESP_086005_1955, 30 November 2024, centered near 15.527° N, 50.85,7° E. The “new” impact crater has a diameter $D = 11$ m. CTX images define the formation date between 12.02.2023 and 09.09.2024.

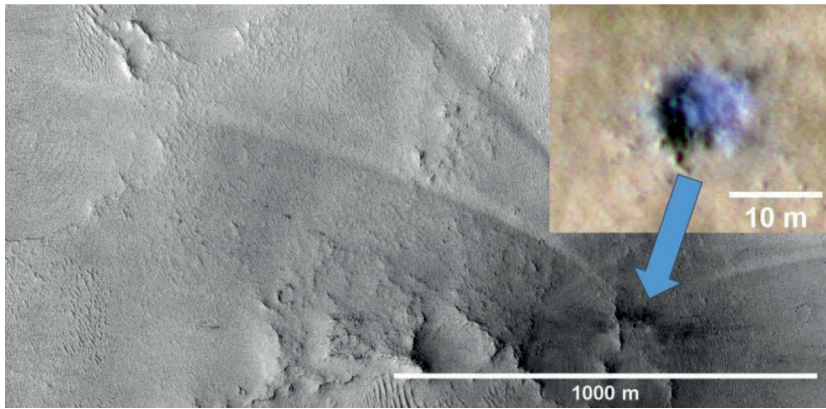


Figure 2. The scimitar near the “new” crater at the HiRISE image ESP_086005_1955

ESP_086871_1750

Figure 3 shows one more example of a scimitar captured in the image ESP_086871_1750 06 February 2025 near -4.888N , 167.052E . “Before” and “after” CTX images pace the formation date between 20.04.2023 and 03.11.2024. The crater diameter is about 8.25 m.

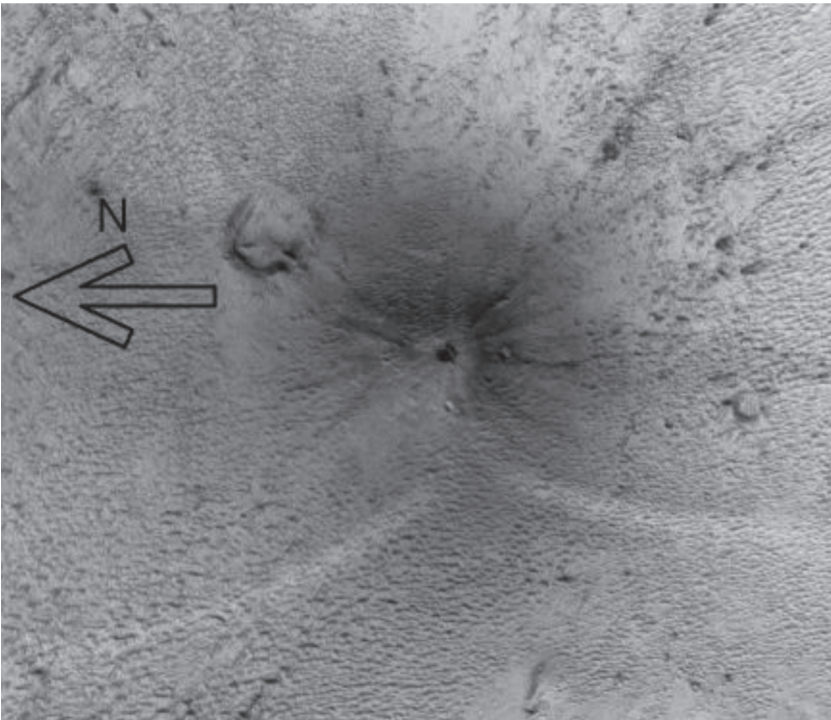


Figure 3. The scimitar near the “new” crater at the HiRISE image ESP_086871_1750. North is to the left

We continue to construct mechanical models of scimitar’s formation to make better conclusions about meteoroid’s orbit inclination and local mechanical properties of the Martian soil at the point of impact.

CONCLUSIONS:

The continuation of the HiRISE/CTX imaging gives a reliable technique to estimate the impact flux on Mars and the impact cratering condition in various regions of Mars.

ACKNOWLEDGMENTS:

The author thanks the HiRise team for the permanent support of public sites <https://www.uahirise.org/catalog/> and <https://jmars.mars.asu.edu>. The project is supported with the state order of Ministry of science and higher education, Russian Federation (project № 122032900178-7).

REFERENCES:

- [1] *Malin M. C., Edgett K. S., Posiolova L. V. et al.* Present-day impact cratering rate and contemporary gully activity on Mars // *Science*. 2006. V. 314. No. 5805. P. 1573–1577. DOI: 10.1126/science.1135156.
- [2] *Daubar I. J., Dundas C. M., McEwen A. S. et al.* New Craters on Mars: An Updated Catalog // *J. Geophysical Research: Planets*. 2022. V. 127. Iss. 7. Article e2021JE007145. <https://doi.org/10.1029/2021JE007149>.
- [3] *Ivanov B. A.* New craters on Mars — expanding catalog in 2023–2024 // 15th Moscow Solar System Symposium 2024. P. 49–51.
- [4] *Burleigh K. J., Melosh H. J., Tornabene L. L. et al.* Impact airblast triggers dust avalanches on Mars // *Icarus*. 2012. V. 217. Iss. 1. P. 194–201. <https://doi.org/10.1016/j.icarus.2011.10.026>.

POLYCYCLIC NATURE OF MARTIAN OUTFLOW CHANNEL ACTIVITY: CHRONOSTRATIGRAPHIC CONSTRAINTS

G. A. Skrebec

*Department of Regional Geology, Belarusian State University, Minsk, Belarus
georg.screbec@geologiya.by)*

*Geological Institute, Research and Production Centre for Geology
Minsk, Belarus*

KEYWORDS:

Mars, Ares Vallis, Hesperian floodings, outflow channels, fluvial resurfacing, polycyclic fluvial activity, climate drivers

INTRODUCTION:

This study builds upon the results of our ongoing analysis of crater size-frequency distributions in the Chryse Planitia region of Mars, the outcomes of which are currently being prepared for publication (Skrebec G.A., Ivanov M.A. Estimates of the absolute model age of the outflow channel floors around the Chryse Planitia. 2025 (manuscript in preparation)). The data reveal a striking temporal contrast between western and eastern outflow channels: while Simud and Tiu Valles show formation ages clustered at 3.7–3.6 Ga, Ares Vallis and Hydaspis Chaos display multiple resurfacing peaks at 3.9, 3.6, 3.5, and 3.0 Ga.

This variability suggests that the eastern systems did not form in a single catastrophic event but were reactivated during at least two or three discrete fluvial phases. Understanding what allowed such episodic reactivation of surface hydrology on a predominantly cold and arid Mars is a key question driving the present study.

Several lines of evidence suggest that transient climatic warming episodes are likely triggers for these events. Global climate models (e.g., MarsWRF, LMD GCM) simulate short-lived periods of surface liquid water stability under specific conditions, including orbital obliquity maxima and episodic volcanic degassing, particularly during the Hesperian epoch.

Here, we investigate whether the observed resurfacing ages of eastern channels align with predicted climate windows. By doing so, we aim to assess the climatic sensitivity of Martian fluvial systems and to test the hypothesis that the eastern sector of the Chryse outflow network functioned as a reactivatable hydrologic domain under marginal warming conditions.

STUDY AREA AND METHODS:

Based on THEMIS daytime mosaics (100 m/pixel) and MOLA topography, photogeological mapping was conducted across representative surfaces in Simud, Tiu, Ares Vallis, and adjacent regions of Hydaspis Chaos. The surveyed localities were subdivided into the western group (Simud, Tiu), and the eastern group (Ares, Hydaspis), based on both geographic position and geomorphological context.

Crater populations were digitised using CraterTools within ArcGIS and analysed using Craterstats2. Model ages were determined using Hartmann–Robbins chronology functions. All count areas were selected to represent morphologically uniform fluvial surfaces, with secondaries excluded. The resulting absolute model ages (AMAs) indicate that western channels formed synchronously around 3.7–3.6 Ga, while the eastern systems underwent multiple resurfacing phases: 3.9–3.6 Ga (Ares I site), 3.5 and 3.0 Ga (Ares II), and 3.6–3.5 Ga (Hydaspis). Formal uncertainties for these estimates range from ± 0.01 to ± 0.07 Ga, depending on the crater population size and surface preservation.

To interpret these age clusters, we compared the fluvial record with outputs from 3D climate models (MarsWRF and LMD GCM), which simulate short-lived warm intervals driven by orbital obliquity cycles and episodic vol-

canic degassing during the Hesperian. Our results support the hypothesis that the eastern channels were reactivated during discrete climate excursions, in contrast to the largely monocyclic nature of the western systems. The eastern valleys, especially Ares Vallis, may thus represent climatically sensitive, reactivatable drainage pathways.

POSSIBLE DRIVERS OF EPISODIC FLUVIAL ACTIVITY:

1. Obliquity-driven orbital forcing: Mars experiences large-amplitude obliquity variations on 0.1–1 Myr timescales due to its lack of a large stabilising moon. According to models [1, 2], periods of high obliquity ($>40^\circ$) would result in poleward redistribution of volatiles and a thickening of the atmosphere due to CO_2 sublimation from polar caps. This, in turn, could lead to increased surface pressure, enhanced greenhouse effect, and the transient stability of liquid water, particularly in lowland regions such as Chryse Planitia. Importantly, the duration of these intervals is predicted to range from 0.01 to 1 Myr — sufficient to permit large-scale water discharge and erosion.
2. Volcanically induced greenhouse spikes: episodic volcanic outgassing, particularly during the late stages of Tharsis activity, could have injected large amounts of SO_2 and H_2O vapour into the atmosphere. As suggested by [3], such degassing events may have induced climate excursions lasting several decades to centuries, sufficient to initiate the melting of near-surface ice deposits or destabilise pressurised aquifers. While brief in geological terms, these pulses may correspond to the resurfacing peaks observed at 3.5 and 3.0 Ga in the Ares II site (*Skrebac G. A., Ivanov M. A. Estimates of the absolute model age of the outflow channel floors around the Chryse Planitia. 2025 (manuscript in preparation)*).
3. Cryospheric reactivation and hydrological cycling: another plausible trigger involves the mechanical destabilisation of buried ice reservoirs. Cycles of sublimation and re-freezing under fluctuating thermal gradients could lead to overpressure and fracturing of cryospheric seals. Such processes may explain the multiple resurfacing signatures seen in Hydaspis Chaos, which is topographically and geologically suited to act as a subsurface drainage hub.

Mechanisms described above differ in both temporal scale and geophysical nature. Table 1 provides a comparative summary of their hypothesised roles in producing the observed resurfacing episodes.

Table 1. Proposed climatic triggers for resurfacing episodes in the study area

Resurfacing age, Ga	Possible climatic or geologic driver	Mechanism	Reference model
3.9–3.6 ¹	High obliquity phase during Early Hesperian	$\uparrow \text{CO}_2$ sublimation \rightarrow \uparrow pressure \rightarrow transient warming	[1, 2]
3.6–3.5 ²	Thermal destabilisation of ground ice	Melting of cryosphere; release through fractured terrain	[3, 4]
3.5 ³	Episodic volcanic degassing (late-stage Tharsis activity)	$\text{SO}_2/\text{H}_2\text{O}$ greenhouse effect \rightarrow brief warming spike \rightarrow aquifer destabilisation	[5, 6]
3.0 ⁴	Orbital forcing and subsurface cryospheric reactivation	Obliquity-induced instability in ground ice \rightarrow phreatic eruption/release	[3, 7]

¹ 3.9–3.6 Ga peak aligns temporally with the main outflow events in the western channels, but in the eastern sector shows evidence for a more extended interval of activity.

² 3.6–3.5 Ga peak is interpreted as the result of episodic cryospheric collapse, facilitated by regional thermal anomalies or subsurface pressure release. These mechanisms are compatible with a declining climate regime and do not require globally elevated temperatures, in agreement with late Hesperian climate models.

³ 3.5 Ga resurfacing may reflect a delayed aquifer response to waning volcanic outgassing or localised climate excursions.

⁴ 3.0 Ga event is especially significant as it represents late-stage fluvial reactivation, potentially under thin atmosphere conditions — a scenario consistent with punctuated warming windows rather than sustained clement climate.

DISCUSSION AND CONCLUSIONS:

Taken together, the climatic and geophysical mechanisms outlined above offer a coherent explanation for the polycyclic fluvial stratigraphy observed in the eastern sector of the Chryse basin. Notably, each of the three resurfacing age peaks (3.9–3.6, 3.5, 3.0 Ga) aligns with a modelled window of transient surface habitability in climate simulations. This strengthens the hypothesis that eastern valleys functioned as reactivable channels, rather than relics of a single fluvial episode.

By contrast, the synchronous formation of the western channels (Simud, Tiu) implies that these systems were formed during a unique global-scale hydrologic event, likely coinciding with early Hesperian peak obliquity and/or initial Tharsis rifting. Their lack of later resurfacing signals suggests that they did not undergo reactivation during subsequent climate excursions—possibly due to geomorphic exhaustion, sealing of aquifers, or tectonic stabilisation.

This dichotomy between polycyclic eastern and monocyclic western channels raises important questions about spatial variability in Mars' hydrosphere–cryosphere system and suggests that regional boundary conditions (e.g., crustal permeability, elevation, latitude) played a major role in modulating the climatic sensitivity of different drainage basins.

REFERENCES:

- [1] *Kite E. S., Gao P., Goldblatt C. et al.* Persistence of intense, climate-driven runoff late in Mars history // *Science Advances*. 2019. V. 5. Iss. 3. Article eaav7710. DOI: 10.1126/sciadv.aav7.
- [2] *Mischna M. A., Baker V., Milliken R. et al.* Effects of obliquity and water vapor/trace gas greenhouses in the early Martian climate // *J. Geophysical Research: Planets*. 2013. V. 118. Iss. 3. P. 560–576. <https://doi.org/10.1002/jgre.20054>.
- [3] *Fastook J. L., Head J. W., Marchant D. R., Forget F.* Early Mars climate near the Noachian–Hesperian boundary: Independent evidence for cold conditions from basal melting of the south polar ice sheet (Dorsa Argentea Formation) and implications for valley network formation // *Icarus*. 2012. V. 219. Iss. 1. P. 25–40. <https://doi.org/10.1016/j.icarus.2012.02.013>.
- [4] *Harrison K. P., Grimm R. E.* Regionally compartmented groundwater flow on Mars // *J. Geophysical Research: Planets*. 2009. V. 114. Iss. E4. Article E04004. <https://doi.org/10.1029/2008JE003300>.
- [5] *Wordsworth R. D., Kerber L., Pierrehumbert R. T. et al.* Comparison of “warm and wet” and “cold and icy” scenarios for early Mars in a 3-D climate model // *J. Geophysical Research: Planets*. 2015. V. 120. Iss. 6. P. 1201–1219. DOI: 10.1002/2015JE004787.
- [6] *Halevy I., Head J. W.* Episodic warming of early Mars by punctuated volcanism // *Nature Geoscience*. 2014. V. 7. No. 12. P. 865–868. DOI: 10.1038/ngeo2293.
- [7] *McCleese D. J., Schofield J. T., Kass D. M. et al.* The Martian lower and middle atmosphere as observed by the Mars Climate Sounder // 4th Intern. Workshop on the Mars Atmosphere: Modelling and Observations. 2011. <https://www-mars.lmd.jussieu.fr/paris2011/>.

IMPACT-INDUCED HYDROTHERMAL CLAY FORMATION ON MARS — GEOMETRICAL EVIDENCE IN HOLDEN CRATER

J. Chu¹, M. A. Ivanov², A. M. Nikishin¹

¹ Lomonosov Moscow State University, Faculty of Geology
Moscow, Russia, vladimirchujun@yandex.ru

² Vernadsky Institute of Geochemistry and Analytical Chemistry RAS
Moscow, Russia, Mikhail_Ivanov@brown.edu

KEYWORDS:

Holden crater, impact, clay, hydrothermal system, volume

INTRODUCTION:

Clay-minerals on Mars is one of evidence of the existence of liquid water activity on Mars in ancient times; they likely indicate climate changes in the history of Mars. Impacts may provide energy for hydrothermal alteration of rocks, which is one of the causes of clay minerals formation [1–3]. There are typical clay-bearing layered outcrops in the southwest portion of Holden crater, which was formed during the transition from the Noachian to the Hesperian [4–6]. Its upper unit is the distal of alluvial fans forming from alcove serving as the source area at the rim of Holden crater [7]. If the energy released by the Holden impact process could promote the alteration of protoliths into clay minerals, then the content of clay-minerals in the alluvial fan could be greater than its content in the original area before the formation of the Holden crater (Figure 1, I).

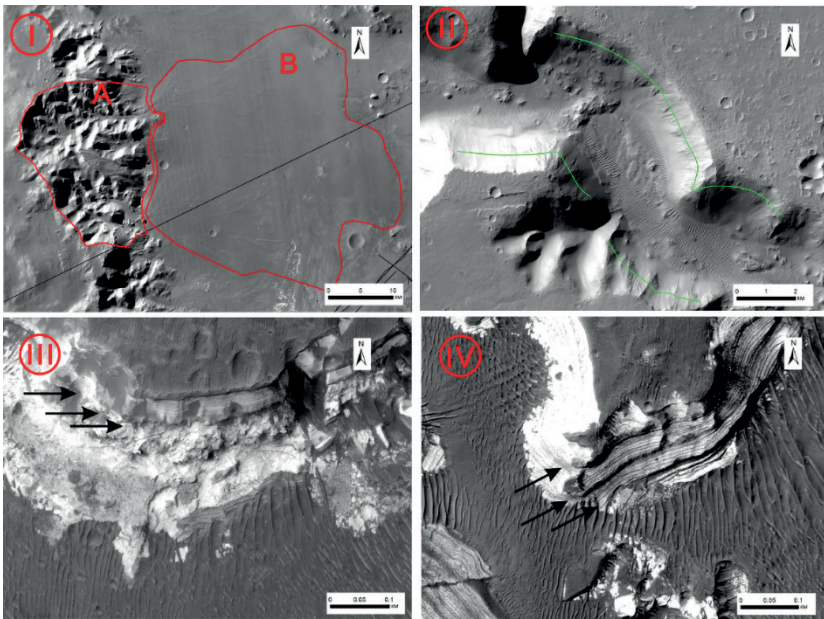


Figure 1. I — Study area, A — alcove at the rim, B — alluvial fan; II — Clay-bearing layer of Nigal Vallis, green lines indicate the subsurface of the clay-bearing layer; III — Southern outcrop of big trough in the SW part of Holden crater, arrows indicate the uncomfortable surface between the upper and lower units; IV — Northern outcrop of big trough in the SW part of Holden crater, arrows indicate three sequences of deposits

This study uses geometric modeling to qualitatively and semi-quantitatively assess the origin of clay minerals in layered deposits in Holden crater. Data of CTX, HiRISE and DTM derived from them, CRISM, MOLA were used.

ESTIMATED THICKNESS OF THE CLAY-BEARING LAYER TO THE WEST OF HOLDEN CRATER:

There are significant exposures of clay minerals on the wall of Nirgal Vallis (Figure 1, II), which cut through Noachian aged terrain to the southwest of the Holden crater [9]. The composition of clay minerals is Fe-Mg smectite, the clay-bearing layer is located above the gullies. So, we assume that the average thickness of the clay-bearing layer of Noachian aged highlands is 50 m as we measured.

GEOLOGIC CONTEXT AND STRATIGRAPHIC RELATIONSHIP OF HOLDEN CRATER:

The paleo-Holden Basin, Eberswalde Crater and Holden Crater were formed in the studied area. We chose the southwestern part of the rim of Holden crater and the alluvial fan inside it as the research object because the Holden impact event cuts through the Noachian highland material here and less effected by preformed paleo-Holden basin and Eberswalde crater (Figure 1, I). The alluvial fan from the west overlays the southern plain material, which has an absolute model age of 3.4 Ga and is the first deposit formed after the formation of Holden crater [10]. The average elevation of the southern plain is -2200 m [10], which is consistent with the unconformity between the layered light-toned upper unit and the non-layered lower unit [4–6] (Figure 1, III, black arrows). Therefore, we consider that all the materials above -2200 m elevation of alluvial fans are formed by materials eroded from alcove at the rim of Holden crater. The results of CRISM data analysis on the rim of Holden crater show that there are little Fe-Mg smectites remaining on its eroded surface, but abundance in low-calcium pyroxene, indicating that the alcove as the source area of alluvial fan has been cut down to the bedrock of highland material.

GEOMETRIC MODEL OF ALLUVIAL FAN AND ALCOVE AT THE RIM OF HOLDEN CRATER:

The geometric model of the Holden crater rim and alluvial fan are shown in Figure 2. R is the original rim of Holden crater when it was formed before erosion. AF is the bottom of alcove at the rim of Holden crater after erosion, which is the source area of the alluvial fan. AB is the surface of the alluvial fan, and BC is the contact surface between the alluvial fan and the southern plain at the bottom of Holden crater. Surface AA'C'C is the inner wall of Holden crater buried by the alluvial fan. We assume that it has not been extensively eroded since the formation of Holden crater. We choose the corresponding eastern edge of Holden crater for measurement, where there is no evidence for fluvial activity [10] and the original slope of crater rim can be preserved there. We got $\tan ACD = 0.21$. Based on the MOLA data and the elevation of the alluvial fan bottom selected as -2200 m, we measured and calculated the volume of the alluvial fan is 385.3 km^3 .

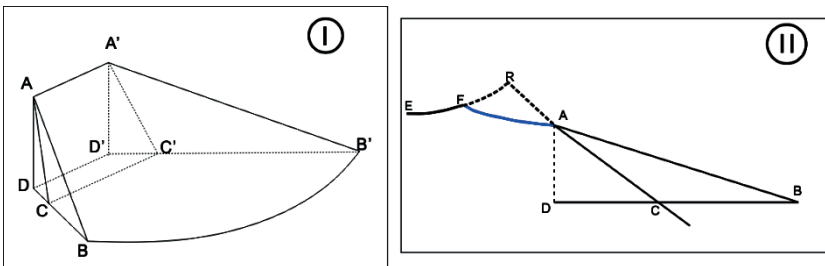


Figure 2. Geometric model of alluvial fan (I), and cross section of alluvial fan and alcove on the rim of Holden crater (II)

The material that formed the alluvial fan came from the alcove to the west at rim of Holden crater (A in Figure 1, I), which has an area of 402 km^2 (Figure 1, I, A). The thickness of the Noachian plateau clay layer measured above is 50 m. We assume that the clay content of this area is similar to that of Mawrth Vallis, which is to 70 % [12], so the volume of clay mineral

contained in the alcove area before the formation of Holden crater does not exceed 14 km^3 .

INTERNAL STRUCTURE OF ALLUVIAL FAN:

The northern part of the Big Trough in the SW portion of Holden crater is within the study area. The outcrop has peninsular-shaped profile (Figure 1, IV). There are three sequences of layered sediments (Figure 1, IV, back arrows). The grain size of each sequence becomes finer upward, indicating the type of alluvial fan is of progradation. We assume that the dark-toned coarse-grained particles are the materials of protolith, while the light-toned fine-grained particles are clay-bearing materials, and the volume ratio we measured is 1:5. We calculated that the volume of clay-bearing layers in the alluvial fan in our study area is 321 km^3 .

The inverted channels on the surface, the structure of clay-bearing layers and the source of material that formed the alluvial fan indicate the similar genesis with fan delta in Eberswalde crater [11]. F. Poulet et al. [12] determined that the clay minerals accounted for less than 25 % of the fan delta in Eberswalde crater, so we assumed that the volume of clay minerals in the alluvial fan in our study area does not exceed 80 km^3 .

DISCUSSION AND CONCLUSIONS:

Through geometric modeling, we found that the volume of clay minerals in the alluvial fan in the study area is about 80 km^3 , which is much greater than the clay content of about 14 km^3 that we estimated in the original strata before the formation of the Holden crater. Therefore, we suggest that the heat released by the Holden impact process caused the original material on the rim of the original Holden crater to be transformed into clay minerals due to hydrothermal processes, and the layered sediments of the alluvial fan in the Holden crater were formed under the action of later erosion. Although only the volume is calculated, and the sorting during the transportation of sediments and the diagenetic effects such as later compaction are not considered, our calculations also reflect the trend of clay content.

ACKNOWLEDGMENTS:

This work is supported by China Scholarship Council and represents a part of the state order of GEOKHI for MAL.

REFERENCES:

- [1] Newsom H.E. Hydrothermal alteration of impact melt sheets with implications for Mars // *Icarus*. 1980. Iss. 1. V. 44. P. 207-216. [https://doi.org/10.1016/0019-1035\(80\)90066-4](https://doi.org/10.1016/0019-1035(80)90066-4).
- [2] Allen C.C., Gooding J.L., Keil K. Hydrothermally altered impact melt rock and breccia: Contributions to the soil of Mars // *J. Geophysical Research: Solid Earth*. 1982. V. 87. Iss. B12. P. 10083–10101. <https://doi.org/10.1029/JB087iB12p10083>.
- [3] Du P., Yuan P., Liu J., et al. Clay minerals on Mars: An up-to-date review with future perspectives // *Earth-Science Reviews*. 2023. V. 243. Article 104491. DOI: 10.1016/j.earscirev.2023.104491.
- [4] Grant J.A., Parker T.J. Drainage evolution in the Margaritifer Sinus region, Mars // *J. Geophysical Research*. 2002. V. 107. Iss. E9. P. 4-1–4-19. <https://doi.org/10.1029/2001JE001678>.
- [5] Pondrelli M., Baliva A., Di Lorenzo S. et al. Complex evolution of paleolacustrine system on Mars: An example from the Holden crater // *J. Geophysical Research*. 2005. V. 110. Iss. E4. <https://doi.org/10.1029/2004JE002335>.
- [6] Grant J.A., Irwin P.R., III, Wilson S.A. Aqueous depositional settings in Holden crater, Mars // *Lakes on Mars*. 2010. P. 323–346. DOI: 10.1016/B978-0-444-52854-4.00012-X.
- [7] Moore M., Howard A.D. Large alluvial fans on Mars // *J. Geophysical Research: Planets*. 2005. V. 110. Iss. E4. <https://doi.org/10.1029/2004JE002352>.
- [8] Grant J.A., Irwin R.P., III, Wilson S.A. et al. A lake in Uzboi Vallis and implications for Late-Noachian-Early Hesperian climate on Mars // *Icarus*. 2011. V. 212. Iss. 1. P. 110–122. <https://doi.org/10.1016/j.icarus.2010.11.024>.
- [9] Wilson S.A., Grant A., Howard A.D., Buczkowski D.L. The Nature and Origin of Deposits in Uzboi Vallis on Mars // *J. Geophysical Research*. 2018. V. 123. Iss. 7. P. 1842–1862. <https://doi.org/10.1029/2017JE005508>.
- [10] Ivanov M.A., Hiesinger H. Topographic characteristics and chronology of the Uzboi-Ladon fluvial system on Mars // *The 11th Moscow Solar System Symposium 2020*.

- [11] *Huges C.M., Rice M.S., Barnhart C.J. et al.* Sources of Clay-rich Sediment in Eberswalde crater, Mars with Implications for Biopreservation Potential // *J. Geophysical Research*. 2023. V. 128. Iss. 4. Article e2022JE007545. <https://doi.org/10.1029/2022JE007545>
- [12] *Poulet F., Carter J., Bishop J.L. et al.* Mineral abundances at the final four curiosity study sites and implications for their formation // *Icarus*. 2014. V. 231. Iss. 1. P. 65–76. <https://doi.org/10.1016/j.icarus.2013.11.023>.

SOME MISCELLANEOUS FINDINGS IN THE SPICAM-IR SURFACE DATASET

A. Lomakin¹, A. Fedorova¹, V. Levashova¹, L. Verdier², O. Korablev¹,
F. Montmessin²

¹ Space Research Institute RAS, Moscow, Russia
aleksander.lomakin96@gmail.com

² LATMOS, UVSQ Université Paris-Saclay, Sorbonne Université, CNRS
Paris, France

KEYWORDS:

IR-spectroscopy, Mars, CO₂ ice, water ice, clouds, mineralogy

ABSTRACT:

SPICAM-IR is an near-infrared (1–1.7 μm) spectrometer on board the Mars-Express mission [1]. It is based on an acousto-optic tunable filter (AOTF), which results in a low-weight (0.8 kg), but high spectral resolution ($R \sim 1800\text{--}2200$). SPICAM-IR started observations in early 2004 and is still working as of August 2025, enlarging its more than 1.5 million nadir spectra dataset. While the main target of nadir observations has always been water vapor in the Martian atmosphere, it was recently exploited to characterize the seasonal and permanent polar caps, since both CO₂ and water ice spectra have diagnostic features in the instruments spectral range [2].

The data revealed that SPICAM-IR is also somewhat sensitive to the water ice clouds using the 1.5 μm water ice band, but discriminating between water ice clouds and surface frost remains challenging with SPICAM data alone. We will show the local time dependence of non-polar water ice detections and discuss the attribution to water ice clouds or surface water ice frost.

Another surface species that is possible to detect in that spectral region are hydrated minerals that have a 1.4 μm absorption band. While sequential scan of the wavelengths decreases detection reliability, spot-tracking observations are able to achieve consistent detections. We will show some selected spot-tracking observations and discuss further possible targets for these observations.

With over 20 years of continuous observations, SPICAM-IR offers unique opportunities for long-term studies. All of these miscellaneous findings may complement and validate findings of other instruments, especially in the case of co-located instruments (OMEGA, SPICAM-UV).

REFERENCES:

- [1] Korablev O., Bertaux J.-L., Fedorova A. et al. SPICAM IR acousto-optic spectrometer experiment on Mars Express // *J. Geophysical Research*. 2006. V. 111. Iss. E9. Article E09S03. <https://doi.org/10.1029/2006JE002696>.
- [2] Lomakin A.A., Fedorova A.A., Berdis J.R. et al. Nine Martian Years of polar caps observations by SPICAM-IR. 2022. Preprint. <https://doi.org/10.1002/essoar.10512788.1>

EFFECT ON THE CHANDLER WOBBLE PERIOD OF MARS BY MANTLE MINERALOGY AND TEMPERATURE PROFILE

E. A. Kulik¹, T. V. Gudkova²

¹ *Moscow Institute of Physics and Technology (National Research University) Dolgoprudny, Russia, kulik.ea@ifz.ru*

² *Schmidt Institute of Physics of the Earth RAS, Moscow, Russia gudkova@ifz.ru*

KEYWORDS:

Mars, Chandler wobble period, mantle mineralogy, areoterm, tidal Love numbers, Andrade rheology

INTRODUCTION:

Seismic experiment on Mars by InSight mission has provided the scientific community by new valuable data, such as the crust density and thickness, the core radius and the thickness of melt layer at the bottom of the mantle. Nevertheless the mineralogy of Mars is under discussion. Chandler Wobble (CW) period is an important parameter, which can provide additional constraint on the structure of Mars. CW for Mars was recently detected. Its value is 206.9 ± 0.5 days [1].

MODELING OF THE MANTLE MINERALOGY:

ix different composition models were chosen: DW85 [2], MA79 [3], T13 [4], LF97 [5], S99 [6] and KC08 [7]. Mineralogy of Martian mantle was modeled by using program *Perple_X*, which is an open-source software (<https://www.perplex.ethz.ch/>). This software provides density, seismic velocities profiles and mineralogy distribution in the mantle.

CALCULATING CHANDLER WOBBLE PERIOD OF MARS:

With the mantle profiles that were obtained in the previous step, the profiles in the whole planet's interior are calculated by using the method from [8]. Andrade rheology was used to account for inelasticity. In order to investigate the effect of the mantle mineralogy and chosen temperature profiles only, parameters of the rheology are fixed at the values: $\alpha = 0.3$, $\eta_0 = 10^{21}$ Pa·s, $\eta_m = 10^9$ Pa·s.

RESULTS:

Models of the internal structure of Mars were constructed for different chemical composition models while varying crust density and thickness, core radius and core density. They were selected by their accordance to the observable values of Love number k_2 , and moment of inertia. Figure 1 represents the process of selection for DW85 model.

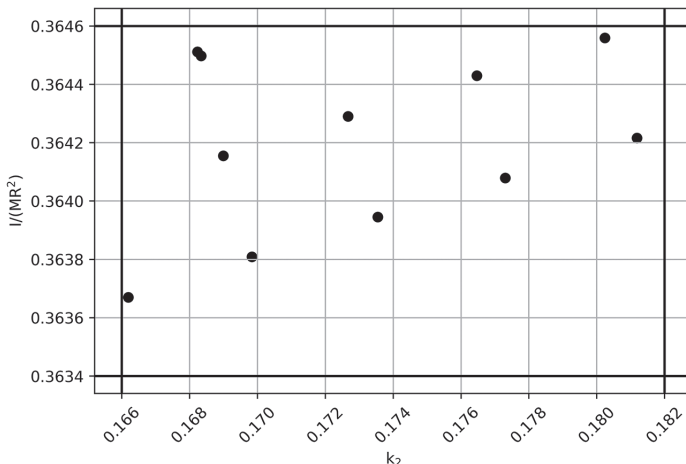


Figure 1. Selection of Martian internal structure models for DW85 chemical model

In order to analyze the difference in CW period values models with close values of Love number and moment of inertia were chosen (Table 1). The models with MA79 composition do not satisfy the moment of inertia and the Love number k_2 .

Table 1. Constructed models and their parameters for DW85, T13, LF97, S99 and KC08 chemical composition models

	DW85	T13	LF97	S99	KC08
Crust thickness, km	70	65	40	40	50
Crust density, kg/m ³	2700	2700	2700	2700	2700
Core radius, km	1685	1688	1684	1678	1687
Moment of inertia I/MR^2	0.36395	0.36396	0.36398	0.36392	0.36395
Love number k_2	0.1735	0.1744	0.1732	0.1734	0.1746
CW period, days	211.6	211.9	211.7	210.4	211.6

According to the obtained results, model values of CW period for inelastic Love number k_2 are in the range 210.4–211.9 days while CW period for elastic k_2 is in the range 200.5–200.9 days. Recently, by numerical simulation authors of [9] have found that in the formula for CW the value between elastic and inelastic Love number k_2 should be used. This brings a little uncertainty in obtaining theoretical CW period and additional investigations on this issue should be made. Nevertheless, it does not reject the results of the effect of mantle mineralogy and temperature profile on CW period.

ACKNOWLEDGMENTS:

This work was carried out under a State Assignment of the Schmidt Institute of Physics of the Earth, Russian Academy of Sciences.

REFERENCES

- [1] *Konopliv A. S., Park R. S., Rivoldini A. et al.* Detection of the Chandler wobble of Mars from orbiting spacecraft // *Geophysical Research Letters*. 2020. V. 47. Iss. 21. Article e2020GL090568. <https://doi.org/10.1029/2020GL090568>.
- [2] *Dreibus G., Wanke H.* Mars, a volatile-rich planet // *Meteoritics*. 1985. V. 20. P. 367–381.
- [3] *Morgan J. W., Anders E.* Chemical composition of Mars // *Geochimica et Cosmochimica Acta*. 1979. V. 43. Iss. 10. P. 1601–1610. [https://doi.org/10.1016/0016-7037\(79\)90180-7](https://doi.org/10.1016/0016-7037(79)90180-7).
- [4] *Taylor G. J.* The bulk composition of Mars // *Chemie der Erde-Geochemistry*. 2013. V. 73. P. 401–420. <https://doi.org/10.1016/j.chemer.2013.09.006>.
- [5] *Lodders K., Fegley B., Jr.* An oxygen isotope model for the composition of Mars // *Icarus*. 1997. V. 126. Iss. 2. P. 373–394. <https://doi.org/10.1006/icar.1996.5653>.
- [6] *Sanloup C., Jambon A., Gillet P.* A simple chondritic model of Mars // *Physics of the Earth and Planetary Interiors*. 1999. V. 112. Iss. 1–2. P. 43–54. [https://doi.org/10.1016/S0031-9201\(98\)00175-7](https://doi.org/10.1016/S0031-9201(98)00175-7).
- [7] *Khan A., Connolly J. A. D.* Constraining the composition and thermal state of Mars from inversion of geophysical data // *J. Geophysical Research: Planets*. 2008. V. 113. Iss. E7. Article E07003. <https://doi.org/10.1029/2007JE002996>.
- [8] *Kulik E. A., Gudkova T. V.* Influence of mantle inelasticity on the model value of the Chandler wobble period of Mars // *Solar System Research*. 2024. V. 58. Iss. 6. P. 650–660. DOI: 10.1134/S0038094624700497.
- [9] *Patočka V., Walterová M.* Formula for the Chandler period (free wobble of planetary bodies) // *Geophysical Research Letters*. 2025. V. 52. Iss. 8. Article e2024GL112997. <https://doi.org/10.1029/2024GL112997>.

SESSION 1. MARS (MS-PS)
POSTER SESSION

NON-HYDROSTATIC STRESSES IN THE INTERIORS OF MARS EXCLUDING LONG-WAVE COMPONENT

A.V. Batov^{1,2}, T.V. Gudkova¹

¹ *Schmidt Institute of Physics of the Earth RAS, Moscow, Russia*
gudkova@ifz.ru

² *Trapeznikov Institute of Control Sciences RAS, Moscow, Russia*
batov@ipu.ru

KEYWORDS:

Mars, gravity, topography, long-wave component, stress state, epicenters of marsquakes

INTRODUCTION:

There was only one seismic station on the InSight mission [1]. The determination of the coordinates and depth of the marsquakes were performed with great uncertainty, represented by ellipsoidal probability density functions [2]. The nature of Martian seismic activity is uncertain. Many marsquakes are thought to be triggered by seismic sources such as faults or cracks. As shown in [3], the gravitational potential of Mars is largely determined by long-wave components and mainly reflects the influence of a massive regional anomaly — the Tharsis bulge. At depths of 100–200 km the predominant contribution to the general stress state is made by the short-wave part of the gravitational field, while long-wave components do not allow localizing stresses associated with specific geological formations. Here we show that global compression and stretching created by the Tharsis zone is not the dominant process.

MARSQUAKE LOCATION DATA:

The main source of information is the Mars Seismic Catalog [4], which includes 2715 events. However, the coordinates of the epicenters (latitude, longitude) are indicated only for 24 of them. We extracted additional information from [2], which provides a table of locations for 31 seismic events (29 marsquakes and 2 meteorite impacts). The work [5] contains a table with locations of 24 marsquakes and 2 impacts, including 6 events in the southern hemisphere, in the Terra Cimmeria area. Even taking into account the high error of location, stable spatial patterns can be distinguished. Most events are concentrated in the area of Cerberus Fossae, where both high levels of tensile and shear stresses are observed. Figures 1 and 2 show the most likely epicenters of marsquakes from different data sources. The colors of the stars correspond to the used catalogs and localization models: white — [4], green — model 1D [2], pink — model 3D Family A, orange — model 3D Family B (both from [2]), blue — [5].

NUMERICAL STRESS MODELING:

The method was detailed in [6]. Non-hydrostatic stresses in the interior of Mars were calculated without taking into account the long-wave component. The numerical solution of the system of elastic equilibrium equations for a gravitating planet was carried out on a grid with a resolution of $1 \times 1^\circ$ in latitude and longitude. As boundary conditions, data on the topography [7] and gravitational field [8] were used. The topography and gravitational field data were determined in relation to the equilibrium spheroid [3]. To eliminate the influence of the Tharsis uplift, summation of spherical harmonics starting from the 7th degree was used. The basis for the calculations was a test interior structure model of Mars from [9], in which the average thickness of the crust was taken equal to 50 km (with a density of 2900 kg/m^3 and a core radius of 1821 km), satisfying the data obtained from the seismic experiment.

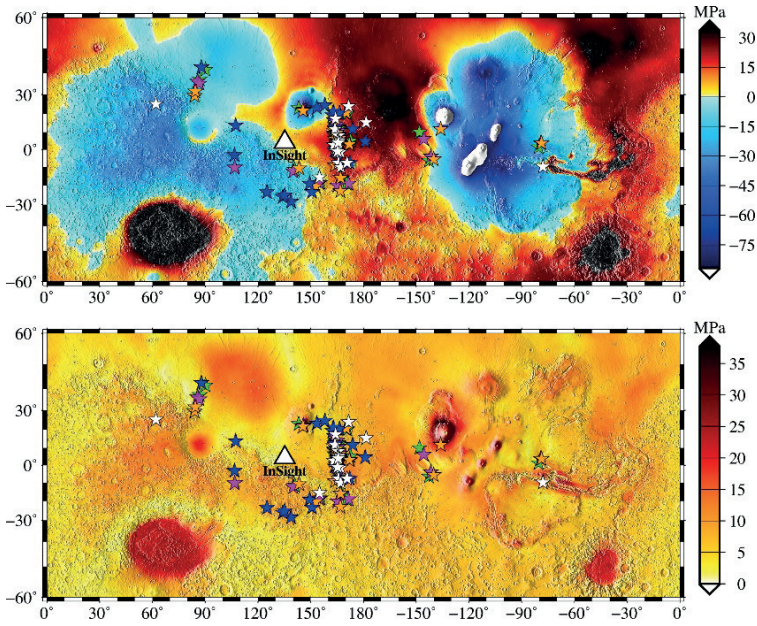


Figure 1. Distribution of model non-hydrostatic stresses in the Martian crust at a depth of 25 km, taking into account the influence of Tharsis: above — tension-compression stresses, below — shear stresses (in MPa). Legend: Δ — location of the seismic receiver; \star — epicenters of recorded marsquakes

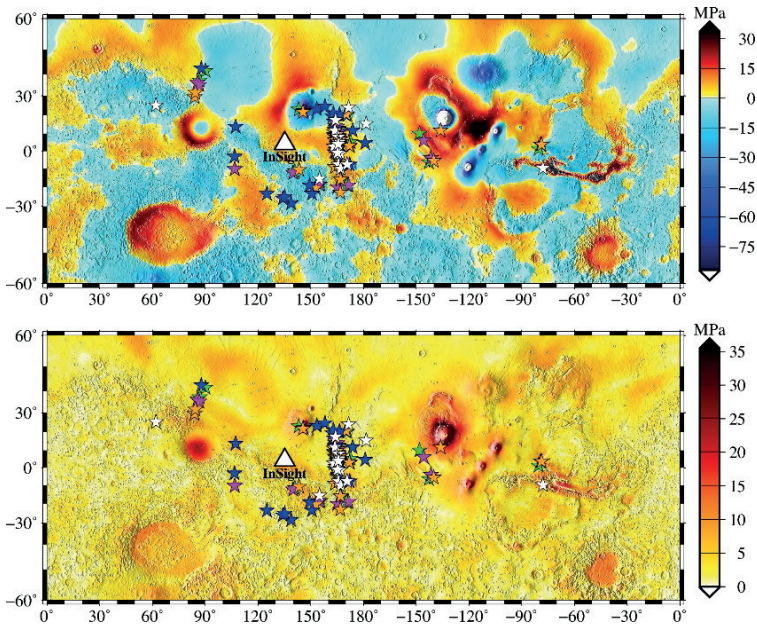


Figure 2. Distribution of model non-hydrostatic stresses in the Martian crust at a depth of 25 km without taking into account the long-wave component: above — tension-compression stresses, below — shear stresses (in MPa). Legend: Δ — location of the seismic receiver, \star — epicenters of recorded marsquakes

RESULTS:

Figures 1 and 2 show stress maps with and without influence of the Tharsis uplift. It is clearly seen that in some areas the tensile stresses change to compressive ones. So, for example, new tensile zones appear within the Tharsis plateau, while between Tharsis and the Elysium volcano, a compression region is formed that was absent earlier. Nevertheless, the main

zone of marsquakes in the area of Cerberus Fossae is preserved in the area of increased tensile and shear stresses, which may serve as an additional criterion in assessing localization models. The centers of the three marsquake areas according to data [2] are on the north of the Isidis Planitia correspond to the tensile region in the model without the influence of Tharsis. At the same time, the cluster identified in [5] is located in the compressive stress zone, which may indicate the need for further refinement of the interior structure model, taking into account the separate density structure of the northern and southern hemispheres, as assumed in [10] when building a model of the thickness of the crust.

CONCLUSION:

We have presented the distributions of non-hydrostatic stresses in the interiors of Mars without taking into account the long-wave component based on a joint interpretation of topography data and the non-equilibrium part of the gravitational field. The results of modeling non-hydrostatic stresses in the interiors of Mars starting from the 7th harmonic are compared with the locations of the marsquake foci obtained during the InSight seismic experiment. Significant shear stresses in the tensile zones, which are not due to the global influence of the Tharsis uplift, correlate well with the identified epicenters of marsquakes.

ACKNOWLEDGMENTS:

This work is financially supported by Budget funding of Schmidt Institute of the Earth RAS.

REFERENCES:

- [1] *Lognonné P., Banerdt W. B., Giardini D. et al.* SEIS: Insight's Seismic Experiment for Internal Structure of Mars // *Space Science Reviews*. 2019. V. 215(1). Article 12. DOI: 10.1007/s11214-018-0574-6.
- [2] *Drilleau M., Samuel H., Garcia R.F. et al.* Constraints on lateral variations of Martian crustal thickness from seismological and gravity field measurements // *Geophysical Research Letters*. 2024. V. 51. Article e2023GL105701. <https://doi.org/10.1029/2023GL105701>.
- [3] *Zharkov V.N., Gudkova T.V.* On the model Structure of the gravity field of Mars // *Solar System Research*. 2016. V. 50(4). P. 235–250. DOI: 10.1134/S0038094616040079.
- [4] *Mars Seismic Catalogue, InSight Mission; V14 2023-04-01 / ETHZ, IPGP, JPL, ICL, Univ. Bristol*. 2023. <https://doi.org/10.12686/a21>.
- [5] *Sun W., Tkalčić H.* Repetitive marsquakes in Martian upper mantle // *Nature Communications*. 2022. V. 13(1). Article 1695. DOI: 10.1038/s41467-022-29329-x.
- [6] *Batov A. V., Gudkova T. V., Zharkov V. N.* Nonhydrostatic stress state in the Martian interior for different rheological Models // *Izvestiya Physics of the solid Earth*. 2019. V. 55. No. 4. P. 688–700. DOI: 10.1134/S1069351319040025.
- [7] *Smith D. E., Zuber M. T., Frey H. V. et al.* Mars Orbiter Laser Altimeter: Experimental summary after the first year of global mapping of Mars // *J. Geophysical Research*. 2001. V. 106. Iss. E10. P. 23689–23722. <https://doi.org/10.1029/2000JE001364>.
- [8] *Konopliv A. S., Park R. S., Folkner W. M.* An improved JPL Mars gravity field and orientation from Mars orbiter and lander tracking data // *Icarus*. 2016. V. 274. P. 253–260. <https://doi.org/10.1016/j.icarus.2016.02.052>.
- [9] *Gudkova T.V., Batov A.V., Zharkov V.N.* Model estimates of non-hydrostatic stresses in the Martian crust and mantle: 1. Two-level model // *Solar System Research*. 2017. V. 51. Iss. 6. P. 457–478. DOI: 10.1134/S003809461706003X.
- [10] *Wieczorek M. A., Broquet A., McLennan S. M. et al.* InSight constraints on the global character of the Martian crust // *J. Geophysical Research: Planets*. 2022. V. 127. Iss. 5. Article e2022JE007298. <https://doi.org/10.1029/2022JE007298>.

PERCHLORATE RADIOLYSIS UNDER SIMULATED MARTIAN CONDITIONS

V. S. Cheptsov^{1,2}, A. Yu. Merkulova³, T. N. Lubkova⁴, O. D. Filatova⁴,
A. K. Pavlov³, O. Yu. Drozdova⁴, A. E. Chumikov², V. N. Lomasov⁵

¹ Space Research Institute of RAS, Moscow, Russia

² Lomonosov Moscow State University, Soil Science Faculty, Moscow, Russia
cheptcov.vladimir@gmail.com

³ Ioffe Physical-Technical Institute, Saint Petersburg, Russia

⁴ Lomonosov Moscow State University, Faculty of Geology, Moscow, Russia

⁵ Peter the Great Saint Petersburg Polytechnic University
Saint Petersburg, Russia

KEYWORDS:

GCR, ionizing radiation, sodium perchlorate, Mars, regolith

INTRODUCTION:

Perchlorate anions are found in Martian regolith in concentrations of about 0.6 wt. % [1]. Their salts have a great importance from astrobiological point of view, since they have high hygroscopicity, and perchlorate-containing brines have low freezing temperatures [2]. So, they probably can promote liquid water formation on the Mars. Some perchlorates are characterized with high solubility, and their distribution in the regolith can shed light on the water cycle of the planet [3, 4]. Due to it understanding of perchlorate origin, transformation and destruction under Martian conditions is needed.

Martian surface is subjected to intense irradiation by ionizing radiation, and it can lead to the perchlorate destruction. There are some studies of this process, estimated effectiveness of these process and perchlorate radiolysis products. In particular, for a pure perchlorate salts it was shown that $G(-\text{ClO}_4^-)$ varies from ~0.8 to ~4.5 molecules/100 eV [5, 6]. There are inconsistencies between studies showing presence or absence of differences in radiolysis effectiveness due to temperature change, and different G-values and sets of radiolysis products for rather similar irradiation conditions [6–9]. Moreover, there is lack of data on perchlorate destruction within any regolith relevant matrix [10].

MATERIALS AND METHODS:

We performed irradiation of sodium perchlorate containing samples by accelerated electrons (~1 MeV) under low pressure (0.01 Torr) and low temperature (–140 °C) conditions with doses of 7.6, 12, and 19.6 MGy. Four compositions were studied:

- 1) pure anhydrous NaClO_4 ;
- 2) water solution of NaClO_4 , 30 % wt/v;
- 3) dry mixture of quartz sand (90 %) and NaClO_4 (10 %);
- 4) mixture of quartz sand (70 %) and 30 % (wt/v) water solution of NaClO_4 (30 %).

Absorbed doses were calculated using NISTESTAR. After irradiation we have measured ClO_4^- anions concentrations in the samples via potentiometry with perchlorate-selective electrode and analyzed ClO_4^- , ClO_3^- , ClO_2^- , and Cl^- via capillary electrophoresis with spectrophotometric detection.

RESULTS:

It was found, that after irradiation with the highest dose (19.6 MGy, which is equal to about $8.8 \cdot 10^{22}$ eV/g) about 12, 5.5, 30, and 9 % of perchlorate was destructed in the samples of composition 1, 2, 3, and 4, respectively. So, the environment significantly affected perchlorate radiolysis: in the presence of quartz sand the lower stability of perchlorate was observed, while in presence of water the lower proportion of perchlorate was destructed. $G(-\text{ClO}_4^-)$ was depending on irradiation dose, and with the dose increase for pure NaClO_4 it linearly declined from ~1 to ~0.7; for the dry mixture of sand and perchlorate — linearly declined from ~0.25 to ~0.18. At the water presence, G-value dependence was not linear — the lowest G-values were

observed after 7.6 MGy irradiation (~0.04 and 0.014 for the NaClO₄ solution and the mixture of sand with solution, respectively). With higher doses they increased and were similar between 12 and 19.6 MGy (~0.09 and ~0.05 for two compositions above, respectively). Among radiolysis products, chlorate anions were found, while chlorite and chloride were not detected. The data obtained can be used for modelling of the perchlorate cycle on Mars.

ACKNOWLEDGMENTS:

The study is funded by Russian Science Foundation, project No. 24-72-00004 (<https://rscf.ru/en/project/24-72-00004/>). Capillary electrophoresis with spectrophotometric detection was performed using CES "Kapel-205" equipment, acquired under the MSU Development Program.

REFERENCES:

- [1] *Hecht M. H., Kounaves S. P., Quinn R. C. et al.* Detection of perchlorate and the soluble chemistry of Martian soil at the Phoenix lander site // *Science*. 2009. V. 325. Iss. 5936. P. 64–67. DOI: 10.1126/science.1172466.
- [2] *Cheptsov V., Belov A., Soloveva O. et al.* Survival and growth of soil microbial communities under influence of sodium perchlorates // *Intern. J. Astrobiology*. 2021. V. 20. Iss. 1. P. 36–47. DOI: 10.1017/S1473550420000312.
- [3] *Marion G. M., Catling D. C., Zahnle K. J., Claire M. W.* Modeling aqueous perchlorate chemistries with applications to Mars // *Icarus*. 2010. V. 207. Iss. 2. P. 675–685. <https://doi.org/10.1016/j.icarus.2009.12.003>.
- [4] *Gough R., Chevrier V., Baustian K. et al.* Laboratory studies of perchlorate phase transitions: Support for metastable aqueous perchlorate solutions on Mars // *Earth and Planetary Science Letters*. 2011. V. 312. Iss. 3–4. P. 371–377. <https://doi.org/10.1016/j.epsl.2011.10.026>
- [5] *Prince L. A., Johnson E. R.* The Radiation—Induced Decomposition of the Alkali and Alkaline Earth Perchlorates. I. Product Yields and Stoichiometry 1a // *The Journal of Physical Chemistry*. 1965. V. 69. Iss. 2. P. 359–377. <https://doi.org/10.1021/j100886a002>.
- [6] *Turner A. M., Abplanalp M. J., Kaiser R. I.* Mechanistic studies on the radiolytic decomposition of perchlorates on the Martian surface // *The Astrophysical J.* 2016. V. 820. Iss. 2. Article 127. DOI: 10.3847/0004-637X/820/2/127.
- [7] *Prince L. A., Johnson E. R.* The radiation—Induced decomposition of the alkali and alkaline earth perchlorates. II. Mechanism of the decomposition 1a // *The J. Physical Chemistry*. 1965. V. 69. Iss. 2. P. 377–384. <https://doi.org/10.1021/j100886a003>.
- [8] *Gobi S., Bergantini A., Kaiser R. I.* In situ detection of chlorine dioxide (ClO₂) in the radiolysis of perchlorates and implications for the stability of organics on Mars // *The Astrophysical J.* 2016. V. 832. Iss. 2. Article 164. 6 p. DOI: 10.3847/0004-637X/832/2/164.
- [9] *Konstantatos J., Katakis D.* Radiolysis of concentrated neutral sodium perchlorate aqueous solutions // *The J. Physical Chemistry*. 1967. V. 71. Iss. 4. P. 979–983. <https://doi.org/10.1021/j100863a033>.
- [10] *Martin P. E., Farley K. A., Douglas Archer Jr, Pet al.* Reevaluation of perchlorate in Gale Crater rocks suggests geologically recent perchlorate addition // *J. Geophysical Research: Planets*. 2020. V. 125. Iss. 2. Article e2019JE006156. <https://doi.org/10.1029/2019JE006156>.

DEEP LEARNING FOR HYPERSPECTRAL UNMIXING OF CRISM DATA: APPLICATION TO MINERAL MAPPING ON MARS

E. D. Faber

Federal Scientific Clinical Center of Space Medicine and Biology FMBA of Russia, faber.cat.rina@gmail.com

KEYWORDS:

hyperspectral unmixing, CRISM, Mars, deep learning, convolutional neural networks, autoencoders, mineral mapping, hydrated silicates

INTRODUCTION:

This ongoing study develops deep learning methodologies for enhanced spectral unmixing of CRISM (Compact Reconnaissance Imaging Spectrometer for Mars) hyperspectral data to advance automated mineral identification on Mars. The research addresses critical limitations in traditional unmixing approaches by leveraging convolutional neural networks (CNNs) and autoencoder architectures to analyze raw CRISM spectra in conjunction with laboratory spectral libraries [1].

METHODOLOGY:

This approach integrates multiple deep learning architectures optimized for hyperspectral unmixing tasks. 1D CNNs was implemented and specifically designed for spectral feature extraction from CRISM's 489-channel targeted observations, focusing on the diagnostic spectral regions for hydrated minerals (1.4, 1.9, and 2.3 μm absorption features) [2]. The CNN architecture incorporates dilated convolutions to capture multi-scale spectral patterns while maintaining computational efficiency.

Complementary autoencoder networks are developed for endmember extraction and abundance estimation. The encoder learns compressed representations of mixed spectra, while the decoder reconstructs pixel spectra as linear combinations of endmember signatures constrained by spectral libraries. In this work I employ the USGS Spectral Library Version 7 convolved to CRISM spectral resolution, supplemented by laboratory spectra of Mars-relevant minerals including phyllosilicates, sulfates, and iron oxides. A hybrid CNN-autoencoder architecture combines the strengths of both approaches: CNN layers extract local spectral features, while autoencoder components perform global spectral unmixing [3]. Attention mechanisms are integrated to weight spectral channels based on their diagnostic value for specific mineral phases.

TARGET MINERALS AND GEOLOGICAL CONTEXT:

The research specifically targets minerals indicative of past aqueous activity on Mars, including hydrated silicates (smectite clays, chlorite, serpentine) and sulfates (jarosite, alunite, gypsum). These phases are critical for understanding Mars' climatic evolution and habitability potential. Focusing on CRISM data from regions with confirmed hydrated mineral detections, including Jezero Crater and Nili Fossae.

TECHNICAL IMPLEMENTATION:

Data preprocessing utilizes the CRISM Analysis Toolkit (CAT) for atmospheric correction and photometric normalization while preserving original spectral information. Synthetic mixing models to generate training datasets were employed with known endmember compositions, addressing the limited ground truth availability for Martian surfaces [4]. The network architectures are optimized for computational efficiency while maintaining spectral fidelity.

CONCLUSIONS:

This research aims to develop automated pipelines for mineral abundance mapping that reduce processing time compared to traditional methods while improving robustness to spectral variability caused by atmospheric effects, particle size variations, and intimate mineral mixing. The approach

addresses current limitations in scaling mineral mapping to CRISM's extensive global dataset.

The developed methodologies will enable systematic analysis of Mars' hydrated mineral inventory, supporting geological interpretations of past environmental conditions and identification of targets for future sample return missions.

REFERENCES:

- [1] *Lin Qi, Jie Li, Ying Wang et al.* Deep spectral convolution network for hyperspectral image unmixing with spectral library // *Signal Processing*. 2020. V. 176. P. 107–115. <https://doi.org/10.1016/j.sigpro.2020.107672>.
- [2] *Viviano-Beck C. E., Seelos F. P., Murchie S. L. et al.* Revised CRISM spectral parameters and summary products based on the currently detected mineral diversity on Mars // *J. Geophysical Research: Planets*. 2014. V. 119. Iss. 6. P. 1403–1431. <https://doi.org/10.1002/2014JE004627>.
- [3] *Palsson B., Sigurdsson J., Sveinsson J. R.* Hyperspectral Unmixing Using a Neural Network Autoencoder // *IEEE Access*. 2018. V. 6. P. 25646–25656. DOI: 10.1109/ACCESS.2018.2818280.
- [4] *Plebani E., Ehlmann B. L., Leask E. K. et al.* A machine learning toolkit for CRISM image analysis // *Icarus*. 2022. V. 376. Article 114849. <https://doi.org/10.1016/j.icarus.2021.114849>.

EFFECT OF SODIUM PERCHLORATE ON SOIL PROKARYOTIC COMPLEXES UNDER LIMITED AVAILABLE MOISTURE CONDITIONS

V. S. Cheptsov^{1,2}, P. M. Sazonova¹, A. A. Belov¹

¹ Space Research Institute RAS, Moscow, Russia
cheptcov.vladimir@gmail.com

² Lomonosov Moscow State University, Soil Science Faculty, Moscow, Russia
sazonova.polina.5555@gmail.com

KEYWORDS:

Mars, bacteria, regolith, soil, perchlorate effect, available moisture deficiency

INTRODUCTION:

It has been established that perchlorate, a compound widespread globally in Martian regolith [3], could be one of primary inhibitors of microbial growth. However, in addition to their inhibitory effect, perchlorates have the capacity to absorb water vapor, resulting in the formation of a saturated solution and the expansion of the range of temperature conditions at which liquid water exists [2, 4]. However, due to the instability of liquid solutions under Martian conditions [1], the assessment of perchlorates influence on organisms under conditions of available moisture deficit is the most relevant.

In this study, we examined the impact of sodium perchlorate on the abundance and potential metabolic activity of soil microorganisms under conditions of liquid water deficit in a model experiment.

EXPERIMENT:

A sample of lithic leptosol obtained from the southern region of the Tenerife Island, along with pure cultures of bacteria *Bacillus subtilis* B-9865 and *Deinococcus radiodurans* VKM B-1422¹ immobilized on kaolinite, served as the objects of this study. For the experiment, soil sample (TT4) and cultures were amended with anhydrous sodium perchlorate or sodium chloride at concentrations of 0.8M (~4.8 %) and 2M (~11.9 %) NaCl and 0.8M (~10 %) and 2M (~25 %) NaClO₄. Subsequent to the addition of these substances, the samples were placed in vials and stored in desiccators containing anhydrous copper sulfate as a desiccant. The desiccators were further subjected to a 24-month incubation period at ambient temperature. A soil sample without salt addition was used as control.

The abundance of cultured heterotrophic bacteria was estimated using the plating method on R2A (for the soil sample) and R3A (for cultures) media [5]. The total number of culturable bacteria for the control sample was approximately $6.3 \cdot 10^7$ CFU/g, which remained constant for the sample with the addition of 0.8M sodium perchlorate. However, it decreased to $2.2 \cdot 10^7$ CFU/g for the sample with the addition of 2M sodium perchlorate. The abundance decreased to $3.5 \cdot 10^7$ CFU/g at addition of 0.8M sodium chloride and increased to $1.0 \cdot 10^8$ CFU/g in the soil with 2M of sodium chloride.

The total bacterial abundance in soil samples was determined by epifluorescence microscopy and was $6.1 \cdot 10^8$ cells/g for the control sample. The total cells count in soils with 0.8M and 2M perchlorate added decreased to $3.2 \cdot 10^8$ and $3.4 \cdot 10^8$ cells/g, respectively. For the sample with 0.8M sodium chloride, the abundance remained constant and decreased to $3.7 \cdot 10^8$ cells/g for the variant with 2M sodium chloride.

Moreover, a general decrease in morphological diversity of cultured bacteria was observed in the incubated samples. Representatives of the *Luteimonas* and *Stenotrophomonas* genera were identified as dominants.

Multi-substrate testing revealed the preservation of high functional diversity after incubation for all soil samples, as well as a decrease in potential metabolic activity in the presence of sodium perchlorate and its increase in the presence of 2M sodium chloride.

The bacterial abundance in the control kaolinite samples with a *B. subtilis* culture was found to be approximately $8.0 \cdot 10^8$ CFU/g. However, for samples with 0.8 and 2M perchlorate the abundance decreased to $5.8 \cdot 10^8$ and $3.7 \cdot 10^8$ CFU/g, respectively. For samples with 0.8 and 2M of sodium chloride, the abundance decreased to $2.4 \cdot 10^8$ and $3.2 \cdot 10^8$ CFU/g, respectively.

Incubation of the kaolinite samples containing *D. radiodurans* culture resulted in the absence of viable microorganisms.

Conclusion:

Presence of perchlorates in Martian regolith, in the absence of available water, is not a factor that strictly limits the preservation of microorganisms between periods of liquid water formation, but it can affect the viability of microorganisms. Consequently, the influence of this factor must be considered when constructing astrobiological models and evaluating the potential for preserving and/or detecting life and/or its traces in the Martian regolith.

ACKNOWLEDGMENTS:

The study was conducted under the state assignment of Lomonosov Moscow State University and was partially supported by Ministry of Education and Science of the Russian Federation, topic no. 122012400153 (in terms of data analysis).

REFERENCES:

- [1] Diaz B., Schulze-Makuch D. Microbial survival rates of *Escherichia coli* and *Deinococcus radiodurans* under low temperature, low pressure, and UV-irradiation conditions, and their relevance to possible Martian life // *Astrobiology*. 2006. V. 6. No. 2. P. 332–347. DOI: 10.1089/ast.2006.6.332.
- [2] Gough R. V., Chevrier V. F., Tolbert M. A. Formation of liquid water at low temperatures via the deliquescence of calcium chloride: Implications for Antarctica and Mars // *Planetary and Space Science*. 2016. V. 131. P. 79–87. <https://doi.org/10.1016/j.pss.2016.07.006>.
- [3] Hecht M. H., Kounaves S. P., Quinn R. C. et al. Detection of perchlorate and the soluble chemistry of Martian soil at the Phoenix lander site // *Science*. 2009. V. 325. No. 5936. P. 64–67. DOI: 10.1126/science.1172466.
- [4] Möhlmann D., Thomsen K. Properties of cryobrine on Mars // *Icarus*. 2011. V. 212. Iss. 1. P. 123–130. <https://doi.org/10.1016/j.icarus.2010.11.025>.
- [5] Reasoner D. J., Geldreich E. E. A new medium for the enumeration and subculture of bacteria from potable water // *Applied and environmental microbiology*. 1985. V. 49. No. 1. P. 1–7. DOI: 10.1128/aem.49.1.1-7.1985.

CO-LOCATED SPICAM-IR AND OMEGA OBSERVATIONS OF MARTIAN POLAR CAPS

A. Lomakin¹, V. Levashova¹, L. Verdier², A. Fedorova¹

¹ Space Research Institute RAS, Moscow, Russia
aleksander.lomakin96@gmail.com

² LATMOS, UVSQ Université Paris-Saclay, Sorbonne Université, CNRS
Paris, France

KEYWORDS:

Mars, polar caps, CO₂ ice, H₂O ice, ice spectroscopy, cross-validation, IR-spectroscopy

INTRODUCTION:

SPICAM-IR is an acousto-optical tunable filter spectrometer onboard Mars Express (MEX), operating in the 1.0–1.7 μm range with high spectral resolution ($\lambda/\Delta\lambda \approx 2000$), capable of detecting narrow CO₂ and H₂O ice absorptions [1]. OMEGA is an imaging spectrometer onboard MEX covering 0.36–5.09 μm with hyperspectral mapping capabilities, enabling large-scale seasonal monitoring of Martian polar caps [2, 3]. Their strengths — SPICAM-IR's spectral resolution and OMEGA's broad spectral range and mapping capabilities complement each other in joint analysis in co-located observations.

JOINT OBSERVATIONS:

We compiled a dataset of co-located SPICAM-IR and OMEGA observations over the Martian Polar Regions, matched by solar longitude, local time, and footprint geometry. This enables direct spectral comparison in overlapping ranges, linking OMEGA's spatial detail with SPICAM-IR's high-resolution profiles.

CALIBRATION AND CROSS-VALIDATION:

OMEGA raw cubes were processed using a Python pipeline with radiometric calibration, thermal emission removal and atmospheric correction. We used SPICAM-IR Level-1B FITS with calibrated reflectance and atmospheric correction. For comparability, OMEGA spectra were convolved to SPICAM-IR's resolution over the 1.25–1.65 μm range.

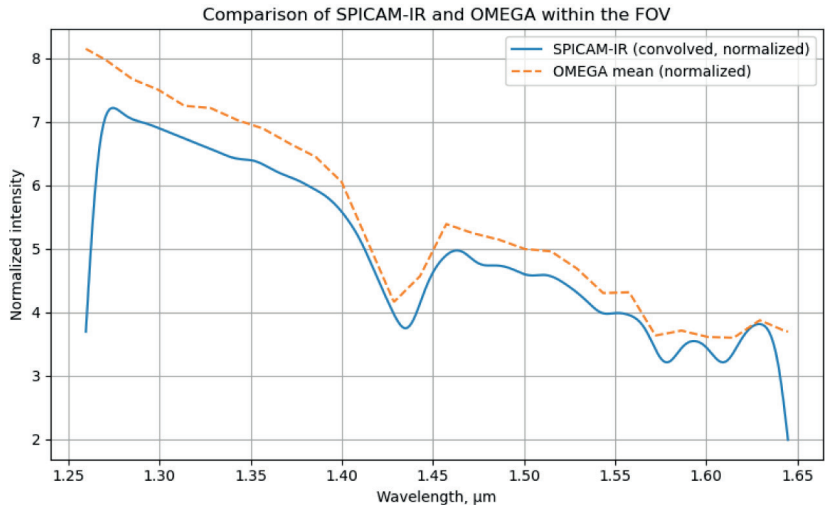


Figure 1. Normalized SPICAM-IR (convolved) and OMEGA mean spectra for a co-located observation over the polar region, illustrating agreement after

RESULTS:

For selected joint orbits (e.g., ORB1765_1, $L_s \approx 221.7^\circ$), CO₂ (1.43 μm band) and H₂O (1.5 μm band) ice index maps derived from OMEGA agree with

SPICAM-IR-derived ice metrics. Differences are attributed to spatial sampling, viewing geometry and instrumental effects.

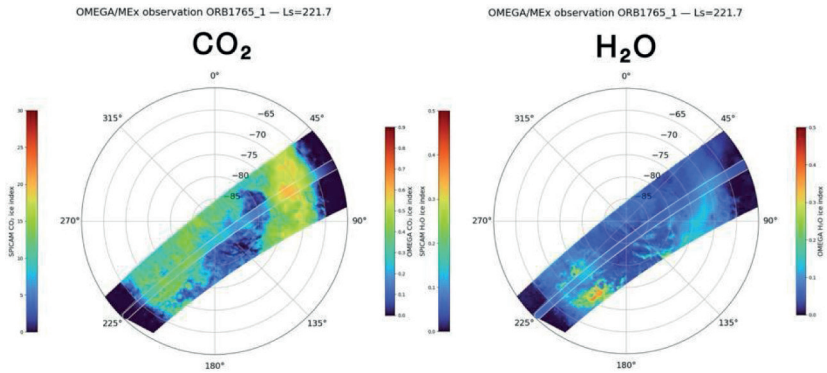


Figure 2. CO_2 (left) and H_2O (right) ice metrics maps from OMEGA/MEx (color scale) for ORB1765_1 ($L_s \approx 221.7^\circ$) over the south seasonal cap. White contour shows SPICAM-IR coverage, with the gradient inside representing SPICAM-derived ice metrics. The maps illustrate strong spatial agreement between instruments.

We will also show multi-wavelength comparison of two instruments and expanded ice metrics comparison. Future work in these combined datasets will improve retrieval robustness and enable a more detailed view of selected regions on seasonal caps.

REFERENCES:

- [1] Korabev O., Bertaux J.-L., Fedorova A. et al. SPICAM IR acousto-optic spectrometer experiment on Mars Express // J. Geophysical Research. 2006. V. 111. Iss. E9. Article E09S03. <https://doi.org/10.1029/2006JE002696>.
- [2] Langevin Y., Bibring J.-P., Montmessin F. et al. Observations of the south seasonal cap of Mars during recession in 2004–2006 by the OMEGA visible/near-infrared imaging spectrometer on board Mars Express // J. Geophysical Research: Planets. 2007. V. 112. Iss. E8. Article E08S12. P. 1–32. <https://doi.org/10.1029/2006JE002841>.
- [3] Appéré T., Schmitt B., Langevin Y. et al. Winter and spring evolution of northern seasonal deposits on Mars from OMEGA on Mars Express // J. Geophysical Research: Planets. 2011. V. 116. Iss. E5. Article E05001. P. 1–27. <https://doi.org/10.1029/2010JE003762>.

STRUCTURE OF THE UPPER MARTIAN ATMOSPHERE FROM THE HOMOPAUSE TO THE CO₂ EXOBASE AS OBSERVED BY ACS/TGO

D. A. Kossova^{1,2}, D. A. Belyaev¹, E. D. Starichenko¹, A. S. Medvedev³,
A. A. Fedorova¹, A. Trokhimovskiy¹, O. I. Korablev¹

¹ Space Research Institute RAS, Moscow, Russia, dakossova@edu.hse.ru

² National Research University Higher School of Economics, Faculty of Physics, Moscow, Russia

³ Max Planck Institute for Solar System Research, Göttingen, Germany

KEYWORDS:

upper atmosphere, Mars, homopause, exobase, eddy diffusion

ABSTRACT:

In this paper we examine the altitudes of the middle and upper atmosphere of Mars, specifically the mesosphere (above ~50 km) and the thermosphere (above 100–120 km) up to the exobase for the CO₂ molecule (180–200 km). These altitudes include transition zones where the diffusion regime of atmospheric particles changes: namely the homopause, located at 100–130 km [1], and the exobase, above which the atmosphere is considered collisionless for each molecule within its scale height. Variations in the altitude and temperature of the homopause, as well as the exobase, are influenced by seasonal variability, solar activity [2] and vertical energy transfer due to global circulation and atmospheric gravity waves [3, 4]. Our research is based on the analysis of temperature and CO₂ density vertical profiles measured during solar occultations by the Atmospheric Chemistry Suite (ACS) on board the Trace Gas Orbiter (TGO) of the ExoMars-2016 mission [5]. The statistics of the analyzed profiles covers seasons spanning 2.5 Martian years (MY), from the middle of MY 34 (May 2018) to the end of MY 36 (December 2022), with atmospheric altitudes ranging from 10 to 180 km. Based on the processed altitude profiles, the coefficients of molecular and turbulent diffusion were evaluated (under the approximation of saturated vertical gravity waves), seasonal variations in the altitude and CO₂ density of the homopause and CO₂ exobase were obtained. Due to our data, the altitude of the homopause varies from 100 km at aphelion to 140 km at perihelion with CO₂ density ranging from 10¹⁰ to 10¹² cm⁻³ and diffusion coefficients between 5·10⁶ and 1.5·10⁸ cm²/s. The altitude of CO₂ exobase decreases to 150 km at aphelion and rises to 200 km at perihelion. The obtained results could be utilized to refine circulation models in calculations of vertical particle transport in the upper atmosphere.

INTRODUCTION:

In the vertical structure of a planetary upper atmosphere there are two transition regions caused by a change in the particle mixing regimes. That is the homopause, located on Mars at altitudes of 100–130 km, where photolysis of some molecules occurs under the influence of solar radiation, as well as the exobase (about 200 km), where the mean free path of a molecule becomes equal to the atmospheric scale height. The homopause is the layer that separates two distinct regions based on the mixing of gases. Below this layer, in the homosphere, gases are well mixed due to the turbulent mixing caused by winds, convection and other atmospheric dynamics. Above the homopause, in the heterosphere, the molecular mixing with diffusive separation of individual gas components prevails. The vertical transport of species can be described by the continuity equation for Fickian diffusive flux Φ_i :

$$\Phi_i = -(K_{eddy} + D_i) \frac{\partial n_i}{\partial z} - n_i \left[K_{eddy} \left(\frac{mg}{kT} + \frac{1}{T} \cdot \frac{\partial T}{\partial z} \right) + D_i \left(\frac{m_i g}{kT} + \frac{1}{T} \cdot \frac{\partial T}{\partial z} \right) \right], \quad (1)$$

where n is the number density [cm^{-3}], T is the temperature [K], K_{eddy} and D_i are eddy and molecular (i^{th}) diffusion coefficients respectively [cm^2/s]. The diffusion coefficients are differently variable with altitude z changing from $K_{\text{eddy}} \gg D_i$ in the lower atmosphere (homosphere) to $K_{\text{eddy}} \ll D_i$ in the upper atmosphere (heterosphere) and $K_{\text{eddy}} \approx D_i$ at the homopause level.

The coefficient K_{eddy} encompasses effects of turbulent mixing and gravity waves. Physically, it is defined by fluctuations of wind velocity on a characteristic distance of the atmospheric scale height $H = kT/mg$ [6]. In this study an approach based on wave effects in the atmosphere taking into account wind speed variations was used to analyze the homopause and estimate the turbulent diffusion coefficient.

This paper presents estimates of the diffusion coefficients for the upper atmosphere of Mars, as well as variations in the homopause and CO_2 exobase altitudes. The results are obtained based on the analysis of the altitude profiles of temperature and CO_2 density measured by the ACS instrument onboard the ExoMars/TGO spacecraft. We revise the homopause data presented earlier in the paper of Belyaev et al. [7] with the extended statistics to 2.5 Martian years (MY), from the mid-MY 34 to the end of MY 36. Here, a wave approach was applied to the altitude profiles in order to estimate the turbulent diffusion coefficient around homopause. In addition, the variation in CO_2 exobase altitudes is presented for the first time from ACS data.

METHODOLOGY:

The middle infrared channel of ACS (ACS-MIR) has been measuring atmospheric transmission spectra at 2.3–4.2 μm range in solar occultation mode since April 2018 [5]. The spectral resolving power ($\lambda/\Delta\lambda \approx 30,000$) of ACS-MIR allows sensing the rotational absorption of CO_2 lines around the 2.7 μm band in a broad altitude range, from 10 to 180 km, that gives a possibility to retrieve vertical profiles of CO_2 density and temperature under the hydrostatic assumption for pressure as described in the previous papers of Belyaev et al. [7]. The vertical resolution of 1–3 km allows revealing small-scale gravity waves and their characteristics from the temperature profiles [8]. According to these studies, wave saturation and breaking was observed at altitudes between 80 and 120 km, likely impacting the turbulent diffusion near the homopause.

In this study we revise the estimates of the diffusion coefficients near the homopause using an approach that takes into account atmospheric gravity waves as a mechanism for vertical mixing. At altitudes of the wave saturation, turbulent mixing can be described through wave parameters using a formula first proposed by Lindzen [6] for the Earth's atmosphere and adapted by Sliński et al. [9] for the Martian atmosphere:

$$K_{\text{eddy}}(z) = \frac{k_h(c-u)^4}{2HB^3(z) \cdot (1 + l^2/k_h^2)^{3/2}}.$$

Here k_h and l are the wave numbers in the zonal and meridional directions [km^{-1}], respectively, B is the Brent-Väisälä frequency [s^{-1}], which is the resonant frequency of stable oscillations of the air mass. The difference between the phase and zonal wind speeds $|c-u|$ can be expressed through the dispersion relation B/v [6, 10], where v is the wave number in the vertical direction [km^{-1}]. Thus, for the case of vertically saturated gravity waves one can estimate the eddy mixing as:

$$K_{\text{eddy}}(z) = \frac{1}{2H} \cdot \frac{k_h B(z)}{v^4 (1 + l^2/k_h^2)^{3/2}}.$$

We assume the horizontal wavelength $k_h = l = 2\pi/300 \text{ km}^{-1}$ due to general circulation models [11, 12]. The temperature profile $T(z)$ retrieved from one occultation session is shown in Figure 1a, together with its mean profile $T_{\text{mean}}(z)$ smoothed by an algorithm of [8]. The dominant vertical harmonic $\lambda_v = 2\pi/v \approx 30 \text{ km}$ was determined from the Fourier analysis applied to

the difference profile $dT = T(z) - T_{mean}(z)$ (Figure 1b). This altitude wavelength was found to be average for the analyzed set of profiles. The atmospheric scale height is calculated as $H(z) = RT/\mu g$, where R is the universal gas constant, $T(z)$ — retrieved temperature profile.

The molecular diffusion D_{CO_2} is defined by collisional geometry of CO_2 and its thermal speed [13]. We derive it directly from the retrieved temperature and CO_2 density by the same manner as described in Belyaev et al. [7]. The intersection of these two profiles $D_{CO_2}(z) = K_{eddy}(z)$ indicates the homopause altitude (Figure 1c). CO_2 exobase altitude is indicated as the intersection of the other two profiles $H(z) = l(z)$ (Figure 1d), where $l(z) = (Q_i n_i(z))^{-1}$ with effective gas kinetic cross section $Q_{CO_2} = 0.52 \text{ nm}^2$.

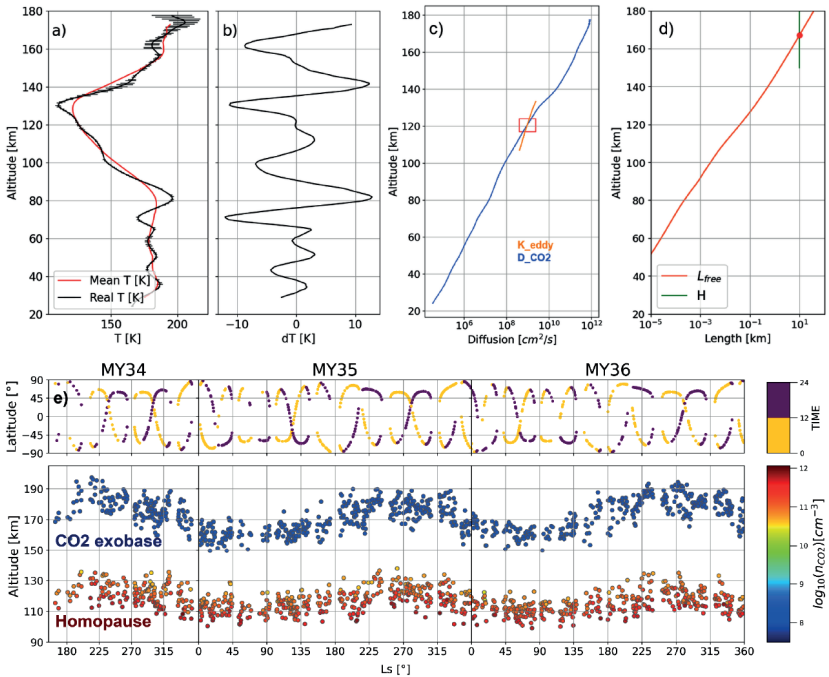


Figure 1. Example of the vertical temperature profile T (black line with error bars) and the mean temperature profile T_{mean} (red line) according to ACS data (a). The vertical profile of the atmospheric gravity wave ($dT = T - T_{mean}$) (b). Example of altitude profiles of turbulent (K_{eddy}) and molecular (D_{CO_2}) diffusions with intersection in the homopause region (with errors) (c). Example of altitude profiles of the mean free path of the molecule (L_{free}) and the atmospheric scale height (H) with intersection in the CO_2 exobase (d). Seasonal distribution of homopause and CO_2 exobase altitudes as a function of solar longitude L_s over 2.5 MY (e). The color scale reflects the corresponding CO_2 density. The upper panel shows the latitude coverage of measurements for the morning (ocher) and evening (violet) eclipse sessions

RESULTS AND CONCLUSION:

We have analyzed 968 vertical profiles observed by ACS-MIR for 2.5 MY at $2.7 \mu\text{m}$ bands. Depending on season, altitudes of the homopause vary from 90–100 km at aphelion to 130–140 km at perihelion; and the CO_2 exobase — from 150 km at aphelion to 200 km at perihelion. The concentration of CO_2 at the homopause altitude varies in the range of values from 10^{10} to 10^{12} cm^{-3} . The concentration of carbon dioxide at the exobase altitudes is about 10^8 cm^{-3} . The range of diffusion values at the homopause point changes from $5 \cdot 10^6$ to $1.5 \cdot 10^8 \text{ cm}^2/\text{s}$. The values of altitudes and CO_2 concentrations are in good agreement with the results of experiments in previous Martian years [14–16]. The difference in altitudes of the exobase and homopause is 50 km on average per season. The obtained values of the diffusion coefficients and the altitudes of the transition regions can be used to refine circulation models and to calculate the vertical particle flux in the upper atmosphere of Mars using formula (1).

ACKNOWLEDGMENTS:

This study is supported by the Russian Science Foundation grant, RSF No. 25-22-00494, <https://rscf.ru/project/25-22-00494/>.

REFERENCES:

- [1] *Bougher S.W., Brain D.A., Fox J.L. et al.* Chapter 14: Upper Neutral Atmosphere and Ionosphere // *The Atmosphere and Climate of Mars* / eds. B. Haberle et al. Cambridge University Press, 2017. P. 433–463.
- [2] *Bougher S.W., Pawlowski D., Bell J.M. et al.* Mars Global Ionosphere-Thermosphere Model: Solar cycle, seasonal, and diurnal variations of the Mars upper atmosphere // *J. Geophysical Research: Planets*. 2015. V. 120. Iss. 2. P. 311–342. <https://doi.org/10.1002/2014JE004715>.
- [3] *González-Galindo F., López-Valverde M.A., Forget F. et al.* Variability of the Martian thermosphere during eight Martian years as simulated by a ground-to-exosphere global circulation model // *J. Geophysical Research: Planets*. 2015. V. 120. Iss. 11. P. 2020–2035. <https://www-mars.lmd.jussieu.fr/>.
- [4] *Medvedev A.S., González-Galindo F., Yiğit E. et al.* Cooling of the Martian thermosphere by CO₂ radiation and gravity waves: An intercomparison study with two general circulation models // *J. Geophysical Research: Planets*. 2015. V. 120. Iss. 5. P. 913–927. DOI: 10.1002/2015JE004802.
- [5] *Korablev O.I., Montmessin F., Trokhimovskiy A. et al.* The Atmospheric Chemistry Suite (ACS) of Three Spectrometers for the ExoMars 2016 Trace Gas Orbiter // *Space Science Review*. 2018. V. 214. Article 7), <https://doi.org/10.1007/s11214-017-0437-6>.
- [6] *Lindzen R.S.* Turbulence and stress owing to gravity wave and tidal breakdown // *J. Geophysical Research: Oceans*. 1981. V. 86. Iss. C10. P. 9707–9714. <https://doi.org/10.1029/JC086iC10p09707>.
- [7] *Belyaev D.A., Fedorova A.A., Trokhimovskiy A. et al.* Thermal structure of the middle and upper atmosphere of Mars from ACS/TGO CO₂ spectroscopy // *J. Geophysical Research: Planets*. 2022. V. 127. Article e2022JE007286. <https://doi.org/10.1029/2022JE007286>.
- [8] *Starichenko E.D., Belyaev D.A., Medvedev A.S. et al.* Gravity wave activity in the Martian atmosphere at altitudes 20–160 km from ACS/TGO occultation measurements // *J. Geophysical Research: Planets*. 2021. V. 126. Iss. 8. Article e2021JE006899. <https://doi.org/10.1029/2021JE006899>.
- [9] *Slipiski M., Jakosky B.M., Benna M. et al.* Variability of Martian turbopause altitudes // *J. Geophysical Research: Planets*. 2018. V. 123. Iss. 11. P. 2939–2957. <https://doi.org/10.1029/2018JE005704>.
- [10] *Fritts D.C., Alexander M.J.* Gravity wave dynamics and effects in the middle atmosphere // *Reviews of Geophysics*. 2003. V. 41. Iss. 1. 64 p. <https://doi.org/10.1029/2001RG000106>.
- [11] *Yiğit E., Medvedev A.S., Hartogh P.* Influence of gravity waves on the climatology of high-altitude Martian carbon dioxide ice clouds // *Annales Geophysicae*. 2018. V. 36. P. 1631–1646. <https://doi.org/10.5194/angeo-36-1631-2018>.
- [12] *Roeten K.J., Bougher S.W., Yiğit E. et al.* Impacts of gravity waves in the Martian thermosphere: The Mars Global Ionosphere-Thermosphere Model coupled with a whole atmosphere gravity wave scheme // *J. Geophysical Research: Planets*. 2022. V. 127. Iss. 12. Article e2022JE007477. <https://doi.org/10.1029/2022JE007477>.
- [13] *Sanchez-Lavega A.* An introduction to planetary atmospheres. Taylor and Francis Group, 1st ed. 2010. 629 p. <https://doi.org/10.1201/9781439894668>.
- [14] *Fu M.H., Wu X.S., Wu Z.P., Li J. et al.* The variations of the Martian exobase altitude // *Earth and Planetary Physics*. 2020. V. 4. Iss. 1. P. 4–10. <https://doi.org/10.26464/epp2020010>.
- [15] *Gu Y., Cao Y., Li Z. et al.* MAVEN-based investigation of Martian exobase temperatures: Diurnal and solar cycle variations // *Reviews of Geophysics and Planetary Physics*. 2023. V. 54. No. 1. P. 91–99. <https://doi.org/10.19975/j.dqyxx.2022-051>.
- [16] *Rao N.V., Leelavathi V., Gupta N. et al.* Exobase and homopause altitudes in the Martian upper atmosphere: Solar cycle variability and response to the 2018 global dust storm // *Icarus*. 2025. V. 435. Article 116565. <https://doi.org/10.1016/j.icarus.2025.116565>.

RADIATIVE TRANSFER IN THE NIR BANDS OF CO₂ AND CO MOLECULES UNDER BREAKDOWN OF VIBRATIONAL LTE IN THE DAYTIME MARTIAN ATMOSPHERE. EFFECT OF RADIATION ABSORPTION BY AEROSOLS ON VIBRATIONAL STATE POPULATIONS

V. P. Ogibalov

*Admiral Makarov State University of Maritime and Inland Shipping
Saint Petersburg, Russia*

*Saint Petersburg State University, Department of Atmospheric Physics
Saint Petersburg, Russia, vpo563@yandex.ru*

KEYWORDS:

radiative transfer, infrared molecular bands, vibrational non-LTE, carbon dioxide, Martian atmosphere, aerosol extinction

INTRODUCTION:

Since the Martian atmosphere is sufficiently rarified already near the surface, the breakdown of vibrational local thermodynamic equilibrium (LTE) for the CO₂ and CO molecules starts in the daytime from the troposphere. As the lower atmosphere of Mars is dusty, the scattering of infrared solar radiation by aerosols should affect the vibrational state populations of these molecules.

The aerosol scattering increases the loss of solar radiation by the atmosphere into the space and, accordingly, decreases the average density of the solar photons in the atmosphere. In the upper part of a dusty atmosphere, where the direct solar radiation is still practically not attenuated, the density of photons is higher due to the aerosol scattering than that in a dust-free atmosphere. Accordingly, the density of photons is less below some altitude level. Since the vibrational states of molecules are excited by the absorption of the solar photons, in a dusty atmosphere, in comparison with a dust-free atmosphere, the populations of vibrational states are higher above this level and less below it.

The intensities of infrared emissions of a planetary atmosphere at wavelengths of rovibrational (R-V) bands of the molecules included in its composition are determined by the population (degree of excitation) of vibrational molecular states. In tenuous planetary atmosphere, molecular collisions are becoming so rare that the Boltzmann distribution for population of molecular vibrational states is broken down. In other words, it takes place the breakdown of the vibrational local thermodynamic equilibrium (LTE), called non-LTE (NLTE) conditions. In this case, the vibrational state population is determined by the joint solution of the radiative transfer equation for considered R-V bands and the kinetic equations for these populations.

The subject of this study is the CO₂ and CO vibrational state populations in the daytime atmosphere of Mars. The Martian atmosphere is sufficiently rarefied already near the surface since the surface pressure is in a range of $\sim 10^2$ – 10^3 Pa. Therefore, the vibrational NLTE for the CO₂ and CO R-V bands in a wavelength range of ~ 1 – 5 μm start in the daytime Martian atmosphere from the troposphere [1, 2]. For the CO₂ bands at wavelengths of 1.4 μm and shorter and the CO bands at 1.6 and 1.2 μm , the NLTE start even from the surface. In the cold high-latitude troposphere, this occurs, beginning even from the CO₂ band at 2.0 μm and the CO band at 2.3 μm .

The troposphere of Mars, as a rule, is dusty, and the dust can be raised to ~ 50 km. Thus, the radiation transfer in the above bands under NLTE in the daytime Martian atmosphere should be considered taking into account the radiation scattering by aerosols. However, most estimates of the molec-

ular state population s were obtained in the approximation of a dust-free atmosphere (e. g., [1–3]).

The first attempt to estimate the aerosol effect on the populations of vibrational states of molecules was made in the paper [4], where for the infrared CO_2 bands only the effect of solar radiation absorption by dust was considered. In the next paper [5], there has already taken into account the effect of radiation scattering by aerosols, using the so-called transport approximation for single scattering phase function, which is convenient for calculations. In transport approximation, some of the photons interacting with an aerosol particle do not change initial directions of propagation, and the remaining photons are scattered with equal probability in any direction. The study has shown that aerosol scattering can significantly change the populations. However, the papers [4-5] did not present a comprehensive study of the aerosol scattering effect on the populations.

The realistic Henyey-Greenstein (H-G) phase function is used in the evaluations performed in this paper. The goal of the present study is to obtain general ideas about the aerosol effect on the populations of the CO_2 and CO vibrational states. Therefore, a number of simplifying assumptions were accepted in the given study with respect to the optical aerosol model discussed in the next section. The most important of these is the use of an exponential change in the aerosol extinction coefficient with altitude. This work presents the aerosol effect on the CO_2 bands at 4.3, 2.7, 2.0, 1.6, 1.4, 1.3, 1.2, and 1.05 μm and the CO bands at 4.7, 2.3, 1.6, and 1.2 μm . We study the effect dependence on both solar zenith angle and an uncertainty in rate constant data for inelastic molecular collisions. The dependence of vibrational state populations on the parameters of aerosol optical model is also tested.

The study of daytime populations of molecular states in a dusty atmosphere is directly related to the problem of atmospheric heat balance. However, the latter is much more complicated than the consideration presented in this paper. Firstly, along with heating due to the absorption of the solar radiation by molecules, the heating of aerosols themselves by this radiation should be taken into account. The aerosols, when heated, transfer the received energy to the atmosphere by molecular thermal conductivity and thermal radiation. Hence, secondly, it follows that the transfer of thermal radiation of the atmosphere will also have to be taken into account. Thus, the problem of heating the atmosphere by solar radiation is combined with the problem of cooling the atmosphere by thermal radiation, which leads to a significant cooling of the atmosphere at the surface, observed on Mars and Earth during dust storms

MODEL:

As already indicated in the Introduction, the molecular state populations under vibrational NLTE result from the joint solution of radiative transfer equations for R–V bands considered and kinetic equations for the populations of the molecular vibrational states, the transitions between which form these bands. Our consideration involves 545 vibrational states (64200 R–V transitions) belonging to 7 isotopologues of the CO_2 molecule and 2 isotopologues of the CO molecule. The overlap of lines in the band head of R-branches and in Q-branches of the bands and the overlap of lines belonging to different vibrational transitions are taken into account. The specifics of methodology for calculating the populations and updated formulas for the rate constants of V–T and V–V processes used are given in the papers [1, 2]. To include the scattering of radiation by aerosols into the problem, additional terms were introduced into the radiative transfer equations [5]. Those take into account the emissivity and opacity, which are associated with the interaction of radiation with aerosols. Since the main goal of the works [4, 5] was to show the possibility of combining the problems of the vibrational NLTE and the scattering of radiation by aerosols, the rough transport approximation for the single scattering phase function was used in the emissivity coefficient in these works. In this paper, this phase function is replaced by the one in the more realistic Henyey-Greenstein form.

We compare the populations of molecular states in a dusty atmosphere with those in a dust-free atmosphere, which were the subject of research in the paper [2]. All the numerical experiments were performed using the model 3 of the Martian atmosphere, described in [2]. The temperature-versus-pressure dependence for this model is presented in Figure 1. The surface albedo of the Martian bright soils is taken into account for the case of orthotropic reflection.

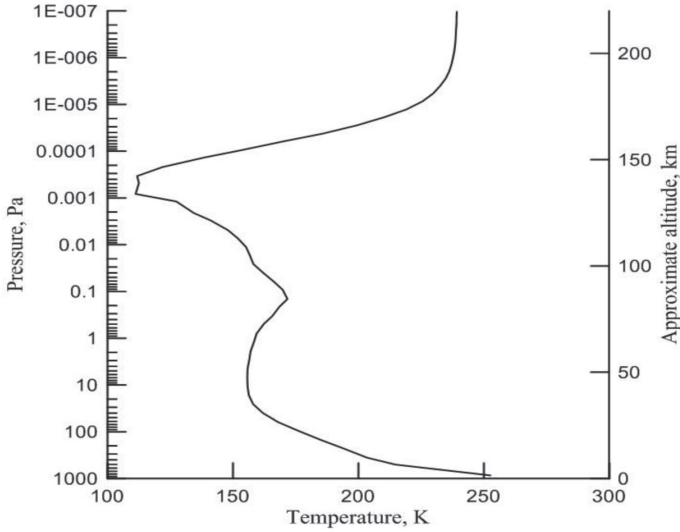


Figure 1. The temperature-versus-pressure dependence used in the model of the Martian atmosphere

The simple exponential change with altitude z was used for aerosol extinction coefficient

$$k_a = k_{a_0} \exp(-z/H_a), \quad (1)$$

where k_{a_0} is this coefficient at the surface, and H_a is the aerosol scale height. Accordingly, the aerosol optical depth of the atmosphere is

$$\tau_a = \int_0^{\infty} k_a(z) dz = k_{a_0} H_a. \quad (2)$$

The values of τ_a and H_a were used as parameters characterizing the abundance and vertical distribution of aerosols, respectively. This model of aerosol distribution was used to retrieve aerosol parameters from observations. As reference magnitudes, $\tau_a = 0.5$ and 2 are used in this work. These can be considered characteristic for regional and major dust storms, respectively. For numerical experiments, we used $H_a = 7$ km as the characteristic value and $H_a = 11.5$ km, which can be regarded as the maximum order of H_a .

The information on single scattering albedo, Λ , in the 1–3 μm range is shown in Figure 16 of the paper [6]. In most of this range, Λ exceeds 0.92. Only near 2.9 μm , where the absorption band of water ice is located, Λ decreases to ~ 0.8 . We used a same value of $\Lambda = 0.95$ for all the bands. However, the case of aerosols which scatter radiation fully ($\Lambda = 1$) was also tested.

In this study we used the one-parameter Henyey-Greenstein phase function. The use of the H-G phase function is justified, since a simplified but realistic expression is needed for phase function to reveal highlights in the problem of aerosol effect on the population of molecular vibrational states. Following the paper [7], we used the magnitude of 0.63 for the asymmetry factor g of the H-G phase function. The effect of degree of elongation for phase function was also tested. We performed the numerical experiments for $g = 0.9$ (strong elongation) and $g = 0$ (scattering in all directions are equally probable).

RESULTS AND DISCUSSION:

The results of numerical experiments are presented in Figures 2, 3 as ratios of the vibrational state population obtained with taking account of radiation scattering by aerosols to the population calculated in the neglect of scattering. The effect of radiation absorption by aerosols and of degree of phase function elongation are shown in Figures 2, 3, respectively.

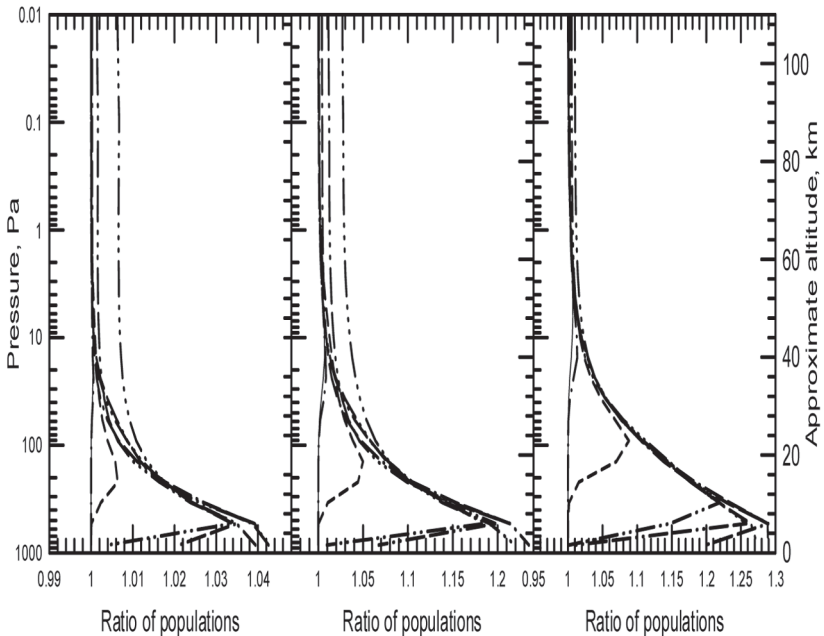
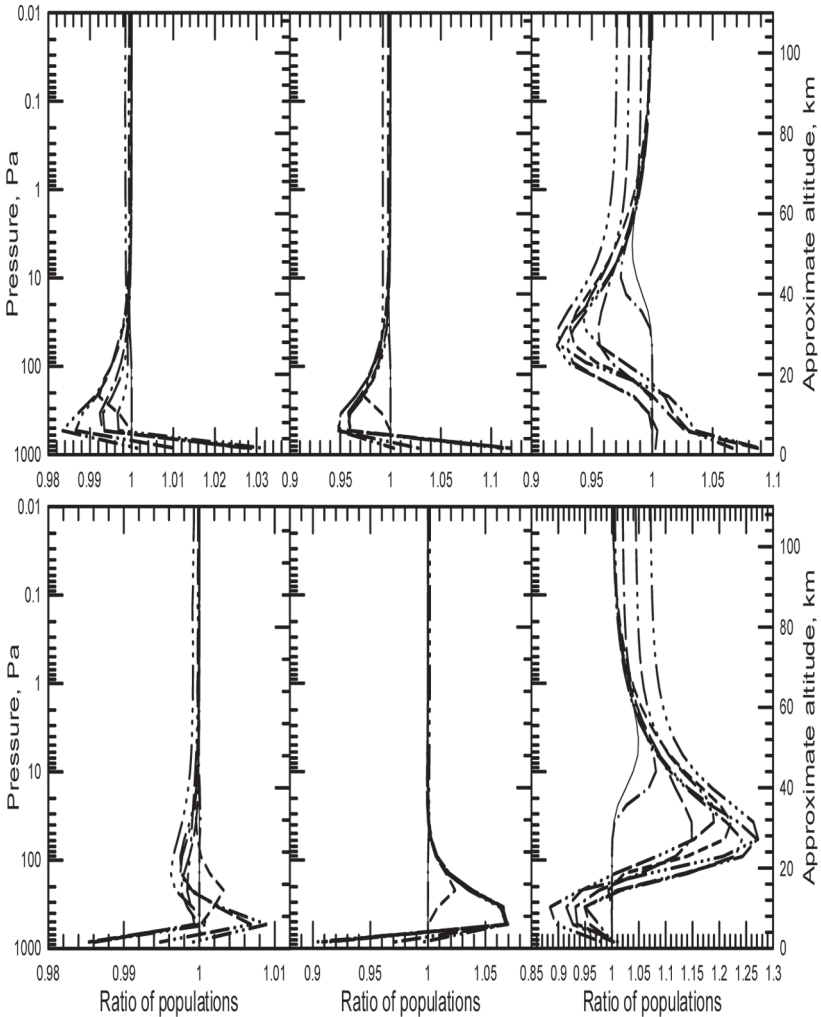


Figure 2. The ratio of the vibrational state population with using $\Lambda = 1$ to the population with using $\Lambda = 0.95$ for $g = 0.63$. Left panel: $\tau_a = 0.5$, $H_a = 7$ km, $SZA = 60^\circ$; middle panel: $\tau_a = 2$, $H_a = 11.5$ km, $SZA = 60^\circ$; right panel: $\tau_a = 2$, $H_a = 11.5$ km, $SZA = 85^\circ$. The curves present the vibrational states, transitions from which form the $^{12}C^{16}O_2$ bands at 4.3 (solid), 2.7 (dotted-dashed), 2.0 (dashed), 1.6 (a dash with two dots), 1.4 (two dashes with two dots), 1.3 (two dashes with three dots), 1.2 (two dashes with a dot), and 1.05 μm (a dash with three dots). The scale of horizontal axis is different for different panels. The scale of horizontal axis is different for different panels

The effect of aerosols on vibrational state population manifests itself as an increase in population above a certain altitudinal level with a pressure p_0 and its decrease below this level (Figures 2, 3). Such change in 'sign' of the effect is expected and has been previously derived in the papers [4, 5]. In order to explain the sign change it is necessary to take into account that the aerosol scattering by the upper part of the aerosol layer increases the loss of solar radiation by the atmosphere into the space. Accordingly, the average density of the solar photons in the lower part of this layer is decreased in comparison with a dust-free atmosphere. In the upper part of the dusty atmosphere, where the direct solar radiation is still practically not attenuated, the density of photons due to the aerosol scattering is higher than that in the dust-free atmosphere. Accordingly, the photon density is less below some altitude level. Since the vibrational states of molecules are excited by the absorption of the solar photons, in the dusty atmosphere, in comparison with the dust-free atmosphere, the population of vibrational states is higher above this level with the pressure p_0 and less below it. The described qualitative nature of the effect of aerosol scattering on the population of vibrational states does not depend on the characteristics of aerosol distribution with height. This allows to assume that the obtained here dependences of the populations on the problem parameters used are fulfilled for any altitudinal distribution of aerosols.

Numerical experiments have shown that the pressure p_0 corresponds to heights at which the optical path length of direct solar radiation, due to

the combined effect of molecular absorption of radiation and aerosol extinction, reaches the magnitudes of an order of 1. An increase in the numerical density of aerosols at any height while maintaining the type of altitudinal distribution of aerosols aerosol, determined by H_a in the model used, leads to an increase in the aerosol optical depth τ_a . Therefore, the pressure p_0 decreases with increasing τ_a .



Figures 3. The ratio of the vibrational state population with using $g = 0$ (top) and $g = 0.9$ (bottom) to the population with using $g = 0.63$ for $\Lambda = 1$. Left panels: $\tau_a = 0.5$, $H_a = 7$ km, SZA = 60° ; middle panels: $\tau_a = 2$, $H_a = 7$ km, SZA = 60° ; right panels: $\tau_a = 2$, $H_a = 11.5$ km, SZA = 85° . The notation of curves is as in Figure 2. The scale of horizontal axis is different for different panels

Some bands does not show the aerosol effect in a near-surface layer: the greater the optical thickness τ_b , the thicker this layer, all other things being equal. That is explained by the fact that the LTE for the population of appropriate vibrational state is fulfilled in this layer [see also the paper [2].

Effect of radiation absorption by aerosols:

The less the single scattering albedo Λ , the lower the energy density of solar radiation in the atmosphere due to the absorption of the radiation by aerosols. Therefore, the decrease of Λ results in a decrease in vibrational state population at all altitudes (Figure 2). For $\Lambda = 0.95$, the populations do not decrease by more than $\sim 3\%$ for the pressures $p < p_0$. However, these can decrease by $\sim 30\%$ for the pressure $p > p_0$.

Dependence on single scattering phase function:

The numerical experiments with the H-G phase function demonstrate a rather complicated effect of the parameter g variation on the vibrational state populations (Figure 3). However, if we ignore population changes not exceeding $\sim 1\%$, then following dependences on the elongation degree for the phase function are revealed. The decrease of phase function elongation results in population decrease above a certain altitudinal level with a pressure p' . Below this level, on the contrary, the population increases. The population decrease at the pressures $p < p'$ is explained by the decrease in the density of the scattered radiation, since the less the phase function is elongated, the more solar photons return back to the space after the first scattering event. The population increase at the pressures $p > p'$ should be attributed to the increase of scattered radiation density, since the less the phase function is elongated, the more photons reflected from the surface are returned to it after the first scattering event. Using the approximation of equiprobable scattering in all the directions ($g = 0$) does not change the populations by more than $\sim 10\%$

CONCLUSIONS:

For the first time, the effect of radiation scattering by aerosols on the populations of vibrational states of the CO_2 and CO molecules in the daytime Martian atmosphere has been studied in the realistic formulation of the problem using the methodology described in the paper [5]. These populations were studied depending on the optical thickness both of the aerosol layer and of the bands, the vertical distribution of aerosols, the solar zenith angle, and the aerosol parameters describing the scattering and absorption of radiation.

The main results obtained in this paper are as follows.

1. The weaker the band, the stronger the aerosol effect on the populations. The effect on the populations of vibrational states, the transitions from which form the most strong bands, what are the $^{12}\text{C}^{16}\text{O}_2$ bands at 4.3 and 2.7 μm , occurs only at the low sun.
2. The aerosol effect manifests itself as an increase and a decrease in population above and below a certain altitudinal level, respectively. The maximum population changes due to aerosols, realized for the weakest bands, are an increase in the population by $\sim 30\%$ above this level and a decrease by an order of magnitude below it. The pressure at this level decreases with increasing the solar zenith angle down to the pressures ~ 1 Pa at the low sun.
3. The use of the approximation of equiprobable radiation scattering by aerosols in all directions does not change the populations by more than $\sim 10\%$.

ACKNOWLEDGMENTS:

V.P. Ogibalov would like to express his extreme gratitude to all colleagues from the ANTARES (LSU-SPbU, 1985–1988) for very useful cooperation in various fields and for constant moral support in his professional activity.

REFERENCES:

- [1] *Ogibalov V.P., Shved G.M.* An improved model of radiative transfer for the NLTE problem in the NIR bands of CO_2 and CO molecules in the daytime atmosphere of Mars. 1. Input data and calculation method // *Solar System Research*. 2016. V. 50. No. 5. P. 316–328. DOI: 10.7868/S0320930X16050042.
- [2] *Ogibalov V.P., Shved G.M.* An improved model of radiative transfer for the NLTE problem in the NIR bands of CO_2 and CO molecules in the daytime atmosphere of Mars. 2. Population of vibrational states // *Solar System Research*. 2017. V. 51. No. 5. P. 373–385. DOI: 10.1134/S0038094617050070.
- [3] *Ogibalov V.P., Shved G.M.* An improved optical model for the non-LTE problem for the CO_2 molecule in the atmosphere of Mars: Nighttime populations of vibrational states and the rate of radiative cooling of the atmosphere // *Solar System Research*. 2003. V. 37. No. 1. P. 23–33.
- [4] *Ogibalov V.P.* Radiative Transfer in the near-infrared CO_2 bands taking account of continuum absorption by aerosol particles in the Martian atmosphere // *Vestnik of St. Petersburg Univ. (Series 4)*. 2008. V. 3. P. 27–36.

- [5] *Ogibalov V.P.* Non-equilibrium radiation in the infrared bands of the CO₂ and CO molecules in the planetary atmospheres (in the application to Mars) // Proc. SPIE. V. 10466. Pt. 1: 23rd Intern. Symp. Atmospheric and Ocean Optics: Atmospheric Physics. Irkutsk, Russia, 3–7 July 2017. P. 1–14. DOI: 10.1117/12.2292238.
- [6] *Wolff M. J., Smith M. D., Clancy R. T. et al.* Wavelength dependence of dust aerosol single scattering albedo as observed by the Compact Reconnaissance Imaging Spectrometer // J. Geophysical Research: Planets. 2009. V. 114. Article E00D04. DOI: 10.1029/2009JE003350.
- [7] *Ockert-Bell M. E., Bell J. F., III, Pollack J. B. et al.* Absorption and scattering properties of the Martian dust in the solar wavelengths // J. Geophysical Research: Planets. 1997. V. 102. P. 9039–9050. DOI: 10.1029/96je03991.

SESSION 2. MOON AND MERCURY (MN) ORAL SESSION

MGNS: FIRST DATA ON MERCURY'S GAMMA-RAY RADIATION

A. S. Kozyrev¹, J. Benkhoff², M. L. Litvak¹, I. G. Mitrofanov¹,
A. B. Sanin¹

¹ Space Research Institute RAS, Moscow, Russian Federation
m.litvak@np.cosmos.ru

² European Space Agency, Noordwijk, The Netherlands

KEYWORDS:

BepiColombo, MPO, Mercury, MGNS, nuclear planetology

ABSTRACT:

The Mercury Gamma-ray and Neutron Spectrometer onboard BepiColombo's Mercury Planetary Orbiter [1] measures the gamma-ray and neutron fluxes from Mercury's surface hence and provides studies of its elemental composition [2, 3]. Launched in October 2018, BepiColombo will continue until December 2026 its cruise phase on a near-Mercurian elliptical Sun orbit. BepiColombo has already performed two flybys at Venus and six flybys at Mercury. We present the experimental results obtained during 5 Mercury flybys in which gamma-rays lines of Silicon, Sodium/Magnesium and Potassium were observed along with a lack of a significant observation of Thorium. The readiness of the MGNS to begin the Mercury mapping phase is discussed along with operational and experimental strategies.

REFERENCES:

- [1] Benkhoff J., Murakami G., Baumjohann W. et al. BepiColombo — Mission Overview and Science Goals // Space Science Reviews. 2021. V. 217. Article 90. <https://doi.org/10.1007/s11214-021-00861-4>.
- [2] Mitrofanov I. G., Kozyrev A. S., Kononov A. et al. The Mercury Gamma and Neutron Spectrometer (MGNS) onboard the Planetary Orbiter of the BepiColombo mission // Planetary and Space Science. 2010. V. 58. Iss. 1–2. P. 116–124. DOI: 10.1016/j.pss.2009.01.005.
- [3] Mitrofanov I. G., Kozyrev A. S., Lisov D. I. et al. The Mercury Gamma-Ray and Neutron Spectrometer (MGNS) Onboard the Mercury Planetary Orbiter of the BepiColombo Mission: Design Updates and First Measurements in Space // Space Science Reviews. 2021. V. 217. Iss. 5. Article 67. DOI: 10.1007/s11214-021-00842-7.

GALACTIC COSMIC RAYS IN THE VICINITY OF MERCURY

V. D. Gubarev^{1,2}, A. S. Kozyrev¹, I. G. Mitrofanov¹, M. L. Litvak¹

¹ Space Research Institute RAS, Moscow, Russia, m.litvak@np.cosmos.ru

² National Research Nuclear University MEPhI, Moscow, Russia

KEYWORDS:

Galactic cosmic rays, MGNS, HEND, BTN-M1, Mercury, neutron flux

ABSTRACT:

Galactic cosmic rays (GCRs) are high-energy charged particles (predominantly protons) that enter the Solar System from interstellar space. Their intensity changes under the influence of the solar wind and the Sun's magnetic field, leading to a decrease in the GCR flux when approaching the Sun. We present the results of analysis of the neutron flux data from the Russian MGNS experiment onboard the ESA MPO/BepiColombo spacecraft [1]. Neutrons are the secondary particles formed within spacecraft materials under exposure to GCRs. The data along the spacecraft's trajectory to Mercury cover the period from the beginning of the BepiColombo cruise phase (early 2019) to the present. The data from the MGNS experiment [2] are compared with data from the neutron detectors of the HEND/Mars Odyssey [3] and BTN-M1/ISS [4] experiments, which perform measurements in orbits around Mars and Earth, respectively. The comparison of the MGNS instrument data with data from other experiments makes it possible to estimate a relative decrease in the average GCR flux when approaching to the Sun from Earth's orbit.

The obtained results can be useful for verification and adjustment of mathematical models describing the propagation of GCRs in the heliosphere.

REFERENCES:

- [1] Benkhoff J., Murakami G., Baumjohann W. et al. BepiColombo — Mission Overview and Science Goals // *Space Science Reviews*. 2021. V. 217. Article 90. <https://doi.org/10.1007/s11214-021-00861-4>.
- [2] Mitrofanov I. G., Kozyrev A. S., Konovalov A. et al. The Mercury Gamma and Neutron Spectrometer (MGNS) on board the Planetary Orbiter of the BepiColombo mission // *Planetary and Space Science*. 2010. V. 58. Iss. 1–2. P. 116–124. DOI: 10.1016/j.pss.2009.01.005.
- [3] Mitrofanov I. G., Litvak M. L., Kozyrev A. S. et al. Search for Water in Martian Soil Using Global Neutron Mapping by the Russian HEND Instrument Onboard the US 2001 Mars Odyssey Spacecraft // *Solar System Research*. 2003. V. 37. P. 366–377. <https://doi.org/10.1023/A:1026018811877>.
- [4] Tretyakov V. I., Mitrofanov I. G. et al. The first stage of the “BTN-Neutron” space experiment onboard the Russian segment of the International Space Station // *Cosmic Research*. 2010. V. 48. No. 4. P. 293–307. DOI: 10.1134/S0010952510040027.

DETERMINATION OF THE MERCURY'S INTERNAL DIPOLE PARAMETERS USING MESSENGER SPACECRAFT DATA

A. S. Lavrukhin¹, I. I. Alexeev¹, D. V. Nevsky^{1,2}

¹ Skobeltsyn Institute of Nuclear Physics Lomonosov Moscow State University
Moscow, Russia, demidova.si@yandex.ru

² Lomonosov Moscow State University, Faculty of Physics, Moscow, Russia

KEYWORDS:

Mercury, magnetosphere, magnetic dipole, MESSENGER

INTRODUCTION:

Mercury is the smallest planet in the Solar System and possesses the smallest magnetosphere. MESSENGER (MErcury Surface, Space ENvironment, GEochemistry, and Ranging) spacecraft completed more than 4000 orbits around Mercury in 2011–2015. Using MESSENGER magnetometer data we refine the position and magnitude of Mercury's dipole field for each MESSENGER flyby and consider the contribution of the induced dipole.

METHOD:

To refine the positions of the Mercury's dipole we use the data on the magnetic equatorial plane crossings by MESSENGER spacecraft and simultaneous fitting of the magnetic field in the region of MESSENGER's closest approach to the planet using a shifted dipole model. To accomplish this task, the FUMILIM program [1], an updated and optimized implementation of the chi-square functional minimization program, is used to fit the model parameters to the MESSENGER data, as was previously done by authors for a small number of MESSENGER orbits [2]. In parallel, we determine the magnetic equatorial plane crossings using magnetometer data. As a result, the offset (x, y, z) of the center of Mercury's planetary dipole and its tilt (θ, ϕ) are determined. Based on the results of refining the internal magnetic field of Mercury and the method for determining annual variations in Mercury's magnetosphere [3], the contribution of the induced dipole to the planetary magnetic field of the planet was determined depending on external conditions and parameters.

REFERENCES:

- [1] Sitnik I. M., Alexeev I. I., Nevsky D. V. Debugging the FUMILIM minimization package // Computer Physics Communications. 2024. V. 294. Article 108868. <https://doi.org/10.1016/j.cpc.2023.108868>.
- [2] Lavrukhin A. S., Alexeev I. I., Nevsky D. V. Determining Optimal Parameters for Mercury's Magnetospheric Current Systems from MESSENGER Observations // Solar System Research. 2024. V. 58. Iss. 5. P. 526–536. DOI: 10.1134/S0038094624700400.
- [3] Nevsky D. V., Lavrukhin A. S., Alexeev I. I. Mercury's Bow Shock and Magnetopause Variations According to MESSENGER Data // Universe. 2024. V. 10. Iss. 1. Article 40. DOI: 10.3390/universe10010040.

ABOUT THE ORIGIN OF HIGH-SPEED Ca ATOMS IN THE HERMEAN EXOSPHERE

A. A. Berezhnoy¹, V. V. Shuvalov², G. V. Belov³, A. E. Ivanova⁴

¹ Sternberg Astronomical Institute Moscow University, Moscow, Russia, aatolok72@gmail.com

² Sadovsky Institute of Geosphere Dynamics RAS, Moscow, Russia

³ Joint Institute of High Temperatures RAS, Moscow

⁴ Space Research Institute RAS, Moscow, Russia

KEYWORDS:

Mercury, exosphere, ejecta, Ca, impact events, condensation

INTRODUCTION:

Energy of Ca atoms in the exosphere of Mercury is about 5 eV [1] while energies of atoms of other elements is below 2 eV K. Several mechanisms including shock-induced dissociative ionization [2] and photodissociation of Ca-containing molecules [3] were considered for explanation of the presence of high-energy Ca atoms in the Hermean exosphere. However, CaO photodissociation is able to provide only about additional 0.6 eV to photolysis-generated Ca atoms [4] while the mechanism of dissociative recombination was not studied in details yet. In this work new mechanism able to explain higher energy of Ca atoms in comparison with atoms of other elements is proposed.

HYDRODYNAMICS OF IMPACT EVENTS:

Hydrodynamical processes during collisions of meteoroids and Mercury were simulated by numerical studies of vertical collisions between dunite impactors and dunite targets using the SOVA code [5]. Impact-produced clouds were divided into 15–20 fragments, and for each fragment temporal evolution of temperature, pressure, and hydrodynamic time scale was studied. Simulations were performed for impact velocities of 20, 30, 50, and 110 km/s. Size of impactors was taken as 0.2, 0.6, and 2.0 mm.

It was found that pressure in all regions of the clouds at 4000 K is 13.5 bar for impact velocities equal to 20, 30, and 50 km/s, because the vapor at this temperature begins to condense, and the pressure is defined by a phase equilibrium curve. However, for 110 km/s impacts a part of vapor begins to condense at higher temperatures, and pressures at 4000 K are decreasing with increasing distance from the center of the cloud and can be as low as 0.7 bar at 4000 K in outer boundaries of the clouds.

CHEMISTRY OF IMPACT EVENTS:

Equilibrium chemical composition of impact-produced clouds was studied considering condensation of minerals and adiabatic expansion of clouds into vacuum with variable adiabatic index [6]. Quenched chemical composition of clouds was estimated by comparison of typical time scales of main chemical reactions and hydrodynamic time scales.

For 110 km/s impacts main Ca-containing gas-phase species in the clouds are Ca and CaO. For 20 and 30 km/s impacts main Ca-containing species are Ca, CaO, and CaOH. Due to a sharp decrease of pressure at the same temperature in outer regions of the clouds formed by 110 km/s impacts Ca uncondensed fraction increases with increasing distance from the center of the clouds. It leads to formation of Ca gas-phase species mainly in outer regions of clouds formed by high-speed 110 km/s impactors. For 20, 30, and 50 km/s impacts pressure at 4000 K is the same over the total volume of cloud and gas-phase Ca species are located mainly in inner regions of clouds.

Let us note that ejecta velocities in impact-produced clouds increase with increasing distance from the center of the clouds and impact velocity [7]. Ejecta velocities for high-speed 110 km/s impacts can reach 5 km/s, this value is comparable to detected velocities of Ca exospheric atoms. It means that energetic Ca atoms detected in the exosphere of Mercury can be orig-

inated in outer envelopes of clouds formed by high-speed meteoroid impacts. The same mechanism is valid for Al as a refractory element with dependence of uncondensed fraction on temperature and pressure similar to that of Ca.

Mg and Fe often observed in the Hermean exosphere are almost not condensed during expansion of the clouds at the considered range of temperatures and pressures. It means that Mg, Fe-containing gas-phase species are located mainly in the center of the clouds because mass of impact-produced clouds is mainly concentrated in inner regions of the clouds. It leads to smaller ejecta velocities of Fe and Mg atoms than that of Ca and Al atoms. So, the proposed mechanism is able to explain higher temperature of Ca atoms in the Hermean exosphere in comparison with that of Fe and Mg atoms.

CONCLUSIONS:

It is proposed that high-speed Ca atoms detected in the Hermean exosphere are produced in outer envelopes of clouds formed by 110 km/s impacts. It is predicted that Al atoms delivered to the exosphere by the same mechanism are also very hot. Additional hydrodynamic simulations of 70, 90, and 130 km/s impact events are required for deeper understanding of ejecta velocities distribution and condensation of Ca and Al in impact-produced clouds. Findings of this work can be applied to analysis of BepiColombo mission data [8].

REFERENCES:

- [1] *Burger M. H., Killen R. M., McClintock W. E. et al.* Seasonal variations in Mercury's dayside calcium exosphere // *Icarus*. 2014. V. 238. P. 51–58. DOI: 10.1016/j.icarus.2014.04.049.
- [2] *Killen R. M.* Pathways for energization of Ca in Mercury's exosphere // *Icarus*. 2016. V. 268. P. 32–36. <https://doi.org/10.1016/j.icarus.2015.12.035>.
- [3] *Moroni M., Mura A., Milillo A. et al.* Micro-meteoroids impact vaporization as source for Ca and CaO exosphere along Mercury's orbit // *Icarus*. V. 401. Article 115616. <https://doi.org/10.1016/j.icarus.2023.115616>.
- [4] *Valiev R. R., Berezchnoy A. A., Sidorenko A. D. et al.* Photolysis of metal oxides as a source of atoms in planetary exospheres // *Planetary and Space Science*. 2017. V. 145. P. 38–48. <https://doi.org/10.1016/j.pss.2017.07.011>.
- [5] *Shuvalov V. V.* Multi-dimensional hydrodynamic code SOVA for interfacial 794 flows: application to the thermal layer effect // *Shock Waves*. 1999. V. 9. Iss. 6. P. 381–390. DOI: 10.1007/s001930050168/
- [6] *Berezchnoy A. A., Belov G. V., Wöhler C.* Chemical processes during collisions of meteoroids with the Moon // *Planetary and Space Science*. 2024. V. 249. Article 105942. <https://doi.org/10.1016/j.pss.2024.105942>.
- [7] *Shuvalov V. V., Trubetskaya I. A.* Numerical simulation of high-velocity ejecta following comet and asteroid impacts: Preliminary results // *Solar System Research*. 2011. V. 45. Iss. 5. P. 392–401.
- [8] *Milillo A., Fujimoto M., Murakami G. et al.* Investigating Mercury's environment with the two-spacecraft BepiColombo mission // *Space Science Reviews*. 2020. V. 216. Iss. 5. Article 93. DOI: 10.1007/s11214-020-00712-8.

MONTE CARLO SIMULATION OF THE GLOBAL MIGRATION OF LUNAR HYDROXYL FROM A MAGNETIC-SHIELDED SOLAR WIND SOURCE

Lianghai Xie, Lei Li

National Space Science Center, Chinese Academy of Sciences, State Key Laboratory of Space Weather, Beijing, China, xielianghai@nssc.ac.cn

KEYWORDS:

Solar wind-derived water, Monte-Carlo simulation, Global migration

ABSTRACT:

Solar wind has been regarded as an important source for the surficial water on the Moon. Here we investigate the global migration of solar wind-derived OH molecules with a Monte Carlo model, in which the shielding effects of both the Earth's magnetosphere and the lunar magnetic anomalies are considered. It is found that the OH surface concentration depends on the latitude, the local time, and the lunar phase. Specifically, the surface concentration can increase from nearly zero ppm near the subsolar point to about 1000 ppm near the polar regions, and there is a local peak near the morning terminator that can bring a diurnal variation of about 150 ppm. Moreover, the OH abundances can be reduced by about 15% in the magnetotail when at low and middle latitudes. But when in the polar region, the OH abundance can keep increasing, resulting in an average deposition rate of $1.0 \cdot 10^{12} \text{ m}^{-2} \text{ s}^{-1}$. In addition, a south-north asymmetry can be caused by the magnetic anomalies, in which the OH abundance in the southern hemisphere is generally lower than that in the northern hemisphere, with maximum difference of about 23 % near 75° latitude. In the exosphere, the OH number density shows a dawn-dusk asymmetry, with relatively higher number densities on the dawnside, and the maximum density can reach $3.9 \cdot 10^9 \text{ m}^{-3}$ near the subsolar region. These results can greatly improve our understanding on the migration and distribution of OH molecules on the Moon.

SURFACE MORPHOLOGY OF PARTIALLY SHADOWED FLOORS OF THREE NEAR-POLE LUNAR CRATERS

A.T. Basilevsky¹, S.S. Krasilnikov², A.S. Krasilnikov¹, Yuan Li³, G.G. Michael⁴

¹ Vernadsky Institute of Geochemistry and Analytical Chemistry RAS
Moscow, Russia, atbas@geokhi.ru, krasilnikov_as@geokhi.ru

² Hong Kong Polytechnic University, Hong Kong, China
sergey.krasilnikov@polyu.edu.hk

³ Suzhou Polytechnic University, SuZhou, China, YuanLi_SciRes@outlook.com

⁴ Institute of Geochemistry Chinese Academy of Sciences, Guiyang, China
gregory@mail.gyig.ac.cn

KEYWORDS:

Moon, surface morphology, craters, permanently shadowed craters' floors, crater ejecta, regolith

INTRODUCTION:

This work continues our studies of surface morphology of floors of near-polar lunar craters [1, 2]. The focus of this work is to study the surface morphology of crater floors that are only partly shadowed. This shadowing may affect a peculiar temperature regime and conditions of accumulation or loss of volatiles, including H₂O, in the crater floor material. The studied craters are 1) Schomberger A, 78.8° S, 24.4° E, $D = 31$ km, 2) Rozhdstvenskiy K, 82.7° N, 215.4° E, $D = 42$ km and 3) Lovelace, 82.3° N, 253.6° E, $D = 54$ km.

DESCRIPTION OF SURFACE MORPHOLOGY OF THE CRATER'S FLOORS:

Crater Schomberger A

Crater Schomberger A is the smallest among the three considered. On its floor is the 6×9 km central peak consisting of two parts (Figure 1). At the base of its western, northeastern and southern inner slopes large landslide bodies are seen (LS on Figure 1a). Positions of the 4.5×6.0 km Study areas 1 and 2 were determined by the intention to have within them the predominance of plain-like terrain. Similar approach was used in the cases of two other considered by us craters. Study area 3, also 4.5×6.0 km, is on the northern inner slope. Study area 4 is located in the northern part of the crater rim. Its size is only 3×4 km due to intention not to have within it the large rock blocks. In photogeological analysis of Study areas 1, 2 and 3 the ShadowCam images were used, in the analysis of Study area 4 were used the LROC NAC images.

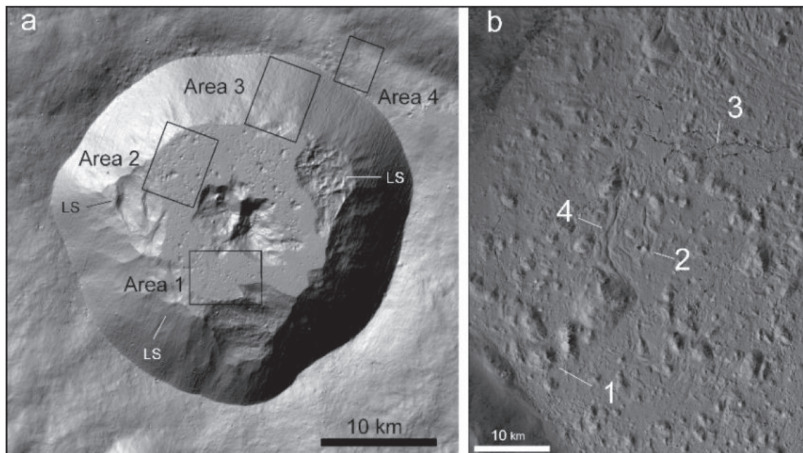


Figure 1. Hill-shade image of crater Schomberger A with shown Study areas (a); ShadowCam image of Study area 2 (b)

In Figure 1 and especially in Figure 1b can be seen prominent irregular steep-sided hills (1), probably fallen back rock fragments, rather rare craters (2), probably impact ones, fractures (3) and channel-like features (4), probably made by flow of impact melt.

The photogeologic analysis of images of Study areas 1, 2, 4 and 4 showed that crater Schomberger A is very young that agrees with its dating as Copernican on the geologic maps of [3] and [4]. On the crater floor regolith is almost absent and small craters have no lobate rims and their outlines are somewhat irregular. Study area 3 on the inner crater slope also shows no evidence for thick regolith. So it is expectable that the neutral spectrometer LEND does not show the increased content of hydrogen associated with this crater (Private communication of A. S. Sanin).

Crater Rozhdestvenskiy K

This crater is intermediate in size ($D = 42$ km) among the three considered. On its floor is the 6×8 km central peak. The crater inner slopes are complicated with subsidence terraces. The 4.5×6.0 km Study areas 1, 2 and 3 are on the crater floor. Study area 4 is in the upper part of its southern inner slope. Its size is also 4.5×6.0 km.

It is seen in Figure 2 that surface of the crater floor is complicated by the hills (h in Figure 2b) and on the hills and on the plain-like terrain are superposed craters, probably impact ones. Three craters with diameters 842, 432 and 405 m have lobate-like rims (numbers 1, 2 and 3 correspondingly in Figure 2b). Surface morphology within Study area 4 on the crater inner slope shows the “elephant hide” texture suggesting rather thick regolith (e.g., [5]).

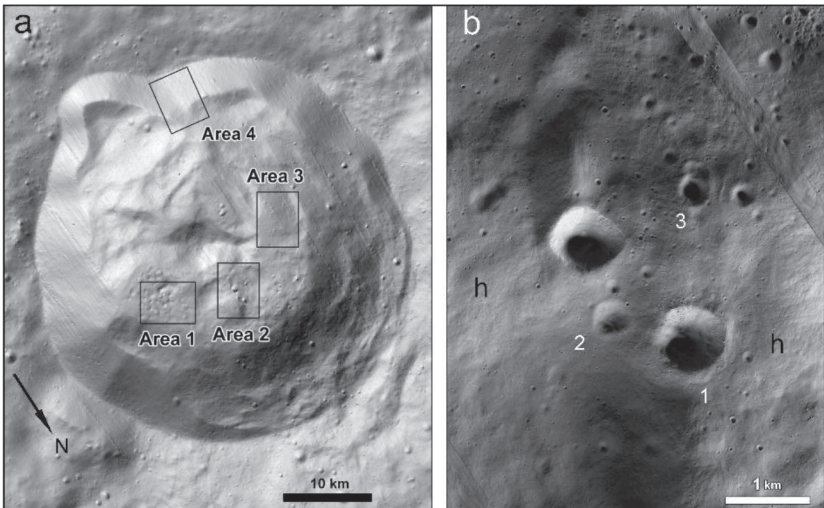


Figure 2. Hill-shade image of crater Rozhdestvenskiy K with shown Study areas (a); ShadowCam image of Study area 2 (b)

The photogeologic analysis of ShadowCam images within crater Rozhdestvenskiy K showed that this craters is not very young that agrees with its classification as Eratosthenian by [3]. On its floor was accumulated rather thick regolith and the lobate-rimmed craters are observed, suggesting presence of significant amount of water ice in the target material [6]. But the neutral spectrometer LEND did not show the increased content of hydrogen associated with this crater [5].

Crater Lovelace

This crater is the largest ($D = 54$ km) among those considered. On its floor is the 5×9 km central peak. The crater inner slopes are complicated with subsidence terraces. Position of the 4.5×6.0 km Study areas 1, 2 and 3 was determined by the intention to have within them the predominance of plain-like terrain. Study area 4 is in the upper part of its southern inner slope. Its size is also 4.5×6 km.

It is seen in Figure 3 that surface morphology of the floor, in general, and within Study area 1, in particular, is dominated with small craters, probably impact ones. Within Study area 1 from 69 mapped craters six have lobate rims (see white numbers nearby).

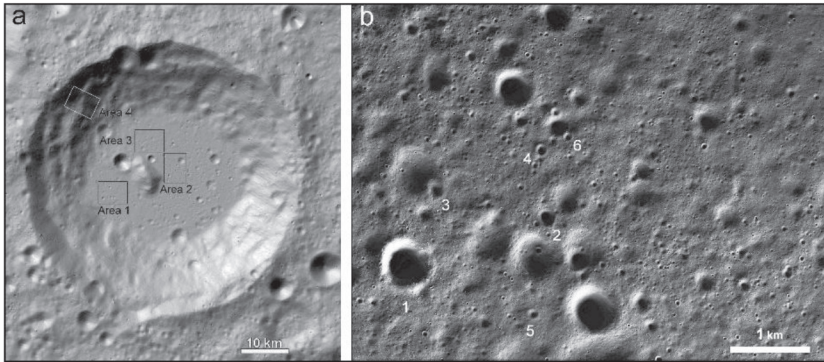


Figure 3. Hill-shade image of crater Lovelace with the shown Study areas (a); ShadowCam image of Study area 1 (b)

The photogeologic analysis of ShadowCam images within crater Lovelace showed that this crater is not young that agrees with its classification as Upper-Imbrian by [3]. On its floor was accumulated rather thick regolith and the lobate-rimmed craters are observed. But as in the two previous cases, the neutral spectrometer LEND did not show the increased content of hydrogen associated with this crater (Private communication of A. S. Sanin).

CONCLUSIONS:

Near polar craters are interesting as source of volatiles, first of all H_2O , for the needs of future lunar bases and being decomposed into H_2 and O_2 as a fuel for rockets. Presence of H_2O in the crater floor materials is supported by two pieces of evidences: 1) the low neutral flux from the surface measured by the LEND instrument, and 2) by presence of lobate rimmed craters. Interesting that partly shadowed floors do not have the low-H anomalies while completely shadowed do. These results demand additional studies.

No	Crater name and diameter, km	Diameter range, m	Crater number, N	LR crater number, n	$n/N, \%$
1	Schomberger A, 31	48–158	55	0	0
2	Rozhdestvenskiy K, 42	101–629	141	8	5.7
3	Lovelace, 54	101–1289	278	21	7.5
4	Faustini, 42,5	150–1141	292	14	4.8
5	Shoemaker, 51	150–1179	123	14	11.1
6	Haworth, 51	150–1287	232	8	3.5

REFERENCES:

- [1] *Basilevsky A. T., Li Yuan* Surface morphology inside the PSR area of lunar polar crater Shoemaker in comparison with that of the sunlit areas // *Planetary and Space Science*. 2024. V. 241. Article 105839. 10 p. <https://doi.org/10.1016/j.pss.2024.105839>.
- [2] *Basilevsky A. T., Krasilnikov A. S., Li Yuan, Michael G.G.* Comparison of surface morphology of floors of the near-pole craters and craters being at middle latitudes of the Moon // *Solar System Research*. 2025. V. 59. Iss. 6. Article 63. 28 p. DOI: 10.1134/S0038094624601671.
- [3] *Fortezzo C. M., Spudis P.D., Harrel S.L.* Unified geologic map of the Moon / USGS TBD. 2020.
- [4] *Krasilnikov S.S., Ivanov M.A., Head J.W., Krasilnikov A.S.* Geologic history of the south circumpolar region (SCR) of the Moon // *Icarus*. 2023. V. 394. Article 115422. 19 p. <https://doi.org/10.1016/j.icarus.2022.115422>.
- [5] *Kreslavsky M. A., Bondarenko N. V., Head J.W.* Ubiquity of “elephant hide” texture on the Moon // 52nd Lunar and Planetary Science Conf. 2021. Article 1826.
- [6] *Robinson M. S., Mahanti P., Bussey D.B.J et al.* Seeing in the shadows // 55th Lunar and Planetary Science Conf. 2024. Article 1669.

METAL-SULFIDE MINERALIZATION OF CHANG'E-5 SOIL SAMPLE

S. I. Demidova¹, C. A. Lorenz¹, L. A. Lakhmanova^{1,2}

¹ Vernadsky Institute of Geochemistry and Analytical Chemistry RAS
Moscow, Russia, demidova.si@yandex.ru

² Lomonosov Moscow State University, Department of Geology
Moscow, Russia

KEYWORDS:

Chang'E-5, soil sample, metal-sulfide association, impact glasses, lunar basalts

INTRODUCTION:

Fe-metal — sulfide particles are widespread on the surfaces and interiors of the lunar impact glasses, recording space weathering and regolith gardening processes occurring on the Moon surface. They have been heavily studied in the Chang'E-5 lunar impact glasses [1–7]. In the latter they are mostly larger than 10 nm and are spherical and hemispherical in shape [6]. We have found that some Fe-metal – sulfide association is related not to the impact glasses alone but to the late-stage mesostasis areas in Chang'E-5 basalts suggesting their possible relation to the volcanic or post-volcanic processes.

SAMPLE AND METHODS:

Magnetically separated 0.01 mg of the Chang'E-5 soil sample was placed on the carbon tape and carbon coated for EDS analysis (energy dispersive spectroscopy) and imaging with a Tescan Mira 3 FEG SEM equipped with an Oxford Instruments EDS detector (Vernadsky Institute, Moscow, Russia). The secondary electron (SE) imaging of the particles was carried out with an electron beam accelerating voltage of 10 kV at a working distance of 5 mm. Acquisition of additional BSE and qualitative elemental maps was performed with an electron beam accelerating voltage of 20 kV at a working distance of 15 mm.

RESULTS:

Two types of metal-sulfide association were found in the Chang'E-5 soil sample. They are related to 1) the primary basaltic fragments or their derivatives and 2) to the impact-induced glassy fragments. Besides that isolated Fe-metal filamentous crystals as well as rounded fibrous troilite aggregates and their rare intergrowths are present in the soil sample as loose particles.

Basaltic-associated Co-Ni-Cu-Fe-sulfides and metal-sulfide aggregates

Eight objects of sulfide or metal-sulfide association with coverage-like irregular shape were found embedded into a late-stage mesostasis areas of the basaltic fragments or related to the mineral fragments of <50 μm soil fraction. Most aggregates do not fit tightly to the surrounding material with frequent cracks between them. Rare cracks cross inside the sulfide aggregate as well. Minerals in contact with these objects are mainly fayalite, Ca-Fe-rich pyroxene, K- or K-Ba-feldspar, ilmenite, REE-merrillite. Sometimes fragmentary nano-sized condensate emulsion coats the contacting minerals. The mineral association is dominated by worn-like troilite forming dendrite-like fibrous network with the 20–50 nm thickness of the composing fibers. Sometimes fibers demonstrate parallel orientation. On the surface of the fibrous substrate rare whiskers-like Fe metal occurs as 0.5–1,0 μm densely packed aggregates of elongated filamentous crystals of 50–150 nm in width.

A Ni-bearing metal aggregate of irregularly shape is present on the sulfide surface at a distance of 5 μm from the Ni-free metal whiskers. A single Cu-bearing sulfide represented by a skeletal 1 μm-sized crystal is attached to the fibrous troilite substrate along with filamentous Fe-metal as well. Another stellate crystal aggregate (2 μm in size) of Cu-rich Fe-bearing sulfide is attached to the sulfide film (35×35 μm area) observed on the flat

surface of silicate grain. The film is composed of sulfide nano-particles of 50–100 nm in size, demonstrating overlaying clusters of concentric rings which could reflect either underlying silicate chip surface or two centers of film growth. The film consists of Cu-bearing troilite (up to 1.5 wt.% Cu) with the Cu-rich Fe-bearing (77.5 wt.% Cu, up to 0.5 wt.% Ni) sulfide aggregate grown on the surface. Small crystals of Co-Ni bearing Fe-sulfide (8.6 wt.% Co, 4.1 wt.% Ni) and Cu-bearing Fe-sulfide (7.4 wt.% Cu) are also settled on the film surface.

Impact glass-associated metal-sulfide spherules

These objects are common on the surfaces and interiors of some glassy particles and are represented by spherules with flat or elevated surfaces reaching 3–5 μm in diameter. Sulfide demonstrates porous texture. Fe-metal is commonly situated in the central part of the spherules forming spherical lenses thought to be initial stages of filamentous crystal growth. Filamentous Fe-metal aggregates up to 0.5 μm are rarely found on the surface of the spherules. Different metal to sulfide ratios are observed on the surface of the spherules from pure sulfide to pure Fe-metal composition.

Some vesicular impact glasses contain nano-sized sulfide particles precipitated on the inner surface of vesicle channel and around its outlet to the glass surface. This can be interpreted as condensation from gas or fluid phase formed in the closed vesicle before pressure and temperature dump when the vesicle became opened.

Individual Fe-metal and sulfide grains and intergrowth fragments

Besides that isolated Fe-metal filamentous crystal aggregates up to $3 \times 4 \mu\text{m}$ are found in the soil sample. Most of them are characterized by Ni-free composition. Some of them are attached to the fibrous like troilite and reach 2.5 μm in length. The largest individual troilite is $17 \times 20 \mu\text{m}$ in size and has fibrous surface texture almost completely covering the particle similar to the observed in metal-sulfide association. An aggregate of flattened crystals arranged in parallel is present in some area of the studied particle suggesting the growth in free space.

DISCUSSION:

Common relation of the Cu-Ni-Fe-S mineralization to the late-stage mesostasis areas suggests that this association is a result of the late-stage magmatic or post-magmatic processes supporting the hypothesis of a possible fluid-vapor transport and deposition of metals and sulphides in the lunar rocks [8]. The metal-troilite veinlet and inclusions of Cu-bearing troilite found in the polished sections of the basaltic fragments exclude their relation to the regolith reprocessing on the lunar surface and point to their endogenous origin similar to sulfide finds in basalts [9].

The unique find of copper-bearing sulfide film and copper sulfide crystals precipitated on the surface of silicate grains has signs of multistage formation that cannot be realized in the rapid impact process under the quick pressure drop of the impact vapor. The more likely it is a product of fumarolic gases condensation in a semi-closed system like a lava tube or fracture where the components income and gas pressure were pulsed and high enough to deposition of the Cu and Fe sulfides. The following points: 1) occurrences of Cu-Ni-bearing sulfides in magmatic rocks; 2) Ni-free composition of metal iron, 3) a lack of correlation of Cu and Ni in the sulfides, 4) and absence of separation mechanism for Fe and Ni in impact vapor; 5) general low abundance of copper and exceptional rarity of Cu-minerals in the meteorites together with regular finds of copper mineralization in the Chang'E-5 samples strongly contradict to the meteorite impact origin of the copper-bearing sulfides found on the surface of regolith particles in association with iron metal whiskers (e.g. [10]) and consistent with a lunar source of these metals. We observed two distinct populations of the sulfide-iron whiskers different in texture and composition and associated with basalts and impact glasses. We suggested that both of them are resulted from similar process of decomposition of sulfides of different genesis under the exogenous processes on the lunar surface. The copper enrichment

could be specific feature of the volcanic complexes and a marker for perspective mineral resources near the Chang'E-5 landing site region.

REFERENCES:

- [1] Long T., Qian Y., Norman M. D. et al. Constraining the formation and transport of lunar impact glasses using the ages and chemical compositions of Chang'e-5 glass beads // Science Advances. 2022. V. 8(39). Article eabq2542. DOI: 10.1126/sciadv.abq2542.
- [2] Yang W., Chen Y., Wang H. et al. Geochemistry of impact glasses in the Chang'e-5 regolith: Constraints on impact melting and the petrogenesis of local basalt // Geochimica et Cosmochimica Acta. 2022. V. 335. P. 183–196. <https://doi.org/10.1016/j.gca.2022.08.030>.
- [3] Guo Z., Li C., Li Y., Wen Y. et al. Sub-microscopic magnetite and metallic iron particles formed by eutectic reaction in Chang'E-5 lunar soil // Nature Communications. 2022. V. 13. Article 7177.
- [4] Wu Y., Liao S., Yan P. et al. Impact-related chemical modifications of the Chang'E-5 lunar regolith // Geochimica et Cosmochimica Acta. 2023. V. 363. P. 94–113. DOI: 10.1016/j.gca.2023.10.031.
- [5] Pang R., Yang J., Li R. et al. Redox condition changes caused by impacts: Insights from Chang'e-5 lunar glass beads // Science Bull. 2024. V. 69. P. 1495–1505. <https://doi.org/10.1016/j.scib.2024.03.004>.
- [6] Yan P., Xiao Z., Wu Y. et al. Iron-rich grain-decorated depressions on surfaces of lunar impact glasses // J. Geophysical Research: Planets. 2024. V. 129. Iss. 4. Article e2024JE008284. DOI: 10.1029/2024JE008284.
- [7] Cao Z., Guo Z., Li C. et al. Submicroscopic magnetite may be ubiquitous in the lunar regolith of the high-Ti region // Science Advances. 2024. V. 10. Iss. 38. Article eadn2301.
- [8] Colson R. O. Mineralization on the Moon? Theoretical consideration of Apollo 16 "Rusty Rocks", sulfide replacement in 67016 and surface-correlated volatiles on lunar volcanic glasses // Proc. 22th Lunar and Planetary Science Conf. 1992. P. 427–436.
- [9] Tang X., Tian H., Sun S. et al. Origin and implication of pentlandite in Chang'e-5 lunar soils // Lithos. 2023. V. 458. Article 107342. <https://doi.org/10.1016/j.lithos.2023.107342>
- [10] Li J., Gu L., Tang X. et al. First discovery of impact-induced vapor deposition of native copper, FeCo alloy and digenite from Chang'e-5 lunar soil // Icarus. 2024. V. 415. Article 116082. <https://doi.org/10.1016/j.icarus.2024.116082>.

DETERMINATION OF THE MIXING FACTOR OF LOCAL AND FOREIGN MATERIAL IN THE LANGRENUS AND CAVALERIUS CRATERS EJECTA

A. S. Krasilnikov, M. A. Ivanov

Vernadsky Institute of Geochemistry and Analytical Chemistry RAS, Moscow, Russia, krasilnikov_as@geokhi.ru

KEYWORDS:

Moon, Langrenus, Cavalerius, Mare Fecunditatis, Oceanus Procellarum, rays, ejecta, mixing factor

INTRODUCTION:

Based on the data on the iron oxide content in the rays of the Langrenus and Cavalerius craters, a relationship has been defined that describes the ratio of the regolith from Mare Fecunditatis and Oceanus Procellarum, respectively, to the material of the crater ejecta. This ratio represents a mixing factor of local and foreign material formed during the fall of craters' ejecta. The data obtained make it possible to refine the currently existing mixing models.

MIXING FACTOR OF LOCAL AND FOREIGN MATERIALS:

During the emplacement of the ejecta deposit, broad-sized materials fall out, forming secondary impact craters in a wide range of diameters. As a result, the regolith of the near-surface layers is mixed with the ejecta material. An approach to solving the mixing problem was proposed by Oberbeck et al. (1975) [1]. They managed to create an empirical relation of the change in the value of μ as the distance from the crater increases: $\mu = 0.0183R^{0,87}$ (1), where R — distance from the middle of the crater radius to the point where its ejecta is calculated.

In their work, Petro and Pieters (2006) [2] determined that the results obtained using the mixing model of Oberbeck et al. (1975) [1] are poorly comparable with the geochemical and petrographic features of the Apollo 16 soil. This discrepancy led authors to conclude that the mixing factor μ , calculated from formula (1), should be reduced by about a factor of two.

ESTIMATION OF THE MIXING OF LOCAL AND FOREIGN MATERIALS BY THE DATA ABOUT THE CONTENT OF IRON OXIDE IN THE RAYS OF THE LANGRENUS AND CAVALERIUS CRATERS:

Currently, there is no definitive confirmation of the accuracy of the material mixing models. To refine them, the models were compared with data on the iron oxide content in the lunar regolith, estimated from the results of the Clementine mission [3].

The rays of the Langrenus crater (Figure 1a) were taken as the object of study, which was selected because: 1) it is located on the border of the Mare Fecunditatis and the highlands, and part of its rays are visible on the dark and smooth mare surface; 2) the age of the crater, 3.44 Ga [4], almost matches with the age of the mare surface of the Mare Fecunditatis, 3.37 Ga [4], which minimizes the difference in the regolith aging of the rays and the mare surface as a result of mechanical reworking of regolith by ejected particles.

The Cavalerius crater's rays (Figure 1b) were taken for the same reasons: 1) the crater ejected the continental material onto the smooth surface of Oceanus Procellarum; 2) the ages of the crater (~3.2 Ga [5]) and the mare surface (~3,18 Ga [6]) are almost a match.

In our study, only those rays that lie on the smooth surface of the mare were used. Within each of them, we have selected randomly distributed points at which the model determined the FeO content. The obtained estimates of FeO content for Langrenus crater rays form a clearly defined trend of increasing iron oxide, as the distance (D) from the centre of the crater in-

creases (Figure 2a), which is described by a linear function: $\text{FeO} = 2.397133004E-005D + 9.585152604$ (2), where D — distance from the crater centre in meters, FeO — iron oxide content in wt.%.

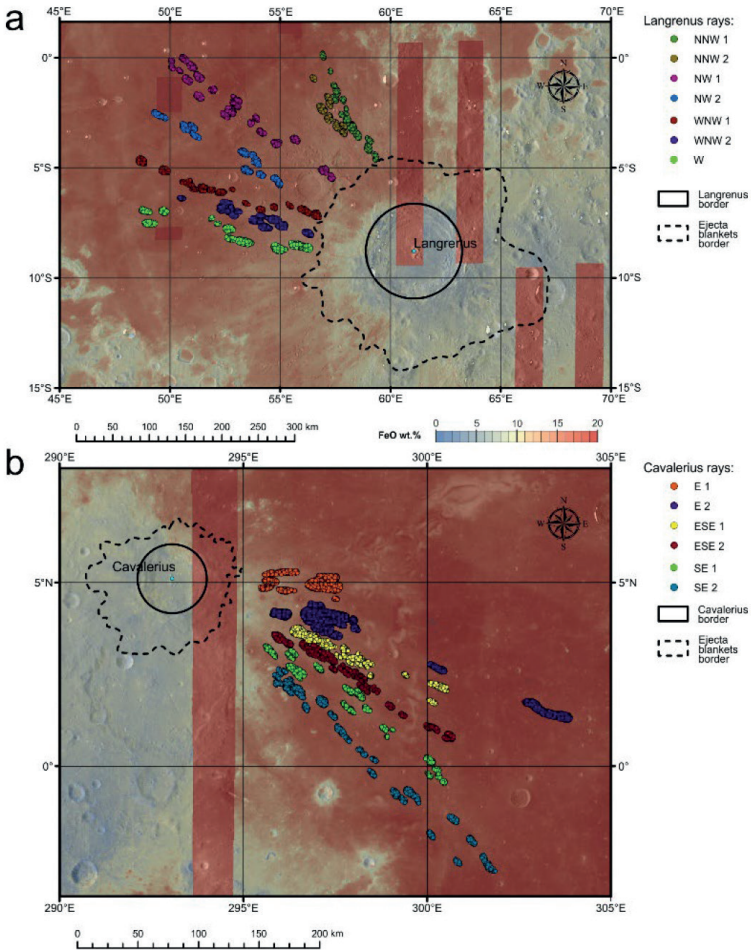


Figure 1. Map of the FeO content in the area of the Langrenus (a) and Cavalierius (b) craters, and the rays used in the calculations

For the Cavalierius crater, the two trends were formed (Fig. 2b), which are described by the following functions: 1) $\text{FeO} = 5.370100657E-005D + 8.732873672$ (3); 2) $\text{FeO} = 3.310274722E-005D + 10.32005953$ (4).

We consider the increase in iron oxide as a result of the mixing of two end members: mare material with an average FeO content of 17.5 wt.%, and highland materials with an average FeO content of 5.5 wt.%. The determined function (2) shows that directly outside the zone of continuous ejecta at a distance of ~150 km from the center of the crater, the content of iron oxide is ~13.16 wt.%, which, at the indicated contents of iron oxide in the end-members, corresponds to a mix of ~36 and 64 % of the highland and mare components. At a distance of 330 km, where the horizontal part of the trend begins, the iron oxide content is estimated to be ~17.5 wt.%, which practically matches with the average FeO content in the Mare Fecunditatis regolith and, therefore, corresponds to almost 100 % of the mare component.

The obtained dependence (2) allows us to propose a formula for estimating the proportion of foreign/local material (L/F) in the range of distances from the zone of contiguous ejecta (~100 km) to the one where the local rego-

lith dominates (~300 km): $L/F = 0.00031457D^{0.63219}$ (5), where D — distance from the crater center in meters.

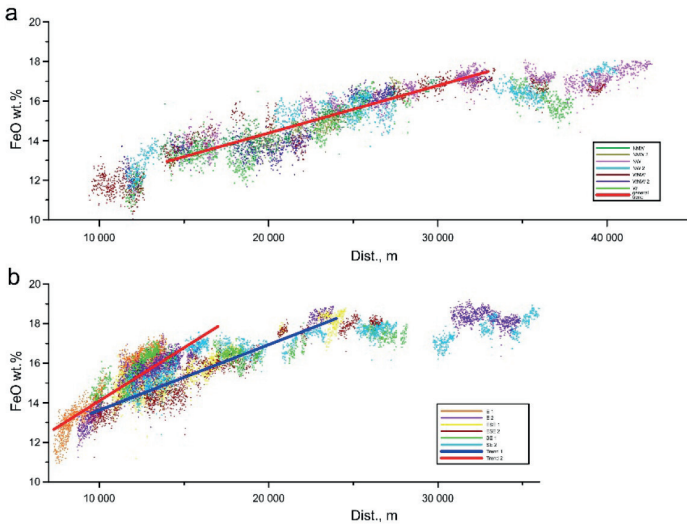


Figure 2. Change in the amount of iron oxide in the rays of the Langrenus (a) and Cavalerius (b) craters depending on the distance from its center

Using a similar approach, we researched the Cavalerius crater rays. As end members of the mixing, we consider the FeO content of ~18 wt.% haw 100 % mare material and ~8.2 wt.% haw 0%. According to trend 1, mare material reaches 100% values over a distance of ~170 km from the crater center. According to trend 2 ~240 km. At the place where the calculations begin, the mare material content is ~47 % for trend 1 (~75 km from the crater center) and ~49 % for trend 2 (~85 km).

As a result, we obtained the following formulas:

- 1) $L/F = 0.0000152395D^{0.92009}$ (6) for trend 1;
- 2) $L/F = 0.0001797478D^{0.6949444}$ (7) for trend 2.

Formulas (5)–(7) are not an alternative for estimating the degree of mixing, but allow one to obtain an integral estimate of the proportions of local and foreign material.

ACKNOWLEDGMENTS:

Sources of funding: The work was done under the GEOKHI RAS state assignment.

REFERENCES:

- [1] Oberbeck V.R., Quaide W.L., Gault D.E. et al. On the origin of the lunar smooth-plains // *Earth, Moon, and Planets*. 1975. V. 12. P. 19–54. DOI: 10.1007/BF02626332.
- [2] Petro N.E., Pieters C.M. Modeling the provenance of the Apollo 16 regolith // *J. Geophysical Research: Planets*. 2006. V. 111. Iss. E9. P. 1–13. <https://doi.org/10.1029/2005JE002559>.
- [3] Lucey P.G., Blewett D.T., Jolliff B.L. Lunar iron and titanium abundance algorithms based on final processing of Clementine ultraviolet-visible image // *J. Geophysical Research: Planets*. 2000. V. 105. Iss. E8. P. 20297–20305. <https://doi.org/10.1029/1999JE001117>.
- [4] Ivanov M.A., Head J.W., Hiesinger H. New insights into the regional and local geological context of the Luna 16 landing site // *Icarus*. 2023. V. 400. Article 115579. <https://doi.org/10.1016/j.icarus.2023.115579>.
- [5] Hood L.L. The enigma of lunar magnetism // *EOS*. 1981. V. 62. Iss. 16. P. 161–163. <https://doi.org/10.1029/EO062i016p00161>.
- [6] Stöffler D., Ryder G. Stratigraphy and isotope ages of lunar geologic units: Chronological standard for the inner solar system // *Space Science Reviews*. 2001. V. 96. Iss. 1/4. P. 9–54. DOI: 10.1023/A:1011937020193.

THE LUNAR SEGMENT OF THE FEDERAL SPACE SCIENCE PROJECT

L. M. Zelenyi, I. G. Mitrofanov, A. A. Petrukovich

Space Research Institute RAS, Moscow, Russia, mitrofanov@np.cosmos.ru

KEYWORDS:

Moon exploration, lunar poles, Russian lunar program

ABSTRACT:

Recently, the State Program of the Russian Federation “Space Activities of Russia” was adopted for the period up to 2036. It includes Space Science project proposed and developed by Russian Academy of Sciences. This project is aimed at the exploration of the Solar system, including the development of technologies for interplanetary flights and preparation of human activities outside Earth orbit. The significant and important segment of this project is related with the lunar exploration. It formulates key robotic lunar missions and its objectives that should be completed before 2036 and even continued beyond this time limit.

LUNAR EXPLORATION FROM POLAR ORBIT: LUNA-26

A. A. Petrukovich, L. M. Zelenyi, K. V. Anufreichik

Space Research Institute RAS, Moscow, Russia, m.litvak@np.cosmos.ru

KEYWORDS:

Moon, Luna-26, orbital mapping

ABSTRACT:

Russian Lunar orbiter Luna-26 is planned for launch in 2028 and targeted to map lunar surface and subsurface composition, as well to study neutral, dust and plasma exosphere. It also provides support for Luna-27 polar landers including high resolution digital elevation models (DEM) for landing site selection and relay service. We present the mission objectives, instrumentation, science plan and discuss the role of the mission in the Russian lunar program.

SCIENCE AT THE LUNAR POLES: LUNA-27.1 AND LUNA-27.2

I. G. Mitrofanov, L. M. Zelenyi, A. A. Petrukovich

Space Research Institute RAS, Moscow, Russia, mitrofanov@np.cosmos.ru

KEYWORDS:

Moon exploration, lunar poles, Russian lunar program, Luna-27

ABSTRACT:

Luna-27 mission is a one of critical milestones of Russian lunar program accepted for the period up to 2036. This mission includes the launch of two identical robotic landers to explore the south and north poles of the Moon and combines ambitious scientific objectives, testing new space technologies, and searching/exploring areas potentially suitable for the creation of a future lunar base.

The primary science goals of the Luna-27 mission both on the south and north poles are the following:

- Studies of the mineralogical, chemical, elemental, and isotopic composition of subsurface layer of lunar regolith using remote and contact science including analysis of regolith samples extracted and delivered by a drill unit from various depths up to 1 m.
- Search for water ice in the subsurface layer of the lunar regolith and estimation of its depth distribution.
- Studies of the ionic, neutral, and dusty components of the Moon's exosphere and the effects of the interaction of the Moon's surface with the interplanetary medium and the solar wind.
- Studies of the physical (mechanical, thermal, dielectric, etc.) properties of the soil of the upper layer of the lunar surface.

TOWARD MULTIWAVELENGTH DISTRIBUTED ASTRONOMICAL OBSERVATIONS FROM THE MOON

M. Sachkov¹, A. Shugarov¹, H. Wang^{3,4}, X. Jiang^{3,4}, M. Kirsanova¹, V. Arefiev², A. Pozanenko², S. Svertilov⁵, J. Wang³

¹ Institute of Astronomy RAS, Moscow, Russia, shugarov@inasan.ru

² Space Research Institute RAS, Moscow, Russia, arefiev@iki.rssi.ru

³ National Astronomical Observatories, Chinese Academy of Sciences Beijing, China, wanghj@nao.cas.cn

⁴ University of Chinese Academy of Sciences, Beijing, China

⁵ Skobel'syn Institute of Nuclear Physics Lomonosov Moscow State University Moscow, Russia, Moscow, Russia

KEYWORDS:

lunar base, ILRS, Moon-based telescope, UV, X-ray, Gamma-ray, long-wave radio interferometer

ABSTRACT:

The prospects for building a multipurpose International Lunar Research Station (ILRS) and the prospects for using robots on the Moon open up opportunities for using the main fundamental advantages of the Moon over classical spacecraft — the ability to create large structures on a solid surface in vacuum conditions and their subsequent maintenance by astronauts and robots. In this regard, the Moon is a unique site in the Solar System for deployment of the next generation astronomical facilities in different wavelengths. All other bodies, such as Mars, are located at a noticeably longer distance and have a number of disadvantages that make them unusable as an astronomical base at least in the near future.

Since many astrophysical phenomena require multiwavelength observations, it makes sense to deploy several telescopes on the Moon close to each other, e.g. on the south pole of the Moon. It enables simultaneous observations of the same area of the sky, allowing for continuous and synchronous multiwavelength monitoring of transients and other sources. The multiwavelength distributed astronomical observatory on the Moon is compliant with the vision of the ILRS, where many countries may contribute to ILRS to carry out their scientific research with their own facilities and benefit from international cooperation.

The creation of an observatory on the Moon may start in the next decade. At the first stage, on the time scale of a decade, we offer to build several small (3–10 kg) technological pathfinders of the Moon-based telescopes for different wavelengths. The main goals are to test critical technologies, to evaluate some technological aspects of astronomical observations at different wavelength from the Moon and to probe new methods of astronomical observations from the Moon that cannot be done from other orbits close to the Earth. These small telescopes should be capable of studying several astronomical scientific goals with limited efficiency due to the size of the instruments. Currently, we are considering technological pathfinders for UV-optical-IR spectral range, long-wave radio range, X-ray and Gamma-ray. They may be proposed as an additional payload for Chinese, Russian and other missions to the Moon. To speed up the development, high Technology Readiness Levels (TRL) components may be used.

For the UV-optical-IR spectral range, two types of technological pathfinders are proposed by a Chinese team from NAOC and Russian team from INASAN. To evaluate the idea of a wide-field multiaperture survey from the Moon (Figure 1, left), its pathfinder (Figure 2, left) may use an advanced star tracker (TRL = 9) with a UV-optimized lens and UV-enhanced sCMOS, which provides a field of view of $\sim 5.5 \times 5.5^\circ$ [1]. It can be fixed on the Moon lander and observation will be performed in a passive scan mode, the required mass is only 3–5 kg.

As a pathfinder of a large Moon-based UV-optical-IR telescope (ILRS-5, Figure 1, *right*), a small 7–15 cm UV telescope (Figure 2, *right*) is proposed. It has a long focus and high angular resolution of up to 2 arcsec in FUV. 2-axis mount and set of filters allows a flexible scientific observation program. The required mass budget started from 10 kg.

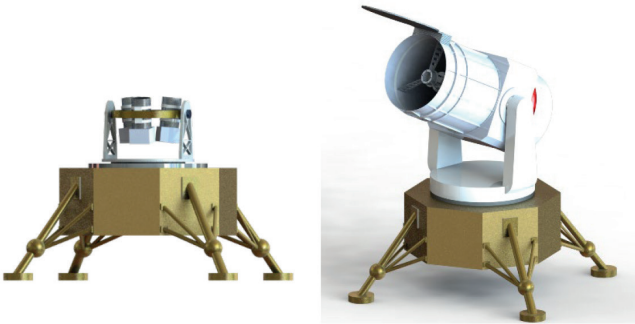


Figure 1. Conceptual view of wide-field multiaperture UV telescope (*left*) and multipurpose Moon-based UV-optical-IR telescope (*right*), NAOC

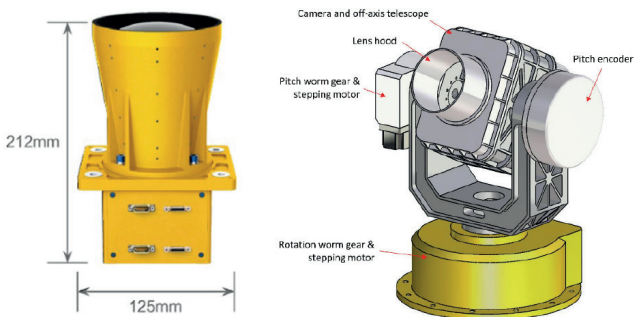


Figure 2. Technological pathfinders for Moon-based wide-field multiaperture UV survey (*left*) and Moon-based UV-optical-IR telescope (*right*)

For the long-wave radio range, the technological pathfinder of a single node of a future large radio interferometer on the Moon's back side may be proposed.

For X-ray IKI RAS offers to build a technological pathfinder (Figure 3, *left*) within a 10 kg mass budget to operate in 4–100 keV without optics (field of view of 20°) to study the operation of X-ray detectors on the Moon and to observe bright objects. For the second step, they propose to build a universal X-ray module (MBH M-2) for a narrow-field mirror X-ray telescope (Figure 3, *center*) with an energy range of 2–30 keV, effective area of 600 cm², field of view of 60 arcmin, angular resolution of 45 arcsec and total mass of 65 kg.

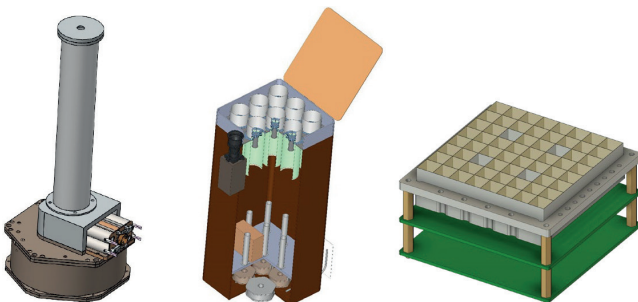


Figure 3. Technological pathfinders: X-ray telescope without optics (*left*), universal X-ray module with optics (*center*), gamma-ray detector (*right*)

For Gamma-ray IKI RAS and SINP offer a broadband omnidirectional spectrometer-polarimeter for observations in the 10 keV – 10 MeV range. At the first step, using heritage [5] from Chibis-AI Segmented Gamma Spectrometer, a 10 kg technological pathfinder is proposed with 256 cm² geometric area of the detector (Figure 3, *right*).

At the second stage (2035–2040) of ILRS building, several medium-class astronomical telescopes [3] may be proposed for future dedicated large Lunar astronomical missions (Figure 1), e.g. ILRS-5, LUNA-32. Medium-class astronomical telescopes will produce world-class scientific results and will become the first true full-featured astronomical telescopes on the Moon.

We expect that after 2040 the ILRS base will involve humans and robots. In the third stage of the Moon astronomical base construction (2040–2060), large astronomical telescopes can be considered to be deployed on the Moon, including those that require the installation of multiple modules spread across the Moon, e.g. interferometers, long focus telescopes and large structures.

REFERENCES:

- [1] *Shugarov A., Sachkov M., Wang H. et al.* A concept of a simple small-sized (5–10 kg) lunar astronomical UV telescope using high TRL components // 15th Moscow Solar System Symp. 15M-S3. 2024. P. 166–168.
- [2] *Wang H., Sachkov M., Dong S. et al.* Recent progress on the lunar-based UV-optical-IR telescope for ILRS // 15th Moscow Solar System Symp. 15M-S3. 2024. P. 173–174.
- [3] *Shugarov A. S., Wang H., Dong S. et al.* The concept of Lunar-based astrophysical telescope for international lunar research station // Vestnik NPO Lavochkina. 2022. No. 1(55). P. 3–9 (in Russian).
- [4] *Sachkov M., Shugarov A., Shmagin V., Gómez de Castro A. I.* The concept of lunar-based astrophysical telescope for international lunar research station (ILRS) // Proc. SPIE. 2022. V. 12181. Article 121812V. 5 p. DOI: 10.1117/12.2629619.
- [5] *Mkrtchyan A., Pozanenko A., Minaev P. et al.* Calibration of segmented BGO scintillation detectors for space-based gamma-ray polarimeter // Experimental Astronomy. 2025. V. 59. Article 12. <https://doi.org/10.1007/s10686-025-09977-9>.

SALIENT SCIENCE OUTCOME FROM CHANDRAYAAN-3 MISSION

S. Megala

*Science Programme Office, Indian Space Research Organisation
Bangalore, India, megala@isro.gov.in*

KEYWORDS:

lunar south polar region, Lunar Magma Ocean, South Pole Aitken (SPA) basin, lunar mantle, complex cratering process

ABSTRACT:

Chandrayaan-3 was launched on 14th July 2023 by LVM3 M4 from Sriharikota. The integrated module carried out five Earth bound maneuvers, Trans lunar injection and was inserted in the lunar orbit on 5th August. After several lunar burns, the lander module was separated from the propulsion module on 17th August. Following two de-boost maneuvers, the Lander along with the 26 kg Rover executed a flawless landing with an Autonomous Landing Sequencer, marking a significant milestone on 23rd August 2023. This accomplishment has placed India as the fourth country to master the soft-landing on the Moon and first country to land in the southern high latitudes on the Moon.

Post landing, the Rover moved around the landing site and traversed a total of ~100 m distance. Payloads on the Lander and Rover were deployed for in-situ investigations. First-ever scientific data about the lunar surface and the near-surface environment at the Shiv Shakti point are intriguing and provided new insights about the Moon.

Elemental composition measurements validated the Lunar Magma Ocean (LMO) hypothesis, which is one of the leading theories on the evolution of the Moon. Further, the presence of excess Magnesium-rich minerals in the regolith shows that material excavated during the formation of the South Pole Aitken (SPA) basin, the largest impact basin in the solar system has been mixed with upper layer material at Shiv-Shakti point.

Seismometer detections indicated that the polar regions are not seismically-quiet and detected ~50 events which were probably from natural sources.

Analysis of Rover NavCam images revealed that the Vikram lander landed on a buried crater that is of semi-circular structure (160 km in size, ~4.4 km deep). It was highly degraded due to thick ejecta deposits from the SPA basin, indicative of complex cratering throughout the geological history of the Moon.

First-ever in-situ measurement of the temperature of the Moon's surface to the depth of 10cm indicated that the lunar surface temperatures show a significant spatial variability at metre scales at high latitudes, unlike the equatorial regions.

X-ray spectrometer revealed potential presence of primitive lunar mantle materials at the landing site, which was excavated during formation of the South Pole-Aitken (SPA) basin 4.3 Ga ago and redistributed by subsequent impacts on the SPA basin ejecta. The primitive mantle contributed the excess sulfur, which got mixed up with the materials at the landing site.

PRELIMINARY CONSIDERATIONS ON THE AI REQUIREMENTS IN LUNAR-BASED ASTRONOMICAL OBSERVATIONS AT ILRS

H. Wang^{1,9}, G. Zhao^{1,9}, M. Sachkov², S. Dong³, X. Bai^{1,9}, A. Shugarov², Y. Chen^{1,9}, X. Jiang^{1,9}, H. Tian⁴, N. Jiang⁵, W. Wang^{1,9}, Q. Zong⁶, Y. Deng^{1,9}, G. Zhao^{1,9}, X. Zhang^{1,9}, X. Zhang⁶, V. Shmagin², Y. Liu^{1,9}, B. Shustov², S. Sichevskij², A. Buslaeva², I. Savanov², Q. Xing^{1,9}, W. Wang⁶, J. Wang^{1,9}, J. Wang¹, H. Zhi¹, L. Wang¹, B. Yan^{7,8}, Y. Tang^{7,8}, X. Zeng¹, P. Qiu^{1,9}

¹ National Astronomical Observatories, Chinese Academy of Sciences
Beijing, China, wanghj@nao.cas.cn, gzhao@nao.cas.cn

² Institute of Astronomy RAS, Moscow, Russia, msachkov@inasan.ru

³ Department of Astronomy, School of Physics, Peking University
Beijing, China, dongsubo@pku.edu.cn

⁴ School of Earth and Space Sciences, Peking University, Beijing, China
huitian@pku.edu.cn

⁵ Department of Astronomy, University of Science and Technology of China
Hefei, China, jnac@ustc.edu.cn

⁶ Macau University of Science and Technology, Macau, China
qgzong@pku.edu.cn

⁷ School of Physics, Zhejiang University of Technology, Hangzhou, China
boyan@zjut.edu.cn

⁸ Collaborative Innovation Center for Bio-Med Physics Information
Technology of ZJUT, Zhejiang University of Technology, Hangzhou, China

⁹ University of Chinese Academy of Sciences, Beijing, China, xybai@nao.cas.cn

KEYWORDS:

lunar-based astronomical observations, UV-Optical-IR observations, International Lunar Research Station (ILRS), Artificial Intelligence (AI)

INTRODUCTION:

Multiple nations are actively advancing lunar exploration through initiatives such as the Artemis Program, the Moon Village concept, and the International Lunar Research Station (ILRS) initiative. The establishment of the ILRS presents unprecedented opportunities for conducting astronomical observations by leveraging the Moon's unique environment and location. The lunar surface, unaffected by Earth's atmosphere, ionosphere, and artificial radio signals, offers a stable platform for observations across the full electromagnetic spectrum — from ultra-long wavelength radio waves to high-energy gamma rays — and potentially for the detection of neutrinos and gravitational waves [1–13]. Building upon in-depth conceptual design and scientific objective studies conducted by our international collaborative team for the lunar-based UV-Optical-IR telescope/array at ILRS, this report uses lunar-based UV-Optical-IR astronomical observation as an example to briefly introduce our preliminary considerations on the Artificial Intelligence (AI) requirements for lunar-based astronomical observations at ILRS.

Realizing the potential of lunar-based astronomical observation necessitates integrating AI capabilities throughout its entire lifecycle, given the Moon's extreme environmental challenges and inherent operational constraints. The severe challenges posed by the lunar environment primarily manifest in extreme day-night temperature variations, lunar dust, high radiation levels, power limitations during lunar nights, and communication delays with Earth. These factors demand a paradigm shift towards highly autonomous astronomical observation systems. AI is crucial for mitigating these constraints and enabling efficient and reliable observations. AI can play key roles in autonomous operation and health management of astronomical instruments, intelligent observation planning and scheduling, in situ intelligent data processing and compression, robust perception and navigation for deployment/maintenance, resource optimization and coord-

dination, and scientific discovery and anomaly detection. Meeting these requirements demands AI systems that are robust, explainable, adaptive, and efficient, capable of effective integration with the broader ILRS infrastructure, communication systems, and data management framework.

REFERENCES:

- [1] Wang C., Lin Y., Pei Z. et al. Key Scientific Questions Related to the Lunar Research Station // Bull. National Natural Science Foundation of China. 2022. V. 36(6). P. 830–840. DOI: 10.16262/j.cnki.1000-8217.2022.06.004.
- [2] Pei Z., Wang Q., Xu L. et al. Strategic Analysis of Scientific Activities and Study on the Overall Plan of Scientific Operation Platforms Based on the Lunar Research Station // Chinese J. Space Science. 2025, V. 45(1). P. 1–14. DOI: 10.11728/cjss2025.01.2024-0188.
- [3] Wang H., Jiang X., Wang J. et al. Research on Methods to Expand Stellar Infrared Flux for Lunar-based Astronomical Observations // J. Space Science and Experiment. 2025. V. 2(2). P. 54–61. DOI: 10.19963/j.cnki.2097-4302.2025.02.006.
- [4] Wang H., Jiang X., Deng Y., et al. Research on Methods for Site Selection for Lunar-based UV-Optical-IR Astronomical Observations // J. Space Science and Experiment. 2024. V. 1(1). P. 33–39. DOI: 10.19963/j.cnki.2097-4302.2024.01.004.
- [5] Wang H., Sachkov M., Dong S. et al. Optimizing Scientific Objectives for the Lunar-based UV-Optical-IR Telescope for ILRS // 14th Moscow Solar System Symposium 14M-S3: Abstr. book. Moscow: IKI RAS, 2023. P. 119–120. DOI: 10.21046/14MS3-2023.
- [6] Shugarov A. S., Sachkov M., Wang H. et al. Astrophysical UV-Optical-IR Telescope for the International Lunar Research Station // 14th Moscow Solar System Symposium 14M-S3: Abstr. book. Moscow: IKI RAS, 2023. P. 154–156. DOI: 10.21046/14MS3-2023.
- [7] Wang H., Sachkov M., Dong S. et al. A Brief Introduction about the Science of the Lunar-based UV-Optical-IR Telescope for ILRS // 2023 Asia-Pacific Regional IAU Meeting (APRIM 2023). 2023.
- [8] Wang H., Chen X, Sachkov M., Dong S. et al. A brief introduction to the astronomical research for ILRS // Intern. Workshop on Overall Science Objectives of ILRS. 2023.
- [9] Shugarov A. S., Huijuan Wang, Subo Dong et al. The concept of Lunar-based astrophysical telescope for international lunar research station // Vestnik NPO Lavochkina. 2022. No. 1(55). P. 3–9. DOI: 10.26162/LS.2022.71.64.001.
- [10] Shugarov A., Dong S., Wang H. et al. The Concept Moon-based UV Survey to Study Transients and Variables // 13th Moscow Solar System Symposium 13M-S3. Abstract book. 2022. P. 106–107. DOI: 10.21046/13MS3-2022.
- [11] Wang H., Sachkov M., Dong S. et al. Science of the Lunar-based UV-Optical-IR Telescope for ILRS // 13th Moscow Solar System Symposium 13M-S3. Abstract book. 2022. P. 108. DOI: 10.21046/13MS3-2022.
- [12] Shugarov A., Sachkov M., Wang H. et al. The concept of Lunar-based UV-Optical-IR Telescope for ILRS // 12th Moscow Solar System Symposium 12M-S3. Abstract book. 2021. P. 441–443. DOI: 10.21046/12M-S3.
- [13] Sachkov M., Shugarov A., Shmagin V., de Castro A. I. G. The concept of lunar-based astrophysical telescope for international lunar research station (ILRS) // Proc. SPIE. V. 12181. Space Telescopes and Instrumentation 2022: Ultraviolet to Gamma Ray. 2022. DOI: 10.1117/12.2629619.

PERMANENT PROTECTION SYSTEM OF THE ASTRONAUT SPACESUIT, OPTICAL SURFACES AND ALL OTHER EQUIPMENT AGAINST CHARGED PARTICLES OF LUNAR DUST

H. I. Abdussamatov

Pulkovo Observatory RAS, Saint Petersburg, Russia, abduss@gaoran.ru

KEYWORDS:

charged lunar dust particles, electrically conductive shells equipment, electrical repulsion forces, dust-protecting bowl, dust particle protection system, Lunar Observatory, special optical telescope SOTR-300VM

INTRODUCTION:

The illuminated surface areas of the Moon become positively charged as a result of photoionization under the influence of mainly the UV part of the solar radiation spectrum. And the shadowed areas of the surface acquire a negative charge due to the incision of the solar wind flow and the plasma layer of the Earth's magnetosphere tail. As a result, dust particles lying on these charged areas of the surface and having received the same electric charge are subject to the action of electric forces exceeding the sum forces of gravity and van Der Waals adhesion. Which push them away from the surface and create a rarefied plasma shell near the lunar surface and conditions for their levitation and transportation along the surface due to the electric fields in the plasma shell [1–6]. Indeed, "streams of light" just above the lunar surface, caused by the scattering of sunlight by these rarefied charged dust particles, lifted by electrostatic forces from the illuminated surface, were directly recorded during sunset by the Surveyor spacecraft in 1967 [6–8] and Blue Ghost M1 on March 16, 2025 [9]. Such charged particles of lunar dust of regolith of submicron and micron sizes, levitating above the surface at altitudes of about 100–300 mm, settle on optical surfaces, the astronauts' spacesuit and the surface of equipment, and also penetrate into cracks and moving parts of the spacesuit, into rotating parts and mechanisms of equipment. They pose a serious danger to the successful work of astronauts and all optical-mechanical equipment on the lunar surface and are a serious obstacle to further exploration of the Moon. The development of scientific research on the Moon requires the creation of a reliable permanently protection system for engineering systems and humans located on the its surface from the settling and adhesion of levitating above surface charged particles of lunar dust to them.

UNIVERSAL EFFECTIVE SYSTEM OF PERMANENT PROTECTION AGAINST CHARGED PARTICLES OF LUNAR DUST OF THE ASTRONAUT SPACESUIT AND ALL EQUIPMENT BOTH DURING THE DAY AND AT NIGHT:

The most effective system for permanent protection of the astronaut's spacesuit as well as the optical surface and all other equipment from charged particles of lunar dust levitating above the surface of the Moon both during the day and at night are:

- For the first time, optical instruments and all other equipment are installing in a special dust-proof bowl more than 700 mm high, shaped like an inverted truncated cone (Figure 1). A durable bowl with a rigid and solid bottom is raised by support posts to a height of about 300 mm above the surface of the Moon, protected by two Russian invention patents [1, 2]. The location of the upper level of the bowl at a height of more than 1,000 mm above the surface will practically ensure the protection of the scientific and technical equipment located inside the bowl from possible penetration and settling on their surface of charged particles of lunar dust levitating on the underlying (~100–300 mm) layers [7–10]. The active operation of the unprotected from lunar dust Chinese Lu-

nar-based Ultraviolet Telescope (LUT), launched on December 2, 2013, during the daytime on the lunar surface shows a fairly high stability of its photometric characteristics during the 18-month lunar experiment, i.e., the absence of any adhesion of lunar dust to the telescope mirrors [11]. This allows us to state that charged micron and submicron near-surface lunar dust particles will not be able to rise above the surface to such a height. However, only such protection of equipment from charged lunar dust is necessary, but not sufficient for its complete protection over a long period of time, as well as for the protection of the astronaut's spacesuit.

- For the first time, the outer surface of the equipment, the astronaut's spacesuit, optical surfaces and dust-proof cup are covered with electrically conductive electrically insulated shells (by flexible and stretchable material for the spacesuit), connected to a power supply unit having the necessary electric charge with a given frequency of continuous polarity reversal, protected by two Russian invention patents [1, 2]. In vacuum and low gravity conditions, the excess of the electrical repulsion forces of their surface over the forces of gravity repels and throws back levitating charged particles with the same charge from settling on their surface both during the day and at night, since intermolecular van der Waals forces are absent. To ensure reliable repulsion from the surface of the optics, the astronaut's spacesuit, the dust bowl and all other equipment of individual charged particles of lunar dust of submicron and micron sizes, levitating above the surface at heights of 100–300 mm, it is necessary that the repulsive electrostatic force of their shells be comparable to the force of detachment of such particles from the lunar surface under the influence of electrostatic forces of the regolith charge [10].

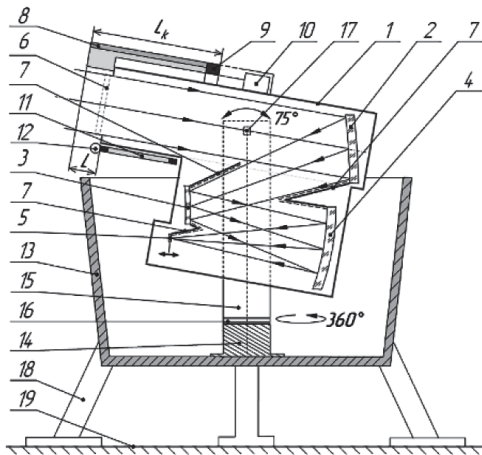


Figure 1. A longitudinal section of the SOTR-300V of the Lunar Observatory (with the ground glass removed) in a special protective bowl for studying the climate and the energy imbalance between the Earth and space [12, 13], where 1 — is the reliable hermetic enclosure of a telescope tube; 2 — the concave mirror; 3 — the convex mirror; 4 — the concave mirror; 5 — the CMOS image sensor; 6 — the entrance pupil; 7 — the antflash lens hood; 8 — the sliding visor; 9, 10 — the mechanisms of the displacement of the sliding visor; 11 — the diffusing glass; 12 — the joint; 13 — dust-protecting bowl; 14 — basement of the mount; 15 — upper part of the mount, azimuth-rotating; 16 — means of azimuth rotation; 17 — means of altitude rotation of the tube; 18 — support feet of the bowl; 19 — the lunar surface

Earlier, when developing the concept of the Lunar Observatory (LO) for studying the climate and the energy imbalance between the Earth and space in 2016 and 2017 years [12, 13], we were the first to patent our inventions for effective protecting only the mirrors of the special robotic optical telescope with the primary mirror of the diameter 300 mm and with sliding visor (SOTR-300V) in a special protective bowl from levitating charged

particles of lunar dust using a similar effective system (Figure 1) [1, 2]. Later modernized SOTR-300VM LO for continuous simultaneous monitoring of the asteroid-comet hazard throughout the entire celestial sphere and the Earth's climate [14, 15] is installed in the central zone of the dust-protective bowl, and its entrance pupil is located at a height of more than 1,000 mm above the surface of the Moon to reliably protect its mirrors from the settling and adhesion of charged particles of lunar dust, levitating above the surface at heights of about 100–300 mm, raised from the surface by electrostatic forces.

CONCLUSIONS:

- Protection of all scientific and technical equipment on the surface of the Moon from the settling and adhesion of charged particles of lunar dust levitating above the surface is primarily carried out by installing (placing) them in a special dust-proof bowl with an upper level at a height of more than 1,000 mm above the surface [1, 2]. The absence of dust particles deposited on the mirrors of the LUT telescope and the preservation of their high photometric efficiency of reflectivity during 1.5 years of active operation during lunar daytime hours indicate the practical absence of charged dust particles at the height of the LUT installation (significantly more than 300 mm) above the surface of the Moon.
- The astronaut's spacesuit, optical surfaces and other equipment, as well as the dust-proof bowl, are covered with electrically conductive, electrically insulated outer shells (by flexible and stretchable material for the spacesuit), connected to a power supply unit. The power supply unit produces the necessary electric charge with a given frequency of continuous polarity inversion, which repels and throws away from their outer shells like-charged particles of lunar dust in conditions of reduced gravity and vacuum of the Moon both during the day and at night.
- As a result, the specified frequency of polarity inversion of the required electric charge of the electrically insulated outer shells of the equipment, the astronaut's spacesuit, optical surfaces and dust-proof bowl will ensure their permanent reliable protection from the settling and adhesion of levitating particles of charged lunar dust.

Thus, the proposed universal system of continuous and reliable protection of equipments both during the day and at night from charged particles of lunar dust levitating above the surface consist in: (1) placing scientific and technical equipment in a special dust-proof bowl at the maximum possible distance from the surface; and (2) covering the astronaut's spacesuit, optical surfaces and other equipment, as well as the dust-proof cup with electrically conductive electrically insulated outer shells, connected to a power supply unit with the necessary electric charge with a given frequency of continuous polarity inversion [1, 2]. Such a round-the-clock effective system of protection of the spacesuit and all other equipment on the surface of the Moon from levitating charged particles opens up a broad reliable prospect for the creation of scientific, industrial, habitable infrastructure and permanent scientific bases using the latest technologies. And, finally, a global scientific task will be successfully solved – the organization of the Lunar Observatory on the Moon's surface with a system of round-the-clock simultaneous monitoring of asteroid danger throughout the celestial sphere and the Earth's climate [12–15].

REFERENCES:

- [1] *Abdussamatov H.I.* Device for protecting an optical telescope from charged lunar dust. Patent of Russia. No. 164303. 2016.
- [2] *Abdussamatov H.I.* Optical telescope. Patent of Russia. No. 2613048. 2017.
- [3] *Colwell J.E., Batiste S., Horányi M. et al.* Lunar surface: dust dynamics and regolith mechanics // *Reviews of Geophysics*. 2007. V. 45. No. 2. P. 1–26. <https://doi.org/10.1029/2005RG000184>.
- [4] *Sana T., Mishra S.K.* Revisiting lunar dust charging and dynamics // *Physics of Plasmas*. 2024. V. 31. Article 102901. <https://doi.org/10.1063/5.0225693>.

- [5] *Zakharov A.V., Zelenyi L.M., Popel S.I.* Lunar dust: properties and potential hazards // *Solar System Research*. 2020. V. 54. No. 6. P. 455–476. <https://doi.org/10.1134/S0038094620060076>.
- [6] *Popel' S.I.* Moon dust // *Chemistry and Life*. 2018. V. 5. P. 5–9.
- [7] *Norton R.H., Guinn J.E., Livingston W.C. et al.* Surveyor 1 observations of the solar corona // *J Geophysical Research*. 1967. V. 72. No. 2. P. 815–817. <https://doi.org/10.1029/JZ072i002p00815>.
- [8] *Rennilson J.J., Criswell D.R.* Surveyor observations of lunar horizon-glow // *Moon*. 1974. V. 10. P. 121–142. <https://doi.org/10.1007/BF00655715>.
- [9] Blue Ghost Mission 1 — Firefly Aerospace; Blue Ghost Mission 1 to Deliver NASA Electric Moon Dust Shield | AIAA. 2025.
- [10] *Abdussamatov H.I.* Permanent protection system of the astronaut spacesuit, optical surfaces and all other equipment against charged particles of lunar dust // *Intern. J. Environmental Sciences and Natural Resources*. 2025. V. 35. No. 4. Article 556420. DOI: 10.19080/IJESNR.2025.35.556420.
- [11] *Wang J., Meng X.M., Han X.H. et al.* 18-months operation of lunar-based ultra-violet telescope: A highly stable photometric performance // *Astrophysics and Space Science*. 2015. V. 360. No. 10. P. 1–5. <https://doi.org/10.1007/s10509-015-2521-2>.
- [12] *Abdussamatov H.I.* A study of climate from the lunar surface and the energy imbalance between the Earth and space // *Geomagnetism and Aeronomy*. 2022. V. 62. No. 7. P. 952–959. DOI: 10.1134/S0016793222070027.
- [13] *Abdussamatov H.I.* Lunar Observatory for monitoring the radiation balance of the Earth and climate // *IOP Conf. Ser.: Earth and Environmental Science*. 2022. V. 1040. Article 012001. <https://doi.org/10.1088/1755-1315/1040/1/012001>.
- [14] *Abdussamatov H.I.* Moon-based monitoring of the Earth's energy imbalance and climate, near-Earth asteroids and comets, potentially habitable exoplanets, supernovae and novae // *J. Indian Society of Remote Sensing*. 2024. V. 52. No. 11. P. 2593–2608. <https://doi.org/10.1007/s12524-024-01971-6>.
- [15] *Abdussamatov H.I.* Continuous simultaneous monitoring of the asteroid hazard throughout the celestial sphere and the Earth's climate by the Lunar Observatory // *Intern. J. Environmental Sciences and Natural Resources*. 2025. V. 35. No. 2. Article 556411. DOI: 10.19080/IJESNR.2025.35.556411.

GEOPHYSICAL EXPLORATION OF THE MOON XI: 3D PITS AND CAVES

A. V. Gusev¹, J. G. Meng²

¹ *Institute of Geology and Oil — Gas Technologies, Kazan Federal University
Kazan, Tatarstan, Russia, agusev33@gmail.com*

² *Institute of Geology, Jilin University, Changchun, China*

KEYWORDS:

Moon, development, breakthrough, pits, caves

ABSTRACT:

The review discusses scientific and technical, infrastructure and breakthrough, industrial and construction problems of developing pits and caves on the Moon.

The implementation of modern long-term programs for industrial development of the Moon Chang'E 1–8 (China), Chandrayaan 1–4 (India), Artemis 1–4 (NASA, USA), Luna 26–28 (RSA, Russia) are aimed at creating long-term lunar bases and geological development of the lunar subsurface. The Moon has a variety of minerals in significant quantities for commercial extraction and transportation to Earth, including rare and rare-earth metals: platinum, nickel, silicon, cobalt and others (up to 14 million tons). The predicted integral cost of lunar resources reaches 16 quadrillion dollars [1].

Currently, methods are being developed for the industrial production of metals, oxygen and building materials from lunar regolith, clarification of water ice deposits and the infrastructure of caves on the Moon. Although scientists have speculated about the possibility of the existence and use of extraterrestrial caves for over 50 years, we have now entered the initial phase of planetary cave exploration [2].

This report provides a detailed overview of the geological origin, exploration history, and distribution of lunar lava tubes on the Moon. Four distinct advantages and typical concepts for building bases inside lava tubes are discussed in detail, and terrestrial attempts to build bases inside lunar lava tubes to date are summarized [3].

Lunar lava tubes are special underground caverns formed by volcanic eruptions that are considered ideal natural shelters and scientific laboratories for the construction of lunar bases. Caves are important because they provide records of the geological, meteorological, and environmental history of planetary bodies in the Solar System. For the Moon, caves can protect human explorers from the harmful and inhospitable surface environment, cosmic rays, and solar flares. Earth represents the highest level of cave exploration and knowledge. Beyond Earth, identification of potential caves is most advanced for the Moon, with hundreds of documented potential cave entrances and several proposed cave exploration mission concepts [4].

To date, the scientific community has catalogued 2,660 caves on eight planetary bodies (excluding Earth) throughout the Solar System. To systematically advance planetary cave exploration, a roadmap is proposed consisting of three major phases: **1.** Identification (spin-orbit parameters), **2.** Characterization (topographic features), and **3.** Exploration (geophysical surveys) [5].

IDENTIFICATION:

To date, most planetary cave entrances, skylights, and collapse pits have been identified using standard remote context imaging. On Earth, cave entrances can be identified using combined thermal, visible, and seismic approaches. Such strategies should be further refined and expanded to detect caves on other planetary bodies.

Combining these methods with orbital subsurface geophysical methods, including radar, seismic, and gravimetry, may provide optimal achievements in cave identification. However, additional orbital spacecraft with sensors capable of accurately detecting these geological features are need-

ed to conduct a broader inventory of cave entrances throughout the Solar System [4].

CHARACTERIZATION:

Candidate cave entrances on the Moon need to be carefully evaluated before selecting a survey target. Exploration of lunar and Martian caves requires high-resolution, oblique-angle imaging, systematic study of these images, and ranking of features by scientific and commercial importance. Current and future missions include Titan's Mars Ingenuity and Dragonfly helicopters to explore numerous caves on planets and moons of the Solar System: Triton (3 caves), Charon (1), Titan (1,297 caves), Moon (221 caves), Mars (1,036 caves), Enceladus (100 caves), and Pluto (caves). [3, 4].

EXPLORATION:

Exploration of lunar caves can be used to confirm and/or study in situ thermodynamics of scientific interest. Surface missions can map cave geometry around the entrance and potentially determine cave extent and volume if equipped with ground-penetrating sensors. The resulting mapped cave architectures and hazards will inform lunar exploration planning and help reduce the risk of lunar missions.

Power will include tethering, alternative internal power sources (e.g. fuel cells), or recharging by returning to the solar surface. Navigating complex cave architectures will require further development of AI. Planetary cave science has the potential to expand significantly over the next decade [5].

On Earth, analog, technological research and development will be paramount. The advent of aerial drones for bodies with atmospheres could be a game changer. These systems could be used to both detect and characterize cave entrances. For lunar rovers, flight-worthy instruments capable of detecting (and characterizing) cave entrances and their internal structure will be indispensable. For the Moon and Mars, missions in the near future (years or decades) are achievable, provided adequate investment in robotics development is made. In particular, the platforms discussed here must be developed to flight-worthy status to achieve the required technical maturity. By applying this roadmap and advancing these key technologies, we will be able to explore the planetary interior, one of the most promising potentially habitable environments to search for evidence of life. This will facilitate the technological developments needed for human exploration and settlement of lunar caves [6].

REFERENCES:

- [1] *Changa W., Meng Z.G., Gusev A. et al.* Planning a lunar long-term research station in MARE SMYTHII // Proc. IEEE Intern. Geoscience and Remote Sensing Symp. 2024. P. 1–4.
- [2] *Mei L., Liu C., Shi Y. et al.* Complex deposits in Lacus Moritis Demonstrated by Ce-2 MRM Data // Proc. IEEE Intern. Geoscience and Remote Sensing Symposium (IGARSS'2024). 2024. P. 6150–6153. DOI: 10.1109/IGARSS53475.2024.10642006.
- [3] *Horvath T., Hayne P.O., Paige D.A.* Thermal and illumination environments of lunar pits and caves: Models and observations from the Diviner Lunar Radiometer Experiment // Geophysical Research Letters. 2022. V. 49. Iss. 14. Article e2022GL099710. <https://doi.org/10.1029/2022GL099710>.
- [4] *Feng Y., Pan P.-Z., Tang X. et al.* A comprehensive review of lunar lava tube base construction and field research on a potential Earth test site // Intern. J. Mining Science and Technology. 2024. V. 34. Iss. 9. P. 1201–1216. <https://doi.org/10.1016/j.ijmst.2024.06.003>.
- [5] *Meng J.G., Sun H., Gusev F. et al.* Thermophysical properties of surface deposits in Tsiolkovsky crater and its geologic significance revealed by CE-2 MRM data // Icarus. 2024. V. 408. Article 115808. <https://doi.org/10.1016/j.icarus.2023.115808>.
- [6] *Gusev A. V., Meng J., Ping Z.* Construction and breakthrough development of the Moon VIII: 3D printing on the Moon // Proc. 59th Scientific Readings in Memory of K. E. Tsiolkovsky. 2024. P. 164–168 (in Russian).

EXPERIMENTAL STUDY OF THE DEPENDENCE OF THE COMPRESSIVE STRENGTH OF SAMPLES OF THE LUNAR REGOLITH SIMULANT ON THE PARAMETERS OF SELECTIVE LASER MELTING

A. M. Lysenko^{1,2}, T. M. Tomilina^{1,2}, I. G. Mitrofanov²,
P. R. Savvatimova^{1,2}

¹ Mechanical Engineering Research Institute RAS, Moscow, Russia
lysenko@imash.ac.ru

² Space Research Institute RAS, Moscow, Russia

KEYWORDS:

Moon exploration, lunar regolith, 3D printing, SLM

ABSTRACT:

Lunar regolith is currently being considered as possible nature material for construction on the Moon.

One of the key scientific tasks is to develop a construction technology suitable for the use of extraterrestrial materials, and additive selective laser melting (SLM) of regolith powder is currently considered the most promising [1, 2]. However, the SLM method, which was originally developed for metal powders, must be adapted to use lunar regolith as a starting material, which has significantly different properties: chemical composition, morphology and particle size distribution.

The purpose of this study is to determine fusion conditions and optimize SLM parameters that ensure the production of volumetric samples with the highest possible strength characteristics. A regolith simulator based on crushed gabbro-dabase and an industrial 3D laser printer with a beam diameter of 50 microns and a laser power of 100 watts were used for the study.

The report presents the method based on detailed study of laser melting of single tracks to obtain samples with improved characteristics compared to earlier studies by the authors [3, 4]. A melting mode was determined in which samples with an average porosity of 15 % and a compressive strength of 37 MPa were obtained, which corresponds to the strength of ceramic bricks, and concrete. A certain dependence of the compressive strength of the samples on melting conditions has been established for a wide range of energy parameters.

REFERENCES:

- [1] *Fateri M., Gebhardt A.* Process parameters development of selective laser melting of lunar regolith for on-site manufacturing applications // Intern. J. Applied Ceramic Technology. 2015. V. 12. Iss. 1. P.46–52. <https://doi.org/10.1111/ijac.12326>.
- [2] *Goulas A., Binner J. G. P., Harri R. A. et al.* Assessing extraterrestrial regolith material simulants for in-situ resource utilization based 3D printing // Applied Materials Today. 2017. V. 6. P. 54–61. <https://doi.org/10.1016/j.apmt.2016.11.004>.
- [3] *Tomilina T.M., Kim A.A., Lisov D.I., Lysenko A.M.* Laboratory Tests of Selective Laser Melting of Simulants of Lunar Regolith with Various Granulometric Properties // Cosmic Research. 2024. V. 62. No. 5. P. 495–509. <https://doi.org/10.1134/S0010952524600781>.
- [4] *Tomilina T., Kim A., Lisov D., Lysenko A.* Porosity and compressive strength of test samples produced by SLM using rock gabbro-dabase based powder as a lunar regolith simulant // Acta Astronautica. 2024. V. 215. P. 493–495. <https://doi.org/10.1016/j.actaastro.2023.12.028>.

PRELIMINARY RESULTS ON THE APPLICATION OF SELECTIVE MICROWAVE SINTERING FOR LUNAR SOIL ANALOGUE VI-LH1

I. A. Agapkin, E. M. Sorokin, K. M. Ryazantsev

Vernadsky Institute of Geochemistry and Analytical Chemistry RAS
Moscow, Russia, 15331533@mail.ru

KEYWORDS:

lunar soil analogue, ISRU, additive manufacturing, selective microwave sintering

INTRODUCTION:

As early as 1985, microwave sintering was considered by researchers as an advanced technology for the extraction of water, oxygen, primary metals, and the creation of lunar infrastructure [1]. The primary advantage of microwave sintering lies in its low energy consumption and its ability to heat materials volumetrically. Potentially, this method could become the most energy-efficient among all investigated technologies in terms of energy expenditure [2]. For example, compared to selective laser sintering (SLS), selective microwave sintering (SMS), due to its volumetric heating, requires 23 % less energy, which also reduces manufacturing time [3].

SAMPLE:

As a starting material, lunar soil analogue VI-LH1, developed at the GEOKHI RAS laboratory, was used. VI-LH1 consists of crushed labradorite, possessing a similar chemical-mineralogical and granulometric composition to lunar highland regolith [4].

EXPERIMENTAL PROCEDURE:

The experiment was conducted using a standard household microwave oven at a power of 800 W. The VI-LH1 material was further milled to a particle size of 100 μm . A 7.3-gram soil sample was placed in a corundum crucible. To achieve a hybrid heating effect, the sample was placed within a ceramic fiber mold internally lined with a silicon carbide layer (Figure 1) [5].

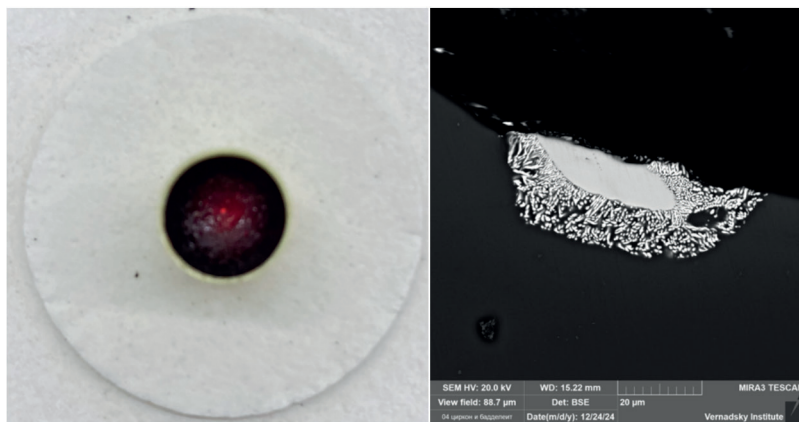


Figure 1. Top view photograph of the soil sample in the crucible immediately after the experiment (left) and SEM image (zircon and baddeleyite) (right)

RESULTS:

Based on previous studies, a sintering time of 15 min was determined, which proved sufficient to completely melt the sample.

The resulting sample was investigated using scanning electron microscopy (SEM) (Figure 1). Observations revealed that the sample consists of a homogeneous glass with minor compositional variations. Signs of frontal crystallization (microscopic crystals) of plagioclase were observed in the meniscus region. The glass also contains inclusions, consisting of:

1. Partially altered zircons, which are likely transforming into baddeleyite.
2. Regions with elevated concentrations of La, Ce, and Th, which may correspond to molten phosphate or orthite.

CONCLUSION:

Preliminary calculations indicated that, under these experimental conditions, the energy consumption for 1 kg of lunar regolith analogue VI-LH1 would be approximately 98 MJ. However, it is anticipated that further investigations will enable a reduction in the experimental duration and, consequently, the required energy for sintering.

The next stage of research will focus on establishing a temperature profile — the dynamics of soil temperature measurement over time, including the determination of the melting temperature. This will also involve investigating the effect of microwave power on the quality of the obtained samples and evaluating their mechanical properties. Furthermore, a crucial direction of research will be the conduction of experiments under vacuum conditions.

REFERENCES:

- [1] *Meek T.T., Vaniman D.T., Cocks F.H., Wright R.A.* Microwave processing of lunar materials: Potential applications // Lunar bases and space activities of the 21st century. 1985. P. 479.
- [2] *Farries K. W., Visintin P., Smith S. T. et al.* Sintered or melted regolith for lunar construction: state-of-the-art review and future research directions // Construction and Building Materials. 2021. V. 296. Article 123627. <https://doi.org/10.1016/j.conbuildmat.2021.123627>.
- [3] *Lim S., Anand M.* Numerical modelling of the microwave heating behaviour of lunar regolith // Planetary and Space Science. 2019. V. 179. Article 104723. <https://doi.org/10.1016/j.pss.2019.104723>.
- [4] *Mironov D.D., Uvarova A.V., Slyuta E.N. et al.* Lunar Highlands Soil Simulant VI-LH1 for Testing Developing In-Situ Technologies and Large-Scale Experiments // 55th Lunar and Planetary Science Conf. 2024. V. 3040. Article 1948.
- [5] *Liu Z., Li J., Yang X. et al.* Sintering of lunar regolith simulants using a domestic microwave: A rapid and energy-efficient strategy for construction material fabrication // J. European Ceramic Society. 2025. V. 45. No. 3. Article 117047. <https://doi.org/10.1016/j.jeurceramsoc.2024.117047>.

COMPARATIVE ANALYSIS OF POTENTIAL SITES FOR LUNAR BASE DEPLOYMENT IN THE NORTHERN POLAR REGION

O. I. Turchinskaya, E. A. Grishakina, O. S. Tretyukhina, E. N. Slyuta
*Vernadsky Institute of Geochemistry and Analytical Chemistry RAS
Moscow, Russia, turchinskaya@geokhi.ru*

KEYWORDS:

Moon, Luna-27, landing sites, solar illumination, visibility of Earth, Surface slopes, digital elevation model

INTRODUCTION:

The selection of an optimal site for a lunar base and its associated infrastructure is a key factor influencing the overall scenario of the lunar program, including equipment delivery logistics, surface operations, energy supply, and the utilization of local resources. A strategically chosen location with safe terrain, high solar illumination, and direct Earth visibility can significantly reduce maintenance costs and provide a clear advantage over less favorable areas.

The selection and comparative analysis of potential sites for a lunar base were conducted not only according to requirements determined by specific scientific and operational tasks [1], but also based on general criteria for the placement of a crewed lunar base. These criteria include radiation and environmental safety, stable and direct communication with Earth, maximum habitability under lunar environmental conditions, and cost-effectiveness of long-term operations, ensured by the use of local resources and continuous, renewable energy sources.

The polar regions of the Moon have unique illumination conditions due to the small axial tilt ($\sim 1.5^\circ$) [2]. It is known that the floors of impact craters near the poles are permanently shadowed and never receive direct sunlight [3, 4]. As a result, crater rims may experience prolonged sunlight, while their floors remain in permanent darkness, forming cold traps — potential reservoirs of water ice [5].

The study area is characterized by complex terrain with relatively steep slopes and numerous impact craters ranging from the resolution limit of the images to tens of kilometers. Illumination and Earth visibility, which in polar regions depend not only on latitude but also on local topography, are critical factors. The relatively small area available due to technical requirements further complicates site selection.

A suitability map for the deployment of a crewed lunar base in the northern polar region (up to 80° N) was developed based on an analysis of key parameters. Potential sites were identified through a comprehensive evaluation of terrain, solar illumination, Earth visibility, and the spatial distribution of water ice. Areas characterized by slopes exceeding 15° , solar illumination below 35 %, and Earth visibility under 50 % were classified as unfavorable. The most promising sites are located near points with maximum insolation, which is crucial for solar panel operation and thus for the energy autonomy of the base.

Special attention was given to the distribution of water equivalent hydrogen (WEH), which indicates the possible presence of water ice in the regolith. This resource can be utilized to produce water, oxygen, and hydrogen — essential components for life support systems and fuel production. The selected sites combine geotechnical and resource-related advantages, making them the most promising for future lunar exploration strategies.

The analysis included the creation of digital elevation models, slope maps derived from DEMs, image mosaics, maps of average solar illumination and Earth visibility based on [6], and maps of WEH distribution using LEND (LRO) spectrometer data [7]. For each of the 11 sites, a series of maps was gener-

ated at the highest available spatial resolution provided by the source data: 0.6–5 m for image mosaics (LROC NAC) and 5–20 m for digital elevation models (LOLA LRO).

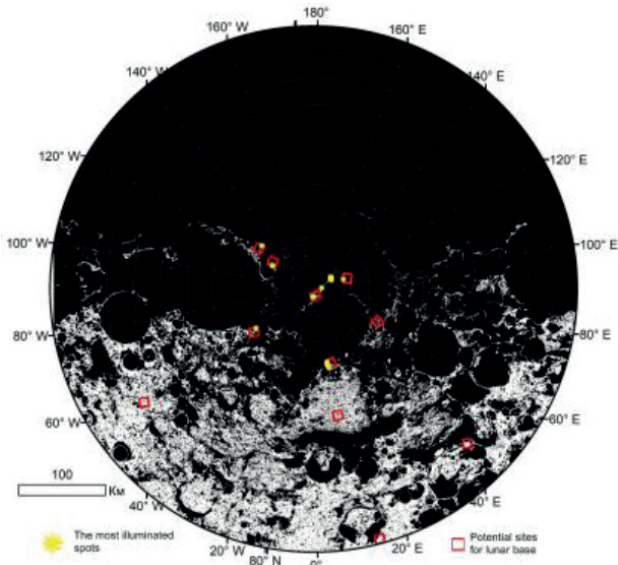


Figure 1. Suitability map of the Northern Polar region for lunar base deployment. Areas meeting engineering and technical requirements for base construction are shown in white

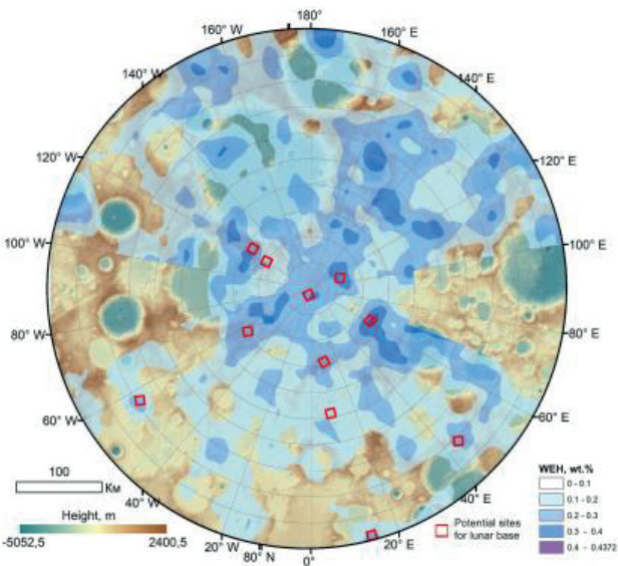


Figure 2. Map of the Northern Polar region based on NASA's LROC data with an overlaid distribution of water-equivalent hydrogen (WEH) deposits according to [7]

Based on the analysis of the aforementioned parameters, eleven candidate sites were identified in the northern polar region of the Moon (Figure 3).

These selected areas represent an optimal combination of high solar illumination, relatively smooth terrain, stable Earth visibility, and proximity to potential sources of water ice, making them the most promising locations for the deployment of a crewed lunar base. Each site constitutes a unique topographic formation with varying elevation characteristics and relief gradients within its boundaries.

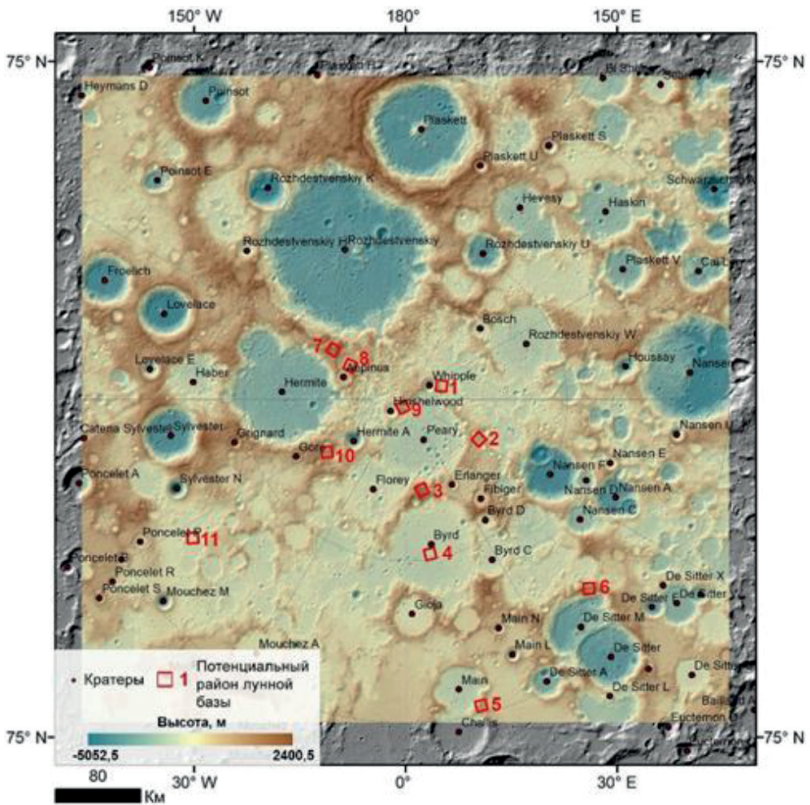


Figure 3. Overview map of potential sites in the Northern Polar region of the Moon for lunar base deployment. Site numbering is arbitrary. The map is based on laser altimetry data from NASA's LOLA instrument aboard LRO

Among the evaluated sites, N3, N9, and N10 stand out as the most favorable for base placement. These locations combine several critical factors: the presence of zones with prolonged sunlight exposure (up to 76–82 %), a predominance of gentle slopes less than 15°, stable Earth visibility (averaging 40–60 %), and positioning in areas with elevated water-equivalent hydrogen content (0.2–0.3 %, locally up to 0.4 %). This balance of parameters ensures high priority for these sites in terms of energy autonomy, engineering reliability, and resource availability.

Sites N1, N4, and N7 are also of interest due to their relatively smooth terrain, the presence of high-illumination points, and the potential occurrence of water ice. However, their utilization may require partial engineering adaptation, due to limited Earth visibility (N1, N7) or moderate insolation levels (N4). With appropriate technical solutions, these sites could serve as backup or auxiliary zones within a broader infrastructure network.

Sites N5, N6, N8, and N11 are considered less favorable. N5 and N6 exhibit significant elevation variation and insufficient water-equivalent hydrogen levels; N8 offers high energy potential but suffers from extremely low Earth visibility; and although site N11 has favorable topography and good Earth visibility, it lacks strong indicators of ice presence and is characterized by low insolation. These areas may still be used for specific purposes, for instance, as temporary or resource extraction zones, provided that adequate logistical and energy support is in place.

REFERENCES:

- [1] *Slyuta E. N., Galimov E. M., Marov M. Ya.* Thematic geological survey and preliminary geological exploration (on the Moon) // *Fundamental'nye kosmicheskie issledovaniya*. Moscow: Fizmatlit, 2014. V. 2. P. 103–128 (in Russian).
- [2] *Ward W.R.* Past orientation of the lunar spin axis // *Science*. 1975. V. 189. Iss. 4200. P. 377–379. DOI: 10.1126/science.189.4200.377.

- [3] *Vasavada A. R., Paige D. A., Wood S. E.* Near-surface temperatures on Mercury and the Moon and the stability of polar ice deposits // *Icarus*. 1999. V. 141. P. 179–193. <https://doi.org/10.1006/icar.1999.6175>.
- [4] *Paige D. A., Foote M. C., Greenhagen B. T. et al.* The Lunar Reconnaissance Orbiter Diviner Lunar Radiometer Experiment // *Space Science Reviews*. 2010. V. 150. No. 1–4. P. 125–160. <https://doi.org/10.1007/s11214-009-9529-2>.
- [5] *Nozette S., Spudis P. D., Robinson M. et al.* Integration of lunar polar remote-sensing data sets: Evidence for ice at the lunar south pole // *J. Geophysical Research*. 2001. V. 106. Iss. E10. P. 23253–23266. <https://doi.org/10.1029/2000JE001417>.
- [6] *Mazarico E., Neumann G. A., Smith D. E. et al.* Illumination conditions of the lunar polar regions using LOLA topography // *Icarus*. 2011. V. 211. Iss. 2. P. 1066–1081. <https://doi.org/10.1016/j.icarus.2010.10.030>.
- [7] *Slyuta E. N., Turchinskaya O. I., Tretyukhina O. S. et al.* Forecast water ice reserves in the Moon Polar regions by the “LEND” data // 54th Lunar and Planetary Science Conf. (LPSC). 2023. V. 54. Article 1089.

REMOTE SENSING OF LUNAR SURFACE: THE SEARCH FOR ISOTOPIC FORMS OF WATER

S. A. Voropaev¹, A. P. Krivenko¹, V. S. Fedulov¹, N. V. Dushenko¹,
Yan Jianguo²

¹ Vernadsky Institute of Geochemistry and Analytical Chemistry RAS
Moscow, Russia, voropaev@geokhi.ru

² State Key Laboratory of Space Weather, National Space Science Center,
Chinese Academy of Sciences, Beijing, China

KEYWORDS:

Moon, isotopes, water, surface rocks, IR mapping, remote sensing

INTRODUCTION:

Moon is the closest planetary body to us with a complex tectonic history and structure significantly different from Earth's structure. Its proximity makes it possible to send orbital and landing stations and even people to work out methods for studying other, more distant than Moon planets of the Solar System (SS). One of the models of its origin (namely the mega-impact model) suggests that the Moon formed ~100 My after the Sun from a collision between a Mars-sized body, Theia, and the proto-Earth [1]. In the resultant lunar magma ocean (LMO), iron settled out to form a small core, followed by a crystallization sequence that produced the lunar mantle and primary crust [2]. Experiments and models based on estimates of the lunar bulk composition show that Mg-rich olivine was the first mineral to crystallize and sink from the LMO, followed by pyroxene and more Fe-rich olivine. At ~80 % LMO crystallization, plagioclase formed, floated to the surface, and accumulated as the Moon's primary anorthosite crust. Under the buoyant plagioclase crust, the dense cumulates (ilmenite and clinopyroxene) continued to crystallize, concentrating incompatible elements including K, REE, P, U, and Th (commonly referred to as KREEP). Because ilmenite and Fe-rich clinopyroxene are dense, the resultant mineral stratification would have been gravitationally unstable. By solid-state convection, the dense late magma ocean cumulates may have sank into the lunar interior in a process termed cumulate mantle over-turn [3]. Finally, on the Moon's surface, olivine is more abundant in the basalt-dominated mare regions compared to the Ca-feldspar (anorthositic) lunar highlands.

LUNAR ROCKS:

The FHT is usually regarded as the central part of the highly anorthositic region, which corresponds to the thickest part of the crust and is largely concentrated on the lunar far side. It is centered around 10° N, 180° E and occupies over 60 % of the moon's surface. It is characterized by high albedo, extensive cratering, elevated topography, and high local relief. Back in 1959, Soviet researchers launched the Luna-3 probe, thanks to which earthlings finally saw an image of the entire far side of the Moon. It had all the same craters and mountains, but there is practically no lunar mare on the far side. The proportion of these dark plains, composed of volcanic basalt, is only 1 % on it, while on the near side they cover 31 % of the area. Minerals without volatile elements as essential structural constituents are typically referred to as nominally anhydrous minerals (NAM) or nominally volatile-free minerals. These phases can store volatiles within crystallographic defects typically at trace abundances. The most commonly studied nominally anhydrous minerals include olivine (Fe,Mg)₂SiO₄, pyroxenes (Fe,Mg,Ca)₂Si₂O₆, garnets (Fe,Mg,Ca)₃Al₂(SiO₄)₃, and feldspars Cax(Na,K)_{1-x}Al_{1+x}Si_{3-x}O₈. Experimental studies have shown that F, Cl, and H can be stored in the above NAM phases; however, the mineral-melt partition coefficients for Cl are typically much smaller than for F and H, likely due to the large ionic radius of Cl-. Lunar samples commonly have olivines, pyroxenes, and feldspars, but the only NAM for which H₂O abundances have been quantified in lunar samples is feldspar.

WATER ON THE MOON:

Hui with colleagues used polarized micro-FTIR to measure the abundances of H₂O in anorthitic plagioclases from troctolite 76535,164 and ferroan anorthosites (FAN) 15414,238 and 60015,787 [4]. They demonstrated that the plagioclase in the FAN's had up to 6 ppm H₂O, and the plagioclase in the Mg-suite troctolite had 2.7 ppm H₂O. Mills with colleagues used SIMS to measure the H₂O abundances of alkali feldspar in a granitoid clast in breccia 15405,78, reporting up to 1000 ppm H₂O [5].

From these measurements, water accumulating in the final residuum of the LMO could have reached 1.4 wt%, an amount sufficient to explain water contents measured in lunar volcanic rocks. The presence of water in the primary crust implies a more prolonged crystallization of the lunar magma ocean than a dry Moon scenario and suggests that water may have played a key role in the genesis of lunar basalts and pyroclastic deposits. So, water and other volatiles converts the lunar magma from a liquid containing gas bubbles to a gas entraining liquid droplets whose sizes are linked to the bubble size distribution during this fragmentation process. The “wet” Moon implied by these findings is inconsistent with wholesale volatile loss due to giant impact and supports either a less energetic formation scenario or a later, meteorite-derived volatile addition to the Moon (a “late veneer”). The isotopic composition of water adsorbed on the surface or incorporated into the crystal structure of the above mentioned minerals could solve this important question.

REMOTE SENSING:

Reflectance and emittance spectroscopy from visible (~0.35 μm) to far-infrared (~50 μm) wavelengths are among the core measurements made in support of planetary exploration from the very beginning. Data from instruments used for spectroscopic measurements are essential in determining surface mineralogy and phase abundance [6]. Quantitative analysis of the observations is fundamental to understanding planetary formation and evolution.

The advantage of the mid-IR spectroscopy is the correspondence of the range to the wavelengths (frequencies) of molecules vibrations of organic and inorganic compounds, which causes absorption. This is the interval of electromagnetic (EM) wavelengths from 2 to 25 microns or (in wave numbers) the average mid-IR range is 5000–400 cm⁻¹. Two types of molecular vibrations are mainly used for analysis: valence and deformation vibrations. Valence oscillations are accompanied by a change in the length of the chemical bond along its axis, while symmetrical and asymmetric oscillations are distinguished. Deformation vibrations are accompanied by a change in the angle between the bonds. To be active, the oscillations must cause a change in the dipole moment of the molecule and the greater the change of the dipole, the stronger the intensity of the band in the IR spectrum.

The fundamental inputs into radiative transfer of EM wave (with frequency ω , or wavelength $\lambda = 2\pi c/\omega$) are $n(\omega)$ and $k(\omega)$, the real and imaginary components of the complex index of refraction,

$$n^* = n + ik.$$

By the absorption, the real part $n(\omega)$ of the complex refractive index n^* demonstrates an anomaly. At visible to near-IR (VNIR) wavelengths, where k is small in many geologic materials, optical constants can be derived using several methods. Traditionally, transmission measurements of thin films or crystal thin sections were used to calculate the wavelength-dependent imaginary index of refraction. Direct measurement of the refractive index and extinction coefficient in some cases is impossible. A practically effective method of obtaining information about optical properties in this case is the use of the Kramers-Kronig relations for the logarithm of the complex reflection coefficient.

$$r(\omega) = [R(\omega)]^{1/2} \exp(i\cdot\varphi(\omega)),$$

where $R(\omega)$ — the reflection coefficient of the EM wave (in intensity), $\varphi(\omega)$ — the phase shift between the reflected and incident waves. Using

the known reflection coefficients and the phase of the reflected wave, it is possible to restore, using Fresnel's formulas, the imaginary and real part of the complex index of refraction n^* .

Reflectance for normal incidence and large (compared to the wavelength) mineral grains can be described by the Fresnel equation as

$$R = [(n - 1)^2 + k^2] / [(n + 1)^2 + k^2].$$

Laboratory specular reflectance spectra with incidence and emergence angles $<15^\circ$ can be well modeled using this simple relationship. For larger incidence and emergence angles, reflectance is described by a much more complicated set of equations where shortcomings of the basic Fresnel equation are revised. Also, elastic scattering has a strong influence only when the size of the particles and the wavelength of the light are comparable. In the mid-infrared region, classical scattering theory can only be applied to particles with sizes about 2–25 μm . Below this size range it is no longer suitable to describe infrared spectra since the molecular structure of the particle starts to dominate them. So, classical scattering theory is useful as an analytical tool, for example to determine rough particle size distributions. It is, however, not capable of providing detailed information about particle shape, or architecture, nor of the properties of very small aggregates (with size about 10–100 nm) through band shape analysis.

RESULTS:

The isotopic composition of water is an important indicator of its quality and determines its suitability for the human use. In this work, the IR spectra features of the various isotopic forms of water ($-\text{OH}$, $-\text{OD}$, H_2O , HDO and D_2O) included in the crystal structure and adsorbed on the surface of the main rock-forming minerals of lunar crust have been studied. The results of numerical modeling with ALT/CUSTEP module (Biovea Materials Studio software) and experimental studies using the FT-801 IR Fourier spectrometer with plug-in for mirror/diffuse reflection (Simex Ltd, Novosibirsk) as well as Raman InVia Renishaw Reflex spectrometer are presented.

ACKNOWLEDGMENTS:

This research was supported by the grant of the Russian Science Foundation No. 25-17-00051, <https://rscf.ru/project/25-17-00051/>.

REFERENCES:

- [1] Hartmann W. K., Davis D. R. Satellite-sized planetesimals and lunar origin // *Icarus*. 1975. V. 24. Iss. 4. P. 504–515. [https://doi.org/10.1016/0019-1035\(75\)90070-6](https://doi.org/10.1016/0019-1035(75)90070-6).
- [2] Elkins-Tanton L. T., Burgess S., Yin Q. Z. The lunar magma ocean: reconciling the solidification process with lunar petrology and geochronology // *Earth and Planetary Science Letters*. 2011. V. 304. Iss. 3–4. P. 326–336. <https://doi.org/10.1016/j.epsl.2011.02.004>.
- [3] Zhang N., Dygert N., Liang Y., Parmentier E. The effect of ilmenite viscosity on the dynamics and evolution of an overturned lunar cumulate mantle // *Geophysical Research Letters*. 2017. V. 44. iss. 13. P. 6543–6552. <https://doi.org/10.1002/2017GL073702>.
- [4] Hui H., Peslier A. H., Zhang Y., Neal C. R. Water in lunar anorthosites and evidence for a wet early Moon // *Nature Geoscience*. 2013. V. 6. No. 3. P. 177–180.
- [5] Mills R. D., Simon J. I., Alexander C. M. O. et al. Chemical zoning of feldspars in lunar granitoids: Implications for the origins of lunar silicic magmas // 45th Lunar and Planetary Science Conference. 2014. Article 1547.
- [6] Stuart B. H. *Infrared Spectroscopy: Fundamentals and Applications*. John Wiley and Sons Ltd, 2004. DOI: 10.1002/0470011149.

DEVELOPMENT OF A SELENOCENTRIC DYNAMIC REFERENCE SYSTEM BASED ON DATA FROM MODERN LUNAR MISSIONS AND THE APPLICATION OF REGRESSION MODELING METHODS

A. O. Andreev¹, Y. A. Nefedyev²

¹ Kazan State Power Engineering University, Kazan, Russia
andreev.alexey93@gmail.com

² Kazan Federal University, Kazan, Russia, star1955@mail.ru

KEYWORDS:

selenocentric dynamic reference system, modern lunar missions, lunar navigation

INTRODUCTION:

One of the primary objectives of this work is the development of a precision selenocentric dynamic navigation network based on satellite observations, aimed at solving navigation problems for future space missions. This includes applications involving onboard high-precision angle-measuring instruments, as well as the use of optical laser beacons deployed on the lunar surface.

METHODS:

For the construction of the selenocentric navigation system, global topographic data from modern space missions — Apollo, Kaguya, Clementine, and LRO — reduced to a dynamic coordinate system were utilized. To this end, specialized software packages and robust estimation systems were developed. The method for determining the coordinates of objects on the near and far sides of the Moon surpasses, in systematic accuracy, many existing modern approaches used for establishing reference selenodetic coordinate systems. This method involves bringing observations of objects on the near and far sides of the Moon, obtained by various space assets, into a unified system, as well as constructing a single selenocentric reference network for both lunar hemispheres in the coordinate system defined by the Moon's center of mass and principal axes of inertia. The coordinate transformation method was developed as a result of thorough investigations into the comparative effectiveness of the following approaches: affine transformation; optimal polynomial approximation; orthogonal transformation with and without accounting for systematic errors; solutions of systems of simultaneous equations. In transforming coordinates from one rectangular system (X) to another (Y), an affine transformation model was employed.

RESULTS:

In this study, heterogeneous satellite observations were consolidated into a unified system for high-precision numerical integration, and a selenocentric dynamic model was constructed using specialized transformation software packages and data from the Apollo, Kaguya, Clementine, and LRO space missions. An analysis of the selenocentric dynamic model was performed employing a system of neural network construction, robust modeling, expansion of the altimetry using spherical functions, as well as methods of harmonic analysis and fractal geometry. As a result, a reference selenocentric network comprising 275,000 reference objects was established

CONCLUSIONS:

A comparison of the results obtained in this study with the results of previous research reveals the following. The existing navigation coordinate and time support systems, primarily developed abroad, the most advanced among which is ULCN 2005 [1], do not provide sufficiently accurate positioning of spacecraft relative to the reference network of lunar surface objects for the following reasons [2]. All the current topographic models

derived from space observations generally possess uncertain coordinate reference surfaces, and thus the coordinates of objects represented within these models are imprecise. Moreover, without a reference catalogue of lunar objects that optimally covers the investigated surface region, it is impossible to perform densification and extension of space-based navigation networks. This is corroborated by the unsuccessful attempt to reference the topographic data from the 'Kaguya' mission. The results of this work will find application in the crewed exploration of the Moon and in the implementation of planned Russian projects Luna-26, -27, -28, -29, as well as in the development of a satellite navigation network in lunar orbit similar to the GLONASS system, and in the deployment of a lunar telescope [3]. These objectives are incorporated into the space program carried out by the Roscosmos State Corporation.

ACKNOWLEDGMENTS:

This work was supported by Russian Science Foundation, grant No. 24-22-00260.

REFERENCES:

- [1] *Archinal B., Acton C., A'Hearn M. et al.* Report of the IAU Working Group on Cartographic Coordinates and Rotational Elements, *Celestial // Mechanics and Dynamical Astronomy*. 2018. V. 130. Iss. 3. Article 22. 46 p. DOI: 10.1007/s10569-017-9805-5.
- [2] *Andreev A.O., Nefedyev Yu.A., Demina N.Yu. et al.* Development of Methods for Navigational Referencing of Circumlunar Spacecrafts to the Selenocentric Dynamic Coordinate System // *Astronomy Reports*. 2020. V. 64. Iss. 9. P. 795–803. DOI: 10.1134/S1063772920100017.
- [3] *Churkin K.O., Petrova N.K., Nefedyev Y.A. et al.* Creation of a multiparameter model of a space telescope observation system // *Technical Physics*. 2024. V. 69. Iss. 6. P. 1518–1520. DOI: 10.1134/S1063784224060070.

LUNAR ORBIT SATELLITE FORMATION: DISTRIBUTED LOW FREQUENCY INTERFEROMETRIC IMAGING SPECTROMETER

Li Deng¹, Jingye Yan¹, Lin Wu¹, Ailan Lan¹, Yu Chen¹, Li Zhou¹,
Chao Yao²

¹ *National Space Science Center, Chinese Academy of Science, Beijing, China*
dengli@nssc.ac.cn

² *Tsinghua University, Beijing, China*

KEYWORDS:

lunar orbit, satellites formation, low-frequency, interferometer

ABSTRACT:

The Discovering Sky at the Longest wavelength (DSL) project, which will consist of a mother satellite and nine daughter satellites, flying on the same circular orbit around the Moon, and forming a linear interferometer array. The main scientific goal is to achieve high-precision measurement of the average radio spectrum and to achieve the first ultra-long wavelength sky survey with high angular resolution. At the same time, it will observe the activities of the sun and planets, and reveal the interaction between them and the interplanetary space environment.

Based on the principle of interferometry, the distributed low frequency interferometric imaging spectrometer realizes the imaging detection and spectrum measurement with high precision from 0.1 to 30 MHz. The detection requirements include: through 0.1–30 MHz all-sky imaging, identify the all-sky ultra-long wave radiation source, obtain the large-scale structure information of the all-sky, realize the first high-resolution ultra-long wave survey, and open the last window of the electromagnetic spectrum. Through continuous spectrum monitoring of solar eruptions and planetary activities, the ultra-long wave activities of the sun and planets are observed to reveal the interaction law of the space environment.

The distributed low frequency interference imaging spectrometer consists of five instruments, including the low frequency interferometer, the low frequency calibration source, the correlation processor, the inter-satellite communication and ranging synchronization instrument and the inter-satellite goniometer.

The low frequency interferometer is responsible for receiving and collecting the 0.1–30 MHz low frequency detection data, completing the synchronous reception of ultra-long wave cosmic radiation, and realizing high-precision imaging detection and spectrum measurement. It is deployed on eight daughter satellites.

The correlation processor is deployed on the main satellite, which is responsible for the complex correlation processing of the received detection data of the eight-daughter satellite low-frequency interferometric imaging spectrometers to form the visibility function.

The inter-satellite communication ranging synchronizer and the inter-satellite goniometer complete the measurement of the baseline vector together. The inter-satellite communication and ranging synchronizer is responsible for the inter-satellite communication, ranging, clock synchronization and other functions between the main satellite and the daughter satellite.

The inter-satellite goniometer is responsible for measuring the relative angle between the main satellite and the daughter satellite. A starry sky camera is arranged on the low-frequency daughter satellite to observe the light array arranged on the main satellite and obtain the angle value of the connecting line vector (baseline vector) of the main satellite and the daughter satellite in the inertial coordinate system.

The low-frequency calibration source subsystem is deployed on the main satellite to send out calibration signals, and the daughter satellite receives the calibration signals to realize the system-level calibration of the low-frequency interferometric imaging spectrometer.

This presentation mainly introduces the design scheme of the Distributed low frequency interferometric imaging spectrometer.

**SESSION 2. MOON AND MERCURY (MN-PS)
POSTER SESSION**

BASALTIC CLASTS POPULATION IN THE LUNAR METEORITE DHOFAR 280

L. A. Lakhmanova^{1,2}, S. I. Demidova¹, N. N. Korotaeva²

¹ Vernadsky Institute of Geochemistry and Analytical Chemistry RAS
Moscow, Russia, lakhmanova.lida@list.ru

² Lomonosov Moscow State University, Department of Geology
Moscow, Russia

KEYWORDS:

mare basalts, lunar meteorite

INTRODUCTION:

Dhofar 280 (Dho 280) is a lunar highland breccia containing a variety of mineral fragments and lithic clasts [1]. A single fragment of the Dhofar 280 meteorite is represented by basaltic fragmental breccia similar to the Dhofar 287 mare meteorite [2]. Here we report the preliminary study of petrography, mineralogy and chemical composition of the basaltic clasts population of this fragment and discuss the possibility of a single magma source for them.

SAMPLES AND METHODS:

A polished section of the Dho 280 stored in the Meteorite Collection of the Russian Academy of Sciences was investigated using methods of electron microscopy with Jeol JSM-6480LV SEM (Lomonosov Moscow State University, Moscow) equipped with Oxford Instruments EDS detectors at an accelerating voltage of 20 keV, a working distance of 15 mm, and a beam diameter of 1 μm . For clear phase identification X-Ray element maps were obtained using Tescan Mira 3 FEG SEM (Vernadsky Institute, Moscow) at a 20 keV accelerating voltage. The bulk compositions of the basaltic clasts were estimated by combining average mineral phase compositions with modal abundances derived from the element distribution maps.

RESULTS:

Basaltic clasts of the Dho 280 mare basaltic breccia fragment are represented by crystalline and vitrophyric rocks. They have substantial variety in size from 50 μm (fine-grained) to 6 mm (coarse-grained). Six fragments of crystalline rocks are defined by ophitic texture (Figure 1). They consist mainly of pyroxene ($\text{En}_{3-70}\text{Wo}_{3-40}$) and plagioclase (An85) with accessory phases such as ilmenite, chromite, silica. A single fragment is characterized by a presence of olivine phenocrysts (Fo56-66). Large fragments contain complex mesostasis areas which include fayalite, K-Si-rich glass, apatite, silica. Pyroxene of the crystalline fragments are low- and high-Ca varieties changing from Mg-rich pyroxene in the cores to Fe-rich in the edges (MG# 6-70). TiO_2 and Al_2O_3 contents are generally 1–2 wt %.

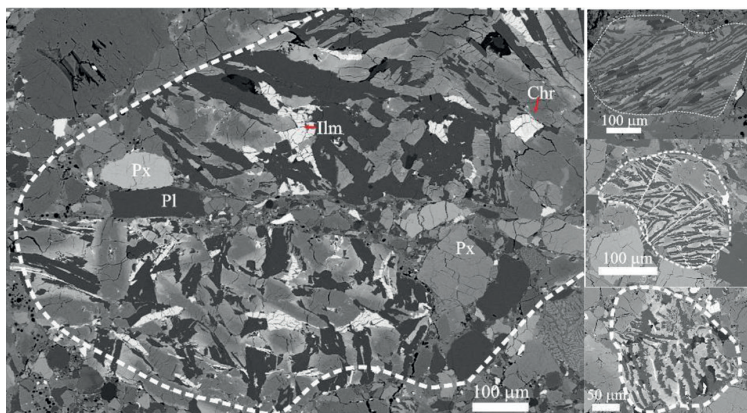


Figure 1. Crystalline rocks of the basaltic clasts in Dho 280 (backscattered electron images)

Two vitrophyric basaltic clasts consist mainly of zoned idiomorphic crystals of pyroxene (En₂₇-67Wo₆-37) with rare olivine crystals (Fo₅₆) embedded in a fine-grained matrix with intersertal texture. Pyroxene are low-Ca and high-Ca varieties with no Fe-rich end-members (MG# 39-72) in contrast to crystalline basalts. Besides that TiO₂ and Al₂O₃ contents are highly variable (1–3 and 1–9 wt% correspondingly) in the vitrophyres.

DISCUSSION:

Although the reconstructed bulk compositions may have large errors because of small size of the clasts and strong zonation of the major minerals, this approach can yield reasonable approximations of bulk rock compositions [3]. In terms of modal and chemical composition the studied clasts belong to the Low-Ti basaltic group that is supported by pyroxene chemistry. In particular Ti/Al ratio in pyroxene is generally 1/4 for Mg-rich varieties that is constituent to the low-Ti basaltic source [4]. Meanwhile basaltic clasts of Dho 280 fragmental breccia has different texture and composition of the mineral phases that could be explained by different cooling rates of the single low-Ti basaltic magma source. Still, the presence of some other basalt types in the Dho 280 breccia cannot be excluded [2].

REFERENCES:

- [1] *Nazarov M. A., Demidova S. I., Anosova M. O. et al.* Native silicon and iron silicides in the Dhofar 280 lunar meteorite // *Petrology*. 2012. 20(6). P. 506–519. DOI: 10.1134/S0869591112060021
- [1] *Demidova S. I., Nazarov M. A., Brandstatter F., Ntaflou T.* A basaltic breccia clast from the Dhofar 280 lunar meteorite: Possible pairing of Dhofar 280 and Dhofar 287 // 44th Lunar and Planetary Science Conf. 2013. Article 1616.
- [1] *Demidova S. I., Nazarov M. A., Anand M., Taylor L. A.* A lunar regolith breccia Dhofar 287B: A record of lunar volcanism // *Meteoritics and Planetary Science*. 2003. V. 38. No. 4. P. 501–514.
- [1] *Papike J. J., Simon S. B., Shearer C. K.* The effects of contrasting Ti and Al activities on Mn/Fe systematics in pyroxene from lunar mare basalts // *American Mineralogist*. 2019. V. 104. No. 6. P. 838–843. <https://doi.org/10.2138/am-2019-6875>.

CONCEPTUAL DESIGN AND PERFORMANCE SIMULATION OF A DUAL-PARTICLE ALBEDO DETECTOR FOR CHANG'E-8 MISSION IN THE LUNAR SOUTH POLAR REGION

Pradiphat Muangha¹, Koth Amratisha², Kanatip Anuchit¹, Sunruthai Burom¹, Popefa Charoenvicha¹, Kullapha Chaiwongkhot², Sarawit Chindaratchakul², Donghui Hou³, Paparin Jamlongkul¹, Pakorn Khonsri¹, Jidapa Lakronwat², Shariff Manuthasna¹, Tanawish Marsri¹, Warit Mitthumsiri², Thanayuth Panyalert¹, Yaowarat Pittayang¹, Kunlanan Puprasit⁴, David Ruffolo², Woradon Sophonamphonsucha¹, Peerapong Torteeka¹, Shenyi Zhang³

¹ National Astronomical Research Institute of Thailand

Chiang Mai, Thailand, Muangha.p@gmail.com

² Mahidol University, Bangkok, Thailand

³ National Space Science Center, Chinese Academy of Sciences, Beijing, China

⁴ Chulabhorn Royal Academy, Bangkok, Thailand

KEYWORDS:

International Lunar Research Station, Chang'E-8 mission, albedo neutrons, albedo protons, Geant4 simulation, galactic cosmic rays, solar energetic particles

INTRODUCTION:

The Chang'E-8 mission represents a pivotal step towards the establishment of the International Lunar Research Station (ILRS), which aims to advance technologies crucial for sustainable human presence and the exploration of lunar resources. A comprehensive understanding of the lunar surface environment is therefore paramount for both ongoing and future human exploration of the Moon. This environment is influenced by galactic cosmic rays (GCRs), high-energy particles originating from outside our solar system, and solar energetic particles (SEPs), bursts of energetic particles from the Sun. The fluxes of both GCRs and SEPs exhibit significant variability driven by solar activity across various timescales. These energetic particles interact with the lunar regolith, leading to the generation of secondary particles, notably "albedo" particles [1], specifically protons and neutrons, that are continuously emitted from the surface. Consequently, the fluxes of these albedo particles display crucial temporal variations directly linked to the evolving solar activity, making their study essential for characterizing the lunar radiation environment.

To address these critical needs, we propose the conceptual design of a compact albedo particle detector for the Chang'E-8 lander. This detector is specifically designed to measure albedo protons and neutrons generated from the lunar surface. The detector system incorporates advanced particle discrimination techniques, enabling the unambiguous separation of both albedo proton and albedo neutron events within a single measurement geometry. This capability is crucial for accurate measurements, especially given the complex and mixed radiation field prevalent on the lunar surface. Preliminary simulations using Geant4 [2] have been performed to assess the detector's performance. These simulations specifically evaluate its efficiency, energy resolution capability for neutron-proton discrimination, and background rejection capabilities within the complex lunar radiation environment. Furthermore, these simulations are being utilized to optimize the detector's geometry, thickness, and shielding. This optimization aims to maximize sensitivity to albedo protons and neutrons and to achieve the highest quality of scientific data for both particle species from this specific measurement geometry, ultimately supporting monitoring of albedo particle flux. This work will detail these comprehensive simulation studies and present the detector's expected performance.

REFERENCES:

- [1] *McCord T. B., Taylor L. A., Combe J.-P. et al.* Sources and physical processes responsible for OH/H₂O in the lunar soil as revealed by the Moon Mineralogy Mapper (M3) // *J. Geophysical Research: Planets*. 2011. V. 116. Iss. E6. Article E00G05. <https://doi.org/10.1029/2010JE003711>
- [2] *Agostinelli S., Allison J., Amako K. et al.* Geant4 — a simulation toolkit // *Nuclear Instruments and Methods in Physics Research Section A: Accelerators, Spectrometers, Detectors and Associated Equipment*. 2003. V. 506. Iss. 3. P. 250–303. DOI: 10.1016/S0168-9002(03)01368-8.

THE UNDERGROUND PROPAGATION OF NEW CONICAL SHOCK WAVES GENERATED BY THE FALLING IMPACTORS ON PLANETS

R. T. Ferreyra¹, M. I. Shpekin²

¹ National University of Córdoba, Córdoba, Argentina
ricardo.tomas.ferreyra@unc.edu.ar

² Kazan Federal University, Kazan, Tatarstan, Russia

ABSTRACT:

In this paper, the classical idea of a shock wave in compressible flow evolved to a hose in matter and then to a conical hose or a conical funnel. These concepts were previously considered in [1] and [2]. The idea of conical funnel was a consequence of a long research process after several publications devoted to the problem of hypersonic wave propagation in the Earth's atmosphere [3–7] and its application and adaptation to the study of complex cratering. The report attempts to consider how the energy and momentum of a conical hose (a new concept of conical shock wave) propagates in the bowels of the planet. Then, the problem of complex craters becomes a case of study.

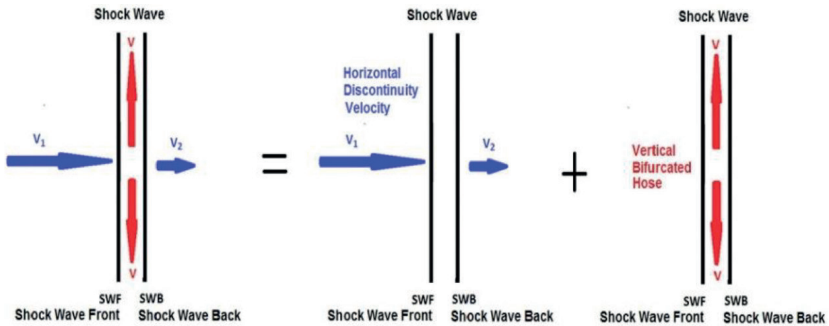


Figure 1. The motion of a new shock wave model [1] for cratering analysis

Figure 1 shows the geometry of a hose [1]. The existence of conical hoses was considered in [2]. The classical plane waves were changed to conical ones after the geometry and then to hoses to form the new model of conical shock waves for cratering analysis. In this paper we deal with the fact that how conical hoses propagates underground through magma.

REFERENCES:

- [1] Ferreyra R. T., Shpekin M. I. A fluid dynamical model for the shape of complex craters // 34th Intern. Conf. Equations of State for Matter (EOS-2019): Book of Abstr. 2019. P. 113.
- [2] Ferreyra R. T. Coupled twin conical funnels or conical hoses: an internal process of dynamic flow distribution // 16th World Congress on Computational Mechanics and 4th Pan American Congress on Computational Mechanics. WCCM. 2024. https://www.scipedia.com/public/Ferreyra_2024a.
- [3] Ferreyra R. T., Tamagno J. P. A non local technique to approach the solutions of nonlinear boundary value problems applied to a supersonic flow model // Problems of Nonlinear Analysis of Engineering Systems PNAES. Bull. 2(38). 2012. V. 18. No. 38. P. 48–63.
- [4] Ferreyra R. T. An infinite number of closed-form solutions for the Taylor-Maccoll model // Problems of Nonlinear Analysis of Engineering Systems. 2014. V. 20. No. 2(42). P. 52–59. https://kpfu.ru/portal/docs/F1781483639/PNAES2_42_2014.pdf.
- [5] Ferreyra R. T. New tools and results in the study of supersonic flow over a solid cone // Problems of Nonlinear Analysis of Engineering Systems. 2015. V. 21. No. 1(43). P. 93–122. https://kpfu.ru/portal/docs/F373391325/PNAES.1_43_rus.2015.pdf.

- [6] *Ferreya R. T.* Supersonic Cones at Zero Incidence // 46th AIAA Fluid Dynamics Conf. AIAA 2016-4275. Session: Shock-Dominated Flows II. Washington, D.C., 2016. <https://doi.org/10.2514/6.2016-4275>.
- [7] *Ferreya R. T.* A shock wave front model applied to very thick and very thin supersonic cones at zero incidence // 8th AIAA Theoretical Fluid Mechanics Conf. Denver, Colorado, 2017. <https://doi.org/10.2514/6.2017-3347>.

THE PROBLEM OF PROPAGATION AND SOME PROPERTIES OF SHOCK WAVES GENERATED BY THE FALLING IMPACTORS ON THE SOLAR SYSTEM PLANETS

M. I. Shpekin¹, R. T. Ferreyra²

¹ Kazan Federal University, Kazan, Tatarstan, Russia

² National University of Córdoba, Córdoba, Argentina
ricardo.tomas.ferreyra@unc.edu.ar

KEYWORDS:

shock wave, impact craters, fluid dynamical model

ABSTRACT:

The classical idea of a shock wave is that it is considered a priori as flat. The first doubts were raised by the authors of the work [1] in 2018 at the ELBRUS Physics Conference (EOS) because in one of the drawings in their poster presentation, they mentioned a conical shock wave. The initiator and author of modified conical waves in the crater formation should be recognized as Ricardo Tomás Ferreyra, who is a specialist in the field of nonlinear processes and had by that time a number of publications devoted to the problem of hypersonic wave propagation in the Earth's atmosphere [2–5].

The report attempts to consider the new concept of a “conical wave” and try to describe some of its basic properties: the energy of a conical shock wave, how the energy of a conical wave propagates in the bowels of the planet. Other properties relate to the interaction of a conical wave with the bowels of the planet, what happens in the bowels is there a way to estimate the energy of such an interaction and whether a magma chamber can form in the bowels of the planet [5].

The report presents attempts at a geometric interpretation of the conical wave [5], which we first described earlier [5]. The main problem in this case is the question of what kind of motion this wave has in the bowels of the planet. There are two points of view on this issue: the wave converges to a point inside the planet's lithosphere, or the wave diverges from the point where the impactor touches the surface when it comes into contact with it. The first point of view is supported by the fact that, a priori, in this case, the energy of the conical wave should be concentrated in a focus at the tip of the wave cone. The second point of view tells us that the energy of the wave should be dissipated in the bowels without focusing. It is also interesting that, as stated in [5], for a planet with an atmosphere, when an impactor passes through it, a hypersonic shock wave is formed that penetrates deep into the planet. The classical point of view was studied before, as happens in the case of a plane wave [6].

There is reason to believe that such a wave also occurs on the atmosphere-free Moon. At the same time, the planetary matter heats up to a high temperature, forming a magma chamber of considerable size at great depth. The substance inside the magma chamber cools down gradually. Cooling takes place on a geological time scale and depends on the state of the heated substance. If the temperature of the substance in the magma chamber is high enough, then the substance may be in a molten (liquid) state. The substance gradually cools down and decreases in volume. In this case, part of the camera volume becomes empty. The formed cavity affects the passage of seismic waves formed by impacts of falling bodies. Since there is more than one cavity on the Moon, seismic waves are reflected many times, which leads to the Moon “buzzing” when it is illuminated. This was first “noticed” by the seismographs of the Apollo expeditions in 1968–1972. The authors did not find in the publications the reason for the mentioned buzz, except for one rather exotic one, which is that the Moon is an artificially created hollow ball. Our proposed scheme for the “buzzing Moon” seems very plausible and so far, the only one.

Another unresolved problem of impact craters is related to the presence of central peaks in the so-called complex craters. Figure 2 shows the geometry of such a crater. The geometry of the conical shock wave gives us a chance to understand this peculiar phenomenon, which has occupied the minds of scientists since the time of Galileo. The porous multilayer substance of the Moon causes a conical wave to provoke a reflected (reverse) conical shock wave. Depending on the depth of the reflecting layer, the energy of this wave is often enough to go beyond the surface of a lava lake (crater floor) and create a "peak" on it, often of a very intricate shape. Figure 1 shows the approximate geometry of the forward and reverse conical waves. Here SWB and SBF are the leading and trailing edges of the reverse wave. Figure 1 shows a model of the motion of a new conical shock wave. To hold the classical notation, we denote the (new) shock waves and their fronts: SWF, SWB (F — front, B — rear).

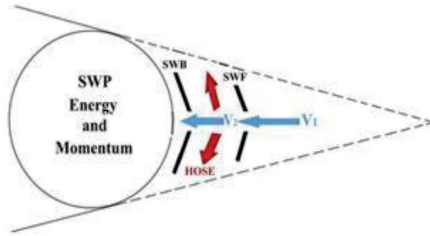


Figure 1. A slice of a new conical shock wave model to show the form of the forward and reverse new conical ones or conical shock waves for cratering analysis [5]

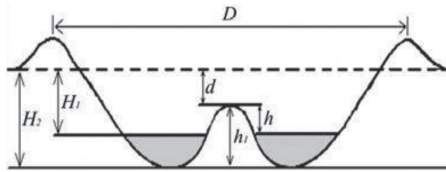


Figure 2 Geometry of a typical complex crater according to [7]

Nowadays, new research considers the new model of conical shock waves for the complex crater analysis [8].

REFERENCES:

- [1] *Ferreira R. T., Shpekin M. I., Ferreira M. A. et al.* A dynamical model as a shock wave pattern to predict the shape of some craters // 3rd Intern. Conf. Equations of State for Matter (EOS-2018): Book of Abstr. 2018. Article 245.
- [2] *Ferreira R. T.* An infinite number of closed-form solutions for the Taylor-Maccoll model // Problems of Nonlinear Analysis of Engineering Systems. 2014. V. 20. No. 2(42). P. 52–59. https://kpfu.ru/portal/docs/F1781483639/PNAES2_42_2014.pdf.
- [3] *Ferreira R. T.* New tools and results in the study of supersonic flow over a solid cone // Problems of Nonlinear Analysis of Engineering Systems. 2015. V. 21. No. 1(43). P. 93–122. https://kpfu.ru/portal/docs/F1607621014/PNAES.N.2_44_v.21.rus.2015.pdf.
- [4] *Ferreira R. T.* A shock wave front model applied to very thick and very thin supersonic cones at zero incidence // 8th AIAA Theoretical Fluid Mechanics Conf. 2017. <https://doi.org/10.2514/6.2017-3347>.
- [5] *Ferreira R. T., Shpekin M. I.* A fluid dynamical model for the shape of complex craters // 34th Intern. Conf. Equations of State for Matter (EOS-2019): Book of Abstr. 2019. Article 113.
- [6] *Barenbaum A. A.* Galxycentric Paradigm in Geology and Astronomy. Moscow: Librokom, 2010. 642 p.
- [7] *Ivanov B. A., Bazilevskiy A. T., Sazonova L. V.* Formation of the central uplift in meteoric craters / NASA Technical Memorandum, 1982. TM-88427 (= Ob obrazovanii tsentralnogo podnyatiya v meteoritnykh kraterakh // Meteoritika. Akademiya nauk SSSR. 1982. No. 40. P. 67–81 (in Russian)).
- [8] *Shpekin M. I., Ferreira R. T., Shishkina V. S.* Shock wave processes on the Moon on the Aitken crater example // Experiment in Geosciences. 2025. V. 1. 6 p. (in print).

APOSTERIORY ANALYSIS OF THE ORBITAL MOTION OF THE APOLLO 17 SPACECRAFT IN NEAR-LUNAR SPACE

M. I. Shpekin, A. D. Gabdulkhakov

Kazan Federal University, Kazan, Tatarstan, Russia

MichaelS1@yandex.ru, blyyt.sky@mail.ru

KEYWORDS:

Photogrammetric processing, mascon, Apollo-17

ABSTRACT:

The report proposes a method for aposteriory tracking of the motion of the spacecraft in the circumlunar space. The method was tested using the example of the Apollo-17 spacecraft. The authors carried out photogrammetric processing of a series of images of the 23rd revolution of Apollo-17 during its passage over Aitken crater and tried to track the behavior of the spacecraft in orbit on approach to the crater, above the crater and away from its center. As a result of image processing, the actual positions of the spacecraft were obtained at the time the images were taken. The authors compared these positions with the ephemeris coordinates of the spacecraft obtained by NASA. The comparison showed that there are noticeable deviations from ephemeris values in the movement of the spacecraft over the crater. These deviations depend on the position of the crater relative to the center of the crater and its central peak. The authors of the report interpret these deviations as a possible effect of mascon in the area of the central Aitken peak.

THE TECHNICAL FEASIBILITY OF DUST TRACKING AND CHARACTERIZATION TECHNOLOGY FOR LUNAR BASE SETTLEMENT

Bintang Alam Semesta Wisran AM

*Skolkovo Institute of Science and Technology, Space Generation Advisory Council, Space Cyber Research Group, Vienna, Austria
bintangalamsemesta.wisranam@gmail.com*

KEYWORDS:

In-Situ Resources Utilization, ISRU, tracking and characterization of lunar dust, portable X-ray fluorescence spectroscopy, pXRF, technique, sensor calibration, dust dynamics prediction

ABSTRACT:

Establishing a sustainable lunar base is a pivotal step toward long-term space habitation and interplanetary exploration. Central to this vision is In-Situ Resources Utilization (ISRU), which minimizes dependence on earth-based supply chains. However, a critical and underexplored challenge in ISRU implementation is the effective tracking and characterization of lunar dust including regolith which is an abrasive, electrostatically charged medium that poses hazards to equipment, habitats, and even to the impact on human health. On top of that, this study investigates the technical feasibility of developing the integrated systems capable of tracking as well as characterizing lunar dust in real-time. Furthermore, a breakthrough in the quantitative surface of lunar dust measurement has been demonstrated through an adapted portable X-ray fluorescence spectroscopy (pXRF) technique [1]. Litofsky, et.al (2024) present a high-throughput, non-destructive technique enabling in-situ quantification of dust load on various surface substrates within seconds. This approach leverages commercial off-the-shelf (COTS) hardware adapted for the lunar environment, providing accurate, high-fidelity dust loading data in mg/cm² units with minimal calibration dependence. The robustness across different substrate materials and environmental testing scenarios, combined with potential adaptation for operational use in spaceflight conditions (radiation, vacuum, thermal extremes), pXRF as a technically feasible tool for continuous surface dust tracking in lunar habitats. Beyond that, precise quantification can inform dust mitigation measures, monitor surface contamination, and contribute to habitat maintenance protocols. On the other hand, the insightful reviews of current dust mitigation and characterization techniques confirming the on-going progression from passive dust control to more active ones, i.e. sensor-driven methodologies [2]. Zanon (2023) outlines the technological readiness of current dust prevention strategies and highlights the gap in the integrated monitoring systems. Aside from it, [3] Fox et al. (2025) discuss detailed characterization of dust impacts inside crew compartments, underscoring the need for precise, real-time monitoring for toxicological assessments and mitigation effectiveness in habitable modules. Last but not least, [4] Tan et al. (2025) present their findings in understanding lunar dust's electrostatic behavior and charging characteristics through multi-source irradiation studies enable refined sensor design and mitigation systems which can exploit those behaviors for more effective dust tracking and removal. Apart from it, such fundamental research underpins technical feasibility by informing sensor calibration, dust dynamics prediction, and environmental interaction models that crucial for integrated dust characterization systems.

REFERENCES:

- [1] *Litofsky J.H., Nagpal S.R., Hull M.W.* Demonstration of Portable X-ray Fluorescence Spectroscopy for High-Throughput In-Situ Quantification of Surface Lunar Dust for Testing and Future Surface Missions / National Aeronautics and Space Administration. 2024. Article NASA/TM-20240012216.

- [2] *Zanon P.* Current Lunar Dust Mitigation Techniques and Future Directions // *Acta Astronautica*. 2023. V. 213. P. 627–644. <https://doi.org/10.1016/j.actaastro.2023.09.031>.
- [3] *Fox R. T. et al.* Lunar Dust Fates in the HLS Crew Compartment: NASA Technical Report. 2025.
- [4] *Yun Chen, Lifang Li, Jihong Yan et al.* Characterization of Charged Lunar Dust in Multi-Source Irradiation Environments and Its Ground Simulation // *J. Earth Science Reports*. 2025. V. 36. Iss. 4. P. 1867–1876. DOI: 10.1007/s12583-025-0196-3.

MONS MUTON ON THE MOON

E. A. Feoktistova¹, M. P. Shcherbina²

¹ Sternberg Astronomical Institute Moscow University, Moscow, Russia
hrulis@yandex.ru

² Institute of Astronomy RAS, Moscow, Russia, mpshcherbina@inasan.ru

KEYWORDS:

Moon, polar regions, landing sites

INTRODUCTION:

Mons Mouton (84.6° S, 31° E) is a large elevation in the region of the south pole of the Moon. This area is currently being considered as one of the possible landing sites for the future Russian lunar missions Luna-27B. The mountain is impressive in size: about 80 km in the north-south direction and up to 100 km in the east-west direction. Mons Mouton is located on the rim of the ancient South Pole — Aitken basin. The average height of the mountain exceeds 6 km above the surrounding surface. To the east, the mountain borders the Nobile crater (85.3° S, 53.3° E). The crater rim is the highest part of Mons Mouton. To the west is Mons Malapert and the crater of the same name (83.9° S, 19.8° E). To the northeast is the Scott crater (82.3° S, 48.4° E). Several small craters, less than 10 km in diameter, are located on the mountain itself. Mons Mouton is of interest as a possible landing site because it is located on the visible side of the Moon (within direct line of sight of the Earth), high above the surrounding terrain, and well illuminated by the Sun during the lunar day. It is possible that there are areas on the plateau containing water ice deposits. Increased hydrogen content in the lunar soil in the plateau region was detected by the probes Lunar Prospector [1], LRO (Lunar Reconnaissance Orbiter) [2, 3]. In 2024 and 2025, the Mons Mouton region became the site of unsuccessful landings of the lunar expeditions Intuitive Machines Im-1 (Odysseus) and Im-2 (Athena).

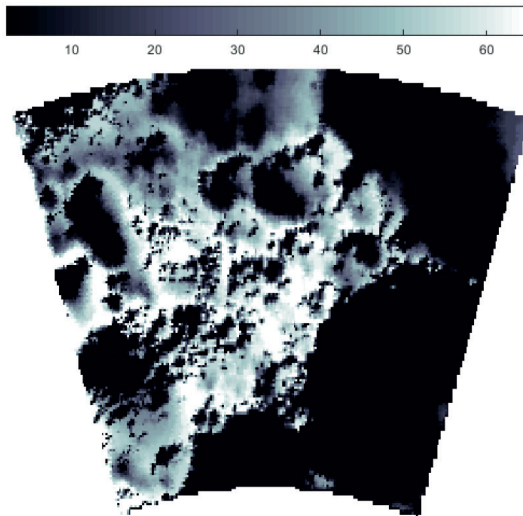


Figure 1. Visibility of Mount Mouton from Earth. Earth visibility is shown from 0 to 100 %. There are areas on the plateau that remain visible from Earth for ~80 % of the lunar year

To determine the geomorphological parameters of the surface of Mons Mouton, we used the data from the LOLA altimeter of the LRO probe (<https://ode.rsl.wustl.edu/moon/>). The calculation of the geomorphological parameters was carried out in the same way as described in [4]. The difference in altitude in this area reaches ~10 km. The maximum altitude (7 km) is observed in the southeastern part of the mountain, and the minimum (-3 km) in the Scott Crater area. The slope values in the mountain area

range from 1° at the summit to 44° on the slopes. The height of the relief surrounding each surface element and the orientation of this surface element relative to the visible position of the Sun and Earth at each moment in time during one lunar year when calculating the illumination and visibility of Mons Mouton from Earth. To study the temperature regime of the lunar surface in the area of Mons Mouton, we used the model described in [5]. The following parameters: terrain slopes, solar illumination level, visibility of the potential landing site from Earth, maximum temperature values, the possibility of the existence of water ice deposits or any other volatile compounds in the area under consideration, and the area of the site were taken into account when determining the positions of possible landing sites on Mons Mouton. The visibility of this area from Earth is shown in Figure 1. We have identified several areas on the surface of the mountain that may be of interest as landing sites for future lunar missions.

REFERENCES:

- [1] *Feldman W.C., Maurice S. et al.* Evidence for water ice near the lunar poles // *J. Geophysical Research*. 2001. V. 106. Iss. E10. P. 23231–23252. <https://doi.org/10.1029/2000JE001444>.
- [2] *Mitrofanov I.G., Sanin A.B., M. L. Litvak.* Water in the Moon's Polar areas: Results of LEND Neutron Telescope Mapping // *Doklady Physics*. 2016. V. 61. Iss. 2. P. 98–101. DOI: 10.1134/S1028335816020117.
- [3] *Hayne P.O., Hendrix A., Sefton-Nash E. et al.* Evidence for exposed water ice in the Moon's south polar regions from Lunar Reconnaissance Orbiter ultraviolet albedo and temperature measurements // *Icarus*. 2015. V. 255. P. 58–69. DOI: 10.1016/j.icarus.2015.03.032.
- [4] *Pugacheva S.G., Feoktistova E.A., Shevchenko V.V.* On the possibility of the existence of volatile compounds in the region of the Scott crater on the Moon // *Cosmic Research*. 2018. V. 56. No. 3. P. 169–179. DOI: 10.1134/S0010952518030048.
- [5] *Vasavada A.R., Bandfield J.L., Greenhagenet B.T. et al.* Lunar equatorial surface temperatures and regolith properties from the Diviner Lunar Radiometer Experiment // *J. Geophysical Research: Planets*. 2012. V. 117. Iss. E12. <https://doi.org/10.1029/2011JE003987>.

ANALYSIS OF LUNAR CRATERS LARGER THAN 10 KM FORMED IN THE MOON'S FIRST BILLION YEARS

E. A. Grishakina

*Vernadsky Institute of Geochemistry and Analytical Chemistry RAS
Moscow, Russia, grishakina@geokhi.ru*

KEYWORDS:

Moon, lunar craters, crater diameter, lunar highlands, morphology

ABSTRACT:

Most lunar craters formed within approximately the first billion years after the formation of the Moon and Earth. In this study, the number of lunar craters larger than 10 km in diameter is analyzed for a number of diameter ranges. The count of ancient craters is carried out primarily in lunar highlands, excluding craters in transition zones and mare areas, in order to exclude areas with lava-filled craters in advance. For comparison, the number of craters of this age is also studied for the entire lunar surface. The craters are selected based on the Morphological Catalog of Lunar Craters [1] in accordance with the characteristics suitable for the task, where the clarity or degree of preservation of the crater rim is defined as "degraded rim" and "ruins". The catalog of lunar craters [2], which includes information on the age of craters based on the works [3, 4], is also used to estimate the number of craters. If it is necessary to clarify the morphological characteristics of craters, altitude profiles are constructed based on the digital elevation model of the Moon using LRO LOLA data in the ArcGIS software package. The results of this study can be used to estimate the average number of impactors that crossed the Earth's orbit during the late-heavy bombardment. If the relation between the diameters of a crater and an impactor for intermediate values of the velocities and impact angles is known, the flux of bodies that form these craters may be determined from the observations, analysis, and counting of impact craters on the Moon [5].

REFERENCES:

- [1] *Rodionova Zh. F., Karlov A. A., Skobeleva T. P. et al.* Morphological Catalog of Lunar Craters. Moscow: Publ. MSU, 1987. 173 p. (in Russian).
- [2] *Losiak A., Kohout T., O'Sullivan K. et al.* Lunar Impact Crater Database // Lunar and Planet. Inst. Lunar exploration Intern Program, 2009. Updated by Ohman T. 2015. <https://www.lpi.usra.edu/scientific-databases/>.
- [3] *Wilhelms D. E., McCauley J. F., Trask N. J.* The geologic history of the Moon. U.S. Geological Survey: Professional Paper 1348. 1987. <https://doi.org/10.3133/pp1348>.
- [4] *Wilhelms D. E., Byrne C. J.* Stratigraphy of lunar craters. 2009. <http://www.imagegain.com/Strata/StratigraphyCraters.2.0.htm>.
- [5] *Ipatov S. I., Feoktistova E. A., Svetsov V. V.* Number of Near-Earth Objects and Formation of Lunar Craters over the Last Billion Years // Solar System Research. 2020. V. 54. Iss. 5. P. 384–404. DOI: 10.1134/S0038094620050019.

CHEMICAL COMPOSITION OF METALLIC IRON SPHERULES IN THE LUNAR SOIL OF CHANG'E-5

E. M. Sorokin¹, M. V. Gerasimov², V. Ya. Shklover³, A. V. Bondarev³

¹ Vernadsky Institute of Geochemistry and Analytical Chemistry RAS
Moscow, Russia, egorgeohim@ya.ru

² Space Research Institute RAS, Moscow, Russia

³ LLC "Systems for Microscopy and Analysis", Moscow, Russia

KEYWORDS:

lunar soil, Chang'E-5, FIB, TEM, iron nanospherules, npFe⁰, siderophile element-impurities, space weathering

INTRODUCTION:

The regolith of the Moon is a product of space weathering, during which the material is mechanically and chemically reworked by micrometeorites and the solar wind. One of the key products of these processes are metallic iron nanospherules (npFe⁰), which affect the optical and magnetic properties of regolith [1, 2].

The present study focuses on metallic iron nanoparticles identified in agglutinate particles in regolith delivered by the Chang'E-5 mission. Up to now there have been no special systematic studies of the impurity composition of metallic iron nanospherules, there have only been isolated analyses of nanosulfides, iron silicides and large iron spherules [3–8]. The aim of the work was to determine the chemical composition of npFe⁰ spherules.

OBJECTS AND METHODS OF ANALYSIS:

A 0.1 mg sample was collected from a fine fraction of mare regolith from the Rümker Mountains. Investigations included scanning (SEM) and transmission (TEM, STEM) electron microscopy, focused ion polishing (FIB), elemental mapping and spot EDS analysis.

Lamellae samples were obtained on a Helios NanoLab 660 system using a Ga⁺-ion beam. Chemical composition was measured in points and along profiles on an FEI G20 F20 S-TWIN microscope at an accelerating voltage of 200 kV. The use of STEM allowed us to achieve a spatial resolution of 1–2 nm.

RESULTS AND DISCUSSIONS:

A lamella was cut out of agglutinate particles (particles formed from rock and mineral fragments sintered by glass under the action of micrometeoritic impact) by the FIB method together with npFe⁰ clusters. This lamella also contained chains and scatterings of metallic iron spherules ranging in size from 10 to hundreds of nm. The npFe⁰ are found both on the surface and inside the glass. They are often organized in linear chains, indicating their formation in zones of active melt agitation.

Forty-six metallic spherules were analyzed by the STEM EDS method. Such spherules contained not only iron, but also a number of impurities, primarily siderophilic elements: Ni, P and S. Their concentrations reached up to 4.5 wt. % Ni, up to 6 wt. % P, up to 8 wt. % S (Figure 1).

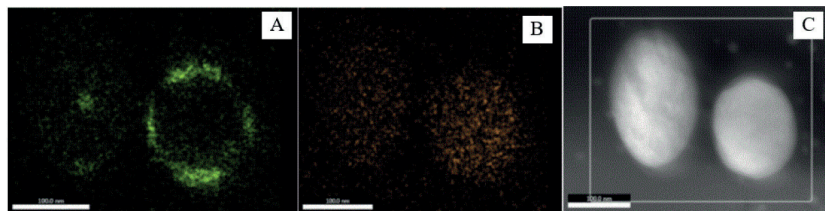


Figure 1. Distribution maps of chemical elements, STEM EDX: *a* — distribution of sulfur; *b* — distribution of phosphorus; *c* — general view of submicron spherules of metallic iron. Scale bar – 100 nm

Sulfur distribution is uneven, in large spherules there are areas with local sulfur enrichment, which may indicate the formation of Fe-sulfide inclusions. Phosphorus is more uniformly distributed, and the oxygen content is lower than in the surrounding glass (Figure 1).

Differences in elemental content in different spherules at the same size may reflect heterogeneities in the local chemical environment during formation as well as different thermal history.

Comparative analysis of the host glass matrix revealed oxygen deficiency (up to 70 % of stoichiometry) and high SiO₂ content (up to 99 wt%), which may be typical of VRAP and GASP condensation glasses [9, 10]. It is likely that the observed elevated matrix silicon contents in this sample indicate relics of similar deposition products incorporated into the glass of this lamella. Such an environment favors the reduction of both iron, and its subsequent organization into spherules, and siderophilic elements that can be sorbed by nascent spherules [11].

Calculated estimates show that the zone from which the spherule “pulls” impurities covers up to 3–4 of its radii.

A simple geometric model is used to estimate the volume of the glass matrix from which npFe⁰ siderophilic elements (Ni, P, S) are absorbed:

$$\frac{R_{gm}}{R_{sph}} = \sqrt[3]{\frac{C_{sph}}{C_{gm}}},$$

where C_{sph} is the concentration of the element of interest in the npFe⁰ spherulas; C_{gm} is the concentration of this element in the glass matrix.

The calculated values (at $C_{sph} = 0.1\%$) range from 1.5 to 4, with no appreciable correlation with the size of the spherulas. This confirms the active role of diffusion and mixing in the melt.

CONCLUSION

The study shows that the spherules of nanophase metallic iron (npFe⁰) found in the regolith of the Moon delivered by the Chang'E-5 mission are not chemically inert formations consisting of pure iron, as has long been assumed. On the contrary, they are enriched with siderophilic impurities — primarily nickel, phosphorus, and sulfur — whose concentrations are much higher than their average levels in the surrounding silicate glass. Such enrichment can be explained by the formation of spherules under conditions of high-temperature melt with reduced oxygen content, where the above elements are reduced and actively diffuse into the metallic phase.

The fixation of npFe⁰ in the volume of glass agglutinates, not only on the surface of regolith particles, indicates their formation in situ at the time of micrometeorite impact [12].

Using a simple matter balance model, it was possible to quantitatively estimate the volume of the “feeding zone” around the spherules from which they capture siderophilic elements: it can reach 3–4 spherule radii, which is consistent with the idea of a high mass transfer rate in a turbulent molten medium.

Thus, npFe⁰ spherules in regolith can be considered as a reservoir and carrier of siderophile elements. Their study not only deepens the understanding of physical and chemical processes on the lunar surface, but also allows us to take a new look at the behavior of reduced elements under conditions of extreme temperatures and low pressure, which is important both for planetary and for the tasks of airless bodies geochemistry.

REFERENCES:

- [1] Hapke B. Space weathering from Mercury to the asteroid belt // J. Geophysical Research. 2001. V. 106. Iss. E5. P. 10039–10073. <https://doi.org/10.1029/2000JE001338>.
- [2] Pieters C.M., Noble S.K. Space weathering on airless bodies // J. Geophysical Research: Planets. 2016. V. 121. Iss. 10. P. 1865–1884. <https://doi.org/10.1002/2016JE005128>

- [3] *Gopon P., Fournelle J., Valley J. et al.* Soft X-Ray EPMA analyses of nanophase lunar Fe-Si compounds // *Microscopy and Microanalysis*. 2014. V. 18. Iss. S2. P. 1728–1729. DOI: 10.17307/wsc.v0i0.18.
- [4] *Gopon P., Spicuzza M., Thomas F.K. et al.* Ultra-reduced phases in Apollo 16 regolith: Combined field emission electron probe microanalysis and atom probe tomography of submicron Fe-Si grains in Apollo 16 sample 61500 // *Meteoritics and Planetary Science*. 2017. V. 52(9). 1–22. DOI: 10.1111/maps.12899.
- [5] *Gu L., Chen Y., Xu Y. et al.* SpaceWeathering of the Chang'E-5 Lunar Sample From a Mid-High Latitude Region on the Moon // *Geophysical Research Letters*. 2022. V. 49. Article e2022GL097875.
- [6] *Yan P., Xiao Z.Y., Wu Y.H. et al.* Intricate Regolith Reworking Processes Revealed by Microstructures on Lunar Impact Glasses // *J. Geophysical Research: Planets*. 2022. V. 127. Iss. 12. Article e2022JE007260. <https://doi.org/10.1029/2022JE007260>.
- [7] *Yan P., Xiao Z., Wu Y. et al.* Submicroscopic iron-rich grains throughout impact glasses in Chang'E-5 regolith // *Icarus*. 2024. V. 410. Article 115920. <https://doi.org/10.1016/j.icarus.2023.115920>.
- [8] *Shen L., Zhao R., Chang C. et al.* Separate effects of irradiation and impacts on lunar metallic iron formation observed in Chang'E-5 samples // *Nature Astronomy*. 2024. V. 8. P. 1110–1118. <https://doi.org/10.1038/s41550-024-02300-0>.
- [9] *Keller L.P., McKay D.S.* Micrometer-sized Glass Spheres in Apollo 16 soil 61181 implications for Impact Volatilization and Condensation // *Proc. 22nd Lunar and Planetary Science Conf.* 1992. P. 137–141.
- [10] *Warren P.H.* Lunar rock-rain: diverse silicate impact-vapor condensates in an Apollo-14 regolith breccia // *Geochimica et Cosmochimica Acta*. 2008. V. 72. Iss. 14. P. 3562–3585. <https://doi.org/10.1016/j.gca.2008.04.031>.
- [11] *Sorokin E.M., Yakovlev O.I., Sluta E.N. et al.* Chemical composition of the nanophase iron (npFe⁰) obtained in the laser experiment // *Proc. 54th Lunar and Planetary Science Conf.* 2023. V. 2806. Article 2156.
- [12] *Sorokin E.M., Gerasimov M.V., Zaitsev M.A. et al.* Experimental Data on the Formation of Nanophase Iron in the Lunar Soil // *Geochemistry Intern.* 2025. V. 70. No. 2. P. 107–125. <https://doi.org/10.31857/S0016752525020013>.

BREAKING THE SHADOWS: NEW TARGETS ON SHACKLETON CRATER FLOOR, LUNAR SOUTH POLE

A.V. Mitusov¹, V.R. Khrisanov²

¹ YouTube channel "Land and Water CA", Berlin, Germany, a_mitusov@mail.ru

² Institute of Basic Biological Problems RAS, Department of Landscape Ecology, Pushchino, Moscow region, Russia

KEYWORDS:

Moon, LOLA data, ShadowCam, Shackleton Crater, South Pole of the Moon, morphometric variables, geomorphometry

INTRODUCTION:

The recent publication of unique photos of Shackleton Crater's shadowed regions [1] is as important as the emergence of an accurate digital elevation model (DEM) of this area. It is now logical to compare these two independent data sources on surface and landforms. One of the most intriguing locations within Shackleton Crater is the three large elevated structures on its floor (Figure 1).

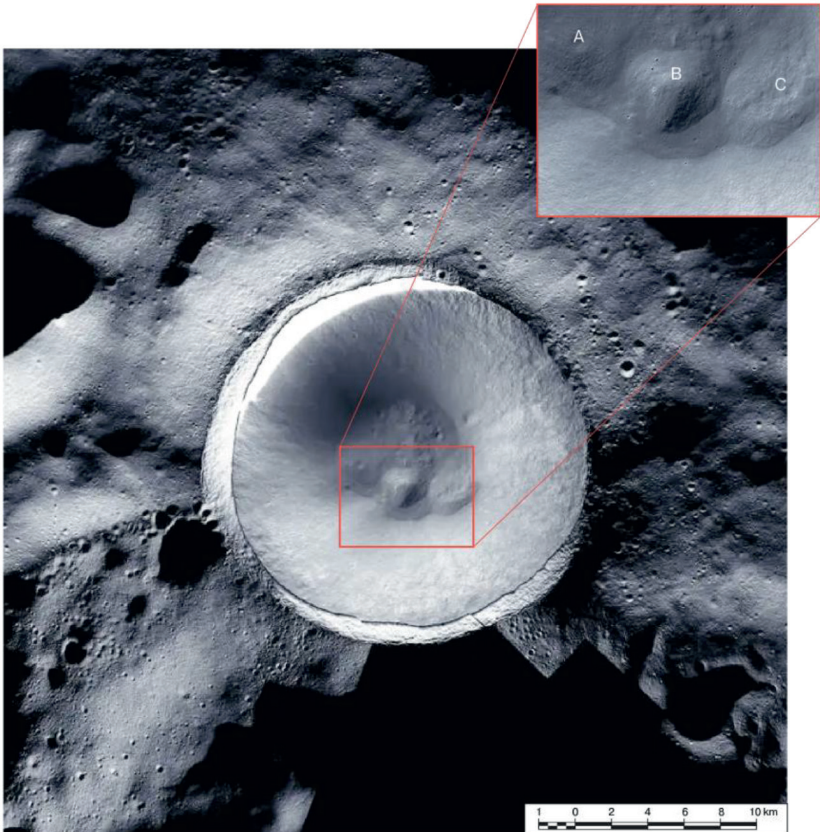


Figure 1. Mosaic of the Shackleton Crater from images provided by NASA [1]. The red rectangle marks the area examined in this study. The letters A, B, and C designate the elevated structures within this region

METHODS:

The inner shadowed area of Shackleton Crater was photographed using ShadowCam [2, 3]. For this study, we use the processed mosaic of Shackleton Crater's shadowed region (Figure 1), published by NASA [1].

The Digital Elevation Model (DEM) with a 20 m horizontal resolution was obtained from the Lunar Orbiter Laser Altimeter (LOLA). This DEM is described in detail in [4]. Based on this DEM, the following curvature types were calculated: vertical (k_v), horizontal (k_h), and minimal (k_{min}). Their physical meaning and computational methods are explained in [4].

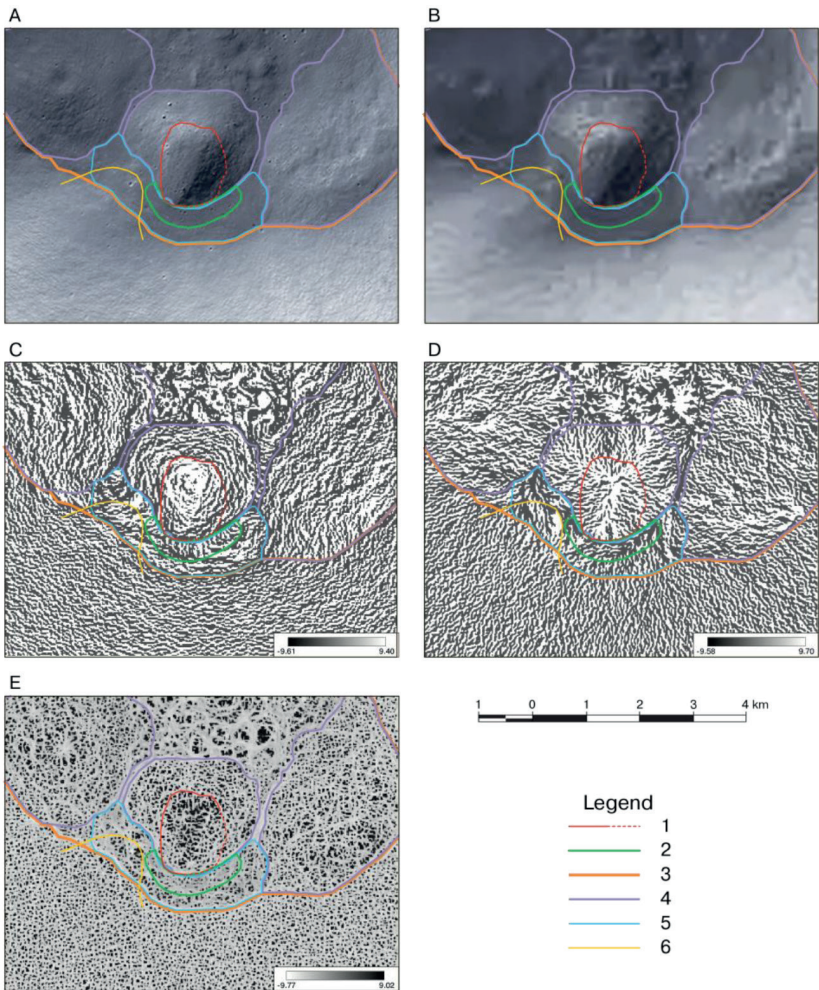


Figure 2. The study area with several regions exhibiting interesting coloration in the ShadowCam images: *a* — Detailed and *b* — Generalized mosaics of the ShadowCam photographs [1]. Gridded Maps: *c* — Vertical curvature map, *d* — Horizontal curvature map, *e* — Minimal curvature map. Legend for contours: 1 — “Beret” Dark smooth area on the summit of Hill B, identified in images A and B. 2 — “Smile” Dark area on the surface of the relatively flat field 5, identified in image B. 3 — Boundary of Shackleton Crater’s floor. 4 — Borders of the elevated structures A, B, and C. 6 — Bright area, visible in images A and B, appearing as an extension of Shackleton Crater’s slope

RESULTS:

This report focuses on three areas with unusual colour gradients on the ShadowCam images (Figure 2*a, b*).

I. BERET

The most noticeable dark patch is located on the summit and slope of elevated structure B (Figure 2, outline 1). Comparison of this colour anomaly with curvature maps revealed a significant number of pixels with positive minimal curvature values (Figure 2*e*). Moreover, the topographic structure on the minimal curvature map (Figure 2*e*) appears more compact than in

the photographic images (Figure 2a, b). The texture with $k_{\min} > 0$ indicates the presence of convex local formations in this area. Their high concentration in a single location suggests that the surface is approximately smooth. This conclusion is further supported by a similar pattern observed on the vertical curvature map (Figure 2c).

Such an extensive area occupied by pixels with $k_v > k_{\min} > 0$ is a rare occurrence. This clearly indicates the presence of unique geomorphological formation mechanisms that differentiate this surface from the surrounding landscape.

II. SMILE

The relatively dark area (Figure 2, outline 2) is barely visible in the detailed image (Figure 2a). However, the dark structure becomes noticeable in the generalized image (Figure 2b). It appears as a narrow strip, approximately one kilometre long, encircling the base of Hill B along the relatively flat field (Figure 2, outline 5). By carefully examining Figure 1, this structure can be identified without relying on outline 2 in Figure 2.

Comparison with curvature maps revealed that outline 2 in Figure 2 closely matches the region of short linear structures on the vertical curvature map (Figure 2c). These structures appear as micro-terraces oriented perpendicular to the flow lines: dark structures are concave, bright structures are convex. The structures themselves are positioned adjacent to the boundary of Hill B.

The detected traces provide clear evidence of flow occurring in this area. However, since the slope gradient in this relatively flat region varies between 2 to 3°, the migration of solid, unconsolidated mineral particles under such conditions would only be possible with very high initial velocities. As an alternative explanation, one could hypothesize that these migrating materials possess special mechanical flow properties, which may be valid for lunar conditions. A simple explanation is that the observed traces are remnants of melt flow from crater formation.

III. YOUNG LANDSLIDE

Outline 6 in Figure 2 was identified in the images as a relatively bright area, visually extending the slope of Shackleton Crater. This outline corresponds well to the dendritic structure observed in the horizontal curvature map (Figure 2d) at this location. Notably, dendritic structures are characteristic of other areas within Shackleton Crater. For example, they are present on the surfaces of elevated structures A, B, and C. This phenomenon has been extensively examined in [4]. However, slope deposits from the crater walls do not form such structures. Thus, the combination of the bright area in images (Figure 2a and b) and the dendritic structure in the horizontal curvature map (Figure 2d) strongly suggests that this feature is a young landslide/s.

CONCLUSIONS:

I. Beret

The existence of a smooth structure on the surface of Hill B has been confirmed. It is likely a rock melt deposit. The hypothesis of an ice cap remains plausible, but only if the ice is covered by a thick layer of dust. Given the limited data, further debate on this matter is not meaningful at this stage. However, future lunar expeditions must conduct detailed geophysical surveys of this area to obtain high-resolution data.

II. Smile

The existence of a complex surface structure on the relatively flat field has been confirmed. Curvature maps (k_v and k_r) support the presence of multi-directional material flows in this region. The presence of structures shaped by material movement in such a flat location leaves no doubt that the migrating substance was in a liquid phase.

III. Young Landslide

Photo image analysis helped identify a relatively young landslide. Its area appears brighter than surrounding regions and is confirmed by the presence of a dendritic structure on the horizontal curvature map (k_r). This is

a significant discovery, as it establishes a connection between dendritic structures and simple linear features on the kh map within the relatively flat field. These features correspond to unconsolidated solid particles “flowing” down the extended slope of Shackleton Crater.

REFERENCES:

- [1] NASA, KARI, SESE. Complicated Lighting // ShadowCam web portal. 2024. Posted by Mark Robinson on 30 January 2024. <https://shadowcam.im-ldi.com/images/1357>
- [2] *Robinson M. S., Brylow S. M., Caplinger M. A. et al.* ShadowCam instrument and investigation overview // *J. Astronomy and Space Sciences*. 2023. V. 40(4). P. 149–171. <https://doi.org/10.5140/JASS.2023.40.4.149>.
- [3] *Estes N. M., Bowley K. S., Hoppe R. et al.* Shedding Light: A First Look at ShadowCam PDS Data // *LPI Contributions*. 2024. V. 3040. Article 1543.
- [4] *Mitusov A. V., Stark A., Khrisanov V. R., Oberst J.* Hidden morphology of Shackleton Crater, lunar South Pole // *Planetary and Space Science*. 2023. V. 238. Article 105795. <https://doi.org/10.1016/j.pss.2023.105795>.
- [5] *Shary P. A., Sharaya L. S., Mitusov A. V.* Fundamental quantitative methods of land surface analysis // *Geoderma*. 2002. V. 107(1-2). P. 1–32. DOI: 10.1016/S0016-7061(01)00136-7.

EXCHANGE OF EJECTED MATERIAL BETWEEN THE MOON AND THE TERRESTRIAL PLANETS

S.I. Ipatov

Vernadsky Institute of Geochemistry and Analytical Chemistry RAS
Moscow, Russia, sipatov@hotmail.com

KEYWORDS:

Motion of bodies, ejection of bodies, probabilities of collisions, Moon, terrestrial planets, Earth

CONSIDERED MODEL:

Planets and the Moon collided with bodies-impactors mainly during formation of planets and at the stage of late-heavy bombardment. After such collisions some material was ejected from planets and the Moon. In each my calculation variant, the motion of 250 bodies ejected from a planet or the Moon was studied for the fixed values of an ejection angle i_{ej} (measured from the surface plane), and a velocity v_{ej} of ejection. In different variants, the values of i_{ej} varied from 15 to 90°, and v_{ej} varied from a parabolic velocity to 20 km/s. Bodies started directly from a planet. Also some calculations were made at the height h of ejection above the Earth's surface equaled to $h = 3r_E$, $h = 5r_E$, $h = 7r_E$ and $h = 36r_E$ (the distance from the center of the Earth is greater than h by r_E), where r_E is the radius of the Earth. There were also calculations for the present orbit of the Moon (its mean distance from the center of the Earth is $60r_E = 385\,000$ km and is a little greater than the semi-major axis of the Moon equaled to 384 748 km due to eccentricity $e = 0.054$). Such calculations with $h > 0$ correspond to the motion of bodies ejected from the Moon, though the gravitational influence of the Moon and its motion about the Earth were not included in integrations. In this case, real velocities of ejection of bodies from the Moon differed a little from those used in calculations. The calculations at $3r_E \leq h \leq 36r_E$ correspond to the case when the Moon had not yet reached its present orbit. Six points on the planet's surface were considered as a starting point of ejection. For point F , the motion of bodies started from the height h from the point of planet's surface located most far from the Sun in the direction from the Sun to the planet. For point C , the motion of bodies started from the point of planet's surface located most close to the Sun in the direction from the planet to the Sun. For points W and B on planet's surface, the bodies started in the direction of the planet's motion and from the opposite side of the planet, respectively. Bodies started from points U and D with the maximum and minimum values of z (with the Oz axis perpendicular to the plane of the planet's orbit), respectively. Only point F (relative to the Earth) was considered for ejection from the Moon. The gravitational influence of all eight planets was taken into account. Calculations were made until all bodies collided with the Sun or planets or reached 2000 a. u. from the Sun. The considered time interval usually equaled to a few hundreds of Myr. More details about the model and the code used for calculations are presented in [1–3].

PROBABILITIES AND VELOCITIES OF COLLISIONS OF BODIES EJECTED FROM THE EARTH WITH THE MOON:

In [1] I studied the probabilities of collisions of bodies ejected from the Earth with the Moon and velocities of collisions of ejected bodies with the Earth and the Moon. The Moon was not included in the integration of motion of bodies. Based on the arrays of orbital elements of migrated bodies and on analytical formulas, I calculated the probabilities of collisions of bodies with the Moon and the Earth and the ratio of probabilities of collisions of bodies with the Earth and the Moon. The probability of a collision of a body ejected from the Earth with the Moon in its present orbit was by a factor 15–35 smaller than the probability of a collision of a body with the Earth at $v_{ej} \geq 11.5$ km/s. The factor was about 35–45 at $v_{ej} = 11.3$ km/s and 15–30 at $v_{ej} = 16.4$ km/s. The probability of a collision of such bodies with the Moon

was mainly about 0.004–0.008 at ejection velocities of at least 14 km/s and about 0.006–0.01 at $v_{ej} = 12$ km/s. It was greater at lower ejection velocities and was in the range of 0.01–0.02 at $v_{ej} = 11.3$ km/s. It was concluded in [1] that in order to contain the present fraction of iron, the Moon should form not far from the Earth.

Values of velocities of collisions of bodies with the Moon and the Earth depended on ejection angles i_{ej} , ejection velocities v_{ej} , and on ejection points. The average velocities of collisions of ejected bodies with the Earth are greater at a greater ejection velocity. The values of these collision velocities were about 13, 14–15, 14–16, 14–20, and 14–25 km/s for ejection velocities equal to 11.3, 11.5, 12, 14, and 16.4 km/s, respectively. The velocities of collisions of bodies with the Moon were also higher at higher ejection velocities and were mainly in the range of 7–8, 10–12, 10–16, and 11–20 km/s at v_{ej} equal to 11.3, 12, 14, and 16.4 km/s, respectively.

PROBABILITIES OF COLLISIONS OF BODIES EJECTED FROM MARS, MERCURY AND VENUS WITH THE MOON:

The probability p_{moon} of a collision of a body ejected from a terrestrial planet with the Moon in its present orbit can be estimated to be mainly about by a factor of 15–30 smaller than the probability p_e of a collision with the Earth. The ratio $k_{em} = p_e / p_{moon}$ can be different for different ejected bodies and typically is less for greater v_{ej} . For example, for $i_{ej} = 45^\circ$ and point F , the ratio equaled to 30, 29, and 18 for ejection from Venus at v_{ej} equal to 10.5, 12, and 20 km/s, k_{em} equaled to 23, 23, and 14 for ejection from Mars at v_{ej} equaled to 5.3, 6, and 20 km/s, and k_{em} equaled to 19, 16, and 21 for ejection from Mercury at v_{ej} equaled to 5.3, 6, and 20 km/s, respectively.

Probabilities p_e of collisions of bodies **ejected from Mars** with the Earth for points C , D , F , U , and W were mainly about 0.08–0.16 and 0–0.16 at $5.05 \leq v_{ej} \leq 10$ and $15 \leq v_{ej} \leq 20$ km/s, respectively. For point B , p_e could exceed 0.24. At $p_e = 0.1$ and $k_{em} = 20$, the probability of a collision with the Moon can be estimated as $p_{moon} = 0.005$.

Probabilities p_e of collisions of bodies **ejected from Mercury** with the Earth were less than 0.03–0.05 (depending on a point of ejection) at $4.23 \leq v_{ej} \leq 6$ km/s. For large velocities in some variants, p_e reached 0.2. At $p_e = 0.04$ and $k_{em} = 20$, the probability of a collision of a body with the Moon can be estimated as $p_{moon} = 0.002$.

For middle points C , D , F , and U at $10.4 \leq v_{ej} \leq 16$ km/s, the fraction p_e of bodies **ejected from Venus** and collided with the Earth was about 0.04–0.1 at $i_{ej} = 45^\circ$, and could be about 0.2 at $i_{ej} = 89^\circ$. At $p_e = 0.09$ and $k_{em} = 30$, the probability of a collision of a body with the Moon can be estimated as $p_{moon} = 0.003$.

PROBABILITIES OF COLLISIONS OF BODIES EJECTED FROM THE MOON WITH THE EARTH:

For ejection of bodies from **the present orbit of the Moon**, $T = 10$ Myr and $30 \leq i_{ej} \leq 60^\circ$, p_e was about 0.2–0.25 at $v_{ej} = 2.5$ km/s, 0.13–0.14 at $v_{ej} = 5$ km/s, and 0.06–0.07 at $12 \leq v_{ej} \leq 16.4$ km/s. At $T = T_{end}$ (at the end of evolution) and $15 \leq i_{ej} \leq 89^\circ$, p_e was about 0.27–0.35 at $v_{ej} = 2.5$ km/s, 0.2–0.25 at $v_{ej} = 5$ km/s, and 0.1–0.14 at $12 \leq v_{ej} \leq 16.4$ km/s. That is, at velocities slightly greater than the parabolic velocity, the values of p_e are approximately the same for the ejection of bodies from the Earth and the Moon, but for different ejection velocities. These p_e values show the fraction of bodies that could collide with the Earth after being ejected from the Moon moving in its present orbit. This fraction is approximately the same as for bodies ejected from the Earth, if we take into account the lower minimum velocities of bodies ejected from the Moon.

For $h = 36r_E$, the probabilities p_e of collisions of bodies ejected from the Moon with the Earth were in the range 0.07–0.2 for $30 \leq i_{ej} \leq 60^\circ$ and $11.2 \leq v_{ej} \leq 16.4$ km/s, and were greater for smaller velocities. At $v_{ej} = 5$ km/s, $T = T_{end}$ and $h = 5r_E$, the value of p_e was about 0.3 (0.26–0.37) for $15 \leq i_{ej} \leq 89^\circ$.

Bodies ejected from the **lunar embryo, which was moving close to the Earth**, fell back to the Earth and the Moon if their initial velocity was

less than the corresponding parabolic velocity. At $v_{ej} = 2.5$ km/s and $h = 3r_{E'}$, the dynamic lifetime of the ejected bodies was less than 5 days. At $h = 5r_{E'}$, $i_{ej} \geq 30^\circ$, and $v_{ej} = 2.5$ km/s, most of the ejected bodies quickly fell to the Earth. For $h = 7r_{E'}$, $v_{ej} = 2.5$ km/s, $30 \leq i_{ej} \leq 60^\circ$, and $(h = 5r_{E'}$, $v_{ej} = 2.5$ km/s, $i_{ej} = 15^\circ)$, and $(h = 3r_{E'}$, $v_{ej} = 5$ km/s, $15 \leq i_{ej} \leq 45^\circ)$, more than a half of bodies still moved around the Earth after more than 100 Myr. The collisions with the Moon were not included in integrations. So actually such bodies should collide with the Moon. At $v_{ej} = 5$ km/s, the values of p_e were in the range (for different i_{ej}) 0.26–0.37, 0.25–0.29, and 0.20–0.22 for $h = 5r_{E'}$, $h = 7r_{E'}$, and the present orbit, respectively. At $v_{ej} = 12$ km/s, the values of p_e were in the range 0.13–0.14, 0.11–0.14, and 0.11–0.16 for $3r_{E'} \leq h \leq 5r_{E'}$, $h = 7r_{E'}$, and the present orbit of the Moon, respectively. The ratios of probabilities of collisions of bodies with other planets to that of the Earth for ejections from the Moon were mainly similar to the ratio for ejection from the Earth. The probabilities of collisions of bodies ejected from the Earth with planets were considered in [2]. For ejection from the Moon, I will present such probabilities in a publication with a larger number of pages than is allowed in this abstract.

ACKNOWLEDGMENTS:

The studies were supported by the Russian Science Foundation, project No. 25-17-00051.

REFERENCES:

- [1] *Ipatov S.I.* Growth of the Moon due to bodies ejected from the Earth // Solar System Research. 2024. V. 58. P. 94–111. <https://doi.org/10.1134/S0038094624010040>.
- [2] *Ipatov S.I.* Probabilities of collisions of bodies ejected from forming Earth with the terrestrial planets // Icarus. 2025. V. 425. Article 116341. 24 p. <https://doi.org/10.1016/j.icarus.2024.116341>.
- [3] *Ipatov S.I.* Exchange of meteorites between the terrestrial planets and the Moon // Modern Astronomy: from the Early Universe to Exoplanets and Black Holes. 2024. P. 904–909. <https://doi.org/10.26119/VAK2024.143>.

PRELIMINARY ALGORITHM FOR DATA PROCESSING OF THE RADAR COMPLEX RLK-L

V. N. Marchuk, O. V. Yushkova

Kotel'nikov Institute of Radio Engineering and Electronics RAS, Fryazino branch, Fryazino, Moscow region, Russia, Marchuk@ms.ire.rssi.ru

KEYWORDS:

lunar surface, lunar soil structure, orbiting spacecraft, space-based radars

INTRODUCTION:

Replace these instructions with the text of your abstract. If you are including tables or figures, they **MUST** be imported into this file. The total abstract's text with figures and tables is no more than 1–3 pages.

INTRODUCTION:

A preliminary set of algorithms for data processing of the RLK-L radar complex, designed to study the subsurface structure of the Moon to a depth of several kilometers, is considered [1, 2] (<https://iki.cosmos.ru/research/missions/luna-26>). The complex is expected to operate in the Luna-Resurs-1 mission (Luna-26) in orbits from 30 to 100 km above the surface. Based on the radar data obtained, it is planned to create a map of surface roughness, a map of the thickness distribution of regolith, and the allocation of areas with an abnormally high amplitude of reflected signals characteristic of areas of increased conductivity on the map, which will subsequently allow us to identify promising areas for examination by landers to detect metals or helium-3.

RADAR COMPLEX DESCRIPTION:

The RLK-L complex consists of two radars: Radar 20 and Radar 200. Both radars use linear frequency modulation signals with a duration of 250 microseconds and a recording time interval of 350 microseconds. Measurements are carried out once per second, during which time the sub-locator point on the surface is shifted by about 1.5 km, while the radars operate quasi-simultaneously — as soon as the Radar 20 completes recording the received data, the Radar 200 begins emitting and receiving, that is, the time interval between their measurements is only a few milliseconds. Thus, it can be assumed that within one measurement cycle, radars irradiate almost the same area of the surface, therefore, Radar 200 data can be used when processing Radar 20 data to account for reflections from the relief of the lunar surface. Before each measurement, radar methods estimate the distance to the surface to select the optimal time for recording signals, so registration begins earlier over hills than over valleys and “seas” and, on the one hand, there is no loss of important radar data, and on the other hand, measurements contain only useful data, without areas where the signal has not reached the surface yet.

The Radar 200 is designed to study the lunar surface, as well as to assess the thickness of the regolith on it. The frequency range is 140–180 km, which makes it possible to achieve a range resolution of 4 m. To reduce the amount of transmitted data on board, the frequency is lowered by obtaining the difference frequencies between the received and reference LFM signals. An intermediate frequency with a bandwidth of about 5 MHz is filtered out, which is digitized and transmitted to the ground-based storage and processing complex.

The Radar 20 is designed to study the subsurface structure of the Moon to a depth of 3 km. The radar frequency range is 17.5–22.5 MHz, which provides a range resolution of 30 m in vacuum and about 10 m in lunar basalts. To reduce the amount of data, the Radar 20 signals are converted to the frequency range of 0–5 MHz.

When probing from an orbit 100 km above the surface, both radars detect reflections from objects on the surface (and below the surface) in an area with a radius of about 100 km. In an orbit 30 km above the surface, the size of the site will be three times smaller. The signals can be separated by time

of arrival, but not by direction, that is, all signals from objects lying on a circle determined by the inclined range r will arrive at the radar receiver simultaneously, regardless of whether the reflecting object is located in front of, behind or to the side of the radar point. To eliminate these effects, methods of synthesizing the antenna aperture [3–5] or migration methods [6–9] developed for processing seismic acoustic data can be used.

Another problem may be the overlap of reflections coming from under the surface with signals reflected from inhomogeneities on the surface [10]. Since the signals in the ground are significantly attenuated, they may be faintly distinguishable against the background of reflections from surface roughness, which may also be small, but are attenuated only due to spherical divergence, but not absorption. The solution to this problem may be to create a roughness model based on known measurements of the laser altimeter and refined from Radar 200 data and then subtracting the signals calculated from this model from Radar 20 data.

DATA PROCESSING ALGORITHM:

Thus, the following algorithm is proposed:

1. Data from Radar 20 and Radar 200 are recorded.
2. Measurements that are damaged during transmission and noisy with interference, are rejected. The data are reduced to a single height level relative to the Moon's spheroid.
3. The measurement data are linked to the coordinates on the surface of the moon.
4. Radar patterns of Radar 20 and Radar 200 are formed by the method of coordinated filtering [13].
5. Areas with an abnormally high level of reflected signal are selected and mapped.
6. Based on the data from the laser altimeter and Radar 200 radarograms processed using antenna aperture synthesis and data migration [3–9], a model of the signal reflected from the surface are created for each point of the orbit.
7. The signals calculated on the basis of the model are subtracted from the Radar 20 data, reflections from under the surface are highlighted.
8. By solving the inverse problem in relation to the electrophysical model [10], the subsurface structure of the lunar soil is determined.
9. By analyzing the spectral characteristics of the reflected signals, the electrophysical parameters of the soil are refined: dielectric constant and absorption capacity [11–13].
10. By analyzing the data obtained in nearby orbits, the contours of subsurface objects are formed, which are mapped.

The development of these algorithms will make it possible to process the data of the radar complex RLK-L in an optimal way.

ACKNOWLEDGMENTS:

The work was performed within the framework of the state task of the Kotel'nikov's FIRE RAS.

REFERENCES:

- [1] *Smirnov V.M., Yushkova O.V., Marchuk V.N. et al.* Luna-Glob project: Radio sounding of the lunar soil // *J. Communications Technology and Electronics*. 2013. V. 58. P. 911–918. <https://doi.org/10.1134/S106422691309012X>.
- [2] *Marchuk V.N., Yushkova O.V.* Estimation of the maximum depth of the Moon soil sounding // *Physical Bases of Instrumentation*. 2023. V. 12. No. 3(49). P. 75–81 (in Russian). <https://doi.org/10.25210/jfop-2303-GNGASY>.
- [3] *Oliver C., Quegan S.* Understanding Synthetic Aperture Radar Images. Boston: Artech House, 1998. 479 p.
- [4] *Yildirim I., Tezel N.S., Erer I., Yazgan B.* A comparison of non-parametric spectral estimators for SAR imaging // *Recent Advances in Space Technologies*, 2003. RAST'03. Intern. Conf. Proc. 2003.

- [5] Larsson E. G., Stoica P. Li J. Amplitude spectrum estimation for two-dimensional gapped data // IEEE Trans. Signal Processing. 2002. V. 50. Iss. 6. P. 1343–1354. <https://doi.org/10.1109/tsp.2002.1003059>.
- [6] Stolt R.H. Migration by Fourier Transform // Geophysics. 1978. V. 43. Iss. 1. P. 23–48. DOI: 10.1190/1.1440826.
- [7] Gazdag J. Wave equation migration with the phase-shift method // Geophysics. 1978. V. 43. No. 7. P. 1342–1351 DOI: 10.1190/1.1440899 ISSN 0016-8033.
- [8] Rickett J., Sava P. Offset and angle-domain common image-point gathers for shot-profile migration // Geophysics. 2002. V. 67. No. 3. P. 883–889. <https://doi.org/10.1190/1.1484531>.
- [9] Yilmaz Öz, Doherty S. M. Seismic data analysis: Processing, inversion, and interpretation of seismic data / Society of Exploration Geophysicists. 2001. V. 2. 2nd ed. 2027 p. <https://doi.org/10.1190/1.9781560801580>.
- [10] Yushkova O., Iushkov V., Rudamenko R. Simulation of the radar signal reflection from the lunar surface // J. Physics: Conf. Series. 2020. V. 1632. Article 012014. <https://doi.org/10.1088/1742-6596/1632/1/012014>.
- [11] Yushkova O. V., Marchuk V. N. The reflected signal spectrum calculation in sub-surface probing of the lunar soil // J. Radio Electronics. 2025. No. 1. 13 p. (in Russian). <https://doi.org/10.30898/1684-1719.2025.1.11>.
- [12] Yushkova O. V., Kibardina I. N., Dymova T. N. Electrophysical Model of the Moon's Soil // Solar System Research. 2020. V. 54. P. 488–496. <https://doi.org/10.1134/S0038094620060064>.
- [13] Marchuk V. N., Yushkova O. V. Features of receiving signals of the radar complex in the Luna-Resource-1 Project // J. Radio Electronics. 2023. No. 11. 14 p. (in Russian). <https://doi.org/10.30898/1684-1719.2023.11.11>.

GROUND STATION FOR RADIO SCIENCE EXPERIMENT WITH KA-BAND RECEIVER (PKD) ONBOARD OF LUNA-26 ORBITER

A. S. Kosov, L. S. Roshkov, V. S. Roshkov

Space Research Institute RAS, Moscow, Russia, Moscow, akosov@cosmos.ru

KEYWORDS:

microwaves, Moon, gravity anomaly, Ground Station

INTRODUCTION:

The Objectives of the PKD and Ground Station experiment are: investigation of the gravitation field anomaly and orbit parameters by precise one way Doppler shift measurement (PKD – Ground Station).

The Ka-band receiver (PKD) has been included into scientific payload of the Luna-Resource-1 orbiter. The receiver is intended to obtain the signal from Earth's transmitter. It will allow precise measurements of Doppler shift and, therefore, of the relative velocity and acceleration.

The main parameters of the Lunar Orbiter Ka-band Receiver:

Central frequency — channel in frequency band	34.7–35.2 GHz (Ka-band)
Bandwidth	0.5 MHz
Noise temperature	150 K
Antenna beam width	120°
Antenna polarization	Circular right
Short term frequency stability (Allan variance)	$2 \cdot 10^{-13}$
Accuracy of the dV/dt measurements	$3 \cdot 10^{-3} \text{ cm/s}^2$

The layout of the PKD experiment has shown on Figure 1.

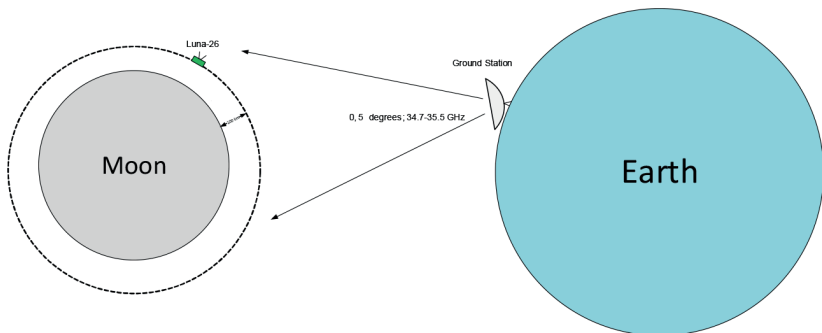


Figure 1. Layout of Radio Science experiment including PKD and Ground Station

The PKD experiment competes with most successful GRAIL experiment performed by NASA.

The comparison of PKD and GRAIL is in the Table 2.

Table 1. The main parameters of the PKD experiment and GRAIL NASA experiment

Parameter	PKD experiment	GRAIL experiment
Allan Deviation:		
1 s	$\leq 1 \cdot 10^{-13}$	$\leq 3 \cdot 10^{-13}$
10 s	$\leq 8 \cdot 10^{-14}$	$\leq 3 \cdot 10^{-13}$
100 s	$\leq 1 \cdot 10^{-13}$	$\leq 3 \cdot 10^{213}$
Accuracy, mGal	3–5	5–10
Resolution, km	5–10	10–20
Area of investigation	Visible side of the Moon	Full Moon
Ground network	Yes	Yes

REFERENCES:

- [1] *Gromov V.D., Kosov A.S.* The Objectives of the Radioscience Experiment in Luna-Resource and Luna-Glob Space Projects // 6M-S3 Symp.: Abstract Book. 2015. P. 43–44.
- [2] *Dehant V., Oberst J., Nadalini R. et al.* Geodesy instrument package on the Moon for improving our knowledge of the Moon and the realization of reference frames // Planetary and Space Science. 2012. V. 68. Iss. 1. P. 94–104. <https://doi.org/10.1016/j.pss.2012.02.008>.
- [3] *Kosov A. S., Gromov V. D., Skulachev D. P. et al.* Radioscience experiments for Martian and Lunar missions // 8M-S3 Symp.: Abstract Book. 2017.
- [4] *Turyshv S. G., Williams J. G.* Space-based tests of gravity with laser ranging // Intern. J. Modern Physics. 2007. V.16. Iss. 12a. P. 2165–2179. DOI: 10.1142/S0218271807011838.
- [5] *Williams J. G., Turyshv S. G., Murphy T. W., Jr.* Improving LLR tests of gravitational theory // Intern. J. Modern Physics. 2004. V. D 13. No. 3. P. 567–582. <https://doi.org/10.1142/S0218271804004682>

UNLOADING, TRANSPORTING AND ASSEMBLING LUNAR STATION MODULES ON THE LUNAR SURFACE: DESIGN DEVELOPMENT OF THE MOBILE ROBOTICS CONCEPT

M. I. Malenkov, V. A. Volov, I. V. Barmin, A. N. Bogachev, N. K. Guseva, E. A. Lazarev

*Scientific and Technical Center "ROCAD", Saint Petersburg, Russia
m.i.malenkov@gmail.com*

KEYWORDS:

lunar station module, unloading device, self-propelled automatic chassis (SAP), intelligent mobile platform (IMP)

INTRODUCTION:

At 13MS3, based on domestic developments [1], with the participation of Dr. A.T. Bazilevsky and Dr. M.A. Ivanov, the authors proposed a new concept of modern lunar trains — multi-link mobile robotic complexes (MRTC). At 15MS3, the design of the SASH was presented, and then some of the results of the developments were summarized [2]. This report reveals new technologies for unloading lunar station modules onto the Moon, transporting them to the construction site, and assembling the lunar station.

TECHNOLOGY OF TURNING THE MODULE ON THE CARGO PLATFORM OF THE SPACECRAFT (SC) AFTER LANDING ON THE MOON:

The authors proceed from the assumption that the MNLS modules, as well as the ISS modules, will be delivered to the construction site fully assembled and will be structures that fit into cylinders, convenient for transportation in space using launch vehicles (LRV). The authors also believe that the new project can be guided by the dimensions (diameter 4 m, length 8 m) and weight (up to 18 000 kg) of the modules proposed in the Long-Term Lunar Base (LTB) project, carried out under the supervision of V.P. Barmin. These initial parameters do not contradict the real parameters of the International Space Station (ISS) modules.

There is no reason to deviate from the idea proposed in the LTB project of building a station on pre-leveled lunar soil. Moreover, studies of Lunokhod-1 have shown that lunar regolith is compacted during deformation, and its load-bearing capacity increases. The authors also believe that by the time work on the Moon to build the MNLS begins, the proven, vertical methods of landing spacecraft on the Moon on their own supports will remain unchanged.

The main problem of unloading modules from the landing spacecraft onto the transport vehicle will be the operation of turning the module over. It is possible to turn over and then place the module on board the lunar rover using lifting and transport equipment using earthly technologies, but for this it will be necessary to first deliver this crane to the Moon in a compact, transport version and assemble this crane at the site of operation. All this requires the participation of astronauts and increases financial costs.

The project proposes a new technology for turning the module over and its subsequent unloading, using the gravitational field of the Moon and simple devices of small mass, built into the landing platform of the same spacecraft. Without going into the technological and design details given in [3], we note that in the initial position at the R-N launch, module 1, with guides 2 installed on it, is secured to the cargo platform of the spacecraft 8 using pyrotechnic bolts 16. The module is hingedly connected to two vertical symmetrical rigid struts 5 and 11, rigidly secured to the same platform 8 in such a way that the axis of the mentioned hinge passes through the center of mass 14 of this module. Such fastening allows reducing the loads on the pyrotechnic bolts 16 during R-N maneuvering in flight.

After landing on the Moon and leveling the spacecraft in a vertical position using special jacks built into supports 17, pyrobolts 16 are torn, which allows winches 7 and 9, operating in coordinated modes, to tear the lower end of the module away from platform 8 and lift the module's rotation axis, which leads to its rotation under the action of the Moon's gravitational field to a horizontal position, in which the same winches lay the module in such a way that guides 2 lie on the roller track of the cargo platform.

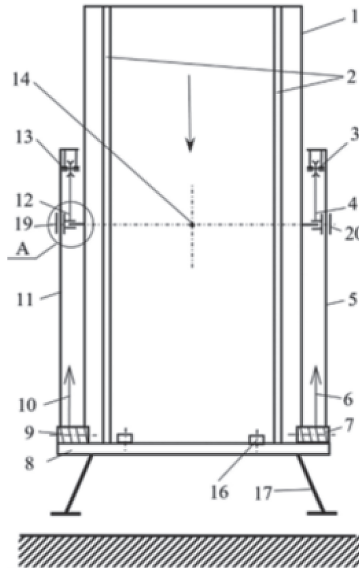


Figure 1. Diagram of the connection of the module (1) with the cargo platform (8) of the spacecraft

TECHNOLOGY FOR RELOADING MODULES ONTO A VEHICLE AND INSTALLING A LUNAR STATION ON THE GROUND OF LUNA FROM WHEELS:

With a nose cone diameter of $D = 5$ m (Figure 2), it is possible to design a four-wheel all-wheel drive chassis with a torsion bar suspension and longitudinal swing of its levers, which has proven itself during the operation of Soviet lunar rovers, with the following geometric characteristics: wheel-base L and track B : $L = B = 3.14$ m, wheel diameter $d = 1.1$ m, wheel width (based on Lunokhod-1 experience) $b = 0.4$ m, wheel turning angle $\theta = \pm 45^\circ$. With such dimensions, a bundle of two intelligent mobile platforms (IMP) based on a single ASP is required to transport the module. IMP are unified ASPs with automatic docking and coupling devices (ADCD) and local navigation systems installed on them. Since the rigid cylinder of the module, all movements of which after its transfer to the coupling are limited by special cradles (Figure 3), will exclude the hinged connection of two IMPs, the coupling becomes similar to the eight-wheeled Lunokhod-1 in its chassis.

Both SASH couplings, in addition to traction drives, are equipped with steering drives, active suspension drives, cradles that ensure the safety of the modules during transportation and a single steering drive. Steering drives facilitate maneuvering for the convergence of the docking lunar rovers. Active suspension drives allow first to ensure the coincidence of the longitudinal axes of these lunar rovers for their reliable docking, and then to align the roller tracks of the coupling in one horizontal plane with the same tracks of the spacecraft cargo platform.

This allows the station module to be moved from the spacecraft cargo platform to the IMP beds along a single roller track using two winches at the rear of the coupling. All operations are performed automatically. One operation that requires the personal participation of the cosmonaut is to hang the winch cable hooks on the eyes attached to the left end of the module.

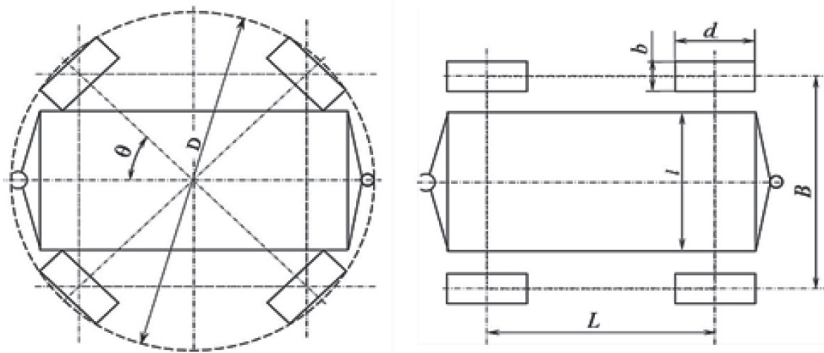


Figure 2. Layout of the SASH on the R-N with a head fairing $D = 5$ m

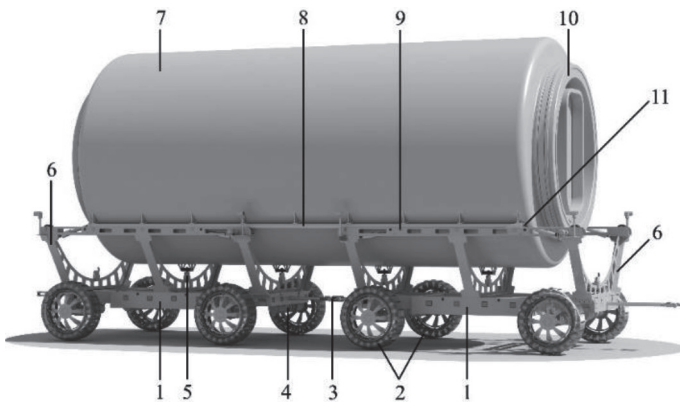


Figure 3. Design concept of a coupling of two IMPs for transporting lunar station modules from the landing site to the automatic assembly site: 1 — self-propelled chassis IMP-1 and IMP-2; 2 — rigid metal wheels; 3 — automatic docking and coupling devices (ADCD)

At the command of the cosmonaut to rotate the winches, the cables pull the module from the spacecraft platform to the coupling beds. Stopping in the required position and locking the module in this position is ensured automatically.

The module can be transported from the landing site to the assembly site at a speed of no more than 0.8 km/h on slopes of no more than 12° along a pre-prepared route at a low speed (less than 1 km/h). The route preparation includes only work with the regolith: leveling and deformation to compact the regolith, after which the coefficient of resistance to movement is reduced. Unloading of modules onto pre-compacted regolith at the lunar station assembly site is carried out using roller tracks and winches.

REFERENCES:

- [1] Egorov A. V., Barmin I. B. Long-term Lunar Base Project. Initial stage // 55th Intern. Astronautical Congress. 2004. IAC-04-IAA.3.7.1.07.
- [2] Malenkov M. I., Volov V. A., Basilevsky A. T. et al. Development of the Concept of Intelligent Mobile Platforms for the International Scientific Lunar Station // Solar System Research. 2025. V. 59. Article 1. DOI: 10.1134/S0038094624600987.
- [3] Volov V. A., Malenkov M. I., Bogachev A. N., Guseva N. K., Lazarev E. I. Method for unloading cylindrical modules of a lunar station from a landing vehicle onto a transport vehicle and a device for implementing it: Patent No. 2837430 (Russia). Application No. 2024120111. 17.07.2024.

MAGNETIC FIELD ANOMALIES OF BOSUMTWI AND ZHAMANSHIN CRATERS ON THE EARTH: ANALYSIS BASED ON NUMERICAL SIMULATIONS

M. Y. Kuzmicheva

*Sadovsky Institute of Geosphere Dynamics RAS, Moscow, Russia
mukuzmigm@gmail.com*

KEYWORDS:

Impact meteorite crater, magnetic field anomaly, demagnetization, numerical simulation

INTRODUCTION:

The most of impact craters found on the Earth are characterized by the presence of negative gravitational and magnetic anomalies [1]. Magnetic field anomalies have been created by a displacement of target rocks and by impact shock wave demagnetization. Magnetic anomalies associated with craters have been found on the surface of Mars [2]. The demagnetization of the lunar surface is also associated with the process of impact cratering [3].

NUMERICAL SIMULATIONS OF MAGNETIC FIELD ANOMALIES WITH VARIOUS TYPES AND VOLUMES OF IMPACTITES:

The author has carried out numerical simulations of the magnetic anomalies of the Bosumtwi and Zhamanshin craters [4, 5]. On the one hand, the ejection of target rocks by a high-speed impact of an asteroid on the planetary surface and the passage of a shock wave into the target, which destroys and weakens the magnetic properties, leads to the formation of a negative magnetic anomaly. On the other hand, in a result of the impact, impactites are formed — rocks with increased magnetic susceptibility, capable of creating a positive magnetic anomaly in the presence of a planetary magnetic field. In the most craters positive magnetic anomalies are observed within crater diameters. Fulfilled numerical simulations of crater magnetic field anomalies permit to make suggestions about a volume and magnetic properties of rocks, buried inside the craters.

ACKNOWLEDGMENTS:

The work was carried out within the framework of the state assignment of the Ministry of Science and Higher Education of the Russian Federation (the Theme № 125012200624-5).

REFERENCES:

- [1] *Grieve R. A. F., Robertson P. B., Dence M. R.* Constraints on the formation of ring impact structures // Multi-ring basins: Formation and evolution: Proc. Lunar and Planetary Science Conference / eds P. H. Schultz, R. B. Merrill. N. Y.; Oxford: Pergamon Press, 1981 P. 37–57.
- [2] *Mohit P. S., Arkani-Hamed J.* Impact demagnetization of the martian crust // *Icarus*. 2004. V. 168. No. 2. P. 305–317. <https://doi.org/10.1016/j.icarus.2003.12.005>.
- [3] *Wieczorek M. A.* Strength, Depth, and Geometry of Magnetic Sources in the Crust of the Moon from Localized Power Spectrum Analysis // *J. Geophysical Research: Planets*. 2018. V. 123. Iss. 1. P. 291–316. <https://doi.org/10.1002/2017JE005418>.
- [4] *Kuzmicheva M., Ivanov B.* Simulation of the Magnetic Anomaly Associated with a Complex Crater Using the Example of the Bosumtwi Crater // *Solar System Research*. 2020. V. 54. No. 5. P. 372–383.
- [5] *Kuzmicheva M., Ivanov B.* Anomalous Magnetic field of the Zhamanshin Meteorite Crater: Numerical Simulation // Proc. IGD RAS “Dynamical Processes in Geospheres”. 2024. V. 16. Iss. 4. P. 46–53 (in Russian).

FAST FREE-RETURN TRAJECTORIES IN THE EARTH-MOON SYSTEM

A.V. Ivanyukhin^{1,2}, **V.V. Ivashkin**³

¹ *Research Institute of Applied Mechanics and Electrodynamics
(Moscow Aviation Institute), Moscow, Russia, ivanyukhin.a@yandex.ru*

² *RUDN University, Moscow, Russia*

³ *Keldysh Institute of Applied Mathematics RAS, Moscow, Russia*

KEYWORDS:

free-return trajectories, resonant orbit, lunar missions, gravity assist, off-nominal situation

ABSTRACT:

This study focuses on Earth-Moon free-return trajectories that enable either Earth return or repeated lunar approach without orbital corrections. These trajectories hold particular significance for lunar missions as they substantially enhance mission safety and ensure overall success, especially for crewed expeditions. This trajectory type was extensively investigated during mid-20th century lunar programs in the USSR and USA [1, 2], involving thorough analysis of periodic orbits in the three-body problem that sequentially approach both Earth and Moon. Specifically, such trajectories were employed for early lunar probes, sample return missions [1], and crewed Apollo flights [2]. With the renewed lunar exploration efforts involving spacecraft, planned crewed orbital stations, and surface bases, these trajectories have regained scientific interest [3]. For future missions, it is essential to consider both Earth free-return trajectories that guarantee crew return [1, 2] and lunar free-return trajectories exhibiting lunar resonance [4], which provide opportunities for repeated lunar orbit insertion in case of anomalies during initial approach.

Clearly, the solution space for such trajectories is extensive, and free-return trajectories can be achieved through various mechanisms: either by selecting appropriate lunar approach parameters and gravity-assist maneuvers, or by leveraging solutions from the three- and four-body problems (including libration point orbits, invariant manifolds, and Weak Stability Boundary trajectories). The first type corresponds to "classical" ("fast") Earth-Moon transfer schemes, while trajectories employing complex three- and four-body dynamics represent low-energy ("long-duration") transfer architectures.

This study focuses on analyzing "fast" free-return trajectories and determining the lunar approach parameters and gravity-assist maneuvers that enable transitions to either Earth- or Moon-bound trajectories. The spacecraft's motion within the Earth-Moon system is modeled using the zero-sphere-of-influence method. Trajectory determination is achieved through solving Lambert's problem [5].

This study presents a preliminary analysis of the essential parameters for Earth-Moon transfer corresponding to free-return trajectories with passive lunar flyby during initial encounter, including estimates of the required velocity costs (ΔV) for trans-lunar injection from low Earth orbit (LEO) and subsequent low lunar orbit (LLO) insertion using the obtained solutions, while evaluating the feasibility of employing such free-return trajectories for prospective lunar missions in terms of mission safety requirements, propellant budget constraints, and operational flexibility needs, with particular applicability to crewed mission abort scenarios, robotic sample return architectures, and flexible mission design approaches.

ACKNOWLEDGMENTS:

The study was supported by the Russian Science Foundation grant No 25-79-30009, <https://rscf.ru/project/25-79-30009/>.

REFERENCES:

- [1] *Egorov V.A.* On some problems of lunar flight dynamics // *Uspekhi fizicheskikh nauk.* 1957. V. 63. No. 1. P. 73–117 (in Russian). <https://doi.org/10.3367/UFNr.0063.195709f.0073>.
- [2] *Arenstorf R.F.* Existence of periodic solutions passing near both masses of the restricted three-body problem // *AIAA J.* 1963. V. 1. No. 1. P. 238–240. <https://doi.org/10.2514/3.1516>.
- [3] *Peng Q.B., Shen H.X., Li H.Y.* Free return orbit design and characteristics analysis for manned lunar mission // *Science China Technological Sciences.* 2011. V. 54. No. 12. P. 3243–3250. <https://doi.org/10.1007/s11431-011-4622-7>.
- [4] *Liu L.-B., Qian Y.-J., Yang X.-D.* Initial parameter analysis about resonant orbits in Earth-Moon system // *Advances in Astronomy.* 2019. Article 6324901. 17 p. <https://doi.org/10.1155/2019/6324901>.
- [5] *Ivanyukhin A.V., Ivashkin V.V.* Solution of the Euler–Lambert problem based on the Okhotsimsky–Egorov ballistic approach // *Solar System Research.* 2024. V. 58. No. 6. P. 769–779. <https://doi.org/10.1134/S0038094624700527>.

SESSION 3. VENUS (VN)
ORAL SESSION

THE VENERA-D MISSION FOR A COMPREHENSIVE STUDY OF VENUS

L. M. Zelenyi¹, O. I. Korablev¹, L. V. Zasova¹, D. A. Gorinov¹,
M. V. Gerasimov¹, N. I. Ignatiev¹, D. S. Rodionov¹, D. V. Strelnikov¹,
M. A. Ivanov², N. A. Eismont¹, D. G. Evdokimova¹, A. Y. Trokhimovsky¹

¹ Space Research Institute RAS, Moscow 117997, Russia

dmitry_gorinov@cosmos.ru

² Vernadsky Institute of Geochemistry and Analytical Chemistry RAS
Moscow, Russia

KEYWORDS:

Venus, mission, spacecraft, orbiter, lander, balloon

ABSTRACT:

Venera-D is a planned mission to study atmosphere and surface of Venus to resolve the fundamental difference between climate histories of Venus and Earth. The Venera-D mission architecture combines the orbiter, the lander and two airborne balloons to use a complex approach to obtain scientific information about Venus.

The Orbiter on the polar orbit is focused on studying thermal structure, dynamics and the composition of the atmosphere (both above and below clouds).

The Lander contains the scientific payload to study the elemental and mineralogical composition of the surface and near subsurface materials, as well as the structure and chemical composition of the atmosphere down to the surface, including the abundances and isotopic ratios of the trace and noble gases, direct chemical analysis of cloud aerosols.

The mission will also include aerial platforms — paired balloons to operate for up to one month at the 53–55 km altitudes. Such modules can provide unique in situ information on the meteorological parameters, composition of the atmosphere, cloud structure, composition and microphysics, nature and distribution of the UV absorber.

The Venera-D project, planned for launch in 2030s, will be an important complementation to the other future Venus missions (Indian Venus Orbiter Mission, VERITAS, DAVINCI and EnVision [1]). A coordination of efforts between missions and their scientific instruments will be crucial to answer the most important fundamental questions about Venus.

REFERENCES:

- [1] *Widemann T., Smrekar S.E., Garvin J.B. et al.* Venus Evolution through Time: Key Science Questions, Selected Mission Concepts and Future Investigations // *Space Science Reviews*. 2023. V. 219. Article 56. <https://doi.org/10.1007/s11214-023-00992-w>.

THE HISTORY OF THE LONG-WAVELENGTH TOPOGRAPHY ON VENUS

M. A. Ivanov¹, J. W. Head²

¹ Vernadsky Institute of Geochemistry and Analytical Chemistry RAS
Moscow, Russia, mikhail_ivanov@brown.edu

² Brown University, Providence RI, USA, James_Head@brown.edu

KEYWORDS:

Venus, global topography, hypsogram, resurfacing, geologic history

INTRODUCTION:

Planetary topography provides substantial clues about the nature of current and past geological and geodynamic processes, the composition of planetary crusts, the efficiency of erosion, degradation and planation processes, and the styles, rates and ages of tectonic processes. Elements of the observed planetary topography can date from different parts of planetary history [1–13]. In our study, we analyzed the global topographic distribution on Venus in the historical aspect using the global geological map of the planet [14]. We investigated the following set of questions closely related to the Venus' geodynamics. (1) What is the history of the global topography of Venus? (2) Does the narrow main peak of the Venus' hypsogram suggest tectonic quiescence of the planet, or does it reflect fairly uniform thickness of crust? (3) Which units of the global geological map correspond to which major topographic domain of the planet? (4) Does the topographic configuration of units correlate with their globally averaged stratigraphic position? (5) Does the assessable topographic evolution of Venus consist of specific episodes or was it a continuous process?

MAJOR TOPOGRAPHIC DOMAINS OF VENUS:

The unimodal hypsogram of Venus allows division of its global topography into three domains [15] relative to the mean planetary radius of 6051.84 km [16]: lowlands (below -0.3 km, 43 % of the Venus surface), midlands (0.3–2 km, 43 %), and highlands (above 2 km, 5 %).

SEQUENCE OF MAJOR GEOLOGIC UNITS/STRUCTURES:

The density of tectonic structures on the surface of units divides them into categories of tectonic and volcanic units [17, 18]. The tectonic and volcanic units occur in the same stratigraphic sequence at both the local global scales [13, 20–24], which permits establishment of three major episodes of resurfacing [18] that correspond to specific periods of the geologic history of Venus [21]. The older Global Tectonic Regime (GTR, Fortunian and Early Guineverian periods, Figure 1) was characterized by the intensive and extensive tectonism. The major units of the GTR are: tessera (t), ridged plains/ridge belts (pr/RB), groove belts (gb). The following Global Volcanic Regime (GVR, Late Guineverian period, Figure 1) was characterized by the emplacement of vast volcanic plains (shield plains, psh, and two units of regional plains, rp1, rp2) that overlie ~ 60 % of Venus. The final, network rifting-volcanism regime (NRVR, Figure 1, Atlian period) includes two major units, lobate plains (pl) and rift zones (rz) that occupy much smaller area (~ 14 %) comparing with units of previous regimes. The rate of resurfacing during the NRVR regime was about an order of magnitude lower [25, 26].

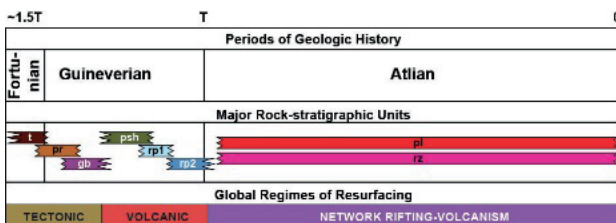


Figure 1. Major divisions (periods and regimes of resurfacing) of the visible portion of the geologic history of Venus

TOPOGRAPHIC CONFIGURATION OF UNITS OF THE GTR (FIGURE 2):

Tessera, ridged plans/ridge belts, and groove belts characterize the oldest recognizable topographic pattern of the planet (Figure 1). The hypsogram of tessera is characterized by a weak bimodality. The apparent saddle between the true major peak and the second possible peak is at about 2,600 m. The lower tesserae compose the majority of tessera terrain (~79 % of its entire area); their mean elevation is about 783 ± 903 m. The higher tesserae compose ~72 % of the highlands; their mean elevation is about 4270 ± 548 m. The hypsogram of ridged plains is strongly unimodal with the peak at about -60 m. It is slightly skewed to the right and has a tail within the highlands. The mean elevation of rp/RB is about -36 ± 806 m. The hypsogram of groove belts is very similar to that of ridge belts. The mean elevation of groove belts is shifted to the right (159 ± 745 m).

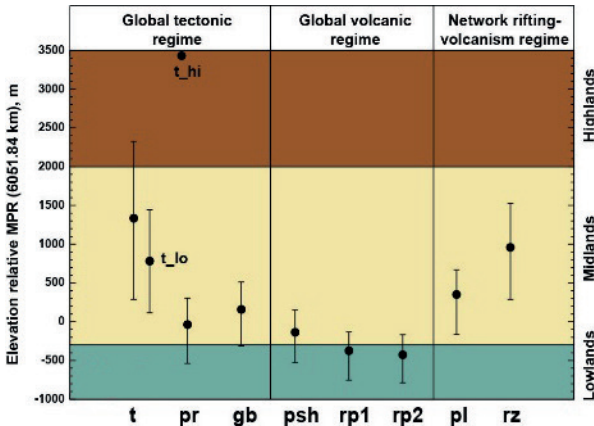


Figure 2. The topographic position of the major units on Venus (units from t through rp2 are in stratigraphic order; units rp and rz are at about the same stratigraphic level)

TOPOGRAPHIC CONFIGURATION OF UNITS OF THE GVR (FIGURE 2):

The hypsogram of shield plains is more symmetrical with the mode at about -300 m and practically coincides with the peak of the global hypsogram. The mean elevation of psh is about -135 ± 637 m. Shield plains make up ~21 % of the area of the lowlands and ~23 % of the midlands. The lower unit of regional plains (rp1) is the most widespread on Venus, covering ~32 % of its surface. The hypsogram of rp1 is unimodal, its mode is between about -500 and -375 m, which is noticeable lower than the peak of the global hypsogram. The mean elevation of the unit is about -370 ± 680 m. The lower unit of regional plains preferentially occurs within the lowlands and makes up about 50% of this topographical domain. The hypsogram of rp2 has the major peak between about -750 and -375 m. Mean elevation of unit rp2 is about -426 ± 570 m. The majority of the unit (~67 %) occurs within the lowlands and makes up about 16% of this domain.

TOPOGRAPHIC CONFIGURATION OF UNITS OF THE NRVR (FIGURE 2):

Units of the NRVR represent the topographic pattern of Venus during the later stages of its evolution. Lobate plains (pl) are distributed in a spot-like manner and are concentrated around prominent volcanic centers. The mean elevation of lobate plains is about 350 ± 815 m. Rift zones occur in close spatial association with broad dome-like rises and likely reflect mantle upwelling associated with these. The hypsogram of rift zones is significantly wider, with the broader peak between ~960–1000 m. The mean elevation is $\sim 960 \pm 1500$. Rift zones and tesserae are the major units of the highlands and compose ~65 % of this domain.

DISCUSSION/CONCLUSIONS:

The results of our study and their interpretations result in the following conclusions.

(1) The formation of the main topographic domains on Venus coincides with the GTR (Figure 3). The largest tessera regions represent a large portion of the modern highlands. (2) The lowlands also began to form during the GTR (Figure 3). The narrow hypsograms of the plains imply that their topographic position/configuration did not change significantly since their emplacement. (3) The topographic position and configuration of rp2 suggest that the topographic changes have essentially vanished by the end of the GTR. (4) The GVR with its lower level of deformation and topographic changes likely represent an aftermath of significant topographic perturbations during the GTR. (5) The stratigraphic position of units formed during the GTR and GVR is well correlated with their topographic position (Figure 2). The progressively younger units occur at lower elevations, which is expected if the embayment relationships determine the stratigraphic sequence. (6) During the observable portion of the Venus' geologic history there were two episodes of the major topographic changes (Figure 3). The first characterized the earlier about one third of the history; it was global in extent and caused both vertical and horizontal displacements of the crust/lithosphere. The second episode characterized the later about two thirds of the history and was related to localized formation of the large topographic swells and the vertical displacements of the crust/lithosphere. (7) These two episodes (Figure 3) likely reflect both the different pattern of mantle circulation and the thickness of the lithospheric lid. The lid was likely thinner and more mobile during the GTR [26, 27] and became thicker and less mobile during the NRVR.

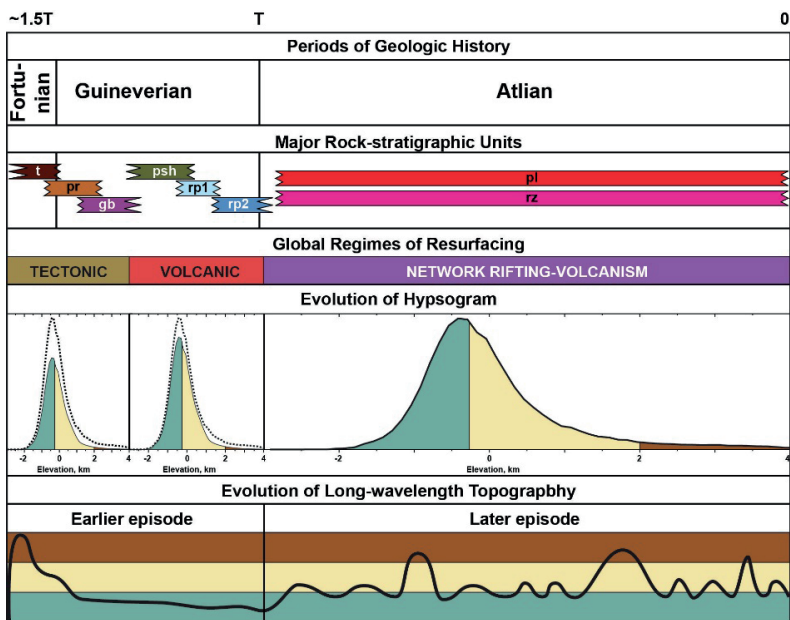


Figure 3. Model of the evolution of the long-wavelength topography of Venus

ACKNOWLEDGMENTS:

The study was carried out within the state assignment of the Vernadsky Institute of Geochemistry and Analytical Chemistry of the Russian Academy of Sciences (GEOKHI RAS).

REFERENCES:

- [1] Taylor S. R., McLennan S. M. The continental crust: Its composition and evolution. Oxford, 1985. 312 p.
- [2] Smith D. E., Zuber M. T., Solomon S. C. et al. The global topography of Mars and implications for surface evolution // Science. 1999. V. 284. Iss. 5419. P. 1495–1503. DOI: 10.1126/science.284.5419.1.
- [3] Zuber M. T., Solomon S. C., Phillipset R. J. et al. Internal structure and early thermal evolution of Mars from Mars Global Surveyor topography and gravity // Science. 2000. V. 287. Iss. 5459. P. 1788–1793. DOI: 10.1126/science.287.5459.1788.

- [4] *Neumann G. A., Zuber M. T., Wieczorek M. A. et al.* Crustal structure of Mars from gravity and topography // *J. Geophysical Research: Planets*. 2004. V. 109. Iss. E8. Article E08002. DOI: 10.1029/2004JE002262.
- [5] *Marinova M. M., Aharanson O., Asphaug E.* Mega-impact formation of the Mars hemispheric dichotomy // *Nature*. 2008. V. 453. DOI: 10.1038/nature07070.
- [6] *Nimmo F., Hart S. D., Korycansky D. G., Agnor C. B.* Implications of an impact origin for the Martian hemispheric dichotomy // *Nature*. 2008. V. 453. P. 1220–1223.
- [7] *Smith D. E., Zuber M. T., Neumann G. A. et al.* Initial observations from the Lunar Orbiter Laser Altimeter (LOLA) // *Geophysical Research Letters*. 2010. V. 37. Iss. 18. Article L18204. DOI: 10.1029/2010GL043751.
- [8] *Wieczorek M. A., Neumann G. A., Nimmo F. et al.* The crust of the Moon as seen by GRAIL // *Science*. 2013. V. 339. P. 671–675. DOI: 10.1126/science.1231530.
- [9] *Neumann G. A., Zuber M. T., Smith D. E., Lemoine F. G.* The lunar crust: Global structure and signature of major basins // *J. Geophysical Research*. 1996. V. 101. Iss. E7. P. 16841–16863. <https://doi.org/10.1029/96JE01246>.
- [10] *Barsukov V. L., Basilevsky A. T., Burba G. A. et al.* The Geology and geomorphology of the Venus surface as revealed by the radar Images obtained by Veneras 15 and 16 // *J. Geophysical Research*. 1986. V. 91. Iss. B4. P. 378–398. <https://doi.org/10.1029/JB091iB04p0D378>.
- [11] *Saunders R. S., Spear A. J., Allin P. C. et al.* Magellan mission summary // *J. Geophysical Research*. 1992. V. 97. P. 13067–13090. DOI: 10.1029/92JE01397.
- [12] *Head J. W., Crumpler L. S., Aubele J. C. et al.* Venus volcanism: Classification of volcanic features and structures, associations, and global distribution from Magellan data // *J. Geophysical Research*. 1992. V. 97. Iss. E8. P. 13153–13197. <https://doi.org/10.1029/92JE01273>,
- [13] *Solomon S. C., Smrekar S. E., Bindshchadler D. L. et al.* Venus tectonics: An overview of Magellan observations // *J. Geophysical Research: Planets*. 1992. V. 97. Iss. E8. P. 13199–13255. <https://doi.org/10.1029/92JE01418>.
- [14] *Ivanov M. A., Head J. W.* Global geological map of Venus // *Planetary and Space Science*. 2011. V. 59. P. 1559–1600. DOI: 10.1016/j.pss.2011.07.008.
- [15] *Masursky H., Eliason E., Ford P. G. et al.* Pioneer-Venus radar results: geology from the images and altimetry // *J. Geophysical Research*. 1980. V. 85. Iss. A13. P. 8232–8260. <https://doi.org/10.1029/JA085iA13p08232>.
- [16] *Ford P. G., Pettengill G. H.* Venus topography at kilometer-scale slopes // *J. Geophysical Research*. 1992. V. 97. Iss. E8. P. 13103–13114. DOI: 10.1029/92JE01085.
- [17] *Ivanov M. A., Head J. W.* The history of volcanism on Venus // *Planetary and Space Science*. 2013. V. 84 P. 66–92. <https://doi.org/10.1016/j.pss.2013.04.018>.
- [18] *Ivanov M. A., Head J. W.* The history of tectonism on Venus: A stratigraphic analysis // *Planetary and Space Science*. 2015. V. 113–114. P. 10–32. <https://doi.org/10.1016/j.pss.2015.03.016>.
- [19] *Sense D. A., Schaber G. G., Stofan E. R.* Regional topographic rises on Venus: Geology of western Eistla Regio and comparison to Beta Regio and Atla Regio // *J. Geophysical Research: Planets*. 1992. V. 97. Iss. E8. P. 13395–13420. <https://doi.org/10.1029/92JE01167>.
- [20] *Basilevsky A. T., Head J. W.* The geologic history of Venus: A stratigraphic view // *J. Geophysical Research: Planets*. 1998. V. 103. Iss. E4. P. 8531–8544. <https://doi.org/10.1029/98JE00487>.
- [21] *Basilevsky A. T., Head J. W.* Geologic units on Venus: Evidence for their global correlation // *Planetary and Space Science*. 2000. V. 48. Iss. 1. P. 75–111. [https://doi.org/10.1016/S0032-0633\(99\)00083-5](https://doi.org/10.1016/S0032-0633(99)00083-5).
- [22] *Bender K. C., Sense D. A., Greeley R.* Geologic map of the Carson Quadrangle (V-43), Venus // U.S. Geological Survey Geologic Investigations Series Map I-2620, 1 plate. 2002. <https://pubs.usgs.gov/imap/2620/>.
- [23] *Rosenberg E., McGill G. E.* Geologic map of the Pandrosos Dorsa Quadrangle (V-5), Venus // U.S. Geological Survey Geologic Investigations Series I-2721. 2001. <https://pubs.usgs.gov/imap/i2721/>.
- [24] *Ivanov M. A., Head J. W.* Volcanically embayed craters on Venus: testing the catastrophic and equilibrium resurfacing models // *Planetary and Space Science*. 2015. V. 106. P. 116–121. <https://doi.org/10.1016/j.pss.2014.12.004>.
- [25] *Kreslavsky M. A., Ivanov M. A., Head J. W.* The resurfacing history of Venus: Constraints from buffered crater densities // *Icarus*. 2015. V. 250. P. 438–450. <https://doi.org/10.1016/j.icarus.2014.12.024>
- [26] *Phillips R. J., Kaula W. M., McGill G. E. et al.* Tectonics and evolution of Venus // *Science*. 1981. V. 212. P. 879–887. DOI: 10.1126/science.212.4497.879.
- [27] *Grimm R. E., Hess P. C.* The crust of Venus // *Venus II Geology, Geophysics, Atmosphere, and Solar wind environment* / eds. S. W. Bougher, D. M. Hunten, R. J. Phillips et al. Univ. Arizona Press Tucson, 1997. 1362 p. P. 1163–1204. <https://www.jstor.org/stable/j.ctv27tct5m>.

ASSESSING THE EVIDENCE FOR ACTIVE VOLCANISM ON VENUS: CURRENT LIMITATIONS AND PROSPECTS FOR FUTURE INVESTIGATIONS

J. Filiberto¹, M. Yu. Zolotov², E. Kohler³, P. D’Incecco⁴, D. A. Gorinov⁵, S. S. Bhiravarasu⁶, M. B. Weller⁷, J. F. Brossier⁸, I. López⁹, P. J. Mason¹⁰, J. A. Edmond¹, N. Mari¹¹, G. Komatsu¹², G. Di Achille⁴, J. B. Garvin³

¹ *Astromaterials Research and Exploration Science Division, NASA Johnson Space Center, Houston, TX, USA, Justin.R.Filiberto@nasa.gov*

² *School of Earth and Space Exploration, Arizona State University Tempe, Arizona, USA*

³ *NASA’s Goddard Space Flight Center, Greenbelt, USA*

⁴ *INAF — Astronomical Observatory of Abruzzo, Teramo, Italy*

⁵ *Space Research Institute RAS, Moscow, Russia*

⁶ *Space Applications Centre (ISRO), Ahmedabad, India*

⁷ *Department of Earth and Environmental Sciences, Rensselaer Polytechnic Institute, Troy, NY, USA*

⁸ *INAF/IAPS, Rome, Italy*

⁹ *Tecnolrisc Research Group. Departamento de Biología, Geología, Física y Química Inorgánica, Universidad Rey Juan Carlos, Madrid, Spain*

¹⁰ *Imperial College London, London, UK*

¹¹ *Department of Biology, Ecology and Earth Sciences, University of Calabria Rende, Italy*

¹² *International Research School of Planetary Sciences (IRSPS), Università d’Annunzio, Pescara, Italy*

KEYWORDS:

Venus, volcanism, weathering, radar, emissivity, atmosphere, geodynamics

ABSTRACT:

Venus is often considered Earth’s sister planet due to its similar size and density, and therefore, it is expected to be volcanically active. However, confirming current volcanic activity and its rate has remained elusive despite being a top scientific priority. Recent investigations have provided tantalizing hints of currently active or recent volcanism. Confirmation of the level of activity is hindered by the thick, omnipresent, optically opaque clouds that obstruct traditional observations of the lower atmosphere and surface. Additionally, corrosive surface conditions pose challenges to long-term landed missions that aim to probe the interior or directly monitor volcanic activity. Despite these challenges, we are entering a new decade of Venus exploration with multiple orbital and probe missions. Here, we review what is known about active volcanism, identify gaps in knowledge to be addressed, and highlight techniques and approaches that need to be developed for this new decade of Venus exploration.

The best evidence for active volcanism comes from combining multiple data sets and approaches, rather than relying on a single study or data set. Venus is likely volcanically active today, with the strongest evidence for activity at Idunn Mons, Maat Mons, and Aramaiti Corona. Without global coverage and regular monitoring, the rate of volcanic activity remains unconstrained. The fleet of new missions, in combination with previous mission data, can be used to provide time-sequence data for monitoring. Our study shows that there are important caveats to combining and comparing data from different instruments. Specifically, differences in look angles and illumination conditions must be accounted for when comparing different datasets.

As we enter the decade of Venus exploration, these new missions must collaborate to collect repeat observations of high-resolution imaging, radar polarimetry, and high-resolution topographical data for any potentially active volcano. The ability to integrate these data is required for understand-

ing Venus's geological activity, particularly in regions where ongoing volcanic processes are suspected.

VENUS SURFACE STUDIES USING VSAR ONBOARD ISRO'S VENUS ORBITER MISSION

S. S. Bhiravarasu, R. Nagori, Y. Sahu, P. Parasher, P. Sinha

Space Applications Centre, Ahmedabad, India, sriram.saran@sac.isro.gov.in

KEYWORDS:

Venus, radar, polarimetry, volcanism, craters

ABSTRACT:

Microwave remote sensing data acquired with ground-based and orbit-based radar instruments are the major source of information about the surface of Venus due to its dense, optically opaque atmosphere. Even though the Magellan mission mapped ~98 % of the surface of Venus in 1990s, there are several gap areas in our understanding of the geologic evolution and resurfacing history of the planet due to the Magellan synthetic aperture radar (SAR) instrument's coarse resolution and single polarization measurements. In this context, the S-band (2385 MHz) fully polarimetric SAR (PolSAR) instrument VSAR on board ISRO's Venus orbiter mission will target the full range of geologic and volcanic processes operating on Venus to address the overarching science questions related to surface processes. Especially, the PolSAR techniques will be utilized to confirm one of the biggest scientific questions about Venus: whether it is still volcanically active, what is the current rate of activity, and what is the volcanic resurfacing rate through time. The VSAR instrument's active and passive imaging capabilities enable detection of recently active volcanism, and provide new constraints to understand the microwave emissivity anomalies on Venus' surface, using repeated PolSAR imagery aided with high resolution, stereo-derived topography. We will present on the VSAR top-level specifications and targeted surface mapping approach during the conference.

CLUSTERING OF VOLCANOES AND CORONAE ON VENUS BASED ON NEURAL NETWORK PROCESSING

D. G. Malyshev¹, N. V. Belyakov², M. A. Ivanov¹

¹ Vernadsky Institute of Geochemistry and Analytical Chemistry RAS
Moscow, Russia, malyshev.danil13@gmail.com

² Artificial Intelligence Center, Moscow, Russia

KEYWORDS:

Venus, volcanoes, coronae, variational autoencoder, clustering, machine learning, SAR images

INTRODUCTION:

The classification of volcanic structures on Venus remains a significant challenge in planetary science despite three decades of research following the Magellan mission (1990–1994). While previous studies have cataloged over 1,700 volcanic edifices, the distinction between coronae (annular tectonic features) and large volcanoes remains ambiguous due to subjective manual classification methods. Traditional approaches rely on topographic profiles or diameter-based criteria, but these methods lack objectivity and scalability for planetary-scale analysis.

This study presents an automated machine learning framework combining variational autoencoders (VAEs) with clustering algorithms to: 1) Extract high-level features from SAR and topographic data; 2) Identify natural subclasses of volcanic structures; 3) Evaluate spatial distribution patterns of clustered features.

METHODOLOGY:

Data Preparation

The dataset comprised 688 structures (446 coronae, 136 large volcanoes, 106 medium volcanoes) from published catalogs [4–7]. Each Magellan SAR image (75 m/px) and corresponding topographic map (5 km/px) was tiled into 512×512 patches (44,032 total), with augmentation applied to improve generalization (Figure 1).

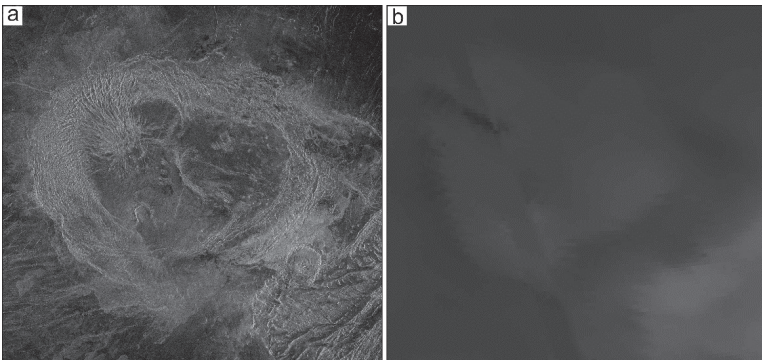


Figure 1: Example of input data: *a* — SAR image of Pomona Corona (79.3° N, 299.4° E); *b* — Topographic map of same region. Image width: 466 km. Source: Processed from Magellan mission data [1]

VAE Architecture

Two separate VAEs were implemented: 1) SAR-VAE: 5-layer encoder with latent dimension 512; 2) Topo-VAE: 3-layer encoder with latent dimension 16. Training utilized composite loss functions combining: 1) Reconstruction loss (MSE); 2) Structural similarity (MS-SSIM) [5]; 3) KL divergence for latent space regularization.

Clustering Pipeline: 1) Feature extraction from latent spaces; 2) Dimensionality reduction to 70 principal components (95 % variance retained);

3) Application of four clustering algorithms: K-Means, DBSCAN, Hierarchical clustering, Gaussian Mixture Models.

RESULTS:

Reconstruction Performance:

Topographic maps achieved superior reconstruction (SSIM = 0.941 vs 0.397 for SAR) due to lower noise (Figure 2). SAR-VAE showed pixel-level artifacts but preserved structural patterns critical for geological interpretation.

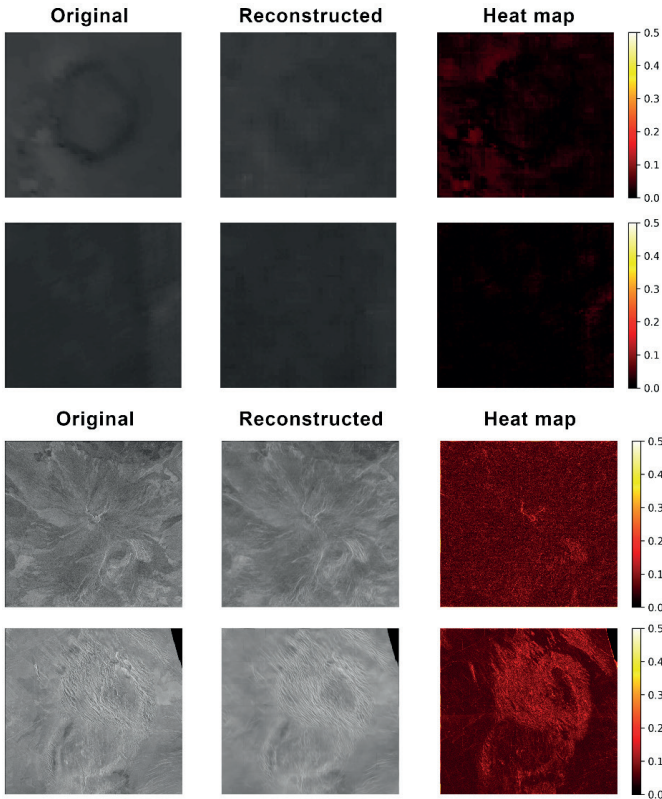


Figure 2: Reconstruction comparison (Left: Original, Center: Reconstructed, Right: Error heatmap). Top row: Topographic data. Bottom row: SAR images

Clustering Results:

Clustering using K-Means, hierarchical clustering, Gaussian Mixture Models (GMM), and DBSCAN methods was performed on the data obtained. The clustering results for the 3rd clusters of the first three models are presented in Table 1. K-Means and GMM produced the most interpretable clusters (Silhouette score = 0.03), though with significant overlap. Spatial analysis revealed longitude-dependent clustering, suggesting potential biases in Magellan data acquisition or geological processes.

Table 1. Clustering results for 3 clusters using three methods

Method	Silhouette score	Cluster content								
		1			2			3		
		cor	vlc	vlcInt	cor	vlc	vlcInt	cor	vlc	vlcInt
K-Means	0.0301	247	94	77	49	0	0	149	42	29
Hierarchical clustering	0.0245	296	106	79	141	27	22	8	3	5
Gaussian Mixture Models	0.0308	246	92	73	49	0	0	150	44	33

Notes: cor — coranae, vlc — large volcanoes, vlcInt — intermediate volcanoes.

In addition to the above examples, experiments were conducted: with a nonlinear method of dimensionality reduction (Kernel PCA), clustering without using coordinates (to test their effect on cluster formation), without dimensionality reduction over the entire space of features obtained from the latent space. All the experiments performed showed either worse results according to the Silhouette Score metric, or were poorly interpreted.

CONCLUSIONS:

1. A unique dataset combining SAR images, topographic maps, coordinates, and sizes of 688 volcanic centers on Venus was created.
2. Two VAE models were developed, showing acceptable reconstruction quality, particularly for topographic maps (SSIM = 0.941).
3. Clustering algorithms partially separated the data by type, but significant overlap remained.
4. The low Silhouette Coefficient suggests weak internal structure, with spatial separation by longitude observed.

Future work includes improving VAE models for better feature extraction, applying the features for cluster analysis, and using the results to automate Venusian surface analysis for future missions.

CODE AND DATA AVAILABILITY:

<https://github.com/MalDan13/Venus-coronae-and-volcanoes-clustering-with-VAE>.

ACKNOWLEDGMENTS:

The study was carried out within the state assignment of the Vernadsky Institute of Geochemistry and Analytical Chemistry of the Russian Academy of Sciences (GEOKHI RAS).

REFERENCES:

- [1] *Saunders R.S., Spear A.J., Allin P.C. et al.* Magellan Mission Summary // *J. Geophysical Research*. 1992. V. 97. Iss. E8. P. 13067–13090. <https://doi.org/10.1029/92JE01397>.
- [2] *Crumpler L. S., Aubele J. C., Senske D. A. et al.* Volcanoes and Centers of Volcanism on Venus // *Venus II: Geology, Geophysics, Atmosphere, and Solar Wind Environment*. 1997. P. 697–756. <https://doi.org/10.2307/j.ctv27tct5m.26>.
- [3] *Stofan E. R., Sharpton V. L., Schubert G. et al.* Global Distribution and Characteristics of coronae and related features on Venus: Implications for origin and relation to mantle processes // *J. Geophysical Research*. 1992. V. 97. Iss. E8. P. 13347–13378. <https://doi.org/10.1029/92JE01314>.
- [4] *Ronneberger O., Fischer P., Brox T.* U-Net: Convolutional Networks for Biomedical Image Segmentation: Lecture Notes in Computer Science // *International Conference on Medical Image Computing and Computer-Assisted Intervention*. 2015. V. 9351. P. 234–241. DOI: 10.1007/978-3-319-24574-4_28.
- [5] *Wang Z., Simoncelli E.P., Bovik A.C.* Multiscale Structural Similarity for Image Quality Assessment. Conference Record of the Asilomar Conference on Signals // *Systems and Computers*. 2003. V. 2. P. 1398–1402. DOI: 10.1109/ACSSC.2003.1292216.

MODELING THE INTERNAL STRUCTURE OF VENUS USING THE MONTE CARLO METHOD

I. A. Boronin, T. V. Gudkova

*Schmidt Institute of Physics of the Earth RAS, Moscow, Russia
anarsull23@yandex.ru, gudkova@ifz.ru*

KEYWORDS:

Monte-Carlo method, inverse problem, Bayesian statistics, Markov chains, internal structure of the planets, Venus

INTRODUCTION:

One of the main problems in studying Venus's internal structure related to its extreme conditions: a dense CO_2 atmosphere with surface pressure 92 times Earth's, temperatures around 470°C , and sulfuric acid clouds. These factors hinder long-term probe operation and data collection. The absence of plate tectonics and a weak magnetic field complicate understanding its geological activity and internal structure. Limited missions and insufficient seismic data also impede accurate modeling of its core, mantle, and crust. A Markov Chain Monte Carlo (MCMC) method is employed [1, 2] to connect observational or hypothetical geodetic data, what allows to determine the posterior probability distribution and the optimal values of the internal structure parameters of Venus.

DATA:

We consider that the interior of Venus is spherically symmetric, isotropic and in hydrostatic equilibrium. The model consists of 3 layers: a liquid core, a viscous mantle and a solid crust. The parameters of each layer are radius, mean density, viscosity, and velocities V_s and V_p . The geodetic data of Venus are summarized in Table 1.

Table 1. The geodetic data of Venus

Parameter	Value
Mean radius R	6051.8 ± 1 km
Standard gravitational GM	$(324858.592 \pm 0.006) \cdot 10^9 \text{ m}^3 \cdot \text{s}^{-2}$
Mean Mol, I/MR^2	0.337 ± 0.024
Tidal Love number k_2	0.295 ± 0.066
Mean density ρ	$5242.7 \pm 2.6 \text{ kg} \cdot \text{m}^{-3}$

A priori Data is summarized in Table 2.

Table 2. A priori data for MCMC

Parameter	Value
Core radius	2500–4000 km
Core density	$< 13\,000 \text{ kg} \cdot \text{m}^{-3}$
Mantle density	$3300\text{--}4600 \text{ kg} \cdot \text{m}^{-3}$
Mantle V_s	$8\,000\text{--}12\,000 \text{ m} \cdot \text{s}^{-1}$
Mantle V_p	$5000\text{--}9000 \text{ m} \cdot \text{s}^{-1}$

We assume that the parameters of Venus's crust are fixed, given that the crust's mass constitutes approximately 0.5 % of the planet's total mass. The modeled core is in a liquid state, which means that shear wave velocity is zero within the core. Consequently, out of the 12 model parameters, only five remain.

MCMC METHOD:

To apply the Monte Carlo method, it is necessary to define the model space as well as the sampling algorithm used for selecting models to construct the probabilistic characteristics. It is assumed that normal distributions are

employed for the core parameters and observed data, while uniform distributions are used for the remaining parameters listed in Table 2. The model selection criterion is based on the following rule: the next model m_{i+1} is always accepted if $L(m_{i+1}) > L(m_i)$ and accepted with probability $L(m_{i+1})/L(m_i)$ otherwise, where $L(m)$ is likelihood function, which measures the degree of fit between geodetic data and data obtained from model m and i is iteration number:

$$L(m) = k_1 \exp \left(- \frac{|d_{\text{Mol}}^{\text{obs}} - d_{\text{Mol}}^{\text{cal}}(m)|^2}{2\sigma_{\text{Mol}}^2} - \frac{|d_{k_2}^{\text{obs}} - d_{k_2}^{\text{cal}}(m)|^2}{2\sigma_{k_2}^2} - \frac{|d_{\rho}^{\text{obs}} - d_{\rho}^{\text{cal}}(m)|^2}{2\sigma_{\rho}^2} \right),$$

where d^{obs} is observed data and d^{cal} is calculated data based on the parameters of model m ; k_1 is normalization constant.

SIMULATION RESULTS:

Five Markov chains was generated with length of 1 million. More than a half of each chain was thrown away as burned up period [1], after autocorrelation analysis was collected about 3000 models. The posterior probability distribution of the obtained models parameters is shown in Figures 1 and 2.

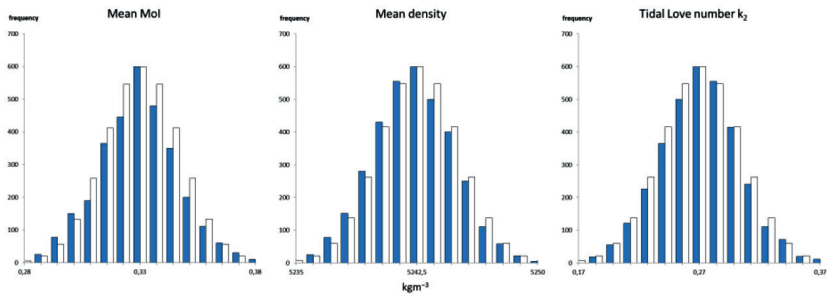


Figure 1. Mean Mol, mean density and tidal Love number k_2 for geodetic data (white) and MCMC inversion results (blue)

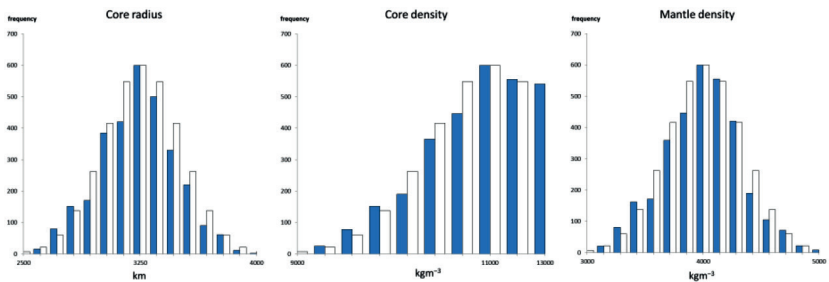


Figure 2. Mean Mol, mean density and tidal Love number k_2 for Gaussian distribution (white) and MCMC inversion results (blue)

Based on the assumption of 3-layered model it was shown, that the interior parameters can be obtained by using the MCMC method with close to normal distribution of parameters.

REFERENCES:

- [1] Mosegaard K., Tarantola A. Monte Carlo sampling of solutions to inverse problems // J. Geophysical Research. 1995. V. 100. Iss. B7. P. 12431–12447. <https://doi.org/10.1029/94JB03097>.
- [2] Xiao C., Li F., Yan J.-G. et al. Inversion of Venus internal structure based on geodetic data // Research in astronomy and astrophysics. 2020. V. 20. No. 8. P. 127–141. DOI: 10.1088/1674-4527/20/8/127.

VENUS LOWER ATMOSPHERE AND SURFACE FROM SPICAV-IR/VEX OBSERVATIONS IN NIR TRANSPARENCY WINDOWS AT 0.8–1.3 μm

D. G. Evdokimova¹, A. A. Fedorova¹, N. I. Ignatiev¹, M. S. Zharikova¹, O. I. Korablev¹, F. Montmessin², J.-L. Bertaux³

¹ Space Research Institute RAS, Moscow, Russia
daria.evdokimova@cosmos.ru

² LATMOS, CNRS, UVSQ, Guyancourt, France

³ LATMOS, CNRS, Sorbonne Université, Paris, France

KEYWORDS:

Venus, cloud optical depth, water vapor, transparency windows

INTRODUCTION:

The dense CO_2 atmosphere (~96.5 %) and H_2SO_4 -cloud layer at 47–70 km greatly obstruct remote sensing of Venus. As a result, the atmosphere below the clouds and the planet's surface remain insufficiently studied. One of the most effective tools for remotely observing Venus's lower atmosphere and surface is the measurement of the atmospheric infrared (IR) transparency windows at 0.8–2.5 μm . These windows are narrow spectral intervals between the strong CO_2 absorption bands and they regulate the thermal radiation escaping from the hot surface and deep atmospheric layers. This weak infrared radiation can be observed on the Venus's night side [1].

The present study examines the spectral interval of 0.8–1.3 μm , which includes transparency windows at 0.85, 0.9, 1.02, 1.1, 1.18, 1.28, and 1.31 μm . In this spectral range, the thermal emission originates from the hot surface and the atmosphere at 0–20 km. The radiation intensity is primarily influenced by the scattering in the sulfuric acid clouds. Additionally, it depends on the surface emissivity and the absorption of H_2O at 0.9–1.0 and 1.1–1.2 μm . It should be noted that the 1.28- μm window is contaminated by an O_2 ($\alpha, \Delta g$) airglow at 1.27 μm produced at 96 km [1].

DATASET OF THE SPICAV IR SPECTROMETER:

The infrared (IR) channel of the SPICAV spectrometer on board the Venus Express (VEx) spacecraft performed observations of the planet night side in 2006–2014. The instrument measured spectra of the transparency windows with a high resolving power of ~1400 [2].

RADIATIVE TRANSFER MODEL:

The measured spectra are analyzed using a multiple scattering radiative transfer model. The model is based on the DISORT program package, which implements the discrete ordinate method for pseudo-spherical geometry [3]. Vertical profiles of atmospheric temperature, pressure, and density were obtained from the VIRA database. The absorption of CO_2 , H_2O , and HDO is calculated from the "High-T", BT2, and VTT spectroscopic databases [4]. It is assumed that H_2O is uniformly mixed beneath clouds. The HDO/ H_2O ratio is fixed at a value that is 127 times lower than the terrestrial one [4]. Aerosol particles are assumed to be spherical and consist of 75 % H_2SO_4 -solution. The optical depth, single scattering albedo and asymmetry parameter are calculated using Mie theory based on the cloud model of Haus et al., 2016 [5]. The variable parameters of the model are the H_2O volume mixing ratio (VMR), cloud opacity and surface emissivity. The model synthesizes the O_2 ($\alpha, \Delta g$) airglow spectrum using the HITRAN database [6].

RESULTS:

The Venus's cloud opacity averages 36.7 ± 6.1 at 1 μm and depends on latitude, with a minimum at 50–55° N. In the Southern Hemisphere, the reduced spatial resolution of the experiment obstructs study of the cloud opacity latitude dependence. Clouds exhibit strong variability at short time scales, more pronounced in the equatorial region. No persistent longitude or local time trends were detected [7].

The volume mixing ratio of deep-atmosphere H₂O (10–16 km) was constrained in the range of 23.6–27.7 ppmv. Water vapor is largely uniform with latitude and local time, showing only a slight high-latitude decrease. Eight years of observations reveal no significant long-term trends or periodicities of H₂O [8].

The surface emissivity variations were studied for the first time for a set of full SPICAV IR spectra.

REFERENCES:

- [1] Pollack J. B., Dalton J. B., Grinspoon D. et al. Near-infrared light from Venus' night-side: a spectroscopic analysis // *Icarus*. 1993. V. 103. No. 1. P. 1–42. DOI: 10.1006/icar.1993.1055.
- [2] Korablev O., Fedorova A., Bertaux J.-L. et al. SPICAV IR acousto-optic spectrometer experiment on Venus Express // *Planetary and Space Science*. 2012. V. 65. No. 1. P. 38–57. DOI: 10.1016/j.pss.2012.01.002.
- [3] Lin Z., Stamnes S., Jin Z. et al. Improved discrete ordinate solutions in the presence of an anisotropically reflecting lower boundary: Upgrades of the DISORT computational tool // *J. Quantitative Spectroscopy and Radiative Transfer*. 2015. V. 157. P. 119–134. DOI: 10.1016/j.jqsrt.2015.02.014.
- [4] Fedorova A., Bézard B., Bertaux J.-L. et al. The CO₂ continuum absorption in the 1.10- and 1.18- μ m windows on Venus from Maxwell Montes transits by SPICAV IR onboard Venus express // *Planetary and Space Science*. 2015. V. 113. No. P. 66–77. DOI: 10.1016/j.pss.2014.08.010.
- [5] Haus R., Kappel D., Tellmann S. et al. Radiative energy balance of Venus based on improved models of the middle and lower atmosphere // *Icarus*. 2016. V. 272. P. 178–205. DOI: 10.1016/j.icarus.2016.02.048.
- [6] Bertaux J.-L., Hauchecorne A., Lefèvre F. et al. The use of the 1.27 μ m O₂ absorption band for greenhouse gas monitoring from space and application to Micro-Carb // *Atmospheric Measurement Techniques*. 2020. V. 13. No. 6. P. 3329–3374. DOI: 10.5194/amt-13-3329-2020.
- [7] Evdokimova D., Fedorova A., Ignatiev N. et al. Cloud Opacity Variations from Nighttime Observations in Venus Transparency // *Atmosphere*. 2025. V. 16. No. 5. Article 572. DOI: 10.3390/atmos16050572.
- [8] Evdokimova D., Fedorova A., Ignatiev N. et al. Near-Surface Water Vapor Content Based on SPICAV IR/VEX Observations in the 1.1 and 1.18 μ m Transparency Windows of Venus // *Atmosphere*. 2025. V. 16. No. 6. Article 726. DOI: 10.3390/atmos16060726.

VIRAL EXPERIMENT FOR ISRO'S VENUS ORBITER MISSION: SCIENTIFIC CONCEPT

D. A. Belyaev¹, A. S. Patrakeev¹, A. Trokhimovskiy¹, A. A. Fedorova¹,
D. Gorinov¹, I. I. Vinogradov¹, S. A. Haider², F. Montmessin³,
O. I. Korablev¹

¹ Space Research Institute RAS, Moscow, Russia, dbelyaev@cosmos.ru

² Physical Research Laboratory, Ahmedabad, India

³ LATMOS/IPSL, Guyancourt, France

KEYWORDS:

Venus atmosphere, minor species, solar occultation, infrared spectroscopy

ABSTRACT:

This paper presents the scientific concept of the VIRAL experiment (Venus InfraRed Atmospheric Linker), which is devoted to study the composition and structure of Venus' atmosphere at the top and above the cloud layer. The instrument was selected by the Indian Space Research Organisation (ISRO) as a scientific payload on board of the Venus Orbiter Mission. The VIRAL instrument includes distinct two infrared (IR) channels: a high-resolution mid-IR echelle spectrometer (VIRAL-C) and an ultra-high resolution near-IR laser heterodyne spectrometer (IVOLGA). The instrument has been designed to perform solar occultation measurements, thereby providing an optimal photon yield combined with a high spectral resolving power exceeding 22,000 (VIRAL-C). The instrument has a high vertical resolution (approximately 1 km at the limb), which enables the detailed altitude profiling of the Venusian upper atmosphere in terms of its composition and structure. The instrument will measure the major and trace species present at the altitudes from 65 to 160 km. The list of species that absorb in the VIRAL-C wavelength range (2.2–4.2 μm) includes CO_2 and its main isotopologues (allowing the retrieval of atmospheric temperature), H_2O and HDO (related to the evolution of water on Venus), other trace gases (CO , SO_2 , HCl , HF) and layers of H_2SO_4 aerosols. Enhanced sensitivity will facilitate the improvement of upper limits or the detection of new trace gases, including H_2CO , OCS , C_2H_2 , H_2S , PH_3 may be upgraded as allegedly detected. The IVOLGA channel will resolve the frequency profile of a single CO_2 line at 1.6 μm with an ultrahigh resolving power of $\sim 10^6$ with an objective to retrieve the vertical profile of the wind. The VIRAL results will contribute to our understanding of the gaseous species variability, as well as the structure and dynamics of the Venusian upper atmosphere.

LONG DURATION PAYLOAD BAY FOR VENUS EXPLORATION

J. Sharma

Moscow Aviation Institute, Moscow, Russia, sharma.joshita14@gmail.com

KEYWORDS:

Multi-Layer Insulation, Heat Flux, Coefficient of Thermal Expansion, Energy Losses, Compressor

INTRODUCTION:

This work intends to present the design of a long duration Venus Lander that is capable of operating for 60 days under the Venus surface conditions of 475 Celsius and 9.3 MPa. The proposed system integrates advanced support systems that enable this extended functioning, including multi staged thermal control system which contains Multi-Layer Insulation, Phase Change Materials and active cooling methods suitable to be used in the Venusian conditions and a Power system to support its continuous operation. The Thermal management system employs active cooling to maintain critical components within their operational limits. Additionally, it includes strategic landing site selection to ensure hazard avoidance with low fuel requirements while maintaining critical data collection opportunity. The end-to-end mission architecture incorporates trajectory optimisation, launch vehicle compatibility and orbital insertion strategies tailored for the lander. While maintaining the 60-day milestone, this work also identifies the limitations prohibiting the development of a lander beyond this limit due to lack of technological advancement, pertaining to the lack of material testing for a longer duration for the required conditions.

THERMAL REGULATION:

Upon landing on the surface of Venus, a module is expected to face temperatures around 475 °C (~748 K) with atmospheric pressure of around 9.2 MPa. Thus, it is most imperative to maintain the temperature within the Payload Bay so as to allow the proper functioning of the electronic devices, which are generally expected to function until the temperature of 125 °C (~398 K). This concept divides the task into two parts, initially before entering the payload bay, the heat flux entering the system should be minimised, for this purpose, few layers of insulations have to be placed for reduction of conductive as well as radiative flux. The outermost layer, which shall interact with the environment will remain to be Titanium to prevent corrosive reactions, beneath its placement of twenty layers of gold foil will be required to reduce the radiative heat flux, following which would be a layer of vacuum, supported by Carbon-Carbon Composite layers on each side, as well as support rods between both, of the same material, this would minimise the conductive heat flux.

Once the heat flux is minimised, the temperature inside would be needed to be maintained, which shall allow comfortable functioning of the Equipment, for this purpose, the atmospheric Carbon Dioxide can be utilised, the pressure difference between the Venus Atmosphere and the payload cooling pipeline, which should be at 0.3 MPa would allow rapid suction as well as cooling of this Carbon Dioxide, to prevent excess speed and energy loss, the intake can be divided into six stages, each with 1.77 pressure ratio, overall this would reduce the gas temperature to ~80 Celsius, which upon flowing through small channels beneath the insulating layers would absorb the already lowered heat flux, thus maintaining the temperature. Finally, to maintain a continuous gas flow and thus by, cooling, this carbon dioxide would need to be removed at the same rate as its intake, for this purpose, the mostly conserved energy can be passed through five stages of diffuser, each with a pressure ratio of 0.52, this would bring up the final pressure at the end of these stages to 7.59 MPa, a single stage centrifugal compressor, would use the pressure ratio of 1.24, to finally increase the pressure beyond the Venusian atmospheric pressure and thus eject the gas, ensuring a continuous flow and cooling.

MASS AND SIZE:

The expected mass of the lander would be 1000 kg, including the landing capsule, the aerodynamic heat shielding and aerodynamic surfaces, scientific equipment, service platform and thermal regulation system. With the mass of the Thermal Protection Layers to be ~223 kg, and the overall service platform mass as ~244 kg including the active thermal regulation.

Summary:

The design of a long-duration Venus Lander presents extraordinary challenges due to its extreme surface conditions, with inclusion of the high temperature conditions, the crushing pressure of the atmosphere as well as the highly corrosive chemistry. This work explored the solutions to overcome these obstacles enabling sustained operations leading to deeper scientific exploration on Venus surface. By the integration of multiple systems, the proposed explorer (lander) design provides a feasible pathway towards the course of extending mission lifetimes beyond the limitations encountered by the previous missions.

REFERENCES:

- [1] *Marov M. Ya.* Venus: A perspective at the beginning of planetary exploration // *Icarus*. 1972. V. 16. Iss. 3. P. 415–461. [https://doi.org/10.1016/0019-1035\(72\)90094-2](https://doi.org/10.1016/0019-1035(72)90094-2).
- [2] *Johnson N. M., de Oliveira M. R. R.* Venus Atmospheric Composition in situ Data: A Compilation // *Earth Space Science*. 2019. V. 6. Iss. 7. P. 1299–1318. <https://doi.org/10.1029/2018EA000536>.
- [3] *Lukco D., Spry D. J., Harvey R. P. et al.* Chemical analysis of materials exposed to Venus temperature and surface atmosphere // *Earth and Space Science*. 2018. V. 5. Iss. 7. P. 270–284. <https://doi.org/10.1029/2017EA000355>.
- [4] *Kosenkova A. V.* Methodology for designing a maneuverable landing vehicle on the surface of Venus: Diss. cand. engineering sciences. Moscow, 2022. 235 p. (in Russian).

SIMULATION MODELING APPLICATION FOR THE DESIGN ANALYSIS OF THE OPERATION OF A VENUS EXPLORATION AEROBOT

N. A. Tkachev, E. V. Loskutova, A. V. Kosenkova

Lavochkin Association, Khimki, Moscow Region, Russia

TkachevNA@laspace.ru

KEYWORDS:

Venus, simulation modeling, aerobot, spacecraft design

INTRODUCTION:

Currently, Venus is of great interest to the global scientific community. The new generation of missions planned for the 30s of the 21st century is focused on the perspective of understanding the evolutionary history of the planet atmosphere and geology [1, 2]. One of the intriguing subjects is the potential cloud habitability [3].

Aerobots as a part of modern Venus exploration missions can provide unique in situ data on meteorological parameters, atmospheric composition, the nature and distribution of the UV absorber, as well as on the structure, composition and microphysics of clouds, including the presence of biomarkers there [3]. For the first time, aerobots were used to explore Venus in the 80s in Soviet missions, but the research was limited by the low aerobot battery power capacity and their visibility from ground stations — the operation time of the aerobots was about 46 hours [4]. An increase in both the drift duration and available resources of the power system are required to improve the quality and quantity of atmospheric data received by the aerobot from various regions on both the night and day sides [5]. The formation of an operation scheme of the aerobots in the atmosphere during their design is also of fundamental importance [6].

The use of simulation modeling is proposed for the design analysis of the operation of an aerobot in the Venus atmosphere. Simulation modeling allows you to perform virtual tests and analyze the operation of the product under various external influences during the spacecraft design process [7].

The paper analyzes the cyclograms of the aerobot's equipment operation during its movement in the cloud layer of the Venus atmosphere in a selected range of latitudes and makes suggestions on the use of simulation modeling in forming the scheme of aerobot operation in the Venus atmosphere.

The results could be applied in the development of missions for the comprehensive exploration of planets with an atmosphere.

REFERENCES:

- [1] *Widemann T., Smrekar S.E., Garvin J.B. et al. Venus Evolution through Time: Key Science Questions, Selected Mission Concepts and Future Investigations // Space Science Reviews. 2023. V. 219. No. 56.*
- [2] *Limaye S.S., Garvin J.B. Exploring Venus: next generation missions beyond those currently planned // Frontiers in Astronomy and Space Sciences. 2023. V. 10. Article 1188096. <https://doi.org/10.3389/fspas.2023.1188096>.*
- [3] *Zelenyi L.M., Korablev O.I., Zasova L.V. et al. Venera-D Mission for Comprehensive Study of Venus // 15th Moscow Solar System Symposium. 2024.*
- [4] *Automated Spacecrafts for Basic and Applied Scientific Research /eds. G.M. Polishchuk, K.M. Pichkhadze. Moscow: Publ. MAI-PRINT, 2010. 660 p. (in Russian).*
- [5] *Loskutova E.V., Yudin A.D. The Possibility of Using a Discharged Balloon in the Process of Balloon Drift in the Atmosphere of Terrestrial Planets // 48th Academic Readings on Cosmonautics, Dedicated to the Memory of Academician S.P. Korolev and Other Outstanding Russian Scientists, Pioneers of Space Exploration: abstr. Moscow, 2024. (in Russian).*
- [6] *Efanov V.V., Shevalev I.L. Design of automated spacecraft for basic scientific research: v 3 t. V. 1. 2-e ed. Moscow: MAI-PRINT, 2013. 492 p. (in Russian).*
- [7] *Tkachev N.A., Kosenkova A.V. Simulation modeling and electronic prototyping of rocket and space technology products in the process of their creation and*

operation // 48th Academic Readings on Cosmonautics, Dedicated to the Memory of Academician S. P. Korolev and Other Outstanding Russian Scientists, Pioneers of Space Exploration: abstr. Moscow, 2024. (in Russian).

THE VENUS-ASTEROID RESONANCE TRANSFERS FOR EXPANDING THE PLANETARY EXPLORATION FRAMEWORK

Zubko V. A., Pupkov M., Chernenko O., Eismont N. A., Fedyaev K. S.

Space Research Institute RAS, Moscow, Russia, v.zubko@cosmos.ru

KEYWORDS:

Resonant orbit, gravity assist maneuver, Venus, space mission, asteroids exploration

The exploration of asteroids has been a primary focus for many years, as there is still much that is unknown about these small bodies in our solar system. While there are more than 1 million asteroids listed in databases such as JPL and MPC, only a small number have been characterized by the SMASSII spectral classification system, and even fewer by the Tholen system. Consequently, the exploration of these asteroids remains a significant challenge for space exploration. This study aims to develop trajectories that include flybys of asteroids as an extension to the main scientific mission.

This particular study focuses on asteroids encountered in near-Venus space, which are of significant interest due to their proximity to both Venus and the potential for capturing spacecraft for studying both. The transfer of a spacecraft into a resonant orbit around Venus facilitates a short transfer arc to asteroids while maintaining proximity to Venus. This allows the spacecraft to encounter asteroids every 224.7 days, enabling the selection of new asteroid targets at each gravitational assist from Venus.

The primary objective of this research is to establish the trajectories for asteroid flybys and spacecraft transfers into mean orbital resonance around Venus by utilizing Venus gravity assists. Three potential scenarios have been explored: (1) an Earth-to-Venus transfer involving a periodic or non-periodic orbit around Venus (PA/NPA), (2) a series of Venus-PA-Venus transfers, and (3) a sequence that includes Venus -NPA1-Venus-NPA2-Venus. Special consideration is given to flybys of potentially hazardous asteroids, which are included in the PA term in schemes 2 and 3. Additionally, the study investigates the possibility of returning to Earth following the final gravity assist of Venus.

For this study, ephemeris data for about 2,000 asteroids were obtained from the JPL database based on their estimated diameters and perihelion distances. This included 69 asteroids with mean motion resonances around Venus and 169 potentially hazardous objects with approximate minimal orbit intersection distance less than 1 lunar diameter. Trajectories were then calculated based on the scenarios described above and results for the years 2029–2031 were obtained. The results from applying the search for trajectories both using patched conics and high-fidelity models demonstrated the feasibility of the proposed approach.

Collecting data on Venus through future missions using the planet's gravitational assistance opens up new possibilities for science and represents a significant step towards establishing partnerships between scientific communities. The practical advantage of implementing asteroid fly-bys due to Venus' gravity assists is, among other things, the ability to pass small bodies whose orbits are highly inclined to the ecliptic plane. The scientific outcomes of the proposed mission plan will combine atmospheric and geological studies of Venus with spectroscopic and morphological analyses of asteroids, filling in gaps in both fields. Thus, this work creates a model for multi-purpose deep-space missions, demonstrating that trajectories oriented towards resonant Venus open unprecedented opportunities for exploring asteroids and at the same time contributing to the advancement of knowledge about Venus.

ACKNOWLEDGMENTS:

Vladislav Zubko is receiving funding from the Russian Scientific Foundation, project No. 25-79-00042.

SESSION 3. VENUS (VN-PS)
POSTER SESSION

THERMAL STRUCTURE OF THE UPPER ATMOSPHERE OF VENUS FROM OCCULTATION EXPERIMENTS

E. S. Stepanova, D. A. Belyaev, A. A. Fedorova, O. I. Korablev
Space Research Institute RAS, Moscow, Russia, lisaoneechan@gmail.com

KEYWORDS:

Venus atmosphere, SOIR, solar occultation, temperature and density profiles, retrieval algorithm

INTRODUCTION:

The mesosphere of Venus, extending from approximately 65 to 120 km above the planet's surface, transitions into the lower thermosphere at the mesopause, which is located between 95–120 km altitude. These atmospheric regions host numerous complex phenomena, including the formation of detached haze layers, observed at 80–90 km with diurnal altitude variation [1, 2], and water escape processes, evidenced by deuterium-to-hydrogen ratio more than 100 times higher than Earth's [3, 4]. Prior to the launch of Venus Express in 2006, these layers of Venus' atmosphere were relatively poorly studied. Nevertheless, some missions (for example, Pioneer Venus and the Soviet Venera missions), as well as ground-based observations, were aimed at investigating this layer of the atmosphere. Detailed review articles have been published which include an extensive description of the results obtained during that period [5, 6].

Previous missions to Venus carried instruments that enabled the study of the atmospheric thermal structure using multiple methodologies, each with their own advantages and disadvantages. For example, radio occultation technique was used to retrieve temperature profiles between 35–90 km above surface starting with Mariner 5. Then, the technique was refined with subsequent missions (Mariner 10, Pioneer Venus, Magellan). The VeRa experiment was an integral part of the Venus Express mission, aimed to investigate the atmosphere of Venus through radio occultations [7]. The geographic coverage of the temperature profiles derived from VeRa data reflects the trajectory of Venus Express spacecraft. Because of its elliptical orbit, measurements were lacking in the northern mid-latitude regions. The advantage of this experiment was the high vertical resolution of the temperature profiles, about 500 m. This property made it possible to study small variations in temperature depending on local time and latitude and reveal gravitational wave activity above the tropopause [8, 9].

Solar and stellar occultation techniques were both widely represented in Venus Express mission, with SOIR (Solar Occultation at Infrared) [10] and SPICAV (Spectroscopy for the Investigation of the Characteristics of the Atmosphere of Venus) [11] instruments. SPICAV was designed with two channels, one operating in the ultraviolet range (110–320 nm) and the other in the near-infrared range (1–1.7 μm). While it could operate several methods to acquire data, such as nadir pointing, solar occultation and stellar occultation, the most effective way to get temperature profiles was to utilize the UV channel measurements in stellar occultation mode. SPICAV-UV performed more than 500 stellar occultation measurements covering all latitudes on the nightside. Not only temperature profiles were retrieved, but also vertical profiles of CO_2 density and aerosols in the upper atmosphere (90–140 km). Main findings include a warm layer at 90–100 km and a constant temperature decline above 120 km, reaching minimums of 100–130 K [12].

The SOIR (Solar Occultation in the InfraRed) instrument on Venus Express conducted solar occultation measurements on altitudes of 65–170 km. Operating in the 2.29–4.43 μm spectral range, this high-resolution spectrometer detected narrow absorption lines from various atmospheric constituents. During its eight-year mission (2006–2014), SOIR accumulated a large spectral dataset, making it possible to perform detailed studies of temperature, density, and trace gas distributions.

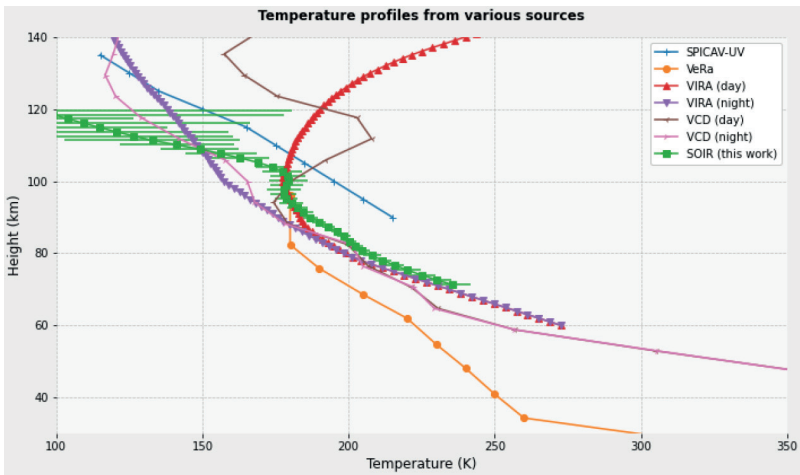


Figure 1. Mean temperature profiles retrieved from several Venus Express instruments' occultations data at mid-northern latitudes, VIRa and VCD temperature profiles included for reference

Overall, the Venus Express mission greatly improved the understanding of Venus's atmospheric thermal structure. Instruments using occultation methods, like VeRa, SPICAV and SOIR delivered a great amount of temperature profiles, unveiling new features of the atmosphere. These discoveries greatly enhanced atmospheric models, and LMD Venus GCM was also updated [13]. The model was extended up to 150 km and shifted its main focus to the thermal structure and the processes in the upper atmosphere, from 90 to 50 km. The Venus Climate Database (VCD) is built on the on base of LMD Venus GCM, and its outputs are mostly analogous to the Mars Climate Database (MCD). The VCD extends and updates legacy atmospheric databases like the Venus International Reference Atmosphere (VIRA) [14] by integrating new observational data from recent missions and incorporating advancements in climate modeling techniques. Core components of the VCD include temperature, density, pressure, wind speeds, and moreover, information on the vertical distribution of major atmospheric species. It also provides a high-resolution mode, and intra-hour and day-to-day variability of meteorological variables based on extensive GCM simulations [15]. The Venus Climate Database serves as a valuable resource, integrating all available observational data through climate modeling. It is an essential reference for validating future observational data and an important planning tool for designing upcoming missions to Venus.

Regarding the aforementioned solar occultation measurements by SOIR, it should be noted that prior thermal structure investigations using this instrument's data established some important foundations. The study derived vertical number density and temperature profiles from SOIR spectra [16], which subsequently enabled the retrieval of other species, including water vapor and HDO vertical distributions [17]. However, there were constraints in the retrieval algorithm that limit data coverage at lower altitudes and introduce uncertainties in atmospheric density profiles.

This study introduces a new retrieval algorithm developed at IKI RAS, distinct from previous approaches, which adapts the methodology applied for analogous solar occultation experiment ACS/ExoMars in Martian atmosphere [18, 19]. Our algorithm's key advantages include enhanced sensitivity to absorption lines at lower altitudes and reduced uncertainties in the mesopause region.

To retrieve the altitude profiles of density and temperature, measurements in the spectral ranges where CO_2 absorption bands are observed in the altitude range available for SOIR observations, from 70 to 170 km, are best suited. In this work, mainly the range of $3308\text{-}3381\text{ cm}^{-1}$ (corresponding to the $21002\text{-}00001$ transition) was used.

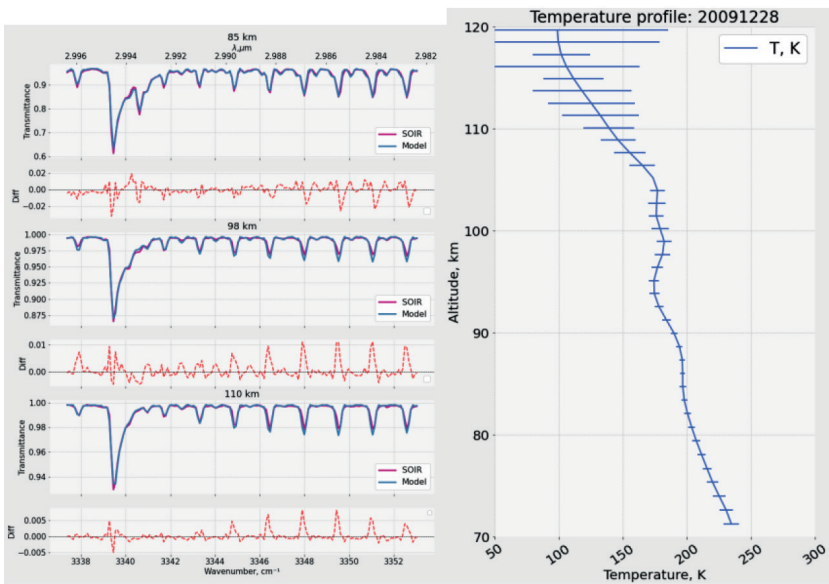


Figure 2. Spectra fitting example and the corresponding temperature vertical profile retrieved

By applying this algorithm to the full SOIR dataset, we could obtain the most precise characterization to date of Venus' atmospheric structure at 65–170 km. The results would advance our understanding of atmospheric dynamics and photochemistry and enable future studies of other molecular species present in the corresponding region (H_2O , HDO , HCl , SO_2) through derived number density and temperature profiles.

ACKNOWLEDGMENTS:

This work is funded by grant No 23-12-00207 of the Russian Science Foundation (<https://rscf.ru/project/23-12-00207/>).

REFERENCES:

- [1] Luginin M., Fedorova A., Belyaev D. et al. Aerosol properties in the upper haze of Venus from SPICAV IR data // *Icarus*. 2016. V. 277. P. 154–170. <https://doi.org/10.1016/j.icarus.2016.05.008>.
- [2] Luginin M., Fedorova A., Belyaev D. et al. Scale heights and detached haze layers in the mesosphere of Venus from SPICAV IR data // *Icarus*. 2018. V. 311. P. 87–104. <https://doi.org/10.1016/j.icarus.2018.03.018>.
- [3] Fedorova A., Korablev O., Vandaele A.-C. et al. HDO and H_2O vertical distributions and isotopic ratio in the Venus mesosphere by Solar Occultation at Infrared spectrometer on board Venus Express // *J. Geophysical Research*. 2008. V. 113. Iss. E5. <https://doi.org/10.1029/2008JE003146>.
- [4] Mahieux A., Viscardy S., Yelle R.V. et al. Unexpected increase of the deuterium to hydrogen ratio in the Venus mesosphere // *Proc. National Academy of Sciences*. 2024. V. 121(4). Article e2401638121. <https://doi.org/10.1073/pnas.2401638121>.
- [5] Taylor F.W. Venus before Venus Express // *Planetary and Space Science*. 2006. V. 54. Iss. 13–14. P. 1249–1262. DOI: 10.1016/j.pss.2006.04.031.
- [6] de Bergh C., Moroz V.I., Taylor F.W. et al. The composition of the atmosphere of Venus below 100km altitude: An overview // *Planetary and Space Science*. 2006. V. 54. No 13–14. P. 1389–1397. <https://doi.org/10.1016/j.pss.2006.04.020>.
- [7] Haesler B., Pätzold M., Tyler G.L. et al. Radio science investigations by VeRa onboard the Venus Express spacecraft // *Planetary and Space Science*. 2006. V. 54. Iss. 13–14. P. 1315–1335. DOI: 10.1016/j.pss.2006.04.032.
- [8] Tellmann S., Pätzold M., Häusler B. et al. Structure of the Venus neutral atmosphere as observed by the Radio Science experiment VeRa on Venus Express // *J. Geophysical Research: Planets*. 2009. V. 114. Iss. 9. DOI: 10.1029/2008JE003204.
- [9] Tellmann S., Häusler B., Hinson D.P. et al. Small-scale temperature fluctuations seen by the VeRa Radio Science Experiment on Venus Express // *Icarus*. 2012. V. 221. Iss. 2. P. 471–480. <https://doi.org/10.1016/j.icarus.2012.08.023>.
- [10] Nevejans D., Neefs E., Van Ransbeeck E. et al. Compact high-resolution spaceborne echelle grating spectrometer with acousto-optical tunable filter based

- order sorting for the infrared domain from 2.2 to 4.3 μm // *Applied Optics*. 2006. V. 45. P. 5191–5206. DOI: 10.1364/AO.45.005191.
- [11] *Bertaux J.-L., Nevejans D., Korablev O. et al.* SPICAV on Venus Express: three spectrometers to study the global structure and composition of the Venus atmosphere // *Planetary and Space Science*. 2007. V. 55. Iss. 12. P. 1673–1700. DOI: 10.1016/j.pss.2007.01.016.
- [12] *Piccialli A., Montmessin F., Belyaev D. et al.* Thermal structure of Venus nightside upper atmosphere measured by stellar occultations with SPICAV/Venus Express // *Planetary and Space Science*. 2015. V. 113–114. P. 321–335. DOI: 10.1016/j.pss.2014.12.009.
- [13] *Gilli G., Lebonnois S., González-Galindo F. et al.* Thermal structure of the upper atmosphere of Venus simulated by a ground-to-thermosphere GCM // *Icarus*. 2016. V. 281. P. 55–72. DOI: 10.1016/j.icarus.2016.09.016.
- [14] *Zasova L.* Reference atmospheres: VIRI II — Venus International Reference Atmosphere update // 39th COSPAR Scientific Assembly. 2012. Article 2248.
- [15] *Lebonnois S., Millour E., Martinez A. et al.* The Venus Climate Database // European Planetary Science Congress. 2021. Article EPSC2021-234. DOI: 10.5194/epsc2021-234.
- [16] *Mahieux A., Vandaele A. C., Bougher S. W. et al.* Update of the Venus density and temperature profiles at high altitude measured by SOIR on board Venus Express // *Planetary and Space Science*. 2015. V. 113–114. P. 309–320. DOI: 10.1016/j.pss.2015.01.017.
- [17] *Mahieux A., Robert S., Piccialli A. et al.* The SOIR/Venus Express species concentration and temperature database: CO₂, CO, H₂O, HDO, H³⁵Cl, H³⁷Cl, HF individual and mean profiles // *Icarus*. 2023. V. 405. <https://doi.org/10.1016/j.icarus.2023.115713>.
- [18] *Fedorova A., Montmessin F., Korablev O. et al.* Stormy water on Mars: The distribution and saturation of atmospheric water during the dusty season // *Science*. 2020. V. 367(6475). Article eaay9522. DOI: 10.1126/science.aay9522.
- [19] *Belyaev D., Fedorova A. A., Trokhimovskiy A. et al.* Revealing a High Water Abundance in the Upper Mesosphere of Mars with ACS Onboard TGO // *Geophysical Research Letters*. 2021. V. 48. Iss. 10. Article e2021GL093411. <https://doi.org/10.1029/2021GL093411>.

VOLCANIC FEATURES OF CONCENTRATION REGIONS OF LARGE VOLCANOES AND CORONAE, VENUS

E. N. Guseva, M. A. Ivanov

Vernadsky Institute of Geochemistry and Analytical Chemistry RAS, Moscow, Russia, guseva@geokhi.ru, ivanov.m@geokhi.ru

KEYWORDS:

Venus, topography, morphology, coronae, volcanoes, groove belts, rifts, lobate plains and volcanic activity

INTRODUCTION:

Coronae and volcanoes are large landforms (hundreds of kilometers in diameter) on the surface of Venus [1–3]. Three main topographic classes characterize coronae: (1) class D, dome uplifts; up to 530 km in diameter, in the progressive stage of evolution of the parent diapir; (2) class W, complex depressions with a central peak; up to 660 km in diameter, the dome uplift loses the thermal support of the diapir and subsides; (3) class U, simple depressions; up to 530 km in diameter, corresponding to the regressive stage of evolution of the diapir [4]. Three size groups characterize large volcanoes: (1) the largest flattened, up to 740 km in diameter; (2) medium conical, up to 425 km in diameter; and (3) small conical, up to 240 km in diameter [5].

Volcanic activity in most coronae died out mainly during the pre-Atlian period [6, 7]. Only a 17 % of the total population of corona exhibit younger volcanic activity in the form of lobate plain flows [8]. Most of the studied volcanoes formed during the late Atlian period [1, 5, 7, 9]. Their slopes are covered with numerous lava flows, which, when merged, form vast complexes of young lobate plains [1, 10–12].

Coronae are often found in spatial-stratigraphic association with Guineverian groove belts and, less commonly, with rift zones of younger Atlian age [13]. Such typical spatial associations of coronae indicate their probable genetic relationship with linear extension zones [14]. Volcanoes are more widespread on the surface of Venus and are less associated with regional zones of extension, groove belts and rift zones [5, 15].

Previously, we analyzed the spatial and genetic relationships of the coronae — sources of lobate plains and large volcanoes of Venus and found that they are genetically unrelated [15]. We identified regions of concentration of these features in which they are spatially separated, for example, in the Metis, Ulfrun, Rusalka, Atla, Imdr and Alpha regions and co-occur, for example, in Tethus, Hinemoa-Beta, Laufey, Eistla, Bell, Ovda-Tellus, Parga-N and -S (Figure 1). In some regions, such as Lakshmi, Aino and Lada, the only sources of lobate plains are coronae, while in the Kawelu region, only volcanoes are present.

In all the regions identified, the coronae are associated with regional extension zones: groove belts and/or rift zones. Volcanoes are associated with these zones to a lesser extent [15].

RESULTS:

We analyzed the regions of concentration of these structures and identified the following areas:

(1) areas where mainly coronae with annulus made by ancient groove belts dominate and volcanoes are absent: Lakshmi, Aino and Lada. Coronae of the regressive stage of evolution are widespread there; these are mainly of the U class. In the Lada area, coronae of the subsidence stage dominate; these are mainly of the W class (blue outlines in Figure 1). An exception is the Atla area, where in addition to coronae of the regressive stage with ancient annulus of groove belts, large flattened and medium-sized conical volcanoes are found (white outline in Figure 1);

(2) areas where small cone volcanoes and coronae with annulus of ancient groove belts dominate: Tethus, Eistla, Alpha, Laufey and Imdr (yellow outline in Figure 1). In the Tethus, Eistla, Alpha and Imdr areas, coronae of the subsidence stage (class W) are common. In the Laufey area, coronae of the progressive stage (class D) are more common;

(3) areas where rift-annulus coronae dominate, mainly of class D: Parga-N and -S, Ulfrun (outlined in orange, Figure 1). In the Rusalka area, in addition to the progressive stage coronae, subsidence stage coronae (class W), are common (this area is shown in black, Figure 1). In all these areas, conical volcanoes of medium and small diameter are common;

(4) areas where the large flattened volcanoes dominate: Metis, Hinemoa-Beta, Bell and Ovda-Tellus (outlined in red, Figure 1). In these areas, coronae of all three stages of evolution are found in approximately equal proportions, mainly with an annulus of ancient groove belts. In the Kawelu area, large flattened volcanoes are also common, but coronae are not found (green outline, Figure 1).

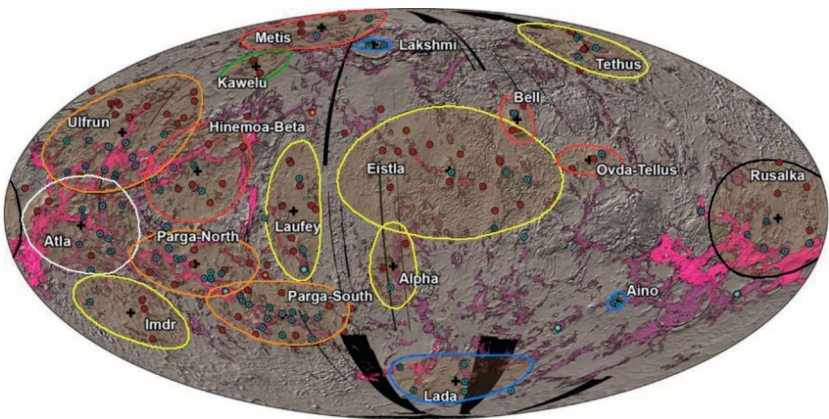


Figure 1. Regions of Venus where large volcanoes and coronae-sources of lobate plains are predominantly concentrated. Coronae are blue dots, volcanoes are red dots, groove belts are violet zones and rifts are pink. The base is the hillshade topography. The map is in the Mollweide equal-area projection, central meridian 180°. Geological boundaries by map of Venus [7]

For each region of the features concentration, we estimated the ratios of the average volcano diameters to the corona diameters, except for areas where coronae of the regressive stage of evolution dominate and volcanoes are absent (Lakshmi, Aino, Lada). The exception is the Atla region, where mature U-class coronae with annulus of ancient groove belts and large flattened and medium-sized conical volcanoes are common. The ratios of the average diameters of these volcanoes to the coronae are about 2.2.

For areas where small cone volcanoes and coronae are predominantly distributed, mainly of the subsidence stage (mainly class W) with an annulus of ancient groove belts: Tethus, Laufey, Eistla, Alpha and Imdr, the ratio of the average diameters of volcanoes and coronae is about 0.8, the average diameter of volcanoes (187 km) is smaller than that of coronae (230 km).

For areas where coronae of the progressive stage (class D) with rift annulus dominate: Parga-N and -S, Ulfrun; the ratio of average diameters of volcanoes and coronae is about 1.3, the average diameter of volcanoes (275 km) is larger than the average diameter of coronae (217 km).

For areas where the large flattened volcanoes dominate and coronae of all three stages of evolution are in approximately equal proportions: Metis, Hinemoa-Beta, Bell and Ovd-Tellus; the ratio of the average diameters of volcanoes and coronae is about 1.3, the average diameter of volcanoes (420 km) is significantly larger than that of coronae (315 km).

CONCLUSION:

The areas of concentration of coronae and volcanoes can be characterized as volcanically mature and immature. (1) Mature areas: dominating by coronae of the regressive stage of evolution with an annulus of ancient groove belts and either the absence of volcanoes (Lakshmi, Aino and Lada) or with abundant small conical volcanoes (Tethus, Laufey, Eistla, Alpha and Imdr). The average diameter of volcanoes in these areas is smaller than the average diameter of coronae, which is probably explained by the relatively small supply of volcanic material from the source area of volcanoes. (2) Immature areas: coronae of the progressive stage of evolution with rift-annulus dominate and abundant either medium and small conical volcanoes (Parga-N and -S and Ulfrun) or large flattened volcanoes (Metis, Hinemoa-Beta, Bell, Ovda-Tellus). The average diameter of the volcanoes in these areas is larger than the average diameter of the coronae. It's probably areas where deep mantle plumes (sources of large volcanoes) dominated, and mantle diapirs (sources of coronae) were of subordinate importance.

ACKNOWLEDGMENTS:

The study was carried out within the state assignment of the Vernadsky Institute of Geochemistry and Analytical Chemistry RAS.

REFERENCES:

- [1] *Head J., Crumpler L., Aubele J. et al.* Venus volcanism: Classification of volcanic features and structures, associations, and global distribution from Magellan data // *Geophysical Research: Planets*. 1992. V. 97. Iss. E8. P. 13153–13197. <https://doi.org/10.1029/92JE01273>.
- [2] *Stofan E., Sharpton V., Schubert G. et al.* Global distribution and characteristics of coronae and related features on Venus: Implications for origin and relation to mantle processes // *Geophysical Research: Planets*. 1992. V. 97. Iss. E8. P. 13347–13378. <https://doi.org/10.1029/92JE01314>.
- [3] *Crumpler L., Aubele J.* Volcanism on Venus // *Encyclopedia of Volcanoes* / eds. Houghton B., Rymer H., Stix J. et al. San Diego: Acad. Press, 2000. P. 727–770.
- [4] *Guseva E., Ivanov M.* Coronae of Venus: geological, topographic and morphometric characteristics // *Solar System Research*. 2022. V. 56(2). P. 76–83. DOI: 10.1134/S0038094622020046.
- [5] *Ivanov M., Head J.* Large volcanoes on Venus: Morphology, morphometry, and stratigraphy // *Icarus*. 2025. V. 429. Article 116404. <https://doi.org/10.1016/j.icarus.2024.116404>.
- [6] *Basilevsky A., Head J.* Geologic units on Venus: Evidence for their global correlation // *Planetary and Space Science*. 2000. V. 48. Iss. 1. P. 75–111. [https://doi.org/10.1016/S0032-0633\(99\)00083-5](https://doi.org/10.1016/S0032-0633(99)00083-5).
- [7] *Ivanov M., Head J.* Global geological map of Venus // *Planetary and Space Science*. 2011. V. 59. Iss. 13. P. 1559–1600. <https://doi.org/10.1016/j.pss.2011.07.008>.
- [8] *Guseva E., Ivanov M.* Spatial and genetic relationships of coronae, lobate plains and rift zones of Venus // *Solar System Research*. 2023. V. 57(2). P. 112–121. DOI: 10.1134/S003809462302003X.
- [9] *Crumpler L., Aubele J., Senske D. et al.* Volcanoes and centers of volcanism on Venus // *Venus II: Geology, geophysics, atmosphere, and solar wind environment* / eds. Bougher S., Hunten D., Phillips R. The University of Arizona Press, 1997. P. 697–756.
- [10] *Basilevsky A., Head J.* Beta Regio, Venus: Evidence for uplift, rifting, and volcanism due to a mantle plume // *Icarus*. 2007. V. 192. Iss. 1. P. 167–186. <https://doi.org/10.1016/j.icarus.2007.07.007>.
- [11] *Ivanov M., Head J.* The history of volcanism on Venus // *Planetary and Space Science*. 2013. V. 84. P. 66–92. <https://doi.org/10.1016/j.pss.2013.04.018>
- [12] *Hahn R., Byrne P.* Morphological and Spatial Analysis of Volcanoes on Venus // *Geophysical Research: Planets*. 2023. V. 128. Iss. 4. Article e2023JE007753. <https://doi.org/10.1029/2023JE007753>.
- [13] *Ivanov M., Head J.* The history of tectonism on Venus: A stratigraphic analysis // *Planetary and Space Science*. 2015. V. 113–114. P. 10–32. <https://doi.org/10.1016/j.pss.2015.03.016>.
- [14] *Solomon S., Smrekar S., Bindshadler D.* Venus tectonics: An overview of Magellan observations // *Geophysical Research: Planets*. 1992. V. 97. Iss. E8. P. 13199–13256. <https://doi.org/10.1029/92JE01418>.
- [15] *Guseva E., Ivanov M.* Spatial and genetic relationships of volcanic coronae and large volcanoes on Venus // *Solar System Research*. 2025 (in print).

1:500,000 SCALE MAPPING AND ANALYSIS OF RADIATING, CIRCUMFERENTIAL AND LINEAR DYKE SWARM PATTERNS OF BETA REGIO, VENUS

A. S. Shimolina¹, R. E. Ernst², H.El. Bilali²

¹ Tomsk State University, Faculty of Geology and Geography, Tomsk, Russia
arina051299@gmail.com

² Department of Earth Sciences, Carleton University, Ottawa, Canada

KEYWORDS:

Beta Regio, Theia Mons, Rhea Mons, Venus, giant dyke swarms, planetary geology

INTRODUCTION:

Beta Regio is a part of the BAT (Beta-Atla-Themis) region, an area of most recent tectonic and magmatic activity on Venus. BAT represents a currently active mantle plume in that it is topographically elevated, has an associated geoid high, and is also the locus of a triple junction rifting system defined by Hecate Chasmata to the west and Devana Chasma to both the north and south. The main volcanic center of Beta Regio is Theia Mons, a large shield volcano, 500 km in diameter.

PREVIOUS WORK AND GOALS:

Mapping of dyke systems that included part of present study area was previously done by Ernst et al. (2003) [1]. This work provisionally suggested that a radiating graben-fissure-fracture system (interpreted as a dyke swarm) of Theia Mons changed from radiating to linear 1000 km away from the center, and located several points of convergence of radiating swarms near 40° N parallel. My more recent 1:500,000 scale mapping focused on Theia Mons focused on flows, grabens and rift systems associated with Theia Mons [2]. It helped to identify two distinct magmatic centers 200 km apart, TM1 and TM2 each defined by fanning lava flows, grabens (representing dykes) and rift systems. The shift between the centers is postulated to indicate relative movement between the lithosphere and the underlying plume head.

Our detailed mapping of graben-fissure-fracture systems (interpreted in dyke swarms) in a broader area of Beta Regio that includes Theia Mons is done with following goals: 1) searching for cryptic magmatic centers in the area, 2) characterizing age relationships between swarms, 3) finding correlations between patterns in separated tessera areas. To achieve this, we created a map of dyke swarms in the area of 95 to 65° W, 40 to 10° N at the scale of 1:500,000.

DATA AND SOFTWARE USED:

We used data of synthetic aperture radar (Cycle 1 left look at 75 m per pixel) and altimetry from the Magellan mission (1989–1994), obtained from USGS Astropedia. Mapping was done using ArcGIS Desktop 10.8.1 software. In addition, JMARS was used for tracking swarms and possible related centers outside the study area.

MAPPING OF GRABENS:

We mapped about 90 000 separate graben-fissure-fracture lineaments (Figure 1). They are generalized into main sets — linear, circumferential, and radiating systems interpreted as dyke swarms (Figure 2), including a number swarms not previously recognized.

The new mapping allowed to expand Theia Mons' two radiating swarms to a radius of about 1500 km each. Inside the study area, no evidence was found for them having a shift to a more linear, northward-facing swarm, as suggested by R. E. Ernst [1]. However, it was noted that the swarm of central caldera may be curved by influence of coeval stress due to Kono Mons activity to the south-west.

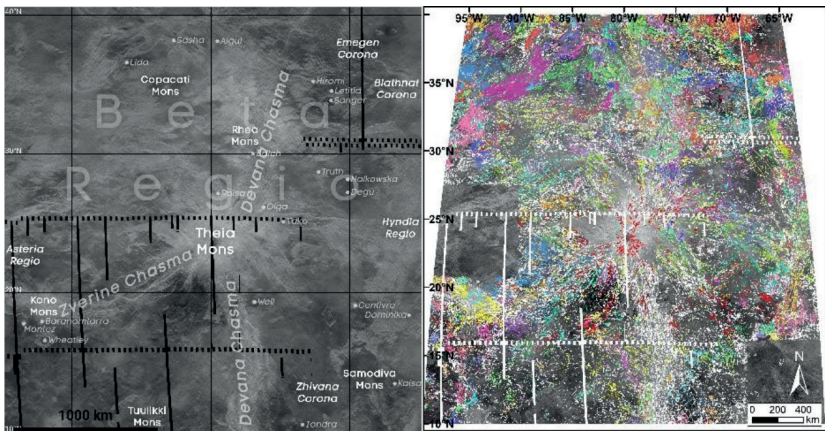


Figure 1. Extent of study area of Beta Regio with nomenclature (left) and the same area with about 90 000 mapped graben units (right)

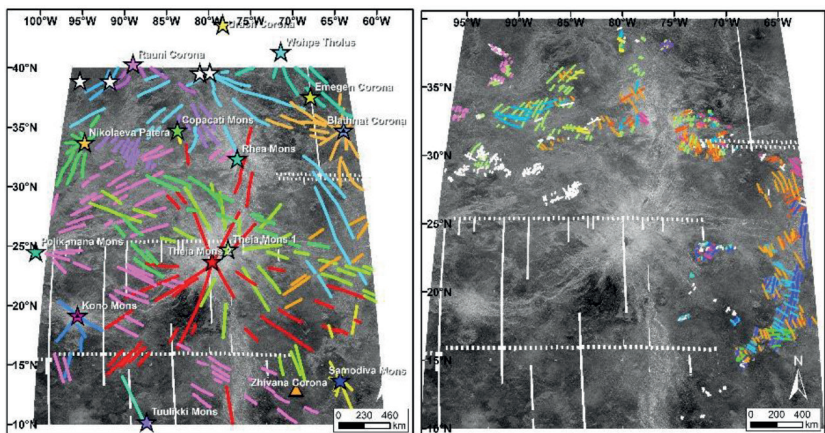


Figure 2. Generalized radiating dyke swarms and associated centers (left) and generalized graben patterns inside tessera terrain areas (right)

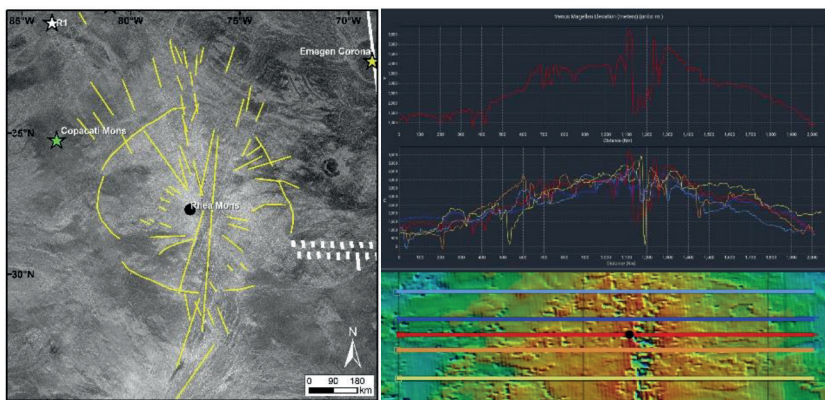


Figure 3. Radiating graben patterns possibly associated with Rhea Mons and circular boundary of elevated tessera (left) and topographic profiles across Rhea Mons and northern part of Devana Chasma (right)

Several new small circumferential features were found, mostly on far north and far south areas of Beta Regio. However, no circumferential swarm has been identified for either of the Theia Mons' centers.

Across southern part of Beta Regio, a giant NW linear trend was noted. However, searching outside the area with JMARS did not reveal any magmatic center that could be the source of this swarm. For now, it is suggested that this may be a coincidence of overlapping parts of different radiating swarms.

Mapping of extensional lineament patterns within separate tessera terrains of the study area reveals matching trends between the tessera terrains, and suggests no rotation of separate blocks of crust.

RHEA MONS ANALYSIS:

Rhea Mons is a topographic high located 960 km to the north from Theia Mons' central caldera. Its lack of visible center or associated flows, high position in very disturbed area and negative Bouguer anomaly allowed the assumption that Rhea Mons is not a magmatic center, but a part of tessera terrain on thick crust [3, 4].

However, the sub-circular extent of this tessera terrain, and our newest mapping suggests that there may be both a radiating (radius 1000 km) and circumferential (radius 350 km) pattern of extensional lineaments centered Rhea Mons (Figure 3). This suggests that Rhea Mons' area is elevated not just because of high crustal thickness, but by uplift due to a plume that did not develop to a point of fueling the volcanic activity in this area.

REFERENCES:

- [1] Ernst R. E., Desnoyers D. W., Head J. W., Grosfils E. B. Graben–fissure systems in Guinevere Planitia and Beta Regio (264–312° E, 24–60° N), Venus, and implications for regional stratigraphy and mantle plumes // *Icarus*. 2003. V. 164. Iss. 2. P. 282–316. [https://doi.org/10.1016/S0019-1035\(03\)00126-X](https://doi.org/10.1016/S0019-1035(03)00126-X).
- [2] Shimolina A. S., Ernst R. E., El Bilali H. et al. Geological history of Theia Mons, Beta Regio plume, Venus: Recognition of two main magmatic centers for flows, radiating dyke swarms and triple junction rifting // *Planetary and Space Science*. 2025. V. 257. Article 106050. <https://doi.org/10.1016/j.pss.2025.106050>.
- [3] Stofan E. R., Head J. W., Campbell D. B. et al. Geology of a rift zone on Venus: Beta Regio and Devana Chasma // *Geological Society of America Bulletin*. 1989. V. 101(1). P. 143–156. [https://doi.org/10.1130/0016-7606\(1989\)101<0143:GOARZO>2.3.CO;2](https://doi.org/10.1130/0016-7606(1989)101<0143:GOARZO>2.3.CO;2).
- [4] Sukhanov A. L., Pronin A. A., Burba G. A. et al. Geomorphic/geologic map of part of the northern hemisphere of Venus // R. M. Batson et al. *Atlas of Venus 1:15,000,000 topographic series*. 1989. DOI: 10.3133/i2041.

NON-HYDROSTATIC STRESSES BENEATH ATLA REGIO AND BETA REGIO ON VENUS

T.V. Gudkova¹, A.V. Batov^{1,2}

¹ *Schmidt Institute of Physics of the Earth RAS, Moscow, Russia*
gudkova@ifz.ru

² *Trapeznikov Institute of Control Sciences RAS, Moscow, Russia*
batov@ipu.ru

KEYWORDS:

Venus, gravity, topography, compressional and extensional stresses, shear stresses

INTRODUCTION:

Venus is assumed to be a seismically active planet. For upcoming seismic experiments on Venus [1] it is of importance to know the areas of large stresses. The surface of Venus has a wide range of volcanic and tectonic features, which could be sources of seismic activity. Part of volcanoes on Venus show spatial concentration in the Beta-Atla region [2].

DATA:

Gravity and topography data are the datasets with which we can study the stress state of Venus. Topography data up to the 360th degree and order (SHTJV360u model) [3]. The resolution of gravity field is about from 400 to 1000 km, the spherical harmonic model (SHGJ180u model) is presented to degree and order 180 [4]. We use the coefficients up to the 70th degree and order, because of bad correlation of the gravity and topography data for higher harmonics. The topography and gravitational data we determine with respect to the reference surface (effectively equilibrium Venus) [5].

STRESS MODELING:

The used numerical modeling method was described in detail in [6]. The numerical solution of the system of elastic equilibrium equations for an elastic self-gravitational spherical planet was carried out on a grid with a resolution of $1 \times 1^\circ$ in latitude and longitude. Data on the topography and gravitational field were used as boundary conditions.

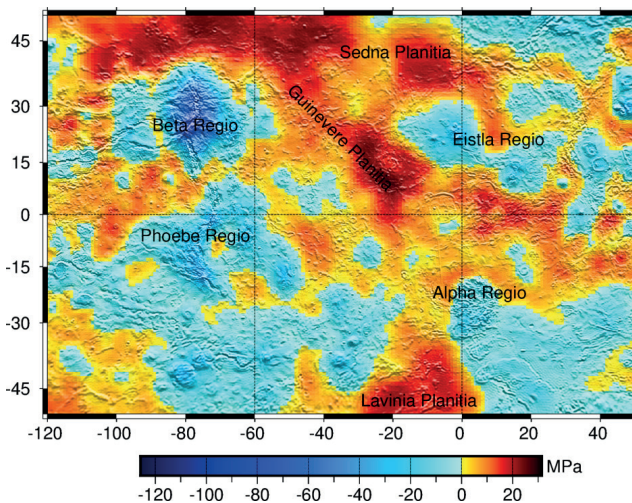


Figure 1. Extensional (positive values) and compressional (negative values) stresses (in MPa) beneath Atla Regio and Beta Regio on Venus in the crust at depths of 25 km for a model with a lithosphere of 300 km for model V_16 from [7]

RESULTS:

The Figures 1 and 2 show stress maps beneath Atla Regio and Beta Regio on Venus. Beneath Beta Regio, strong compressional stresses are observed. To the north and east, these transition into extensional stresses reaching up

to approximately 20 MPa. The region of maximum extension within the selected area is located in Guinevere Planitia. This area also exhibits the highest shear stresses in the analyzed region, exceeding 25 MPa.

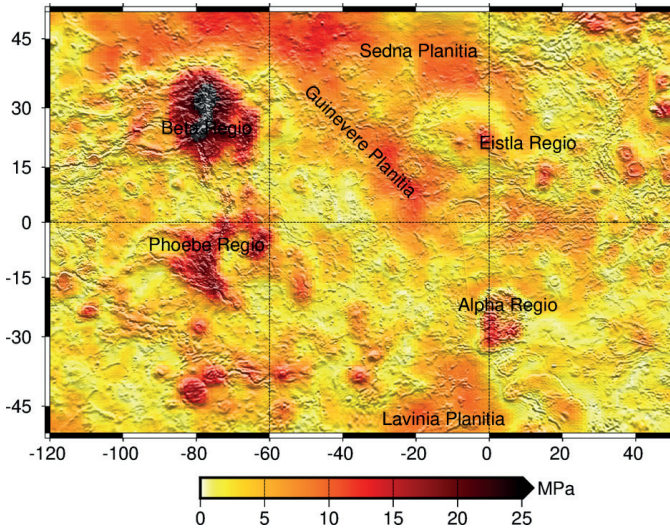


Figure 2. Shear stresses (in MPa) beneath Atla Regio and Beta Regio on Venus in the crust at depths of 25 km for a model with a lithosphere of 300 km for model V_16 from [7]

Beneath the central part of Atla Regio, compressional stresses are dominant and extend southeastward. However, extensional stresses are observed in other directions, with particularly strong extension in the Lavinia Planitia area. Shear stresses in the Atla region are also high, but lower than those beneath Beta Regio.

CONCLUSION:

We have presented the distributions of non-hydrostatic stresses in the interiors of Venus based on a joint interpretation of topography data and the non-equilibrium part of the gravitational field. The results of modeling non-hydrostatic stresses in the interiors of Venus can be of interest for choosing the location of the seismometer site in connection with the future seismic experiments.

ACKNOWLEDGMENTS:

This work is financially supported by Budget funding of Schmidt Institute of the Earth RAS.

REFERENCES:

- [1] *Kremic T., Ghail R., Gilmore M. et al.* Long-duration Venus lander for seismic and atmospheric science // *Planetary and Space Science*. 2020. V. 190. Article 104961. DOI: 10.1016/j.pss.2020.104961.
- [2] *Hahn R. M., Byrne P. K.* Kernel density analysis of volcanoes on Venus at varying spatial scales // *53rd Lunar and Planetary Science Conf.* 2022. Article 2437.
- [3] *Rappaport N. J., Konopliv A. S., Kucinskas A. B.* An improved 360-degree and order model of Venus topography // *Icarus*. 1999. V. 139. Iss. 1. P. 19–31. <https://doi.org/10.1006/icar.1999.6081>.
- [4] *Konopliv A. S., Banerdt W. B., Sjogren W. L.* Venus gravity: 180th degree and order model // *Icarus*. 1999. V. 139. Iss. 1. P. 3–18. <https://doi.org/10.1006/icar.1999.6086>.
- [5] *Zharkov V. N., Gudkova T. V.* On parameters of the Earth-like model of Venus // *Solar System Research*. 2019. V. 53(1). No. 1. P. 1–4. <https://doi.org/10.1134/S0038094618060084>.
- [6] *Batov A. V., Gudkova T. V., Zharkov V. N.* Nonhydrostatic stress state in the Martian interior for different rheological models // *Izvestiya, Physics of the Solid Earth*. 2019. V. 55(4). P. 688–700. DOI: 10.1134/S1069351319040025.
- [7] *Gudkova T. V., Zharkov V. N.* Models of the internal structure of the Earth-like Venus // *Solar System Research*. 2020. V. 54(1). P. 20–27. <https://doi.org/10.1134/S0038094620010049>.

THE EFFECT OF THE CONTOUR SHAPE OF SPECTRAL LINES ON THE EMISSION IN THE 4.3 MM BAND OF CO₂ MOLECULES OUTGOING FROM THE PLANETARY ATMOSPHERE IN THE PRESENCE OF MACROSCOPIC WIND VELOCITY GRADIENT

V. P. Ogibalov^{1,2}, L. V. Belyakova¹, I. V. Voytko¹, E. M. Pastushok¹, E. I. Rasputina¹, S. A. Starostina¹, A. A. Sosnovskaya¹

¹ *Admiral Makarov State University of Maritime and Inland Shipping Saint Petersburg, Russia*

² *Saint Petersburg State University, Department of Atmospheric Physics Saint Petersburg, Russia, vpo563@yandex.ru*

KEYWORDS:

Radiative transfer, planetary atmospheres, wind field gradient, Venus, molecular bands, carbon dioxide

INTRODUCTION:

The discovery of the existence of large-scale currents in the atmospheres of planets with velocities of the order of the speed of sound and significant large-scale wind velocity gradients (for example, the phenomenon of super rotation above the cloud layer on Venus [1]) underscores the significance of incorporating this phenomenon into account in modeling radiation in the IR bands of atmospheric gas molecules. When observing from angles other than the nadir, there exists a non-zero component of wind velocity projected along the line of sight. Consequently, due to the Doppler effect, there is a variation in the frequency of radiation absorption, resulting in a substantial change in the value of the volume radiation absorption coefficient, σ_v , and, consequently, to a change in the radiation transfer pattern. In the center of the strongest line of the 4.3 μm band of the principal isotopologue $^{12}\text{C}^{16}\text{O}_2$, the optical thickness of Venus' atmosphere above approximately 85 km is approximately $2.3 \cdot 10^8$. Therefore, it becomes crucial to consider the accurate representation of spectral line shapes.

In the paper [2], within the framework of a simplified model, the problem of radiative transfer in the spectral lines of the 4.3 μm band of the CO₂ molecules in the planetary atmosphere was considered with taking into account the frequency shift of the volume radiation absorption coefficient due to the Doppler Effect.

In this paper, we continue our previous investigation and explore the effect of the shape of spectral lines on the values of the radiation intensity outgoing from the planetary atmosphere in the 4.3 μm CO₂ band, assuming both the Doppler and more realistic Voigt and Lorentz contours for planetary atmospheres.

MODEL:

In general, the model of the structural parameters of the planetary atmosphere and the model of the parameters of the vertical wind velocity profile adopted in this work follow the models described in [2]. We consider a planet whose atmosphere is stationary relative to the surface, with the exception of a certain layer that moves parallel to the equator at a speed of the order of the speed of sound. The atmosphere is considered to be plane-parallel with pressure distributed according to the barometric law with values characteristic of the above-cloud layer in the atmosphere of Venus, with a temperature having a linear vertical gradient (see in [2] Figure 1, left panel), and consisting entirely of CO₂ molecules. The isotopologues $\text{C}^{12}\text{O}^{16}_2$, $\text{C}^{13}\text{O}^{16}_2$, $\text{C}^{12}\text{O}^{16}\text{O}^{18}$ and $\text{C}^{12}\text{O}^{16}\text{O}^{17}$ are taken into account (hereinafter the designations 626, 636, 628 and 627 are used and their abundance values for

the Earth are assumed: 0.984204, 0.011077, 0.003947 and 0.0007339, respectively). For simplicity, it is assumed that a local thermodynamic equilibrium is maintained at all altitudes in the planetary atmosphere.

For the vertical distribution of the modulus of horizontal wind speed, a Gaussian dependence with 3 parameters is assumed: u_0 is the maximum wind speed (in units of the speed of sound), which is reached at a height of z_m , the layer has a half-width of Δz_m . In the coordinate system of an observer stationary relative to the surface of the planet, an expression was obtained in [2] for the frequency shift of radiation emitted in a certain direction by gas molecules moving in a wind current at a given height. This shift is taken into account in the expression for the values of σ_ν when modeling radiation coming out of the planet's atmosphere at the upper boundary with different values of the zenith angle.

For all spectral lines, a Voigt contour with a width parameter of $\gamma_0 = 0,068 \text{ cm}^{-1} \cdot \text{atm}^{-1}$ (at $p_0 = 1 \text{ atm}$, $T_0 = 296 \text{ K}$) and a temperature dependence parameter of $n = 0.7$ is adopted. Since this work is of a demonstration nature, the radiation field at frequencies is considered only for the most intense line of fundamental transitions with values of the central frequency ν_0 and the Einstein coefficient of spontaneous emission A_0 , characteristic of the $4.3 \text{ }\mu\text{m}$ band of molecules of the considered 4 CO_2 isotopologues.

RESULTS:

The values of the radiation intensity exiting the upper boundary of the planetary atmosphere have been modeled for cases involving a stationary (i.e. atmosphere without the moving layer) and moving atmosphere (i.e., one with a moving layer). The results are presented in Figure 1 in the form of a ratio of outgoing radiation intensities, q , for a moving vs. stationary atmosphere, depending on the dimensionless frequency (the difference between the current frequency ν and the central frequency ν_0 , expressed in units of Doppler width $\Delta\nu_D$). This dimensionless frequency is useful for studying the effects of macroscopic wind speed gradients on the outgoing radiation spectrum.

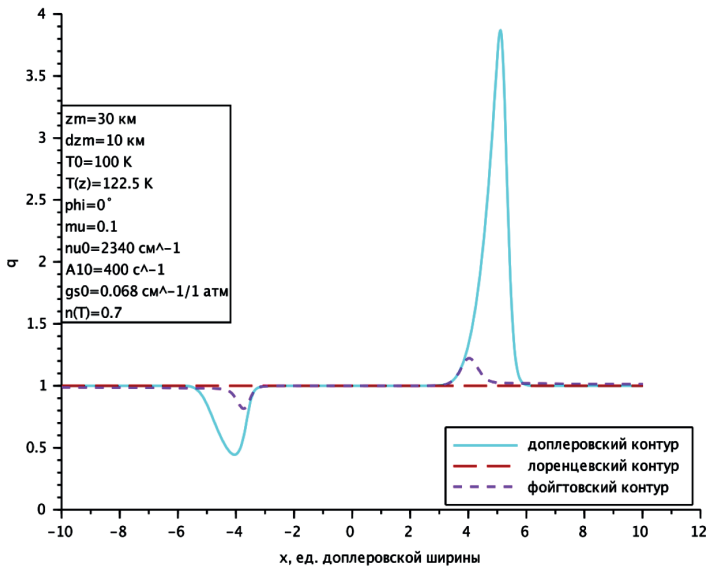


Figure 1. The ratio q of the spectrum of outgoing radiation for a moving atmosphere (wind velocity in the center of the moving layer is 1 Max) to the spectrum of outgoing radiation for a stationary one for the principal isotopologue $^{12}\text{C}^{16}\text{O}_2$ from the Doppler (solid), Voigt (long dotted line) and Lorentz (short dotted line) contours of the spectral line in the $4.3 \text{ }\mu\text{m}$ band.

In order for the wind profile model to approximately correspond to the observed velocity field in the layer above clouds in the atmosphere of Venus, the following values were selected: velocity in the center of the layer

$u_0 = 1$ Max, height of the center of the moving layer $z_m = 30$ km, half-width of the moving layer $\Delta z_m = 10$ km (the wind velocity profile is shown in [2] in Figure 1, right panel). The following observation geometry was adopted: the ray of sight has the cosine of the zenith angle $\mu = 0.1$, and the azimuth angle is 0° .

The following characteristic values were taken as the main optical parameters on which the optical thickness of the planetary atmosphere in the $4.3 \mu\text{m}$ band of the $^{12}\text{C}^{16}\text{O}_2$ molecule depends: the frequency of the center of the line $\nu_0 = 2340 \text{ cm}^{-1}$ and the Einstein coefficient of spontaneous emission $A_0 = 400 \text{ s}^{-1}$.

From the Figure 1, it can be concluded that the Doppler effect is most noticeably taken into account when taking the Doppler contour of the spectral line, because in this case the wings of the spectral lines are not developed: the volume absorption coefficient of radiation, σ_ν , decreases very quickly at all altitudes in the atmosphere with increasing distance from the central frequency of the line. The least noticeable manifestation of this effect is when assuming the Lorentz contour, since in this case the rate of decrease of σ_ν is too slow at all altitudes in the atmosphere (inversely proportional to the square of the dimensionless frequency). Both of these contours are marginal cases. In the case of the Voigt contour, which is more realistic for planetary atmospheres, with the Voigt parameter proportional to pressure (and, consequently, exponentially increasing with decreasing altitude in the atmosphere), the influence of the Doppler effect on the outgoing radiation remains significant, although it is an order of magnitude weaker than in the case of the Doppler contour.

It is also evident that the locations of the maxima and minima in the values q are shifted away from the centerline as the rate of decline in the values σ_ν (Doppler shift) increases.

CONCLUSIONS:

It has been shown that the presence of a moving layer in the planetary atmosphere, for a certain range of frequencies in the near and middle parts of the wings of the spectral lines, can significantly affect the intensity of radiation outgoing from the planetary atmosphere at its upper boundary. These variations can reach hundreds of percent, both upwards and downwards. Furthermore, these variations do not cancel each other out, as they are significantly non-linear in nature.

The main conclusions are as follows. 1) The spectral distribution of radiation escaping from the atmosphere at the upper boundary in the presence of a large-scale vertical gradient of horizontal velocity strongly depends on the parameters of the spectral line of the band (the central frequency ν_0 and the Einstein coefficient of spontaneous emission A_0). 2) When the spectral parameters of the line vary, the intensity of the outgoing radiation changes in different ways for frequencies located at different distances from the central frequency. 3) In this case, the change in radiation intensity in the presence of a moving layer in the atmosphere has a very different character from line (band) to line (band).

The latter circumstances can be used to diagnose the characteristics of large-scale wind movements in planetary atmospheres. Based on the analysis of the results of this work, it suggests that further studies of this problem using more realistic models, both for spectral bands and for large-scale vertical wind velocity gradients, may be appropriate.

REFERENCES:

- [1] *Mendonça J.M., Read P.L.* Exploring the Venus global super-rotation using a comprehensive general circulation model // *Planetary and Space Science*. 2016. V. 134. P. 1–18. DOI: 10.1016/j.pss.2016.09.001.
- [2] *Ogibalov V.P., Bordovskaya Yu.I.* Influence of wind fields with macroscopic velocity gradients on the IR CO_2 band emissions outgoing from a planetary atmosphere // *Proc. SPIE*. V. 12341. 28th Intern. Symp. Atmospheric and Ocean Optics: Atmospheric Physics. 2022. Article 1234110 DOI: 10.1117/12.2645401.

SESSION 4. SMALL BODIES (SB) ORAL SESSION

WATER ICE EXPOSURE ON THE SURFACE OF COMET 67P/CHURYUMOV-GERASIMENKO

S. Krasilnikov¹, B. Wu¹, Y. Xin^{2,3}, H. Li¹, W. Xun¹

¹ Research Centre for Deep Space Explorations, Department of Land Surveying and Geo-Informatics, The Hong Kong Polytechnic University, Hong Kong, sergey.krasilnikov@polyu.edu.hk, bo.wu@polyu.edu.hk

² Key Laboratory of Planetary Sciences, Purple Mountain Observatory, Chinese Academy of Sciences, Nanjing, PR China

³ School of Astronomy and Space Science, University of Science and Technology of China, Hefei, PR China

KEYWORDS:

comet, 67P, nucleus, water ice, volatiles, exposure

INTRODUCTION:

The exposure of volatiles could be spotted on the surface of comets as bright spots. Firstly, bright spots were discovered on the surface of comets 9P/Tempel 1 [1] and 103P/Hartley 2 [2]. Under the Rosetta mission, bright features on the comet's surface were identified using OSIRIS and VIRTIS-M multispectral imaging systems (Figure 1). The component analysis revealed that these bright spots primarily consist of water ice (e.g., [3]). The estimated water ice abundance significantly varies from 10 % to up to 80 %. The lifetime of bright spots varies from the diurnal cycle of frost recondensation [4], up to months for bright spots in consolidated material (e.g., [5]).

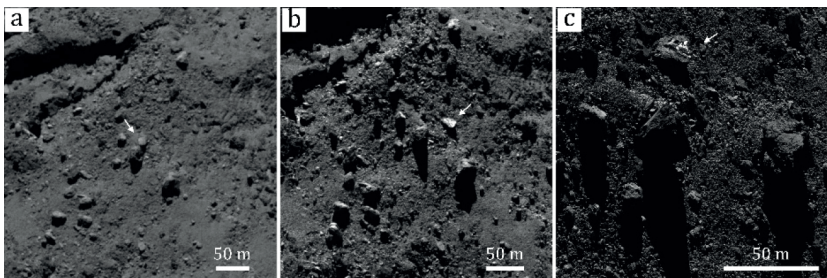


Figure 1. An example of water ice exposure and evolution: *a* — boulder before destruction and exposure; *b* — boulder after cracking and exposure; *c*) close-range image of the boulder

In our investigation, we present a comprehensive spatial and temporal analysis of water exposure on the surface of Comet 67P, highlighting active areas that depend on the comet's position in its orbit. Based on this knowledge and morphological analysis of active spots, we aim to investigate the primary mechanisms responsible for exposing water ice on 67P's surface. The next step will be to integrate morphological and thermophysical analyses.

MORPHOLOGY, SPATIAL DISTRIBUTION AND TIME-SERIES ANALYSIS:

In our research, we rely on previous publications in classification [3, 6] and the mapping of bright features [6, 7]. However, we have developed a combined classification based on the morphology and origin of these features. While we focused on the erosional exposure of volatiles, it has allowed us to exclude sublimational deposition of frost from our analysis. The frost sublimation and deposition process will be studied in separate research. Therefore, studying the erosional mechanism of volatile exposure allows us to distinguish three types with several subtypes for future heat and mass modelling:

1. Volatile exposure in a smooth material:
 - 1a) areal exposure,
 - 1b) scarp-related exposure.

2. Volatile exposure in a consolidated material:

- 2a) consolidated material,
- 2b) separated boulders.

3. Volatile exposure caused by slope collapse.

To explain the mechanism of exposure formation, we focused on (1a) areal volatile exposure in smooth material and (2) volatile exposure in a consolidated material, because the other types required the use of additional methods and will be studied in the future.

Volatile exposure in a smooth material

The variations of volatile exposure in a smooth material allowed us to subdivide these features into (a) areal exposure and scarp-related exposure (Figure 1b). The first subtype (1a) is related to the areal exposure of volatiles in a smooth material. This subtype is characterized by both a localized exposure within one month and a prolonged active period that spans a large area. The main feature of this subtype is the formation of volatile exposure in smooth material without an obvious external erosional process. It is assumed that exposure occurs due to internal driving forces. The most common is the 1b subtype related to the active transient surface changes that appeared on the surface due to the formation of erosional circular scarps. The speed of scarps migration reaches 7.6 m/day, which is much faster than the erosion by H₂O or CO₂, suggesting non-sublimation-driven erosion. This explains why this mechanism was excluded from our numerical calculations. Therefore, volatile exposure in smooth materials is mainly related to the fast-growing and short-lived process, which appears on the surface through the erosional removal of dust material.

Volatile exposure in a consolidated material

Compared to volatiles exposed in a smooth material, the process in consolidated material (Figure 1) is usually active for a longer time and localized to a few meters. This is facilitated by the rough, partially shaded surface and slow material erosion, which slows down the sublimation rate. Time-series analysis revealed that this process can be prolonged for up to 10 months in some cases, with breaks for several months. This process is less dependent on orbital position and exhibits only a slight increase in activity detection after perihelion. In the after-perihelium period, the mean exposure latitude shifted more to the south, which is explained by better illumination of the southern hemisphere at this part of the orbit.

Volatile exposure caused by slope collapse

This type of volatile exposure is associated with highly inclined slopes and cliffs, including the break line at the inclined surface and redeposited material, such as talus and individual boulders, at the base of the slopes. A combination of processes, including water-ice sublimation, metamorphism, material thermal stress, and local gravity, drives the formation mechanism. Higher local gravity accelerates the breakdown of consolidated material, leading to its fragmentation into larger fragments and subsequent downslope transport, which forms taluses and individual boulders at the bottom of the slope. Volatile-rich areas are exposed at the break line areas and on the eroded material. Within this process, the assumed influence of subsurface ice sublimation on material erosion could be more significant. A combination of processes acting on the material leads to more active erosion and, consequently, an acceleration of the erosional cycle. The time-series analysis confirmed this assumption and revealed a relatively uniform temporal distribution of this process with the significant presence of prolonged or reactivated exposures.

RESULTS:

The results of the mapping revealed 340 places with ice exposure (Figure 2). Totally, 32 exposures for subtypes 1a (8) and 1b (24), 244 exposures for subtypes 2a (154) and 2b (90), and 64 exposures for type 3 were detected. The duration of volatile exposure in 135 places was more than one month, occurring over several consecutive months or appearing separately with intervening inactive periods. This reveals the reactivation mechanism

of exposure. The main density of volatile exposure accrues to Comet 67P's equatorial and southern regions, which are extensively illuminated close to the perihelion period.

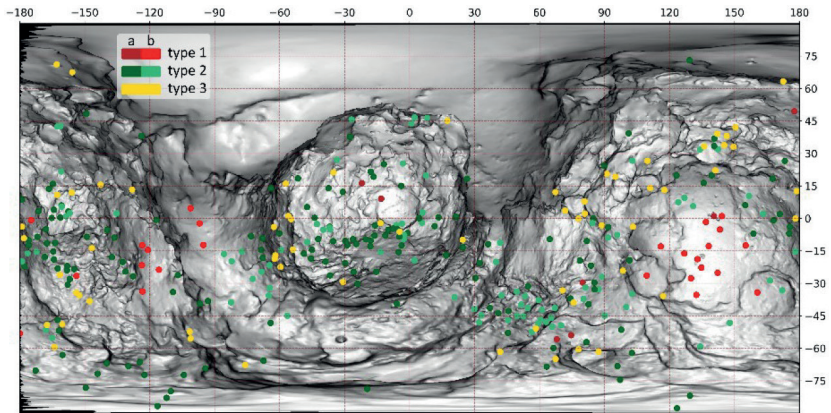


Figure 2. Map of volatile exposure on the Comet 67P

The morphology and dynamics of exposures considered in our work revealed the erosional nature of the processes and indicated that consolidated material remains a primary reservoir for volatile storage (see Figure 1). The reactivation of active places says about the erosional cycle with the gradual destruction of material: (a) drying of the upper layer, (b) erosion of dry crust with underlayer volatile exposure, (c) sublimation of volatiles and repeating the cycle.

ACKNOWLEDGMENTS:

S. Krasilnikov acknowledges support from the Startup Funding P0052619 from the Hong Kong Polytechnic University. B. Wu acknowledges support from the Research Grants Council of Hong Kong (Project No. 15219821). Y. Xin was supported by the National Natural Science Foundation of China (Grant No. 12222307, 12073084).

REFERENCES:

- [1] *Sunshine J.M., A'hearn M.F., Groussin O. et al.* Exposed water ice deposits on the surface of comet 9P/Tempel 1 // *Science*. 2006. V. 311. Iss. 5766. 1453-1455. DOI: 10.1126/science.1123632.
- [2] *Li J.Y., Besse S., A'hearn M.F. et al.* Photometric properties of the nucleus of Comet 103P/Hartley 2 // *Icarus*. 2013. V. 222. Iss. 2. P. 559–570. <https://doi.org/10.1016/j.icarus.2012.11.001>.
- [3] *Pommerol A., Thomas N., El-Maarry M.R. et al.* OSIRIS observations of meter-sized exposures of H₂O ice at the surface of 67P/Churyumov-Gerasimenko and interpretation using laboratory experiments // *Astronomy and Astrophysics*. 2015. V. 583. Article A25. 16 p. <https://doi.org/10.1051/0004-6361/201525977>.
- [4] *Fornasier S., Mottola S., Keller H.U. et al.* Rosetta's comet 67P/Churyumov-Gerasimenko sheds its dusty mantle to reveal its icy nature // *Science*. 2016. V. 354. No. 6319. P. 1566–1570. DOI: 10.1126/science.aag2671.
- [5] *Oklay N., Mottola S., Vincent J.B. et al.* Long-term survival of surface water ice on comet 67P // *Monthly Notices of the Royal Astronomical Society*. 2017. V. 469. Iss. Suppl_2. P. 582–597. <https://doi.org/10.1093/mnras/stx2298>.
- [6] *Deshapriya J.D., Barucci M.A., Fornasier S. et al.* Exposed bright features on the comet 67P/Churyumov-Gerasimenko: distribution and evolution // *Astronomy and Astrophysics*. 2018. V. 613. Article A36. 14 p. <https://doi.org/10.1051/0004-6361/201732112>.
- [7] *Fornasier S., Hoang H.V., Fulle M. et al.* Volatile exposures on the 67P/Churyumov-Gerasimenko nucleus // *Astronomy and Astrophysics*. 2023. V. 672. Article A136. 18 p. <https://doi.org/10.1051/0004-6361/202245614>.

POSSIBILITY OF LIQUID WATER FORMATION IN ICY BODIES DUE TO THE PROCESS OF RAPID RECOMBINATION OF ACCUMULATED RADICALS

A. K. Pavlov¹, G. A. Kucherov^{1,2}, A. Y. Merkulova¹

¹ Ioffe Institute, Saint Petersburg, Russia, anatoli.pavlov@mail.ioffe.ru

² Peter the Great Saint Petersburg Polytechnic University, Saint Petersburg, Russia, glebkucherov2002@gmail.com

KEYWORDS:

free radicals, Kuiper belt, Oort cloud, icy bodies, comets, liquid water

ABSTRACT:

Observations have shown that many icy bodies in the Solar System undergo processes of active energy release. These processes may lead to the formation of liquid water beneath the surface of an icy body. An energy source for such processes remains unknown in many cases. We propose the recombination of accumulated radicals as the energy source. We assume that the accumulation of H and OH radicals occurs in amorphous water ice due to the decay of radionuclides throughout the entire volume of the body. Our previous calculations show that if a certain concentration of radicals accumulates inside an icy body, the recombination process can raise the temperature up to 273 K [1]. However, the formation of liquid water inside the body also requires sufficient gas pressure. In the work [1] we carried out simulations without taking into account the diffusion of volatile gases and, therefore, we did not address the pressure that would develop inside an icy body during the recombination process. In the present work, we examine a more complex model in which the processes of diffusion and crystallization of volatile gases are also taken into account [2]. This model allows us to study the dependence of the possibility of liquid water formation on the composition and porosity of an icy body. In this work, we consider porous bodies with radii up to 20 km (e.g., comets and small bodies of the Kuiper belt). We assume that the bodies are composed of amorphous water ice and dust. At low temperatures, amorphous ice traps volatile gas molecules [3]. At temperatures above 120 K, the process of transition from amorphous ice to crystalline ice occurs, accompanied by sublimation of trapped volatile gases (e.g., CO and CO₂). The release of these gases results in the growth of pressure inside the body. The gases can diffuse through the porous material into unheated layers, where they can recondense. Our calculations show that the maximum pressure front of CO and CO₂ gases is slightly behind the recombination front and propagates throughout the body along with it. The gas pressure inside this region can reach large values necessary for the formation of liquid water. For example, when the molar abundances of CO and CO₂ gases relative to water ice are equal to 0.1, as in works [1, 2], this pressure exceeds 20 atmospheres.

ACKNOWLEDGMENTS:

This work has been supported by the grant of the Russian Science Foundation, RSF 24-22-00257, <https://rscf.ru/project/24-22-00257/>.

REFERENCES:

- [1] Pavlov A. K., Kucherov G. A., Merkulova A. Y., et al. Accumulation and Recombination of Radicals as an Energy Source for Active Processes in Icy Bodies of the Solar System // *Solar System Research*. 2025. V. 59. Article 44. <https://doi.org/10.1134/S0038094624601981>.
- [2] Belousov D. V., Pavlov A. K. Cometary outbursts in the Oort cloud // *Icarus*. 2024. V. 415. Article 116066. <https://doi.org/10.1016/j.icarus.2024.116066>.
- [3] Bar-Nun A., Herman G., Laufer D., Rappaport M. Trapping and release of gases by water ice and implications for icy bodies // *Icarus*. 1985. V. 63. Iss. 3. P. 317–332. [https://doi.org/10.1016/0019-1035\(85\)90048-X](https://doi.org/10.1016/0019-1035(85)90048-X).

OUTBURSTS OF ICY BODIES IN KUIPER BELT AND BEYOND, AS POSSIBLE NEW SOURCE OF DUST TO EXPLAIN NEW HORIZONS OBSERVATIONS

A. K. Pavlov, N. V. Liashenko, A. Y. Merkulova

Ioffe Institute, Saint Petersburg, Russia, anatoli.pavlov@mail.ioffe.ru

KEYWORDS:

Kuiper belt, cometary outbursts, cosmic dust

ABSTRACT:

The New Horizons mission measured an abnormally high density of dust particles at a distance of $R = 42\text{--}55$ au and even an increase in their number with increasing distance from the Sun [1]. Existing models of dust generation in the Kuiper Belt region cannot explain these observations. So far, only two mechanisms of dust formation at large distances from the Sun have been considered: collisions of bodies entering this belt and bombardment of their surfaces with interstellar dust particles.

We propose a new mechanism for the generation of dust at large distances, which is based on our previously proposed model of observed cometary outbursts at $R > 10$ au [2]. Our mechanism is based on the rapid process of recombination of radicals accumulated in the surface layers of icy bodies as a result of long time bombardment by galactic cosmic rays. The process leads to the release of a large amount of energy and the ejection of a large number of dust particles $M > 10^{10}$ g.

In our work, we estimate the required number of icy bodies and their size and distance distribution from the Sun to generate enough to explain the results of the New Horizons mission.

ACKNOWLEDGMENTS:

This work has been supported by the grant of the Russian Science Foundation, RSF 24-22-00257, <https://rscf.ru/project/24-22-00257/>.

REFERENCES:

- [1] *Doner A., Horányi M., Bagenal F. et al.* New Horizons Venetia Burney Student Dust Counter Observes Higher than Expected Fluxes Approaching 60 au // *Astrophysical J. Letters*. 2024. V. 961. No. 2. Article L38. DOI: 10.3847/2041-8213/ad18b0.
- [2] *Pavlov A. K., Belousov D. V., Tsurkov D. A., Lomasov V. N.* Cosmic ray irradiation of comet nuclei: A possible source of cometary outbursts at large heliocentric distances // *Monthly Notices of the Royal Astronomical Society*. 2022. V. 511. Iss. 4. P. 5909–5914. <https://doi.org/10.1093/mnras/>.

DISTANT TRANS-NEPTUNIAN OBJECTS PRODUCED BY PERTURBATIONS OF MIGRATING OUTER PLANETS AND MASSIVE PLANETESIMALS

V.V. Emel'yanenko

Institute of Astronomy RAS, Moscow, Russia, vvemel@inasan.ru

KEYWORDS:

Trans-Neptunian objects, N -body simulations, long-term evolution, migration

ABSTRACT:

We investigate the origin of distant trans-Neptunian objects under collective gravity of the known giant planets, additional outer planets and massive planetesimals. We carry out the full N -body numerical simulations of gravitational interactions of the giant planets and smaller bodies of different mass ranges for 4 Gyr. First, we study the evolution of the Solar system with additional Earth-mass planets. Secondly, we consider systems with additional planets of larger masses. In most cases of numerical simulations, either the destructions of planetary systems or the transitions of planets to orbits significantly different from modern orbits occur. Nevertheless, we have found many cases of the planetary systems that survive for the Solar system age with a configuration close to the present one. In such systems, the presence of distant trans-Neptunian objects is typical. The dynamical features of objects in the remote trans-Neptunian region are very diverse and include mutual secular resonances and close encounters. The combined action of perturbations from the giant planets, additional planets and self-gravity of the planetesimal disk can produce distant trans-Neptunian objects in both high-eccentricity and near-circular orbits. A trend towards an increase in the number of surviving distant trans-Neptunian objects with an increase in the number of additional planets has been noted.

COMETARY OUTBURSTS IN THE EARLY SOLAR SYSTEM

A. Y. Merkulova, A. K. Pavlov, G. I. Vasilyev

Ioffe Physical-Technical Institute, Saint Petersburg, Russia
a.j.merkulova@mail.ioffe.ru

KEYWORDS:

comets, cometary outbursts, early Solar System, gravitational perturbations

INTRODUCTION:

The dynamical evolution of comets is influenced not only by gravitational perturbations, but also by non-gravitational forces such as cometary outbursts [1, 2]. While planetary encounters and migration, as described in the Nice model [3–5], played a dominant role in reshaping the structure of the outer Solar System, additional effects from comet-intrinsic activity could have contributed to the long-term orbital evolution of small icy bodies. In this study, we explore how cometary outbursts may have affected cometary orbits during the early stages of Solar System history. Comets in our simulations were initially distributed between 30 and 50 au from the Sun. We compare two evolutionary scenarios: one involving only planetary gravitational perturbations, and another incorporating both gravitational forces and velocity impulses caused by cometary outbursts.

RESULTS:

Our results show that cometary outbursts can significantly affect orbital evolution by increasing eccentricity. In multiple cases, comets that remained on near-circular or moderately perturbed orbits under purely gravitational influences acquired near-parabolic or even hyperbolic trajectories when outbursts were included. This effect was particularly evident for smaller comets, which experienced stronger velocity changes per unit mass. Even though outbursts were applied infrequently, their cumulative effect led to major divergence between the two scenarios. These findings suggest that cometary activity could have played a substantial role in shaping the dynamical structure of the early outer Solar System.

ACKNOWLEDGMENTS:

The study is funded by Russian Science Foundation, project No. 24-22-00257.

REFERENCES:

- [1] *Belousov D.V., Pavlov A.K.* Non-gravitational mechanism of comets' ejection from the Oort cloud due to cometary outbursts // *Solar System Research*. 2023. V. 57. No. 6. P. 629–635. DOI: 10.1134/s0038094623060023.
- [2] *Merkulova A. Y., Pavlov A. K., Belousov D. V.* The impact of cometary outbursts on the orbits of comets in the Oort cloud // *Icarus*. 2025. V. 434(1). Article 116547. <https://doi.org/10.1016/j.icarus.2025.116547>.
- [3] *Gomes R., Levison H.F., Tsiganis K., Morbidelli A.* Origin of the cataclysmic Late Heavy Bombardment period of the terrestrial planets // *Nature*. 2005. V. 435. P. 466–469. <https://doi.org/10.1038/nature03676>.
- [4] *Tsiganis K., Gomes R., Morbidelli A., Levison H.F.* Origin of the orbital architecture of the giant planets of the Solar System // *Nature* 2005. V. 435. P. 459–461. <https://doi.org/10.1038/nature03539>.
- [5] *Morbidelli A., Levison H.F., Tsiganis K., Gomes R.* Chaotic capture of Jupiter's Trojan asteroids in the early Solar System // *Nature*. 2005. V. 435. P. 462–465. <https://doi.org/10.1038/nature03540>.

DUSTY PLASMA FORMATION NEAR 67P/CHURYUMOV-GERASIMENKO COMET: IMPORTANCE OF ALBEDO

S. I. Popel, A. P. Golub, L. M. Zelenyi

Space Research Institute RAS, Moscow, Russia, popel@cosmos.ru

KEYWORDS:

dusty plasmas, comet coma, 67P/Churyumov-Gerasimenko comet, dynamics of dust particles, albedo

INTRODUCTION:

In the case of a comet [1], in addition to the processes leading to the electrostatic interaction of dusty plasma with the charged surface of the cosmic body, the formation of dusty plasma is influenced by the drag of dust by the flow of gases resulting from the sublimation caused by the heating of the comet nucleus by solar radiation. Here, we present a description of dusty plasma processes in the vicinity of 67P/Churyumov-Gerasimenko comet and discuss the influence of albedo on the processes of dusty plasma formation.

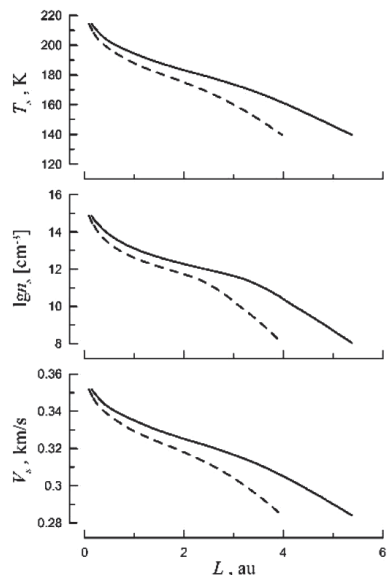
RESULTS OF CALCULATIONS:

Figure 1 presents the comparison of the temperature T_s of gases in the gas flow, their concentration n_s and velocity V_s calculated for two values of the bolometric albedo, namely, 0.06 (solid curves) and 0.63 (dashed curves). The comet nucleus is supposed to correspond to the conditions of the nucleus of the 67P/Churyumov-Gerasimenko comet (in particular, the gravity is 0.0245 cm/s^2 , the nucleus radius is $R_n = 1.65 \text{ km}$, the nucleus mass is $M_n = 10^{13} \text{ kg}$, and the nucleus matter density is $\rho_n = \text{g/cm}^3$).

If the albedo of the comet nucleus is rather high (e.g., 0.63 for pure ice [2]) the dusty plasma processes are manifested significantly when a comet is sufficiently far from the Sun. For example, the dusty plasma near the comet nucleus at distances to the Sun no less than $\sim 2.5\text{--}2.5 \text{ au}$ can be formed [1] due to the electrostatic interactions similar to the situation, e.g., near the Moon. Dust particle dynamics at closer distances from the Sun is determined by the gas flow from the comet nucleus.

The low albedo (e.g., 0.06 for the nucleus of the 67P/Churyumov-Gerasimenko comet) results in a significant change in the parameters of gases resulting from the sublimation caused by the heating of the comet nucleus in comparison with the situation of the high albedo (see Figure 1). In particular, for the same distance L from the Sun, the gas flow from the comet nucleus is stronger for the lower albedo. Figure 2 shows the altitude distributions of the parameters characterizing dusty plasma above the surface of the 67P/Churyumov-Gerasimenko comet nucleus at $L = 5 \text{ au}$. The ratio of the electrostatic and gas-dynamic forces acting on a dust particle, $E_E/E_{fg} \sim 1$ at $L = 5 \text{ au}$ (see Figure 2).

Figure 1. The dependencies on the distance from the Sun L of the parameters of gases flowing from the comet nucleus. Calculations are performed for two values of the bolometric albedo, 0.06 and 0.63



Thus for the 67P/Churyumov-Gerasimenko comet the dusty plasma is formed mainly due to the electrostatic interactions when L is within the range from ~ 5 au to the aphelion of the comet, 5.68 au. For the distances less than ~ 5 au the dynamics of dust particles is determined by the gas flow from the comet nucleus.

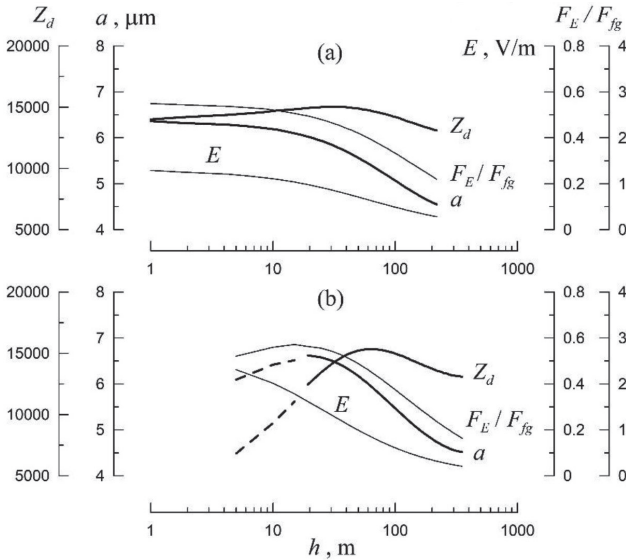


Figure 2. Sizes a and charge numbers Z_d of dust particles, the ratio F_E/F_{fg} of the electrostatic and gas-dynamic forces acting on a dust particle, and the electric field E versus the altitude h over the surface of the comet nucleus for the subsolar angles $\theta = 87^\circ$ (a) and 77° (b). The dashed lines correspond to unstable equilibrium states of dust particles. Calculations are performed for the conditions of the 67P/Churyumov-Gerasimenko comet at $L = 5$ au

DISCUSSION AND CONCLUSIONS:

For a comet exhibiting parameters of the nucleus close to those of the nucleus of the 67P/Churyumov-Gerasimenko comet, the dusty plasma in the vicinity of the nucleus forms due to electrostatic interactions, i.e., analogous to dusty plasma formation near other bodies without atmosphere (e.g., Mercury [3], the Moon [4], Martian satellites [5, 6]), provided that the distance from the comet to the Sun is at least ~ 5 au. On the contrary, if the comet is closer to the Sun, the dynamics of dust particles is determined by the gas flow from the comet nucleus. The reason why for the 67P/Churyumov-Gerasimenko comet the distance of the dusty plasma formation due to the electrostatic interactions is larger than for a comet with nucleus consisting of pure ice is the low value of albedo of the surface of the 67P/Churyumov-Gerasimenko comet. Thus albedo is an important factor for the formation of dusty plasma system in the vicinity of a comet.

The results obtained here can be used for the description of dusty plasmas near active asteroids [7]. Because active asteroids are Main Belt those, and the typical distance from the Sun to an active asteroid is 2.8 au, an appearance of dusty plasmas formed mainly due to the electrostatic interaction at active asteroids is possible only for rather high albedo of their surface (e.g., 0.63).

Although the history of studying dusty plasmas at comets and asteroids is relatively long, there are still unresolved problems, and successful solution of some of them requires accumulating new knowledge about the studied space objects. This goal can be achieved only in the course of future space missions.

ACKNOWLEDGMENTS:

The study was supported by the Russian Science Foundation grant No. 24-12-00064, <https://rscf.ru/project/24-12-00064/>.

REFERENCES:

- [1] *Popel S.I., Golub' A.P., Zelenyi L.M.* Plasma-dust processes in the vicinity of comets // *Solar System Research*. 2025. V. 59(5). Article 47. 11 p. DOI: 10.1134/S0038094624601695.
- [2] *Houpsis H.L.F., Mendis D.A.* On the development and global oscillations of cometary ionospheres // *Astrophysical J.* 1981. V. 243. P. 1088–1102. DOI: 10.1086/158673.
- [3] *Popel S.I., Golub' A.P., Zelenyi L.M.* Dusty plasmas above the sunlit surface of Mercury // *Physics of Plasmas*. 2023. V. 30. Iss. 4. Article 043701. 9 p. DOI: 10.1063/5.0142936.
- [4] *Popel S.I., Zelenyi L.M., Golub' A.P., Dubinskii A.Yu.* Lunar dust and dusty plasmas: recent developments, advances, and unsolved problems // *Planetary and Space Science*. 2018. V. 156. P. 71–84. <https://doi.org/10.1016/j.pss.2018.02.010>.
- [5] *Golub' A.P., Popel S.I.* Nonstationary Processes in the Formation of a Dusty Plasma near the Surface of Phobos // *J. Experimental and Theoretical Physics Letters*. 2021. V. 113. P. 428–432. <https://doi.org/10.1134/S0021364021070079>.
- [6] *Golub' A.P., Popel S.I.* Non-Stationary Processes during the Formation of Dusty Plasma at the Surface of Deimos, the Satellite of Mars // *Plasma Physics Reports*. 2021. V. 47. P. 826–831. DOI: 10.1134/S1063780X21070084.
- [7] *Dubinsky A.Yu., Reznichenko Yu.S., Popel S.I.* The influence of water on the formation of a dusty plasma exosphere above the surface of an asteroid // *Solar System Research*. 2025. V. 59. Article 51. 8 p. <https://doi.org/10.1134/S0038094624602160>.

PRE-PERHELION OBSERVATIONS AND INTERPRETATION OF CH₃OH, CO AND HCN LINE EMISSION IN THE OORT CLOUD COMET C/2017 K2 (PANSTARRS)

M. S. Kirsanova, Ya. N. Pavlyuchenkov
Institute of Astronomy RAS, Moscow, Russia
kirsanova@inasan.ru, pavyar@inasan.ru

KEYWORDS:

comets, Oort cloud, water, hypervolatiles, organics, spectral lines, millimetre observations, non-LTE modelling

INTRODUCTION:

Studying of trans-Neptunian bodies, we address the origin and formation scenario of the Solar System. The distant comets are members of the Oort and Kuiper belts, and therefore they remain the Solar System primary material. The distant comets move at large heliocentric distances and retain the material in the primary, almost no processed state. The ices covering the comet nuclei contain different types of molecules from simple two-atomic to precursors of the complex organic species like methanol. Measuring the molecular composition of the distant comets helps us to understand how deeply their ices were preceded by solar UV radiation. Since methanol can only be formed on dust grains by subsequent hydrogenation of condensed CO, the abundance ratio of primary volatile molecules CH₃OH/CO can be marker of a comet history and its irradiation by solar UV photons.

RESULTS:

We observed 12 lines of methanol, one line of CO and one of HCN in the Oort comet C/2017 K2 (PANSTARRS) during the pre-perihelion phase from April to July 2022 with the APEX and OSO-20m telescopes. Our conclusions are following.

First, the intensities of the methanol lines rise from April to July from 10–20 to 100 % for the lines with $E_u \leq 40$ K and even higher for lines with $E_u > 40$ K. The intensities of the CO and HCN lines did not rise from spring to summer which is probably related with depletion of these hypervolatiles. The coma expansion velocity of 0.3 km/s was unchanged regardless of the position of the comet relative to the Sun.

Second, water production rate $Q_{\text{H}_2\text{O}} = (0.7-1) \cdot 10^{29} \text{ s}^{-1}$ was almost stable during the observed pre-perihelion phase. The non-LTE model appears to be degenerate across the explored gas temperature values. However, we find that the best-fit models correspond to gas temperatures above 100 K by at least a factor of few, whereas the LTE analysis yields values an order of magnitude lower. The ratio of CH₃OH/H₂O is in the interval 0.013–0.017.

Third, while the LTE analysis provides reasonable agreement of the simulated and observed line intensities, the non-LTE intensities are closer to the observed. These two approaches give different values of the gas temperature, CH₃OH/H₂O ratio and $Q_{\text{H}_2\text{O}}$. Since the non-LTE is more general approach, we do our main conclusions using those. Molecular abundances and other physical parameters of comet comas obtained using the LTE approach should be interpreted with caution and must be supplemented by more accurate non-LTE analyses to draw reliable conclusions about the interstellar origin of elements and molecules found on Earth.

CALCULATION OF THE PLUTO SURFACE COMPOSITION MAP USING THE LEISA IR SPECTRUM OF THE NEW HORIZONS

A. E. Drozdov¹, N. V. Emelyanov^{1,2}

¹ Sternberg Astronomical Institute Moscow University, Moscow, Russia
drozdofflekha1997@yandex.ru

² Affili Institut de Mécanique Céleste et de Calcul des Éphémérides —
Observatoire de Paris, Institut de Mécanique Céleste et de Calcul des
Éphémérides, Paris, France

KEYWORDS:

Pluto, IR spectrum, surface, Ices, Image processing

INTRODUCTION:

The existing infrared spectral measurements of Pluto by the New Horizons spacecraft's LEISA instrument make it possible not only to determine the composition of the dwarf planet's surface, but also to find out the spatial distribution of various materials and ices. Despite the fact that there is already very good work [1–3] on calculating the materials distribution on Pluto's surface, only 2 images of the LEISA camera were used in the work, and the spatial resolution was limited to 12 km per pixel due to computational difficulties. In this work, an attempt is also made to calculate the distribution of materials using simultaneously 5 images of the LEISA camera in a spatial resolution of 7 km per pixel. During the processing of the calibrated LEISA fits files, some image defects were detected and removed that could affect the calculation results.

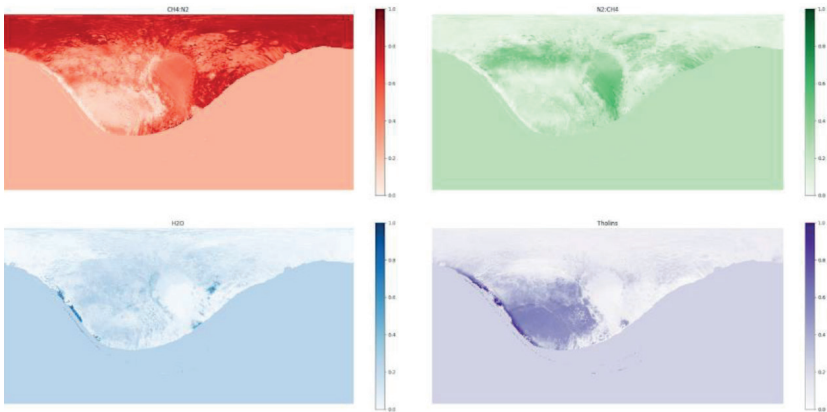


Figure 1. Example of calculated Pluto surface composition: CH₄-rich ice, N₂-rich ice, H₂O-ice and Titan tholins

REFERENCES:

- [1] Protopapa S., Grundy W.M., Reuter D.C. et al. Pluto's global surface composition through pixel-by-pixel Hapke modeling of New Horizons Ralph/LEISA data // *Icarus*. 2016. V. 287. P. 218–228. <https://doi.org/10.1016/j.icarus.2016.11.028>.
- [2] Schmitt B., Philippe S., Grundy W.M. et al. Physical state and distribution of materials at the surface of Pluto from New Horizons LEISA imaging spectrometer // *Icarus*. 2016. V. 287. P. 229–260. <https://doi.org/10.1016/j.icarus.2016.12.025>.
- [3] Emran A., Dalle Ore C.M., Ahrens C.J. et al. Pluto's Surface Mapping Using Unsupervised Learning from Near-infrared Observations of LEISA/Ralph // *The Planetary Science J*. 2023. V. 4. Article 15. DOI 10.3847/PSJ/acb0cc.

COMPARISON OF POLARIZATION PHASE DEPENDENCE OF NEA 2100 RA-SHALOM WITH THE DEPENDENCIES FOR OTHERS LOW-ALBEDO NEAS

N. Kiselev^{1,2}, M. Shcherbina¹, E. Zhuzhulina², H. Dyachenko³,
N. Karpov¹, I. Sokolov¹, D. Andreev¹

¹ Institute of Astronomy RAS, Moscow, Russia, kiselevnn42@gmail.com

² Crimean Astrophysical Observatory RAS, Nauchny, Russia

³ Junior Academy of Sciences "Explorer", Simferopol, Russia

KEYWORDS:

polarimetry, near Earth asteroids, 2100 ra-shalom, albedo

INTRODUCTION:

Since 2019, polarimetric monitoring of near-Earth asteroids (NEAs) has been conducted at the 2.6-m telescope at the Crimean Astrophysical Observatory (CrAO) and the 2-m telescope at the Peak Terskol Observatory (PTO, a branch of INASAN). Polarimetric studies, especially over a wide range of phase angles, are essential for determining polarization phase dependences (PhDP) for different taxonomic classes, as well as estimating albedo and size. To date, polarimetric properties of more than 30 near-Earth asteroids have been measured. This represents a significant contribution to the total number (approximately 26) of observed NEAs published to date.

2100 RA-SHALOM:

In the period from July 23 to August 3, 2025, observations of the low-albedo NEA 2100 Ra-Shalom were carried out in the phase angle range of 84–73° using the CrAO and PTO polarimeters in the V and R bands. Figure 1 shows the R-band PhDP, supplemented by measurements at 60° [1] and by unpublished measurements at 27°.

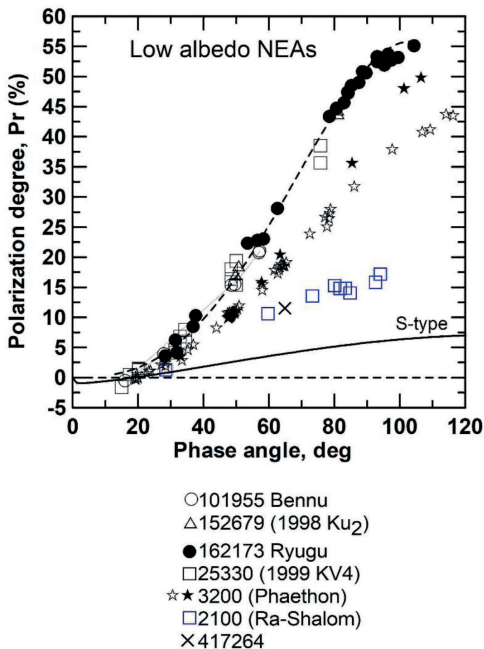


Figure 1. The phase-angle polarization dependencies of low-albedo NEAs. The dashed line represents the average polarization curve of NEAs 101955, 152679, 162173, 25330. For comparison, the synthetic polarization curve for intermediate-albedo S-type asteroids is shown as a solid curve

For comparison, the data of different authors [2] are presented for other low-albedo asteroids 101955 (Bennu), 152679 (1998 Ku2), 162173 (Ryugu), 3200 Phaethon. Additionally, data from NEAs 25330 and 417264 obtained using our program [3] are shown.

The figure shows that the PhDP of Ra-Shalom differs significantly from the data for Phaethon and four asteroids 101955, 152679, 162173, 25330. The latter form a group with close polarization curves. However, the PhDP of Ra-Shalom coincides well with the polarization of NEA 417264. In general, it is obvious that low-albedo asteroids demonstrate significant scattering of the degree of polarization on the plot P_r vs phase angle. Possible reasons will be discussed.

REFERENCES:

- [1] *Kiselev N. N., Rosenbush V. K., Jockers K.* Polarimetry of Asteroid 2100 Ra-Shalom at Large Phase Angle // *Icarus*. 1999. V. 140. Iss. 2. P. 464–466. <https://doi.org/10.1006/icar.1999.6139>.
- [2] *Lupishko D. F.* Asteroid Polarimetric Database (APD) V1.0 / NASA Planetary Data System, urn:nasa:pds:asteroid_polarimetric_database::1.0. 2019. DOI: 10.26033/z7xq-1x46.
- [3] *Shcherbina M. P., Kiselev N. N., Karpov N. V., Zhuzhulina E. A.* Results of Polarimetric Monitoring of Near-Earth Asteroids at the 2.6-m KrAO Telescope and the 2-m Telescope of the Terskol Peak Observatory // *Solar System Research*. 2025. V. 59. No. 6. Article 61. DOI: 10.1134/S0038094624601968.

ASTEROIDS OF THE HUNGARIA FAMILY AND THE EARTH'S CO-ORBITAL POPULATION

N. Adigozalov¹, V.V. Sidorenko²

¹ *Moscow Institute of Physics and Technology, Moscow, Russia*
adigozalov@phystech.edu

² *Keldysh Institute of Applied Mathematics RAS, Moscow, Russia*
vvsidorenko@list.ru

KEYWORDS:

asteroids, near-Earth space objects, co-orbital dynamics

ABSTRACT:

Earth's 1:1-resonant asteroid companions make up a small yet remarkable part of the near-Earth space objects. A Monte Carlo investigation [1] showed that slow, chaotic drift from the main belt can keep this co-orbital group continually supplied, replacing objects that persist for just 10^3 – 10^5 years. These bodies are difficult to detect: they are spread over a wide area of sky and too faint for most telescopes.

Complementing that statistical view, long-term simulations in [2] show that the high-inclination Hungaria family is an active inner-belt source of near-Earth, planet-crossing asteroids with frequent close encounters. In a subsequent study, [3] quantified the co-orbital contribution: approximately 5 % of the test Hungarias escaped over 100 Myr, and about 3 % of these escapees were temporarily captured into 1:1 resonance with Earth or Mars. Once trapped, they typically remain co-orbital with Earth for a few tens of thousands of years before planetary perturbations or close encounters break the resonance. Most captures take the quasi-satellite form, with a smaller contingent on horseshoe or Trojan paths; a bias toward Earth's trailing (L5) region is evident, and lifetimes rarely exceed $\sim 6 \cdot 10^4$ years.

More recently, numerical and spectral studies [4, 5] revived the idea that some co-orbitals may actually be fragments of the Moon. Simulations reveal that just a tiny fraction of ejecta, launched at velocities slightly above lunar escape speed from the Moon's trailing hemisphere, can leave the Earth–Moon system, hover near 1 a.u., and settle into the 1:1 resonance. Spectroscopic observations show an L-type reflectance profile that is virtually indistinguishable from lunar silicates for the long-lived quasi-satellite (469219) Kamo'oalewa, hinting that Earth's co-orbital ranks include not only Hungaria-type asteroids but also occasional lunar shards.

In comparison with [2, 3], our study is based on updated information on the distribution of orbital elements of the Hungaria family of asteroids. Using long-term N-body integrations, we track entries into Earth's 1:1 resonance, classify co-orbital regimes (quasi-satellite, horseshoe, Trojan) and measure residence times. The objective is to quantify the intrinsic supply potential and typical lifetimes of Hungaria-derived co-orbitals.

REFERENCES:

- [1] *Morais M. H. M., Morbidelli A.* The population of near-Earth asteroids in co-orbital motion with the Earth // *Icarus*. 2002. V. 160. P. 1–9. DOI: 10.1006/icar.2002.6937.
- [2] *Galiazzo M. A., Bazsó Á., Dvorak R.* Fugitives from the Hungaria region: Close encounters and impact probabilities of Hungaria asteroids with the terrestrial planets // *Planetary and Space Science*. 2013. V. 84. P. 5–13. <https://doi.org/10.1016/j.pss.2013.03.017>.
- [3] *Galiazzo M. A., Schwarz R.* The Hungaria region as a possible source of Trojans and satellites in the inner Solar System // *Monthly Notices of the Royal Astronomical Society*. 2014. V. 445. Iss. 4. P. 3999–4007. DOI: 10.1093/mnras/stu2016.
- [4] *Sharkey B. N., Reddy V., Malhotra R. et al.* Lunar-like silicate material forms the Earth quasi-satellite (469219) 2016 HO₃ Kamo'oalewa // *Communications Earth and Environment*. 2021. V. 2. Article 231. <https://doi.org/10.1038/s43247-021-00303-7>.
- [5] *Castro-Cisneros J. D., Malhotra R., Rosengren A. J.* Lunar ejecta origin of near-Earth asteroid Kamo'oalewa is compatible with rare orbital pathways // *Communications Earth and Environment*. 2023. V. 4. Article 372. <https://doi.org/10.1038/s43247-023-01031-w>.

DESIGNING HALO ORBITS PASSING THROUGH THE TRAJECTORIES OF NEAR-EARTH ASTEROIDS

M. V. Pupkov¹, N. A. Eismont¹, O. L. Starinova², K. S. Fedyaev¹,
V. A. Zubko¹, O. S. Chernenko¹

¹ Space Research Institute RAS, Moscow, Russia, m.pupkov@iki.rssi.ru

² Samara University, Samara, Russia

KEYWORDS:

libration points, halo orbits, Apophis asteroid, James Webb Space Telescope, spectrum-roentgen-gamma space observatory

INTRODUCTION:

This work is devoted to study the possibilities of redirecting spacecraft from the initial halo orbits in the vicinity of the L_2 Sun-Earth libration point to the required ones, which ensure the spacecraft's approach to one of the near-Earth asteroids and further movement around the libration point. Such an asteroid can be Apophis [1], which will approach Earth on April 13, 2029, passing near the L_2 Sun-Earth libration point two days prior.

The paper focuses on orbits whose parameters are similar to those of existing space observatories and telescopes, such as The James Webb Space Telescope [2] and the Spectrum-Roentgen-Gamma (SRG) [3]. It is shown that, taking into account current fuel reserves, a spacecraft in the SRG-like orbit can approach the Apophis asteroid at a cost of a characteristic velocity of less than 200 m/s in several ways.

SIMULATION RESULTS:

Figures 1 and 2 show the dependencies $x(t)$, $y(t)$, $z(t)$ and $\alpha(t)$ (phase angle), respectively, for one initial (red) and three target orbits, obtained by applying the necessary impulse on different dates: February 18 ($\Delta V = 200$ m/s, purple), March 3 ($\Delta V_{\min} = 175.2$ m/s, blue) and March 15 ($\Delta V = 200$ m/s, green), 2029. The date February 18 is accepted as $t = 0$. The vertical line marks the date of Apophis' flyby near the L_2 Sun-Earth libration point. The spacecraft approaches the asteroid in all three target orbits on April 11, 2029, with a difference of several hours, during which Apophis manages to cover almost 100,000 km along the x -axis. It is important to note that the approach to Apophis can occur at different phase angles.

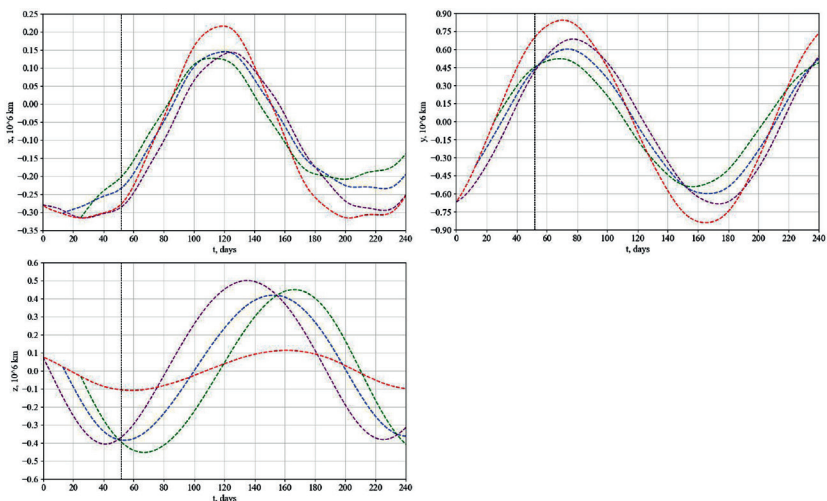


Figure 1. Time dependence of coordinates for the initial and target orbits

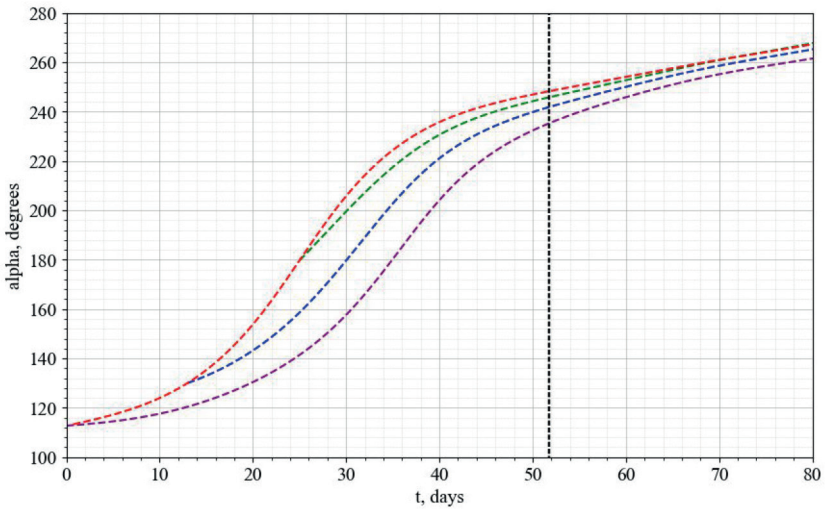


Figure 2. Phase angle as a function of time for the initial and target orbits

CONCLUSION:

The proposed kind of extended mission enable acquiring new scientific data about the target celestial body while simultaneously pursuing primary objectives. Such a concept for designing transfer trajectories within the vicinity of the libration point may be useful for future missions, especially for small spacecraft due to the low fuel consumption to implement the necessary maneuvers.

REFERENCES:

- [1] *Shuvalov V.V., Svetsov V.V., Artem'eva N.A.* Asteroid Apophis: evaluating the impact hazards of such bodies // *Solar System Research*. 2017. V. 51. No. 1. P. 44–58. <https://doi.org/10.1134/S003809461701004X>.
- [2] *Gardner J., Mather J., Abbott R. et al.* The James Webb Space Telescope mission // *Publications of the Astronomical Society of the Pacific*. 2023. V. 135. Iss. 1048. Article 068001. 24 p. DOI: 10.1088/1538-3873/acd1b5.
- [3] *Eismont N.A., Kovalenko I.D., Nazarov V.N.* Orbital motion and attitude control of the Spectrum–Röntgen–Gamma space observatory // *Astronomy Letters*. 2020. V. 46. No. 4. P. 263–274. <https://doi.org/10.1134/S1063773720040040>.

ON THE POSSIBILITY OF FLYBYS OF A LARGE NUMBER OF MAIN BELT ASTEROIDS

A. A. Sukhanov

Space Research Institute RAS, Moscow, Russia, sukhanov@cosmos.ru

KEYWORDS:

spacecraft, main belt asteroids, asteroid flyby, gravity assist maneuver, asteroid mass determination

ABSTRACT:

A concept of a low-cost mission to a large number of main belt asteroids is considered; a similar project called Hannes was being developed in Sweden in the 1990s [1]. It is proposed to launch several spacecraft (SC) by one launch vehicle, each of which approaches several asteroids. To lower the mission cost, it is suggested to use identical SC, perform gravity assists of Venus and Earth (i.e. Venus-Earth Gravity Assist (VEGA) maneuver is used), and explore asteroids from flyby trajectories. After the VEGA, for each of the SC a main target among main belt asteroids is selected; apart from that a few smaller asteroids can be encountered for low additional ΔV by each of the SC. Then each of the SC performs second Earth gravity assist maneuver which directs it to second main target, etc. An illustrative example of such a mission is given. This example includes encounters of one of the SC with such big asteroids as (216) Kleopatra, (112) Iphigenia (or (235) Carolina or (196) Philomela) and a few more small asteroids for 5–6 years. A method for accurately determining the mass of an asteroid from a flyby trajectory, suggested in [2], is described. This method is based on optical observations from the SC of a passive probe that separated from the SC shortly before the asteroid flyby.

REFERENCES:

- [1] *Sukhanov A. Trajectory Design for the Mission 'Hannes' // Acta Astronautica. 1997. V. 39. No. 1–4. P. 25–34. [https://doi.org/10.1016/S0094-5765\(96\)00119-1](https://doi.org/10.1016/S0094-5765(96)00119-1).*
- [2] *Perret A. Mass Determination of a Small Body in Solar System by Using a Test Mass During a Fly-by // Acta Astronautica. 1985. V. 12. No. 1. P. 41–44.*

ABOUT THE INFLUENCE OF NON-GRAVITATION PERTURBATIONS ON THE MOTION OF ASTEROIDS APPROACHING JUPITER

T. Yu. Galushina, O. N. Letner, D. Yu. Kuleshov

Tomsk state university, Tomsk, Russia, tatyana.galushina@mail.tsu.ru, oksana.letner@gmail.com, Danilkakuleshov@mail.ru

KEYWORDS:

near-Earth asteroids, approach to Jupiter, solar radiation pressure, the Yarkovsky effect, automatization

INTRODUCTION:

The study of approaches of Near-Earth asteroids (NEAs) to other planets provides important information about the nature of their motion and further evolution, since this feature can affect the behavior of orbital parameters in a short time. It is especially important to identify approaches to massive planets such as Jupiter, since its gravitational effect can cause the object to become a potentially hazardous asteroid. Earlier, we compiled a list of Near-Earth asteroids approaching Jupiter [1], which contains 1409 such celestial bodies. A detailed study of the dynamics of these asteroids requires constructing a perturbation structure. Formation of this structure will allow us to compile a recommended list of forces that have been taken into account to build a more accurate prediction of the dynamics of Near-Earth asteroids approaching Jupiter. This topic is covered in this paper. A special place in constructing the perturbation structure is occupied by solar radiation pressure and the Yarkovsky effect. These non-gravitational perturbations can have a significant effect on the orbits of small asteroids that regularly pass close to the Sun. The difficulty in taking these factors into account lies in the lack of knowledge of the physical parameters of most asteroids.

STUDY TECHNIQUE:

The impact of perturbing factors on the asteroid motion was assessed using a technique we had developed earlier [2, 3]. The methodology for studying the perturbation structure is based on the assessment of not only the nominal orbit, but also the size of the initial confidence region. These methods are implemented in our software "IDA" [4]. Using the IDA, we obtained estimates of the influence of perturbations for all Near-Earth asteroids approaching Jupiter from [1]. To process an array of 1409 files, a Python script was written, which made it possible to obtain general statistics on perturbations by class of these asteroids and separately for each object.

To assess the influence of solar radiation pressure, it is necessary to know the physical parameters of asteroids, such as diameter, mass, and albedo. To take into account the Yarkovsky effect, it is sufficient to know the transverse acceleration parameter A_2 . To make it easier to find these parameters and reduce the time spent, we created the AstroScan program. This program automatically downloads known parameters for a given list of asteroids from the NASA JPL database (<https://ssd.jpl.nasa.gov>). The user specifies a list of parameters for searching and a list of asteroids and runs the program. AstroScan automatically generates API requests to the NASA server, filters the data and leaves the necessary information. The user receives the results in text format and can save them for further use.

RESEARCH RESULTS:

The conducted study allowed us to identify the following set of perturbations that should be taken into account when constructing the orbital evolution of NEAs approaching Jupiter: gravitational influence of the planets, the Moon, Ceres, Pallas, and Vesta, relativistic effects of the Sun and the Sun oblateness. For 1/3 of the asteroids under study, taking into account the relativistic effects of Jupiter is also valid; the Jupiter oblateness has a slightly lesser effect, which is most likely due to close approaches to

the planet. The influence of these factors should be considered for individual objects.

To account for solar radiation pressure, we were able to download parameters for 113 asteroids, and the Yarkovsky effect parameter was available for only five objects. Using these parameters, we constructed the perturbation structure for these asteroids and found that the Yarkovsky effect should be taken into account for all five asteroids with a known A_2 . Solar radiation pressure has a significant impact on approximately half of the objects with known parameters. When analyzing the dynamics of individual asteroids, it is advisable to assess the influence of these parameters on a case-by-case basis.

The obtained results led us to the idea of performing numerical estimates of the A_2 parameter for all the studied objects. By applying an automated procedure, we obtained the following estimates. For 16 objects, the uncertainty of the Yarkovsky effect parameter does not exceed 10^{-14} a.u.; these are numbered asteroids with well-determined orbits. For 209 NEAs, the uncertainty is less than 10^{-13} a.u.; these results can be considered acceptable. The orbits of the remaining objects are not well enough defined to obtain reliable estimates of the Yarkovsky effect parameter.

ACKNOWLEDGMENTS:

The research was carried out within the state assignment of Ministry of Science and Higher Education of the Russian Federation (theme No. FSWM-2024-0005).

REFERENCES:

- [1] Galushina T. Yu., Letner O. N., Shein A. V. et al. Near-Earth Asteroids Approaching Earth and Jupiter // Vestnik St. Petersburg University. Mathematics. 2025. V. 58. No. 3. P. 446–454. <https://doi.org/10.1134/S106345412570044X>.
- [2] Galushina T. Yu., Ryabova G. O., Skripnichenko P. V. The force model for asteroid (3200) Phaethon // Planetary and Space Science. 2015. V. 118(50). P. 296–301. DOI: 10.1016/j.pss.2015.06.014.
- [3] Galushina T. Yu., Letner O. N., Niganova E. N. Notes on force models for near-Sun asteroids // Planetary and Space Science. 2021. V. 202. Article 105232. <https://doi.org/10.1016/j.pss.2021.105232>.
- [4] Galushina T. Y., Bykova L. E., Letner O. N., Baturin A. P. IDA software for investigating asteroid dynamics and its application to studying the motion of 2012 MF7 // Astronomy and Computing. 2019. V. 29. Article 100301. <https://doi.org/10.1016/j.ascom.2019.100301>

SELECTION OF NEAR-EARTH ASTEROIDS AND INITIAL TRAJECTORY DESIGN FOR TRANSFER TO EARTH-RESONANT ORBIT

O. S. Chernenko, V. A. Zubko, M. V. Pupkov, N. A. Eismont

Space Research Institute RAS, Moscow, Russia, o.chernenko@cosmos.ru

KEYWORDS:

near-Earth asteroids, gravitational capture, planetary defense

INTRODUCTION:

Modern missions to small bodies of the Solar System increasingly rely on energy-efficient ballistic solutions, especially in the context of planetary defense and asteroid deflection technologies. One of the most promising strategies involves transferring an asteroid onto an orbit resonant with Earth, which enables regular encounters with the Earth–Moon system and creates favorable conditions for gravitational capture without the need for high-energy braking maneuvers.

MISSION CONCEPT:

This study considers a transfer scheme for near-Earth asteroids to a heliocentric orbit with a period close to one Earth year [1, 2]. Special attention is given to the selection of suitable targets and the design of the initial phase of the mission, including departure from low Earth orbit (LEO), rendezvous with the asteroid, and a single impulse maneuver that places it on a resonant trajectory. Transfer trajectories were constructed for selected asteroids using chemical propulsion systems. The resulting orbital configurations ensure stable annual encounters with Earth, and minor angular adjustments allow for close approaches to the Moon without the need for additional impulsive corrections. This work lays the foundation for further studies on multi-flyby lunar capture and low-thrust trajectory optimization, forming the initial stage of an extended research project. Numerical simulations were performed using Lambert problem solvers and integration of full equations of motion under the perturbations from the Sun, Earth, and Moon. The analysis used JPL DE ephemerides and an adaptive Runge–Kutta integration scheme.

RESULTS:

The analysis demonstrates that a well-chosen combination of target selection and initial maneuver parameters can significantly reduce the mission's energy budget. A single-impulse transfer to a resonant orbit enables further passive capture through natural dynamics within the Earth–Moon system. Such strategies can be used not only for planetary defense but also for asteroid resource utilization and demonstration of low-energy capture techniques for small-body missions.

REFERENCES:

- [1] Ledkov A. A., Eismont N. A., Nazirov R. R. et al. A method for capturing asteroids into earth satellite orbits // *Astronomy Letters*. 2015. V. 41(8). P. 442–449. DOI: 10.1134/S1063773715080058.
- [2] Ledkov A. A., Eismont N. A., Boyarskii M. N. et al. Control of the motion of near-Earth asteroids // *Astronomy Letters*. 2015. V. 41. Iss. 1–2. P. 67–83. DOI: 10.1134/S1063773715020036.

SCENARIOS FOR THE FORMATION OF THE YOUNG EMILKOVALSKI ASTEROID FAMILY

E. D. Kuznetsov, A. S. Perminov, V. S. Safronova

Ural Federal University, Yekaterinburg, Russia, eduard.kuznetsov@urfu.ru, alexander.perminov@urfu.ru, v.s.safronova@urfu.ru

KEYWORDS:

Emilkowalski family, family formation scenario, numerical modelling, convergence of nodal and apsidal lines, Kholshvnikov metrics, cascade decay, Yarkovsky effect

INTRODUCTION:

The young Emilkowalski asteroid family is located in the central Main Belt: semi-major axis $a = 2.60$ a.u., eccentricity $e = 0.15$, inclination $i = 17.75^\circ$. In 2006 Nesvorný and Vokrouhlický [1] considered Emilkowalski family as a cluster of three asteroids in close heliocentric orbits: (14627) Emilkowalski, (126761) 2002 DW10, and (224559) 2005 WU179. The first estimate of the age of the family at 220 ± 30 kyr [1] showed that it is a young family. Vereš et al. [2] estimated the taxonomic type of asteroid (14627) Emilkowalski based on photometric observations as type D.

Pravec et al. [3] and Fatka et al. [4] discovered new family members and brought the number of asteroids in the family to nine. Age estimates of the "main asteroid (14627) Emilkowalski — secondary asteroid" pairs were obtained in papers [3] and [4]. Estimates of the formation age of the oldest pair (14627) Emilkowalski – (476673) 2008 TN44 are $3.447^{+0.524}_{-0.898}$ Myr [3] and $3.020^{+1.232}_{-1.340}$ Myr [4]. It was shown that at least two decay events of the parent asteroid of this family occurred in the last 5 Myr. This is consistent with the scenario of cascading disintegration of the parent body. Kuznetsov et al. [5] added four new members of the Emilkowalski family. Thus, 13 asteroids that are members of the Emilkowalski family are currently known.

Kuznetsov et al. [6] considered the young Emilkowalski asteroid family from the point of view of studying the formation process and attempting to reconstruct the chronological sequence of the parent body breakup based on nominal orbits. It is possible that the family is significantly younger than previously thought. According to the constructed scenario, the age of the family does not exceed 1.5 Myr.

In this paper, we estimate the ages of asteroid pairs in the Emilkowalski family from the results of probabilistic evolution modeling to verify and refine the family formation scenario.

METHODS:

In the probabilistic evolution modeling, 250 clones were generated for each asteroid. The linear stochastic scheme $\mathbf{e} = \mathbf{e}_0 + \mathbf{L}\mathbf{r}$ was used. Here \mathbf{e}_0 and \mathbf{e} are vectors of orbital elements of the (nominal) asteroid and its (virtual) clone, respectively; \mathbf{L} is the Choletsky decomposition matrix for the covariance matrix of parametric errors $\mathbf{C}: \mathbf{C} = \mathbf{L}\mathbf{L}^T$; \mathbf{r} is a six-dimensional vector of independent standard normally distributed random variables.

Improved orbital elements and covariance matrices for the asteroids of the Emilkowalski family for epoch MJD 60800 (05.05.2025) were obtained from AstDyS Database (<https://newton.spacedys.com/astdys/>). As a result, 250 variants of dynamical evolution were modeled for each asteroid, and 62500 evolutionary variants were considered for each pair. Numerical simulations of the dynamic evolution of asteroids were performed using the Orbit9 software included in the OrbFit software package (<http://adams.dm.unipi.it/orbfit/>). Perturbations from eight major planets and the dwarf planet Pluto, the Sun's oblateness, relativistic effects, and the influence of the Yarkovsky effect as the drift rate of the semi-major axis da/dt were considered. The integration interval was 2 Myr.

Estimation of the drift rate of the semi-major axis da/dt was performed using a modified version of the Orbit9 software included in the OrbFit package (<https://github.com/Fenu24/OrbFit>) [7], which provides the possibility of taking into account the influence of the Yarkovsky effect and the YORP effect on the basis of setting the dynamic (period of axial rotation and inclination of the rotation axis), physical (density) and thermophysical (heat capacity, thermal conductivity, radiation and absorption coefficients of surface layers) parameters of the asteroid.

When considering the influence of the Yarkovsky effect, we used physical and thermophysical parameters for D-type asteroids [8]: density $\rho = 1300 \text{ kg}\cdot\text{m}^{-3}$, thermal inertia $\Gamma = 580 \text{ J}\cdot\text{m}^{-2}\cdot\text{K}^{-1}\cdot\text{s}^{-1/2}$, coefficients of emission $\alpha = 1$ and absorption $\beta = 1$. For asteroids (14627) Emilkowalski, (126761) 2002 DW10, (224559) 2005 WU178, (256124) 2006 UK337, (434002) 2000 SM320 the positions of the rotation axes are known, so only one variant of the Yarkovsky effect was considered for them. For the other asteroids, three variants of the initial position of the rotation axis were considered: the axis is orthogonal to the orbital plane in clockwise and counterclockwise rotation, and the rotation axis lies in the orbital plane. If the pair has both asteroids with known rotational axis position, we get one age estimate. If the position of the rotation axis is known for one asteroid in the pair, we get three age estimates for the pair. If the position of the rotation axis is not known for both asteroids of the pair, then — nine estimates.

We considered three methods for estimating the age of pairs: 1) searching for moments of low relative-velocity close encounters of asteroids, 2) analyzing the moments of encounters of the nodal and apsidal lines, and 3) achieving the minimum of the Kholoshevnikov metric ρ_2 [9]. The low relative-velocity close encounters method yielded large uncertainties in the results and was therefore not used to obtain final age estimates for the pairs. Methods for searching for moments of minima of the Kholoshevnikov metric and approaches of nodal and apsidal lines gave consistent age estimates. In the method of searching for convergence of nodal and apsidal lines, we searched for the time t of reaching the minimum of the function $f(t) = (\Delta\Omega(t)^2 + \Delta g(t)^2)^{1/2}$, where $\Delta\Omega$ and Δg are the differences of longitudes of ascending nodes and arguments of pericenters, respectively. The minimum errors in estimating ages were obtained using a smoothing filter moving average.

RESULTS AND DISCUSSIONS:

Based on age estimates obtained from the results of probabilistic evolution, we adjusted the preliminary scenario for the formation of the Emilkowalski family. Table 1 provides estimates of the age of family pairs as median values with 5 and 95 percentiles. According to the presented scenario, the asteroid family was formed because of the cascade destruction of the parent body. The beginning of the family formation corresponds to an event that occurred with the parent body of the family 1.26 Myr. Then, three intervals can be distinguished during which further destructions of intermediate parent bodies occurred: 957-926, 753-636, and 313-187 thousand years ago.

Table 1. Estimating the age of pairs of asteroids in the Emilkowalski family

Asteroid pair	Age, kyr
(14627) Emilkowalski — 2009 VF107 (N)	1263_{-1}^{+1}
(14627) Emilkowalski — (476673) 2008 TN44 (S)	957_{-22}^{+0}
2009 VF107 (N) — 2015 WH29 (N)	956_{-22}^{+0}
(14627) Emilkowalski — 2022 SA160 (P)	934_{-87}^{+55}
(14627) Emilkowalski — (653857) 2014 UV143 (S)	926_{-0}^{+0}
2016 CS377 (N) — 2022 SA160 (P)	753_{-181}^{+604}
(476673) 2008 TN44 (S) — (679223) 2018 VB69 (N)	744_{-0}^{+0}

Asteroid pair	Age, kyr
(476673) 2008 TN44 (S) — 2017 UY114 (N)	636 $^{+21}_{-18}$
(434002) 2000 SM320 — 2017 UY114 (N)	313 $^{+8}_{-0}$
(14627) Emilkowalski — (224559) 2005 WU178	274 $^{+1}_{-0}$
(14627) Emilkowalski — (256124) 2006 UK337	194 $^{+0}_{-7}$
(14627) Emilkowalski — (126761) 2002 DW10	187.04 $^{+1201}_{-0}$

Notes: The designation N corresponds to the tilt of the rotation axis relative to the orbit plane $\varphi = 0^\circ$, P corresponds to $\varphi = 90^\circ$, S corresponds to $\varphi = 180^\circ$.

CONCLUSIONS:

In this work, a scenario for the formation of the young Emilkowalski asteroid family was developed. The next important stage of the work is to establish the feasibility of the proposed scenario and, if possible, the events that led to the formation of new members of the family: collisions, disintegration of binary and multiple systems, etc.

ACKNOWLEDGMENTS:

The study was funded by the Russian Science Foundation grant No. 24-22-00143, <https://rscf.ru/en/project/24-22-00143/>.

REFERENCES:

- [1] *Nesvorný D., Vokrouhlický D.* New candidates for recent asteroid breakups // *The Astronomical J.* 2006. V. 132. No. 5. P. 1950–1958. DOI 10.1086/507989.
- [2] *Vereš P., Jedicke R., Fitzsimmons A. et al.* Absolute magnitudes and slope parameters for 250,000 asteroids observed by Pan-STARRS PS1 — Preliminary results // *Icarus.* 2015. V. 261. P. 34–47. DOI: 10.1016/j.icarus.2015.08.007.
- [3] *Pravec P., Fatka P., Vokrouhlický D. et al.* Asteroid clusters similar to asteroid pairs // *Icarus.* 2018. V. 304. P. 110–126.
- [4] *Fatka P., Pravec P., Vokrouhlický D.* Cascade disruptions in asteroid clusters // *Icarus.* 2020. V. 338. Article 113554. <https://doi.org/10.1016/j.icarus.2017.08.008>.
- [5] *Kuznetsov E. D., Vasilieva M. A., Perminov A. S., Safronova V. S.* Search for new members of young asteroid families // *Solar System Research.* 2025. V. 59(1). Article 8. 12 p. DOI: 10.1134/S0038094624601129.
- [6] *Kuznetsov E. D., Safronova V. S., Vasilieva M. A., Perminov A. S.* Constructing a scenario for the formation of the Emilkowalski family based on modeling the evolution of nominal orbits of asteroids // *Solar System Research.* 2025. V. 59. Article 10. 9 p. <https://doi.org/10.1134/S0038094624601403>.
- [7] *Fenucci M., Novakovic B.* MERCURY and ORBFIT packages for numerical integration of planetary systems: implementation of the Yarkovsky and YORP effects // *Serbian Astronomical J.* 2022. V. 204. P. 51–63. DOI: 10.2298/SAJ2204051F.
- [8] *Ribeiro T. M., D'Ambrosio A., Calabuig G. J. D. et al.* CARINA: A near-Earth D-type asteroid sample return mission // *Acta Astronautica.* 2023. V. 212. P. 213–225. <https://doi.org/10.1016/j.actaastro.2023.07.035>.
- [9] *Kholshchikov K. V., Kokhirova G. I., Babadzhanov P. B., Khamroev U. H.* Metrics in the space of orbits and their application to searching for celestial objects of common origin // *Monthly Notices of the Royal Astronomical Society.* 2016. V. 462. Iss. 12. P. 2275–2283. <https://doi.org/10.1093/mnras/stw1712>.

izMETEORS: METEOR EVENT DETECTION NETWORK AND DATABASE

M. Yu. Khovrjichev¹, I. S. Izmailov^{1,2}, D. A. Bikulova^{1,2}, S. R. Pavlov¹, A. L. Tolstoy¹

¹ *Institute of Applied Astronomy RAS, Saint Petersburg, Russia*
gmymax@gmail.com

² *Pulkovo Observatory RAS, Saint Petersburg, Russia*

KEYWORDS:

meteor shower, meteor event detection, database, image analysis, AI-instruments

INTRODUCTION:

Over the past decade, we have witnessed the rapid growth of meteor event detection systems operating in the optical bandpass, along with the development of corresponding databases. These databases provide results from raw data analysis, which includes video streams or consecutive image frames. They offer detailed information on individual meteor events, such as the time of occurrence and positions on the celestial sphere, as well as insights that can be derived from a set of individual event data, including radiant evolution, ZHR, and orbital parameters.

Perhaps the most well-known meteor camera network is the Global Meteor Network (GMN, <https://globalmeteornetwork.org/>) [1]. One of the main advantages of the GMN database is a special Python code for data access. The GMN data are extracted from globally distributed small cameras with an angular scale of about ten of arcmins per pixel. This decreases the final data accuracy and applicability to the set of meteor astronomy problems. There are several similar types of data sources that are available at the Meteor Data Center (MDC) of the IAU (<https://www.iaumeteordatacenter.org/>), usually as plain text (sometimes as CSV) tables. A significant improvement in the accuracy and availability of faint meteor data was demonstrated by the Mini-MegaTORTORA (MMT, <http://mmt.favor2.info/>) system [2]. Here, we see simple text tables for different nights and some visualization of individual events.

The natural data set traditionally available from numbered databases usually includes RA and DEC for starting and final points, angular velocity, and minimal and maximal brightness. However, for a significant part of the modern applications, a set of sequential event images is required. Here we present the meteor event detection network izMeteors and the corresponding database (<https://izmeteors.ru/>, and a mirror at izmeteors.puldb.ru). Our database provides access to both traditional meteor event data and a compressed image set, which is one of the main advantages of our data product.

IZMETEORS METEOR EVENT DETECTION NETWORK:

Our meteor event detection network relies on intermediate optics. This approach avoids very short focal length lenses, which have an angular scale of approximately 10 arcmin per pixel. The frame field of view is 50×30° with a scale of 3 arcmin/pix. The fundamental pipeline for event detection is outlined in papers [3] and [4], with partial availability on GitHub (<https://github.com/ymax74/szm>). The link <http://sfa.puldb.ru:9010/MetObs/Assy-Turgen/MetVideo/m2025x05x24T20h17m34s.mp4> demonstrates the typical set of frames for the event.

Our meteor monitoring network was established one year ago. The cameras are located at Pulkovo Observatory (59.771771, 30.326226), Zlobino station (55.414497, 41.554068), Ka-Dar Observatory (43.652548, 41.428386), and Assy-Turgen Observatory of the V. G. Fesenkov Astrophysical Institute (FAI) of the National Center for Space Research and Technology under the Aerospace Committee of the Republic of Kazakhstan (43.227172, 77.872787). Additionally, this high-altitude observatory is home to the Pulkovo 40-cm telescope and the WFOS-40 telescope, designed by FAI specialists.

A distinctive feature of the network is the complete automation of work and the minimization of the efforts of observatory engineers to maintain equipment. The video stream analysis from the cameras is conducted using energy-efficient computers running Windows 10 in real time.

The video feed from Astroverti astrofarm cameras was analyzed simultaneously using software developed for the GMN network and the izMeteor pipeline. It turned out that izMeteor reliably detects about 1.5 times more meteor phenomena.

CONCLUSIONS:

The izMeteors network (<https://izmeteors.ru/>) has been constructed at the IAA RAS and the Pulkovo Observatory. Data on 60,000 individual meteor events are currently available. The system collects 500–1000 events each night. Alongside the standard data set for each event, compressed image sets are available. This data can be utilized for reprocessing and training neural networks to identify the characteristics of meteor events. For instance, meteor phenomena caused by cometary particles can exhibit different behaviors compared to those caused by meteoroids that have been ejected from asteroid surfaces when they enter the atmosphere.

ACKNOWLEDGMENTS:

The research received funding from the Russian Science Foundation and the Saint Petersburg Science Foundation, project 24-22-20044 “Investigation of a low-mass fraction of meteoroid streams associated with the near-Earth asteroids”, <https://rscf.ru/en/project/24-22-20044/>.

REFERENCES:

- [1] *Vida D., Šegon D., Gural P.S. et al.* The Global Meteor Network — Methodology and first results // *Monthly Notices of the Royal Astronomical Society*. 2021. V. 506. Iss. 4. P. 5046–5074. <https://doi.org/10.1093/mnras/stab2008>,
- [2] *Karpov S., Orekhova N., Beskin G. et al.* Two-station Meteor Observations with Mini-MegaTORTORA and FAVOR Wide-Field Monitoring Systems // *Revista Mexicana de Astronomía y Astrofísica Conference Series*. 2019. V. 51. P. 127–130.
- [3] *Izmailov I., Khovritchev M., Tolstoy A. et al.* Detection of meteor event images using the SSA400 telescope at the Assy-Turgen Observatory // *Publications of the Pulkovo Observatory*. 2024. V. 234. P. 22–35.
- [4] *Izmailov I., Khovritchev M., Tolstoy A. et al.* Detecting low signal-to-noise meteor images in the astronomical camera video stream // *Modern Astronomy: From the Early Universe to Exoplanets and Black Holes (VAK2024)*. 2024. P. 911–914. DOI: 10.26119/VAK2024.144.

MODELING THE DYNAMICS OF DUST PARTICLES IN THE GRAVITATIONAL AND ELECTROSTATIC FIELDS OF A PRIMITIVE ASTEROID TAKING INTO ACCOUNT THE SUBLIMATION OF WATER ICE

S. Y. Kuznetsov^{1,2}, V. V. Busarev²

¹ *Lomonosov Moscow State University, Faculty of Space Research
Moscow, Russia, imarpus@gmail.com*

² *Sternberg Astronomical Institute Moscow University, Moscow, Russia
busarev@sai.msu.ru*

KEYWORDS:

active asteroids, dust, dynamics, exosphere, surfaces, regolith

INTRODUCTION:

The solution to the two-body problem for dust particles near asteroids differs significantly from similar problems for objects of greater mass and size. Due to the fact that dust particles are small in size and weight, they are much more significantly affected by various small disturbing forces [1–3]. These forces include the radiation pressure of the Sun, which is the main mechanism for the loss of the dust exosphere of comets and asteroids that are close enough to it. Although radiation pressure weakens in the main asteroid belt, it is still a significant factor influencing the trajectory of dust particles, and if the asteroid itself is small enough, it can be the main mechanism for the loss of the dust exosphere. In addition to radiation pressure, the solar corona emits a stream of ionized particles (mainly helium-hydrogen plasma) that interacts with the asteroid's surface and forms an electrostatic field near it. These electrostatic forces [4–6] are the main forces affecting the dynamics of dust particles near the asteroid's surface.

MATHEMATICAL MODEL:

In general this results in the following differential equation describing the trajectory of a dust particle ejected from the surface of a 5-km asteroid:

$$\ddot{\vec{r}} = -\frac{GM\vec{r}}{r^3} + \frac{Q_d(t)}{m_p} [E(\vec{r}) + \dot{\vec{r}} \times B(\vec{r})] + \frac{1}{m_p} F_{SRP}(\vec{r}), \quad (1)$$

where $Q_d(t)$ is the charge; m_p is the mass of the dust particle; $F_{SRP}(\vec{r})$ is the solar radiation pressure. $E(\vec{r})$ and $B(\vec{r})$ are the electric and magnetic fields, respectively.

The initial potential of the asteroid surface and the electric field are calculated by the interaction of the solar wind plasma with the asteroid surface using the "Particle-in-Cell" method [7]. This method allows the actual number of solar wind ions and electrons to be replaced by a smaller number of macroparticles, which significantly reduces the calculations required for plasma modeling. The edges of the calculated area are open boundaries, and the asteroid's surface is the boundary between two environments: the dust layer of regolith and the drifting field of the solar wind plasma flow. Due to the low density of the solar wind plasma, the motion of plasma particles is considered to be collisionless, and the magnetic field can be neglected. Plasma particles move with a certain initial velocity toward the asteroid under the action of the Lorentz force.

PRELIMINARY RESULTS:

Although the Particle-in-Cell method significantly reduces the amount of calculations required, it still requires considerable computing resources. The method is also demanding in terms of the constructed grid and time step. As a result, a fairly small grid (about 40×20×40 cells) has to be used for a real asteroid, so at this stage of the work, we can only talk about preliminary results (Figure 1). The simulation species include solar wind ions and electrons, and photoelectrons.

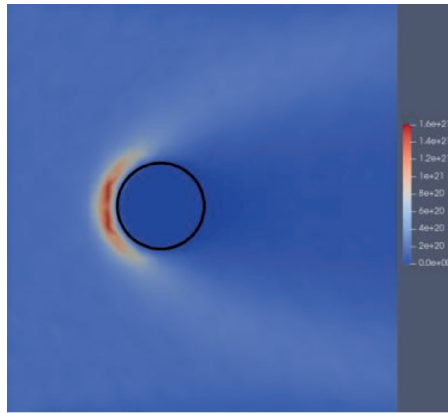


Figure 1. Concentration of charged particles near the asteroid (black circle)

The calculations were performed for an asteroid with a radius of 5 km and a density of $1.7 \text{ g}\cdot\text{cm}^{-3}$ at a distance of 3 a.u. from the Sun. A dust particle with a radius of $1 \mu\text{m}$, a density of $1.7 \text{ g}\cdot\text{cm}^{-3}$, and an optical coefficient of $Q_{pr} = 1$. The dust particle moves only in the gravitational field of the asteroid. Eq. 1 can be represented as follows:

$$\ddot{r} = a_g + a_{ES} + a_{SRP},$$

where a_g , a_{ES} , and a_{SRP} are the gravitational, electrostatic, and solar influences on the dynamics of the dust particle. In this case, we can estimate the order of magnitude of the contribution of all forces:

- a_g up to 10^{-3} near the surface;
- a_{ES} up to 10^{-1} near the terminator;
- a_{SRP} constant due to the order of magnitude 10^{-5} .

As can be seen, the contribution of non-gravitational forces can even exceed the gravitational force of the asteroid. This can be clearly seen in the graphs in Figure 2. They show two trajectories of a dust particle: one due to gravity alone (left graph) and one with the influence of all the above forces. In both cases, the particle is launched at an angle of 70° with a speed of 1.4 m/s, which is one of the possible scenarios for the ejection of a dust particle in the case of water ice sublimation.

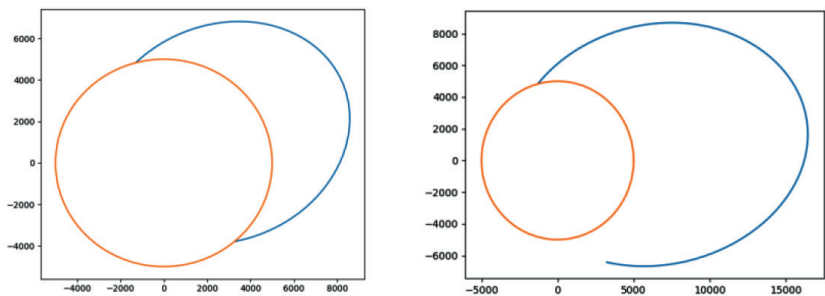


Figure 2. Trajectory due solely to gravitational forces on the left, $t = 10\,000$ s. Trajectory taking into account electrostatic forces and solar wind pressure on the right, $t = 25\,000$ s

CONCLUSION:

The following objectives were achieved during the course of the work:

1. A mathematical model of the dynamics of dust particles in the gravitational and electrostatic fields of a primitive asteroid was developed.
2. A model of the interaction of solar wind plasma with the surface of an asteroid was developed.
3. Estimates were given for the influence of forces on dust particles near an asteroid with a radius of 5 km.

It is possible to talk about the influence of the electrostatic field and solar radiation pressure on the trajectories of dust particles (sometimes even of a higher order than gravitational forces). Dust emissions due to sublimation of water ice near the terminator allow dust particles to remain around the asteroid longer (several times compared to movement only due to gravity Figure 2) owing to the influence of electrostatic forces. As a result, we can say that a thin and relatively stable dust exosphere (with a thickness in the range of 10–1000 m and an optical thickness of $t < 0.5$) can form on the illuminated side of the asteroid consisting of particles of minimum size (0.01–1.0 μm) in the form of a plasma-dust layer close to the surface, provided that the rate of dust particle ejection into this layer during water ice sublimation exceeds the rate of their ejection by the electrostatic field near the terminator.

REFERENCES:

- [1] *Poppe A. R.* An improved model for interplanetary dust fluxes in the outer Solar System // *Icarus*. 2016. V. 264. P. 369–386. DOI: 10.1016/j.icarus.2015.10.001.
- [2] *Hartzell C. M.* Dynamics of 2D electrostatic dust levitation at asteroids // *Icarus*. 2019. V. 333. P. 234–242. DOI: 10.1016/j.icarus.2019.05.013.
- [3] *Yu W., Han D., Wang J. J.* Numerical Modeling of Dust Dynamics Around Small Asteroids // *AIAA SPACE Conf.* 2016. DOI: 10.2514/6.2016-5447.
- [4] *Collier M. R., Farrell W. M., Stubbs T. J.* The lunar dust pendulum // *Advances in Space Research*. 2013. V. 52. Iss. 2. P. 251–261. DOI: <https://doi.org/10.1016/j.asr.2012.09.044>.
- [5] *Nitter T., Havnes O.* Dynamics of dust in a plasma sheath and injection of dust into the plasma sheath above Moon and asteroidal surfaces // *Earth, Moon, and Planets*. 1992. V. 56. P. 7–34. DOI: 10.1007/bf00054597.
- [6] *Lee P.* Dust Levitation on Asteroids // *Icarus*. 1996. V. 124. Iss. 1. P. 181–194. DOI: 10.1006/icar.1996.0197.
- [7] *Han D., Wang J.* 3-D Fully Kinetic Particle-in-Cell Simulations of Small Asteroid Charging in the Solar Wind // *IEEE Trans. Plasma Science*. 2019. V. 47. Iss. 8. P. 3682–3688. DOI: 10.1109/TPS.2019.2919895.
- [8] *Roussel J.-F., Dufour G., Mateo-Velez J.-C. et al.* SPIS Multiscale and Multiphysics Capabilities: Development and Application to GEO Charging and Flashover Modeling // *IEEE Trans. Plasma Science*. 2012. V. 40. P. 183–191. DOI: 10.1109/TPS.2011.2177672.

METEOR OBSERVATIONS FROM RUSSIA AND TAJIKISTAN STATIONS

A. Kartashova¹, G. Kokhirova²

¹ Institute of Astronomy RAS, Moscow, Russia, akartashova@inasan.ru

² Institute of Astrophysics of National Academy of Science of Tajikistan Dushanbe, Tajikistan

KEYWORDS:

meteors, meteoroids, double-stations observations

INTRODUCTION:

Meteor observations are needed to solve various near-Earth environmental fundamental and applied tasks. Ideally, meteor observations should be carried out around the clock and all year round (24 hours per day / 7 days per week / 365 days per year). It is more convenient to analyze the characteristics of both meteoroids themselves and their streams based on the same type of data. Therefore, the location of meteor systems in different parts of the world is an approximation to the non-stop observation option. In order to implement a meteor network with stations spaced by longitude, to study their capabilities and work features, in 2024, the same type of meteor systems were launched on the territory of Russia and Tajikistan. Observations were organized by Institute of Astronomy RAS and Institute of Astrophysics NAST.

OBSERVATIONS AND RESULTS:

The observations were carried out from several stations (Dushanbe-Sanglokh (Tajikistan) and Zvenigorod–Mikhnevo–Ryazan (Russia)) that formed the double-station observations and allowed to get individual parameters for each meteor event. For our observations, we selected cameras that are widely used in the world (as part of the GMN (<https://global-meteor-network.org/>)). Sony IMX 307 cameras with 4 mm lenses are used for observations (with field of view of $87 \times 45^\circ$); RMS software (<https://global-meteor-network.org/>) [1, 2] is used for observations and primary processing. Individual parameters of each meteor event can be calculated by double-stations observations. Two types of software (UFO (sonotaco.com) and RMS (<https://global-meteor-network.org/>)) were used for meteor parameters calculations.

Several hundred basic meteors have been detected since the cameras were first launched in November 2024.

Examples of parameters distributions of the fireball detected in 01.06.2025 in 22:24:56 UTC in Zvenigorod Observatory INASAN (ZV) and Astronomical Observatory of Ryazan State University (RZ) are presented at the Figure 1, 2. The distance between RZ and ZV stations is 220 km.

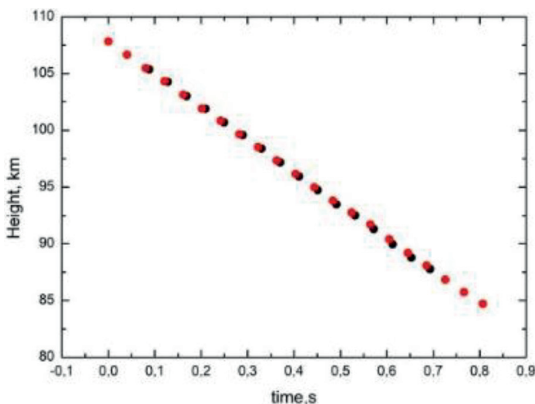


Figure 1. Distribution of the 20240601_222456 meteor height by time. Red line — ZV, Black line — RZ

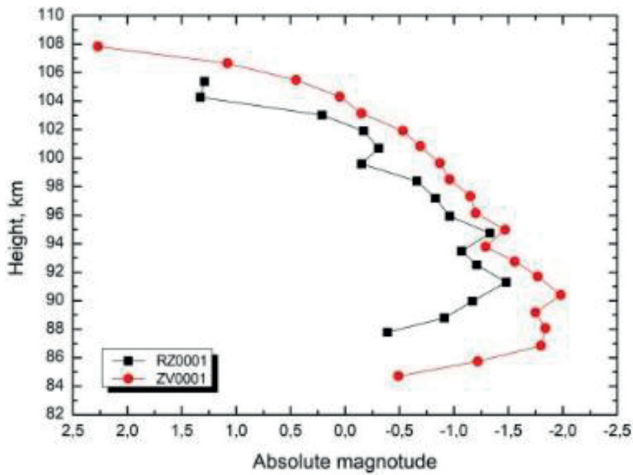


Figure 2. Light curve of the 20240601_222456 meteor. Red line — ZV, Black line — RZ

Examples of parameters of fireballs detected at Tajikistan stations 16.03.2025 in 20:38:53 and at Russian stations 01.06.2025 in 22:24:56 are presented in Tables 1–4.

Table 1. Parameters of the 20240601_222456 meteor obtained by RMS and UFO software

Software	M_a	Mass ($\tau = 0.7\%$), kg	RA, deg	DEC, deg	V_g , km/s	H_{br} , km	H_{cr} , km
RMS	-1.98	$3.32 \cdot 10^{-4}$	355.498 ± 0.171	$+45.897 \pm 0.102$	49.108 ± 0.036	106.660 ± 0.04	85.736 ± 0.03
UFO	-2.034	–	357.192	+45.787	49.112	109.544	86.717

Table 2. Orbital parameters of the 20240601_222456 meteor obtained by RMS and UFO software

Software	a , au	e	q , au	i , deg	peri, deg	node, deg
RMS	6.214 ± 0.111	0.889 ± 0.002	0.686 ± 0.002	88.628 ± 0.146	108.181 ± 0.283	71.317 ± 0.00001
UFO	8.096	0.919	23.045	87.654	105.401	70.358

Table 3. Parameters of the 20250316_203853 meteor obtained by RMS and UFO software

Software	M_a	Mass ($\tau = 0.7\%$), kg	RA, deg	DEC, deg	V_g , km/s	H_{br} , km	H_{cr} , km
RMS	-0.54	$6.78 \cdot 10^{-4}$	166.567 ± 0.046	-3.816 ± 0.223	23.822 ± 0.008	98.617 ± 0.06	76.819 ± 0.03
UFO	-0.405	–	166.826	-3.438	23.249	97.038	78.263

Table 4. Orbital parameters of the 20250316_203853 meteor obtained by RMS and UFO software

Software	a , au	e	q , au	i , deg	peri, deg	node, deg
RMS	5.201 ± 0.079	0.875 ± 0.002	0.648 ± 0.0006	6.358 ± 0.154	75.366 ± 0.124	176.141 ± 0.0004
UFO	4.370	0.851	0.651	5.896	75.578	176.153

CONCLUSION:

Simultaneous observations allow us to obtain different characteristics of each meteor particle and their flux. Meteor observations on the same type of cameras from Russia and Tajikistan were started. A preliminary analysis of the obtained particle characteristics has been carried out. The analysis of the used meteor systems has been carried out. Observations are continuing.

ACKNOWLEDGMENTS:

We would like to thank Dr. D. Vida for his help in the work with RMS software. We would like to thank our colleagues for help in cameras install process.

REFERENCES:

- [1] *Vida D., Segon D., Gural P.S. et al.* The Global Meteor Network — Methodology and first results // *Monthly Notices of the Royal Astronomical Society*. 2021. V. 506. Iss. 4. P. 5046–5074. <https://doi.org/10.1093/mnras/stab2008>.
- [2] *Vida D., Gural P.S., Brown P.G. et al.* Estimating trajectories of meteors: an observational Monte Carlo approach — I. Theory // *Monthly Notices of the Royal Astronomical Society*. 2020. V. 491. Iss. 2. P. 2688–2705. <https://doi.org/10.1093/mnras/stz3160>.

COSMIC DUST COLLECTION NEAR VOSTOK STATION IN CENTRAL ANTARCTICA: RESEARCH PROBLEMS AND PROSPECTS

Y. O. Chetverikov¹, V. F. Ezhov¹, M. S. Glukhov², E. M. Ivankova³,
A. S. Loshachenko⁴, V. D. Kalganov⁴, O. V. Yakubovich⁵

¹ Petersburg Nuclear Physics Institute named by B. P. Konstantinov of NRC "Kurchatov Institute", Gatchina, Leningrad Region, Russia
chetverikov_yo@pnpi.nrcki.ru

² Zavaritsky Institute of Geology and Geochemistry, Ural Branch RAS
Yekaterinburg, Russia

³ Institute of Macromolecular Compounds RAS, Saint Petersburg, Russia

⁴ Saint Petersburg State University, Saint Petersburg, Russia

⁵ Institute of Precambrian Geology and Geochronology RAS
Saint Petersburg, Russia

KEYWORDS:

cosmic dust, meteor showers, resonant orbits, Vostok station, central Antarctica

ABSTRACT:

Cosmic dust (CD) collections obtained in 2017 and winter 2023/2024 by filtering fresh snow near the Vostok station in Central Antarctica (Figure 1), were studied using a scanning electron microscope. Morphology, structure and composition of particles falling to the surface of the Earth have been analyzed (Figure 2).



Figure 1. Collection of snow with cosmic dust in a clean area near Vostok station. 1 — building of the new station, 2 — clean room for changing clothes and preparing equipment, 3 — snow collection area). Photo by PJSC "Zapsibgazprom"

The CD flux distributions according to the time of deposition and the particle size distribution were determined [1]. The main attention was paid to the study of stability and fluctuations in the CD flow during the season of work 2023–2024 (28 days) with the time resolution (the interval between the closest collection samples) of one day. The range of sizes of obtained particles — from three to several hundred micrometers — is associated both with the rate of precipitation of particles (particles less than 3 μm fall down in the atmosphere during the several days) and the collecting technology (fresh snow with CD is transferred by the wind into the trench for collection and, therefore, do not contain massive particles). A comprehensive analysis of the collections of CD based on the results of seasonal work is a step towards the accumulation of such data on stability and fluctuations in the flow as: a) dynamics of the precipitation of the CD on Earth (pos-

sible fluctuations of flow caused by disturbances in resonant orbits of dust particles, associated with both the activity of the sun and the complexity of trajectory of the Earth's movement); b) detailing data on the structure, composition and dynamics of the passage of individual meteoroid showers with a possible identification of parental bodies (comets and asteroids).

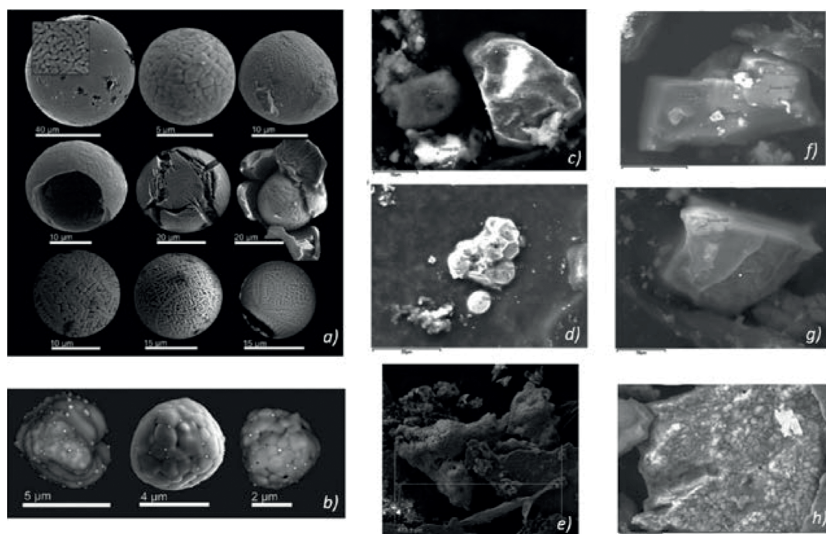


Figure 2. Examples of found cosmic dust particles: completely melted and oxidized in the atmosphere: *a* — iron oxides; *b* — O-Fe-Ni spherules; *c* — partially melted and burnt out in the atmosphere (practically melted olivine crystal; *d* — maussanite with regmaglypts; *e* — scoriaceous-type silicate; *f, g* — particles without visible traces of heating and melting (olivine and pyroxene crystallites; *h* — particle from stuck together micron silicate grains

REFERENCES:

- [1] Chetverikov Y.O., Ezhov V.F., Glukhov M.S. et al. Extraterrestrial dust flux monitoring at Antarctic Vostok station: New collection of extraterrestrial spherules fallen from May to September 2017 // *Meteoritics and Planetary Science*. 2023. V. 58. Iss. 6. P. 815–833. <https://doi.org/10.1111/maps.13991>.

PECULIARITIES OF DYNAMICS OF CHARGED DUST GRAINS EJECTED FROM THE SURFACES OF PHOBOS AND DEIMOS

N. D. Borisov

Space Research Institute RAS, Moscow, Russia, borisov@izmiran.ru

KEYWORDS:

dust motion, electric fields, dust rings, micrometeorites, Phobos and Deimos

ABSTRACT:

The problem of dust rings formation by Phobos and Deimos attracts attention for rather long time. There are publications in which the role of different factors in dust grains motion (the gravity, electric fields, solar radiation pressure, oblateness of Mars) is investigated for particles with various sizes (see, e.g., [1–3]). In these publications calculations are carried out for small initial velocities of dust grains (in accordance with the power-law distribution accepted for dust ejected from the Galilean moons). Based on the results of the LADEE mission quite different initial velocity distribution of dust grains ejected by micrometeorites bombardment from the Moon (with the pronounced maximum at rather high velocities) has been obtained not long ago [4]. As it is unclear what type of the initial velocity distribution for dust grains ejected from Phobos and Deimos is more suitable, it is worthwhile to investigate the behavior in time of dust grains with high enough initial velocities. In this presentation we discuss the influence of the main factors (the gravity, electric fields, and solar radiation pressure) on radial localization of dust particles with rather small sizes (less than a few microns) ejected from Phobos and Deimos. We present the results of numerical computations and argue that there could exist three populations of dust. For dust grains ejected from the front hemisphere (with respect to the orbital motion) by micrometeorites bombardment the orbital initial velocities are higher than the orbital velocity of the corresponding moon. These grains are situated at larger distances from Mars than the moon and their evolution in time is determined mainly by electric forces. The second population is formed by dust grains ejected from the rear hemisphere. These grains have initial orbital velocities smaller than one of the moon and occupy some space at distances between Mars and the moon. The last population is formed by charged dust grains raised from the surface by local electrostatic fields. Such grains have small initial velocities (of the order of a few meters per second). It is shown that some of these grains are accelerated in particular regions (like magnetosheath) and contribute to formation of a dust ring in the vicinity of the moon. In our calculations we take into account recent numerical simulations (based on the results of the MAVEN mission) that predict significant electric potentials in particular regions in plasma (up to 150 V in the magnetosheath of Mars and –100 V in the wake).

ACKNOWLEDGMENTS:

This research was supported by the Russian Science Foundation grant No. 24-12-00064, <https://rscf.ru/project/24-12-00064/>.

REFERENCES:

- [1] *Ip W.-H., Banaszekiewicz M.* On the dust/gas tori of Phobos and Deimos // *Geophysical Research Letters*. 1990. V. 17. Iss. 6. P. 857–860. <https://doi.org/10.1029/GL017i006p00857>
- [2] *Horanyi M., Tatrallyay M., Juhasz A., Luhman J. G.* The dynamics of submicron-sized dust particles lost from Phobos // *J. Geophysical Research: Space physics*. 1991. V. 96. Iss. A7. P. 11283–11290. <https://doi.org/10.1029/91JA00947>.
- [3] *Krivov A. V., Hamilton D. P.* Martian dust belts: waiting for discovery // *Icarus*. 1997. V. 128. Iss. 2. P. 335–353. <https://doi.org/10.1006/icar.1997.5753>.
- [4] *Szalay J. R., Horanyi M.* Lunar meteoritic gardening rate derived from in situ LADEE/LDEX measurements // *Geophysical Research Letters*. 2016. V. 43. Iss. 10. P. 4893–4898. <https://doi.org/10.1002/2016GL069148>.

METEORITE FUSION CRUST AS A RESULT OF THE IMPACT OF ABLATION PROCESSES ON THE METEOROID SUBSTANCE

E. V. Petrova, V. I. Grokhovsky

Ural Federal University, Ekaterinburg, Russia, evgeniya.petrova@urfu.ru

KEYWORDS:

meteorites, fusion crust, ablation, emission spectra, modeling

INTRODUCTION:

The features of the processes occurring in the plasma layer of slow meteoroids can be studied using: i — registration of the emission spectra of fireballs; ii — study of the phase and chemical composition of the fusion crust of meteorites; iii — conducting model experiments on ablation with the meteorite material in a plasma torch. This review examines current achievements in this area and formulates unanswered questions.

SPECTRA OF FIREBALLS

As meteor networks and amateur astronomy develop, the meteoroids pass through the atmosphere are recorded in detail. Not only do eyewitnesses or CCTV cameras give records, but they are remotely controlled and directed into the sky stationary cameras that are united in a network. Today, it has even become possible to observe the falls of asteroids that discovered on their approach to Earth [1, 2].

For a few registered meteorites, there is comprehensive data on their path through the atmosphere. The chemical composition of the Kindberg and Ribbeck meteorites matter was determined from the data of the luminescence spectra [1, 2]. However, measuring the emission spectra of a falling bolide requires a diffraction grating, which is not yet widely used. Nevertheless, the recent fall of a meteorite Smalyavichy in Belarus was recorded by a bolide network. The registered spectrum was compared with the composition of the fragments found [3, 4].

FUSION CRUST

Fusion crust formation occurs under the following conditions: velocity of the meteoroid is from 11 to 20 km/s [5]; duration of the fusion crust formation is of several seconds; temperature gradient on the meteorite surface is above 2000 °C [6]; thickness of the fusion crust depends on the type of meteoritic matter, that is usually less than 2 mm for stony meteorites.

Studies of the composition of the fusion crust in comparison with the internal substance of the meteorite using X-ray diffraction, magnetic measurements and Mössbauer spectroscopy methods showed some features of the fusion crust mineral composition. In particular, the phase ratio transformed, and new minerals formed [7–9]. In addition, the presence of PGE elements was found in the fusion crust of the Chelyabinsk LL5 chondrite, although they were not noted in internal substance, despite many studies in various laboratories [10].

MODELING OF ABLATION

Experiments with a plasmatron to model the ablation process on chondrite matter were carried out in laboratories [11–13]. Measurements of the spectra of the synthesized plasma recorded lines of iron, together with silicon, sodium, potassium, and manganese [11]; and iron, copper (that was pollution from the holder) [12]. The atomic lines of nitrogen and oxygen appear from the air in a plasma flow in both [11] and [12].

Thus, a fusion crust is the result of interaction between meteorite material and the atmosphere under high-energy circumstances of the ablation process. From this point of view “we know what it was, what was gone, and what remained”. It was noticed that non-volatile elements heavier than Ni and Co tend to accumulate in the fusion crust of chondrites.

ACKNOWLEDGMENTS:

This research was funded by the Russian Science Foundation, project No. 24-27-00392, <https://rscf.ru/project/24-27-00392/>.

REFERENCES:

- [1] *Gattacceca J., Mccubbin F.M., Grossman Jeffrey et al.* Meteoritical Bulletin No. 110 // Meteoritics and Planetary Science. 2022. V. 57. P. 2102–2105. DOI: 10.1111/maps.13918.
- [2] *Spurný P., Borovicka J., Shrubny L. et al.* Atmospheric entry and fragmentation of small asteroid 2024 BX1: Bolide trajectory, orbit, dynamics, light curve, and spectrum // Astronomy and Astrophysics. 2024. Article 49735.
- [3] *Grokhovsky V.I., Petrova E.V. Yakovlev G.A. et al.* Matching of the Compositions of Chondrites and Their Fusion Crust with the Emission Spectra of Meteoroids // 87th Annual Meeting of the Meteoritical Society 2025 (LPI Contrib. No. 3088). Article 5208.
- [4] *Dugushkina K.A., Sharygin V.V. Yakovlev G.A. et al.* Mineralogy of Smalyavichy H6 Chondrite, a New Meteorite in Belarus // 87th Annual Meeting of the Meteoritical Society 2025 (LPI Contrib. No. 3088). Article 5268.
- [5] *Drolshagen E., Ott T., Koschny D. et al.* Velocity distribution of larger meteoroids and small asteroids impacting Earth // Planetary and Space Science. 2020. V. 184. Article 104869. <https://doi.org/10.1016/j.pss.2020.104869>.
- [6] *Hezel D.C., Poole G.M., Hoyes J. et al.* Fe and O isotope composition of meteorite fusion crusts: Possible natural analogues to chondrule formation? // Meteoritics and Planetary Science. 2015. V. 50. Iss. 2. P. 229–242. DOI: 10.1111/maps.12414.
- [7] *Maksimova A.A., Petrova E.V., Chukin A.V. et al.* Characterization of the matrix and fusion crust of the recent meteorite fall Ozerki L6 // Meteoritics and Planetary Science. 2020. V. 55. Iss. 1. P. 231–244.
- [8] *Oshtrakh M.I. et al.* Hyperfine Interactions. 2023. V. 224, No. 22.
- [9] *Petrova E.V., Chukin A.V., Varga G. et al.* Characterization of bulk interior and fusion crust of Calama 009 L6 ordinary chondrite // Meteoritics and Planetary Science, 2024. V. 59. Iss. 10. P. 2865–2879. <https://doi.org/10.1111/maps.14249>.
- [10] *Sharygin V.V.* Nickel-rich metal-sulfide globules in fusion crust of Chelyabinsk meteorite // Meteoritics and Planetary Science. 2019. V. 54. SI. Article A6363.
- [11] *Loehle S., Zander F., Hermann T. et al.* Experimental Simulation of Meteorite Ablation during Earth Entry Using a Plasma Wind Tunnel // The Astrophysical J. 2017. V. 837. No. 2. Article 112. DOI: 10.3847/1538-4357/aa5cb5.
- [12] *Wang L., Dang L.N., Yang L.W. et al.* Study of Iron and Stony Meteorite Ablation Based on Simulation Experiments in an Arc Heater // The Astrophysical J. 2024. V. 962. No. 1. Article 23. DOI: 10.3847/1538-4357/ad063c.
- [13] *Kopysov A.S., Petrova E.V., Kokorin A.F. et al.* Identification of the cosmic spherules in the modern urban sediments // Meteoritics and Planetary Science, 2018. V. 53. SI. Article A144. P. 6201–6201.

INVESTIGATION OF ELECTROMAGNETIC PROCESSES IN PLANETARY ATMOSPHERES

M. E. Abdelaal¹, A. V. Zakharov¹, E. A. Malinovskaya²,
O. G. Chkhetiani², I. A. Kuznetsov¹, A. A. Kartasheva¹,
L. O. Maksimenkov², I. V. Dokuchaev¹, A. N. Lyash¹, A. E. Dubov¹,
Y. A. Obod¹, I. A. Shashkova¹, G. G. Dolnikov¹

¹ Space Research Institute RAS, Moscow, Russia

Mohamad.essam@phystech.edu

² Obukhov Institute of Atmospheric Physics RAS, Moscow, Russia

KEYWORDS:

dust particle electrization, electromagnetic activity, planetary atmospheres, Mars, Electromagnetic Analyzer (EMA), atmospheric electrization

ABSTRACT:

Dust particle electrization in arid environments plays a crucial role in atmospheric dynamics, influencing local electric fields and generating electromagnetic activity [1]. This study investigates the low atmospheric electrical and electromagnetic properties of dust-laden arid Kalmykia regions under moderate wind conditions and convective dust aerosol transport (Figure 1). Comprehensive multilevel measurements of wind speed, temperature, humidity, solar radiation, and electric potential were conducted alongside the Dust Complex instrumentation [2], which includes piezoelectric sensors and an Electromagnetic Analyzer (EMA). The analysis reveals a strong correlation between electromagnetic bursts, and fluctuations in electric field strength and wind speed. A significant increase in burst frequency and intensity was observed under low relative humidity conditions (<30%), highlighting its role in enhancing discharge activity. The shift in the relationship between electric field strength and relative humidity suggests that charge formation is driven by the balloelectric effect. Statistical and cross-correlation analyses further indicate lagged effects of temperature variations on electromagnetic activity, emphasizing the complex realtion between thermal and mechanical processes in dust electrization [3]. These findings provide valuable insights into dust charging and discharging mechanisms in arid environments, with implications for understanding similar phenomena in planetary atmospheres, particularly on Mars, and it is in this context that the results obtained are discussed. The study underscores the importance of integrating high-frequency electromagnetic measurements with meteorological data to refine models of dust dynamics and atmospheric electrization.

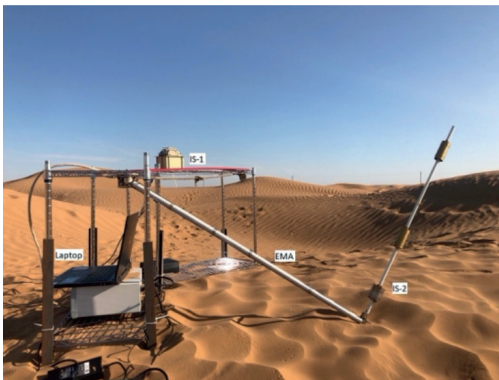


Figure 1. Dust Complex setup in the Kalmykia steppe

ACKNOWLEDGMENTS:

The research was carried out within the state assignment of Ministry of Science and Higher Education of the Russian Federation (theme No. FSWM-2024-0005).

This research was supported in part through computational resources of the supercomputer "SKIF Cyberia" of Tomsk State University

REFERENCES

- [1] *Michael M., Tripathi S. N., Mishra S. K.* Dust charging and electrical conductivity in the day and nighttime atmosphere of Mars // *J. Geophysical Research: Planets*. 2008. V. 113. Iss. E7. <https://doi.org/10.1029/2007JE003047>.
- [2] *Zakharov A. V., Dolnikov G. G., Kuznetsov I. A. et al.* Dust complex for studying the dust particle dynamics in the near-surface atmosphere of Mars // *Solar System Research*. 2022. V. 56. 6. P. 351–368. <https://doi.org/10.1134/S0038094622060065>.
- [3] *Abdelaal M. E., Dokuchaev I. V., Malinovskaya E. A. et al.* Experimental modeling of atmospheric discharge phenomena and charged dust particle interactions // *Frontiers in Astronomy and Space Sciences*. 2024. V. 11. Article 1347048. DOI: 10.3389/fspas.2024.1347048.

OPERATION OF A SPACECRAFT WITH A PARABOLIC SOLAR SAIL FOR SPACE DEBRIS REMOVAL

Y. M. Sorokoletova¹, I. A. Nikolichev¹, O. S. Chernenko²

¹ *Moscow Aviation Institute Moscow, Russia, iulia.sorokoletova@yandex.ru*

² *Space Research Institute RAS, Moscow, Russia, o.chernenko@cosmos.ru*

KEYWORDS:

space debris, parabolic solar sail, space flight mechanics, optimal control

INTRODUCTION:

The outer space around the Earth is becoming more and more loaded with artificial objects. In this regard, the urgency of the problem of space debris is growing [1]. The study examines the ballistic operation of a spacecraft with a solar parabolic concentrator for space debris disposal in Geostationary orbit [2].

MISSION CONCEPT:

The possibility of using a parabolic solar sail to maneuver a spacecraft without fuel consumption is being investigated. Thus, in the course of the work, the problem of optimal control of a solar sail using the Pontryagin maximum principle was posed and solved [3]. An algorithm has been developed to calculate flight paths to debris accumulation zones, taking into account the change in sail orientation and minimizing flight time.

RESULTS:

A complete and detailed formalization of the trajectory problem as an optimal control problem was carried out, special attention was paid to the development of a robust algorithm for numerically determining optimal control, which sets the orientation of the solar concentrator. An expression was obtained for optimal control of the orientation of the solar concentrator for a phase vector corresponding to the use of rectangular planetocentric coordinates; the expressions obtained can also be transformed into a form corresponding to any other set of coordinates of the phase vector (for example, written in the elements of the orbit). A complete set of optimality conditions is obtained and the corresponding optimal control problem is reduced to a two-point boundary value. The numerical solution of the latter was carried out using the developed software. The study shows the fundamental possibility of using a solar concentrator as a propulsion device (i.e., as a solar sail with low "windage"), and new results have been obtained for the corresponding problem of optimal control of sailing systems.

REFERENCES:

- [1] ESA's Annual Space Environment report / European Space Agency, 2025. 144 p. https://www.sdo.esoc.esa.int/environment_report/Space_Environment_Report_latest.pdf.
- [2] *Chernenko O. S., Smirnova Y. M.* Utilization of space debris in geostationary orbit // 14th All-Russian Interdisciplinary Youth competition of scientific and technical works and projects "Youth and the future of aviation and Cosmonautics". Moscow: Pero Publishing House, 2022. P. 129-130 (in Russian).
- [3] *Pontryagin L. C., Boltyansky A. G. et al.* Mathematical theory of optimal processes / ed. Pontryagin L. C. Moscow: Nauka Publ., 1985. 284 p. (in Russian).

APPLICATION OF ARTIFICIAL NEURAL NETWORK TO IDENTIFY ORBITAL RESONANCES IN THE MOTION OF ARTIFICIAL EARTH SATELLITES

S. Wijaya, I. V. Tomilova, T. V. Bordovitsyna

Tomsk State University, Tomsk, Russia, steven.wijaya2001@gmail.com

KEYWORDS:

orbital resonances, orbital dynamics, artificial earth satellites, artificial neural network

INTRODUCTION:

The study of orbital resonances is a fundamental challenge in celestial mechanics that is critical for understanding the long-term evolution of celestial bodies and artificial satellites. A resonance occurs when the satellite's orbital period is commensurate with the central body's rotation, leading to cumulative gravitational perturbations that alter the orbit's long-term behavior. Analyzing these resonances is essential for identifying stable and chaotic regions in space. Numerical study of the structures of near-planetary orbital simples is associated with routine analysis of a large number of graphical data.

To address these limitations, this abstract explores the application of Artificial Neural Network (ANN) to automatically classify orbital resonances. By training a convolutional neural network (CNN) on graphical representations of resonant arguments, we demonstrate that a machine learning model can accurately distinguish between different resonant behaviors. This research shows that the proposed ANN-based approach can significantly enhance the efficiency and accuracy of resonance analysis, allowing for the rapid processing of vast data.

ORBITAL RESONANCE:

Orbital resonance is a phenomenon in celestial mechanics that occurs when two orbiting bodies exert a regular, periodic gravitational influence on each other. This condition typically arises when the ratio of their orbital periods can be expressed as a ratio of two small integers, such as 1:2 or 2:3. These periodic gravitational interactions can significantly perturb a satellite's orbit, leading to distinct dynamical behaviors that are critical for understanding its long-term stability.

This phenomenon has a dual nature. On one hand, it can be a source of profound stability, locking objects into stable configurations that persist over astronomical timescales. On the other hand, resonances can be powerful agents of instability, amplifying orbital perturbations, driving objects into chaotic zones, and ultimately leading to their ejection from the system or collision with other bodies [1].

Resonant Characteristics: Libration, Circulation and Transitional States

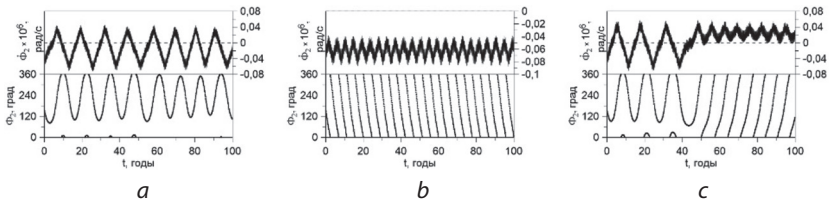
The state of an object with respect to a potential resonance is characterized by the behavior of its critical resonant angle, a variable derived from the orbital elements of the bodies involved. Formulas to calculate resonant critical argument angle were given in the table below [2].

The analysis of this angle reveals three primary dynamical states (Figure 1):

1. Libration (Figure 1a): The critical angle does not circulate through all possible values (0 to 360°) but instead oscillates, or librates, around a stable equilibrium point.
2. Circulation (Figure 1b): The critical angle changes monotonically, continuously increasing or decreasing over time (circulate through all possible values).
3. Mixed States (Circulation-Libration) (Figure 1c): This state involves transitions between circulation and libration.

Table 1. Critical Arguments and Resonance relationships

Critical Arguments	Resonance relationships
$\Phi_1 = u(M + \omega + \Omega) - m\theta$	$\dot{\Phi}_1 = u(\dot{M} + \dot{\omega} + \dot{\Omega}) - m\dot{\theta}$
$\Phi_2 = u(\omega + M) + m(\Omega - \theta)$	$\dot{\Phi}_2 = u(\dot{\omega} + \dot{M}) + m(\dot{\Omega} - \dot{\theta})$
$\Phi_3 = uM + m(\omega + \Omega - \theta)$	$\dot{\Phi}_3 = u\dot{M} + m(\dot{\omega} + \dot{\Omega} - \dot{\theta})$
$\Phi_4 = u(M - \Omega + \omega) - m\theta$	$\dot{\Phi}_4 = u(\dot{M} - \dot{\Omega} + \dot{\omega}) - m\dot{\theta}$
$\Phi_5 = uM + m(-\omega + 2\Omega - \theta)$	$\dot{\Phi}_5 = u\dot{M} + m(-\dot{\omega} + 2\dot{\Omega} - \dot{\theta})$

**Figure 1.** Rules for selecting the type of resonant characteristics

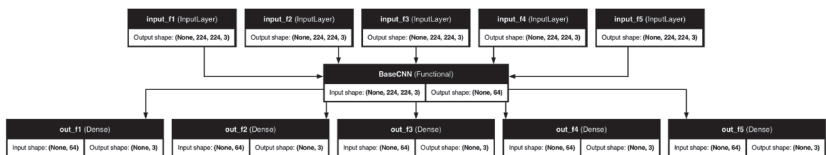
ARTIFICIAL NEURAL NETWORKS:

Artificial Neural Networks (ANNs) have revolutionized the field of visual pattern recognition, a journey that gained significant momentum with Yann LeCun's groundbreaking work in 1989 [3]. His application of backpropagation to recognize handwritten zip codes laid the foundation for the deep learning models that are ubiquitous today. This breakthrough, combined with the integration of other AI techniques, has led to the development of powerful and sophisticated artificial intelligence systems.

As our work deals directly with pattern recognition from the graphical representations of each resonant argument angle (Φ_1 – Φ_5) as seen in the example for the resonant argument Φ_2 in Figure 1. We apply the exact same principle to our problem in celestial mechanics. Just as LeCun's network learned the visual grammar of handwritten numbers, our CNN is designed to learn the visual grammar of the evolution of the critical orbital resonance argument. By training the network on a large dataset of labeled plots, it learns to associate the distinct graphical patterns of libration, circulation and mixed type with their respective classifications.

To accomplish this, we designed a custom multi-input multi-output CNN architecture (Figure 2) to accommodate 5 parallel input data of 5 different resonant arguments (Φ_1 – Φ_5). Each branch processes its respective image independently (through BaseCNN) before their outputs are combined for a final classification.

The core of our model is a base CNN architecture that processes 224×224 pixel color images. The network is made up of several sequential blocks, each performing four key operations:

**Figure 2.** Multi-input multi-output CNN architecture

1. Convolution (Conv2D): This layer finds basic features in the image, such as lines, corners, and textures.
2. Normalization (Batch Normalization): This step helps make the network's training process more stable and faster.
3. Activation (ReLU): A simple function that decides if a detected feature is important enough to be passed on.

4. Pooling (MaxPooling): This layer reduces the image's size while keeping only the most important detected features.

As data passes through these blocks, the network learns to recognize increasingly complex patterns, and the size of the feature map gradually decreases. At the end of this process, the resulting 2D data is "flattened" into one long vector using a Flatten layer. This vector, which contains all the key information about the image, is then passed to two final fully connected layers that form the final data representation.

The final model was trained on a comprehensive dataset combining all three orbital resonance region (1:2, 2:1, and 3:1), which included a total of 69,240 model objects. The Convolutional Neural Network (CNN) was tasked with classifying the five different resonant arguments (Φ_1 – Φ_5) for each object. The network demonstrated excellent performance across the entire dataset. As summarized in Table 2, the fully trained model achieved a high degree of accuracy, correctly predicting the dynamical state in an average of 98.11 % of cases. This result confirms the model's robustness and its ability to accurately classify different critical argument behaviors.

Table 2. Accuracy of resonance classification

Orbital resonances	Φ_1	Φ_2	Φ_3	Φ_4	Φ_5
1:2	0.9892	0.9932	0.9823	0.9853	0.9729
2:1	0.9860	0.9828	0.9777	0.9848	0.9687
3:1	0.9860	0.9828	0.9777	0.9848	0.9687

REFERENCES:

- [1] *Malhotra R.* Orbital resonances and chaos in the solar system // Solar system Formation and Evolution ASP Conference Series. 1998. V. 149. P. 38–63.
- [2] *Tomilova I. V., Blinkova E. V., Bordovitsyna T. V.* Features of the Dynamics of Objects Moving in the Zones of Orbital Resonances 1:4, 1:6, and 1:8 with the Earth's Rotation // Solar System Research. 2021. V. 55. No. 5. P. 420–436. DOI: 10.1134/S0038094621040092.
- [3] *Cun Y. Le, Boser B., Denker J. S. et al.* Handwritten Digit Recognition with a Back-Propagation Network // Advances in Neural Information Processing Systems. 1990. V. 2. P. 396–404.

ACKNOWLEDGMENTS:

The research was carried out within the state assignment of Ministry of Science and Higher Education of the Russian Federation (theme No. FSWM-2024-0005). This research was supported in part through computational resources of the supercomputer "SKIF Cyberia" of Tomsk State University.

MIGRATION OF BODIES EJECTED FROM MERCURY AND VENUS

S.I. Ipatov

Vernadsky Institute of Geochemistry and Analytical Chemistry RAS
Moscow, Russia, sipatov@hotmail.com

KEYWORDS:

motion of bodies, ejection of bodies, Mercury, Venus, probabilities of collisions, terrestrial planets, the Earth

CONSIDERED MODEL:

Collisions of bodies-impactors with planets caused ejection of material from planets. Such collisions took place mainly during the accumulation of the terrestrial planets and at the late heavy bombardment) My studies of the motion of bodies ejected from the Earth have been published in [1, 2]. A review of papers devoted to studies of the motion of bodies ejected from planets can be found in these papers. Short information about the motion of bodies ejected from Mars was published in [3]. Below I discuss the evolution of orbits of bodies ejected from Mercury and Venus. In each calculation variant, the motion of 250 bodies ejected from a considered planet was studied for the fixed values of an ejection angle i_{ej} (measured from the surface plane of the planet), a velocity v_{ej} of ejection, and a time step t_s of integration. The gravitational influence of the Sun and all eight planets was taken into account. Bodies that collided with planets or the Sun or reached 2000 AU from the Sun were excluded from integration. The symplectic code from the SWIFT integration package [4] was used for integration of the motion equations. The initial positions of planets in their orbits were the same as those from this package. I studied the probabilities p_E , p_V , p_{Me} , p_{Ma} , and p_{Sun} of collisions of bodies ejected from a terrestrial planet with the Earth, Venus, Mercury, Mars, and the Sun. Also the fraction p_{ej} of bodies ejected from the Solar system was calculated. Most of calculations were made at $t_s = 1^d$ for ejection from Mercury and at $t_s = 2^d$ for ejection from Venus. For comparison a few calculations for Venus were made at $t_s = 1^d$ and $t_s = 5^d$. The results of calculations with different t_s were compared and gave similar results. The motion of bodies ejected from a planet under the gravitational influence of all planets was studied during the dynamic lifetime T_{end} of all bodies, which was often about several million years in the calculation variants. In some calculations T_{end} exceeded 1 Gyr.

The ejection of bodies from six opposite points of the planet's surface was studied for a number of values of velocities and angles of ejection of bodies. For points F and C , the motion of the bodies started at most and least distant points of the planet's surface from the Sun (located on the line from the Sun to the planet), respectively. For points U and I , the bodies started from points on the planet's surface with the maximum and minimum values of z (with the z axis perpendicular to the plane of the planet's orbit), respectively. For points W and B), the bodies started from the forward point on the planet's surface in the direction of the planet's motion and from the back point on the opposite side of the planet, respectively. Evolution of orbits of bodies launched from points B and W can differ from that of bodies launched from other four points (F , C , U , and D). In different variants, the values of the ejection angle i_{ej} were 15, 30, 45, 60, 89, or 90°. The ejection velocity v_{ej} was mainly equal to 4.23, 4.25, 4.3, 4.5, 5, 6, 8, 10, 15, or 20 km/s for ejection from Mercury, and v_{ej} mainly equal to 10.4, 10.5, 10.7, 11, 12, 14, 16, or 20 km/s for ejection from Venus.

MIGRATION OF BODIES EJECTED FROM MERCURY:

Probabilities of collisions of ejected bodies with planets depend on ejection velocities v_{ej} , ejection angles i_{ej} and ejection points. For $4.23 \leq v_{ej} \leq 6$ km/s and point F , I obtained that $p_{ej} \leq 0.004$, $p_{Sun} \leq 0.1$, $0.6 \leq p_{Me} \leq 0.97$, $0.02 \leq p_V \leq 0.3$, $p_E \leq 0.04$, and $p_{Ma} \leq 0.004$. The probabilities for ejection from points C , D and U did not differ much from those for point F . For $4.23 \leq v_{ej} \leq 6$ km/s and

point B, I obtained that $p_{ej} \leq 0.01$, $p_{Sun} \leq 0.1$, $0.65 \leq p_{Me} \leq 0.85$, $0.1 \leq p_V \leq 0.25$, $p_E \leq 0.03$, and $p_{Ma} \leq 0.004$. For $4.23 \leq v_{ej} \leq 6$ km/s and points W, I obtained that $p_{ej} \leq 0.004$, $p_{Sun} \leq 0.2$, $0.3 \leq p_{Me} \leq 1$, $p_V \leq 0.5$, $p_E \leq 0.05$, and $p_{Ma} = 0$. For point W, the probabilities p_{Me} and p_V can reach larger values than for other points. Often for greater v_{ej} the greater values of p_{ej} , p_{Sun} , p_V , p_E , and p_{Ma} were obtained, but it may not be true for $v_{ej} > 8$ km/s. The values of p_{Me} were typically smaller for greater v_{ej} . The values of p_V were greater than p_E typically by an order of magnitude, the difference was greater for smaller ejection velocities. The probabilities of collisions of bodies ejected from Mercury with the Earth usually did not exceed 0.1 at ejection velocities less than 15 km/s. The probabilities of collisions of bodies ejected from Mercury with Venus were usually about 0.1–0.3 at ejection velocities from 4.3 to 10 km/s.

For large ejection velocities, the above probabilities can differ much for points F, W, and B and for ejection angles. At $v_{ej} = 20$ km/s and point F, I obtained that $0.004 \leq p_{ej} \leq 0.1$, $0.14 \leq p_{Sun} \leq 0.4$, $0.3 \leq p_{Me} \leq 0.44$, $0.12 \leq p_V \leq 0.4$, $0.02 \leq p_E \leq 0.1$, and $p_{Ma} \leq 0.008$. At $v_{ej} = 20$ km/s, $i_{ej} \geq 30^\circ$, and point B, it was obtained that $0.9 \leq p_{Me} \leq 0.95$ and all other bodies collided with the Sun (there were no collisions with other planets and no ejection from the Solar system). At $v_{ej} = 20$ km/s and point W, probabilities were different for different ejection angle: For $i_{ej} = 30^\circ$, it was obtained that $p_{ej} = 0.044$, $p_{Sun} = 0.268$, $p_{Me} = 0.144$, $p_V = 0.284$, $p_E = 0.24$, and $p_{Ma} = 0.02$. For $i_{ej} = 89^\circ$, most of the bodies were ejected from the Solar system ($p_{ej} = 0.744$) and all other bodies collided with the Sun.

MIGRATION OF BODIES EJECTED FROM VENUS:

In this paragraph I discuss the values of the probabilities of collisions with planets for bodies ejected from Venus from the “middle” points C, D, F, and U at ejection velocities between 10.4 and 16 km/s. In this case, the fraction p_{ej} of bodies ejected into hyperbolic orbits did not exceed 0.06, the fraction p_{Sun} of bodies collided with the Sun was about 0.1–0.4, the fraction p_{Me} of bodies collided with Mercury was about 0.01–0.2, the fraction p_V of bodies collided with Venus was about 0.3–0.8, and the fraction p_E of bodies collided with the Earth was about 0.04–0.2 (was smaller by a factor of several than p_V). The values of p_{Sun} were greater by about a factor of 2 at $v_{ej} = 16$ km/s than at $v_{ej} = 10.4$ km/s. The values of p_{Me} at $v_{ej} = 16$ km/s were greater by about a factor of several (from 2 to 10 depending on the point of ejection and i_{ej}) than at $v_{ej} = 10.4$ km/s. The values of p_V have some tendency (but not at all initial data) to be smaller at greater v_{ej} . The probabilities of collisions of bodies with Mars often did not exceed 0.01 for all considered initial data.

For the “middle” points C, D, F, and U at $v_{ej} = 20$ km/s, p_{Me} was about 0.1–0.15; the values of p_V were about 0.23–0.35; the values of p_E were about 0.04–0.1 at $i_{ej} = 45^\circ$, and could be about 0.2 at $i_{ej} = 89^\circ$, the values of p_{ej} were about 0.25–0.32 at $i_{ej} = 45^\circ$, and they could be about 0.02 at $i_{ej} = 89^\circ$; the values of p_{Sun} were about 0.15–0.3.

For the point B, the values of p_{Me} were about 0.02–0.35 (with maximum at $v_{ej} = 20$ km/s), the values of p_V were about 0.4–0.8, the values of p_E were mainly about 0.04–0.2 (but equaled to 0.01 at $v_{ej} = 20$ km/s and $i_{ej} = 89^\circ$), the values of p_{ej} were mainly less than 0.04, and the values of p_{Sun} were about 0.07–0.3.

For the point W at $v_{ej} \leq 12$ km/s, the values of p_{Me} were about 0.01–0.1, the values of p_V were about 0.3–0.8, p_E was about 0.1–0.2, the values of p_{ej} were mainly less than 0.06, and the values of p_{Sun} were about 0.1–0.4. More bodies were ejected from the Solar system at greater v_{ej} . For $v_{ej} = 20$ km/s and the point W, the fraction of ejected bodies was about 0.8 at $i_{ej} = 45^\circ$, and all bodies were ejected at $i_{ej} = 89^\circ$.

CONCLUSIONS:

Most bodies ejected from Mercury fell back onto Mercury. The probabilities of collisions of bodies ejected from Mercury with the Earth usually did not exceed 0.1. The fraction of bodies that collided with Venus was greater than with the Earth, usually by an order of magnitude. The probabilities of colli-

sions of bodies with Venus were usually about 0.1–0.3 at ejection velocities from Mercury from 4.3 to 10 km/s.

For bodies that had been ejected from Venus, the fraction of bodies that collided with Venus was about 0.2–0.8, and the fraction of bodies that collided with the Earth was about 0.04–0.2. The fraction of bodies collided with Mercury varied from 0.01 to 0.2. The probabilities of collisions of bodies with Mars often did not exceed 0.01 for all considered initial data.

ACKNOWLEDGMENTS:

The studies were carried out under government-financed research project for the Vernadsky Institute of Geochemistry and Analytical Chemistry RAS.

REFERENCES:

- [1] *Ipatov S.I.* Growth of the Moon due to bodies ejected from the Earth // *Solar System Research*. 2024. V. 58. P. 94–111. <https://doi.org/10.1134/S0038094624010040>. <http://arxiv.org/abs/2405.19797>.
- [2] *Ipatov S.I.* Probabilities of collisions of bodies ejected from forming Earth with the terrestrial planets // *Icarus*. 2025. V. 425. Article 116341. 24 p. <https://doi.org/10.1016/j.icarus.2024.116341>. <http://arxiv.org/abs/2411.04218>.
- [3] *Ipatov S.I.* Migration of bodies ejected from Mars // 15th Moscow Solar System Symposium (15M-S3). 2024. No. 15MS3-SB-06. P. 236–238. https://elibrary.ru/download/elibrary_80856144_39006326.pdf.
- [4] *Levison H.F., Duncan M.J.* The long-term dynamical behavior of short-period comets // *Icarus*. 1994. V. 108. P. 18–36. <https://doi.org/10.1006/icar.1994.1039>.

COORDINATE SYSTEM TRANSFORMATIONS IN EXTRATERRESTRIAL CARTOGRAPHY

M. V. Nyrtsov¹, M. E. Fleis², A. I. Sokolov¹

¹ *Lomonosov Moscow State University, Moscow, Russia*
nyrtsovmaxim@gmail.com

² *Institute of Geography RAS, Moscow, Russia, fleis.maria@yandex.ru*

KEYWORDS:

extraterrestrial mapping, mathematical cartography, conformal projection, coordinate system, triaxial ellipsoid, map projection

ABSTRACT:

The International Astronomical Union has set a definition of small Solar System bodies (SSSB) by isolating them from larger objects such as planets, dwarf planets, and their satellites. Therefore, SSSB include asteroids, meteoroids, comet nuclei, and others. Their shapes vary from spherical (e.g., the satellite of asteroid 243 Ida Dactyl) to extremely irregular (e.g., asteroid 433 Eros). Bodies like Eros are highly elongated and look like a potato. The shape is a key factor in choosing a reference surface and corresponding projections for the mathematical basis of maps of celestial bodies. Recommendations for the use of a reference surface are contained in the report of the Working Group on Cartographic Coordinates and Rotational Elements [1]. Most SSSB are approximated by a triaxial ellipsoid, but it is noted that the use of triaxial ellipsoids complicates the calculations of cartographic projections. Their use and study of properties are also complicated. In our previous studies [2, 3], formulas for cylindrical, azimuthal, and conical projections of the triaxial ellipsoid with different distortion were derived, and the conformal projection proposed by the German mathematician Carl Jacobi was adapted for cartographic purposes.

To use projections of the triaxial ellipsoid in geoinformation technologies, it is necessary to solve the problems of transformation coordinates from a geographic system into a projection plane system (direct problem) and from planar rectangular coordinates into geographic coordinates (inverse problem) on the approximation surface.

The proposed method for recalculating rectangular coordinates of a projection plane into geographic coordinates is based on the possibility of separating variables and sequentially determining the argument value based on the value of a function of one variable. The calculation uses the method of dividing a segment in half. In this case, the optimal range is selected to find the desired argument value. In cylindrical projections and in the Jacobi projection, a range of longitude and latitude from zero to 90° is used. There is no such need for azimuthal projections, since longitude is calculated using an exact formula, and the sign of longitude does not matter when determining latitude.

The problems that arise when recalculating the coordinates of cylindrical, azimuthal and conic projections are shown using the example of cylindrical and azimuthal projections selected for the implementation of the methodology. The Jacobi projection was chosen because it has its own characteristics both when recalculating coordinates from geographic to rectangular ones, and when determining geographic coordinates with known rectangular ones.

Experiments were conducted with transformation the coordinates of the contours of relief forms on the surface of Phobos from the cylindrical projection of the meridian section into geographic coordinates on a triaxial ellipsoid. A similar recalculation was performed for cartographic grids in the azimuthal projection, which preserves the lengths along the meridians, and the Jacobi projection.

The presented formulas can be included in geoinformation software, which will allow to use projections of the triaxial ellipsoid in geoinformation mapping.

ACKNOWLEDGMENTS:

The research was carried out according to the State assignments No. 121051400061-9 (M.V. Nyrtsov, A.I. Sokolov) and FMWS-2024-0009 No. 1023032700199-9 (M.E. Fleis).

REFERENCES:

- [1] *Archinal B. A., Anton C. H., A'Hearn M. F. et al.* Report of the IAU Working Group on Cartographic Coordinates and Rotational Elements: 2015 // *Celestial Mechanics and Dynamical Astronomy*. 2018. V. 130. P. 131–161. <https://doi.org/10.1007/s10569-019-9925-1>.
- [2] *Nyrtsov M. V., Fleis M. E., Sokolov A. I.* Meridian section projections: a new class of the triaxial ellipsoid projections // *Geodesy and Cartography*. 2021. V. 968. Iss. 2. P. 11–22. DOI: 10.22389/0016-7126-2021-968-2-11-22.
- [3] *Nyrtsov M. V., Fleis M. E., Borisov M. M., Stooke P. J.* Jacobi Conformal Projection of the Triaxial Ellipsoid: New Projection for Mapping of Small Celestial Bodies // *Cartography from Pole to Pole, Lecture Notes in Geoinformation and Cartography* / eds. M. Buchroithner et al. Berlin; Heidelberg: Springer-Verlag; 2014. P. 235–246. DOI: 10.1007/978-3-642-32618-9_17.

**SESSION 4. SMALL BODIES (SB-PS)
POSTER SESSION**

PYRRHOTITE AND ILMENITE AS SUPPLEMENTS FOR LUNAR REGOLITH SIMULANTS IMPROVING THE CONDITIONS OF MICROWAVE BREAKDOWN AND THE FORMATION OF PLASMA-DUST CLOUDS

A. S. Kuzovchikova¹, V. D. Borzosekov^{2,3}, E. M. Sorokin⁴, M. A. Zaitsev¹, V. V. Gudkova^{2,3}, A. A. Letunov², E. V. Voronova², D. V. Malakhov², A. S. Sokolov², E. A. Obraztsova^{2,5}, T. I. Morozova¹, S. M. Kuzovchikov⁶, K. V. Naumova², V. D. Stepakhin², M. V. Gerasimov¹

¹ Space Research Institute RAS, Moscow, Russia, Vasiljek_anna@mail.ru

² Prokhorov General Physics Institute RAS, Moscow, Russia
borzosekov@fpl.gpi.ru

³ RUDN University, Moscow, Russia

⁴ Vernadsky Institute of Geochemistry and Analytical Chemistry RAS
Moscow, Russia

⁵ Moscow Institute of Physics and Technology (National Research University)
Dolgoprudny, Russia

⁶ N. N. Semenov Federal Research Center for Chemical Physics
Moscow, Russia

KEYWORDS:

microwave discharge, plasma-dust clouds, optical emission spectroscopy, OES, scanning electron microscopy, SEM, X-ray diffraction, XRD, lunar regolith simulant, pyrrhotite, ilmenite, Nd:YAG laser

INTRODUCTION:

Plasma-dust clouds formed from the “building material” of the Solar System bodies are an interesting object encountered in natural terrestrial and cosmic processes. For example, the catalytic effect of such a multiphase environment in the abiotic synthesis of organic compounds is possible [1, 2]. To study this issue, plasma-dust clouds must be created from the starting substances, at least repeating the chemical composition of the simulated natural environments, and better yet, repeating their mineral composition.

One of the methods for creating plasma-dust clouds is a discharge that occurs when powder mixtures are irradiated with microwave radiation [3]. However, a feature of this approach is the necessity for the mixture to have a sufficient volume concentration of particles with a decent concentration of free charge carriers, or particles with a high dielectric loss. That is, it is necessary to have particles in the mixture that will ensure the absorption of the electromagnetic wave at the initial stage.

In natural conditions, the initial substance for plasma-dust clouds is often regolith or rocks of cosmic bodies (including the Earth). They may not contain a sufficient concentration of the certain substances capable to absorb microwave radiation to start the discharge. An example of such substances is the lunar regolith, containing mainly olivines and pyroxenes.

The goal of our experimental study was to find mineral components that, when added to mixtures simulating lunar regolith, can ensure the microwave breakdown and the formation of a plasma-dust cloud, but at the same time do not contradict the nature of the simulated environment. As the first samples, we chose ilmenite and pyrrhotite, which are well known from literature for their good microwave absorption and electrical conductivity, respectively.

EXPERIMENTS:

The samples of ilmenite (FeTiO_3) and pyrrhotite ($\text{Fe}_{x-1}\text{S}_x$), close to monomineral composition, were pre-crushed and powdered in an agate mortar. The powdered samples were exposed to microwave radiation of

the gyrotron (frequency $f = 75$ GHz) with the power of 400 kW. This power value corresponds to an average beam cross-section power density of 14 kW/cm^2 and RMS electric field strength of 2.3 kV/cm . Each powdered sample (200 mg of mass) was exposed to one microwave pulse of length 8 ms. Argon at a pressure of 1 atm was used as the initial atmosphere, providing a chemically inert environment. Optical emission spectroscopy and high-speed video recording were used during the experiment to obtain the discharge parameters and its dynamics.

RESULTS AND THEIR DISCUSSION:

For both types of minerals, a microwave breakdown occurred with the formation of plasma-dust clouds. However, with pyrrhotite, the volume and intensity of the cloud visible radiation were significantly lower. This could be the manifestation of strong magnetic properties and/or high electrical conductivity of pyrrhotite. In order to minimize these effects we increased the distance between the pyrrhotite particles and changed the technique for the powder sample placing on the quartz glass bottom of the test chamber for that purpose. After that improvement, we obtained plasma-dust clouds of larger volume and with greater intensity/duration of visible radiation.

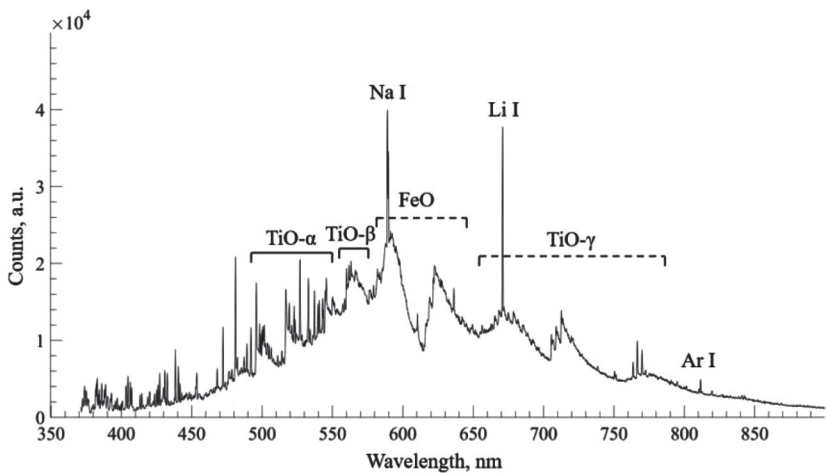


Figure 1. Optical emission spectrum in the experiment with the ilmenite sample

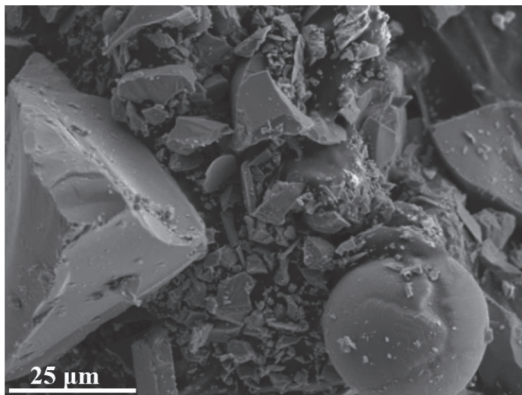


Figure 2 SEM image of the ilmenite sample after the microwave discharge

The emission spectra of the discharge contained emission lines of atoms (Fe, Ti) from the composition of the initial sample substance, which indicates the destruction of the initial substance in the discharge. In the case of ilmenite, intense emission bands of TiO and FeO molecules were observed (Figure 1), which indicates the binding of oxygen from the initial substance.

The vibrational temperature of the gas was determined to be 5500 K from the TiO bands, and the surface temperature of the solid phase was 2500 K from the thermal radiation continuum.

Comparative X-ray diffraction (XRD) study of the initial and microwave irradiated samples has not shown any changes in the structural properties of either ilmenite or pyrrhotite. Metallic iron was not detected using energy dispersive X-ray (EDX) analysis either. This could require further study with higher sensitive methods, since the appearance of metallic iron was observed after ilmenite and pyrrhotite vaporization with the millisecond Nd:YAG laser.

Scanning electron microscopy (SEM) of revealed the appearance of spherical microparticles after the microwave discharge (Figure 2). This spheroidization effect is inherent for dust particles of micron range and lower sizes exposed to plasma [4, 5].

CONCLUSION:

The formation of plasma-dust clouds during microwave irradiation of monomineral samples of ilmenite and pyrrhotite demonstrates the possibility of their use as an additive to simulant mixtures, for example, lunar regolith, to ensure the discharge formation while maintaining the “validity” of the sample.

ACKNOWLEDGMENTS:

This work was supported by the Russian Science Foundation (project No. 25-22-00505, <https://rscf.ru/project/25-22-00505/>).

REFERENCES:

- [1] *Snytnikov V.N.* Abiogenic synthesis of prebiotic matter for the Earth's biosphere as a stage of self-organization on an astrophysical and paleontological time scale // *Paleontological J.* 2007. V. 41. No. 5. P. 473–480. DOI: 10.1134/S0031030107050012.
- [2] *Peters S., Semenov D.A., Hochleitner R., Trapp O.* Synthesis of prebiotic organics from CO₂ by catalysis with meteoritic and volcanic particles // *Scientific Reports.* 2023. V. 13. Article 6843. <https://doi.org/10.1038/s41598-023-33741-8>.
- [3] *Batanov G.M., Kossyi I.A.* Pulsed microwave discharges in powder mixtures: Status, problems, and prospects // *Plasma Physics Reports.* 2015. V. 41. P. 847–857. <https://doi.org/10.1134/S1063780X15090020>.
- [4] *Károly Z., Szépvölgyi J.* Plasma spheroidization of ceramic particles // *Chemical Engineering and Processing.* 2005. V. 44(2). P. 221–224. DOI: 10.1016/j.ccep.2004.02.015.
- [5] *Ji L., Wang C., Wu W. et al.* Spheroidization by Plasma Processing and Characterization of Stainless Steel Powder for 3D Printing // *Metallurgical and Materials Transactions A.* 2017. V. 48. Iss. 10. P. 4831–4841. DOI: 10.1007/s11661-017-4240-5.

ALGORITHM FOR IMAGE SEGMENTATION OF PARTICLE TRACKS IN THE DUSTY PLASMA NEAR THE SURFACE OF ATMOSPHERELESS BODIES

Y. Tian¹, A. Yu. Poroykov¹, I. A. Shashkova^{1,2}, I. A. Kuznetsov²,
A. V. Zakharov², S. I. Popel²

¹ *National Research University "Moscow Power Engineering Institute"*
Moscow, Russia, poroykovay@mpei.ru

² *Space Research Institute RAS, Moscow, Russia*

KEYWORDS:

image processing, instance segmentation, convolutional neural networks, particle tracks, dusty plasma, atmosphereless bodies

INTRODUCTION:

One of the important risk factors for planned automatic and manned scientific missions to the Moon and other atmosphereless bodies of the Solar System is the harmful effect of dust particles on equipment and crew [1].

To understand the processes that determine the behavior of dust particles, a large number of experimental and theoretical studies are being conducted, for example, [2–4]. Experimental studies are focused on laboratory simulation of processes occurring with particles under conditions that imitate the environmental impact typical to atmosphereless bodies. Optical methods are widely used to study the dynamics and characteristics of dust particles in such experiments. In the simplest case, the number of moving particles is estimated post facto based on counting the particles scattered in the area around the test sample. This is primarily due to the fact that the particles move quite quickly and form intersecting tracks in the images. The speed and charge of each particle are estimated based on the height of its trajectory. In a previous study [5], an approach was used in which the trajectories of micron-sized particles were extracted from stereo images of their tracks, and the speeds and charges of the particles were then estimated based on the trajectories found. One of the problems in processing experimental images was the difficulty of separating intersecting tracks and the need for a large amount of manual work when matching these tracks on stereo pair images.

Therefore, this paper proposes the use of an improved algorithm for processing stereo images of particle tracks, based on a convolutional neural network for their instance segmentation, encouraged by [6].

EXPERIMENTAL SETUP:

The small vacuum chamber of the IKI allows to create electric fields with an intensity of up to 10^3 V/cm in the area with the particles under study, as well as irradiating the particles with UV radiation at a wavelength $\lambda = 172$ nm with a flux of up to 18 mW, generated by a high-pressure excimer lamp filled with argon. The pressure in the measuring volume of the vacuum chamber was $4 \cdot 10^{-5}$ – $6 \cdot 10^{-5}$ Torr. Optical access to the measuring volume was provided through vacuum flanges with windows. An MGL-FN-532 laser source with $\lambda = 532$ nm and a power of 2 W was used to illuminate the samples. Stereo pairs of particle tracks were recorded using Contrastech Mars 2300S-40gm CMOS machine vision cameras with a resolution of 1920×1200 pixels and a pixel size of $5.86 \mu\text{m}$. VST SV-7525H lenses with a focal length of 75 mm were used.

IMAGE PROCESSING ALGORITHM:

To improve the algorithm for processing stereo pairs of particle trajectories proposed in [5], it was suggested to use the YOLO11 deep convolutional neural network [7]. Specifically, the possibility of implementing instance segmentation to highlight intersecting trajectories. To train the network, 10,000 synthetic images with a size of 1900×1200 pixels were created using the method described in [8], with a total of about 60,000 tracks. The input

image size for the network was chosen to be 960 pixels to increase the segmentation accuracy. Training was performed for 500 epochs on an NVIDIA GeForce RTX 3060 graphics card. The network size was selected as nano (2.9 million parameters). The best results in terms of segmentation error were achieved at approximately 250–300 epochs. The results achieved so far in training the network are: precision metric 0.989, recall metric 0.73, mAP50 metric 0.855, mAP50-95 metric 0.564.

The trained model was integrated into software developed for processing stereo pairs of tracks and demonstrated its effectiveness, allowing the identification of intersecting tracks in experimental images.

The improved algorithm for separating intersecting particle trajectories in images will allow for more accurate determination (without loss of frame information) of particle motion parameters, such as their initial velocity and mass transfer, when simulating conditions at the surface of atmosphereless bodies. The calculated heights of the motion trajectories will allow us to estimate the lower limit of the particle charge.

ACKNOWLEDGMENTS:

This work was supported by the Russian Science Foundation (project No. 24-12-00064, <https://rscf.ru/project/24-12-00064/>).

REFERENCES:

- [1] *Linnarsson D., Carpenter J., Fubini B. et al.* Toxicity of lunar dust // Planetary and Space Science. 2012. V. 74. Iss. 1. P. 57–71. <https://doi.org/10.1016/j.pss.2012.05.023>.
- [2] *Orger N. C., Toyoda K., Masui H., Cho M.* Experimental investigation on silica dust lofting due to charging within micro-cavities and surface electric field in the vacuum chamber // Advances in Space Research. 2019. V. 63. Iss. 10. P. 3270–3288. <https://doi.org/10.1016/j.asr.2019.01.045>.
- [3] *Wang X., Schwan J., Hsu H. W. et al.* Dust charging and transport on airless planetary bodies // Geophysical Research Letters. 2016. V. 43. Iss. 12. P. 6103–6110. <https://doi.org/10.1002/2016GL069491>.
- [4] *Popel S. I., Zelenyi L. M., Zakharov A. V.* Dusty plasma in the Solar System: celestial bodies without atmosphere // Plasma Physics Reports. 2023. V. 49. Iss. 8. P. 1006–1013. DOI: 10.1134/S1063780X23600780.
- [5] *Zakharov A. V., Poroykov A. Y., Bednyakov S. A. et al.* Recovery of dust particles trajectories in modeling physical processes in the near-surface exosphere of the moon // Measurement. 2021. V. 171. Article 108831. <https://doi.org/10.1016/j.measurement.2020.108831>.
- [6] *Tsalicoglou C., Rösger T.* Deep learning based instance segmentation of particle streaks and tufts // Measurement Science and Technology. 2022. V. 33. No. 11. Article 114005. DOI 10.1088/1361-6501/ac8892.
- [7] *Jocher G., Qiu J.* Ultralytics YOLO11. 2024. <https://github.com/ultralytics/ultralytics>.
- [8] *Tian Y., Poroykov A. Y., Shashkova I. A. et al.* Computer simulation of microparticle trajectories in a laboratory study of lunar dust dynamics // Proc. 2024 6th Intern. Youth Conf. Radio Electronics, Electrical and Power Engineering (REEPE). 2024. P. 1–5. DOI: 10.1109/REEPE60449.2024.10479868.

ESTIMATING OF THE METEOR PARAMETERS

V. Efremov¹, O. Popova¹, A. Kartashova², D. Glazachev¹,
A. Bushmanova¹

¹ *Sadovsky Institute of Geosphere Dynamics RAS, Moscow, Russia*
efremov.vv@phystech.edu

² *Institute of Astronomy RAS, Moscow, Russia*

KEYWORDS:

meteors, meteoroids, ablation, Perseid shower

INTRODUCTION:

The energy deposition due to interaction of the meteor particle with the Earth's atmosphere determines the light and ionization, which are observed by different techniques. The energy deposition depends on ablation rate and deceleration of the meteor particle. The ablation and deceleration are determined by the particle size and density, as well as the entry angle and velocity. To determine the properties of the meteor particles different models should be applied to observational data.

DESCRIPTION OF THE MODELS:

Light curves are usually reproduced with the help of two most common ablation models. The first model assumes that the entire incoming energy flux is consumed for ablation. The second model suggests that the incoming energy is expended on meteoroid heating, thermal radiation and ablation. The mass loss itself is determined by the saturated vapor pressure. Both models include a number of coefficients, which also affect the obtained results.

DISCUSSION:

The work used double-station observations of the 2016 Perseid shower. One of the used ablation models is applicable to small meteoroids, so meteors weaker than -2^m were selected. Light of a number of meteor events were reproduced using two ablation models. Corresponding meteor particles parameters (mass and size) were determined. The presentation will discuss used models, their results and uncertainty, and factors, which affect obtained results.

ACKNOWLEDGMENTS:

V. Efremov, O. Popova, D. Glazachev were funded by the program "Development of an complex model of the entering cosmic objects action on the internal and external geospheres and assessment of the consequences of these impacts" (1021052706222-8-1.5.4). We thank J. Oberst, A. Margonis for their SPOSH observations.

LOWER-HYBRID DRIFT WAVES IN PLASMA OF METEOROID TAILS IN THE EARTH'S IONOSPHERE

T. I. Morozova, S. I. Popel

Space Research Institute RAS, Moscow, Russia, timoroz@yandex.ru

KEYWORDS:

meteoroids, meteoroid tails, electrophonic noises, passages of meteor bodies, modulational instability, low-hybrid drift waves

INTRODUCTION:

Low frequency noises from meteoroid tails which are registered simultaneously with passages of meteor bodies can be associated with plasma waves, instabilities and turbulence in the meteoroid tails. One of such process is the development of modulational instability of low-hybrid drift waves [1]. It produces the same range of frequencies as observed electromagnetic noises and electrophonic noises from meteoroid flight simultaneously with the passage of meteor body. It should be mentioned that these mysterious phenomena still do not have definite explanation.

DISCUSSION:

In plasma-dust systems of meteoroid tails, various wave oscillations can arise. In particular, taking into account the inhomogeneities of the plasma concentration of meteoroid tails and the presence of the Earth's magnetic field, excitation of drift lower-hybrid waves, as well as the development of modulational instability of these oscillations, is possible. One of the phenomena in meteor physics that has not yet been fully explained is the electrophonic sounds that arise simultaneously with the passage of meteoroids and are obviously not associated with ordinary sound waves. It is noted that the appearance of electrophonic sounds simultaneously with the passage of meteoroids can be caused by the development of drift lower-hybrid turbulence in the tails of meteoroids. The frequencies of the observed electrophonic noises from the passage of meteoroids have values lower than the frequencies of the drift lower hybrid waves, which determine the frequency threshold of wave oscillations that can be excited in the tails of meteoroids as a result of the development of modulational instability of the drift lower hybrid waves and thus explain the occurrence of electrophonic noise simultaneously with the passage of meteoroids. The conditions under which the propagation of drift lower hybrid waves in the plasma of meteoroid tails during their passage through the Earth's ionosphere and the development of modulational instability of these waves for different frequency ranges are considered. The corresponding increments of the development of modulational instability of the monochromatic pump wave are derived. The values of the increments of the development of this instability for typical parameters of the plasma of meteoroid tails are calculated.

ACKNOWLEDGMENTS:

The work was supported by Grant of Russian Science Foundation No. 23-72-01066.

REFERENCES:

- [1] *Morozova T.I., Popel S.I. Instability in the tails of meteoroids in the Earth's atmosphere associated with the magnetic field // Radiophysics and Quantum Electronics. 2025. V. 68. No. 7 (in press).*

SYSTEMATIC BIASES IN POSITIONAL OBSERVATIONS OF INTERSTELLAR COMET 3I/ATLAS

Yu. D. Medvedev, S. R. Pavlov

*Institute of Applied Astronomy RAS, Saint Petersburg, Russia
medvedev@iaaras.ru, sr.pavlov@iaaras.ru*

KEYWORDS:

interstellar comet, non-gravitational forces, cometary activity, Rubin Observatory, 3I/ATLAS

ABSTRACT:

The third known interstellar object, designated C/2025 N1 (ATLAS), was first identified on July 1, 2025, by the Asteroid Terrestrial-impact Last Alert System (ATLAS). Orbital calculations revealed its interstellar origin, with an exceptionally high eccentricity exceeding 6.

Serendipitously, the Rubin Observatory collected imaging in the area of the sky in habited by the object. The object was detection by Rubin's telescope spanning 2025 June 21 (10 days before discovery) to 2025 July 7. Thanks to the large aperture and high spatial resolution of the Rubin telescope, cometary activity was detected as early as June 21 [1]. Analysis of Rubin's astrometric data revealed a small but significant systematic offset relative to the predicted positions from JPL Horizons ephemerides. One possible explanation is a shift of the observed photocenter relative to the center-of-mass of the comet, due to asymmetric shape of the cometary coma.

In this work, we quantify the magnitude of this offset in the astrometric measurements and determine the corresponding non-gravitational accelerations affecting the comet's motion. To achieve this, we use a dedicated modeling program that allows us to determine both the values of positional shifts and the parameters of non-gravitational forces over different time intervals. This, in turn, enables us to investigate the evolution of these values and place constraints on the velocity and size distribution of particles in the comet's coma.

REFERENCES:

- [1] *Chandler C.J., Bernardinelli P., Jurić Mario et al.* NSF-DOE Vera C. Rubin Observatory Observations of Interstellar Comet 3I/ATLAS (C/2025 N1) // <https://arxiv.org/2025>. 36 p. <https://doi.org/10.48550/arXiv.2507.13409>.

ON ANOMALOUS DISSIPATION IN DUSTY PLASMAS IN THE VICINITY OF COMET NUCLEI AND ACTIVE ASTEROIDS

A. Yu. Dubinsky¹, Yu. S. Reznichenko^{1,2}, S. I. Popel¹

¹ Space Research Institute RAS, Moscow, Russia, nfcpb@bk.ru

² Moscow Institute of Physics and Technology (National Research University) Dolgoprudny, Moscow Region, Russia, dvju@yandex.ru

KEYWORDS:

dusty plasma, comet, active asteroid, anomalous dissipation, aperiodic mode

ABSTRACT:

One of the main features that distinguishes dusty plasma from ordinary one (which does not contain charged dust particles) is anomalous dissipation associated with the effect of dust particle charging as well as leads to new physical phenomena, effects and mechanisms [1, 2]. In our work we consider the process of anomalous dissipation in the way of describing dust particle dynamics in the dusty plasma of comets [3] and the near-surface dusty plasma of an active asteroid. An analytical description of the motion of a dust particle above the surface of the comet and active asteroid is presented. It is shown that in the case of dust particle periodic motion in the comet and active asteroid dusty plasma attenuation processes are determined by the charging frequency of dust particles, which characterizes anomalous dissipation. In addition, it is shown that under certain conditions the dynamics of dust particles can have an aperiodic character. The results of corresponding numerical calculations are presented [4]. It is shown that anomalous dissipation plays a significant role in justifying the application of the levitating dust particle model describing the dusty plasma above a comet and active asteroid.

ACKNOWLEDGMENTS:

The study was supported by the Russian Science Foundation grant No. 24-12-00064, <https://rscf.ru/project/24-12-00064/>.

REFERENCES:

- [1] Popel S.I., Golub' A.P. On Anomalous Dissipation in the Plasma of the Dusty Lunar Exosphere // J. Experimental and Theoretical Physics Letters. 2022. V. 115. Iss. 10. P. 596–601. <https://doi.org/10.1134/S0021364022100587>.
- [2] Popel S.I., Izvekova Yu.N., Golub' A.P. On Anomalous Dissipation in Plasma of Dusty Mercury's Exosphere // Plasma Physics Reports // Plasma Physics Reports. 2024. V. 50. No. 2. P. 237–246. DOI: 10.1134/s1063780x23601761.
- [3] Popel S.I., Golub' A.P., Zelenyi L.M. Plasma-dust processes in the vicinity of comets // Sol. Syst. Res. 2025. V. 59(5). Article 47. 11 p. DOI: 10.1134/S0038094624601695.
- [4] Dubinsky A. Yu., Reznichenko Yu. S., Popel S.I. The influence of water on the formation of a dusty plasma exosphere above the surface of an asteroid // Solar System Research. 2025. V. 59(5). Article 51. 8 p. DOI: 10.1134/S0038094624602160.

DUST PARTICLES ABOVE THE SURFACE OF ENCELADUS

S. I. Kopnin¹, D. V. Shokhrin², S. I. Popel¹

¹ *Space Research Institute RAS, Moscow, Russia, kopnin@cosmos.ru*

² *National Research University Higher School of Economics, Moscow, Russia*

KEYWORDS:

Enceladus, dusty plasma, photoelectric effect, charging of dust particles

ABSTRACT:

A model of Enceladus' surface charging as a result of its interaction with the surrounding plasma of Saturn's magnetosphere has been developed, taking into account its characteristic parameters. Namely, two types of ions: protons and ions of the so-called "water group" (such as O^+ , OH^+ , H_2O^+ , H_3O^+ , N^+ with an average atomic mass of about 16 a.m.u.); two types of electrons ("cold" and "hot" with corresponding different temperatures); as well as the influence of the photoelectric effect on the surface of Enceladus and taking into account the reverse current of photoelectrons. Within the framework of the proposed model, the surface charge of Enceladus, the characteristic profile of the electric field depending on the height above this surface, as well as the characteristic sizes of dust particles and the corresponding heights to which these particles are capable of rising as a result of the action of electrostatic repulsion forces from the charged surface of Enceladus are determined.

SOLITONS AND PERIODIC NONLINEAR DUST ACOUSTIC WAVES NEAR THE SATELLITES OF MARS

Yu. N. Izvekova¹, S. I. Kopnin¹, S. I. Popel^{1,2}

¹ Space Research Institute RAS, Moscow, Russia, izvekova@cosmos.ru

² National Research University Higher School of Economics, Moscow, Russia

KEYWORDS:

dusty plasma, atmosphereless celestial bodies, Mars satellites, dust acoustic perturbations, nonlinear waves

INTRODUCTION:

Phobos and Deimos are atmosphereless celestial bodies with a weak gravity. Their surfaces consist of small regolith grains that are not connected to one another and have appeared due to bombardment with micrometeorites. Their weak gravity makes these bodies interesting for piloted flights and increases the role of dust, since even a small perturbation leads to the creation of massive dust clouds above their surfaces. The surfaces of these satellites of Mars are charged by the electromagnetic radiation from the Sun and the plasma of the solar wind. The dust grains located at the surface and in the near-surface layer absorb the photons, photoelectrons, electrons, and ions of the solar wind, and, as a result, they obtain electric charge. The action of the electrostatic force under the weak gravity conditions leads to the detachment of dust grains from the surface and the creation of a dusty plasma system together with the electrons and ions. In the dusty plasma system above the surfaces of Mars's satellites, dust acoustic perturbations can propagate. We consider nonlinear periodic and solitary dust acoustic waves with an arbitrary amplitude, which can propagate near the surface of Phobos and Deimos, and discuss the possibility of observing these structures.

THE DUSTY PLASMA SYSTEMS NEAR THE SURFACES OF PHOBOS AND DEIMOS:

The dusty plasma systems near the surfaces of Phobos and Deimos are described using the model, in which the charging of dust grains above the surface is calculated taking into account the effects of solar radiation, photoelectrons, and electrons and ions of the solar wind. The photoelectrons emitted by the surface of the satellite and the surface of the suspended dust grains are accounted for. The problem is solved numerically and is self-consistent, since the photoelectrons affect the distributions of the dust grains while the dust grain distributions determine the number of the photoelectrons. When the distribution function of the photoelectrons is calculated, the important parameters include the solar radiation spectrum, the quantum yield, and the regolith work function. The shape of the solar radiation spectrum is similar to the shape of the spectrum near the Moon [1], yet its intensity is lower due to the solar constant being lower at Mars's orbit (43% of the solar constant value at Earth's orbit). The work function and quantum yield of the regolith are unknown; therefore, they are assumed to be similar to those at the Moon [2]. In calculations, the following parameters of the solar wind are used: the electron temperature $T_{eS} = 1.4 \cdot 10^5$ K, the ion temperature $T_{iS} = 7 \cdot 10^5$ K, the ion density (equal to the electron density) $n_{iS} = n_{eS} = 3.7 \text{ cm}^{-3}$, and the velocity $u = 468 \text{ km/s}$. As the solar wind ions, protons were chosen.

NONLINEAR DUST ACOUSTIC WAVES:

We use the standart Sagdeev's potential method to study nonlinear dust acoustic waves and solitons. The Gurevich's distribution is used for the electrons. The main equation is

$$\frac{1}{2} \left(\frac{d\varphi}{d\xi} \right)^2 + V(\varphi) = E,$$

where φ is the self-consistent plasma potential; $V(\varphi)$ is the Sagdeev potential; E is a parameter. Solution in a form of a soliton corresponds to the case when $E = 0$.

Figure 1 shows the potential profile for the soliton at Phobos. The calculations were conducted for the dimensionless velocity of the structure $M = 60$, which, in dimensional units, corresponds to a velocity of 0.6 m/s. Z_d is the charge of a dust grain expressed in units of the elementary charge. At Phobos, the equilibrium charge was assumed to be $Z_d = 2864$, which corresponds to the particle size $a = 1.445 \mu\text{m}$, while at Deimos, $Z_d = 3440$, which corresponds to the particle size $a = 1.768 \mu\text{m}$. Figure 2 presents the solutions in the form of periodic nonlinear waves at Deimos for $M = 60$ and $Z_d = 3440$. The calculations were carried out for two values of the parameter E : curve 1 corresponds to the value $E = V_{\min}/2$, and curve 2 to the value $E = V_{\min}/10$, where V_{\min} is the minimum value of the Sagdeev potential. The amplitudes of the potential in the nonlinear waves, in dimensional units, reach about 0.5 V (at Phobos) for the calculated parameters. Thus, the electric field in the wave is comparable to the background electric field [3] and it can be measured using Langmuir probes.

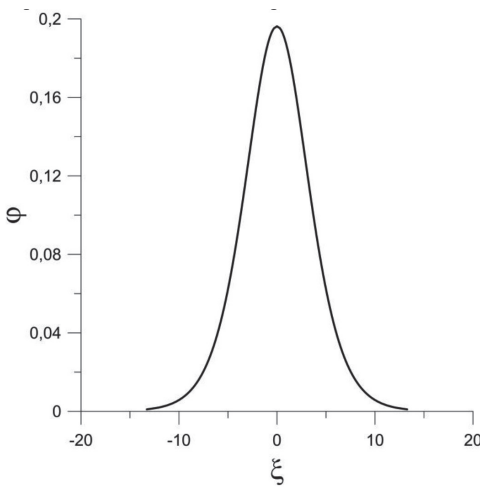


Figure 1. Solitary wave profile in dimensionless units for the conditions above Phobos at $M = 60$, $Z_d = 2864$ (corresponds to a particle size $a = 1.445 \mu\text{m}$)

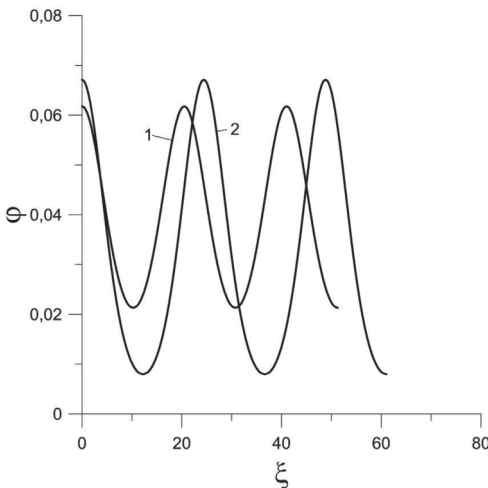


Figure 2. Nonlinear waves at Deimos at $M = 60$, $Z_d = 3440$. Curve 1 corresponds to the value $E = V_{\min}/2$, and curve 2 to the value $E = V_{\min}/10$, where V_{\min} is the minimum value of the Sagdeev potential

CONCLUSIONS:

Near the surface of Mars's satellites, a dusty plasma system exists, in which, similar to the dusty plasma system near the surfaces of the Moon and Mercury, the development of dust acoustic perturbations is possible. The amplitudes of the solitons and the periodic nonlinear dust acoustic waves near the surfaces of Phobos and Deimos can reach measurable values. Additionally, one has to account for the possibility of excitation of these nonlinear wave structures during the analysis of the current-voltage characteristics of the Langmuir probes, which the spacecraft used to study Mars's satellites has to be equipped with.

REFERENCES:

- [1] *Popel S. I., Golub' A. P., Izvekova Yu. N. et al.* On the distributions of photoelectrons over the illuminated part of the moon // JETP Letters. 2014. V. 99. P. 115–120. <https://doi.org/10.1134/S0021364014030114>
- [2] *Willis R. F., Anderegg M., Feuerbacher B., Fitton B.* // Photon and Particle Interactions with Surfaces in Space / ed. R.J.L. Gard. Dordrecht: Reidel, 1973. P. 389.
- [3] *Popel S. I., Golub' A. P., Zakharov A. V., Zelenyi L. M.* // JETP Letters. 2017. V. 106. Iss. 8. P. 485–475. <https://doi.org/10.7868/S0370274X17200012>.

NONLINEAR DUST ACOUSTIC WAVES IN SATURN'S MAGNETOSPHERE

Yu. N. Izvekova¹, S. I. Kopnin¹, D. V. Shokhrin^{1,2}, S. I. Popel^{1,2}

¹ Space Research Institute RAS, Moscow, Russia, izvekova@cosmos.ru

² National Research University Higher School of Economics, Moscow, Russia

KEYWORDS:

dusty plasma, nonlinear dust acoustic waves, kappa distribution, magnetosphere of Saturn

INTRODUCTION:

A characteristic feature of the magnetosphere of Saturn is the presence of two types of electrons, hot and cold ones, which obey kappa distributions. Electrons, magnetospheric ions, and dust particles, which have been discovered within the Cassini mission, form a dusty plasma system in the magnetosphere of Saturn. Nonlinear periodic dust acoustic waves of arbitrary amplitude, which can propagate in the dusty magnetosphere of Saturn, are considered. The obtained results are important for the interpretation of future space observations.

NONLINEAR DUST ACOUSTIC WAVES:

Dust and dusty plasma are important objects of study near the surface of the Moon, Mercury, the satellites of Mars and other atmosphereless celestial bodies, in the atmospheres and magnetospheres of planets, planetary rings, in the tails of comets, and interplanetary space. The plasma of the magnetosphere of Saturn was first studied as part of the Voyager 1 and Voyager 2 missions in the 1980s. Evidence of the existence of waves in the plasma of the atmosphere of Saturn was then obtained. During the Cassini mission, dusty plasma was discovered in the Saturn system in the vicinity of its moon Enceladus. The possible origin of the dusty plasma was also indicated in the studies within this mission: the Cassini spacecraft discovered fountains of dust particles and small water ice particles (which can also be interpreted as dust particles) many hundreds of kilometers high, gushing out of four cracks in the area of Enceladus's south pole. It was also discovered that two types of electrons, hot and cold ones, are simultaneously present in the magnetosphere of Saturn, and the electron distributions are described by kappa distributions. Nonlinear waves, primarily dust acoustic waves, can exist in the dusty plasma with parameters corresponding to the conditions in the magnetosphere of Saturn. We consider nonlinear periodic dust acoustic waves taking into account the presence of two types of electrons.

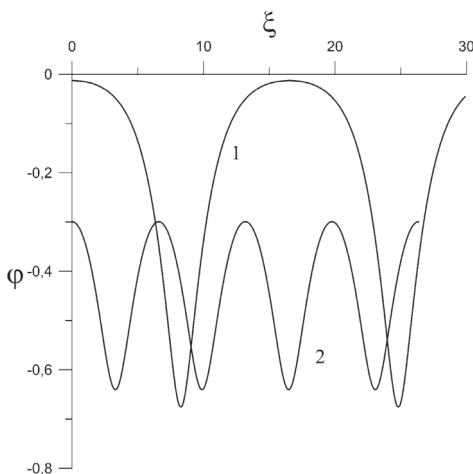


Figure 1. Examples of nonlinear periodic dust acoustic waves in the magnetosphere of Saturn. Plasma potentials versus coordinate in dimensionless units are shown

We write the basic equations for nonlinear periodic dust acoustic waves in the magnetosphere of Saturn. We consider one-dimensional disturbances described by a system of equations, consisting of the Poisson equation for the potential and equations defining the number densities of plasma components. We solve the resulting system using the Sagdeev potential method. The examples of solutions in a form of nonlinear periodic waves are shown in the Figure 1.

CONCLUSIONS:

This work shows the possibility of the propagation of nonlinear periodic dust acoustic waves in the dusty plasma of the magnetosphere of Saturn, which includes hot and cold electrons, magnetospheric ions, and charged dust particles. The amplitudes of nonlinear dust acoustic waves reach fairly large values and are in the region of negative potentials. In order to ensure the possibility of observing nonlinear periodic dust acoustic waves in the magnetosphere of Saturn in future space missions, it is necessary to equip the spacecraft with devices that allow high-precision measurements of electric fields.

SEARCH FOR ORDERED TRAJECTORIES OF DUST PARTICLES IN THE SYSTEM THE SUN AND MARS

N. I. Perov^{1,2}, O. A. Kirshina¹

¹ Cultural and Educational Center named after Valentina V. Tereshkova
perov@yarplaneta.ru

² Yaroslavl State Pedagogical University named after K. D. Ushinsky

KEYWORDS:

Sun, Mars, dust matter, the restricted circle plane three body problem, the choreographic trajectories, researching and reclaiming of the Solar system planets using single-pulse spacecraft flights

INTRODUCTION:

Let's find choreographic trajectories $r_3(x_3, y_3)$ of small bodies and estimates periods of them motion in respect of the baricentric system of coordinates, that uniformly rotates with angular velocity Ω (Sun (m_1) and Mars (m_2) are major bodies). Motion of a particle with negligible mass (m_3) is investigated in the frame of the restricted plane circle three body problem [1]. r_{12} is the distance between the major bodies, G is the gravitational constant. Method Runge–Kutta of numerical simulation is used [1–8].

BASED EQUATIONS:

According to work [1], the differential equation of a particle m_3 motion is presented in the form (1):

$$\begin{aligned} d^2\mathbf{r}_3/dt^2 + Gm_1(\mathbf{r}_3 - \mathbf{r}_1)/\|\mathbf{r}_3 - \mathbf{r}_1\|^3 + \\ + Gm_2(\mathbf{r}_3 - \mathbf{r}_2)/\|\mathbf{r}_3 - \mathbf{r}_2\|^3 - 2[d\mathbf{r}_3/dt, \Omega] - \Omega^2\mathbf{r}_3 = 0. \end{aligned} \quad (1)$$

Here, \mathbf{r}_3 is the radius-vector determined the position of the point m_3 in respect of the barycenter; \mathbf{r}_1 и \mathbf{r}_2 are the radii-vectors of the major bodies with mass m_1 and m_2 ;

$$\mathbf{r}_1 = -(m_2/(m_1 + m_2))\mathbf{r}_{12}, \quad \mathbf{r}_2 = (m_1/(m_1 + m_2))\mathbf{r}_{12}; \quad (2)$$

$$\Omega = \sqrt{G(m_1 + m_2)/r_{12}^3}.$$

For solving of the equations (1) the following units of measurements are used. r_{12} is the unit of length; m_1 is the unit of mass; the unit of time was chosen so that $G = 1$. The initial conditions are following: $x_1 \neq 0$, $dx_1/dt = 0$, $y_1 = 0$, $dy_1/dt = 0$, $x_2 \neq 0$, $dx_2/dt = 0$, $y_2 = 0$, $dy_2/dt = 0$, $x_{30} \neq 0$, $-3.5 < (dx_3/dt)_0 < +3.5$ (unit of length)/(unit of time), $-3.5 < (dy_3/dt)_0 < +3.5$ (unit of length)/(unit of time), $-1 < y_{30} < +1$ (unit of length). The results of numerical simulations devoted researching of m_3 motion in intervals of time corresponded dozens and hundreds revolutions of major bodies are presented in figures (Figures 1–8).

EXAMPLES:

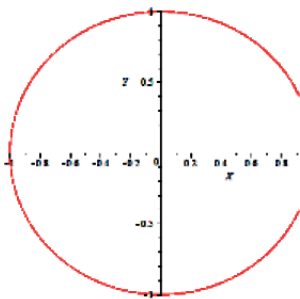


Figure 1. "Rendezvous" m_3 with Mars and the revolution around the Sun

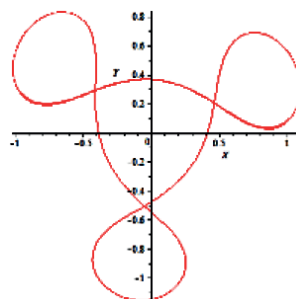


Figure 2. Motion m_3 in the region of Mars and the Earth

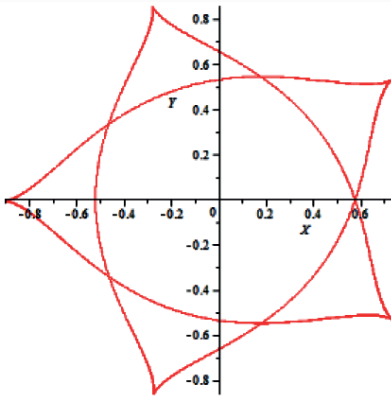


Figure 3. The movement of m_3 along Mars orbit

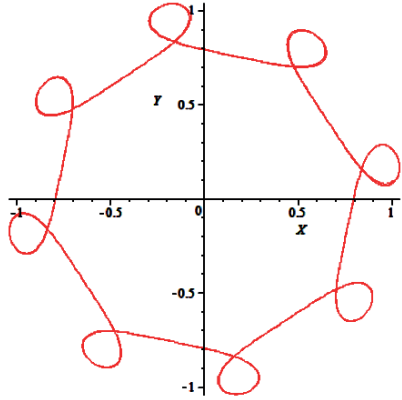


Figure 4. The movement of m_3 inside orbit of Mars

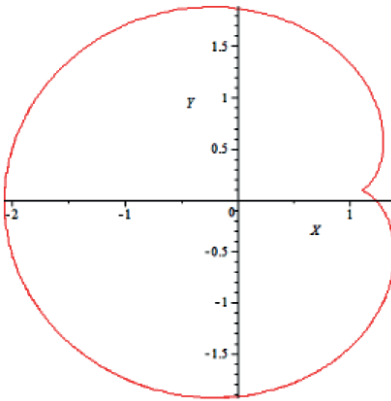


Figure 5. The movement m_3 from Mars to the to the asteroid belt

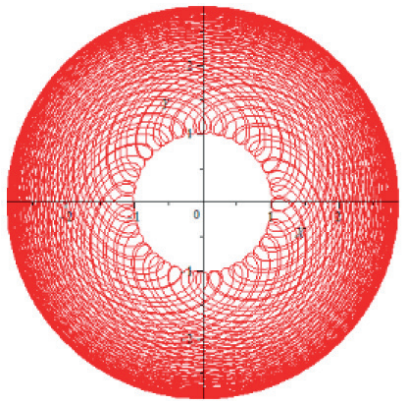


Figure 6. The movement m_3 from Mars asteroid belt and back

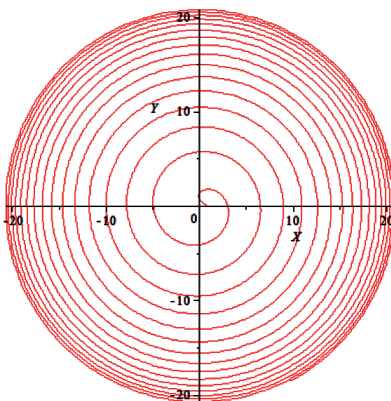


Figure 7. The movement m_3 from Mars to Uranus and back

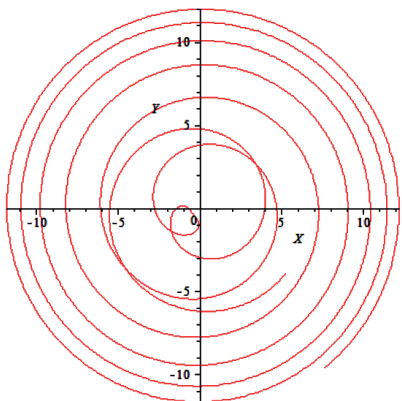


Figure 8. The movement m_3 from Mars to Neptune and back

PERIOD OF M_3 MOTION ALONG HORSESHOE SHAPED TRAJECTORY DEPENDED FROM THE RATIO M_1/M_2 :

In Table 1 period T of m_3 movement along horseshoe-shaped trajectory (Figure 1) in restricted circle plane three body problems depended on the ratio of m_1/m_2 and the number of revolutions n of major body is presented.

Table 1. Period T of movement of m_3 along horseshoe-shaped trajectory (Figure 1) in the restricted circle plane three body problem depended on the ratio of m_1/m_2 and the number of revolutions n of major bodies ($n = T/(2\pi)$).

m_1/m_2	$\lg(m_1/m_2)$	T , units of time	$n = T/(2\pi)$, number of m_2 revolutions	$\lg(n)$
800	2.90309	281.1265	44.242672	1.650722
900	2.954242	281.3416	44.776906	1.651054
10^3	3	293.8707	46.770974	1.669976
$4 \cdot 10^3$	3.60206	725.5877	115.480869	2.062510
$4 \cdot 10^5$	5.60206	10033.39175	1596.863893	3.2032268
$4 \cdot 10^7$	7.60206	110250	17546.83247	4.244199
$4 \cdot 10^9$	9.60206	$9.33963404 \cdot 10^5$	1.489632 \cdot 10^5	5.173079

To estimate the value of n (m_1/m_2), the models (3) and (4) are proposed.

$$\lg(n) = a_0 + a_1 \lg(m_1/m_2) + a_2 [\lg(m_1/m_2)]^2, \quad (3)$$

$$n = 10^{a_0} (m_1/m_2)^{a_1 + a_2 \lg(m_1/m_2)}. \quad (4)$$

where

$$a_0 = -0.2902078693, a_1 = 0.700754946, a_2 = -0.0137246231.$$

(The least squares method was used. $10^2 < m_1/m_2 < 10^{11}$).

CONCLUSIONS:

Choreographic trajectories in the considered model are stated. They may be useful for spacecraft launches. The movement of m_3 along horseshoe-shaped trajectory is stable if the ratio of $m_1/m_2 > 1000$. Horseshoe-shaped trajectories are reserved for zero initial conditions for $m_1/m_2 = 10000$ if $-1.006793 < x_{30} < -0.9936$. (For $m_1/m_2 = 1000$ horseshoe-shaped trajectories are reserved for zero initial conditions if $-1.0095 < x_{30} < -0.987$.)

REFERENCES:

- [1] *Marchal C.* The three-body problem. Elsevier Sciences, 1990. 572 p.
- [2] *Murray C.D., Dermott S.F.* Solar system dynamics. Cambridge University Press, 1999. 592 p.
- [3] *Krivov A. V., Sokolov L. L., Kholshchevnikov K. V., Shor V.A.* The existence of a swarm of particles in the vicinity of the PHOBOS orbit // *Astronomicheskii vestnik*. 1991. V. 25. P. 317–326 (in Russian).
- [4] *Stuber T.A., Kirchschrager F., Pearce T.D. et al.* How much large dust could be present in hot exozodiacal dust systems? // *Astronomy and Astrophysics*. 2023. V. 678. Article A121. 18 p. <https://doi.org/10.1051/0004-6361/202346109>.
- [5] *Ipatov S.I.* Migration of planetesimals from beyond Mars' orbit to the Earth // *Europlanet Science Congress*. 2020. V. 14. Article EPSC2020-71. <https://doi.org/10.5194/epsc2020-71>.
- [6] *Marov M. Ya., Ipatov S.I.* Migration of planetesimals from the feeding zone of the giant planets to the terrestrial planets and the Moon // *INASAN Science Reports*. 2020. V. 5(3). P. 94–96. DOI: 10.26087/INASAN.2020.5.3.003.
- [7] *Perov N.I.* Horseshoe Trajectories of Small Bodies in the Systems of "A Star and a Planet" // *Astronomy-2018 (13th Congress of the Intern. Public Organization "Astronomical Society")*. Ser. Modern Star Astronomy: Abstr. Moscow: IZMIRAN, 2018. P. 259–262.
- [8] *Calleja R., Garcia-Azpeitia C., Lessard J.-P., Mireles James J.D.* Torus knot choreographies in the n -body problem. // *Nonlinearity*. 2021. V. 34. No. 1. DOI: 10.1088/1361-6544/abcb08.

DYNAMIC EVOLUTION OF NEAR-EARTH ASTEROIDS ASSOCIATED WITH THE σ -CAPRICORNIDS METEOROID STREAM

M. V. Sergienko, Y. A. Nefedyev, A. O. Andreev

Kazan Federal University, Kazan, Russia, maria_sergienko@mail.ru

KEYWORDS:

meteoroids, meteoroid streams, asteroids, small bodies of the Solar system, the orbits evolution, orbital resonances

INTRODUCTION:

The issue of establishing genetic relationships among small Solar System bodies is of considerable significance both for advancing evolutionary theories and for refining our understanding of the distribution of meteoroid material in near-Earth space. For the majority of meteoroid associations, genetic connections with small bodies have yet to be conclusively determined. In this study, we investigate the σ -Capricornids meteoroid shower, its probable association with near-Earth asteroids identified via the synthetic approach [1, 2], and conduct an analysis of the long-term dynamical evolution of the orbits of those asteroids associated with the σ -Capricornids shower. The σ -Capricornids is categorized as a minor meteor shower with a low zenithal hourly rate. According to the IAU Meteor Data Center, it is listed under identification number 179 and is associated with the Apollo-type asteroid 2003 MT9 (<https://www.ta3.sk/IAUC22DB/MDC2022/>). However, reference [4] suggests an additional relationship with three other Apollo group asteroids: 2008 BO16, 2011 EC41, and 2013 CT36. Our objective was to verify the association between the σ -Capricornids meteoroid shower and near-Earth asteroids employing our proprietary synthetic method, and to perform long-term orbital evolution studies for the asteroids identified as genetically connected to the σ -Capricornids.

METHODS:

The proprietary synthetic method, described in detail in [2], is employed to identify associations between the meteoroid stream and near-Earth asteroids.

RESULTS:

Using the proprietary synthetic method, associations have been established between the meteoroid shower and the following Apollo-group asteroids: 2003 MT9, 2008 BO16, 2011 EC41, 2013 CT36, 2008 EM9, 2003 OV, 2005 ET70, 2011 FZ22, and 2013 NE19. According to their Tisserand parameters with respect to Jupiter, some of these asteroids move in comet-like orbits, while others follow transitional-type orbits, which does not preclude the possibility that the identified asteroids may be extinct cometary nuclei or their remnants. The conducted analysis of the orbital evolution of these asteroids demonstrates significant perturbations due to planetary influences, particularly from Jupiter. The study also discusses the alteration of asteroid orbits as a result of orbital resonances with planets.

REFERENCES:

- [1] *Sergienko M. V., Nefedyev Y. A., Andreev A. O.* Connection of the sigma-Capricornids meteor shower with Near-Earth asteroids // *Meteoritics and Planetary Science*. 2024. V. 59. Article A380.
- [2] *Sergienko M. V., Andreev A. O., Nefedyev Y. A.* The modernized synthetic method for searching connections between Near-Earth objects // *Meteoritics and Planetary Science*. 2024. V. 59. Article A381.
- [3] *Kokhirova G. I., Babadzhanov P. B.* Current Knowledge of Objects Approaching the Earth // *Solar System Research*. 2023. V. 57. Iss. 5. P. 467–485. DOI: 10.1134/S0038094623050039.

**SESSION 5. EXTRASOLAR PLANETS (EP)
ORAL SESSION**

INTERPRETATION OF ABSORPTION OF HOT EXOPLANETS DURING THE TRANSIT OF HELIUM TAILS

**M. S. Rumenskikh, E. D. Savintseva, I. B. Miroshnichenko,
I. F. Shaikhislamov**

*Institute of Laser Physics SB RAS, Novosibirsk, Russia
marina_rumenskikh@mail.ru*

KEYWORDS:

transit spectroscopy, atmospheres, hot exoplanets, MHD modelling

INTRODUCTION:

The atmosphere of hot Jupiters is heated by intense radiation from the parent star and undergoes an outflow beyond the boundaries of the Roche lobe. Around some exoplanets, extended tails during the outflow of planetary matter can be formed, which have observational evidences. Modeling showed that the magnetic field can significantly affect the structure of the atmosphere, and at some values reduce the outflow of planetary matter and the formation of tails. The study was supported by the Russian Science Foundation grant No. 25-72-10080.

METHODS AND RESULTS:

Transit spectroscopy of hot exoplanets is used to obtain the main characteristics of exoplanetary atmospheres and plasmaspheres, such as composition, temperature, density, and to study the effects that occur during the collision of plasma flows of stellar and planetary winds. It is known that the atmosphere of many hot planets consists mainly of hydrogen. However, the most popular in transit spectroscopy Ly- α line undergoes absorption by the interstellar medium and is also distorted due to the effect of geocoronal emission. The line of metastable helium $\lambda = 10830$ A is not subject to significant distortions, and therefore can be used to obtain higher-quality data on exoplanetary systems. We use a numerical 3D MHD model to simulate the transit absorptions of the planets Wasp-107 b and Wasp-69 b in the 10830 A metastable helium line to determine the influence of planetary system parameters and magnetic field on observational manifestations.

CONCLUSION:

Modeling has shown that the magnetic field can significantly influence the structure of the atmosphere, and at certain values reduce the outflow of planetary matter and the formation of tails.

ACKNOWLEDGMENTS:

This work was done with a support of the Russian Science Foundation grant No. 25-72-10080.

EXPERIMENT ON THE MODELING TRANSIT ABSORPTIONS OF HOT EXOPLANETS

**M. S. Rumenskikh, E. D. Savintseva, A. G. Berezutsky,
A. A. Chibrarov, I. F. Shaikhislamov**

*Institute of Laser Physics SB RAS, Novosibirsk, Russia
marina_rumenskikh@mail.ru*

KEYWORDS:

transit spectroscopy, multipass schemes, hot exoplanets, laboratory modelling

INTRODUCTION:

Exoplanet research is rapidly developing. To date, about 6,000 exoplanets have been discovered, and their number is constantly increasing. New space telescopes are launched, ground-based instruments are improved, and the volume of observational data continues to grow. However, an expanded knowledge base is needed to interpret the data in order to find space weather parameters and chemical composition. One such task is to measure the course of physicochemical reactions that are important for helium-containing plasma environments. Observations have shown that many hot exoplanets contain helium in their atmospheres, and therefore, for a high-quality interpretation of observational data, it is necessary to accurately know the constants describing the processes in helium-containing environments.

METHODS AND RESULTS:

Laboratory modeling of plasma processes has significantly expanded the understanding of a number of fundamental phenomena in near and deep space (waves in the ionosphere and magnetosphere, interaction of the Earth's magnetosphere with the solar wind, magnetic field reconnection, particle acceleration, collisionless shock waves, astrophysical jets). It's possible to reproduce plasma parameters comparable to those observed in real space objects, and to study the dynamics of interactions in controlled and repeatable conditions.

Laboratory modeling of exoplanets is a completely new direction, and there are only a few very limited examples of its implementation. One of the aspects of planetary atmospheres that is difficult to reproduce in the laboratory is the optical path length. Most of the observed deep space objects, including exoplanet atmospheres, are extended, with characteristic distances calculated in hundreds and thousands of kilometers. To reproduce absorptions in such objects in laboratory setups, taking into account the operation at higher gas pressure, an optical path of ~ 1 km is required, for which a multi-pass scheme was used.

CONCLUSION:

The report highlights the specifics of the setup and the first results of a laboratory experiment aimed at measuring the rates of physical and chemical reactions in the upper atmospheres of hot exoplanets, as well as testing the application of the theory of atomic alignment to search for magnetic fields of hot exoplanets.

ACKNOWLEDGMENTS:

This work was done with a support of branch 10 of NCPM.

COMPLEX PLACE NUMERICAL MODELING OF HOT EXOPLANET ATMOSPHERES AND INTERPRETATION OF MULTI-LINE TRANSIT OBSERVATIONS

I. F. Shaikhislamov^{1,2,3}, I. B. Miroshnichenko^{1,3}, M. S. Rumenskikh^{1,2},
A. V. Shepelin¹, A. G. Berezutskiy^{1,2}, S. S. Sharipov^{1,3},
M. P. Golubovskiy^{1,3}, A. A. Chibrinov¹

¹ *Institute of Laser Physics SB RAS, Novosibirsk, Russia*
ShaikhislamovIldar@yandex.ru

² *Institute of Astronomy RAS, Moscow, Russia*

³ *Novosibirsk State Technical University, Novosibirsk, Russia*

KEYWORDS:

exoplanets, atmosphere, transit observations, plasma

ABSTRACT:

Hot gas planets rotating in close orbits form a subclass among a very diverse population of exoplanets. They have a unique feature of extensive outflow of the upper atmosphere. Multicomponent and partially ionized matter, heated by intense ionizing radiation of the parent star, flows through the Roche lobe at supersonic speed and collides with the stellar wind plasma. Such dynamics are fundamentally different from the processes in the rarefied exospheres of the planets of the Solar System. Observational evidence for such an outflow of the atmosphere was found for a number of hot Jupiters and warm Neptunes by measuring their transit absorption in the VUV lines of such elements as H, C, O, Mg, Si, Fe. Recently, rich information was provided by the analysis of the transit absorption of exoplanets in the 1083 nm line in the IR range of the metastable helium triplet. Moreover, the first detection of transit absorption by an oxygen atom at a wavelength of 777.4 nm in the IR range in Kelt-9b promises new possibilities.

Comparison of spectrally resolved transit measurements of individual exoplanets and 3D modeling of their dynamic environment provides compelling evidence for the interaction between planetary and stellar winds, allowing important inferences about exoplanetary atmospheres and stellar wind plasma parameters. The outflow of hot exoplanet atmospheres is a complex phenomenon influenced by a number of physical processes, and quantitative interpretation of observational data requires dedicated numerical modeling, and the corresponding models have undergone significant development since 2003 [1]. In this talk, we present some results from modeling with a 3D aeronomy multifluid MHD model that includes radiative transfer and excited-level kinetic modeling. We studied several hot Jupiters and warm Neptunes for which transit observations were carried out with different spectral resolutions — HD209458b, HD189733b, Wasp107b, Wasp80b, GJ436b, GJ3470b, TOI421b&c, PiMenC. For two of them (GJ436b [2], GJ3470b [3]), modeling showed that the observed strong absorption in the hydrogen Ly α line can be explained only if the corresponding stellar winds interacting with the outflowing atmosphere have parameters comparable to the solar wind. Modeling of HD189733b [4] confirmed that the existing variability of the transit spectra measurements can be explained by changing space weather conditions. The transit absorptions in the H α , OI, CII and HeI lines measured for HD209458b allowed us to estimate the upper limit of the possible magnetic field of this planet [5]. We also modeled two binary planetary systems, TOI421 and HD63433, for which we predict the possibility of interaction of the outflowing atmospheres through stellar wind disturbances [6].

For the ultra-hot Jupiter Kelt9b, we have shown for the first time, based on modeling the kinetics of levels, that the observed absorption in the H α line of hydrogen in the visible range is directly related to a new channel of atmospheric heating — photoionization of excited levels. Such studies of var-

ious stellar-planetary systems create a basis for remote sensing of changing conditions of space weather of different stars. Progress in the quality and quantity of observations, new instruments, including the planned launch of the Spektr-UV telescope, new approaches to sensing exoplanets, including new spectral windows, multispectral and multi-instrument observations require further development of modeling tools capable of complex modeling and interpretation of all available observations.

ACKNOWLEDGMENTS:

The research is supported by RNF projects 23-12-00134, 25-72-20053.

REFERENCES:

- [1] *Lammer H., Selsis F., Ribas I. et al.* Atmospheric Loss of Exoplanets Resulting from Stellar X-Ray and Extreme-Ultraviolet Heating // *Astrophysical J.* 2003. V. 598. No. 2. Article L121. DOI 10.1086/380815.
- [2] *Khodachenko M. L., Shaikhislamov I. F., Lammer H. et al.* Global 3D Hydrodynamic Modeling of In-transit Ly α Absorption of GJ 436b // *Astrophysical J.* 2019. V. 885. No. 1. Article 67. DOI: 10.3847/1538-4357/ab46a4.
- [3] *Shaikhislamov I. F., Khodachenko M. L., Lammer H. et al.* // *Monthly Notices of the Royal Astronomical Society.* 2021. V. 500. Iss. 1. P. 1404–1413. <https://doi.org/10.1093/mnras/staa2367>.
- [4] *Rumenskikh M. S., Shaikhislamov I. F., Khodachenko M. L. et al.* Global 3D Simulation of the Upper Atmosphere of HD189733b and Absorption in Metastable He I and Ly α Lines // *Astrophysical J.* 2022. V. 927. No. 2. Article 238. DOI: 10.3847/1538-4357/ac441d.
- [5] *Khodachenko M. L., Shaikhislamov I. F., Lammer H. et al.* The impact of intrinsic magnetic field on the absorption signatures of elements probing the upper atmosphere of HD209458b // *Monthly Notices of the Royal Astronomical Society.* 2021. V. 507. Iss. 3. P. 3626–3637. DOI: 10.1093/mnras/stab2366.
- [6] *Berezutsky A. G., Shaikhislamov I. F., Rumenskikh M. S. et al.* On the transit spectroscopy features of warm Neptunes in the TOI-421 system, revealed with their 3D aeronomy simulations // *Monthly Notices of the Royal Astronomical Society.* 2022. V. 515. Iss. 1. P. 706–715. DOI: 10.1093/mnras/stac1633.

COMPARISON OF THE MAGNETOSPHERE OF OSIRIS IN THE PARABOLOID AND MHD MODELS

A. S. Krotov^{1,2}, E. S. Belenkaya²

¹ *Lomonosov Moscow State University, Faculty of Physics, Moscow, Russia
a-krotov.2014@mail.ru*

² *Skobeltsyn Institute of Nuclear Physics Lomonosov Moscow State University
Moscow, Russia*

KEYWORDS:

exoplanets, stars, magnetic field, magnetosphere, Alfvén Mach number, Alfvén wings

INTRODUCTION:

The article by Zhilkin and Bisikalo [1] describes the MHD modelling of magnetospheres of hot Jupiters located near the Alfvén point of the stellar wind of their host stars, where the Alfvén Mach number is equal to 1. In particular, the authors model the magnetosphere of the exoplanet HD 209458 b, also known by the unofficial name Osiris. Since this exoplanet lies in the boundary region between regimes of stellar wind flow with Alfvén Mach numbers greater and less than one, both super-Alfvénic and sub-Alfvénic cases are considered correspondingly.

Previously, we conducted a simulation of the magnetosphere of HD 209458 b using the analytical paraboloid magnetospheric model [2], so it is reasonable to compare the results obtained with the paraboloid model to those presented by Zhilkin and Bisikalo MHD simulations [1].

Despite methodological differences, the results show overall agreement in the large-scale structure of the magnetosphere of HD 209458 b. The paraboloid model provides a qualitative presentation of the geometry and orientation of magnetospheric magnetic field structure, serving as a convenient tool for preliminary analysis, while the MHD approach allows for a deeper investigation of physical processes related to plasma flow redistribution and the emergence of local instabilities.

REFERENCES:

- [1] *Zhilkin A.G., Bisikalo D.V. On possible types of magnetospheres of hot Jupiters // Astronomical J. 2019. V.63. Iss.7. P.550–564. DOI: 10.1134/S1063772919070096.*
- [2] *Belenkaya E.S., Krotov A.S., Alexeev I.I., Lavrukhin A.S. Exoplanets on close-in orbits around their host stars (HD 209458 b) // Astronomical and Astrophysical Trans. 2024. V. 34. Iss. 3. P. 277–294. DOI: 10.17184/eac.9179.*

SEARCH FOR HABITABLE WORLDS: POTENTIALLY OBSERVABLE BIOMARKERS TO PROBE IN THE ATMOSPHERES OF EXOPLANETS

D.V. Bisikalo^{1,2}, V.I. Shematovich², G.N. Tsurikov²

¹ National Center of Physics and Mathematics, Sarov, Russia

² Institute of Astronomy RAS, Moscow, Russia, tsurikov@inasan.ru

KEYWORDS:

exoplanets atmospheres, biomarkers, nitric oxide

INTRODUCTION:

The search for potentially habitable exoplanets is a complex observational and theoretical problem. There are many signs of potential habitability of an exoplanet [1] (for example, the location of the planet in the habitable zone [2, 3] is considered a necessary but not sufficient sign). An important additional sign of habitability is the special chemical composition of the planet's atmosphere, which may be a consequence of biological and geological activity on it. Atoms and molecules that indicate such an atmosphere or individual biological processes on the planet are considered potential biomarkers. The search for spectral lines of biomarker molecules in the atmospheres of exoplanets located in the habitable zone is an effective strategy for determining their potential habitability. This task will be included in the scientific program of the Spektr-UF space telescope (ST) [4] being created in Russia.

One of the most important criteria for biomarker molecules on exoplanets is the possibility of their reliable detection in a time not exceeding the time of the telescope's scientific program. This work presents an overview of potentially observable biomarkers in the atmospheres of exoplanets. Particular attention is paid to the molecules — indicators of N₂-O₂ dominant atmosphere, which, according to modern concepts, can be formed on a planet of the terrestrial type as a result of biological and geological activity [5, 6]. It is shown that the nitric oxide molecule is a promising biomarker for search using ultraviolet space telescopes, including Spektr-UF. Using the long-slit spectrograph (LSS, R = 1000) ST Spektr-UF, detection of nitric oxide is possible on typical super-Earths and sub-Neptunes in the habitable zone of G- and K-type stars more active than the Sun [7]. The detection limits of this molecule are up to 30 pc. We provide a list of potential targets for ST Spektr-UF — exoplanets, the detection of nitric oxide on which will allow us to make a conclusion about their potential habitability.

ACKNOWLEDGMENTS:

The work was supported by program 10 "Experimental laboratory astrophysics and geophysics" of the National Center for Physics and Mathematics.

REFERENCES:

- [1] Meadows V.S., Barnes R.K. Factors Affecting Exoplanet Habitability // Handbook of Exoplanets / eds. Deeg H., Belmonte J. Springer, 2018. P.57. DOI: 10.1007/978-3-319-55333-7_57.
- [2] Kasting J.F., Whitmire D.P., Reynolds R.T. Habitable Zones around Main Sequence Stars // Icarus. 1993. V. 101. Iss. 1. P. 108–128. DOI: 10.1006/icar.1993.1010.
- [3] Kopparapu R.K., Ramirez R., Kasting J.F. et al. Habitable Zones around Main-sequence Stars: New Estimates // The Astrophysical J. 2013. V. 765. No. 2. P. 131. DOI 10.1088/0004-637X/765/2/131.
- [4] Sachkov M., Kopylov E. The World Space Observatory — Ultraviolet mission: science program and status report // Proc. SPIE. 2024. V. 13093. Article 130933F. DOI: 10.1117/12.3020257.
- [5] Lammer H., Sproß L., Grenfell J.L. et al. The Role of N₂ as a Geo-Biosignature for the Detection and Characterization of Earth-like Habitats // Astrobiology. 2019. V. 19. No. 7. P. 927–950. DOI: 10.1089/ast.2018.1914.
- [6] Sproß L., Scherf M., Shematovich V.I. et al. Life as the Only Reason for the Existence of N₂-O₂-Dominated Atmospheres // Astronomy Reports. 2021. V. 65. No. 4. P. 275–296. <https://doi.org/10.1134/S1063772921040077>.

- [7] *Tsurikov G. N., Bisikalo D. V., Shematovich V. I. et al.* Searching for Biomarkers with Spektr-UF Observatory: Nitric Oxide Molecule in Atmospheres of Exoplanets near the Active Host Stars // *Astronomy Reports*. 2024. V. 68. Iss. 12. P. 1406–1422. DOI: 10.1134/S1063772925701355.

PLANETARY MAGNETIC FIELD AS A PROPERTY OF WEAKENING THE PRECIPITATING ELECTRONS FLUX INTO THE EARTH'S ATMOSPHERE

D.V. Bisikalo^{1,2}, V.I. Shematovich², A.G. Zhilkin², G.N. Tsurikov²

¹ National Center of Physics and Mathematics, Sarov, Russia

² Institute of Astronomy RAS, Moscow, Russia, tsurikov@inasan.ru

KEYWORDS:

planetary magnetic field, nitric oxide, precipitating electrons

INTRODUCTION:

The nitric oxide molecule is an indicator of N_2 - O_2 atmosphere of a terrestrial planet [1] (which can be formed due to biological activity [2]) and, therefore, a potential atmospheric biomarker on exoplanets. Spectral lines of nitric oxide can be detected on nearby (<30 pc) exoplanets in the habitable zone of active stars using the planned Spektr-UF space telescope [3]. It is known from observations of the Earth's thermosphere [4] that nitric oxide is effectively formed by the precipitation of electrons with energies of 1–10 keV. Moreover, nitric oxide concentration depends on the energy flux of precipitating electrons [5], Q_0 . Thus, if we determine the nitric oxide content on a planet with different intrinsic magnetic fields, B_{pl} , it is possible to estimate how B_{pl} affects the weakening of Q_0 independently.

To make such an estimate, we compared the nitric oxide content for two cases with different B_{pl} values: a) on Earth ($B_{pl} = B_{Earth}$) and b) on a planet without its own magnetic field ($B_{pl} = 0$). Calculation at an intermediate value of B_{pl} is possible only with correct modeling of the entire complex of physical and chemical processes leading to the precipitation of electrons of magnetospheric origin [6]. This complex problem can be solved quite simply only in the case of a zero magnetic field value, $B_{pl} = 0$.

The nitric oxide content for a planet with $B_{pl} = B_{Earth}$ was taken from satellite observations of the Earth's atmosphere. The numerical model of nitric oxide formation [5] tested on Earth was used for a planet with $B_{pl} = 0$. To determine the parameters of precipitating e^- for case b), we used the MHD model of the interaction of the stellar wind with the atmosphere of a terrestrial planet with $B_{pl} = 0$, which was tested on Venus [7].

Based on the calculation results, it was determined that the total number of nitric oxide molecules on a planet with $B_{pl} = 0$ is nearly 10 times greater than on Earth (the conditions of a quiet Sun are considered). The corresponding conclusion can also be made for the energy flux Q_0 , which, due to the presence of B_{pl} on the planet, is weakened by an order of magnitude compared to a planet without a magnetic field. The resulting estimate shows the role of the Earth's magnetic field as a protective mechanism against electron precipitation.

ACKNOWLEDGMENTS:

The work was supported by the Russian Science Foundation (project No. 22-12-00364-p).

REFERENCES:

- [1] Sproß L., Scherf M., Shematovich V.I. et al. Life as the Only Reason for the Existence of N_2 - O_2 -Dominated Atmospheres // *Astronomy Reports*. 2021. V. 65. No. 4. P. 275–296. <https://doi.org/10.1134/S1063772921040077>.
- [2] Lammer H., Sproß L., Grenfell J.L. et al. The Role of N_2 as a Geo-Biosignature for the Detection and Characterization of Earth-like Habitats // *Astrobiology*. 2019. V. 19. No. 7. P. 927–950. DOI: 10.1089/ast.2018.1914.
- [3] Tsurikov G.N., Bisikalo D.V., Shematovich V.I. et al. Searching for Biomarkers with Spektr-UF Observatory: Nitric Oxide Molecule in Atmospheres of Exoplanets near the Active Host Stars // *Astronomy Reports*. 2024. V. 68. Iss. 12. P. 1406–1422. DOI: 10.1134/S1063772925701355.

- [4] *Barth C.A., Mankoff K.D., Bailey S.M. et al.* Global observations of nitric oxide in the thermosphere // *J. Geophysical Research: Space Physics*. 2003. V. 108. Iss. A1. Article 1027. <https://doi.org/10.1029/2002JA009458>.
- [5] *Shematovich V., Bisikalo D., Tsurikov G. et al.* Non-Thermal Processes of Nitric Oxide Formation during Precipitation of Auroral Electrons into the Upper Atmospheres of Terrestrial Planets // *Astronomy Reports*. 2024. V. 68. P. 843–864. <https://doi.org/10.1134/S1063772924700744>.
- [6] *Zelenyi L. M., Malova H. V., Grigorenko E. E. et al.* Thin current sheets: from the work of Ginzburg and Syrovatskii to the present day // *Physics Uspekhi*. 2016. V. 59. P. 1057–1090. DOI: 10.3367/UFNe.2016.09.037923.
- [7] *Zhilkin A. G., Shematovich V. I., Tsurikov G. N. et al.* 3D Numerical Model for Studying Electron Precipitation in the Upper Atmospheres of Venus-Like Exoplanets // *Astronomy Reports*. 2024. V. 68. P. 1252–1265. <https://doi.org/10.1134/S1063772925701252>.

TECHNIQUES FOR EXOPLANET DIRECT IMAGING, UPDATED ANALYSIS AND THE PROPOSAL FOR A HIGH CONTRAST IMAGING INSTRUMENT ONBOARD THE WSO-UV 1.7 METER TELESCOPE

A. Tavrov, I. Shulgina, A. Yudaev

Space Research Institute RAS, Moscow, Russia, tavrov@iki.rssi.ru

KEYWORDS:

exoplanets, direct imaging, high-contrast instrument, WSO-UV telescope

ABSTRACT:

In eve of IR Roman 2.4 m space telescope of wait to launch with having onboard the imaging coronagraph instrument (CGI) with active extreme adaptive optics and IFS — integral field spectrometer, we revisit what to recommend as a high contrast instrument within WSO-UV aiming direct observe exoplanets.

Critical analysis was performed for the stellar coronagraph that principally uses an apodization in pupil plane with an LC-SLM matrix, that is simultaneously used to compensate wavefront aberrations as coming from meters sized optics primary and secondary mirrors and apertures of the WSO-UV telescope.

For an unaberrated optics, the simulated coronagraphic contrast exceeds a 109 in magnitude at a $5 \lambda/D$ stellocentric separation within an image area inside the 90 degree sector.

In the proposed configuration, the active wavefront sensing in the focal plane, where the since camera is mounted can use the similar wavefront sensing techniques as were developed in Roman space telescope: e. g. pair-wise-probing, self-coherent camera.

MULTICOLOR PHOTOMETRIC VALIDATION OF THE EXOPLANET CANDIDATE AROUND SOI-3

O.Y. Yakovlev¹, M.S. Berezhnaya², K.A. Antoniuk³

¹ *Special Astrophysical Observatory, Nizhnij Arkhyz, Russia, yko-v@ya.ru*

² *Kazan Federal University, Kazan, Tatarstan, Russia*

³ *Crimean Astrophysical Observatory, Nauchnyi, Russia*

KEYWORDS:

exoplanets, photometry, follow-up observations

INTRODUCTION:

Hot Jupiters can be detected using small ground-based telescopes with the transit photometry method. If the stellar parameters are known with large uncertainties, transits with a depth of 0.01–0.05 mag may be caused by a planet, a brown dwarf, or another star. To distinguish between these cases, it is usually sufficient to determine the mass of the companion using the radial velocity method. If radial velocity data are not available, a preliminary validation can be performed using multicolor photometry of the system. This work is devoted to the validation of an exoplanet candidate around the star SOI-3, in the light curve of which dips with period $P = 45.99$ h, duration $\tau = 2.17$ h, and depth $\Delta m = 0.056$ mag were detected [1]. Additional results for other candidates are also discussed.

METHOD:

Photometric data obtained in broadband filters i -, r -, v -, and b - with the 1-m AZT-11 telescope (CrAO RAS) are analyzed, along with additional unfiltered (white-light) data from the 50-cm robotic telescope of SAO RAS (the instrument that originally detected this candidate). Using different transit models, the transit depth, other parameters, and the radius of the eclipsing body are determined in various filters, as well as for odd and even transits separately. These values are then compared to identify effects that are characteristic of binary stars [2]. If the eclipse is caused by a planet, the estimated radius should remain consistent (within the given accuracy) across all transits and filters.

RESULTS:

Modeling for different cases yields an estimated radius of the eclipsing body in the range of 1.71–2.64 Jupiter radii (in some cases up to 2.8). A dependence of the radius on wavelength and on odd/even transit number was also found. Based on these results, we conclude that SOI-3 is a binary star, and thus the presence of an exoplanet around this star is not confirmed.

REFERENCES:

- [1] *Yakovlev O. Y., Valeev A. F., Valyavin G. G. et al. Eight Exoplanet Candidates in SAO Survey // Astrophysical Bull. 2023. V. 78. Iss. 1. P. 79–93. <https://doi.org/10.1134/S1990341323010108>.*
- [2] *Colón K.D., Ford E.B., Morehead R.C. Constraining the false positive rate for Kepler planet candidates with multicolour photometry from the GTC // Monthly Notices of the Royal Astronomical Society. 2012. V. 426. Iss. 1. P. 342–353. <https://doi.org/10.1111/j.1365-2966.2012.21711.x>.*

VALIDATION OF EXOPLANET CANDIDATES USING SPECTROSCOPIC OBSERVATIONS FROM BTA-6

A. E. Ivanova¹, M. S. Berezhnaya², O. Y. Yakovlev³, S. S. Kotov³,
A. V. Moiseev³, G. G. Valyavin³

¹ *Space Research Institute RAS, Moscow, Russia*

anastasia.ivanova@cosmos.ru

² *Kazan Federal University, Respublika Tatarstan, Kazan, Russia*

³ *Special Astrophysical Observatory, Nizhny Arkhyz, Karachai-Cherkessian Republic, Russia*

KEYWORDS:

exoplanets, photometry, spectra, observations

INTRODUCTION:

The search for exoplanet candidates and their subsequent validation is one of the main areas of exoplanet research. This report is devoted to the development of this topic in Russia.

VALIDATION OF EXOPLANET CANDIDATES:

Using the transit method, it is possible to determine the radius of the body that causes the darkening of the star. If the size of this body is typical for planetary bodies, then it is considered that an exoplanet candidate has been discovered. However, the estimated radius of the eclipsing body depends on the estimated radius of the host star. Therefore, to verify whether the eclipse is caused by a planet, it is essential to know the stellar radius as accurately as possible.

This report is devoted to the validation of exoplanet candidates discovered during survey observations at SAO RAS [1]. Spectroscopic observations of these stars were carried out using the SCORPIO-2 focal reducer at 6-m telescope SAO RAS [2]. At this stage, we determine the class of the parent star, from which we can conclude its radius, and from the ratio of sizes obtained by the transit photometry method and the radius of the star, we can find the size of the companion.

As a result of the modeling using photometric data from 50-cm robotic telescope of SAO RAS, the radii of the studied exoplanet candidates have been refined. In addition, a software package has been developed that will allow validation for new candidates.

REFERENCES:

- [1] *Yakovlev O. Y., Valeev A. F., Valyavin G. G. et al. Catalog of Variable Stars in the WD 0009501 and GRW 708247 Fields Based on Photometric Survey Data on Transiting Exoplanets // Astrophysical Bull. 2024. V. 79. V. 126–136. <https://doi.org/10.1134/S1990341323600400>.*
- [2] *Afanasiev V. L., Moiseev A. V. Scorpio on the 6-m Telescope: Current State and Perspectives for Spectroscopy of Galactic and Extragalactic Objects // Baltic Astronomy. 2011. V. 20. P. 363–370. <https://doi.org/10.1515/astro-2017-0305>.*

MASS DISTRIBUTION OF GIANT PLANETS IN TRANSIT DISCOVERED BY THE TESS MISSION

V. I. Ananyeva, A. V. Tavrov

Space Research Institute RAS, Moscow, Russia, a-lada@yandex.ru

KEYWORDS:

exoplanets, transit, TESS, statistics

ABSTRACT:

The presence of a planet in a transiting configuration allows its physical mass m to be measured, rather than just its minimum mass $m \sin i$, where i is the inclination of the planet's orbit to the line of sight, which is unknown for non-transiting planets. To date, the number of transit candidates labeled as TOI (TESS object of interest) discovered by the TESS mission has exceeded 7,600, of which 686 have been confirmed as planets (TESS planets in the NASA Exoplanet Archive, https://exoplanetarchive.ipac.caltech.edu/cgi-bin/TblView/nph-tblView?app=ExoTbls&config=PS&constraint=default_flag=1&constraint=disc_facility+like+%27%25TESS%25%271), and 514 of them have had their mass measured. The mass distribution of giant transiting planets $0.3 < m < 13 m_{\text{Jupiter}}$ found by TESS has been studied and compared with similar distributions of planets discovered by ground-based observation programs and the Kepler space telescope.

Therefore, we extend our previous study with new data revealing new refined selection effects and confirm the discovered before statistical distribution of masses and orbital periods for the demographics and cosmogony of exoplanets.

APPROACH OF THE ORION SWORD COMPLEX (NGC 1977) TO STARS WITH PLANETARY SYSTEMS (TOI-2796)

L. A. Maksimova, V. V. Vereshchagin, M. D. Sizova

Institute of Astronomy RAS, Moscow, Russia, lomara.maksimova@gmail.com

KEYWORDS:

exoplanet, planetary system, TOI-2796, open star cluster, NGC 1977

ABSTRACT:

The problem of the kinematics of the approach of open star clusters and stars with exoplanets is considered. It was found that the cluster NGCv1977, located in the region of Orion's Sword, in past epochs approached in space the star TOI-2796, which has a planetary system. The parameters of the approach — time and distance between the objects — were obtained. For this, numerical calculations of the orbit around the Galactic Center were carried out. It is shown that these objects approached at a distance of ~ 7.8 pc about ~ 4.4 million years ago. This approach could have had a gravitational effect on the Oort cloud analogue TOI-2796, leading to a change in the orbital elements of small bodies located in its outer parts. It is important to note that the observed effect could be the loss of objects from the TOI-2796 planetary system into interstellar space.

CHARACTERISTICS OF EXOPLANETS DEPENDING ON THE SPECTRAL CLASS OF THE PARENT STAR

G. A. Morozov^{1,2}, E. S. Belenkaya²

¹ *Lomonosov Moscow State University, Moscow, Russia*
morozov.ga21@physics.msu.ru

² *Skobel'syn Institute of Nuclear Physics Lomonosov Moscow State University*
Moscow, Russia

KEYWORDS:

exoplanets, mini-Neptunes, super-Earths, Fulton small radius gap, planet occurrence rate, spectral classes of stars

INTRODUCTION:

The characteristics of exoplanets, such as radius, mass, density, etc., directly depend on the formation of a planetary system. An important characteristic of the system is the spectral class of the parent star. We check the dependence of the characteristics of exoplanets on the spectral class of the parent star, assuming that when forming planetary systems, an important role for the future of the system is played by the amount of material in the protoplanetary disk and the influence of the star on the formation of planets, based on [1]. The data are taken from the NASA exoplanet catalog.

It is shown that with an increase in the temperature of the star (a change in the spectral class), the range of radii and masses increases, and the range of densities of exoplanets in systems decreases. At high temperatures of parent stars, the median radius and median mass of exoplanets increase, which indirectly indicates that with an increase in the amount of material and its mass for the formation of planets and stars, the temperature of the star also increases.

The so-called Fulton small radius gap was studied — in the distribution of exoplanets by radius, a decrease in the number of planets in the region of 1.5–2.0 Earth radii is observed. We give a possible explanation for this phenomenon. According to [2], the position of the dip should depend on the parent star, this statement is tested. The proportion of occurrence of super-Earths and mini-Neptunes among all planets is compared, as well as the proportion of low-mass planets for different spectral classes of parent stars.

The occurrence rate of exoplanets with different spectral classes of parent stars was investigated. The occurrence rate for different spectral classes of parent stars is compared. The occurrence rate is calculated depending on the radii of the planets and their orbital periods, based on [3].

REFERENCES:

- [1] *D'Angelo G., Lissauer J. J.* Formation of Giant Planets // Handbook of Exoplanets. / eds. Deeg H., Belmonte J. Springer, 2018. P. 2319–2343. arXiv:1806.05649.
- [2] *Fulton B. J., Petigura E. A.* The California-Kepler Survey. VII. Precise Planet Radii Leveraging Gaia DR2 Reveal the Stellar Mass Dependence of the Planet Radius Gap // The Astronomical J. 2018. V. 156. Iss. 6. Article 264. 13 p. DOI: 10.3847/1538-3881/aae828.
- [3] *Dressing C. D., Charbonneau D.* The occurrence rate of small planets around small stars // The Astrophysical J. 2013. V. 767. Iss. 1. Article 95. 20 p. DOI: 10.1088/0004-637X/767/1/95.

THE INFLUENCE OF STELLAR METALLICITY ON PLANET FORMATION

E. E. Buslaeva^{1,2}, E. S. Belenkaya¹

¹ Skobel'syn Institute of Nuclear Physics Lomonosov Moscow State University
Moscow, Russia, buslaeva.ee21@physics.msu.ru

² Lomonosov Moscow State University, Faculty of Physics, Moscow, Russia

KEYWORDS:

stellar metallicity, planet formation, exoplanet systems, protoplanetary disk, planet density, orbital characteristics

ABSTRACT:

It is believed that stars with exoplanets have higher metallicity than stars without planets [1]. This may be due to the greater amount of solid material available for planetesimal formation in protoplanetary disks [1]. In this study, the metallicity distribution of parent stars was constructed for systems with one to seven exoplanets. No correlation was observed between the number of systems with a larger number of planets and higher metallicity of the parent star. The highest number of systems with one or multiple planets was confirmed for stars with metallicity close to solar. Moreover, the metallicity distribution of the star for each considered number of exoplanets in the system has the same shape and peak position.

In the study by Adibekyan, it was found that giant planets are more frequently detected around stars with higher metallicity [2]. This is attributed to the fact that a high metal content in the protoplanetary disk promotes the formation of massive cores, which can then accrete gas and form giant planets [2]. In this work, the dependence of planet density on the metallicity of the parent star was examined for systems containing one to five exoplanets. Higher density is characteristic of rocky planets, while gas giants typically have lower density. It was expected that stars with higher metallicity would exhibit an increase in the number of low-density planets. This study shows that the highest number of planets of all types is confirmed for stars with metallicity close to or slightly higher than solar. The growth in the number of gas planets around more metal-rich stars plateaus at 0.3 dex for multiplanet systems and 0.4 dex for single-planet systems.

For systems with one and multiple exoplanets (up to five), a comparison was made of the distributions of characteristics determining planet density: mass and radius. Distributions of orbital radius and orbital period were also constructed. If differences in these distributions were found between single-planet and multiplanet systems, it could suggest the existence of a large number of single-planet systems that are truly single due to their formation conditions rather than detection limitations. The distributions of orbital radius and orbital period for systems with one and multiple planets do not differ in shape. In the planet radius distribution, systems share a common peak at 1.6–3.2 Earth radii, while a second peak at 11.2–12.8 Earth radii is observed only in systems with one confirmed planet and may correspond to genuinely single-planet systems. The mass distribution differs between single-planet and multiplanet systems: multiplanet systems more frequently host lower-mass planets, and the number of planets drops sharply with increasing mass. In single-planet systems, the number of planets decreases more gradually, which may indicate that during system formation, less material in the protoplanetary disk was allocated to each planet in multiplanet systems compared to planets in single-planet systems.

REFERENCES:

- [1] Fischer D. A., Valenti J. The planet-metallicity correlation // *The Astrophysical J.* 2005. V. 622. Iss. 2. P. 1102–1117. DOI: 10.1086/428383.
- [2] Adibekyan V. Heavy metal rules. I. Exoplanet incidence and metallicity // *Geosciences*. 2019. V. 9. No. 3. Article 105. <https://doi.org/10.3390/geosciences9030105>.

VENUS AND EARTH AS LABORATORIES FOR UNDERSTANDING TERRESTRIAL EXOPLANETS: SURFACE SPECTRAL SIGNATURES, PLANETARY SYNERGIES, AND THE AVENGERS INITIATIVE

P. D’Incecco¹, G. Arney², J. Filiberto³, D. Gorinov⁴, S. S. Bhiravarasu⁵, I. Pagano⁶, J. Garvin⁷, E. Kohler⁷, G. Andreuzzi^{8,9}, A. Ghedina⁸, R. Cosentino^{8,9,6}, Y. Miguel^{10,11}, S. Kane¹², C. Ostberg¹², J. Lustig-Yaeger¹³, G. Di Achille¹, V. Cottini¹⁴, J. Head¹⁵, J. Brossier¹⁶, S. Branca¹⁷, R. A. Corsaro¹⁷, C. Monaco^{17,18}, I. López¹⁹, P. Mason²⁰, G. Gallardo i Peres²⁰, G. Thangjam²¹, L. Majumdar²¹, S. Bhattacharya⁵, N. Truong⁷, R. Ernst²², H. El Bilali²², G. Komatsu²³, G. Covone²⁴, G. Di Rico¹, M. Cantiello¹, M. El Yazidi²⁵, V. Ortega-Ramos²⁶, N. Mari²⁷, S. Parisini²⁵, I. T. W. Flynn²⁸, L. Bruzzone²⁹, M. Way^{30,31}, J. Crandall³², J. Cabrera³³

¹ National Institute for Astrophysics (INAF) — Astronomical Observatory of Abruzzo, Teramo, Italy, piero.dincecco@inaf.it

² NASA Goddard Space Flight Center, Greenbelt, MD, USA

³ Astromaterials Research and Exploration Science (ARES) Division, NASA Johnson Space Center, Houston, TX, USA

⁴ Space Research Institute RAS, Moscow, Russia

⁵ Space Applications Centre, Indian Space Research Organization (ISRO) Ahmedabad, India

⁶ INAF — Osservatorio Astrofisico di Catania, Catania, Italy

⁷ NASA Goddard Space Flight Center, Greenbelt, MD, USA

⁸ Fundación Galileo Galilei — INAF, La Palma, Canary Islands, Spain

⁹ INAF — Osservatorio Astronomico di Roma, Monte Porzio Catone, Italy

¹⁰ Leiden Observatory, University of Leiden, Leiden, The Netherlands

¹¹ SRON Netherlands Institute for Space Research, Leiden, The Netherlands

¹² Department of Earth and Planetary Sciences, University of California Riverside, CA, USA

¹³ Johns Hopkins University Applied Physics Laboratory, Laurel, MD, USA

¹⁴ Italian Space Agency (ASI), Rome, Italy

¹⁵ Department of Geological Sciences, Brown University, Providence, RI, USA

¹⁶ National Institute for Astrophysics (INAF) — Institute for Space Astrophysics and Planetology (IAPS), Rome, Italy

¹⁷ Istituto Nazionale di Geofisica e Vulcanologia (INGV) — Osservatorio Etneo, Catania, Italy

¹⁸ Dipartimento di Scienze Biologiche Geologiche e Ambientali, Università di Catania, Italy

¹⁹ Tecvolrisk Research Group, Departamento de Biología, Geología, Física y Química Inorgánica, Universidad Rey Juan Carlos, Madrid, Spain

²⁰ Department of Earth Science and Engineering, Imperial College London London, UK

²¹ National Institute of Science Education and Research (NISER) Jatani, Odisha, India

²² Department of Earth Sciences, Carleton University, Ottawa, ON, Canada

²³ IRSPS, Università G. d’Annunzio, Pescara, Italy

²⁴ Dipartimento di Fisica “Ettore Pancini”, Università Federico II, Napoli, Italy

²⁵ National Institute for Astrophysics (INAF) — Istituto di Radioastronomia, Bologna, Italy

²⁶ Instituto Volcanológico de Canarias (INVOLCAN), Tenerife, Canary Islands, Spain

²⁷ Department of Earth and Environmental Sciences, University of Pavia, Italy

²⁸ Department of Geology and Environmental Science, University of Pittsburgh, PA, USA

²⁹ Department of Information Engineering and Computer Science, University of Trento, Italy

³⁰ *NASA Goddard Institute for Space Studies, New York, USA*

³¹ *Theoretical Astrophysics, Department of Physics and Astronomy
Uppsala, Sweden*

³² *Eastern Illinois University, Charleston, Illinois, USA*

³³ *German Aerospace Center, Berlin, Germany*

KEYWORDS:

Exoplanets, Venus, Earth, Analogs, Volcanism, Spectroscopy

ABSTRACT:

The growing availability of exoplanet observations — especially with upcoming exoplanet missions such as ESA's PLANetary Transits and Oscillations of stars (PLATO) [1], Atmospheric Remote-sensing Infrared Exoplanet Large-survey (ARIEL) [2], and NASA's Habitable Worlds Observatory (HWO) [3], alongside a new wave of the Venus missions, including NASA's Deep Atmosphere Venus Investigation of Noble gases, Chemistry, and Imaging (DAVINCI) [4], NASA's Venus Emissivity, Radio Science, InSAR, Topography and Spectroscopy (VERITAS) [5], ESA's EnVision [6], Roscosmos' Venera-D [7], ISRO's Venus Orbiter Mission (VOM) [8], complemented by ground-based facilities such as the high resolution spectrographs HARPS-N [9] (visible) and GIANO-B (IR) installed at the Telescopio Nazionale Galileo (La Palma, Canary Islands), the James Webb Space Telescope (JWST), and the Extremely Large Telescope (ELT) in Chile - requires robust frameworks to characterize the surface and atmospheric properties of terrestrial planets beyond our Solar System. Venus, with its thick atmosphere and possibly ongoing volcanic-tectonic processes, provides a powerful backyard analog for these distant worlds.

In this context, the Analogs for VENus' GEologically Recent Surfaces (AVENGERS) initiative promotes interdisciplinary research bridging Venus, Earth, and exoplanetary science [9]. Here, we propose a novel spectral strategy to infer geological activity on rocky exoplanets, based on lessons learned from Venus' surface emissivity studies.

The 1- μm absorption band, associated with fresh mafic minerals (e.g., olivine, pyroxenes), is known to fade quickly on Venus due to rapid oxidation caused by its hot, dense atmosphere [11,12]. Detecting this absorption band on exoplanets with similarly extreme conditions could indicate the presence of unweathered basaltic materials, suggesting recent or even ongoing volcanic resurfacing. Although a single eruptive center may not be observable, a planet-scale volcanic regime (Io-like) could generate a globally integrated spectral signature at 1 μm detectable by future space observatories.

To support this approach, we are currently analyzing the 0.8–2.5 μm reflectance spectra of fresh lava flows from Mount Etna (Italy) [13] and Cumbre Vieja (La Palma, Spain) [14], both serving as terrestrial analogs for volcanic terrains on Venus and (rocky) exoplanets. These datasets will help calibrate the expected spectral behavior of unweathered basaltic surfaces under Venus and Earth-relevant conditions, providing key constraints for future space observations. This perspective is consistent with recent JWST studies on rocky exoplanets in the habitable zone, which place strict limits on potential secondary atmospheres [15].

In the future, we also plan to include additional mafic and felsic-dominated volcanic environments — such as the active volcanoes of Kamchatka (Russia) — to expand the spectral library to more evolved, compositionally differentiated terrains. Spectral features of felsic volcanic materials (e.g., felsic-rich glass, feldspars) may also be accessible. Their presence would suggest the onset of crustal differentiation or even plate tectonic-like regimes, offering valuable insight into the internal evolution of rocky exoplanets.

AVENGERS aims to establish a scientific bridge between current and upcoming Venus missions (DAVINCI, VERITAS, EnVision, Venera-D, VOM), and the exoplanet community (PLATO, ARIEL, HARPS-N and GIANO-B at TNG, JWST, ELT, HWO), in coordination with NASA's Venus Exploration Analysis Group (VEXAG) and NASA's Exoplanet Exploration Program Analysis Group

(ExoPAG). In doing so, it also connects the planetary science community with Earth-based geologists through the joint analysis of terrestrial analogs. We advocate for a comparative planetary approach that integrates surface processes, volcanism, and atmospheric evolution to better characterize (rocky) exoplanets using Venus and Earth as key references.

REFERENCES:

- [1] *Rauer H., Aerts C., Cabrera J. et al.* The PLATO mission // *Experimental Astronomy*. 2025. V. 59(1). Article 26. <https://doi.org/10.1007/s10686-025-09985-9>.
- [2] *Tinetti G., Drossart P., Eccleston P. et al.* A chemical survey of exoplanets with ARIEL // *Experimental Astronomy*. 2018. V. 46(1). P. 135–209. <https://doi.org/10.1007/s10686-018-9598-x>.
- [3] *Vaughan S.R., Gebhard T.D., Bott K. et al.* Chasing rainbows and ocean glints: Inner working angle constraints for the Habitable Worlds Observatory // *Monthly Notices of the Royal Astronomical Society*. 2023. V. 524(4). P. 5477–5485. <https://doi.org/10.1093/mnras/stad2127>.
- [4] *Garvin J.B., Getty S.A., Arney G.N. et al.* Revealing the mysteries of Venus: the DAVINCI mission // *Planetary Science. J.* 2022. V. 3. Article 117. 17 p. <https://doi.org/10.3847/PSJ/ac63c2>.
- [5] *Smrekar S., Hensley S., Nybakken R. et al.* VERITAS (Venus Emissivity, Radio Science, InSAR, Topography, and Spectroscopy): A Discovery Mission // *IEEE Aerospace Conf. Proc.* 2022. <https://doi.org/10.1109/AERO53065.2022.9843269>.
- [6] *Ghail R., Wilson C., Widemann T. et al.* The science goals of the EnVision Venus orbiter mission // *Europlanet Science Congress 2020: EPSC abstr.* 2020. V. 14. <https://doi.org/10.5194/epsc2020-599>.
- [7] *Zasova L.V., Gorinov D.A., Eismont N.A. et al.* Venera-D: A design of an automatic space station for Venus exploration // *Solar System Research*. 2019. V. 53. P. 506–510. <https://doi.org/10.1134/S0038094619070244>.
- [8] *Sundararajan V.* Tradespace exploration of space system architecture and design for India's Shukrayaan-1, Venus Orbiter Mission // *AIAA ASCEND 2021: Proc.* 2021. <https://doi.org/10.2514/6.2021-4103>.
- [9] *Cosentino R., Lovis C., Pepe F. et al.* Harps-N: the new planet hunter at TNG // *Proc. SPIE — The International Society for Optical Engineering*. 2012. V. 8446. Iss. Ground-based and Airborne Instrumentation for Astronomy IV. Article. 8446IV. 20 p. DOI: 10.1117/12.925738.
- [10] *D'Incecco P. et al.* The AVENGERS (Analogues for VENUS' GEologically Recent Surfaces) initiative: using terrestrial analogs to study recent volcano-tectonic activity on Venus and inform the characterization of terrestrial exoplanets // *J. Geophysical Research: Planets*. 2025. (in press).
- [11] *Filiberto J., Trang D., Treiman A.H., Gilmore M.S.* Present-day volcanism on Venus as evidenced from weathering rates of olivine // *Science Advances*. 2020. V. 6(1). Article eaax7445. <https://www.science.org/doi/10.1126/sciadv.aax7445>.
- [12] *D'Incecco P., Filiberto J., Lopez I. et al.* Idunn Mons: Evidence for ongoing volcano-tectonic activity and atmospheric implications on Venus // *Planetary Science J.* 2021. V. 2. Article 215. 9 p. <https://doi.org/10.3847/PSJ/ac2258>.
- [13] *Eggers G.L., Filiberto J., D'Incecco P. et al.* Spectroscopy of Mount Etna Lava Flows as a Proxy for Age: A Potential Analogue to Recent Volcanism on Venus // *54th Lunar and Planetary Science Conf.* 2023. Article 2480. 2 p. <https://www.hou.usra.edu/meetings/lpsc2023/pdf/2480.pdf>.
- [13] *Filiberto J. et al.* La Palma as an Analog for Hot Spot Volcanism on Venus: Insights from Mineralogical Detection Techniques // *GSA Meeting*. 2025.
- [15] *Piaulet-Ghorayeb C., Benneke B., Turbet M. et al.* 2025. Strict limits on potential secondary atmospheres on the temperate rocky exo-Earth TRAPPIST-1 d // *The Astrophysical J.* 2025. V. 989. No. 2. Article 181. <https://doi.org/10.3847/1538-4357/adf207>.

MIGRATION OF EARTH-LIKE PLANETS IN PLANETESIMAL DISKS CAUSING THE FORMATION OF DEBRIS DISKS

O. S. Oleynik, V. V. Emel'yanenko

Institute of Astronomy RAS, Moscow

olgaoleynik93@gmail.com, vvemel@inasan.ru

KEYWORDS:

debris disk, exoplanets, planetesimals, migration, planet-disk interaction

ABSTRACT:

We investigate the interaction of Earth-mass planets with a disk of planetesimals. It is shown that an Earth-like planet, initially located near the inner boundary of the planetesimal disk, migrates inside the disk. The magnitude of penetration of the planet into the disk is determined by the angular momentum distribution of planetesimals approaching the planet. The direction of the planet's migration always changes, and the planet returns to the inner boundary of the disk. During such reversible migration, the planet perturbs the orbits of planetesimals and increases their relative velocities in the region of the disk where it was during its migration. The relative velocities of planetesimals increase to values sufficient for their fragmentation during collisions. We show that after the passage of an Earth-mass planet through the outer planetesimal disk, the average relative velocities in the main part of the disk increase to values sufficient for the fragmentation of monolithic basaltic planetesimals up to 40 km in size. Thus, the interaction of even a small planet (of the order of Earth's mass) with a planetesimal disk can lead to the formation of dust particles observed in outer debris disks.

ULTRA-COOL BROWN DWARFS WITH AND WITHOUT CIRCUM-SUBSTELLAR PLASMA DISKS: POSSIBLE CONSEQUENCES

G. P. Malygin^{1,2}, E. S. Belenkaya¹, I. I. Alexeev¹

¹ *Skobel'syn Institute of Nuclear Physics Lomonosov Moscow State University
Moscow, Russia, malygin.gp22@physics.msu.ru*

² *Lomonosov Moscow State University, Moscow, Russia*

KEYWORDS:

brown dwarfs, red dwarfs, giant planets, infrared emission, magnetodisk, aurora

ABSTRACT:

Brown dwarfs are substellar objects that occupy an intermediate position between stars and planets. Their masses range from approximately ~ 13 to $\sim 80M_J$, where $M_J = 1.9 \cdot 10^{27}$ kg is the mass of Jupiter. The upper limit ($80M_J$) corresponds to the mass at which thermonuclear hydrogen burning begins in the object's core, while the lower limit ($13M_J$) is the minimum mass required for deuterium burning inside the celestial body. The goal of this work is to give an answer to the question: Why does one of two nearly identical isolated ultracold brown dwarfs exhibit auroras and a temperature inversion with altitude in its atmosphere, while the other does not? We suggest that the possible reason lies in the fact that one brown dwarf (W1935) possesses a magnetic field and a surrounding plasma magnetodisk. When the magnetic dwarf rotates rapidly, its interaction with the magnetodisk may produce the observed phenomena. If the second brown dwarf (W2220) lacks its own magnetic field and/or a magnetodisk, it does not meet the necessary conditions for generating auroras and temperature inversion with altitude in its atmosphere (Figure 2). We demonstrate how these phenomena depend on the brown dwarf's characteristics and the parameters of the circum-substellar plasma disk. Additionally, this work focuses on comparing brown dwarfs with stellar red dwarfs and giant planets (Figure 1).

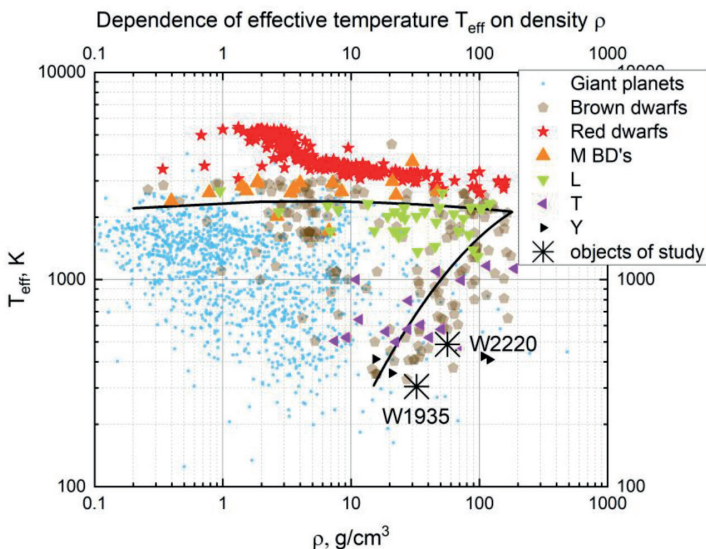


Figure 1. The graph highlights brown dwarfs for which the spectral class is known. In the background there are all brown dwarfs (in brown), for which two characteristics are known: temperature and density. The black curves are polynomial approximations of the most common brown dwarfs with these parameters on a logarithmic scale. Two ultra-cool brown dwarfs W1935 and W2220 discussed in this paper are shown by asterisks

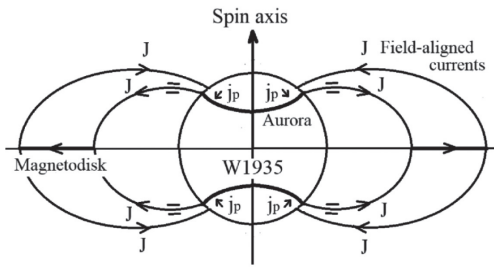


Figure 2. Current system of magnetodisk, including field-aligned currents J , magnetodisk currents and ionospheric Pedersen currents j_p . Current directions are shown by asterisks. Arcs are the auroral ovals at the brown dwarf

STABILITY AND DYNAMICS OF THE COMPACT PLANETARY SYSTEM KEPLER-51

E. D. Kuznetsov, A. S. Perminov

Ural Federal University, Yekaterinburg, Russia

eduard.kuznetsov@urfu.ru, alexander.perminov@urfu.ru

KEYWORDS:

compact planetary system, mean-motion resonances, dynamic evolution, stability

INTRODUCTION:

The compact three-planet system Kepler-51 was announced in 2013 [1]. Kepler-51 is $a \lesssim 1$ Gyr-old Sun-like star hosting three transiting planets with radii $\sim(6-9)R_{\oplus}$ (radii of the Earth) and orbital period ratios close to 1:2:3 (45, 85, and 130 days for Kepler-51b, c, and d, respectively) detected with Kepler photometry. Transit timing variations measured with past Kepler and Hubble Space Telescope observations have been successfully modeled by considering gravitational interactions between the three transiting planets, yielding low masses and low mean densities ($\lesssim 0.1 \text{ g}\cdot\text{cm}^{-3}$) for all three planets.

Antoniadou and Voyatzis [2] demonstrate three possible scenarios safeguarding compact planetary system Kepler-51, each followed by constraints. Firstly, there are the 2:1 and 3:2 two-body mean-motion resonances (MMRs), in which eccentricity $e_b < 0.02$, such that these two-body MMRs last for extended time spans. Secondly, there is the 1:2:3 three-body Laplace-like resonance, in which $e_c < 0.016$ and $e_d < 0.006$ are necessary for such a chain to be viable. Thirdly, there is the combination comprising the 1:1 secondary resonance inside the 2:1 MMR for the inner pair of planets and an apsidal difference oscillation for the outer pair of planets in which the observational eccentricities, e_b and e_c , are favored as long as $e_d \approx 0$.

D. Jontof-Hutter et al. [3] refined parameters of the Kepler-51 planetary system using data from the TESS space telescope. Kuznetsov and Perminov [4] examined the dynamic evolution of the compact three-planet system Kepler-51 using refined parameters [3]. It is shown that the compact planetary system Kepler-51 is not resonant. Under initial conditions corresponding to the masses and elements of the planets' orbits, determined from observations considering their errors, the evolution of the system is stable and regular over the studied interval of 100 Myr.

K. Masuda et al. [5] reported the discovery of a fourth planet in the Kepler-51 system. They obtained solution, the one in which Kepler-51e is around the 2:1 MMR with Kepler-51d implies low orbital eccentricities ($\lesssim 0.05$) and comparable masses ($\sim 5M_{\oplus}$) for all four planets, as is seen in other compact multi-planet systems.

In this paper, we will consider the dynamic evolution of the compact four-planetary system Kepler-51 and study stability and resonant property.

METHODS:

Since compact systems, an important factor influencing orbital evolution is tidal interaction. We simulated the evolution of the Kepler-51 system over a time interval of 100 Myr using the Posidonius (<https://www.blancocuaresma.com/s/posidonius>) software [6], which considers tidal interaction. We varied the mass of the star ($0.96 \pm 0.05 M_{\odot}$ [5]) and the masses of the planets (see [5], Table 6) within the limits of determination errors for nominal values of orbital elements. The orbital elements were varied for the nominal masses of the star and planets. The values of the period and eccentricity were varied within the limits of determination errors, the inclinations of the orbits and the longitudes of the ascending nodes were assumed to be equal to zero, and the arguments of the periastron were assumed to be equal to the nominal values.

RESULTS AND DISCUSSIONS:

In the first stage, we analyzed how the addition of the fourth outer planet affects the dynamic evolution of the three inner planets. The results of the modeling show that both the inner three-planet part of the system and the full four-planet system maintain a stable evolution of the positional elements of the orbit. The evolution of the longitudes of the ascending nodes and the arguments of the pericenters is regular.

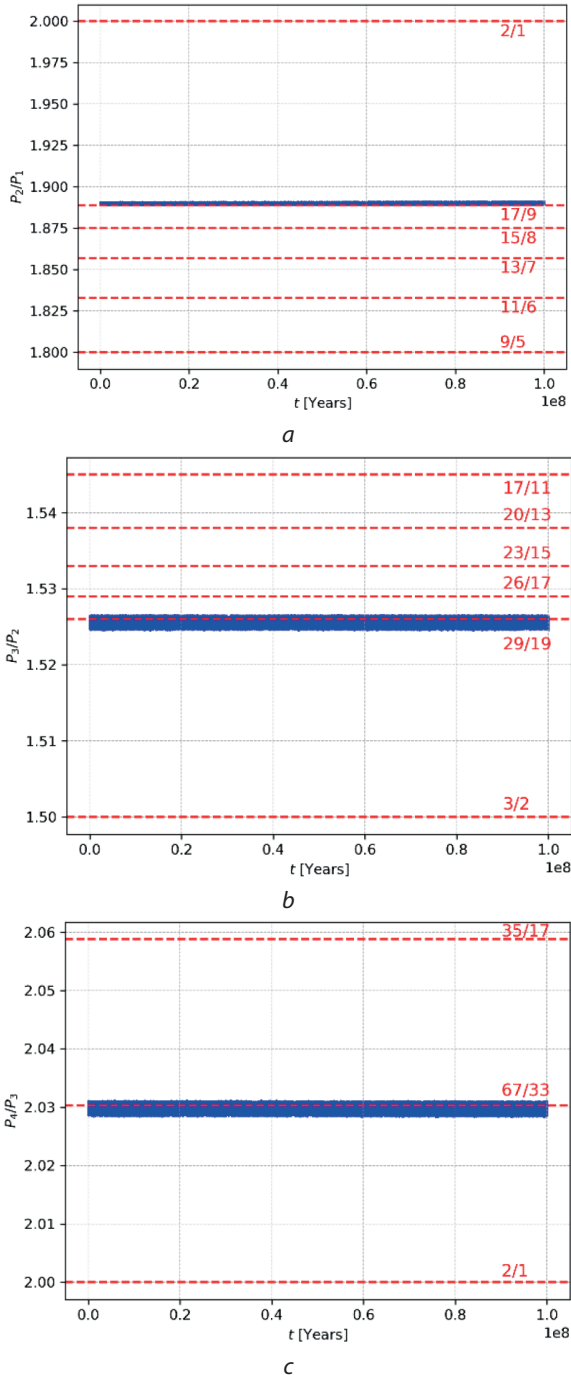


Figure 1. Evolution of the period ratios of adjacent planets over time t : P_1, P_2, P_3, P_4 are orbital periods of Kepler-51b, c, d, e, respectively (blue points are the period ratios, dashed red lines correspond to MMRs)

The study of the resonance properties of the system shows that pairs of adjacent planets are not in low-order mean motion resonances. It is possible to indicate high-order resonances corresponding to the ratio of the periods of adjacent planets. Numerical modeling shows that the semi-major axes of the orbits and periods are located in the vicinity of the following resonances over the entire considered interval of 10 Myr: 17:9 for Kepler-51c and Kepler-51b (Figure 1a), 29:19 for Kepler-51d and Kepler-51c (Figure 1b), 67:33 for Kepler-51e and Kepler-51d (Figure 1c), but the corresponding resonance arguments circulate. It can be concluded that there are no MMRs in the system.

CONCLUSIONS:

The orbital evolution of the Kepler-51 system was simulated using the Posidonius software package, considering tidal interaction. The complete study shows that the compact planetary system Kepler-51 is not resonant. Under initial conditions corresponding to the masses and elements of the planets' orbits, determined from observations considering their errors, the evolution of the Kepler-51 system is stable and regular over the studied interval of 100 Myr.

ACKNOWLEDGMENTS:

The study was supported by the Russian Ministry of Science and Higher Education via the State Assignment Project FEUZ-2025-0003.

REFERENCES:

- [1] *Steffen J. H., Fabrycky D. C., Agol E. et al.* Transit timing observations from Kepler-VII. Confirmation of 27 planets in 13 multiplanet systems via transit timing variations and orbital stability // *Monthly Notices of the Royal Astronomical Society*. 2013. V. 428. Iss. 2. P. 1077–1087. DOI: 10.1093/mnras/sts090.
- [2] *Antoniadou K. I., Voyatzis G.* Periodic orbits in the 1:2:3 resonant chain and their impact on the orbital dynamics of the Kepler-51 planetary system // *Astronomy and Astrophysics*. 2022. V. 661. Article A62. 16 p. <https://doi.org/10.1051/0004-6361/202142953>.
- [3] *Jontof-Hutter D., Dalba P. A., Livingston J. H.* TESS observations of Kepler systems with transit timing variations // *The Astronomical J.* 2022. V. 164. No. 2. Article 42. DOI: 10.3847/1538-3881/ac7396.
- [4] *Kuznetsov E. D., Perminov A. S.* Study of the dynamical evolution of the compact planetary system Kepler-51 // *Solar System Research*. 2024. V. 58. Iss. 5. P. 594–611. DOI: 10.1134/S0038094624700394.
- [5] *Masuda K., Libby-Roberts J. E., Livingston J. H. et al.* A Fourth Planet in the Kepler-51 System Revealed by Transit Timing Variations // *The Astronomical J.* 2024. V. 168. No. 6. Article 294. 36 p. DOI: 10.3847/1538-3881/ad83d3.
- [6] *Blanco-Cuaresma S., Bolmont E.* Studying tidal effects in planetary systems with Posidonius. A N-body simulator written in Rust // *EWASS Special Session 4 (2017): Star-planet interactions (EWASS-SS4-2017)*. 2017. DOI: 10.5281/zenodo.1095095. 10.5281/ZENODO.1095095.

THE INFLUENCE OF WATER CONTENT IN THE CORES OF MINI-NEPTUNES ON THE RATE OF PRIMARY ATMOSPHERE'S CORE-POWERED MASS-LOSS

R. A. Evdokimov¹, V. I. Shematovich²

¹ *Rocket and Space Corporation "Energia", Korolev, Moscow Region, Russia*
evdokimovrom@yandex.ru

² *Institute of Astronomy RAS, Moscow, Russia, shematov@inasan.ru*

KEYWORDS:

mini-Neptunes, Fulton gap, atmospheric dissipation, core heat flux, internal structure, thermal energy sources

ABSTRACT:

The distribution of exoplanets discovered to date by observed (transit) radii features the so-called Fulton gap — a region between radii of 1.6 and 1.8 R_{\oplus} where exoplanets are relatively rare [1]. This gap likely separates the two most common populations of exoplanets: super-Earths and mini-Neptunes, which generally possess extensive water mantles and primary atmospheres. The formation of this gap may be attributed to the loss of hydrogen-helium envelopes by mini-Neptunes, leaving behind bare cores that, depending on water content, could become either ocean worlds or rocky super-Earths [2]. The leading mechanisms of atmospheric loss believed to shape the Fulton gap are photoevaporation [3] and core-powered mass-loss [4, 5]. The first mechanism involves heating of the outer layers of the gas envelope by short-wavelength radiation from the parent star (primarily X-rays and extreme ultraviolet — EUV), while the second is driven by infrared radiation heating due to heat flux from the interior [4]. In [5], it was shown that photoevaporation contributes more significantly to the formation of the Fulton gap, but core-powered mass-loss noticeably affects its profile. Currently, several mini-Neptunes have been identified near the boundary of the Fulton gap, likely undergoing the process of losing their primary gas envelopes, making them a transitional form of exoplanets. Examples include HD207496b (TOI-1099b) [2] and HD235088b (TOI-1430b) [6]. For HD235088b, observational data confirming helium loss from its atmosphere are available. For these mini-Neptunes, studies [2, 6] have demonstrated the high efficiency of photoevaporation, both currently and in the past, for various models of their internal structure. For the mini-Neptune HD207496b, with a mass of approximately 6.1 M_{\oplus} and a radius of 2.25 R_{\oplus} , [2] proposed two extreme models of internal structure: a rocky core without a water mantle surrounded by a hydrogen-helium envelope, and an ocean world (a rocky core with an extensive water mantle and a steam atmosphere). In our works [7, 8], we investigated the efficiency of primary atmosphere loss for HD207496b due to core-powered mass-loss. It was shown that for a moderate equilibrium temperature of about 743 K [2], this mechanism is ineffective for the model with a waterless core [7]. However, if HD207496b is an ocean world with a water content of 30–45 % (consistent with observational data), the process of atmospheric loss due to core heat flux could have occurred in the past with high efficiency — a significant portion of the gas envelope might have been lost in the first few million to tens of millions of years of the exoplanet's evolution [8]. Thus, in addition to the planet's mass and equilibrium temperature, the water fraction in its composition significantly affects the rate of gas envelope loss, as shown to be linked to the dependence of the core's radius and heat capacity on water content. This study explores the relationship between the efficiency of primary atmosphere loss in mini-Neptunes due to core-powered mass-loss mechanism and the mass fraction of water in the core. Alongside results for mini-Neptune models varying in mass, equilibrium temperature, and relative water content, calculations are presented for several exoplanets with extensive observational data, including HD207496b and HD235088b.

Estimates of primary atmosphere loss rates and possible initial masses of hydrogen-helium envelopes are provided for different water mass fractions compatible with observational data. In calculating the internal heat flux, in addition to thermal energy accreted during formation and gravitational energy, the energy from radioactive decay, including short-lived elements, is accounted for. The possibility of higher equilibrium temperatures for exoplanets shortly after formation, due to the evolutionary tracks of low-mass stars, is also considered.

REFERENCES:

- [1] *Fulton B.J., Petigura E.A., Howard A.W. et al.* The California-Kepler Survey. III. A Gap in the Radius Distribution of Small Planets // *Astronomical J.* 2017. V. 154. Iss. 3. Article 109. 19 p. DOI: 10.3847/1538-3881/aa80eb.
- [2] *Barros S.C.C., Demangeon O.D.S., Armstrong D.J. et al.* The young mini-Neptune HD 207496b that is either a naked core or on the verge of becoming one // *Astronomy and Astrophysics.* 2023. V. 673. Article A4. 18 p. <https://doi.org/10.1051/0004-6361/202245741>.
- [3] *Owen J.E., Jackson A.P.* Planetary evaporation by UV and X-ray radiation: basic hydrodynamics // *Monthly Notices of the Royal Astronomical Society.* 2012. V. 425. Iss. 4. P. 2931–2947. DOI: 10.1111/j.1365-2966.2012.21481.x.
- [4] *Ginzburg S., Schlichting H.E., Sari R.* Super-Earth Atmospheres: Self-consistent Gas Accretion and Retention // *Astrophysical J.* 2016. V. 825. Iss. 1. Article 29. 12 p. DOI: 10.3847/0004-637X/825/1/29.
- [5] *Owen J.E., Schlichting H.E.* Mapping out the parameter space for photoevaporation and core-powered mass-loss // *MNRAS.* 2024. V. 528. P. 1615–1629.
- [6] *Nardiello D., Akana Murphy J.M., Spinelli R. et al.* The GAPS Programme at TNG: LXV. Precise density measurement of TOI-1430 b, a young planet with an evaporating atmosphere // *Astronomy and Astrophysics.* 2025. V. 693. Article A32. 26 p. <https://doi.org/10.1051/0004-6361/202452236>.
- [7] *Evdokimov R.A., Shematovich V.I.* Evolutionary History of the Atmosphere of the Young Mini-Neptune HD 207496b // *Solar System Research.* 2025. V. 59(3). DOI: 10.1134/S0038094624601579.
- [8] *Evdokimov R.A., Shematovich V.I.* Estimate of Core-Powered Mass-Loss of Primary Atmosphere of the Mini-Neptune (Ocean Planet) HD 207496b // *Solar System Research.* 2025. V. 59(6). Article 68. 17 p. DOI: 10.1134/S0038094624602172.

**SESSION 5. EXTRASOLAR PLANETS (EP-PS)
POSTER SESSION**

NUMERICAL MODELING OF THE HOT SATURN ATMOSPHERE HAT-P-18B

E. D. Savintseva, M. S. Rumenskikh, I. F. Shaikhislamov

*Institute of Laser Physics SB RAS, Novosibirsk, Russia
savintsevaed49@gmail.com*

KEYWORDS:

transit spectroscopy, atmospheres, hot exoplanets, MHD modelling

INTRODUCTION:

Hat-P-18b is a hot gas giant orbiting close to its parent star at a distance of ~ 0.056 a.u. The system is located in the constellation Hercules, 529 light years from the Sun. This exoplanet has a mass comparable to Saturn ($M = 0.197M_{\oplus}$), but a radius close to Jupiter's ($R = 0.995R_{\oplus}$). The average surface temperature of Hat-P-18b is 841 ± 15 K, which classifies it as a "hot Saturn". The star Hat-P-18 belongs to the orange dwarfs of the spectral class K with a temperature of about 4719 K. All this indicates a low atmospheric density and the likely existence of an atmospheric tail, which has been observed during a transit of some hot exoplanets. Using measurements made with JWST and HST, as well as numerous ground-based telescopes, carbon dioxide (CO_2), water (H_2O), sodium (Na), methane (CH_4) were detected in the absorption spectrum of this exoplanet. Extensive spectral analysis data allow the physicochemical parameters of the system to be determined with high accuracy.

This study is devoted to determining the composition of the exoplanet's atmosphere by interpreting transit absorptions in the 1083 nm metastable helium line and identifying sensitivity to changes in space weather conditions in the system.

MODELING AND RESULTS:

A numerical three-dimensional hydrodynamic model was used for interpretation of transit absorptions of the planet Hat-P-18b in the 1083 nm helium line in order to determine the parameters of space weather and the atmosphere of the exoplanet. Due to the good observability of metastable helium from Earth, there are sufficient data for its study. The determination of probable physicochemical parameters of the planetary system was carried out by comparing the measured absorption line with the results of numerical modeling performed with various free modeling parameters.

Analysis of transit absorptions of exoplanet Hat-P-18b demonstrates that the absorption line center does not coincide with observations, being shifted to the blue region of the spectrum in the case of medium and strong stellar wind. Comparison of the calculated absorption profiles with observations reveals Solar content of heavy elements in the upper atmosphere of Hat-P-18b.

CONCLUSION

Our simulations suggest that the observed Hel 1083 nm absorption in HAT-P-18b is consistent with a low-density atmosphere undergoing moderate stellar wind interaction. The absence of metal line absorptions aligns with the expected low UV flux from the K-type host star.

ACKNOWLEDGMENTS

This work was done with a support of the Russian Science Foundation grant No. 25-72-10080.

MOTION OF SUPERFAST EXOPLANETS AND SOLAR SYSTEM

V. A. Kotov

Crimean Astrophysical Observatory, Nauchny, Russia, vkotov@craocrimea.ru

KEYWORDS:

exoplanets, orbital motion, Solar system, the Sun, pulsations, Earth

ABSTRACT:

It is shown superfast exoplanets tend to revolve around «parent» stars with periods commensurable with timescales P_0 and/or $2P_0/\pi$, where the P_0 value presents a period of global pulsations of the Sun: $P_0 \approx 3^{-2}$ days [1–6]. The study of the origin of cosmic timescale P_0 can lead us to the new knowledge about superfast motion of planets and close binary stars, proving the Schrödinger's [7] "tendency for order", triumphant in the World.

As to the Solar System, the remarkable, precise to 0.1 %, correlations of the P_0 timescale with the Sun's and Earth's motions are noted:

$$P_S/P_D \approx 2P_Y/P_S \approx 3P_D/P_0 \approx 3^3, \quad (1)$$

where $P_S = 27.027(4)$ days is the *synodic* period of solar rotation, and P_Y and P_D are orbital and daily periods of Earth, respectively.

Correlations, similar to (1), are found between periodic motions of all components of the Sun–Mercury–Venus–Earth system. A hypothesis is advanced that P_S , P_Y , P_D and P_0 are special timescales, which nature, being at the borders of some "cosmic miracle", is yet hidden under seven seals from us.

REFERENCES

- [1] *Sevin É.* Sur la structure du système solaire // *Comptes Rendus de l'Académie des Sciences.* 1946. V. 222. P. 220–221.
- [2] *Brookes J.R., Isaak G.R., van der Raay H.B.* Observations of free oscillations of the Sun // *Nature.* 1976. V. 259. P. 92–95. <https://doi.org/10.1038/259092a0>.
- [3] *Severny A.B., Kotov V.A., Tsap T.T.* Observations of solar pulsations // *Nature.* 1976. V. 259. P. 87–89. <https://doi.org/10.1038/259087a0>.
- [4] *Grec G., Fossat E., Pomerantz M.* Solar oscillations: full disk observations from the geographic South Pole // *Nature.* V. 288(5791). P. 541–544. <https://doi.org/10.1038/288541a0>.
- [5] *Scherrer P.H., Wilcox J.M.* Structure of the solar oscillation with period near 160 minutes // *Solar Phys.* 1983. V. 82. P. 37–42. <https://doi.org/10.1007/BF00145543>.
- [6] *Kotov V., Haneychuk V.* Sixfold enhancement of solar pulsations: 1974–2018 // *Acta Astrophysica Taurica.* 2023. V. 4. No. 2. P. 1–5. DOI: 10.34898/aat.vol4.iss2.pp1-5.
- [7] *Schrödinger E.* What is life? The physical aspect of the living cell. Dublin: Dublin Inst. Adv. Studies, 1955.

**SESSION 6. GIANT PLANETS (GP)
ORAL SESSION**

THE SEMI-ANALYTICAL MOTION THEORY OF MAJOR PLANETS OF THE SOLAR SYSTEM

A. S. Perminov, E. D. Kuznetsov

Ural Federal University, Yekaterinburg, Russia

alexander.perminov@urfu.ru, eduard.kuznetsov@urfu.ru

KEYWORDS:

semi-analytical motion theory, dynamical evolution, Solar System, Hori-Deprit method

INTRODUCTION:

According to exoplanet.eu database, about 7400 planets have been discovered to date in more than 5000 extrasolar planetary systems, and more than 1000 of these systems are multi-planetary. In the work [1], the authors constructed a semi-analytical motion theory for a four-planetary problem. This theory allows us to study the dynamical evolution of extrasolar planetary systems with up to 4 planets. About two dozen five-planetary systems, about ten six-planetary systems, 5 seven-planetary systems, and 1 eight-planetary extrasolar system Kepler-90 have already been discovered. Thus, the problem of modeling the dynamical evolution of such planetary systems arises to study their stability over long-time intervals. Testing of the eight-planetary theory being created was performed during the modeling of the dynamical evolution of the large planets of the Solar System.

METHODS:

The Hamiltonian of the eight-planetary problem is written in the hierarchical Jacobi coordinate system, which is most convenient for studying the orbital evolution of planetary systems. The expansion of the perturbing part of the Hamiltonian in a Poisson series is constructed using the small parameter μ (the ratio of the sum of planetary masses to the mass of the star) and the elements of the second Poincaré system. For the Solar System, $\mu = 0.001$ can be chosen as the value of the small parameter. Using the elements of the second Poincaré system allows us to significantly reduce the angular part of the expansion, since this system contains only one angular element — the mean longitude. The elements of the second Poincaré system are also convenient for use in this problem in which the osculating eccentricity and inclination retain small values for a long-time intervals.

The Hamiltonian of the problem in osculating elements is averaged by the Hori-Deprit method (otherwise known as the Lie transformation method). All the sought quantities are expressed here through Poisson brackets, which implies their invariance with respect to canonical transformations. The Hamiltonian is averaged over the average longitudes (the period of which is close to the period of orbital motion), which allows us to exclude short-period perturbations of orbital elements and subsequently significantly increase the step of numerical integration of the motion equations.

All analytical transformations are performed in the Piranha (<https://github.com/bluescarni/piranha>) computer algebra system, which is an echeloned Poisson processor. In this case, all orbital elements and mass parameters are saved in series in symbolic form. The coefficients in the Poisson series are fractional rational numbers with arbitrary precision, which allows us to avoid rounding errors in calculations.

The osculating Hamiltonian of the eight-planet problem is constructed with an accuracy of μ^2 . The terms containing the first power of μ are obtained with an accuracy of up to the 6th power from the eccentric and oblique Poincaré elements (which are proportional to the eccentricities and inclinations of the orbits, respectively). The terms with μ^2 are obtained with an accuracy of up to the 4th power from the orbital elements.

The series representing the averaged Hamiltonian of the problem and the right-hand sides of the motion equations in the averaged elements are constructed with an accuracy of up to μ^2 . The eccentric and oblique Poin-

caré elements are preserved in the series representing the averaged Hamiltonian up to the 6th power, and in the series for the equations of motion — up to the 5th power. The transition between the osculating and averaged elements is made using the functions for the change of variables, the series for which are constructed with an accuracy of up to the first power of μ and the 6th power from the orbital elements.

RESULTS AND DISCUSSION:

The dynamic evolution of the eight-planet system Sun–Mercury–Venus–Earth–Mars–Jupiter–Saturn–Uranus–Neptune is studied using the motion equations constructed by the Hori–Depri method in averaged elements. The integration of the second-order motion equations with respect to a small parameter is performed by the 12th-order Gregg–Bulirsh–Stoer method on a time interval of 10 Gyr years with a step of 10000 years. The 15th order Everhart method is also used to integrate the motion equations over a time interval of 100 Myr with a step of 1000 years. This additional integration is performed to more accurately determine the periods and limits of change in the orbital elements. In this case, the Everhart integrator very accurately preserves the value of the total energy of the system, which makes the integration process quite slow. The Gregg–Bulirsh–Stoer integrator, on the contrary, is less accurate, but very fast.

For comparison with the constructed semi-analytical motion theory, a numerical simulation of the orbital evolution of the major planets of the Solar System was carried out. The 15th order Cowell–Stormer integrator and the Wisdom–Holman symplectic integrator were used, namely its specific implementation — WHFast, which is part of the Rebound software package. The integration was performed over a time interval of 100 Myr with a step of 4 days.

The initial conditions for modeling the orbital evolution of the major planets of the Solar System are taken from the DE440 ephemeris relative to the mean ecliptic and equinox J2000.0.

The results obtained within the framework of the semi-analytical motion theory are compared with the results of direct numerical modeling. The periods of oscillations of orbital elements and the amplitudes of their changes were compared. Table 1 presents the values of the periods of change of eccentricities T_e and inclinations T_i of the orbits of the major planets, obtained within the framework of the semi-analytical theory (SA) and from the results of numerical modeling (NM). Several different periods in some cells correspond to different frequencies of oscillations realized in the system.

Table 1. The periods of change of orbital eccentricities and inclinations

Planet	T_e , yr (SA)	T_e , yr (NM)	T_i , yr (SA)	T_i , yr (NM)
Mercury	1111000	~1000000	234740	238000
Venus	97560; 393700	96000; 384000	73150	73700
Earth	97560; 393700	96000; 384000	73150	73700
Mars	101940	110900	73150	73700
Jupiter	54770	54080	49360	49250
Saturn	54770	54080	49360	49250
Uranus	1136400	~1100000	434790	441700
Neptune	380200; 613500	~400000; ~600000	1886800	1880000

CONCLUSIONS:

The constructed semi-analytical eight-planetary motion theory has been tested in modeling the orbital evolution of major planets of the Solar System. The relative accuracy of the periods of change in orbital elements obtained by various methods ranges from fractions of a percent for giant planets to several percents for terrestrial planets. In the future, it is planned to use this motion theory to study the orbital evolution of extrasolar multi-planetary systems.

ACKNOWLEDGMENTS:

The study was supported by the Russian Ministry of Science and Higher Education via the State Assignment Project FEUZ-2025-0003.

REFERENCES:

- [1] *Perminov A.S., Kuznetsov E.D.* The orbital evolution of the Sun–Jupiter–Saturn–Uranus–Neptune system on long time scales // *Astrophysics and Space Science*. 2020. V. 365. Iss 8. Article 144. DOI: 10.1007/s10509-020-03855-w.

**SESSION 6. GIANT PLANETS (GP-PS)
POSTER SESSION**

FEATURES OF METHANE AND AMMONIA ABSORPTION ALONG THE CENTRAL MERIDIAN OF JUPITER AND IN THE GREAT RED SPOT IN 2023

S. K. Salamakhin, A. M. Karimov

Fesenkov Astrophysical Institute, Almaty, Kazakhstan, sergey_ks2002@mail.ru

KEYWORDS:

Jupiter, Great Red Spot, troposphere, methane, ammonia

INTRODUCTION:

This work is part of an extensive multi-year program of research on the instability of Jupiter's atmosphere and the search for patterns in its structure. The program provides for obtaining homogeneous material from spectral observations of Jupiter and analyzing spatiotemporal variations in the intensity of the molecular absorption bands of methane and ammonia in the visible and near-infrared regions of the spectrum of 600–950 nm.

The behavior of methane absorption bands of varying intensity along the central meridian of Jupiter depends on the vertical structure, optical density, and position of the upper boundary of the cloud cover at different latitudes of the planet.

The formation of absorption bands of methane and ammonia does not occur in the same way precisely due to the fact that ammonia condenses, forming clouds at atmospheric level below the tropopause, and at high altitudes its content drops sharply.

In addition, it participates in the formation of deeper cloud layers from ammonium hydrosulfide NH_4SH , and can also enter the water-ammonia cloud layer located even lower. Therefore, the observed variations in the intensity of the NH_3 absorption bands can be considered as a consequence of changes not only in the optical and structural characteristics of clouds, but also with real variations in the relative ammonia content in different regions of the planet.

In this article, we continue our research in this direction [1–4], especially since the significant depletion of gaseous NH_3 in the low latitudes of the Northern Hemisphere in the NEB region is confirmed by the results of a high-resolution microwave VLA study [5]. The lower ammonia content is also confirmed by observations in the visible and near-infrared range [6].

This article differs from the work of our colleagues [4] in that we present a comparison of the results of a study of variations in methane and ammonia along the central meridian of Jupiter for certain longitudes L_2 in the second system, corresponding to:

- the moment of passage of the Great Red Spot ($L_2 = 46^\circ$),
- without it ($L_2 = 16^\circ$).

OBSERVATION CONDITIONS, PROCESSING METHODS AND MAIN RESULTS:

Our spectral observations were performed near the opposition of Jupiter (November 2023) at the observatory of the V.G. Fesenkov Astrophysical Institute (Almaty, 1450 m above sea level) using an SGS diffraction spectrograph with an ST7-XE CCD camera mounted in 7.5-meter focus, a 0.6-meter Cassegrain RC600 telescope. The CCD matrix consists of 765×510 pixels. The dispersion of the spectrograph is 0.43 nm/pixel. In the spectrogram image, the spatial scale is 4.18 pixels per 1 angular second.

The exposures at the time of observation were 60–90 s, which provided for the accumulation of 50 000–55 000 pulses in the continuous spectrum for the center of the disk and 2000–2500 in the center of the deepest absorption band of methane at 886 nm. With a background noise track outside the main spectrum of 50–60 pulses along the entire spectrogram, this pro-

vided a signal-to-noise ratio of 1000 in the continuous spectrum, and 40 in the methane absorption band of 886 nm.

For processing, the best quality spectrograms obtained on the night of November 2–3, 2023 were used. An improved methodology and program for processing observational material are described in the article [7]. This program provides an operational and detailed representation of the characteristics of the bands on the central meridian or in one of the selected latitude zones. The program outputs graphical and tabular data on the equivalent widths, central depths of the absorption bands, and the effective optical thickness of the absorbing gas, calculated from the residual intensities. At the same time, the residual Bostu intensity in each wavelength can be represented as:

$$\text{Bostu} \approx \exp(-\tau^*),$$

where τ^* is the effective optical thickness of the absorbing gas at a given wavelength: either methane τ_m^* or ammonia τ_a^* , or as the sum of both ($\tau_m^* + \tau_a^*$).

Regardless of the conditions of reflected radiation formation in the scattering and absorbing atmosphere of a planet, these parameters remain proportional to the absorption coefficient at a given wavelength and the average number of absorbing gas molecules per line of sight, being a kind of indicator of the optical path or depth of reflected radiation formation.

Therefore, in our opinion, for absorption bands that differ greatly in intensity, as well as for a correct comparison of absorption variations in the center of each band and in its wings (located along its edges), it is optimal to represent the variations in the form of a comparison of effective optical absorption thicknesses $\tau^* \approx \text{Ln}(\text{Bostu})$. Such a comparison can be considered as a peculiar method of optical sensing of a complex atmosphere.

For convenience and clarity of comparing the variations of these values along a particular cloud zone or along the central meridian, the ratio of their values to the value in the reference region is often used. As such, the center of Jupiter's disk or any other area is most often used, depending on the research task.

The result of this representation of absorption variations along the central meridian and the Great Red Spot for all 8 absorption bands of methane and ammonia is presented below.

Figure 1 shows the appearance of Jupiter from November 2–3, 2023, at the time of the passage of the Great Red Spot through the central meridian and the studied zones.

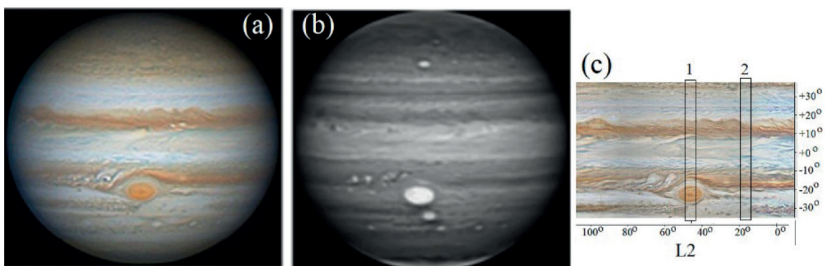


Figure 1. External view of Jupiter on November 2–3, 2023: *a* — in the RGB system (Gary Walker); *b* — in the absorption band of 889 nm (Akutsu Sebu); *c* — study areas: 1 — in the area of the GRS ($L_2 = 46^\circ$) and 2 — in the STRz zone, free from disturbance ($L_2 = 16^\circ$) (<https://alpo-j.sakura.ne.jp/>)

As in previous years, the most characteristic feature of the Great Red Spot is its abnormally high brightness in the absorption band of 886 nm methane. Figure 2 shows the brightness variations along the central meridian in the continuous spectrum of 630 nm and in the absorption band of 886 nm methane at the time of the passage of the Great Red Spot.

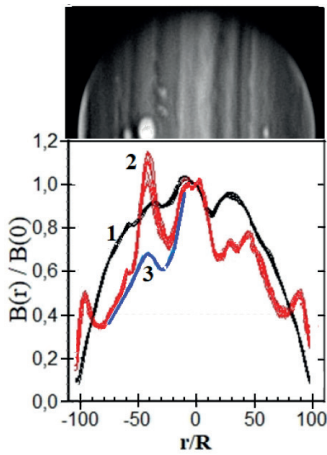


Figure 2. Brightness variations along the central meridian in the continuous spectrum of 630 nm (1) and in the absorption band of 886 nm methane (2) at the time of passage of the Great Red Spot and without it (3). The result of processing 7 spectrograms

To identify the features of methane and ammonia absorption in the Great Red Spot, the Equatorial Zone (EZ) and the Southern Tropical Zone (STrZ), on which this disturbance is located, were chosen as the reference area. The result turned out to be similar, but most pronounced when compared with STrZ.

Figure 3 shows the STrZ spectrum (a) and the ratio of the spectra (GRS/STrZ) (b) and (c). For the 800–950 nm spectral range, the ordinate scale is on the right.

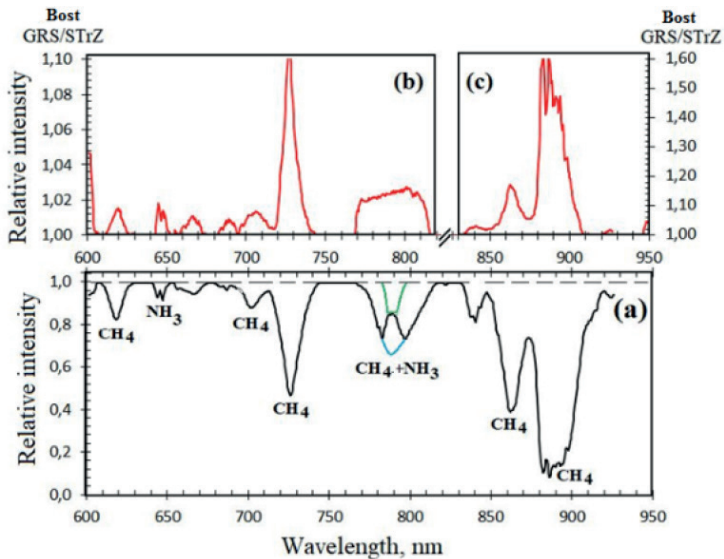


Figure 3. The STrZ spectrum (a) and the ratio of the GRS/STrZ spectra (b). In the CH₄ band of 889 nm, the GRS/STrZ ratio reaches 1.6

Figure 4 shows a comparison of the latitudinal variations of the effective $\tau_m^*(r)$ and $\tau_a^*(r)$ along the central meridian of Jupiter relative to their values in the center of the disk at the time of the passage of the GRS (red line) and without it (black line).

It is noteworthy that variations in the central depths, equivalent widths and τ_m^* , normalized to the center of the disk, for 6 methane absorption bands demonstrate a pronounced deficiency of methane and ammonia in the region of the Great Red Spot (Figure 5).

Comparing the variations of τ_a^* of the studied ammonia absorption bands (Figure 4 on the right), we can draw attention to the fact that in 2023, the ammonia deficiency is most pronounced in the NH₃ band of 645 nm, especially in the area of the BCP. As in previous years, the minimum falls on the border between NEB and NTrZ. This effect is slightly less pronounced in the NH₃ band of 790 nm. However, in the 790 nm band, the boundary of ammonia deficiency in the northern hemisphere is more pronounced between the light Equatorial Zone (EZ) and the dark Northern Equatorial Belt (NEB).

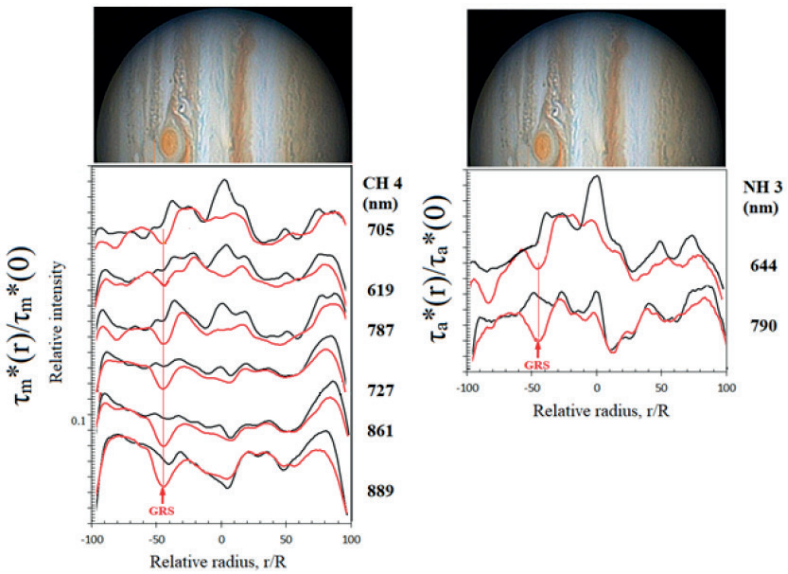


Figure 4. Comparison of the relative latitudinal variations of the effective $\tau_m^*(r)$ and $\tau_a^*(r)$ along the central meridian of Jupiter, normalized to their value in the center of the disk. The red line corresponds to the passage of the GRS along the central meridian, the black line is without the GRS. The curves are reflected on the same scale and shifted along the ordinate axis for clarity

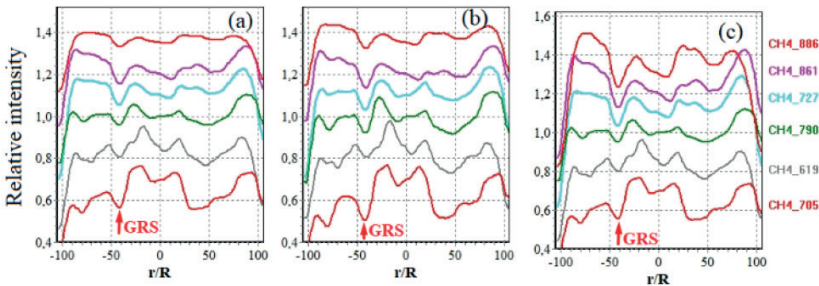


Figure 5. Variations of the central depths (a), equivalent widths (b), and $\tau_m^*(c)$, normalized to the center of the disk, for 6 methane absorption bands. For clarity, the curves are shifted along the ordinate axis and reflected at the same scale

CONCLUSION:

The observed optical and morphological features of Jupiter’s atmosphere are variable in nature and are related to various factors in the formation of reflected and outgoing radiation in the planet’s troposphere.

The main prerequisite for carrying out work in this direction are the results obtained in the course of our previous studies of the atmosphere of Jupiter, especially on the behavior of absorption bands. In particular, the previously discovered significant depression of ammonia absorption in the Northern Equatorial Belt of Jupiter (NEB) is confirmed. In addition, the results obtained from observations in the visible and near-infrared regions of the spectrum practically coincided qualitatively with what studies of Jupiter show in the thermal infrared wavelength range and in the radio range of millimeter and centimeter thermal radiation [5, 6].

This is what determines the future direction of our research on processes in the atmosphere of Jupiter in order to detail the spatiotemporal changes in the atmosphere of the planet by molecular absorption bands.

We hope that this kind of work can be useful both in the general complex of studies of Jupiter’s atmosphere and in modeling its complex multi-tiered layered clouds.

ACKNOWLEDGMENTS:

The authors would like to thank Professor V. G. Teifel for his helpful advice.

The work was carried out within the framework of the program No. BR20280974 "Program of Fundamental Astrophysical Research in Kazakhstan: observations and theory", financed by the Ministry of Education and Science of the Republic of Kazakhstan.

REFERENCES:

- [1] *Vdovichenko V.D., Kiriyyenko G.A.* Investigation of asymmetry during ammonia absorption in the northern and southern hemispheres of Jupiter in 2004–2016 // *Izvestiya NAS RK*. 2017. No. 4. P. 170–178.
- [2] *Vdovichenko V.D., Karimov A.M., Kiriyyenko G.A. et al.* Molecular absorption bands in the study of Jupiter's troposphere // *Izvestiya NAS RK: Physico-mathematical series*. 2020. V. 3. P. 26–33. DOI: 10.32014/2020.2518-1726.33.
- [3] *Teifel V.G., Kharitonova G.A., Karimov A.M.* Features of the latitudinal course of ammonia absorption in the NH₃ 7870 A band on Jupiter // *Izvestiya NAS RK: Physico-mathematical series*. 2006. No. 4. P. 57–61.
- [4] *Vdovichenko V.D., Karimov A.M., Lysenko P.G. et al.* Some Characteristic Features of Latitudinal Variations in Methane and Ammonia Absorption on Jupiter // *Solar System Research*. 2025. V. 59. P. 57–68. DOI: 10.1134/S0038094624601750.
- [5] *De Pater I., Sault R.J., Butler B. et al.* Peering through Jupiter's clouds with radio spectral imaging. *Research Reports. Gas Giant Planets // Science*. 2016. V. 352. Iss. 6290. P. 1198–1201. DOI: 10.1126/science.aaf2210.
- [6] *Hill S.M., Irwin P.G.J., Alexander C., Rogers J.H.* Spatial variations of Jovian tropospheric ammonia via ground-based imaging // *Earth and Space Science*. 2024. V. 11. Article e2024EA003562. <https://doi.org/10.1029/2024EA003562>.
- [7] *Vdovichenko V.D.* Methodological aspects of the study of ammonia-methane absorption variations in the atmosphere of Jupiter // *16th Moscow Solar System Symp*. 2024. P. 138–141/

SPATIAL VARIATIONS OF JOVIAN TROPOSPHERIC AMMONIA OBTAINED FROM SAO RAS OBSERVATIONS

A. E. Ivanova¹, A. V. Moiseev^{1,2}, D. G. Evdokimova¹, D. A. Belyaev¹,
A. A. Fedorova¹

¹ Space Research Institute RAS, Moscow, Russia

anastasia.ivanova@cosmos.ru

² Special Astrophysical Observatory, Nizhny Arkhyz, Karachai-Cherkessian Republic, Russia

KEYWORDS:

Jupiter, Uranus, troposphere, clouds, methane, ammonia

INTRODUCTION:

Study of the latitudinal variations of ammonia and methane in Jupiter's atmosphere is the subject of research for many groups (e. g. [1–3]).

In January 2025 spectra of Jupiter and Uranus were obtained for the first time at the SAO RAS 6-m telescope. We present the results of our study of ammonia variations based on new data obtained at the SAO RAS.

SPATIAL VARIATIONS OF A JOVIAN TROPOSPHERIC AMMONIA:

Jupiter was observed using the long-slit mode of the SCORPIO-2 focal reducer [4] in January and March 2025. Wavelength range 550–780 nm.

We investigated the latitudinal dependence of equivalent width of 647 ammonia band for Jupiter troposphere. Our result is at the agreement with the one published at [1].

Additionally we investigated equivalent width changes for Uranus. Uranus was observed in March 2025 using the SCORPIO 2 in the same configuration.

REFERENCES:

- [1] Hill S. M., Irwin P. G. J., Alexander C., Rogers J. H. Spatial Variations of Jovian Tropospheric Ammonia via Ground-Based Imaging // *Earth and Space Science*. 2024. V. 11. Iss. 8. <https://doi.org/10.1029/2024EA003562>.
- [2] Irwin P. G. J., Hill S. M., Fletcher L. N. et al. Clouds and Ammonia in the Atmospheres of Jupiter and Saturn Determined From a Band-Depth Analysis of VLT/MUSE Observations // *J. Geophysical Research: Planets*. 2025. V. 130. Iss. 1. <https://doi.org/10.1029/2024JE008622>.
- [3] Vdovichenko V. D., Lysenko P. G., Filippov V. A. Absorption variations in the ammonia bands of 645 and 790 nm along the central meridian of Jupiter in 2023 // 15th Moscow Solar System Symp. 2024.
- [4] Afanasiev V. L., Moiseev A. V. Scorpio on the 6 m Telescope: Current State and Perspectives for Spectroscopy of Galactic and Extragalactic Objects // *Baltic Astronomy*. 2011. V. 20. P. 363–370. <https://doi.org/10.1515/astro-2017-0305>

**SESSION 7. ASTROBIOLOGY (AB)
ORAL SESSION**

STIMULATION OF THE ORIGIN-OF-LIFE PROCESS BY HIGH-FREQUENCY OSCILLATIONS IN HYDROTHERMAL MEDIUM: SUGGESTED EXPERIMENTS

V. N. Kompanichenko

*Institute for Complex Analysis of Regional Problems FEB RAS
Birobidzhan, Russia, kompanv@yandex.ru*

KEYWORDS:

astrobiology, origin of life, hydrothermal system, prebiotic chemistry, oscillations of parameters, experiment

ABSTRACT:

The presentation is devoted to consideration of possible experimental ways to verify the concept of thermodynamic inversion (TI) of the origin of life [1]. From a standpoint of the general thermodynamics of systems, an appearance of the initial signs of living state in organic (micro)systems means their transition to the prevalence of free energy contribution over the entropy contribution. Such a transition can only occur in conditions far from equilibrium in the presence of different-rank oscillations of physical and chemical parameters in the environment (temperature, pressure, chemical, and electrical potentials, etc.). Their range must include high-frequency (short-period) oscillations that bring maximum energy to the prebiotic system. Such conditions exist in hydrothermal systems during the fluid migration to the surface.

Some conducted experiments confirm this approach. They reveal the dependence between fluctuations in physicochemical parameters in the medium and the level of polymerization of molecules. In particular, these research have demonstrated that fluctuations in parameters significantly increase the yield of oligomers and polymers of various macromolecules, in comparison with stable conditions in the medium [2–4]. However, the author considers all the listed experiments as indirect support for the TI concept only, since they were set for other tasks. Direct experimental verification of this approach has not yet been carried out. Based on the provisions formulated above, the author suggests several directions for experiments that could check and develop the TI concept.

A key thesis of the developed approach, which requires experimental confirmation, is the following: pumping organic microsystems with high-frequency (short-period) oscillations transmitting high energy is a prerequisite for their transition to life through an intermediate state. Such experiments should be aimed at studying the primary signs of the intermediate state in various prebiotic models (microsystems) placed in an environment with varying oscillations of physicochemical parameters (pressure, temperature, chemical and electrical potentials, etc.). As a result of their implementation, it is necessary to test the thesis that under nonequilibrium oscillatory conditions in prebiotic systems, a response to external influence appears, which, under optimal pumping conditions, transfers the system to the intermediate state between non-life and life [5].

At the initial stage, the following direction of such experiments can be proposed. The general approach is the self-assembly of lipid vesicles (considered as primary prebiological microsystems) under conditions modeling a fluctuating flow of hydrothermal fluid rising to the surface. In this case, the fluctuations of the parameters in the experimental chamber should be regulated in such a way that the trend towards self-assembly of liposomes periodically changes to a trend towards their disintegration, which will facilitate the constant recombination of molecules in the microsystems. Amino acids and low-molecular organic compounds established in hydrothermal systems should be used as additional components. The most important aspect of such studies should be the study of the response to ex-

ternal influences (stress) that occurs in prebiological microsystems, which can be considered as the primary signs of a living state.

REFERENCES:

- [1] *Kompanichenko V.N.* Geothermal energy as an initial factor in the process of life origin // *AIMS Geosciences*. 2025. V. 11. Iss. 2. P. 528–539. DOI: 10.3934/geosci.2025022.
- [2] *Osipovich D.C., Barratt C., Schwartz P.M.* Systems chemistry and Parrondo's paradox: computational models of thermal cycling // *New J. Chemistry*. 2009. V. 33(10). P. 1981–2184. <http://dx.doi.org/10.1039/B900288J>.
- [3] *Sugawara T., Kurihara K., Suzuki K.* Constructive approach toward protocells // *Engineering of Chemical Complexity* / ed. Mikhailov A. 2012. P. 359–374. https://doi.org/10.1142/9789814390460_0018.
- [4] *Varfolomeev S.D.* Kinetic models of prebiological evolution of macromolecules: Thermocycle as the motive force of the process // *Mendeleev Communication*. 2007. V. 17. Iss. 1. P. 7–9. <https://doi.org/10.1016/j.mencom.2007.01.003>.
- [5] *Kompanichenko V.* The Rise of a Habitable Planet: Four Required Conditions for the Origin of Life in the Universe // *Geosciences* 2019. V. 9. No. 2. Article 92. <https://doi.org/10.3390/geosciences9020092>.

FROM PREBIOTIC EARTH TO ASTROSCIENCE EMPOWERMENT: THE NORCEL INSTITUTE'S EDUCATIONAL JOURNEY ACROSS THE GLOBAL SOUTH

Sohan Jheeta

The Network of Researchers on the Chemical Emergence of Life
sohan@sohanjheeta.com

KEYWORDS:

prebiotic Earth, chemical emergence of life, astroscience education, global south outreach, science equity, NoRCEL Institute ERA

ABSTRACT:

The **Network of Researchers on the Chemical Emergence of Life (NoRCEL)** was founded in 2013 to explore how life began on Earth, spanning prebiotic chemistry through the emergence of Archaea, Bacteria, and Eukarya. Following its inaugural conference at The Open University, NoRCEL rapidly grew into a global community of scientists, students, and educators (*norcel.net*).

Building on this scientific foundation, NoRCEL steadily expanded its scope into **public engagement and global outreach**. The **Blue Earth Project (BEP)** added a science-in-society dimension, confronting planetary challenges through hybrid forums that connected scientific knowledge with societal needs. Regional hubs then emerged: the **Latin America Hub (LatAm Hub)**, advancing English-language collaboration among Latin American students and scholars; and the **Microbial World Network (MWN)**, deepening research and dialogue on microbial life as a planetary driver and as an analogue for astrobiological exploration.

In 2022, NoRCEL launched the **Astroscience Exploration Network (ASEN)**, establishing an **African Astroscience Hub**. Here, outreach was deliberately tailored to local contexts, leveraging Africa's landscapes as "natural laboratories" while inspiring new generations to pursue STEM careers. The outreach successes of **LatAm Hub and ASEN** became the proving ground for NoRCEL's next transformation.

NoRCEL is now transitioning into **The NoRCEL Institute**, consolidating a decade of initiatives into a strategic mission: the creation of the **NoRCEL Education & Research Academy (ERA)**. ERA will deliver a **structured on-line curriculum in astroscience**, designed to extend equitable, high-quality science education to developing nations worldwide.

This presentation will trace NoRCEL's evolution from its roots in prebiotic chemistry research to its current role as a **provider of accredited astroscience education**. It will demonstrate how a progression from research to outreach has now culminated in a comprehensive, curriculum-based approach that empowers the Global South with both knowledge and opportunity.

ASTROECOLOGY AS A NEW SCIENTIFIC DIRECTION WITHIN ASTROBIOLOGY

O. R. Kotsyurbenko

Yugra State University, Khanty-Mansiysk, Russia, kotsor@mail.ru

*Network of Researchers on the Chemical Evolution of Life
Leeds, United Kingdom*

KEYWORDS:

astroecology, astrobiology, biosystems, metabiosphere, closed artificial ecosystems

ABSTRACT:

Astrobiology is a highly integrative science that includes knowledge of various natural science disciplines such as biology, chemistry, physics, geology, astronomy and others, as well as some humanities, such as philosophy. Currently, in connection with the active exploration of outer space, astrobiology is increasingly engaged in applied issues related to the influence of space factors on terrestrial organisms, their potential for adaptation, as well as the biological component of the organization of life support for astronauts in various extraterrestrial systems. Like any actively developing scientific discipline, astrobiology accumulates new data and uses new methodological approaches for their interpretation, enriched with new scientific concepts. One of the trends in the development of astrobiology is its integration with ecology, the science of terrestrial ecosystems, their interaction and levels of organization. Ecological approaches and research methods are very useful for solving various problems of astrobiology. methods are very useful for solving various problems of astrobiology. Currently, the integration between ecology and astrobiology is becoming so close that a new direction is being formed within the latter — astroecology, in which ecological knowledge and concepts are key in the study and description of various cosmic phenomena.

The possibility of drawing some conditional boundaries for the new discipline exists based on the field of ecology research — the study of interactions of living organisms with each other and with their habitat at different levels of organization.

It is the interactions between various biosystems in the context of the new astronomical component that is the main area of interest of astroecology. A new level of studying phenomena associated with outer space is added to the existing close scientific integration of ecology and biology, and accordingly the prefix “astro” to the new discipline. Accordingly, the current ecological concepts and methodological approaches to the study of natural phenomena constitute the theoretical basis of astroecology, which is used in the new “cosmic” dimension.

Astroecology includes three main areas of research. The first direction is related to terrestrial issues and is based on the use of approaches and methods of terrestrial ecology with the use of remote sensing tools and other approaches related to space technologies. The second direction is related to the modeling and study of closed artificial ecosystems, the principles of their functioning and the creation of life-support ecosystems for astronauts in space flights or at research stations on other planets. The third direction is related to the study of hypothetical extraterrestrial ecosystems on various cosmic bodies, their formation, features, as well as the creation of concepts for terraforming various cosmic bodies with the involvement of terrestrial organisms in the processes of creating conditions favorable for the development of terrestrial biosystems and human existence.

THEORETICAL AND EXPERIMENTAL STUDIES OF INTERSTELLAR ICES

A. I. Vasyunin¹, K. Borshcheva^{1,2}, V. M. Karteyeva¹, M. G. Medvedev¹, R. S. Nakibov¹, M. E. Ozhiganov¹, I. V. Petrashkevich¹, U. A. Sapunova¹

¹ Ural Federal University, Yekaterinburg, Russia, anton@urfu.ru

² Institute of Astronomy RAS, Moscow, Russia

KEYWORDS:

astrochemistry, molecule formation, laboratory astrophysics, ice spectroscopy, dust processes

ABSTRACT:

The regions of star and planet formation are characterized by extreme physical conditions: ultra-low densities and temperatures of gas and dust, as well as the presence of ionizing action. Despite this, the chemical composition of star-forming regions is very diverse. A variety of molecular species have been discovered in the interstellar medium, ranging from simple diatomic species to complex organic molecules. The number of complex molecules (COMs) of various types discovered in the interstellar medium is continuously growing, which causes a growing interest in astrochemistry as one of the possible mechanisms contributing to the emergence of life in the Universe.

Numerical modeling of the formation of complex organic molecules in the interstellar medium using the MONACO model showed that although COMs can form in cold interstellar gas, the main contribution to their formation is made by chemical processes on the surface of interstellar dust particles covered with ice mantles. At the same time, the so-called non-diffusion chemical processes occurring in interstellar ices play a significant role. It is interesting that the COMs contents in cold ices formed at the early stages of protostar development are close to the COMs contents in the gas of the so-called "hot cores", the next stage of development of low-mass protostars.

The results of numerical modeling are supplemented by laboratory experiments on the ISEAge ultra-high-vacuum setup designed for transmission IR spectroscopy of interstellar ice analogues. The setup created in the laboratory allows growing thin ices of controlled chemical composition and structure under conditions close to those in the interstellar medium ($P < 10^{-13}$ atm, $T \sim 10 \dots 300$ K). The resulting transmission IR spectra of ices in the 2.5–20 μm range are used as references in the analysis of interstellar ice observations obtained with modern ground-based and space telescopes, including the James Webb Space Telescope (JWST). Comparison of laboratory spectra with observational data on JWST allowed for the first time to simultaneously estimate the methane content in the gas and ice mantles of the protostar IRAS 23385+6053, to establish upper limits for the content of the HCN molecule and the IR-inactive N₂ molecule in interstellar ices.

ACKNOWLEDGMENTS:

The research is supported via the Russian Science Foundation via the Project No. 23-12-00315 (https://grant.rscf.ru/prjcard_int?23-12-00315).

NITROUS OXIDE IN INTERSTELLAR ICE

V. M. Karteyeva, R. S. Nakibov, I. V. Petrashkevich, M. E. Ozhiganov,
M. G. Medvedev, A. I. Vasyunin

Ural Federal University, Yekaterinburg, Russia, varvara.karteeva@urfu.ru

KEYWORDS:

interstellar ice, infrared spectra, nitrous oxide, absorption band, astrobiology

ABSTRACT:

Various chemical compounds, including those relevant to astrobiology, efficiently form in the icy mantles of interstellar dust particles. The presence and abundance of molecules in the condensed phase are determined using infrared (IR) telescope data [1, 2]. With the launch of the James Webb Space Telescope (JWST), it is now possible to detect less abundant molecules (concentrations below 1% relative to water). One such candidate molecule is nitrous oxide (N_2O). This molecule has been detected in the gas phase in three objects [3–5] and is currently tentatively detected in interstellar ice of five others [6–8]. Reliable detection of this molecule requires an extensive database of IR spectra of interstellar ice analogs.

We conducted cryogenic ultrahigh-vacuum experiments using the ISEAge (Ice Spectroscopy Experimental Aggregate) [9] setup to produce such ices. In this work we obtained laboratory reference spectra of nitrous oxide at 10 K. Ten mixtures with common interstellar ice molecules (H_2O , CO , CO_2 , CH_3OH , NH_3 , CH_4 , N_2) were analyzed. Nitrous oxide exhibits two distinct absorption bands at 10 K: 2221 cm^{-1} (NN stretch) and 1282 cm^{-1} (NO stretch). The search for N_2O in IR spectra was conducted using the NN stretching band, as it is the most intense. It was found that the largest spectral shift occurs in mixtures with carbon-containing molecules (CO_2 , CO , CH_3OH), with the greatest shift (28 cm^{-1}) observed in the CO_2 mixture.

We also analyzed JWST data for the object B335. The spectral fit in the $2260\text{--}2200\text{ cm}^{-1}$ range includes absorption bands of nitrous oxide in a water-dominated environment (1:20 ratio) and in a mixture with carbon dioxide and nitrogen (1:15:13 ratio). This spectral region also contains water combination bands, gaseous CO emission lines, and an absorption band from the cyanate anion (OCN^-), complicating the detection of N_2O . This marks the first reliable detection of N_2O in interstellar ice.

ACKNOWLEDGMENTS:

This research work is funded by the Russian Science Foundation via 23-12-00315 agreement.

REFERENCES:

- [1] Öberg K. I., Boogert A. C. A., Pontoppidan K. M. et al. The Spitzer ice legacy: Ice evolution from cores to protostars // *The Astrophysical J.* 2011. V. 740. No. 2. Article 109. DOI: 10.1088/0004-637X/740/2/109.
- [2] McClure M. K., Rocha W. R. M., Pontoppidan K. M. et al. An Ice Age JWST inventory of dense molecular cloud ices // *Nature Astronomy.* 2023. V. 7. No. 4. P. 431–443. <https://doi.org/10.1038/s41550-022-01875-w>.
- [3] Ziurys L. M., Apponi A. J., Hollis J. M., Snyder L. E. Detection of interstellar N_2O : A new molecule containing an NO bond // *Astrophysical J. Letters.* 1994. V. 436. No. 2. P. L181–L184. DOI: 10.1086/187662.
- [4] Halfen D. T., Apponi A. J., Ziurys L. M. Evaluating the N/O chemical network: The distribution of N_2O and NO in the Sagittarius B2 complex // *The Astrophysical J.* 2001. V. 561. No. 1. Article 244. DOI: 10.1086/322770.
- [5] Rivilla V. M., Martín-Pintado J., Jiménez-Serra I. et al. Prebiotic precursors of the primordial RNA world in space: Detection of NH_2OH // *The Astrophysical J. Letters.* 2020. V. 899. No. 2. P. L28. DOI: 10.3847/2041-8213/abac55.
- [6] Nazari P., Rocha W. R. M., Rubinstein A. E. et al. Hunting for complex cyanides in protostellar ices with the JWST-A tentative detection of CH_3CN and $\text{C}_2\text{H}_5\text{CN}$ // *Astronomy and Astrophysics.* 2024. V. 686. P. A71. 15 p. <https://doi.org/10.1051/0004-6361/202348695>.
- [7] Nakibov R., Karteyeva V., Petrashkevich I. et al. Solid and Gaseous Methane in IRAS 23385+6053 as seen with Open JWST Data // *The Astrophysical J. Letters.* 2025. V. 978. No. 2. Article L46. DOI: 10.3847/2041-8213/ada290.

- [8] *Rocha W.R.M., McClure M.K., Sturm J.A. et al.* Ice inventory towards the protostar Ced 110 IRS4 observed with the James Webb Space Telescope-Results from the Early Release Science Ice Age program // *Astronomy and Astrophysics*. 2025. V. 693. P. A288. 28 p. <https://doi.org/10.1051/0004-6361/202451505>.
- [9] *Ozhiganov M., Medvedev M., Karteyeva V. et al.* Infrared Spectra of Solid HCN Embedded in Various Molecular Environments for Comparison with the Data Obtained with JWST // *The Astrophysical J. Letters*. 2024. V. 972. No. 1. Article L10. DOI: 10.3847/2041-8213/ad6d5c.

METHANE ENVIRONMENT IN INTERSTELLAR ICE

**R. S. Nakibov, V. M. Karteyeva, I. V. Petrashkevich, M. E. Ozhiganov,
M. G. Medvedev, A. I. Vasyunin**

Ural Federal University, Yekaterinburg, Russia, nakibov.ruslan@urfu.ru

KEYWORDS:

interstellar ice, infrared spectra, methane, laboratory ice analogues, astrobiology

ABSTRACT:

Methane is one of a few molecules of astrobiological importance that is securely detected in interstellar ices by its infrared spectral features. As a precursor to complex carbonaceous molecules, it plays a key role in forming complex carbonaceous molecules [1, 2] and carbon-chain chemistry [3]. Methane also has astrobiological significance, serving as a potential biosignature [4] and a valuable tracer in planetary studies [5].

Despite its widespread detection, methane is typically fitted in observational data using water-dominated ice environments [6, 7]. However, recent work suggests that methane can also reside in CO₂-rich ices [8], and alternative formation pathways, such as methanol photolysis, may contribute to its abundance [9]. Laboratory studies show that methane spectral features are highly sensitive to its molecular environment, making it essential to consider diverse ice mixtures when interpreting observational data.

In this study, we examine the 7.7 μm methane deformation band in the protostar IRAS 23385+6053 using JWST observations. We report the detection of gaseous methane emission and find a new spectral interpretation based on laboratory ice analogs: CH₄:H₂O = 1:10 (8.4 K) and CH₄:CO₂ = 1:5 (27.4 K). Additionally, we identify a residual spectral feature tentatively attributed to nitrous oxide (N₂O), supported by experimental ice spectra.

ACKNOWLEDGMENTS:

This research work is funded by the Russian Science Foundation via 23-12-00315 agreement.

REFERENCES:

- [1] *Harada N., Herbst E.* Modeling carbon chain anions in L1527 // *The Astrophysical J.* 2008. V. 685. No. 1. Article 272. DOI 10.1086/590468.
- [2] *Hassel G.E., Herbst E., Garrod R.T.* Modeling the lukewarm corino phase: is L1527 unique? // *The Astrophysical J.* 2008. V. 681. No. 2. Article 1385. DOI: 10.1086/588185.
- [3] *Sakai N., Sakai T., Hirota T., Yamamoto S.* Abundant carbon-chain molecules toward the low-mass protostar IRAS 04368+ 2557 in L1527 // *The Astrophysical J.* 2008. V. 672. Iss. 1. P. 371–381. DOI: 10.1086/523635.
- [4] *Thompson M.A., Krissansen-Totton J., Wogan N. et al.* The case and context for atmospheric methane as an exoplanet biosignature // *Proc. National Academy of Sciences.* 2022. V. 119. No. 14. Article e2117933119. DOI: 10.1073/pnas.2117933119.
- [5] *Kobayashi K., Geppert W.D., Carrasco N. et al.* Laboratory studies of methane and its relationship to prebiotic chemistry // *Astrobiology.* 2017. V. 17. No. 8. P. 786–812. DOI: 10.1089/ast.2016.1492.
- [6] *McClure M.K., Rocha W.R.M., Pontoppidan K.M. et al.* An Ice Age JWST inventory of dense molecular cloud ices // *Nature Astronomy.* 2023. V. 7. No. 4. P. 431–443. <https://doi.org/10.1038/s41550-022-01875-w>.
- [7] *Rocha W.R.M., van Dishoeck E.F., Ressler M.E. et al.* JWST Observations of Young protoStars (JOYS+): Detecting icy complex organic molecules and ions-I. CH₄, SO₂, HCOO⁻, OCN⁻, H₂CO, HCOOH, CH₃CH₂OH, CH₃CHO, CH₃OCHO, and CH₃COOH // *Astronomy and Astrophysics.* 2024. V. 683. Article A124. 32 p. <https://doi.org/10.1051/0004-6361/202348427>.
- [8] *Nakibov R., Karteyeva V., Petrashkevich I. et al.* Solid and Gaseous Methane in IRAS 23385+6053 as seen with Open JWST Data // *The Astrophysical J. Letters.* 2025. V. 978. No. 2. Article L46. DOI: 10.3847/2041-8213/ada290.
- [9] *Islam F., Baratta G.A., Palumbo M.E.* Simultaneous UV-and ion processing of astrophysically relevant ices-The case of CH₃OH: N₂ solid mixtures // *Astronomy and Astrophysics.* 2014. V. 561. Article A73. 9 p. <https://doi.org/10.1051/0004-6361/201322010>.

ON THE FORMATION AND STABILITY OF RESIDUAL HYDROGEN-HELIUM ATMOSPHERES OF MINI-NEPTUNES DEPENDING ON POSSIBLE ATMOSPHERIC LOSS PROCESSES

R. A. Evdokimov¹, V. I. Shematovich²

¹ *Rocket and Space Corporation "Energia", Korolev, Moscow Region, Russia
evdokimovrom@yandex.ru*

² *Institute of Astronomy RAS, Moscow, Russia, shematov@inasan.ru*

KEYWORDS:

mini-Neptunes, Hyceans, atmospheric dissipation, core-powered mass-loss, photoevaporation, habitable zone

INTRODUCTION:

A brief overview is given of the problem of potential habitability of Hycean planets formed as a result of the loss of extended and massive primary hydrogen-helium envelopes by mini-Neptunes with relatively small masses and low equilibrium temperatures (after the parent star has entered the main sequence). The loss of primary atmospheres by such exoplanets may be due to the core-powered mass-loss mechanism. The stability of residual atmospheres is considered taking into account the photoevaporation process.

HYCEANS AS A NEW CLASS OF POTENTIALLY HABITABLE EXOPLANETS:

Hyceans (hydrogen-water worlds) are a hypothetical class of exoplanets with thin hydrogen-helium atmospheres and water oceans. They differ from ordinary mini-Neptunes in the presence of liquid water and a clear boundary between the atmosphere and the ocean (water surface) [1, 2]. Despite a number of problematic issues (stability of the climate system, possible deficiency of a number of elements important for life in the ocean, etc.), the presence of liquid water places the Hyceans among potentially habitable exoplanets. Moreover, it has been suggested that the oceans of these exoplanets may contain a large biomass, and the biodiversity and rate of evolution of microbial life may exceed those on Earth in some cases [3]. Since hydrogen is a greenhouse gas at sufficiently high pressure [4], but unlike, for example, CO₂ and H₂O, it does not condense even at very low temperatures, an atmosphere of primordial composition can provide conditions suitable for the existence of a liquid ocean even at very large distances of the exoplanet from the parent star. Even free-floating exoplanets can be Hyceans. In this case, only the heat flow from the planet's interior is present, and there is no radiation from the parent star. Thus, the Hycean potential habitability zone actually has no outer boundary. In [1], arguments were made in favor of the fact that the so-called "dark Hyceans" (tidally locked Hyceans with a permanently shadowed hemisphere) could have an inner boundary of the potential habitability zone located closer to the parent star than for Earth-like exoplanets. It was also noted that the gaseous envelopes of this class of exoplanets are preferable for study by transmission spectroscopy due to the relatively high altitude of the homogeneous atmosphere and the larger radius [1]. A number of potential biomarkers were proposed for Hyceans [1]. Among the mini-Neptunes discovered to date, a number of candidates for hycean planets have been identified [1], of particular interest is K2-18b [5, 6], which, according to initial estimates, should have an equilibrium temperature of 250–300 K. In addition, according to [7, 8], the transmission spectroscopy method (using the results of observations on JWST) made it possible to identify signs of the presence of dimethyl sulfide in the atmosphere of this mini-Neptune, which the authors of the aforementioned papers classified as a biomarker. Both the biogenic origin of dimethyl sulfide in the atmosphere of K2-18b and its pres-

ence are questionable. In particular, a strong argument is given in favor of a high (exceeding critical) temperature at the boundary of the gas envelope and the water mantle. First, the moderate temperature at the ocean surface is compatible only with the maximum possible water content in K2-18b [8], which is unlikely. Second, the work [9] shows that the albedo of K2-18b should be relatively low (no more than 0.2–0.3), and the equilibrium temperature should significantly exceed 250 K. Third, a more detailed examination of the climate features of the Hyceans [10] indicates the presence of a strong greenhouse effect in the surface layer of the atmosphere, which should contain a large amount of water vapor. For these reasons, the Hycean candidates discovered to date may have too high temperature at the boundary of the atmosphere and the water layer, incompatible with a liquid ocean. The inner boundary of the potential habitability zone for them may be located significantly further from the parent star, where the illumination level corresponds to distances of several a. u. for sun-like stars [10]. However, this fact does not reduce interest in exoplanets of this class. Light (with masses from 1 to $4M_{\oplus}$) mini-Neptunes and super-Earths may be common in fairly wide orbits, which is confirmed indirectly by statistical data on discovered exoplanets, as well as by recent observations. In addition, even relatively hot mini-Neptunes, lacking oceans but having a cloud layer of liquid water droplets in the shallow layers of the atmosphere, may be of some interest from the point of view of astrobiology.

POSSIBLE WAYS OF FORMING THIN HYDROGEN-HELIUM ATMOSPHERES:

Mini-Neptunes on wide orbits can be hyceans only if the relative mass of their gas envelope does not exceed 10^{-5} – 10^{-3} of the exoplanet mass (a higher mass corresponds to lower illumination). The probability of forming such thin envelopes is relatively small. As a rule, the atmosphere is several percent of the mini-Neptune mass [11]. Almost complete or significant loss of primary envelopes as a result of photoevaporation is possible only at low orbital distances, i.e. outside the habitable zone for hyceans [12]. In this work, it is shown that the loss of massive gas envelopes and the formation of thin atmospheres of primary composition are possible for light mini-Neptunes (1.5 – $0.3M_{\oplus}$), rich in water, on wide orbits due to core-powered mass-loss [13, 14]. This mechanism of formation of potential hyceans is most effective for exoplanets around red dwarfs, which are distinguished by relatively high luminosity at the initial stage of evolution. Relatively high equilibrium temperature of exoplanets in the first millions — tens of millions of years after formation can ensure the loss of most of the gas envelope. Its further evolution is associated with photoevaporation, the rate of which will decrease with a decrease in the luminosity of the parent star and its activity. Ultimately, the equilibrium temperature of the exoplanet decreases to values compatible with the existence of an ocean. The results of calculations for models of mini-Neptunes of different masses, with different proportions of water in the composition and with different equilibrium temperatures after formation for parent stars of different spectral classes are presented. An assessment is given (based on the conditions at the boundary of the atmosphere and the water mantle) of their belonging to hyceans. The stability of residual gas envelopes is estimated taking into account photoevaporation.

REFERENCES:

- [1] *Madhusudhan N., Piette A. A. A., Constantinou S.* Habitability and Biosignatures of Hycean Worlds // *Astrophysical J.* 2021. V. 918. No. 1. DOI: 10.3847/1538-4357/abfd9c.
- [2] *Nixon M. C., Madhusudhan N.* How deep is the ocean? Exploring the phase structure of water-rich sub-Neptunes // *Monthly Notices of the Royal Astronomical Society.* 2021. V. 505. Iss. 3. P. 3414–3432. <https://doi.org/10.1093/mnras/stab1500>.
- [3] *Mitchell E. G., Madhusudhan N.* Prospects for biological evolution on Hycean worlds // *Monthly Notices of the Royal Astronomical Society.* 2025. V. 538. Iss. 3. P. 1653–1662. <https://doi.org/10.1093/mnras/staf094>.

- [4] *Pierrehumbert R., Gaidos E.* Hydrogen Greenhouse Planets Beyond the Habitable Zone // *Astrophysical J.* I. 2011. V. 734. Iss. 1. Article L13. 5 p. DOI: 10.1088/2041-8205/734/1/L13.
- [5] *Guinan E. F., Engle S. G.* The K2-18b Planetary System: Estimates of the Age and X-UV Irradiances of a Habitable Zone “Wet” Sub-Neptune Planet // *Research Notes of the American Astronomical Soc.* 2019. V. 3. Iss. 12. Article 189. 5 p. DOI: 10.3847/2515-5172/ab6086.
- [6] *Madhusudhan N., Nixon M. C., Welbanks L. et al.* The Interior and Atmosphere of the Habitable-zone Exoplanet K2-18b // *Astrophysical J. Letters.* 2020. V. 891. No. 1. Article L7. DOI: 10.3847/2041-8213/ab7229.
- [7] *Madhusudhan N., Sarkar S., Constantinou S. et al.* Carbon-bearing Molecules in a Possible Hycean Atmosphere // *Astrophysical J. Letters.* 2023. V. 956. No. 1. Article L13. DOI: 10.3847/2041-8213/acf577.
- [8] *Madhusudhan N., Constantinou S., Holmberg M. et al.* New Constraints on DMS and DMDS in the Atmosphere of K2-18b from JWST Miri // *Astrophysical J. Letters.* 2025. V. 983. Article L40. DOI: 10.3847/2041-8213/adc1c8.
- [9] *Jordan S., Shorttle O., Quanz S. P.* Planetary albedo is limited by the above-cloud atmosphere: Implications for sub-Neptune climate // <https://arxiv.org>. 2025. DOI: 10.48550/arXiv.2504.12030.
- [10] *Innes H., Tsai S.-M., Pierrehumbert R. T.* The Runaway Greenhouse Effect on Hycean Worlds // *Astrophysical J.* 2023. V. 953. No. 2. Article 168. DOI: 10.3847/1538-4357/ace346.
- [11] *Mol Lous M., Helled R., Mordasini Ch.* Potential long-term habitable conditions on planets with primordial H–He atmospheres // *Nature Astronomy.* 2022. V. 6(7). Article 819.
- [12] *Owen J. E., Mohanty S.* Habitability of terrestrial-mass planets in the HZ of M Dwarfs — I. H/He-dominated atmospheres // *Monthly Notices of the Royal Astronomical Society.* 2016. V. 459. Iss. 4. P. 4088–4108. DOI: 10.1093/mnras/stw959.
- [13] *Ginzburg S., Schlichting H. E., Sari R.* Super-Earth Atmospheres: Self-consistent Gas Accretion and Retention // *Astrophysical J.* 2016. V. 825. Iss. 1. Article 29. 12 p. DOI: 10.3847/0004-637X/825/1/29.
- [14] *Owen J. E., Schlichting H. E.* Mapping out the parameter space for photoevaporation and core-powered mass-loss // *Monthly Notices of the Royal Astronomical Society.* 2024. V. 528. Iss. 2. P. 1615–1629. <https://doi.org/10.1093/mnras/stad3972>.

EFFECT OF TWO-YEAR EXPOSURE IN LOW EARTH ORBIT CONDITIONS ON THE PROKARYOTIC COMMUNITY OF GREY FOREST SOIL

I. A. Kozlov, A. A. Belov, V. S. Cheptsov

Lomonosov Moscow State University, Soil Science Faculty, Moscow, Russia
dfyz357@gmail.com

KEYWORDS:

astrobiology, space, low Earth orbit, soil microbiome, extremophiles, metabolic activity

INTRODUCTION:

Currently, outer space is a unique space for interdisciplinary research, allowing us to obtain new information about various physical and biochemical characteristics of natural objects [1, 2]. One of the key areas of astrobiology has become the assessment of the influence of various cosmic factors on microorganisms, in particular on prokaryotic communities [3–8]. Determining the limits of resistance to these conditions is necessary to understand the processes of transformation of the microbial community in outer space, which is important when planning long-term expeditions and missions (for example, to the Moon or Mars), as well as when assessing the risks of “forward” and “back” contamination of planets by various microorganisms [9–13]. Soil can be chosen as a model object for studying the effects of cosmic factors on prokaryotic communities, since it is a complex biological system, being the main pool of microorganisms on our planet that ensure the cyclic use of chemical elements by organisms. Exploration of the microorganism’s biodiversity and physiological activity in soil exposed in LEO (Low Earth Orbit) is the key to understanding the possibility of creating closed ecological systems in spacecraft and future extraterrestrial colonies.

EXPERIMENT:

In this research, a comprehensive assessment of the impact of two years of exposure in the outer shell of the International Space Station (ISS) on the prokaryotic communities of gray forest soil was carried out. To achieve this goal, a systematic methodological approach was applied that allows for a comprehensive analysis of the resistance of bacterial populations to the extreme conditions of outer space.

Soil samples (0–10 cm) from a broad-leaved forest in the vicinity of Pushchino were dried, aseptically crushed to 1 mm and packed in sterile polypropylene bags with pores of 0.2 microns. The packages were placed in special containers to ensure the sterility of the inner surface and direct interaction with the atmosphere.

The epifluorescence microscopy with intercalating dye acridine orange was used to determine the number of bacteria in soil samples. In order to estimate the number of culturable bacteria in soil samples, the plating method on dense nutrient media was used. Culturing were performed at two different temperatures: 10 and 25 °C. The functional diversity of soil microbial communities was assessed using the multisubstrate testing method based on the study of substrate consumption spectra [14]. An *in vitro* study of the stress resistance of bacterial isolates included the determination of tolerance spectra to temperature, pH, and osmotic stress was performed [14].

KEY RESULTS:

The total numbers of prokaryotic cells were in the range of $(8.5–8.6) \cdot 10^8$ cells/g. It was no statistically significant differences between the total number of prokaryotes in the samples of gray forest soil from all experimental variants, which may indicate a slight effect of the cumulative effect of LEO conditions on the number of prokaryotic cells.

The number of culturable bacteria in the studied samples was statistically significantly different in the exposed and control samples: a significant de-

crease in the number of cultured bacteria by 10-100 times in the exposed samples compared with the control variants was found, which may indicate the suppression of cultured bacterial complexes under the influence of stressful conditions of outer space.

Multisubstrate testing has shown that exposure in LEO conditions leads to a decrease in the potential metabolic activity of soil microbial communities while maintaining a relatively uniform representation of representatives of various trophic groups within the communities. Analyzing the consumption spectra of substrates at the class level of bioorganic compounds, it is possible to note a change in the "consumption strategies" of bacterial communities of the studied samples of gray forest soil towards the consumption of the most energy-efficient substrates (amino acids).

It was found that all the analyzed bacterial isolates, regardless of the temperature conditions of their initial secretions and the type of gray forest soil samples, demonstrated the ability to grow on nutrient media at a temperature of 25 °C. It is worth noting that 50% or more of the strains in the complexes isolated from gray forest soil in all experimental variants show active growth over the entire range of temperatures studied (from 10 to 45 °C).

All strains isolated from the researching microbial communities showed maximum activity at a neutral pH of 7. In the pH range from 5 to 11, there was significant variability in the proportion of bacteria capable of growth, ranging from 60 to 100 %. Psychrotolerant strains of the exposed samples show greater resistance compared to mesophilic ones. Also, 70% of the strains isolated from exposed and frozen samples showed the ability to grow at salt concentrations up to 10 % (0.1 M).

ACKNOWLEDGMENTS:

The study was supported by grant No. 69 25-74-00003 from the Russian Science Foundation, <https://rscf.ru/project/25-74-00003/>.

REFERENCES:

- [1] *Cottin H., Kotler J.M., Bartik K. et al.* Astrobiology and the possibility of life on earth and elsewhere... // *Space Science Reviews*. 2017. V. 209. P. 1–42. DOI: 10.1007/s11214-015-0196-1.
- [2] *De Mol M.L.* Astrobiology in space: A comprehensive look at the Solar system // *Life*. 2023. V. 13. No. 3. Article 675. <https://doi.org/10.3390/life13030675>.
- [3] *Horneck G., Moeller R.* Microorganisms in space // *Astrobiology. An Evolutionary Approach*. Boca Raton: CRC Press, 2015. P. 283–299.
- [4] *Senatore G., Mastroleo F., Leys N., Mauriello G.* Effect of microgravity and space radiation on microbes // *Future Microbiology*. 2018. V. 13. No. 7. P. 831–847. DOI: 10.2217/fmb-2017-0251.
- [5] *Checinska Sielaff A., Urbaniak C., Mohan G. B. M. et al.* Characterization of the total and viable bacterial and fungal communities associated with the International Space Station surfaces // *Microbiome*. 2019. V. 7. Article 50. 21 p. <https://doi.org/10.1186/s40168-019-0666-x>.
- [6] *Mora M., Wink L., Kögler I. et al.* Space Station conditions are selective but do not alter microbial characteristics relevant to human health // *Nature communications*. 2019. V. 10. Article 3990. <https://doi.org/10.1038/s41467-019-11682-z>.
- [7] *Beblo-Vranesovic K., Bohmeier M., Schleumer S. et al.* Impact of simulated martian conditions on (facultatively) anaerobic bacterial strains from different Mars analogue sites // *Current Issues in Molecular Biology*. 2020. V. 38. No. 1. P. 103–122. DOI: 10.21775/cimb.038.103.
- [8] *Cheptsov V.S.* Survival and Transfer of Microorganisms beyond the Earth: To What Extent are Microorganisms Tolerant to External Influences? // *Solar System Research*. 2024. V. 58. Iss. Suppl 1. P. S87–S104. DOI: 10.1134/S0038094624601087.
- [9] *Baranov V.M., Novikova N.D., Polikarpov N.A. et al.* The biorisk experiment: 13-month exposure of resting forms of organism on the outer side of the russian segment of the international space station: Preliminary results // *Doklady Biological Sciences*. 2009. V. 426. No. 5. P. 706–709. DOI: 10.1134/S0012496609030223.
- [10] *Zea L., Nisar Z., Rubin P. et al.* Phenotypic changes exhibited by *E. coli* cultured in space // *Frontiers in Microbiology*. 2017. V. 8. Article 1598. DOI: 10.3389/fmicb.2017.01598.
- [11] *Kminek G., Clark B. C., Conley C. A. et al.* Report of the COSPAR Workshop on Refining Planetary Protection requirements for human missions // 2nd COSPAR Work-

- shop on Refining Planetary Protection Requirements for Human Missions. Tech. rep. 2018. 28 p.
- [12] *Garrett-Bakelman F.E., Darshi M.A., Green S.J. et al.* The NASA Twins Study: A multidimensional analysis of a year-long human spaceflight // *Science*. 2019. V. 364. Iss. 6436. Article eaau8650. DOI: 10.1126/science.aau86.
- [13] *Hendrickson R., Urbaniak C., Minich J.J. et al.* Clean room microbiome complexity impacts planetary protection bioburden // *Microbiome*. 2021. V. 9. Article 238. 17 p. <https://doi.org/10.1186/s40168-021-01159-x>.
- [14] *Belov A.A., Cheptsov V.S., Vorobyova E.A. et al.* Stress-tolerance and taxonomy of culturable bacterial communities isolated from a central Mojave Desert soil sample // *Geosciences*. 2019. V. 9. No. 4. Article 166. <https://doi.org/10.3390/geosciences9040166>.

ABIOTIC SYNTHESIS OF ORGANIC COMPOUNDS IN PLASMA-DUST CLOUDS INITIATED BY MICROWAVE DISCHARGE IN THE MINERAL SIMULANT OF LUNAR REGOLITH

M. A. Zaitsev¹, V. D. Borzosekov^{2,3}, A. S. Kuzovchikova¹,
V. V. Gudkova^{2,3}, A. A. Letunov², A. D. Rezaeva^{2,4}, E. V. Voronova²,
D. V. Malakhov², A. S. Sokolov², E. M. Sorokin⁵, E. A. Obratsova^{2,6},
T. I. Morozova¹, V. D. Stepakhin², M. V. Gerasimov¹

¹ Space Research Institute RAS, Moscow, Russia, mzaitsev@cosmos.ru

² Prokhorov General Physics Institute RAS, Moscow, Russia
borzosekov@fpl.gpi.ru

³ RUDN University, Moscow, Russia

⁴ Zelenograd Nanotechnology Center, Zelenograd, Moscow, Russia

⁵ Vernadsky Institute of Geochemistry and Analytical Chemistry RAS
Moscow, Russia;

⁶ Moscow Institute of Physics and Technology (National Research University)
Dolgoprudny, Moscow Region, Russia

KEYWORDS:

abiotic synthesis, organic compounds, early Earth atmosphere, microwave discharge, plasma-dust clouds, lunar regolith simulant, LMS-1D, optical emission spectroscopy, OES, scanning electron microscopy, SEM, pyrolytic gas chromatography-mass spectrometry, Pyr-GC/MS

INTRODUCTION:

More and more organic compounds (OC) are being discovered in outer space, including complex polycyclic compounds of abiotic origin [1]. The abiotic synthesis of complex OC from initial inorganic or/and organic matter has been repeatedly approved due to many types of model experiments, which represent different processes take place on space bodies or in the cosmic medium. For that, different targets placed in model atmospheres, vacuum, or "persistent containers" were exposed to different energy sources: spark discharges, ultraviolet (UV-) and X-ray irradiation, pulsed laser irradiation, hypervelocity impacts, shock waves generated by explosions, etc. The sources of elements for OC formation can be both mineral sample, imitating the regolith or rock of considered space body, and surrounded gas medium (if any) containing different combinations of gases that represent the hypothetical or known atmosphere of the space body (H₂, N₂, CO, CO₂, NH₃, O₂, CH₄, H₂O, etc.).

One of the topical issues of abiotic synthesis is the possible catalytic role of the plasma-dust medium in the synthesis of OC. Plasma here acts as a source of charged particles, UV radiation, radicals, and particles in an excited state, which significantly increase the number of possible chemical reactions. Solid particles, located in plasma regions where heat fluxes are not so large for their evaporation or melting, can act as a heterogeneous catalyst [2].

EXPERIMENTS:

We used a microwave discharge in powdered samples, which occurs when they are exposed to powerful pulsed gyrotron radiation [3], to create a plasma-dust environment and study the formation of organic substances. The target was the lunar regolith simulant LMS-1D [4, 5], which repeats both the mineral (pyroxene, basalt, anorthosite, olivine, and ilmenite) and granulometric compositions of the lunar maria regolith, or rather its smallest fraction, lunar dust [6, 7]. The initial gas medium was argon at atmospheric pressure, but ammonium carbonate was added to each of the prepared samples, which rapidly decomposed into H₂O, CO₂, and NH₃ at the initial stages of discharge, creating an environment of gases and vapors that could have been presented in the early Earth atmosphere. Metal iron powder was added to a part of the samples to facilitate the breakdown conditions.

The microwave radiation power of 400 kW corresponds to an average beam cross-section power density of 14 kW/cm² and RMS electric field strength of 2.3 kV/cm. Two irradiation modes were used to vary the quenching conditions of possible reaction products: 1) a sequence of three short (2 ms) pulses with a pause of 8 ms between them; 2) single long (8 ms) pulses.

RESULTS AND THEIR DISCUSSION:

Optical emission spectroscopy confirmed the appearance of ammonium carbonate constituents in plasma and the destruction of the initial petrogenic oxides.

Scanning electron microscopy revealed the spheroidization of particles and the appearance of porous particles in the samples after exposure to a discharge. This effect was most brightly represented in samples with the addition of metal iron powder.

A comparative study of the composition and content of OC in the samples before and after the exposure to the discharge was carried out by pyrolytic gas chromatography-mass spectrometry (Pyr-GC/MS). The setup consisted of "Pyrolytic vaporizer P4" equipped with a cryofocusing system (liq. CO₂), and "Chromatec Crystal 5000.2" gas chromatograph/mass spectrometer. In order to protect all the exposed materials against contamination with organic substances from the laboratory environment, the preparation of both the chamber and samples for the microwave discharges, as well as the analytical preparation of the irradiated material, was carried out in the microbiological safety boxes (as laminar shelters) with all necessary precautions.

A noticeable release of OC occurred at temperatures of 450 °C and above (with stepwise heating of the samples at 150, 300, 450, 600 and 900 °C), which indicates the presence of high-molecular thermally unstable OC that produce volatile products of their thermal destruction. Among the volatiles isolated were: alkadienes (isoprene, pentadiene-1,3), aromatic hydrocarbons (benzene, toluene, biphenyl, styrene, naphthalene), as well as N-bearing substances (mainly — benzonitrile).

CONCLUSION:

These experiments showed that microwave irradiation of mixtures based on a lunar regolith simulant generates new compounds (mainly high-molecular ones), including those containing bound nitrogen from the model atmosphere.

ACKNOWLEDGMENTS:

This work was supported by the Russian Science Foundation (project No. 25-22-00505, <https://rscf.ru/project/25-22-00505/>).

REFERENCES:

- [1] *Wenzel G., Gong S.* Discovery of the Seven-ring polycyclic aromatic hydrocarbon cyanocoronene (C₂₄H₁₁CN) in GOTHAM Observations of TMC-1 // *The Astrophysical J. Letters*. 2025. V. 984. No. 1. Article L36. 19 p. DOI 10.3847/2041-8213/adc911.
- [2] *Tu X., Whitehead J. C., Nozaki T.* Plasma catalysis: fundamentals and applications // *Springer Series on Atomic, Optical, and Plasma Physics*. V. 106. Berlin: Springer, 2019. 348 p.
- [3] *Batanov G.M., Kossyi I.A.* Pulsed microwave discharges in powder mixtures: Status, problems, and prospects // *Plasma Physics Reports*. 2015. V. 41. No. 10. P. 847–857. <https://doi.org/10.1134/S1063780X15090020>.
- [4] *Isachenkov M., Chugunov S., Landsman Z. et al.* Characterization of novel lunar highland and mare simulants for ISRU research applications // *Icarus*. 2022. V. 376. No. 1. Article 114873. 11 p. DOI: 10.1016/j.icarus.2021.114873.
- [5] *Long-Fox J.M., Britt D.T.* Characterization of planetary regolith simulants for the research and development of space resource technologies // *Frontiers in Space Technologies*. 2023. V. 4. Article 1255535. 16 p. <https://doi.org/10.3389/frspt.2023.1255535>.
- [6] *Kuznetsov I.A., Zakharov A.V., Dolnikov G.G. et al.* Lunar dust: properties and investigation techniques // *Cosmonautics and rocket engineering (Vestnik "NPO im. S. A. Lavochkina")*. 2016. No 4(34). P. 20–32 (in Russian).
- [7] *Zakharov A.V., Zelenyi L.M., Popel' S.I.* Lunar Dust: Properties and Potential Hazards // *Solar System Research*. 2020. V. 54. Iss. 6. P. 455–476. DOI: 10.1134/S0038094620060076.

ALTERNATIVE LIFE FORMS UNDER EXTREME CONDITIONS

T. I. Morozova

Space Research Institute RAS, Moscow, Russia, timoroz@yandex.ru

KEYWORDS:

non-carbon life forms in the Universe, extreme chemistry, non-carbon compounds, life forms based on ammonia, life forms based on silicon principles, self-organization, self-reproducing and self-organizations, dusty plasma structures

ABSTRACT:

The possibilities of using non-carbon life forms in the Universe and, in particular, in the Solar System are considered. Special mechanisms for the arrangement of living organisms in the depths of giant planets have been developed in fundamental extreme chemistry and the synthesis of a complex method of non-carbon compounds and the diversity of their forms based on ammonia. Life based on silicon principles, self-organization in dusty plasma as one of the possible forms of life, and even clouds in the Earth's atmosphere as independent self-reproducing and self-organizing structures are considered.

**SESSION 7. ASTROBIOLOGY (AB-PS)
POSTER SESSION**

EFFECT OF PERCHLORATE ON BACTERIA RADIORESISTANCE UNDER SIMULATED MARTIAN CONDITIONS

V. S. Cheptsov^{1,2}, A. A. Belov¹, A. Yu. Merkulova³, A. K. Pavlov³,
V. N. Lomasov⁴

¹ Space Research Institute of RAS, Moscow, Russia

² Lomonosov Moscow State University, Soil Science Faculty, Moscow, Russia
cheptcov.vladimir@gmail.com

³ Ioffe Physical-Technical Institute, Saint Petersburg, Russia

⁴ Peter the Great St. Petersburg Polytechnic University
Saint Petersburg, Russia

KEYWORDS:

Mars, habitability, radiotolerance, bacteria, perchlorates

INTRODUCTION:

Perchlorates are found in Martian regolith and have a great importance from astrobiological point of view. In one hand, they can serve as an energy source for microorganisms and can promote liquid water formation, and in other hand they are able to kill microorganisms through oxidative and osmotic stress [1]. Despite that, it is found that perchlorate presence significantly (in several times) enhances bactericidal effect of UV radiation [2]. Hypothetical microbial cells in Martian soil can be shielded from UV by thin layers of minerals ([3], and references therein), so this factors combination probably could be effective only in the shallow regolith. But Mars is subjected to irradiation with intensive ionizing radiation, which penetrates few meters depth [4]. It is unknown, is there any synergistic bactericidal effects of ionizing radiation and perchlorates, like it is shown for UV. There are data on higher rates of organics radiolysis at the perchlorates presence [5–7], but effects on microbial viability are not studied yet.

EXPERIMENT:

We performed irradiation of *Bacillus subtilis* bacteria by accelerated electrons under simulated Martian conditions — temperature about –65 °C and pressure about 1 Torr. Bacterial cells were within pure water ice and perchlorate-containing (1 and 2.5 wt.%) water ice. Irradiation was performed with 5, 10, and 15 kGy doses. Bacterial viability was assessed using solid nutrient media culturing.

Bacteria have demonstrated high radiotolerance under model conditions — cells count decreased no more than two orders of magnitude after irradiation with the highest dose. It was found, that sodium perchlorate presence at concentrations up to 2.5 % does not alter bacteria survivability under ionizing radiation (in contrast to previously shown effect of UV). This result testifies in favor of habitability of perchlorate-containing eoniches on Mars.

ACKNOWLEDGMENTS:

The study is funded by Russian Science Foundation, project №24-72-00004 (<https://rscf.ru/en/project/24-72-00004/>).

REFERENCES:

- [1] Cheptsov V., Belov A., Soloveva O. et al. Survival and growth of soil microbial communities under influence of sodium perchlorates // Intern. J. Astrobiology. 2021. V. 20. Iss. 1. P. 36–47. DOI: 10.1017/S1473550420000312.
- [2] Wadsworth J., Cockell C.S. Perchlorates on Mars enhance the bacteriocidal effects of UV light // Scientific reports. 2017. V. 7(1). Article 4662. <https://doi.org/10.1038/s41598-017-04910-3>.
- [3] Rummel J.D., Beaty D.W., Jones M.A. et al. A new analysis of Mars “special regions”: findings of the second MEPAG Special Regions Science Analysis Group (SR-SAG2) // Astrobiology. 2014. V. 14(11). P. 887–968. DOI: 10.1089/ast.2014.1227.
- [4] Dartnell L.R., Desorgher L., Ward J.M., Coates A.J. Modelling the surface and subsurface Martian radiation environment: Implications for astrobiology

- // *Geophysical Research Letters*. 2007. V. 34. Iss. 2. Article L02207. <https://doi.org/10.1029/2006GL027494>.
- [5] Pavlov A. A., McLain H. L., Glavin D. P. et al. Rapid radiolytic degradation of amino acids in the Martian shallow subsurface: Implications for the search for extinct life // *Astrobiology*. 2022. V. 22(9). P. 1099–1115. DOI: 10.1089/ast.2021.0166.
- [6] Góbi S., Abplanalp M. J., Kaiser R. I. Effect of perchlorates on electron radiolysis of glycine with application to Mars // *The Astrophysical J*. 2016. V. 822. No. 1. Article 8. DOI: 10.3847/0004-637X/822/1/8.
- [7] Góbi S., Bergantini A., Kaiser R. I. Degradation of adenine on the Martian surface in the presence of perchlorates and ionizing radiation: a reflectron time-of-flight mass spectrometric study // *The Astrophysical J*. 2017. V. 838. No. 2. Article 84. DOI: 10.3847/1538-4357/aa653f.

REMOTE SENSING OF EARTH'S ECOSYSTEMS

V. P. Badya, P. I. Besogonova, O. R. Kotsyurbenko

Ugra State University, Khanty-Mansiysk, Russia, lerabada5@gmail.com

KEYWORDS:

astroecology, remote sensing, environmental monitoring, Lidar, Sentinel-2, environmental assessment, satellite devices

Abstract:

Remote sensing is the most well-developed and actively used research method in astroecology. In relation to terrestrial ecosystems, versatility and innovative technologies make remote sensing a powerful tool in the hands of scientists in solving problems in the field of biogeography and ecology. In the context of global environmental challenges such as biodiversity loss and climate change, remote sensing is becoming an indispensable tool for the sustainable management of natural resources and the development of effective environmental protection strategies. The development of remote sensing methods and technologies opens up the possibility to measure the height, topography and geometry of an object (tree) using Lidar, determine the level of chlorophyll in foliage, and study the biochemistry of a plant using spectrometric sensors. This allows scientists to calculate the biomass of the forest. By comparing these data with ground-based studies, conclusions can be drawn about the state and diversity of the forest. Also, the correlation of Lidar and spectral measurement data with information about the soil obtained directly allows us to draw conclusions even about microbial activity. With the help of information about the climate and vegetation obtained using remote sensing technologies, it is possible to predict where a particular type of animal is found and with what density. Within the framework of astroecology, an actively developing field of astrobiology, remote sensing methods make it possible to observe and assess the state of various ecosystems and draw conclusions about the functioning of the Earth's biosphere as a whole. In addition, remote sensing methodology can be effective in exploring various extraterrestrial systems to obtain important information about their potential habitability.

CLOSED ARTIFICIAL ECOSYSTEMS IN SPACE EXPLORATION

P. I. Besogonova, V. P. Badya, O. R. Kotsyurbenko

Ugra State University, Khanty-Mansiysk, Russia, besogonova99red@mail.ru

KEYWORDS:

closed artificial ecosystems, space exploration, life support systems in spacecraft, experiments with closed artificial systems, biosystems on planetary stations, ecosystem interactions

ABSTRACT:

The creation of closed artificial systems with balanced ecosystem relationships is the most important aim in space exploration. They are divided into two main types — biosystems on spacecraft and on stations organized on the surface of planets. Closed ecosystems are self-sufficient autonomous systems in which all the organisms and resources necessary for life are located in a limited space. In conditions of long-term flights on a spacecraft or working on a space station, such systems will provide for vital functions and ensure stable activity of the crew. The higher the degree of closure of such biosystems, the more efficient their functioning and contribution to saving resources. To create the systems, it is necessary to take into account all the trophic connections between its biological agents and simulate ecosystem interactions that should ensure the closure of biogeochemical cycles in a very limited volume. To date, a number of experiments have been conducted in created artificial systems on Earth. Such systems are Biosphere-2 (USA), BIOS-3 (Russia), Yurgong-1 (China) and a number of others. Various biological organisms were used in experiments to create artificial ecosystems, including plants (cereals, legumes, grasses and shrubs), animals (insects, reptiles, amphibians, fish, crustaceans, small mammals), as well as microorganisms (bacteria, fungi, protists) involved in the decomposition of organic substances. Algae served as the main producers in the water component of the systems. In different experiments, different degrees of their closeness were achieved. In general, the results obtained proved to be extremely important for understanding the functioning of such systems and served as the basis for more accurate modeling and further experiments to create effective types of various closed systems. Such ecosystems provide valuable information about how life can exist and adapt in conditions of limited resources, which is important for future exploration and possible colonization of other planets. At the same time, experiments with such systems can give a clue of understanding the principles of ecosystem sustainability and the possibilities of their restoration on Earth.

MAXIMA OF STRONG METEOR SHOWERS IN BLOOD MARKERS

A. V. Tertyshnikov

Institute of Applied Geophysics, Moscow, Russia, atert@mail.ru

KEYWORDS:

meteor showers, ultraviolet radiation, blood markers, generalized portraits, leukocytes, lymphocytes, erythrocytes

INTRODUCTION:

The ordering of variations in solar ultraviolet radiation and an increase in its intensity during the maxima of strong meteor showers at the Russian Antarctic station Novolazarevskaya [1] was used to search for effects in blood tests from the St. Petersburg Clinical Hospital for 2000–2001. The following are selected for the experiment: the rate of erythrocyte sedimentation (ESR), the content of leukocytes and lymphocytes.

The features of the devices used for observations of solar ultraviolet radiation are considered.

THE SCHEME OF THE EXPERIMENT:

Strong meteor showers with fixed peak dates from (https://en.wikipedia.org/wiki/List_of_meteor_showers/) were used to diagnose the effect of increases in the power of solar ultraviolet radiation on blood markers. The criterion for selecting meteor showers was the value of the zenith hour number of at least 5 meteors per hour above a potential observer. The list of events includes streams: January 3, February 8 and 24, March 14, 07.06, 19.06, 30.07, 06.08, 13.08, 01.09, 9 September, October 21, November 17, December 7 and 14.

The duration of the investigated series of blood tests in the St. Petersburg Clinical Hospital was from 28.05.2000 to 20.03.2001, with the exception of July. There were no analyses on public holidays and, partially, on weekends. The average scores from daily blood tests were used as blood markers: 1) erythrocyte sedimentation rate (ESR), 2) lymphocyte count, and 3) leukocyte count. During the day, at least five and up to 15 people took blood tests. The uncertainty in the state of health of those who took the tests determines the main attention to the study of their dispersion and order. For this purpose, the "generalized portrait" method was used in the range of ± 10 days from the dates of the maxima of strong meteor showers, and the fast Fourier transform method, taking into account the small amplitude of potential changes.

ANALYSIS OF THE RESULTS:

The ESR marker evaluates the presence of an inflammatory process and other pathological changes in the body. Estimates of the standard deviation and coefficient of variation of the average daily ESR estimates, the coefficients of skew and kurtosis of the average series of ESR are analyzed.

Increased amplitudes of variations in the estimates obtained are noticeable in the range from -6 to $+9$ days from the date of the maximum of the strong meteor shower. But on the date of the maximum, with an increased level of solar ultraviolet radiation, variations are minimal, and the marker level normalizes. The average ESR estimate on the date of the strong meteor shower was 5.2 mm/hour, with a norm of 2–10 mm/hour for men and 2–15 mm/hour for women. The ESR values on the dates -2 days and $+2$ days are 60 % higher than on the date of the maximum of the strong meteor shower.

On the date of the maxima of strong meteor showers, the kurtosis coefficient of the average daily ESR marker is negative, which corresponds to a uniform distribution law.

The cyclicity in the morphology of spectral-temporal amplitudograms calculated using the fast Fourier transform is shown for a number of average daily ESR markers.

A change in the morphology of the spectral and temporal characteristics of the analyzed markers was noted with respect to the dates of strong meteor showers, dominant cyclical patterns with periods of 3–4 and 6–7 days, as well as normalization of the average daily ESR estimate.

The level of the average daily marker “leukocytes” is lower than the average values within ± 10 days from the date of the maximum meteor shower and increased on -3 days and on $+4$ days. There are also dominant periodicities of 3–4 and 7 days. Ordering the variation of the average daily markers by leukocytes by estimating the kurtosis coefficient as much as one day after the date of the meteor shower maxima. The signal is strong, exceeding the limits of the 95 % confidence interval of the analyzed three-week series and corresponding to the levels of the normal distribution law, which confirms the effect of ordering variations of the analyzed marker, activation of the immune system.

According to the average daily marker “lymphocytes”, the changes are in many ways similar to the estimates for leukocytes. Lymphocytes (blood cells that are involved in the formation of immune defenses) are a type of white blood cell.

DISCUSSION:

The time correspondence between the weak impact of the meteor shower on the upper atmosphere and variations in blood markers necessitates the search for possible mechanisms of interaction. These may include changes in atmospheric conductivity due to meteor dust, an increase in the influx of solar ultraviolet radiation into the maximum of the meteor shower, the influence of solar ultraviolet radiation on pathogenic processes, and variations in the density of the meteor shower in the solar ultraviolet stream.

Models of the distribution of meteoric matter do not take into account changes in the density of the meteor shower in the upper layers of the Earth’s atmosphere. In Russia, priority is given to space debris models, in which special attention should be paid to dust generated by the combustion of Starlink satellites. Possible mechanisms of meteor dust release that affect fluctuations in the solar ultraviolet radiation flux are discussed.

CONCLUSIONS:

As a result of statistical processing of blood tests from the St. Petersburg Clinical Military Hospital, normalization of the erythrocyte sedimentation rate was established on dates of strong meteor showers, which corresponds to an increase in incoming solar ultraviolet radiation. In the dynamics of ESR estimates characterizing the activity of inflammatory processes, dominant cyclical news with periods of 3–4 and 6–7 days was noted. They may be caused by the social effects of the working week and variations in ultraviolet radiation on particles of settling meteor dust.

The content of leukocytes and lymphocytes revealed similar effects with minima on the dates of meteor shower maxima, dominant periodicity, and strong signals of activation of immune system processes after the maxima of strong meteor showers.

The deposition of cosmic and meteoric dust into the ozonosphere is of interest to astrobiology.

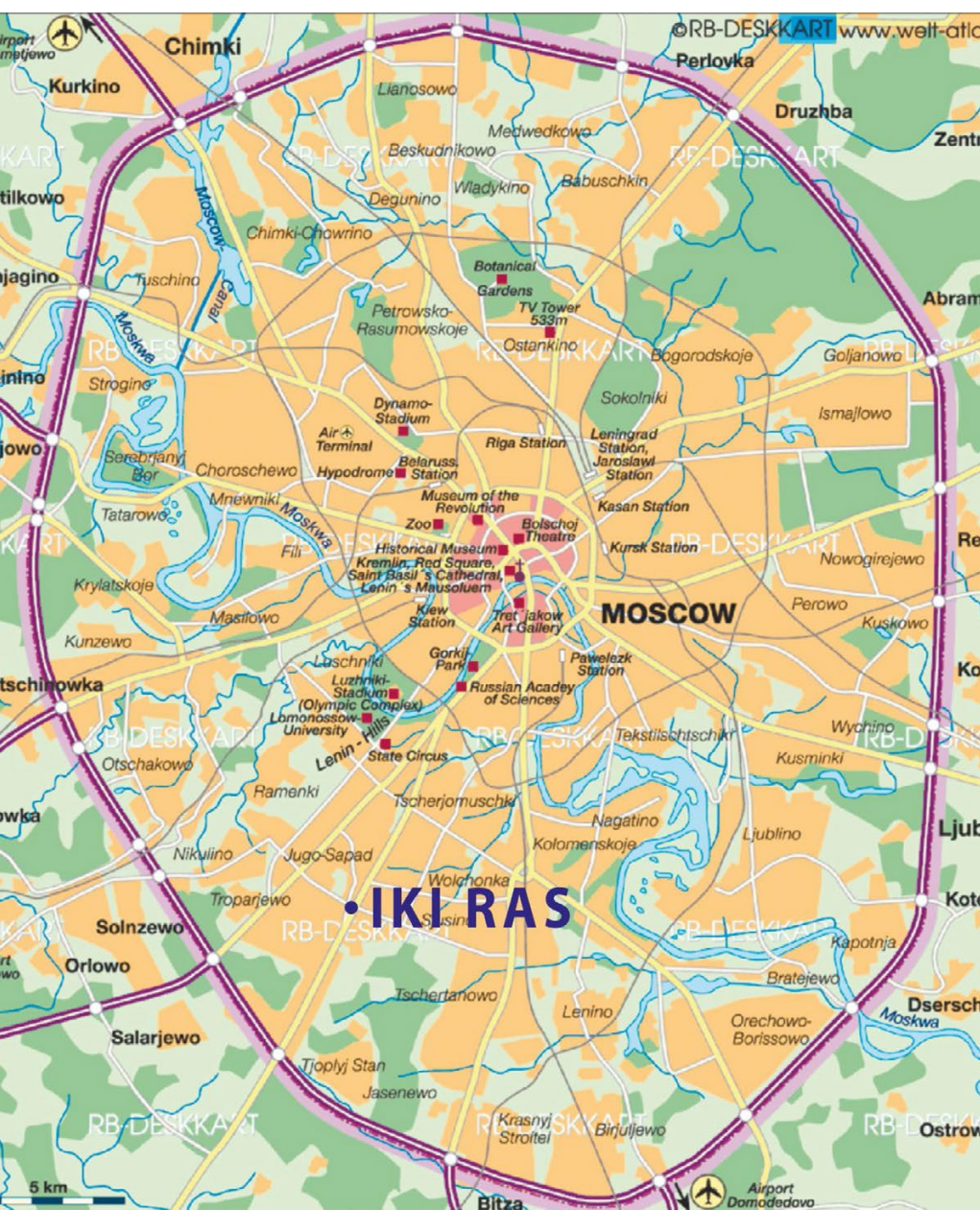
REFERENCES:

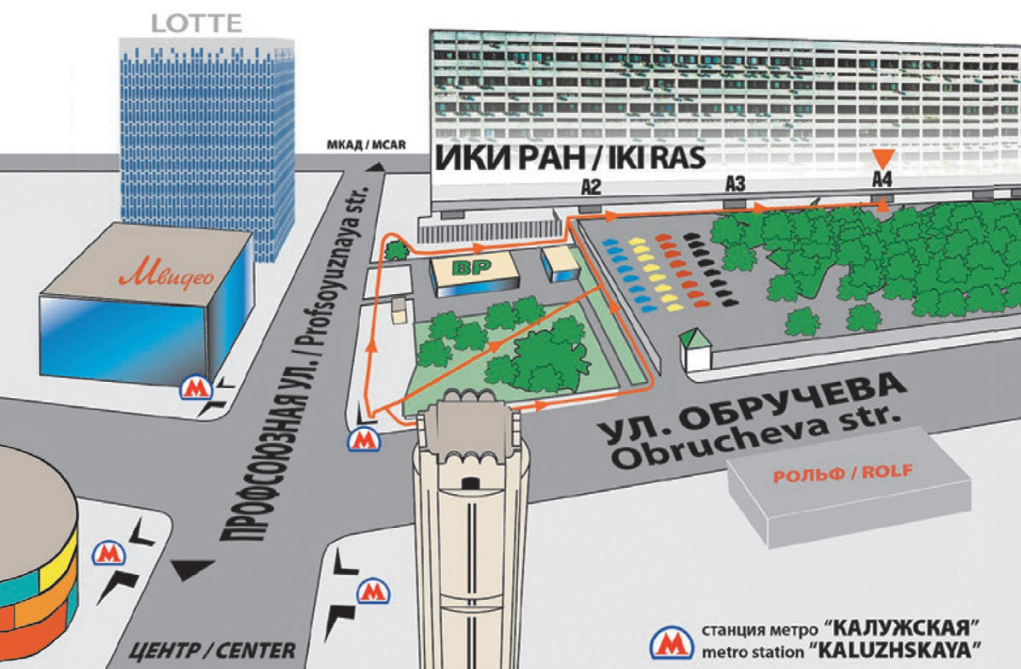
- [1] *Tertyshnikov A. V. Variations in F10.7 by New Dates of Maximum Meteor Streams // Solar System Research. 2025. V.59. Article 56. <https://doi.org/10.1134/S003809462460166X>.*

INFORMATION

address:

Space Research Institute (IKI)
Profsoyuznaya street 84/32
post code 117997
metro station: Kaluzhskaya
Moscow, Russia





ИКИ РАН

площадь академика Келдыша
метро «Калужская», первый вагон из центра, по тоннелю – прямо,
по второму поперечному тоннелю – направо, выход на площадь,
далее по стрелкам на схеме

IKI RAS

You should get off at "Kalyzhskaya" metro station using the southern exit.
After leaving a station lobby through glass doors you should go straight
to the end of the tunnel, then take right and use the stairs to get to the surface.
From this point you may follow either arrow on this map

MOSCOW METRO SCHEME



<ul style="list-style-type: none"> ● Серпуховская ● Звенигородская ● Арбатско-Смольнинская ● Филевская ● Кольцевая ● Кольцевая ● Тимирязевская ● Каширская ● Солнцевская 	<ul style="list-style-type: none"> ● Серпуховская ● Рязанский проспект ● Восточная ● Кольцевая 	<ul style="list-style-type: none"> ● Александровский парк 	<ul style="list-style-type: none"> ● Аэропорт ● Платформа ● Аэропорт
--	--	---	--

ИКИ RAS

Метро-центр

7 495 539-54-54

© 1971 Общественное предприятие

REGISTRATION AND INFORMATION DESK

location: IKI, entrance A-4

time:

20 october, 9:00–18:00

21–24 october, 10:00–18.00

ORAL SESSIONS

location:

- IKI conference hall, second floor
Sessions: Opening, Mars, Moon and Mercury, Venus, Small Bodies, Extrasolar Planets, Giant Planets, Astrobiology
20–24 october

POSTER SESSIONS FOR ALL SESSIONS

- IKI Winter Garden, second floor
20 october, 18.05–18.35

COFFEE BREAKS, WELCOME PARTY, RECEPTION

location:

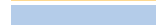
- IKI Winter Garden, second floor – Coffee Breaks
- IKI Winter Garden, second floor – Welcome Party
- IKI Exhibition Hall, ground floor – Reception

INTERNET ACCESS AND WIFI

there is Internet access in and near the conference hall

SOCIAL PROGRAM

	BOLSHOI	OPERETTA	HELIKON	STANISLAVSKY	NOVAYA OPERA	MMDM	KREMLIN PALACE
18.10	12.00, 19.00 opera in four acts, New Stage LE NOZZE DI FIGARO СВАДЬБА ФИГАРО 19.00 ballet, Historic Stage IVAN THE TERRIBLE ИВАН ГРОЗНЫЙ	14.00, 19.00 music performance ANNA KARENINA АННА КАРЕНИНА	19.00 opera, Stravinskiy Hall RAYATSY ПАЯЦЫ	19.00 BALLET EVENING ВЕЧЕР БАЛЕТОВ	19.00 opera TRAVIATA ТРАВИАТА		
19.10	12.00, 18.00 ballet, Historic Stage IVAN THE TERRIBLE ИВАН ГРОЗНЫЙ 12.00, 18.00 opera in four acts, New Stage LE NOZZE DI FIGARO СВАДЬБА ФИГАРО	14.00, 19.00 music performance ANNA KARENINA АННА КАРЕНИНА	16.00 opera, Stravinskiy Hall RAYATSY ПАЯЦЫ	12.00 opera TZAR SALTAN FAIRY-TALE СКАЗКА О ЦАРЕ САЛТАНЕ	18.00 opera TRAVIATA ТРАВИАТА		
21.10	19.00 ballet, New Stage ANYUTA АНЮТА 19.00 opera, Historic Stage LA TRAVIATA ТРАВИАТА	19.00 musical performance GRAF ORLOV ГРАФ ОРЛОВ		19.00 opera MEDEA МЕДЕЯ			
22.10	19.00 ballet, New Stage ANYUTA АНЮТА 19.00 opera, Historic Stage LA TRAVIATA ТРАВИАТА	19.00 musical performance GRAF ORLOV ГРАФ ОРЛОВ		19.00 opera RIGOLETTO РИГОЛЕТТО	19.00 opera LOENGRIN ЛОЭНГРИН	19.00 Svetlanov Hall SPIVAKOV FESTIVAL ФЕСТИВАЛЬ В. СПИВАКОВА	
23.10	19.00 opera, Historic Stage LA TRAVIATA ТРАВИАТА	19.00 musical performance GRAF ORLOV ГРАФ ОРЛОВ	19.00 opera, Stravinskiy Hall BORIS GODUNOV БОРИС ГОДУНОВ	19.00 opera RIGOLETTO РИГОЛЕТТО		19.00 concert, Svetlanov Hall VAGNER AND CHAIKOVSKIY ВАГНЕР И ЧАЙКОВСКИЙ, «ВАЛЬКИРИЯ» И «ЛЕБЕДИНОЕ ОЗЕРО»	
24.10	20.00 concert, Historic Stage CONCERT OF THE LAUREATES OF THE INTERNATIONAL TCHAIKOVSKY COMPETITION КОНЦЕРТ ЛАУРЕАТОВ МЕЖ- ДУНАРОДНОГО КОНКУРСА ИМЕНИ П.И.ЧАЙКОВСКОГО	19.00 musical performance GRAF ORLOV, ГРАФ ОРЛОВ	19.00 opera, Stravinskiy Hall BORIS GODUNOV БОРИС ГОДУНОВ	12.00, 19.00 ballet SWAN LAKE ЛЕБЕДИНОЕ ОЗЕРО	19.00 opera LOENGRIN ЛОЭНГРИН	19.00 concert, Svetlanov hall SERGEY ZHILIN AND THE ORCHESTRA СЕРГЕЙ ЖИЛИН И ОРКЕСТР ФОНОГРАФ-СИМФО-ДЖАЗ 19.00 ballet, Theater hall DON QUIXOTE BALLET БАЛЕТ «ДОН КИХОТ»	19.00 concert ANNIVERSARY CONCERT OF THE SOPRANO OF TURETSKY ART GROUP – "THE WORLD OF WOMEN" ЮБИЛЕЙНЫЙ КОНЦЕРТ АРТ-ГРУППЫ «СОПРАНО ТУРЕЦКОГО» – «МИР ЖЕНЩИН»
25.10	12.00, 19.00 ballet, historic stage RAYMONDA РАЙМОНДА 12.00, 19.00 opera in three acts, New Stage TOSCA, GIACOMO PUCCINI ТОСКА	14.00, 19.00 musical performance GRAF ORLOV ГРАФ ОРЛОВ	19.00 opera, Stravinskiy Hall BORIS GODUNOV БОРИС ГОДУНОВ	12.00, 19.00 ballet SWAN LAKE ЛЕБЕДИНОЕ ОЗЕРО	19.00 OPERA GALA ДЕНЬ ОПЕРЫ	14.00 concert, Svetlanov Hall «WE WILL ROCK YOU» ВЕЛИКИЕ ХИТЫ QUEEN	18.00 concert THE STATE ACADEMIC KUBAN COSSACK CHOIR "RUSSIA FROM EDGE TO EDGE" «РУСЬ ОТ КРАЯ ДО КРАЯ» ГОСУДАРСТВЕННЫЙ АКАДЕМИЧЕСКИЙ КУБАНСКИЙ КАЗАЧИЙ ХОР
26.10	12.00, 18.00 ballet, Historic Stage RAYMONDA РАЙМОНДА 12.00, 18.00 opera in three acts, New Stage TOSCA, GIACOMO PUCCINI ТОСКА	14.00, 19.00 musical performance GRAF ORLOV ГРАФ ОРЛОВ	16.00 opera, Stravinskiy Hall BORIS GODUNOV БОРИС ГОДУНОВ	12.00 ballet SWAN LAKE ЛЕБЕДИНОЕ ОЗЕРО	19.00 dance divertissement VOLERO БОЛЕРО	13.00, 17.00 musical, Theater hall BREMEN TOWN MUSICIANS «БРЕМЕНСКИЕ МУЗЫКАНТЫ»	

	https://bolshoi.ru
	https://mosoperetta.ru
	https://www.helikon.ru
	https://www.stanmus.ru
	https://novayaopera.ru
	https://www.mmdm.ru
	https://kremlinpalace.org

БОЛЬШОЙ ТЕАТР, BOLSHOI THEATRE
 ТЕАТР ОПЕРЕТТЫ, OPERETTA THEATRE
 ГЕЛИКОН-ОПЕРА, HELIKON THEATRE
 МУЗЫКАЛЬНЫЙ ТЕАТР ИМ. К.С. СТАНИСЛАВСКОГО И ВЛ. НЕМИРОВИЧА-ДАНЧЕНКО, STANISLAVSKY AND NEMIROVICH-DANCHENKO MUSICAL THEATER
 НОВАЯ ОПЕРА, NOVAYA OPERA
 МОСКОВСКИЙ МЕЖДУНАРОДНЫЙ ДОМ МУЗЫКИ, MOSCOW INTERNATIONAL HOUSE OF MUSIC
 ГОСУДАРСТВЕННЫЙ КРЕМЛЁВСКИЙ ДВОРЕЦ, KREMLIN PALACE

LUNCH POINTS NEAREST TO IKI



1. **ИНСТИТУТ КОСМИЧЕСКИХ ИССЛЕДОВАНИЙ РАН**,
ул. Профсоюзная, 84/32,
столовая, 1 этаж, секция А3
SPACE RESEARCH INSTITUTE,
Profsoyuznaya street, 84/32,
Food center, Ground Floor, Section A3
2. **ТЦ «КАЛУЖСКИЙ»**,
ул. Профсоюзная, 61А,
зона ресторанов, 2 этаж
"KALUZHSKIY" Market Center,
Profsoyuznaya Street, 61A,
2 Floor
3. **КАФЕ «АНДЕРСОН»**,
ул. Обручева, 30/1
CAFÉ "ANDERSON",
Obrucheva street, 30/1
4. **ИНСТИТУТ ПРИКЛАДНОЙ МАТЕМАТИКИ РАН**,
ул. Профсоюзная 84/32,
столовая, 1 этаж
INSTITUTE OF APPLIED MATHEMATICS,
Profsoyuznaya street 84/32,
Food center, Ground Floor

